Fortieth Anniversary
Pioneering the Future

32nd Aerospace Mechanisms Symposium

Compiled by
S.W. Walker and E.A. Boesiger
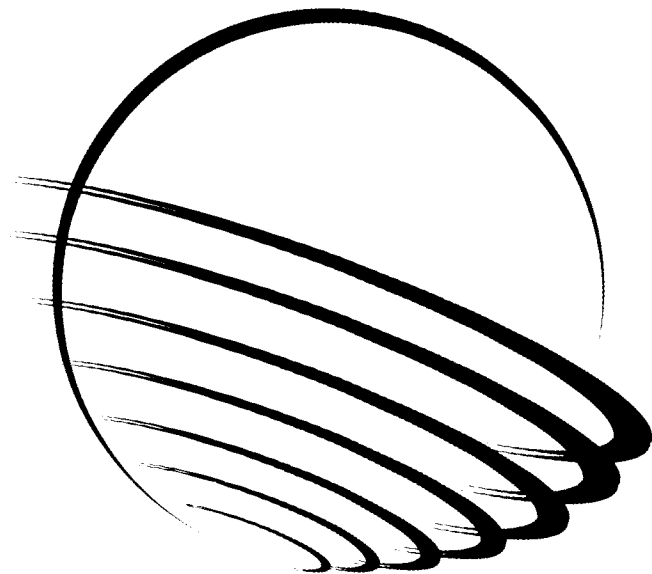
May 1998

NASA/CP-1998-207191

1Əⅰ.

336 Ɏəɏ

Fortieth Anniversary
Pioneering the Future

32nd Aerospace Mechanisms Symposium

Compiled by
S.W. Walker
John F. Kennedy Space Center • KSC, Florida

and

E.A. Boesiger
Lockheed Martin Missiles and Space • Sunnyvale, California

National Aeronautics and Space Administration
John F. Kennedy Space Center • KSC, Florida 32899

May 1998

PREFACE

The Aerospace Mechanisms Symposium (AMS) provides a unique forum for those active in the design, production and use of aerospace mechanisms. A major focus of the AMS is the reporting of problems and solutions associated with the development and flight certification of new mechanisms. The National Aeronautics and Space Administration and Lockheed Martin Missiles and Space (LMMS) share the responsibility for organizing the AMS. Now in its 32nd year, the AMS continues to be well attended, attracting participants from both the U.S. and abroad.

The 32nd AMS, hosted by the NASA John F. Kennedy Space Center (KSC) in Cocoa Beach, Florida, was held May 13, 14, and 15, 1998. During these three days, 28 papers were presented. Topics included robotics, deployment mechanisms, bearings, actuators, scanners, boom and antenna release, and test equipment. Hardware displays during the vendor fair gave attendees an opportunity to meet with developers of current and future mechanism components.

The high quality of this symposium is a result of the work of many people, and their efforts are gratefully acknowledged. This extends to the voluntary members of the symposium organizing committee representing the eight NASA field centers, LMMS, and the European Space Agency. Appreciation is also extended to the session chairs, the authors, and particularly the personnel at NASA KSC responsible for the symposium arrangements and the publication of these proceedings. A sincere thank you also goes to the symposium executive committee at LMMS, who is responsible for the year-to-year management of the AMS, including the paper processing and preparation of the program.

The use of trade names of manufacturers in this publication does not constitute an official endorsement of such products or manufacturers, either expressed or implied, by the National Aeronautics and Space Administration.

Dedication

> The symposium was dedicated to the memory of the late Dr. Charles W. Coale. Dr. Coale provided leadership to the symposium for more than 20 years. His exceptional guidance helped make this symposium the world's best forum for space mechanisms. With his untimely passing, he will be sorely missed.

CONTENTS

SYMPOSIUM SCHEDULE

TUESDAY, 12 MAY 1998

6:30-8:30   EARLY REGISTRATION AND/OR CHECK-IN
            Lobby area

WEDNESDAY, 13 MAY 1998

8:00   Wednesday Authors' Breakfast - Dunes 1 Room

8:30   REGISTRATION AND REFRESHMENTS
            Lobby area

9:00   INTRODUCTORY REMARKS
            Sterling W. Walker, Host Chairman
            NASA Kennedy Space Center, KSC, FL
            Stuart H. Loewenthal, General Chairman
            Lockheed Martin Missiles & Space, Sunnyvale, CA

            CENTER WELCOME
            Roy D. Bridges, Jr., Center Director
            NASA Kennedy Space Center, FL

9:30   **SESSION I - INSTRUMENT MECHANISMS**
            Bill Bialke, Session Chair
            ITHACO Space Systems Inc., Ithaca, NY
            • *A Simple Method for Repeatable Rotational Positioning of Optical
              Components within a Spaceflight Ultraviolet Spectrometer*
              Tom Smiley, AZ Technology, Inc., Huntsville, AL
            • *AXAF Science Instrument Module Mechanisms*
              Robert Renken, Ball Aerospace and Technologies Corp., Boulder, CO
            • *Development and Qualification of the Scan Mechanisms for MHS*
              Winfried Aicher, Dornier Satellitensysteme GmbH,
              Friedrichshafen, Germany
            • *Cryogenic Scan Mirror Mechanism for SIRTF/MIPS*
              Robert Warden & Gerald Heim,
              Ball Aerospace and Technologies Corp., Boulder, CO
            • *Development of a Mirror Pointing Mechanism for an Atmospheric Gas
              Measurement Instrument*
              Michael Graham & Adel Belous, Sverdrup Technology, Moffett Field,
              CA; Jeff Brown & James Podolske, NASA Ames Research Center,
              Moffett Field, CA

12:00   LUNCH

1:15	**SESSION II - DEPLOYABLES** Eric Favre, Session Chair ETEL SA, Motiers, Switzerland • *The FAST Boom Mechanisms* David Pankow, Bobby Besuner & Robert Ullrich, University of California, Berkeley; Bob Wilkes, Lockheed Martin Space Mission Systems & Services, Houston, TX • *Thermal-Vacuum Deployment and Retraction Testing of the* *Photovoltaic Radiator* Ron Hofstad, Lockheed Martin Vought Systems, Dallas, TX • *Non-Explosive Pinpuller and Rotary Actuators* Michael Bokaie & Kevin Barajas, TiNi Aerospace, Inc., San Leandro, CA • *Improvements for Rotary Viscous Dampers used in Spacecraft* *Deployment Mechanisms* Alphonso Stewart & Charles Powers, NASA Goddard Space Flight Center, Greenbelt, MD; Ron Lyons, DEB Manufacturing, Inc., Lakewood, NJ • *Stress Relaxation of Spring Materials* W. David Hanna, Dick Chang & Gary Steckel, The Aerospace Corporation, El Segundo, CA
3:45-4:00	UPDATE ON NASA SPACE MECHANISMS HANDBOOK Robert Fusaro, NASA Lewis Research Center, Cleveland, OH
4:00-5:30	VENDOR DISPLAYS Invited component and software vendors display current products and provide tutorials.
6:00-10:00	RECEPTION AT APOLLO SATURN V FACILITY 6:00 Buses leave Cocoa Beach Hilton 6:30 Tour Saturn V Facility and enjoy reception 9:00 Buses leave facility

THURSDAY, 14 MAY 1998

7:00   Thursday Authors' Breakfast - Dunes 1 Room

8:00   **SESSION III - SAMPLING SYSTEMS**
Les Krumel, Session Chair
Sandia National Laboratories, Albuquerque, NM
- *Compact Drilling and Sample System*
  Greg Gillis-Smith, Jet Propulsion Laboratory, Pasadena, CA;
  Doug Petercsak, American Technology Consortium, Camarillo, CA
- *Active Sample Acquisition System for Micro-Penetrators*
  Chris Voorhees & Benjamin Potsaid, Jet Propulsion Laboratory,
  Pasadena, CA
- *Thermal and Evolved Gas Analyzer*
  M. Williams, W. Boynton, R. James, W. Verts, S. Bailey & D. Hamara,
  University of Arizona, Tucson, AZ
- *"Long Life" DC Brush Motor for Use on the Mars Surveyor Program*
  David Braun & Don Noon, Jet Propulsion Laboratory, Pasadena, CA

10:00   BREAK

10:15   **SESSION IV - BEARINGS & TRIBOLOGY**
William Jones, Jr., Session Chair
NASA Lewis Research Center, Cleveland, OH
- *Liquid Hydrogen Testing of Silicon Nitride Bearings for Use in High-
  Speed Turbomachinery*
  Chip Moore, Howard Gibson, & Robert Thom,
  NASA Marshall Space Flight Center, Huntsville, AL
- *Experiences with Differentiating Ball Bearing Retainer Instabilities*
  Bill Bialke, ITHACO Space Systems Inc., Ithaca, NY;
- *Rex 20/Si3N4 Control Moment Gyroscope Bearing Development*
  Dennis Smith, Honeywell Inc., Glendale, AZ;
  Alan Leveille & Michael Hilton, The Aerospace Corporation,
  El Segundo, CA; Peter Ward, MPB Corporation, Keene, NH
- *Rolling Contact Fatigue and Load Capacity Tests of M62 Bearing Steel*
  Woonsup Park, Michael Hilton, G. Henderson & Alan Leveille,
  The Aerospace Corporation, El Segundo, CA;
  Peter Ward, MPB Corporation, Keene, NH;
  Don McClintock, Timken Co., Canton, OH;
  Dennis Smith, Honeywell Inc., Glendale, AZ

12:15   LUNCH

1:15   **SESSION V - MECHANISMS**
Stewart Meyers, Session Chair
NASA Goddard Space Flight Center, Greenbelt, MD
  • *Development of a Large Rotary Positioning Mechanism*
    Edwin Joscelyn, Richard Casper, Heinz Rott & Alexander Solla,
    Aeroflex Laboratories, Inc., Farmingdale, NY
  • *High-Precision Pointing Gimbal Development*
    D. Hobson Lane & Mark Carroll, TRW Space & Technology Division,
    Redondo Beach, CA
  • *The Challenges of Designing a Retracting Tether for Space
    Applications*
    Jon Salton & Frank James,
    Lockheed Martin Space Mission Systems & Services, Houston, TX
  • *Research on Liquid Lubricants for Space Mechanisms*
    William Jones, Jr., NASA Lewis Research Center, Cleveland, OH;
    Bradley Shogrin, Case Western Reserve University, Cleveland, OH;
    Mark Jansen, AYT Corporation, Brookpark, OH
  • *Considerations on Mechanical Reliability*
    Fabio Panin, European Space Technology Center,
    Noordwijk, The Netherlands

3:45   BREAK

4:00-5:00   SPECIAL PRESENTATION
Colonel Don McMonagle, USAF, Launch Integration Manager
Space Shuttle Program, NASA Kennedy Space Center
With more than 600 hours in space, Col. McMonagle will present an
astronaut's perspective on Extravehicular Activities (EVA) and the use of
mechanisms.

6:00-10:00   Caribbean Theme Dinner
                 6:00-7:00   Social Hour
                 7:00-8:30   Dinner
                 8:30-10:00   Entertainment

FRIDAY, 15 MAY 1998

7:00   Friday Authors' Breakfast - Dunes 1 Room

8:00   **SESSION VI - MORE MECHANISMS**
Alan Littlefield, Session Chair
Kennedy Space Center, FL
* *Ullage Rocket Jettisoning Mechanism for a Typical Launch Vehicle*
  N. Giri, G. Narayanan, S. Nalluveettil, G. Koshy & M. Abdul Majeed,
  Vikram Sarabhai Space Center, Thiruvananthapuram, India
* *International Space Station Blanket Restraint System: Successful
  Mechanism Qualification and Process Development through Analysis
  and Simple Characterization Tests*
  Dan Schmidt, Lockheed Martin Missiles & Space, Sunnyvale, CA
* *Space Station Remote Manipulator System Qualification Model Joint
  Test Program*
  J. Marc Devlin, SPAR Aerospace Limited, Brampton, Ontario, Canada
* *Human Habitat Positioning System for NASA's Space Flight
  Environmental Simulator*
  William Caldwell & John Tucker, NASA Ames Research Center, Moffett
  Field, CA; Paul Keas, Sverdrup Technology, Inc., Moffett Field, CA
* *Testing of the Automated Fluid Interface System*
  Nick Johnston & Tony Tyler, NASA Marshall Space Flight Center,
  Huntsville, AL

10:30   BREAK

10:45   NASA KENNEDY SPACE CENTER OVERVIEW
Loren J. Shriver, Deputy Center Director for Launch and Payload
Processing
NASA Kennedy Space Center, FL

11:15   PRESENTATION OF THE HERZL AWARD
Otto Fedor, Lockheed Martin (ret)

CLOSING REMARKS
Edward A. Boesiger, Operations Chairman
Lockheed Martin Missiles & Space, Sunnyvale, CA

11:30   LUNCH AND CHECK-OUT

12:30   BUSES DEPART HOTEL FOR KSC TOUR

1:00-5:00   NASA KENNEDY SPACE CENTER FACILITY TOUR

SYMPOSIUM ORGANIZING COMMITTEE

Sterling W. Walker, Host Chairman, NASA KSC
Alan C. Littlefield, Co-Host Chairman, NASA KSC

Stuart H. Loewenthal	General Chairman	Lockheed Martin
Edward A. Boesiger	Operations Chairman	Lockheed Martin

Obie H. Bradley, Jr.	NASA LaRC
Michael J. Eiden	ESA/ESTeC
Carlton L. Foster	NASA MSFC
Robert L. Fusaro	NASA LeRC
Claef F. Hakun	NASA GSFC
Edward C. Litty	JPL
Ronald E. Mancini	NASA ARC
Fred G. Martwick	NASA ARC
Stewart C. Meyers	NASA GSFC
John F. Rogers	NASA LaRC
Douglas A. Rohn	NASA LeRC
William C. Schneider	NASA JSC
Donald R. Sevilla	JPL
Edward A. Wegner	Lockheed Martin (ret)

SYMPOSIUM ADVISORY COMMITTEE

Aleck C. Bond	NASA JSC (ret)
H. Mervyn Briscoe	ESA/ESTeC (ret)
David F. Engelbert	NASA ARC (ret)
Otto H. Fedor	Lockheed Martin (ret)
Angelo Giovannetti	NASA ARC (ret)
John E. Harbison	NASA MSFC (ret)
Frank T. Martin	NASA GSFC (ret)
John W. Redmon, Sr.	NASA MSFC (ret)
Alfred L. Rinaldo	Lockheed Martin (ret)
Bowden W. Ward, Jr.	NASA GSFC (ret)
Nathan D. Watson	NASA LaRC (ret)

S) - 19
/6 8 0 8 4

A Simple Method For Repeatable Rotational Positioning of Optical Components Within a Spaceflight UltraViolet Spectrometer

/ 4 P.

Tom Smiley*

33 6 8 4/5 —

Abstract

The performance of materials used in the space environment continues to be a limiting technology for space missions. The Optical Properties Monitor (OPM) is an experiment that studies the effects of the space environment on materials and coatings. The Vacuum UltraViolet (VUV) Spectrometer is one of several optical instruments and environmental monitors developed for the OPM. The VUV Spectrometer examines the effects of the space environment in the vacuum ultraviolet spectrum on various materials and coating samples by in-situ periodic measurement. This paper addresses the use of Geneva drive systems and Hall Effect Sensors to produce periodic, repeatable rotational positioning of several optical components within the VUV instrument.

Introduction

The OPM was carried to the Russian Space Station Mir on the NASA Space Shuttle during STS-81 in January, 1997, and is currently mounted on the exterior surface of the Mir Docking Module for a nine month operational deployment (Figure 1).
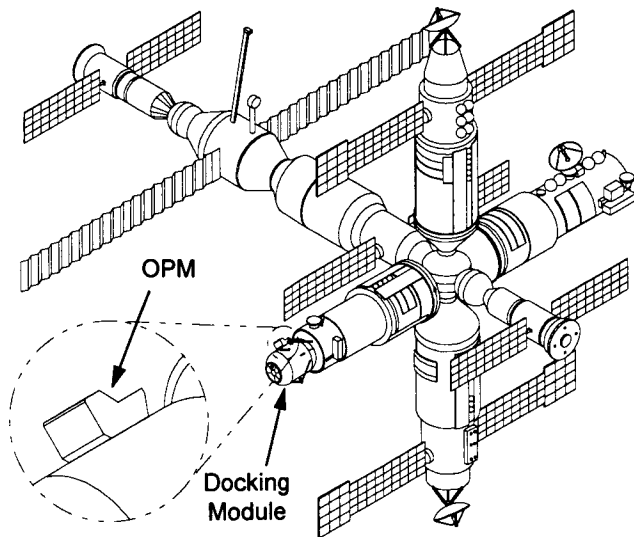
Figure 1. OPM Deployed on Mir Station

* AZ Technology, Inc., Huntsville, AL

Within the OPM, a 64.8 cm (25.5 in) diameter rotating carousel wheel is loaded with 98 material and coating samples positioned in a polar array. Of the 98 samples, 32 are measured by the VUV. The samples are normally exposed to the space environment. Once a week, the OPM carousel rotates the samples that have been exposed to space under the VUV and other instruments for measurement. After the optical measurements are complete, the OPM carousel returns the samples to the exposed position for another week of exposure (Figure 2).
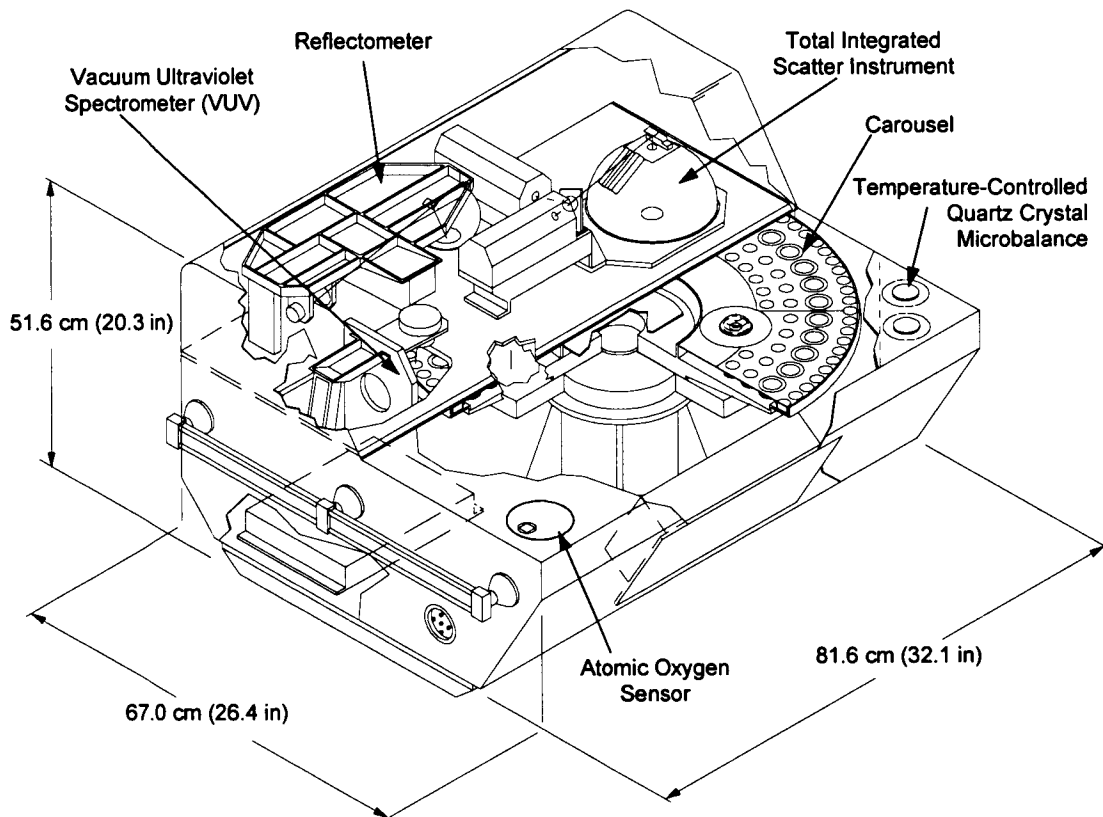
Figure 2. Cut-Away View of OPM Interior

VUV Instrument Description
The VUV spectrometer measures specular reflectance and transmittance of test samples at seven discrete wavelengths in the VUV spectrum. The Optical path of the VUV spectrometer is shown in Figure 3. The source lamp is a standard off-the-shelf deuterium lamp. The internal baffles of the lamp form the source light into a 10° output cone. This output is collected by an off-axis ellipsoidal mirror which focuses the beam through a rotating filter wheel. The filter wheel assembly (Figure 4) contains eight equally spaced positions: seven bandpass filters and one open hole aperture.

2
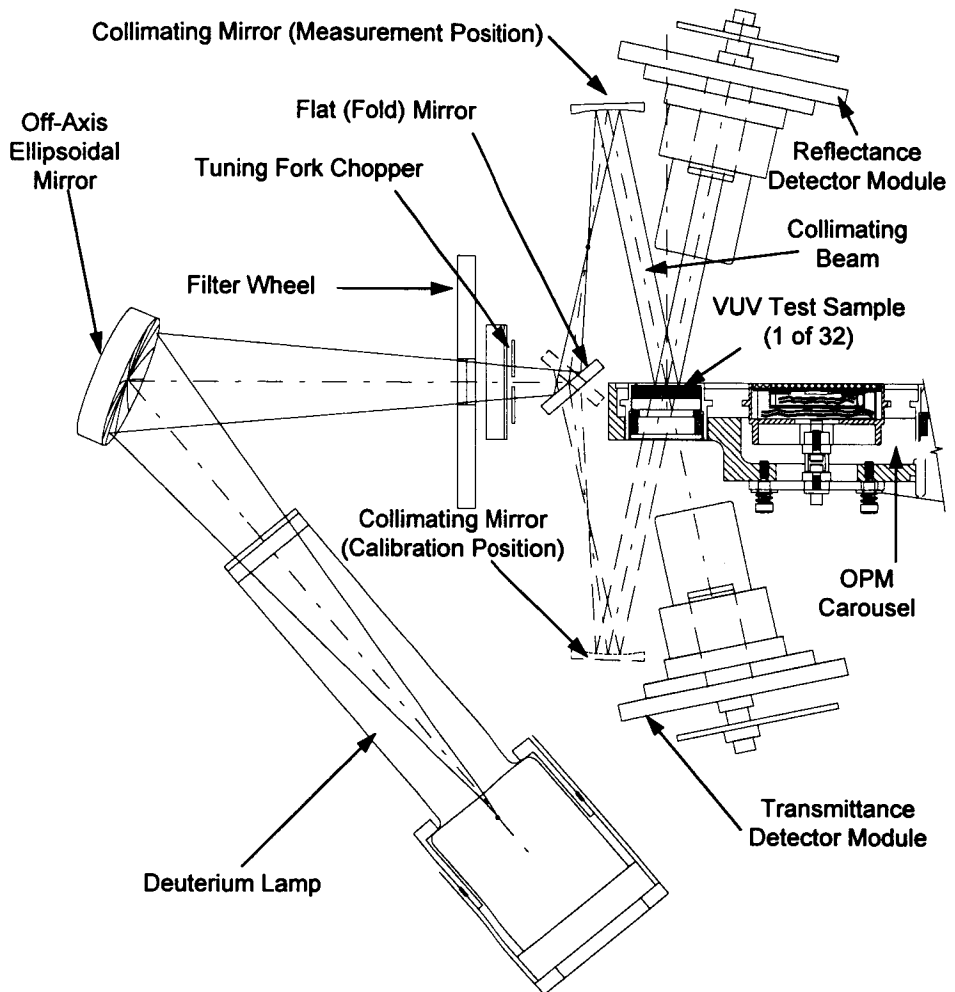
Figure 3. VUV Optical Path
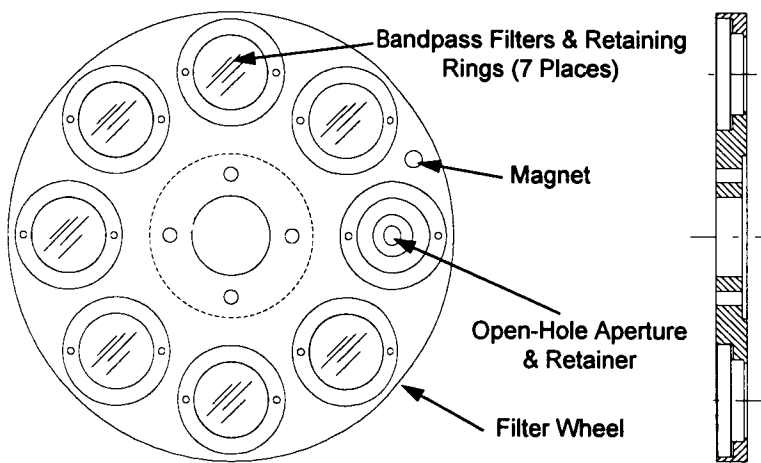
Figure 4. Filter Wheel Assembly

Each bandpass filter alters the source energy to create seven discrete center wavelengths ranging from 121.6 nm to 250 nm. The open hole aperture provides a broadband of VUV energy.

After passing through the filter wheel assembly, the beam is modulated at 150 Hz by a tuning fork chopper and then folded with a flat mirror. The beam is then collected by a collimating spherical mirror which directs the deuterium source energy to the sample being measured. The fold and collimating mirrors are mounted to a swing arm assembly (Figure 5) which is designed to rotate 180° about the central axis of the flat mirror.

SECTION A-A
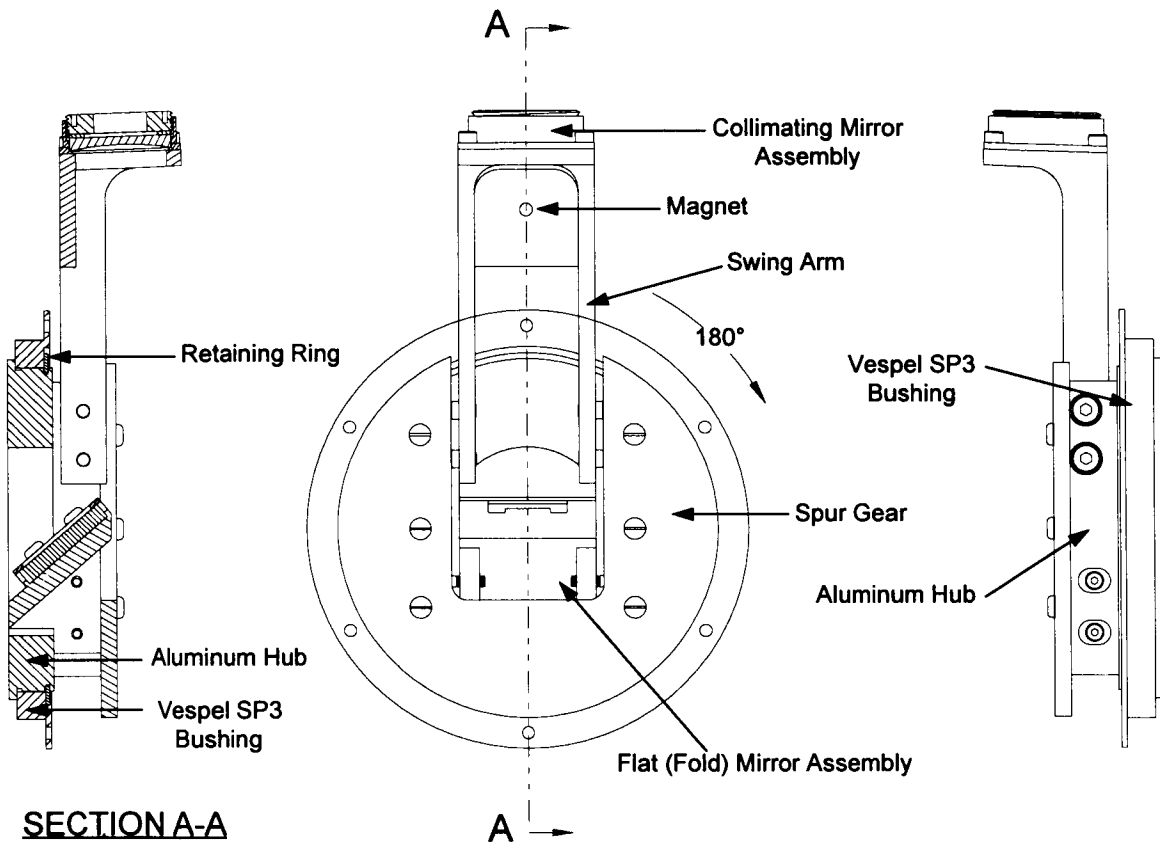
Figure 5. Swing Arm Assembly

Two detector modules collect the reflected and transmitted UV energy from the samples and convert the UV energy to a more easily detectable visible energy. To ensure the accuracy of the VUV measurements, the transmission and reflectance detector modules are periodically calibrated. At every fifth VUV sample position on the OPM carousel, the sample is omitted to provide an open hole. During calibration of the transmission detector, the swing arm assembly remains in the measurement position (Figure 3). All of the energy from the spherical collimating mirror is directed

4

through the open hole into the transmission detector thereby providing a 100% reference point. Calibration of the reflectance detector requires redirection of the optical beam path; this allows all of the source energy to pass through the open hole in the carousel to the reflectance detector (Figure 3). To redirect the beam path, the swing arm assembly rotates 180° about the central axis of the flat mirror. During calibration of both detectors, the filter wheel rotates through all eight positions.

Between the calibration cycles, the VUV makes a measurement of the specular reflectance and transmittance of each sample. Energy from the source is positioned on the surface of the sample and the reflected and transmitted energy is collected by the detectors. During measurement, the source beam is altered by the filter wheel which rotates through all eight positions. The energy collected by each detector is recorded and compared to the energy collected by the detectors during calibration to determine the VUV specular reflectance and transmittance of the sample.

Design Considerations

The positioning of the optical components within the VUV mandated a high degree of precision and repeatability. Also, as any device designed for spaceflight, mass and volume had to be minimized while maintaining structural integrity to limit the effects of vibrational loads at launch (Figures 6 & 7). Stepper motors were chosen to drive both the filter wheel and swing arm assemblies because of their high torque per package size and ease of control. Aside from the two stepper motors in the VUV filter wheel and swing arm assemblies, the OPM has three additional stepper motors used in other applications. Space-qualified stepper motors are expensive and costs are directly related to custom design requirements and quantity purchased. This cost consideration led an effort to apply the same stepper motor design for all applications in the OPM, where possible.

The remaining design considerations for the VUV filter wheel assembly and swing arm assembly gear train were derived from two requirements. 1) Both systems had to be mechanically "locked", not only during shipping and launch (no power), but intermittently during the measurement sequence (power on). 2) The rotation of the filter wheel and swing arm had to be precise, but more importantly, repeatable.

There are several methods to drive a stepper or servo motor to a specified position depending upon the application. Generally, the motor is coupled directly to the driven part or through a chain or gear drive. The rotation of the motor is controlled by one of the following three ways.
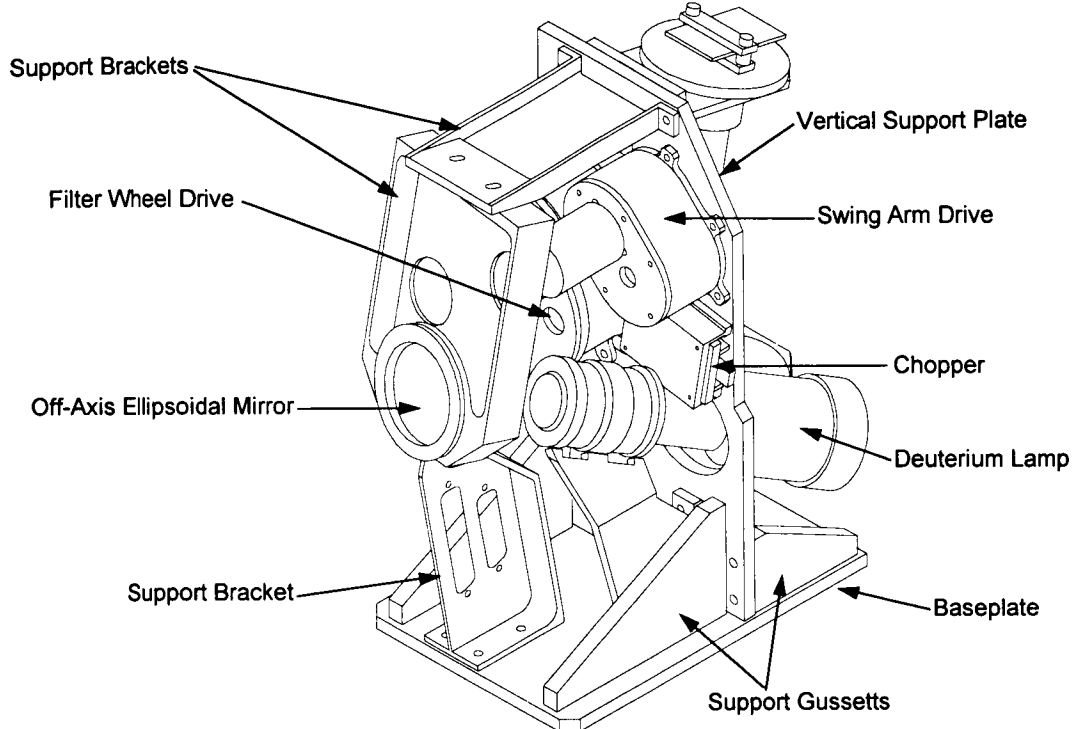
Figure 6. VUV Instrument (Drive Side)
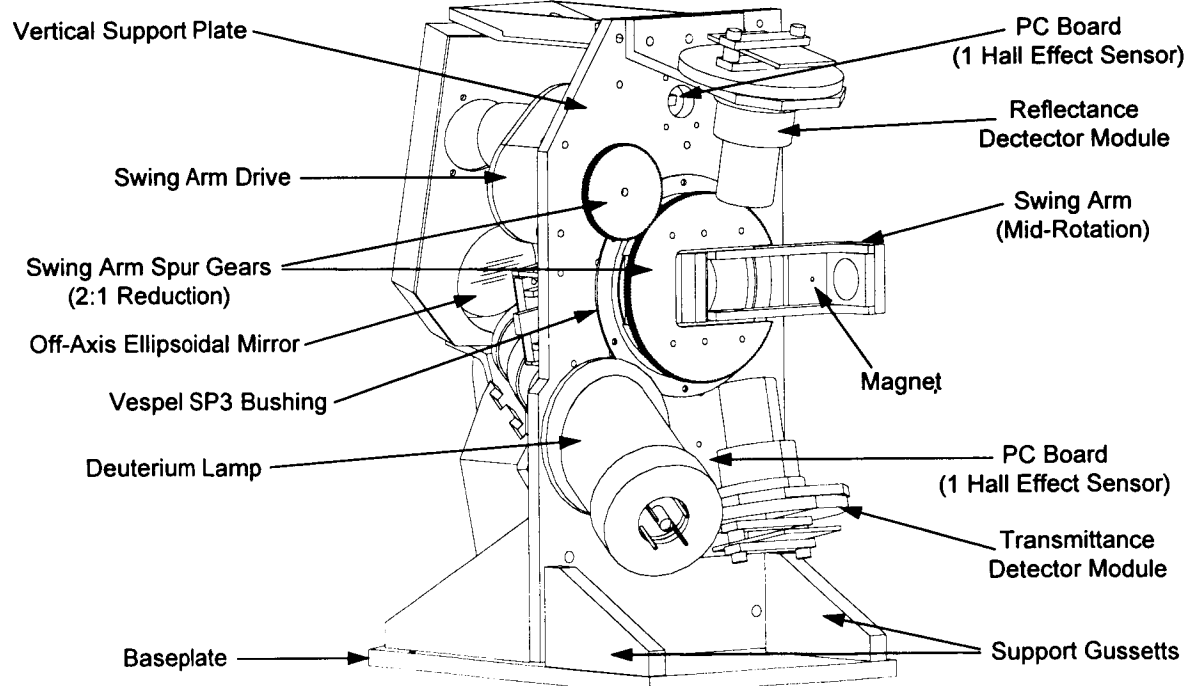
Figure 7. VUV Instrument (Detector Side)

6

1) *A signal is sent to a stepper motor to turn a specified number of steps and stop.*
Although this method is cost effective and mechanically simple, rotational resolution
is limited to the stepper motor or a multiple of the gear train. Another disadvantage
of this system is that it relies on the holding torque of the stepper motor when the
motor is at rest.

2) *A signal is sent to a stepper motor to turn a specified number of steps based on
feedback generated from a potentiometer, optical encoder or other similar device.*
Although this method is similar to the above, it offers greater flexibility since the
system can be calibrated based on data from the feedback device.

3) *A signal is sent to a servo motor to turn a specified number of degrees based on
feedback generated by a servo loop.* Although this method offers uncompromised
accuracy in the positioning of the motor, servo loops are relatively expensive and
mechanically complex compared to the previous two methods.

The filter wheel and swing arm assemblies in the VUV did not require the kind of
positioning needed to justify a servo feedback loop as described in method three.
Method one did not offer the kind of flexibility to make the systems function as
required. For all methods, power must be applied to the motor to prevent movement
and holding power is limited to the motor torque. For these reasons, a derivative of
the second method was chosen that incorporated a Geneva drive system combined
with Hall Effect sensors. Geneva drive systems can be purchased as off-the-shelf
components; however, because of the filter wheel and swing arm assembly
requirements, both VUV Geneva drive systems had to be custom designed
(Figure 8).
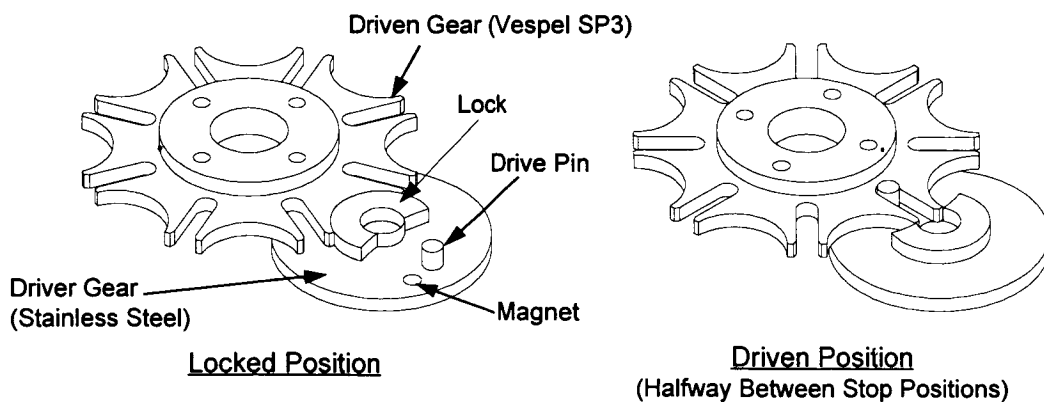
Figure 8. Geneva Drive System (8 Position)

A Geneva drive system consists of a driver gear and a driven gear that can rigidly lock together to prevent any movement of the drive train output even when the drive motor power is off. This feature offers a significant advantage to the VUV design since the filter wheel and swing arm must remain motionless during the measurement and calibration sequences (power-on) and during shipping and launch (power-off).

The Geneva drive has two other inherent advantages. First, a discrete number of precise positions can be designed into the driven gear to match the design requirements. This number may be as small as three or as large as required depending on machining practicality. The drive system's rotational precision is therefore a function of machining precision and not the resolution of the stepper motor. The second advantage is the relatively long dwell time between each index of the Geneva driven gear that converts the constant rotary motion of the stepper motor to an intermittent rotary motion. During this dwell time, the Geneva driven gear remains locked and any overstepping of the motor cannot influence the gear train output. In a conventional gear system, the overstepping tolerance would generally be only two or three steps.

Hall Effect sensors are used to generate the feedback signals controlling the stepper motor drive circuits. Aside from their low cost and durability, Hall Effect sensors have a relatively large activation area which decreases the mechanical precision required by other sensing devices. The VUV filter wheel and swing arm assemblies each contain several sets of Hall Effect sensors mounted on printed circuit boards; each set is activated by a magnet. Each assembly has a magnet and Hall Effect sensor set that monitors the rotation of the Geneva driver gear. The other sets monitor the output rotation of the filter wheel and swing arm as described below.

Filter Wheel Drive Design
The following section describes the mechanical layout of the filter wheel drive train. Unless otherwise noted, refer to Figure 9. A stepper motor is coupled to a 4.5:1 reduction gearhead. A stainless steel Geneva driver gear is mounted to the output shaft and a magnet is positioned near the outer diameter of the gear (Figures 8 & 9). This magnet is aligned with one Hall Effect sensor mounted to a small printed circuit board adjacent to the driver gear. The 7.0 cm (2.75 in) diameter filter wheel assembly consists of eight 1.3 cm (.5 in) diameter optical filters held in place by retaining rings and is coupled directly to the eight position Geneva driven gear machined from Vespel SP3 (Figures 4 & 9). The filter wheel is equipped with a magnet near its outside diameter which is aligned to eight Hall Effect Sensors positioned in a polar array on an adjacent printed circuit board (Figures 4 & 9). The filter wheel, Geneva drive system, and printed circuit boards are shielded from contamination and accidental damage by a protective housing.

8
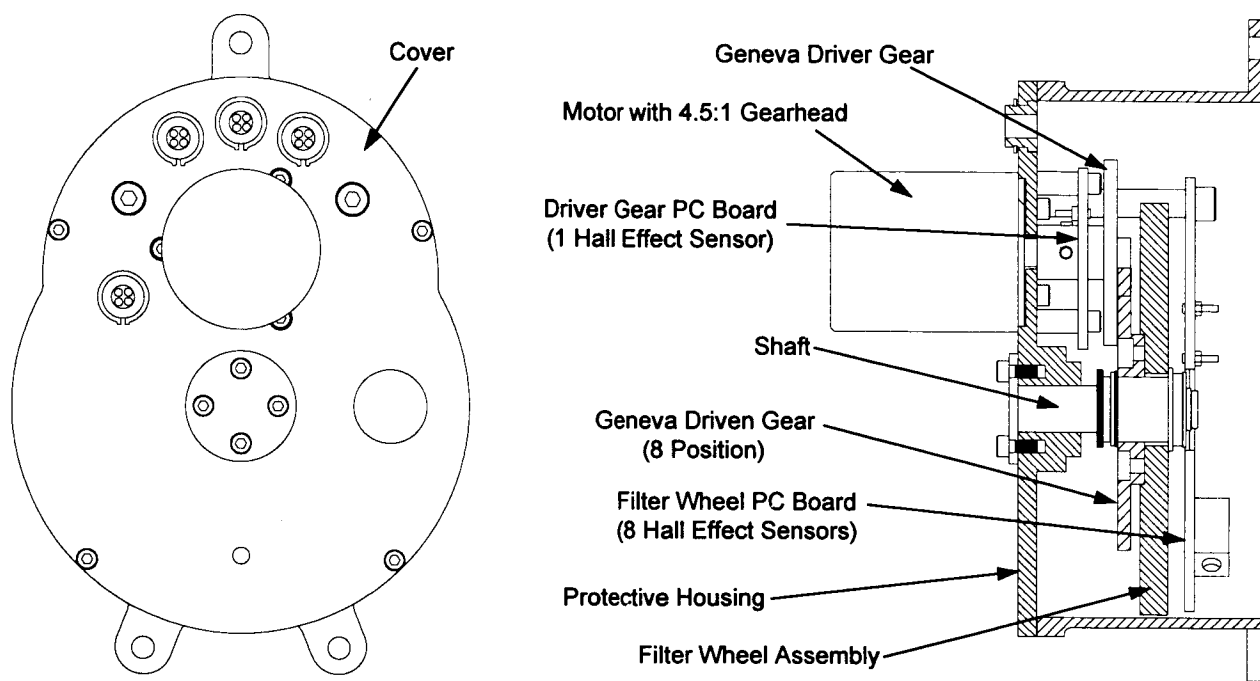
Figure 9. Filter Wheel Drive

Both the Geneva driver gear and the filter wheel Hall Effect sensor sets work in concert to provide the signal logic for the stepper motor. Each time the driver gear magnet sweeps past the Hall Effect sensor, a signal verifying that the driver gear is in the locked position is sent to the instrument processor. Likewise, each time the magnet located on the filter wheel sweeps over one of the eight Hall Effect sensors, a signal is sent to the instrument processor which indicates that the filter wheel has indexed to the next measurement location. In this way, a logical AND statement is generated which forces the correct positioning of the filter wheel in a locked condition ready to take a measurement.

*If the filter wheel has rotated to the correct measurement position **AND** the driver gear has rotated to a locked position, stop rotation of the stepper motor.*

The sensor sets also provide a level of redundancy. If either of the printed circuit boards for the driver gear or filter wheel were to fail, the Geneva drive would still be able to function based on the signal output of one of the printed circuit boards. Although the software would not be able to determine which filter was in place at the time of the measurement, this information could be determined on the ground by analysis of the measurement data.

Swing Arm Design

The mechanical layout of the swing arm drive train is essentially the same as the filter wheel drive train. Unless otherwise noted, refer to Figure 10. A stepper motor is coupled to a 25:1 reduction gearhead. A stainless steel Geneva driver gear is mounted on the gearhead output shaft. The driver gear turns a four position Geneva driven gear machined from Vespel SP3. The output of the Geneva driven gear is coupled to a pair of spur gears which give a 2:1 reduction (Figure 7). The swing arm is mounted to an adjustable central hub fastened to the output spur gear. This adjustable hub is necessary to align the optical path during assembly. The hub rotates on a bushing machined from Vespel SP3 which is held in place with a large snap ring. The rotation axis of the swing arm passes through the center of the flat mirror which is mounted to the swing arm base (Figure 5 & 7). The spherical collimating mirror is mounted near the tip of the swing arm. During the calibration sequence, the swing arm must rotate 180° to redirect the optical beam path.
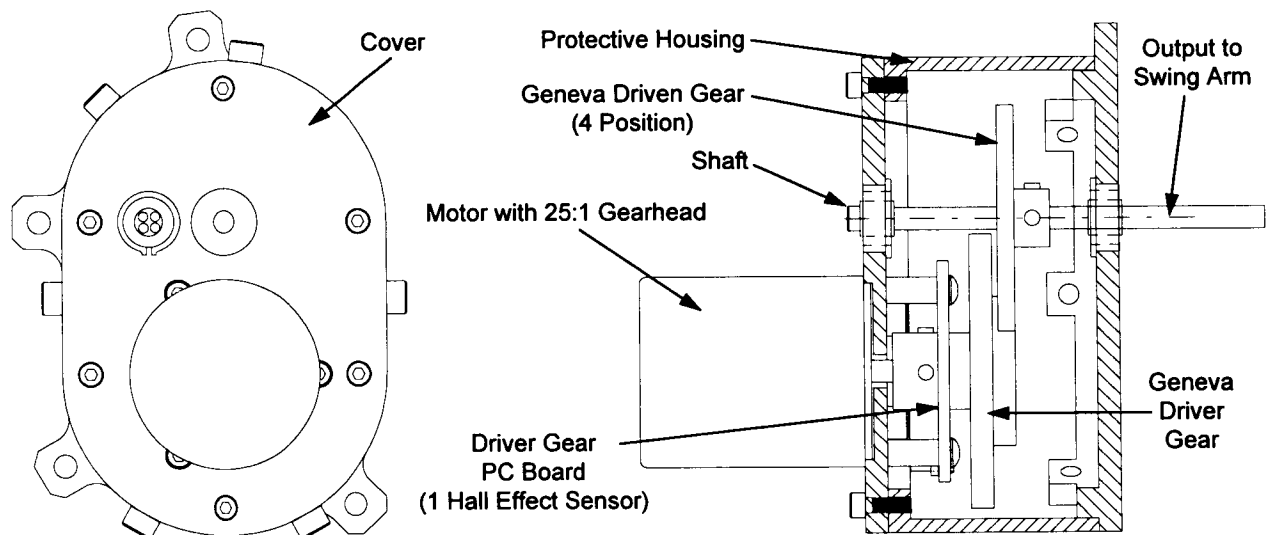
Figure 10. Swing Arm Drive

One magnet is located on the swing arm assembly Geneva driver gear and another magnet is located on the swing arm. Similar to the filter wheel drive, one printed circuit board containing a Hall Effect sensor is adjacent to the Geneva driver gear. But, unlike the filter wheel, there are two (not one) printed circuit boards with Hall Effect sensors that monitor the swing arm output. Each board is positioned 180° apart on the same radius as the magnet mounted on the swing arm (Figure 7). The swing arm Geneva drive system and the driver gear printed circuit board is shielded from accidental damage by a protective housing.

10

Swing Arm Bushing Challenge

The torque analysis for the swing arm included inertial loads, friction, and gravity. Gravity was included in the torque analysis because the swing arm assembly was required to work on the ground for testing as well as in orbit. Analysis showed that approximately 15% of the total required torque comes from the effect of gravity. The torque required to rotate the swing arm assembly was much greater than the torque required to rotate the filter wheel assembly. The large gear reductions of the swing arm drive train were necessary for a positive torque margin.

Analysis showed frictional loads were the largest contributing factor to the torque required to rotate the swing arm and accounted for approximately 80% of the total torque. Therefore, minimizing friction within the swing arm assembly was a priority. Low friction ball bearings were used to support the Geneva gear drive shafts but could not be used for the swing arm hub because of size limitations. The swing arm hub main bushing was custom designed and machined from Vespel SP3 because of its low coefficient of friction. The Vespel SP3 bushing is bolted to a vertical support plate with six screws (Figures 5 & 11). The swing arm is attached to an anodized aluminum hub that is fastened to the bushing with a retaining ring (Figure 11-A). During operation of the swing arm, the aluminum hub rotates inside the bushing.

Note: In air, the dynamic coefficient of friction for Vespel SP3 is .25. In a vacuum, the dynamic coefficient of friction is .03. The SP3 designation for Vespel denotes a 15% (by weight) molybdenum disulfide concentration.

Initial in-house testing of the VUV verified nominal (as designed) rotation of the swing arm. Unfortunately, during the cleaning process prior to final assembly, the swing arm bushing was damaged. Another Vespel SP3 bushing was machined, inspected, and installed in the VUV for testing. A slight vibration of the swing arm was observed during tests with the new bushing. Closer inspection of the bushing revealed that although it was within specification, the hub mating diameter was machined on the high side of its tolerance range. This caused a small excess (approximately .102 mm (.004 in) by design) of diametrical clearance between the hub and bushing resulting in the slight vibration of the swing arm during some of the rotation tests. The VUV passed all subsequent in-house tests. The slight vibration of the swing arm appeared to be an occasional nuisance rather than a problem and another bushing was not machined because of the high cost and time involved.

The VUV was integrated into the OPM and submitted to vibration and thermal-vacuum testing at Marshall Spaceflight Center. Post vibration tests indicated the OPM (and VUV) systems were functioning nominally. Approximately 70 hours into a 250 hour thermal-vacuum test, the swing arm mechanism stalled the stepper motor

in the maximum load condition. The VUV was pulled from the testing chamber, disassembled, and examined in the laboratory. It appeared that during the 70 hours of operation, the mating surfaces of the hub and bushing had worn slightly introducing more "play" into the system (Figure 11-B). This aggravated the vibration of the swing arm to the point that excess friction was generated and the hub could not rotate smoothly inside the bushing.

The bushing was designed to operate with the dry lubricant impregnated in the Vespel SP3 material. Lab tests verified that the Pennzane oil could be used as a filler agent to reduce the excess clearance between the bushing and hub. Pennzane oil is an approved lubricant for optical spaceflight payloads as tested by the Volatile Condensable Materials for Optical Applications (VCMO) NASA-STD-1443 within the OPM thermal design environment. One VCMO approved grease was considered, but was too viscous to work properly. A thin film of Pennzane oil was applied to the bearing surfaces that allowed the swing arm hub to "float" inside the bushing. This reduced the excess clearance and resulting friction inducing vibration. The VUV was reassembled and returned to the thermal-vacuum chamber where it operated nominally for a complete retest of 250 hours.

Note: Each VCMO test requires definition of the anticipated thermal environment and a minimum distance of the desired lubricant to an optical surface.

A. Nominal
Aluminum Hub
Retaining Ring
Bushing

B. Excess Clearance
Pennzane Oil
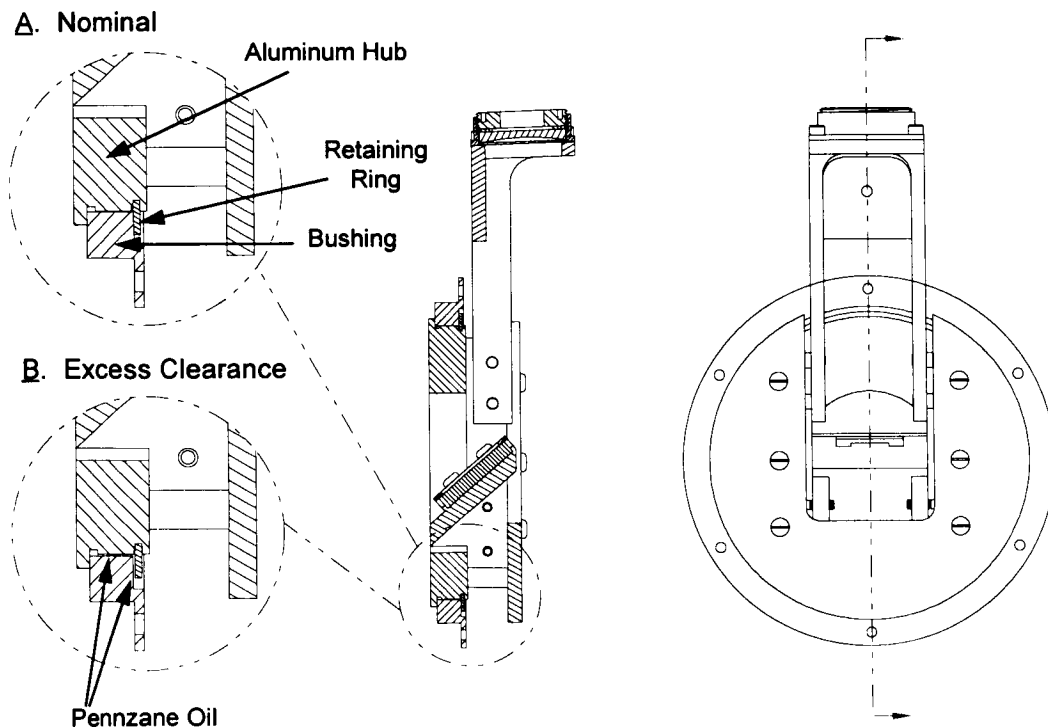
Figure 11. Swing Arm Bushing and Hub

Current Status of the VUV

After a total projected deployment of 8 1/2 months, the VUV will be returned to earth on STS-89 for analysis at AZ Technology. Flight data to date have verified that all of the VUV mechanical systems functioned nominally even after the collision between the Progress cargo ship and the Mir Spektr module on June 25, 1997.
Unfortunately, for reasons not yet determined, the Deuterium lamp source would not strike; therefore, no in-flight data was generated. Below are some tables containing pre-flight data gathered by the VUV while in the thermal-vacuum testing chamber at Marshall Space Flight Center. Each table shows a comparison of two samples previously measured by a commercial vendor of grating spectrometers. Note that data for the open hole aperture is not presented since the vendor did not perform this measurement.

Table 1. Measurement of an ND Filter: VUV versus Vendor

Wavelength (nm)	Transmittance		Reflectance	
	VUV	Vendor	VUV	Vendor
121.6	8.5	10.6	51.8	49.4
140	8.2	8.9	65.8	66.9
160	7.8	8.1	68.7	69.6
170	8.0	8.3	69.5	69.9
180	8.1	8.7	72.2	72.3
200	8.4	9.0	76.7	77.6
250	7.9	8.0	76.0	78.9

Table 2. Measurement of a MgF2 Window: VUV versus Vendor

Wavelength (nm)	Transmittance		Reflectance	
	VUV	Vendor	VUV	Vendor
121.6	79.9	75.7	8.6	9.7
140	86.6	83.5	7.4	7.4
160	86.8	88.5	7.1	6.7
170	89.4	90.3	6.5	6.4
180	91.5	92.2	6.4	6.3
200	91.7	93.8	6.0	5.9
250	92.7	94.8	5.6	5.5

Lessons Learned

- A mechanical system that requires periodic, repeatable, indexed rotation is "the perfect" application for a Geneva drive system. Rotation of a Geneva drive system can be effectively controlled with a combination of magnets and Hall Effect Sensors to generate signals for the drive motor.

  - The mechanical locking feature of a Geneva drive system eliminates the need for stepper motor holding torque during both power-on and power-off situations.

  - Drive system precision and repeatability is an inherent function of the Geneva Drive mechanical design tolerances and not the stepper motor accuracy.

  - One magnet and Hall Effect sensor set monitors the rotation of the Geneva driver gear, and the other sensor set monitors the gear train output. With this method, the Geneva gear is always stopped in a locked position and a level of redundancy is gained.

- Pennzane oil can be effectively used as a filler agent to reduce small excess clearances within bushing assemblies designed to operate in the space environment.

References

1. Harchanko, John S., Wilkes, Donald R., "A Novel Instrument to Measure the Optical Properties of VUV Materials in Space", American Institute of Aeronautics and Astronautics, AIAA 96-4380.

Information on the OPM mission and the VUV spectrometer is available on the internet (http://www.azhsv.com).

AXAF Science Instrument Module Mechanisms

Robert D. Renken[*]

Abstract

The Advanced X-ray Astrophysics Facility (AXAF) Science Instrument Module (SIM) consists of two, high-precision mechanisms and the related graphite structures required to support and move the science instruments to desired positions at the focal point of the telescope. Two axes of operation are accommodated: translation and focus. The translation axis uses linear bearings and a ball screw actuator. Several lessons learned about the mounting of linear rails are discussed. The focus mechanism is a unique design that uses flexures as primary structure and a motor-driven actuator to support the Integrated Science Instrument Module (ISIM) during launch and to focus it after launch. The details of the mechanism and its actuator are described.

Introduction

The AXAF is a large X-ray telescope scheduled to be launched in 1998. As one of NASA's four great observatories, AXAF will study the cosmos in the X-ray spectrum. The Science Instrument Module (SIM) is the package or housing that supports the instruments at the focal plane, which is 10 m (32.8 ft) behind the mirrors. The SIM is supported by the Optical Bench Assembly (OBA), which is a conical graphite part of the spacecraft that connects the SIM to the rest of the spacecraft. The SIM houses two instruments, the AXAF-I CCD Imaging Spectrometer (ACIS) and the High Resolution Camera (HRC). An artist's conception of the AXAF is shown in Figure 1.
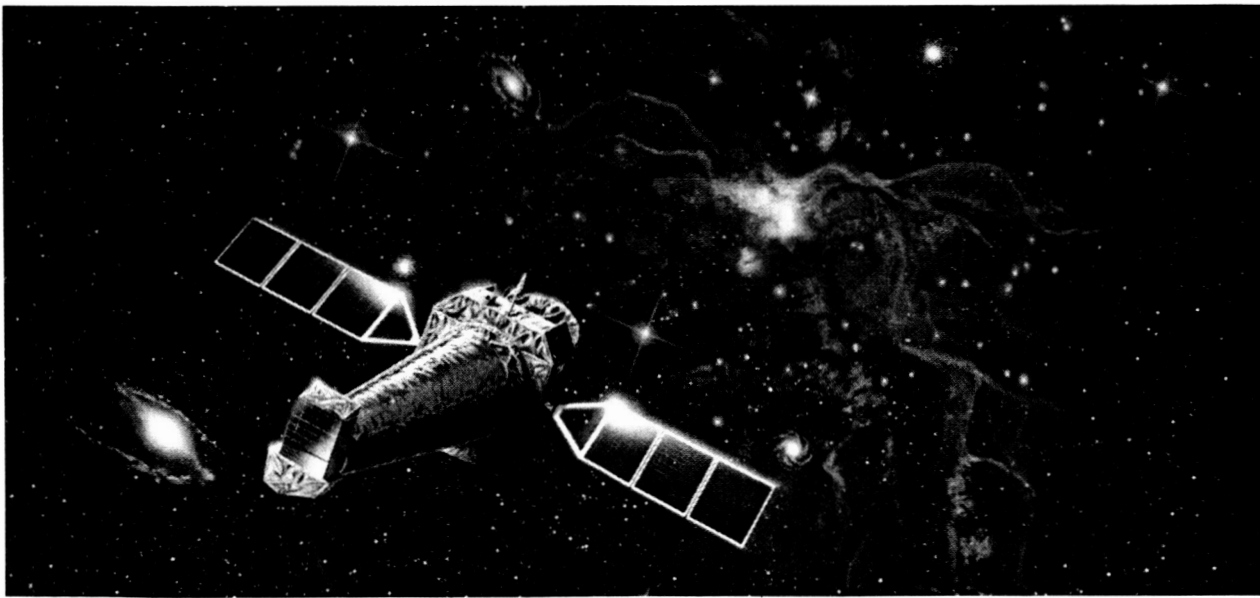

A7265.001a[30A] 96-467c

Figure 1. Artist's Conception of AXAF

---

[*] Ball Aerospace & Technologies Corp.
Boulder, Colorado

Under the auspices of NASA's Marshall Space Flight Center, TRW is the prime spacecraft contractor. Ball Aerospace is the subcontractor responsible to TRW for developing and building the SIM and also integrating the instruments into the complete Integrated Science Instrument Module (ISIM). The ACIS instrument is built by the Massachusetts Institute of Technology and the HRC instrument by the Smithsonian Astrophysical Observatory.

Science Instrument Module Requirements

The purpose of the SIM is to support and enclose the instruments throughout launch and in the space environment. It is required to translate each instrument to the focal point and focus it. The SIM also connects the instruments to the spacecraft structurally and electrically and provides the environment acceptable for their operation. Key parts of the SIM and the axes used for orientation are shown in Figure 2.

Mechanism
The key requirement for the mechanisms is that they move either instrument to the desired aim point with respect to the focal plane of the telescope. Figure 3 shows a pictorial view of the instrument apertures and their relationship with respect to each other. The mechanisms are required to meet the performance and alignment requirements given in Tables 1 and 2, respectively, for any of the four detectors. Total travel in translation is 52.1 cm (20.5 in) minimum with the launch position as indicated in the figure. Travel in focus is required to be ±1.02 cm (±0.400 in) with the launch position being in the mid-range of the travel.

Envelope
The envelope is defined in two ways: (1) All structure and mechanisms had to clear the aperture through the center of the SIM. The aperture is an irregularly-shaped envelope defined by the instrument detectors. The longest cross-sectional diagonal at the focus structure is approximately 34.8 cm (13.7 in). (2) The SIM was required to fit inside the Shuttle in the Y and Z directions and there was a conscious attempt made to minimize its overall length. The final length agreed upon was 72.4 cm (28.5 in) from the OBA interface plane to the telescope focal plane and an overall length of 87.6 cm (34.5 in).

Structural
The SIM is the key structural member between the OBA and the instruments. It is required to support and house both instruments through the launch and then on-orbit. Each of the instruments weighs approximately 113 kg (250 lbf). The minimum primary resonant frequency during launch is 25 Hertz.

Table 1   Mechanism Performance Requirements

Parameter	Translation (Z)	Focus (X)
Positioning μm (in)	±127 (±0.005)	±12.7 (±0.0005)
Repeatability μm (in)	±127 (±0.005)	±12.7 (±0.0005)
Range μm (in)	>0.521 (>20.5)	>0.0203 (>0.800)
Position Readout Resolution μm (in)	<127 (<0.005)	<12.7 (<0.0005)
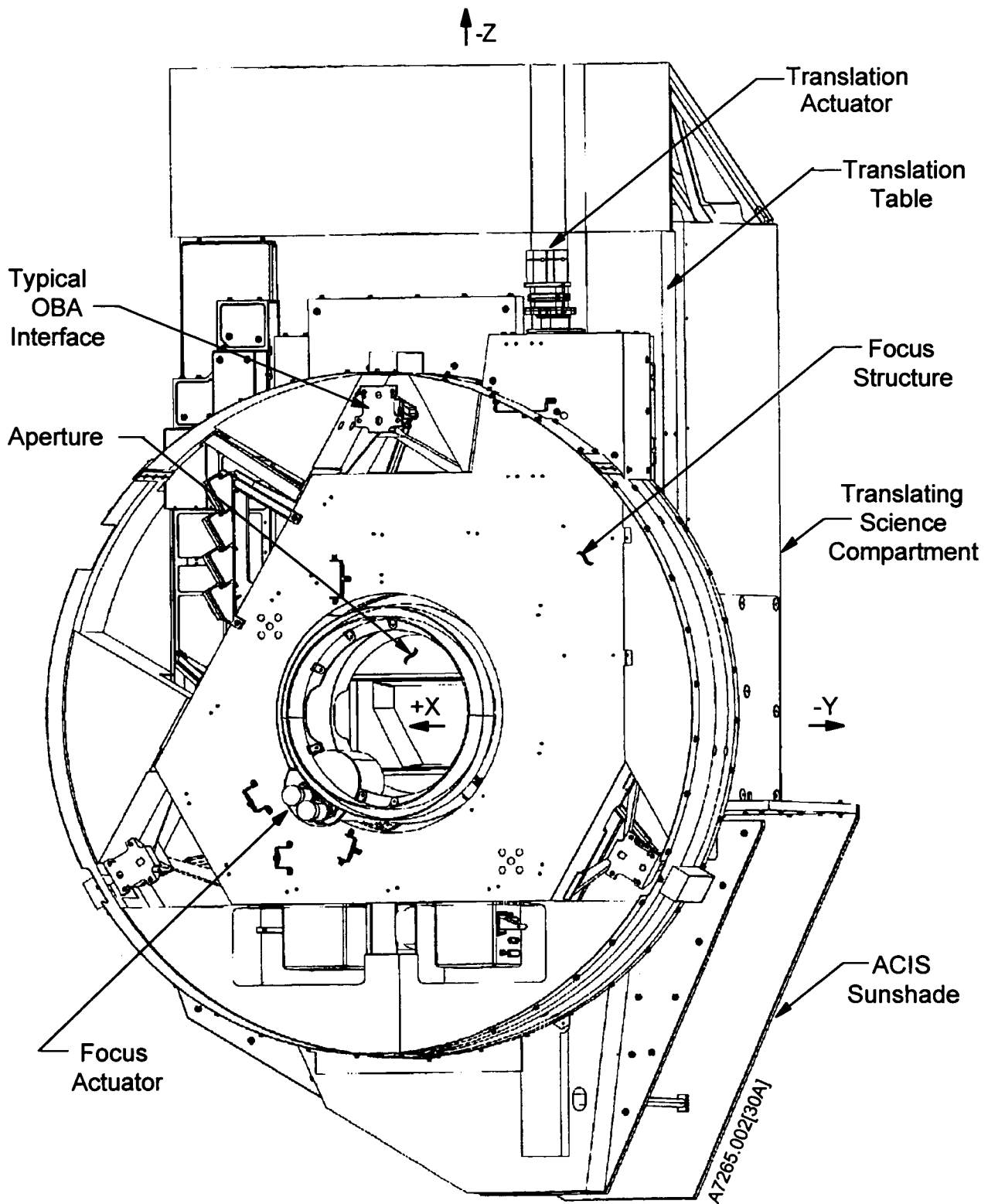
Figure 2. SIM Key Components

TSC Position
(+Z aim point motion)

103,578

ACIS-I

83,858 ——— 83,826 (Tab 3 sensed by SEA A)
——— 80,669 (Tab 3 sensed by SEA B)
80,655 ——— 75,766 (Launch lock position)
ACIS-S
70,877

24,912 (Tab 2 sensed by SEA A)
21,755 (Tab 2 sensed by SEA B)

0 (Origin)

-24,205

HRC-I

-76,514

-84,416 (Tab 1 sensed by SEA A)
-87,553 (Tab 1 sensed by SEA B)
-95,182
HRC-S
-103,143
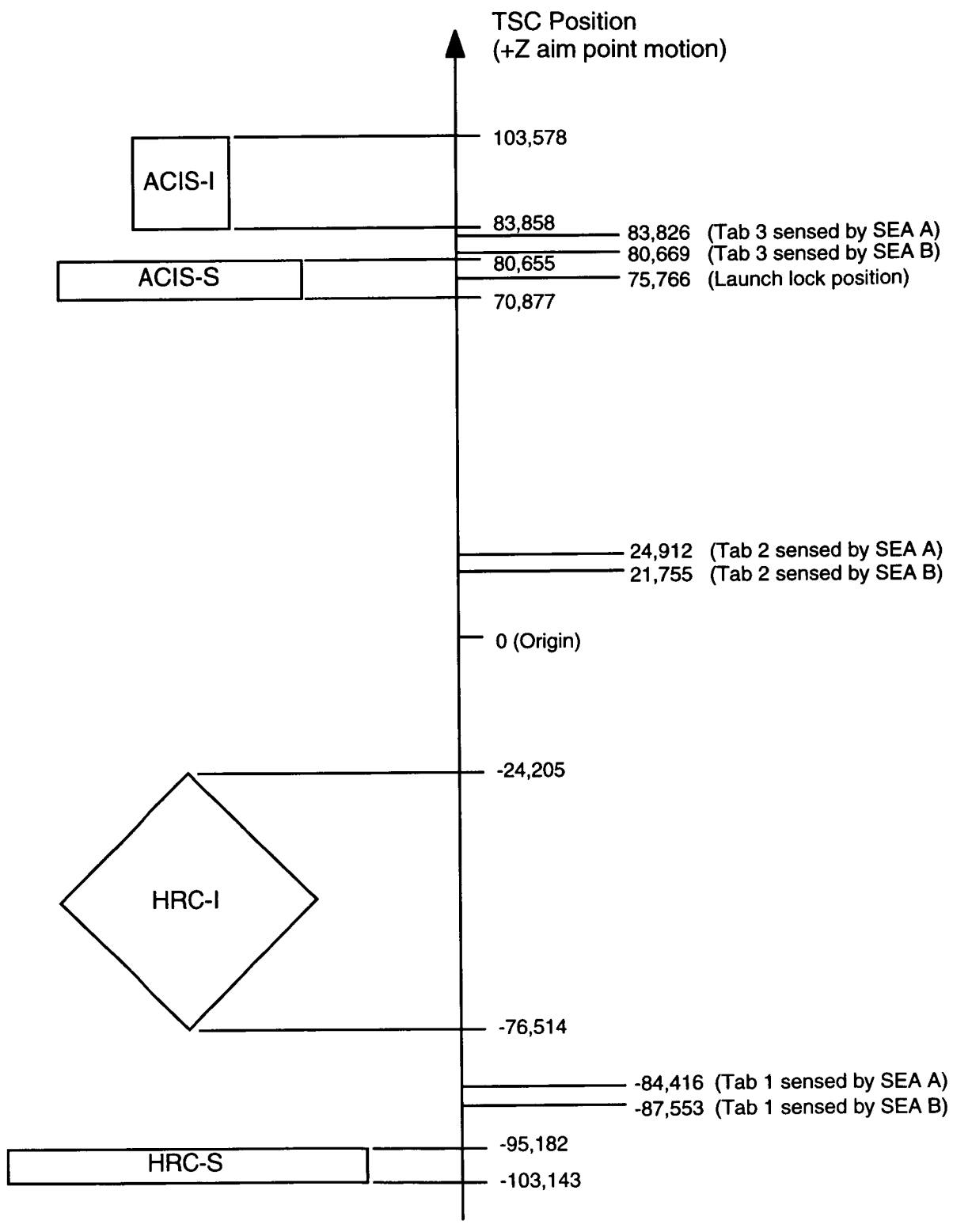
47265.012[30A]

Figure 3. Translating Science Compartment Positions

Table 2   SIM Alignment Requirements

Degrees of Freedom	Not-to-Exceed Value	Thermal Stability
X μm (in)	229 (0.009)	12.7 (0.0005)
Y μm (in)	279 (0.011)	50.8 (0.002)
Z μm (in)	279 (0.011)	50.8 (0.002)
x(sec)	10	2.5
y(sec)	49	9
z(sec)	49	9

Notes:

(1)   These alignment values are obtained between the -X surface of the SIM Translation Table and the OBA/SIM I/F Plane.

(2)   For the SIM, an AXAF-I observation period is defined as a 48-hr (maximum) time period between SIM mechanism actuations.

(3)   The X NTE value is to be obtained with the SIM focus mechanism at the center of its full travel range.

(4)   The X NTE value is to be obtained with either the ACIS or HRC in viewing position.

Thermal:
The AXAF is placed in a high elliptical orbit, 140,000 by 10,000 km (87,000 by 6,200 miles). Normally the sun is always on the same side (-Z) of the spacecraft from within a 45-deg angle of the aperture to dead aft. The ACIS radiator is always on the side away from the sun. It's desired to keep the entrance aperture of the ACIS instrument cold, -10 °C (14 °F). At the same time, both instruments and the other electronics mounted on the SIM are dissipating heat which has to be radiated to space. (This led to a complex thermal control system and rather large thermal gradients within the SIM.) Nominal on-orbit temperatures range down to -35 °C (-31 °F) while warm temperatures are as warm as +17 °C (63 °F). The coldest predicted graphite temperature is -112 °C (-170 °F).

Life
Life is for 3 years of ground operations, a possible 3 years of storage, followed by 5 years of operation on-orbit. The mechanism life is defined by the number of movements that will occur during ground and orbital operations. Normally, on-orbit, the movements will be short, except when instruments are switched or calibration is being performed. During ground test, movements are longer. The specified number of orbital movements is 3,812 for translation and 5,322 for focus. The mechanism life test is for three times this quantity.

Electrical
The electrical requirement that drove the mechanism design was that power and signal circuits had to be transferred from the spacecraft to the instruments across the moving interfaces.

Miscellaneous
Several other miscellaneous requirements that drive the design are listed below:
•   Redundancy: Electrical redundancy was required. Structural redundancy is not required; however, redundancy of rotating joints was a goal.

19

- Fracture: A formal fracture critical program was required.
- Cleanliness: The SIM has to meet requirements of MSFC-SPEC-1248 and all materials have to meet the requirements of MSFC-SPEC-1443.

Structural Arrangement

As shown in Figure 2, the SIM is composed of two major structural parts, which are the translation table and the focus structure. Each is made from bonded graphite fiber reinforced cyanate with two faceplates bonded to an eggcrate internal structure. Composite Optics Incorporated supplied the graphite structures. Metal interfaces to support the instruments, mechanisms, and wiring are bonded internally to this structure and are made from either titanium or Invar, depending on the size of the fitting and the thermal environment in the area of the fitting. The thermal coefficient of expansion of the composite structure is -0.24 micro strain per degree Celsius.

Instruments are mounted directly to the translation table along with their supporting electronics and cabling. Also mounted to the translation table is the Remote Control and Telemetry Unit and the Ball Thermal Control Unit and other electronic boxes. The ACIS radiator is mounted to the +Z panel, which also forms one side of a box that encloses the instruments. The other four sides are covered by a structure called the *Turtle Shell*, which can be seen in the photo in Figure 4. This entire package is mounted to the focus structure on three, linear bearings and is driven by a ball screw actuator, which collectively is called the translation mechanism. Power and signals are transferred across the linear joint by a rolling-loop flexible-cable assembly.
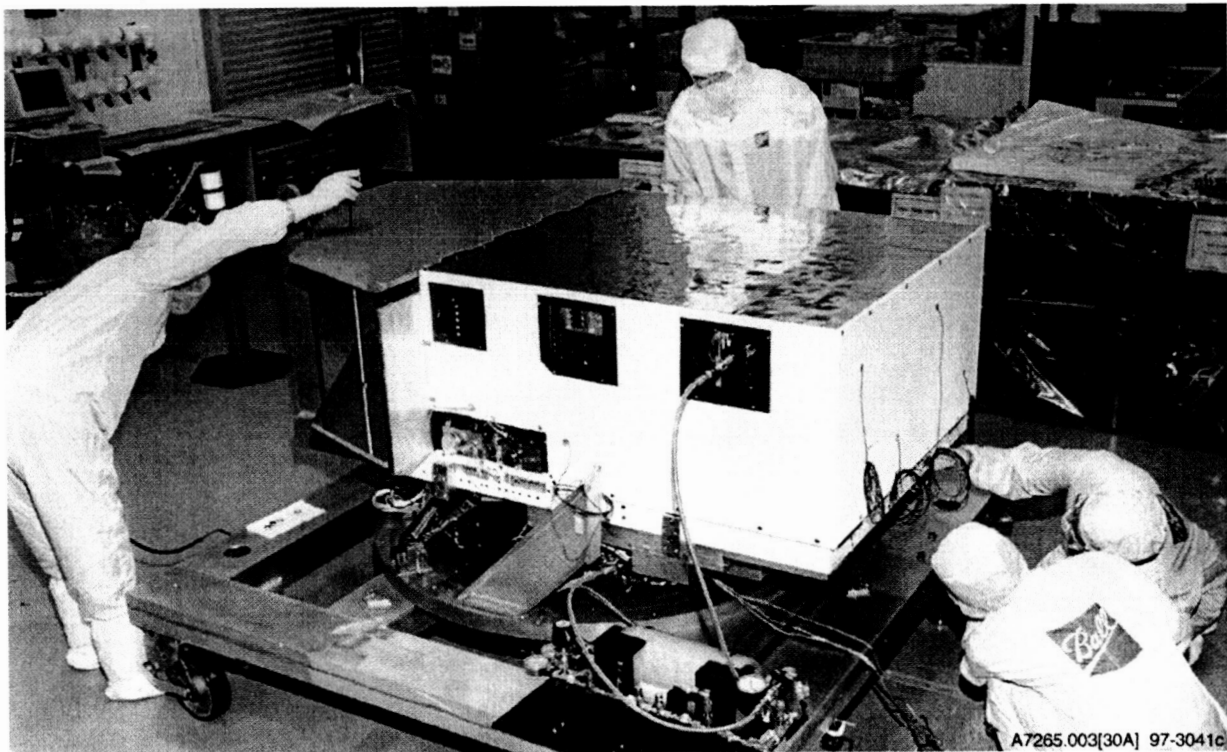
Figure 4. ISIM Photograph

The focus structure is supported and moved in focus by the focus mechanism and is tied to the Optical Bench Assembly through flexures and linkages at three points, called the feet. The focus mechanism is driven by the focus actuator, which is installed in the center of the focus structure and wraps around the aperture.

Translation Mechanism

The translation mechanism is shown in Figure 5. Three linear bearings tie the translation table to the focus structure. Each of the bearings is comprised of a rail and a carriage assembly. There are four recirculating ball tracks per bearing. The limit load capacity of these bearings is 26,900 N (6,050 lbf) with the maximum launch load being 12,200 N (2,740 lbf). This gives a maximum mean compressive stress at the ball/rail contact zone of 2,480 mPa (360,000 psi). To minimize the overall envelope for the assembly, two rails are mounted to the translation table and one to the focus structure. This gives a comparatively large "wheelbase" for launch and still provides adequate separation of the carriages for on-orbit operation.
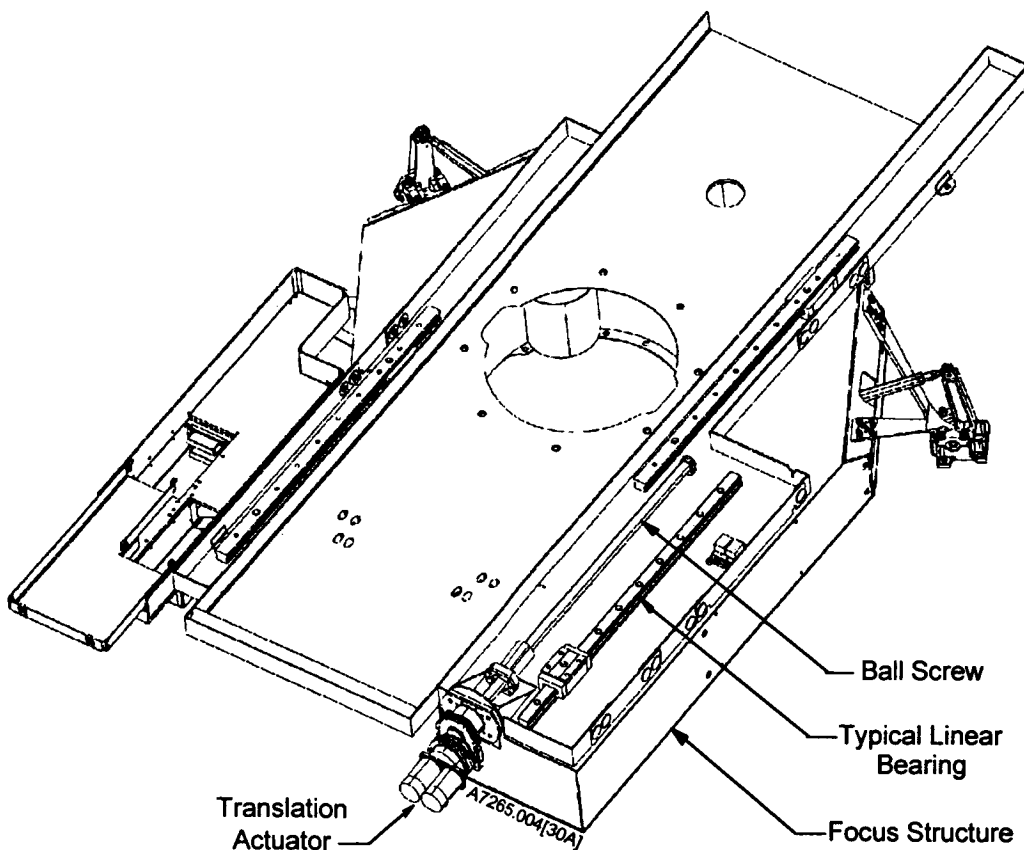
Figure 5. Translation Mechanism

The bearings were supplied with a light preload; hence, on orbit there should be no perceptible freeplay. The metal fittings connecting the bearings to graphite structure are rigid at the launch position and have built-in flexures at other locations to allow thermal expansion and contraction of the steel rails. Further, the "C" carriage is

mounted to a fitting designed to be flexible in the Y direction so the rails are not over-constrained and hence remain virtually unloaded as a result of thermal gradients between the translation table and the focus structure. Assembly alignment of the rails and carriages is provided by offset, splined pins, one for each rail and one for each carriage.

The translation actuator shown in Figure 6 consists of two motors driving a ball screw through a spur gear differential and intermediate gearing. The gearbox housing is mounted to the focus structure and the ball nut is mounted to the translation table. Two motors were chosen for redundancy. Each motor is a direct-current six-pole three-phase device with Hall probe commutation and was supplied by Aeroflex Laboratories.

A7265.005[30A]
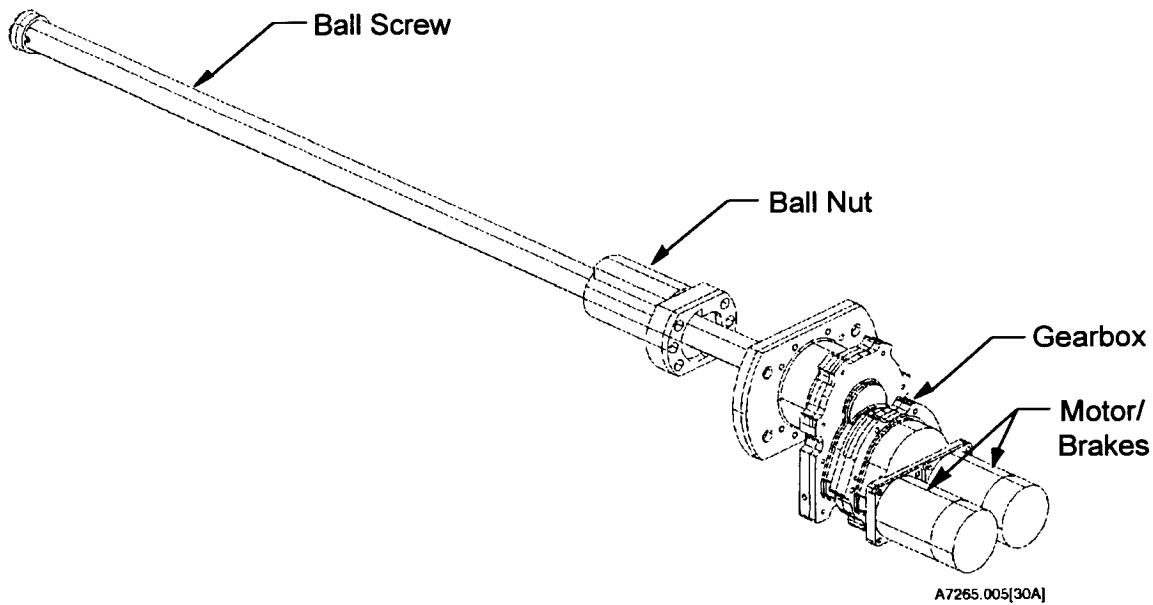
Figure 6. Translation Actuator Assembly

Each motor also has a toothed brake designed to lock the motor in position when it is not used. Unpowered, the brake is spring loaded to the braked position. When power is applied, it is released and the motor can be driven normally. The normal mode of operation is with one motor at a time. Position information is obtained by counting the number of times the Hall probes switch. This is an advantage of the direct current motor over a stepper motor, which may not move every time the current is switched. The motors are designed to be operated at a maximum speed of 2900 RPM, which with 18 switches per revolution means that they are switched 870 times per second. They are capable of providing a minimum torque of 56.6 mN•m per ampere (8.3 inch-ounces per ampere). This is the maximum output torque since the electronics is current limited at one ampere. The brakes are designed to provide a minimum holding torque of 283 mN•m (40 in•oz). The gears are standard 20-deg pressure angle involute tooth forms. When low numbers of pinion teeth were used, the center distance was modified to avoid undercutting. Actuator gear ratios are shown for single motor operation in Table 3.

22

Table 3 Gear Data

Mesh	Pitch	Number of Teeth	Ratio
Motor Input	64	114/15	7.6:1
Differential	64	Ring 78 Planets 28	2:1
Translation Output	48	96/13	7.38:1
Focus Intermediate	48	166/13	12.77:1
Focus Sector	24	376/12	31.33:1

Overall Ratio: Translation: 112:1

                     Focus: 6432:1

The gearing and brakes are designed to serve two functions: (1) they hold the launch loads and lock the actuator through launch, and (2) the brake prevents the non-operating motor from backdriving when the other motor is being operated. This means that no caging device is required other than the actuator itself. Therefore, launch loads drive the sizing of the ball screw, gearing, and the brake. The motor size was selected to lift the translation table in a one-g field during thermal vacuum testing. A major advantage of this configuration is that the actuator is overpowered for the orbital condition.

Focus Mechanism

The focus mechanism is shown in Figure 7. It consists of a central focus actuator, foot mechanisms, and push rods that connect the actuator to the foot mechanisms. Three foot mechanisms provide a three-point stable optical mount to the optical bench assembly. A single foot mechanism is shown in Figure 8, and a stick figure of how it operates is shown in Figure 9. This mechanism is centered around two basic parts, the eccentric lever and the bi-pod flexure. As the lever is rotated, the focus structure is moved in the X direction. The radial component of the motion is absorbed by displacing the flexure in a radial direction. When the three feet operate together in zero g, the reactions in the flexures are exactly equal to each other since they are equally spaced at 120-deg angles about the periphery of the Optical Bench Assembly. On orbit these reactions are purely radial since any X reaction results in movement of the focus structure.

The levers are moved by push rods connected to them and to the focus actuator. All move together since they are connected to the same actuator housing. An external view of the actuator is shown in Figure 10 and a section view of the actuator is shown in Figure 11. The housing is supported by a duplex pair of 35.56 cm (14 inch) bearings that extend completely around the aperture. The focus actuator is driven by identical motor/brake combinations to those that are used on the translation actuator. Initial gearing is the same. There are two additional stages of output gearing as shown in Table 3. Like the translation mechanism, the focus mechanism is designed to hold the ISIM through launch, and to operate it in a one-g field. The ISIM is consequently overdesigned for the zero-g condition, giving a large margin for on-orbit operations.
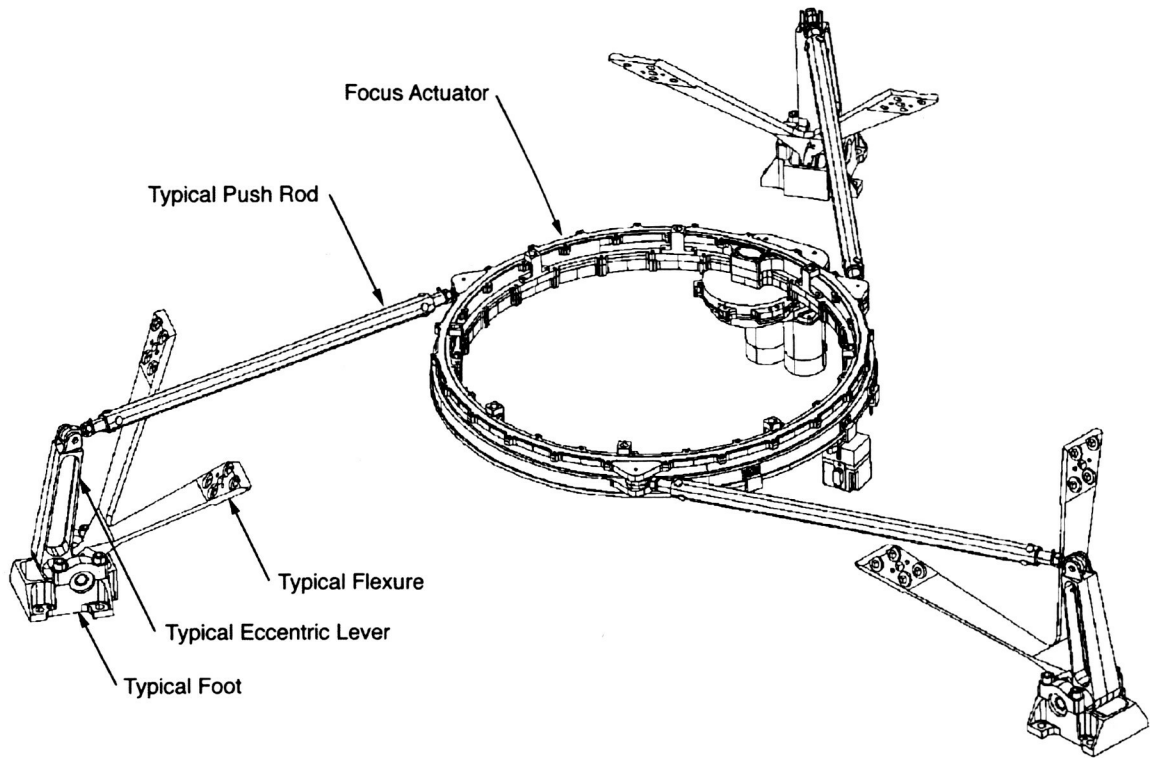
Figure 7. Focus Mechanism

A7265.006[30A]
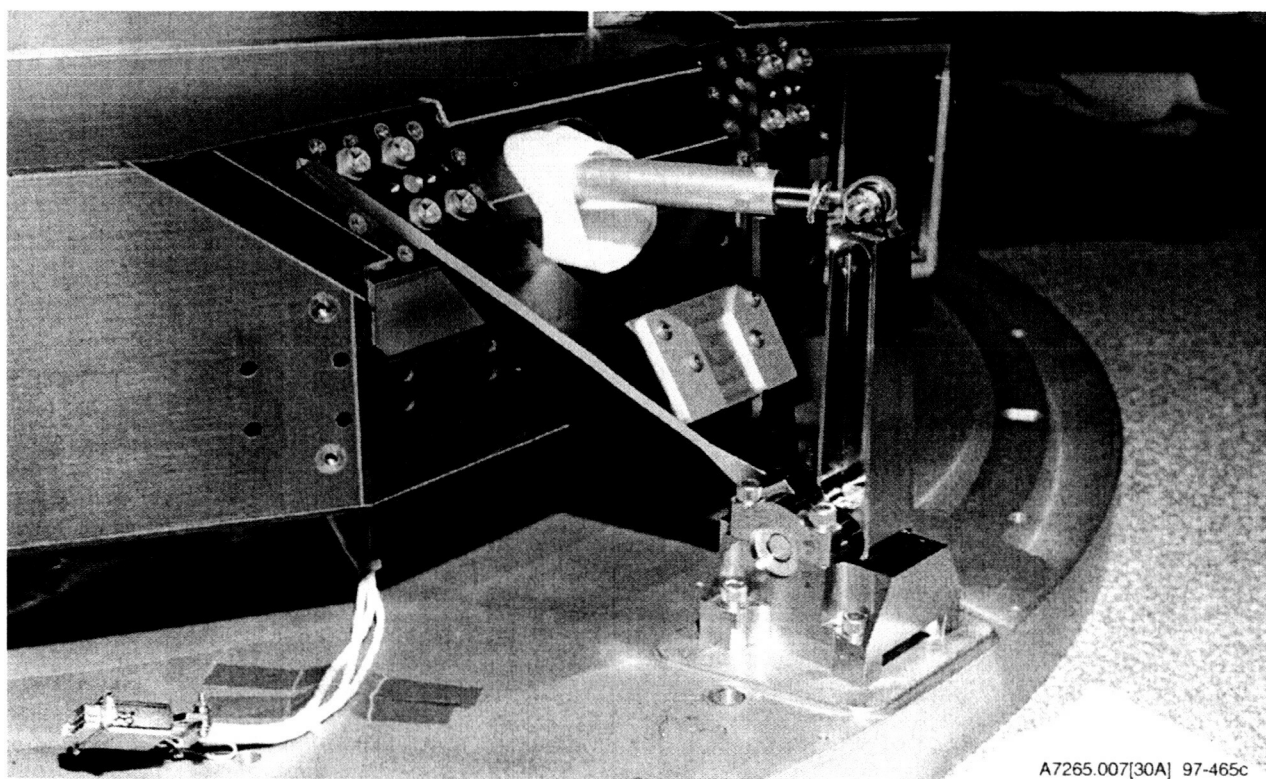
A7265.007[30A] 97-465c

Figure 8. Foot Mechanism

24
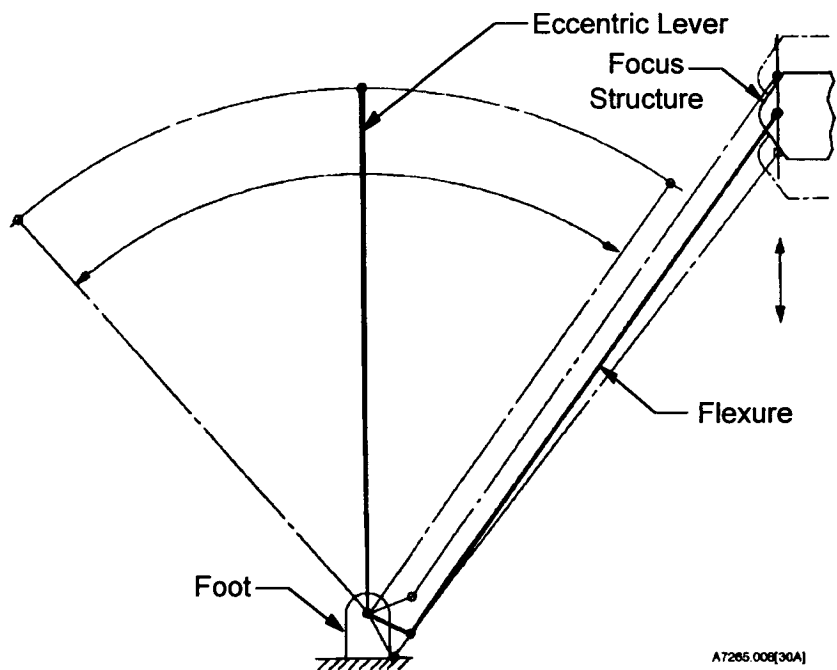
Figure 9. Foot Mechanism Stick Figure
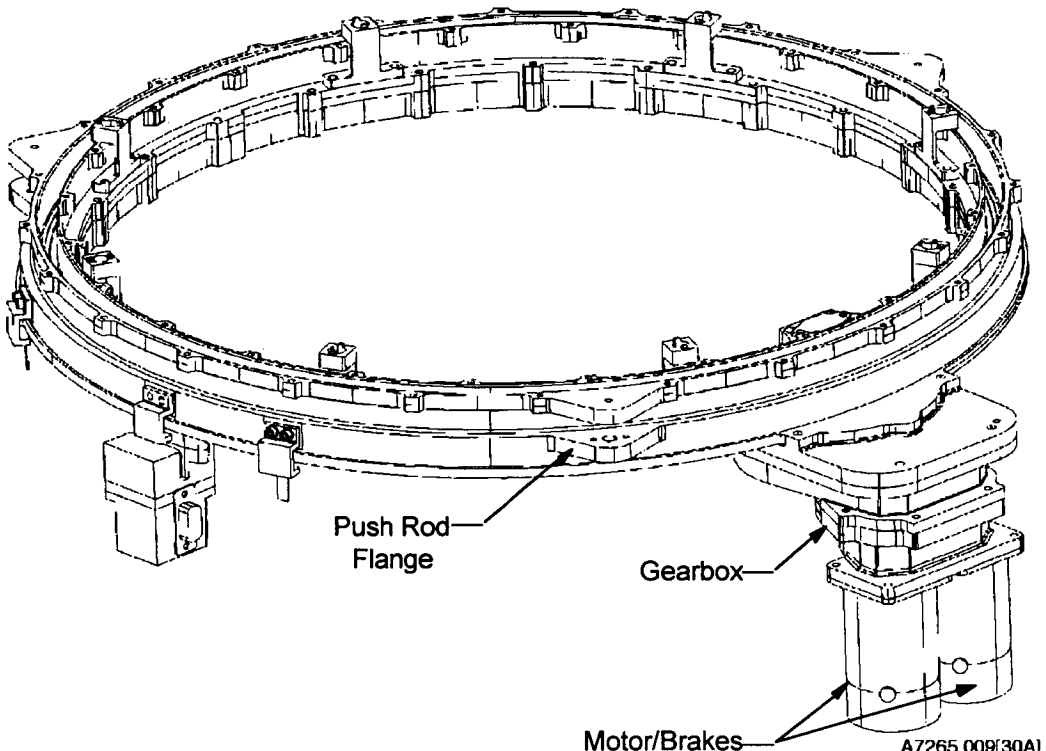
Figure 10. Focus Actuator
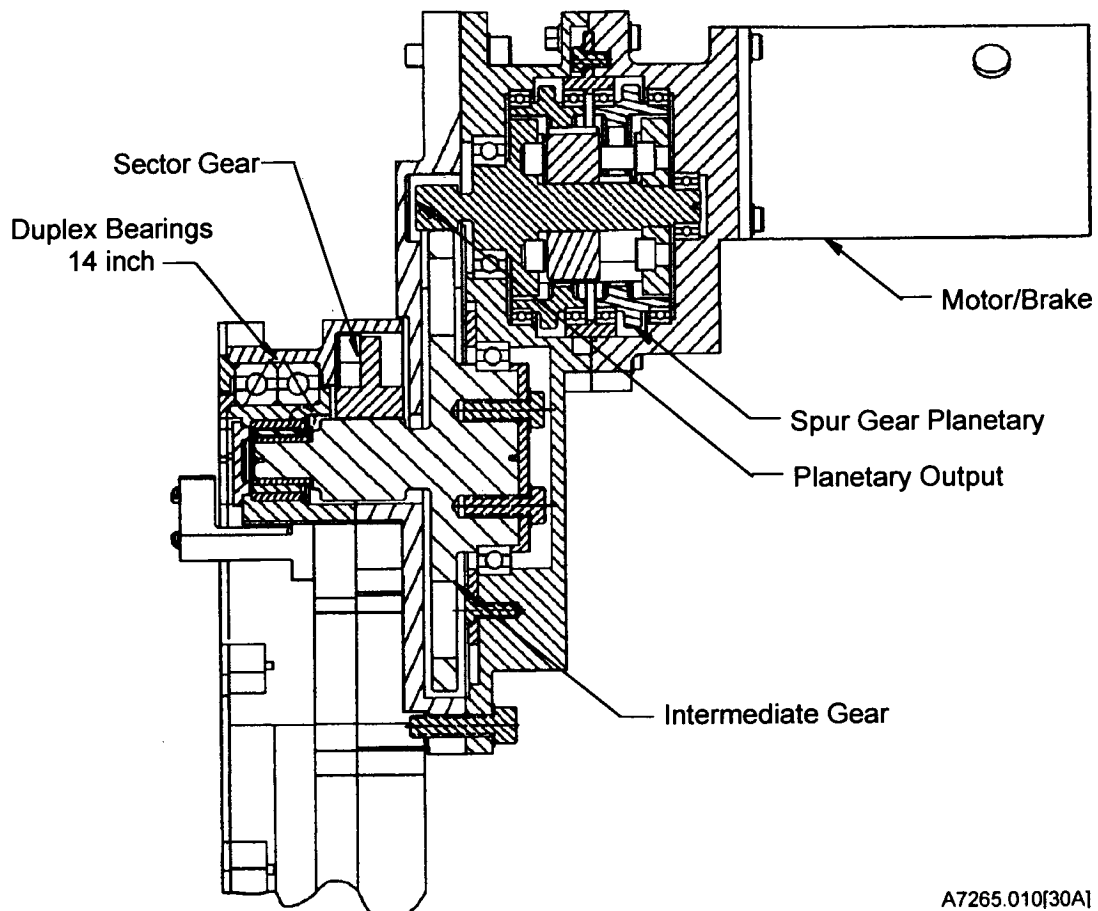
Figure 11. Focus Actuator Section View

Flexible Lead Assembly

Power and signals are transferred across the translating joint with redundant roll loops as shown in Figure 12. One end of the roll loop is fixed to the focus structure on a part called the wire tray. The other end is fastened to the translation table. As the table translates, the loops roll between the wire tray and the translation table. There are five flat cable assemblies inside each other in each loop. The inner 4 are unshielded flat flexible cable, with 13 conductors that have cross-sectional dimensions of 0.005 x 0.160 inches. The outer ribbon consists of 18 twisted pairs of #28 gauge leads. In total, each loop has 52 single conductors that are #24 gauge wire and 18 twisted shielded pair that has #28 gauge conductors. For each loop, there are four layers of flat, flexible cable and one with twisted shielded pair.

Materials

The SIM mechanisms use a variety of materials. As mentioned above, the primary structure is graphite fiber reinforced cyanate.
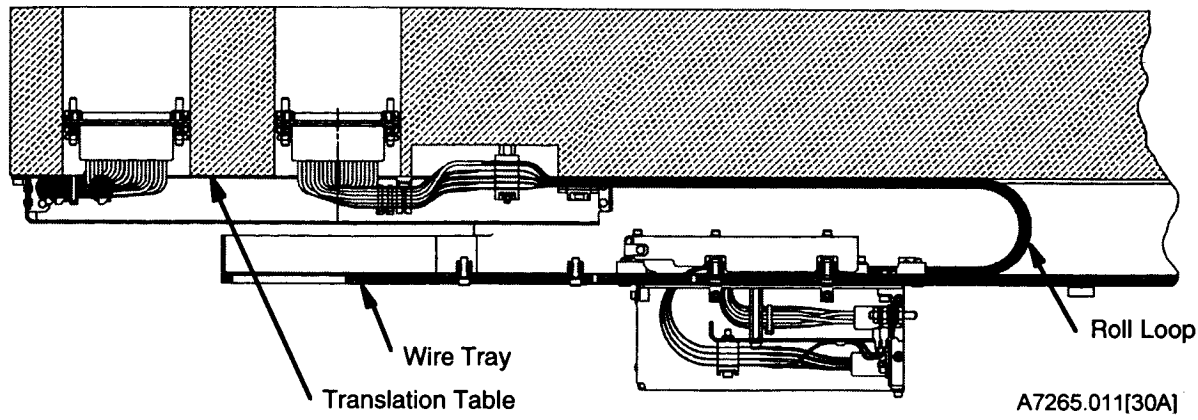
Figure 12. Flexible Wire Assembly

Metals

Gearbox housings are 6Al-4V titanium and the gears are made from Carpenter Custom 455 heat treated to the H1000 condition. Bearings are 440C CRES with phenolic retainers. The carriages for the linear bearings are carburized AISI 8620. The rails are made from AISI 1060, which is induction hardened. Both the rails and the carriages are coated with thin, dense, chrome plating for corrosion resistance. The ball screw is manufactured of similar materials, and balls for both devices are 440C CRES.

The feet are made from 6Al-4V titanium, and the flexures and the eccentric levers are made from 15-5PH Corrosion Resistant Steel. We chose 15-5PH relatively late in the program when we discovered that changing these two parts from titanium to steel increased the fundamental resonant frequency of the ISIM from 24 Hz to 25 Hz. Push rods were made from 6061 aluminum.

Lubricants

We used a variety of lubricants throughout the mechanisms. For the rolling element, bearings vacuum stripped Bray 601 grease was selected. This grease was also used on the ball screw and linear bearings. In every case, barrier film was used to control creep of this low surface energy grease. Gears were lubricated with the same base grease, but 3% moly-disulfide was added to prevent wear. Monoball bearings used at the push rod ends and at the bottom of the flexure were lubricated with Karon B, a trade name of the Karon company. Garlock DU was used as the lubricant for the bushings and thrust washers in the foot assemblies.

Lessons Learned

We learned many lessons during the development of these mechanisms.

Linear Bearings

Initially, we thought it would be easy to adapt linear bearings to space usage. But it turned out to be an interesting challenge when we realized that these were fracture-critical parts. The parts had to be corrosion resistant and the rail and carriage required hard (Rc 58+) races at the rolling element contact points. Yet, they had to have core ductility to meet the fracture requirements.

27

The initial linear bearing selected was a recirculating roller bearing manufactured in Europe. The specification was written to define all of the requirements including handling and material traceability for fracture critical parts. The roller bearing provided the highest load-to-weight ratio for any bearing considered. We immediately received a no-bid when the requirements were reviewed.

Next, the design was changed to a linear recirculating ball bearing design after the loads were reduced. This time, the specification eliminated most of the inspections and tests using the catalog data as a reference. A second specification was generated whereby the purchased parts could be upgraded to meet the fracture-critical requirements by inspection, chemical analysis, and test after receipt. Requirements for corrosion resistance, lot traceability, and raw-stock inspections remained. Extra bearings were ordered as test samples.

We selected a Japanese company that promised delivery. But as the procurement progressed, we realized that it was becoming increasingly difficult to communicate with them. Items we thought had been settled were treated as surprises when they were mentioned. Finally, we learned that the steel to be used was a Japanese counterpart to the 440-C material we thought we were getting. When the chemical analysis of this steel was received, we found that even though it was somewhat corrosion resistant, it did not meet the strict definition of a corrosion resistant steel. After delivery, some of these rails were tested and found to be so brittle that crack propagation almost could not be measured.

At this point, we learned that our ball screw supplier, Thomson, was also making a similar design linear bearing. Subsequently, we switched to their design and were able to rely on them for inspection and handling of fracture-critical parts. This design uses carburized steel to attain the hardness for the races while allowing the core to be softer and hence meet the fracture requirements.

Rail Straightness
We also learned that the rails are not necessarily straight, even though they are parallel. In a typical commercial application, the rail is bolted rigidly to a machine toolbed to achieve the straightness requirement. Since we were mounting them on flexures, the rails had to be straight without rigid support. Eventually, we had to straighten each rail to meet a straightness requirement of 0.002.

Rail Mounting
Another problem encountered throughout the design was interfacing the slightly negative coefficient of expansion graphite structure with metallic parts that have a relatively large positive coefficient of expansion. The most difficult interface was between the steel rails and the translation table or focus structure. For these interfaces, the metal fittings at the launch positions of the bearings were fixed (bonded securely) to the graphite. Other points were flexure mounted using blades so that the rail could expand and contract. With this mounting configuration, the flexures must be able to carry one-g loads with the ISIM in a variety of attitudes. After the graphite was delivered, we found that the bonded flexures could carry tensile and compressive loads well, but not side loads. For this application, our customer worked with us to determine that an

28

operating constraint was possible which stated that the SIM would never be moved from launch position on the ground unless the -X axis was up.

This type of rail mounting should be avoided for this application. One alternative is to incorporate a separate steel fitting into the graphite that is as long as the rail and rigid enough to control rail straightness and to support load in any required attitude. The fitting incorporates both hard points and flexure mounts to support the required loads. Another alternative is to use two bearings, one purely for rail isolation and the other for linear operation.

Flexible Roll Loops

The flexible wire rolling loops were development tested twice because of a failure with the first design. We learned two lessons. First, it is undesirable to use stranded wire in a flexing, high-vacuum environment. The individual strands will cold weld to each other increasing the stiffness of the wire and will eventually fail. Second, we learned that the spring characteristics of the wire loops themselves will support the loops in a one-g field. The original design used flexible springs from steel tape measures to support the leads. This support was found to be unnecessary.

Conclusion

The design is now complete. The ISIM is assembled and testing is in progress. It is scheduled to be shipped to TRW for launch in the second half of 1998. This was a challenging design because of the fine accuracy required for focus and translation, and stability. We devised a novel use of flexures in a moving mechanical design. A mechanism life test is now starting, and we are confident that this test will demonstrate that the mechanisms will meet mission requirements. The flight design meets the requirements as verified by test.

Acknowledgments

References

1. Hamidi, M., R.P. Iwens, J.F. Donaghy, J.A. Spina, J.A. Wynn, D.D. Johnston, G.F. Flanagan, and L.D. Hill. "Design of the Advanced X-ray Astrophysics Facility— Imaging." *AIAA Space Programs and Technologies Conference,* AIAA 93-4199, 1993.

2. Jordan, Steven P. and Scott Texter. "The Science Instrument Module for the AXAF Mission." *AIAA Space Programs and Technologies Conference,* AIAA 94-4565, 1994.

3. Skinner, M.A. and S.P. Jordan. "AXAF: The Science Instrument Module." *EUV, X-ray, and Gamma-ray Instrumentation for Astronomy VIII,* Proc. SPIE 3114, (1997) 2-10.

Development and Qualification of the Scan Mechanisms for MHS

Winfried H. Aicher*

S_3-/9

/65,88

3368Y5

/ Y P.

Abstract

In the Microwave Humidity Sounder (MHS) Instrument Program, several Scan Mechanisms were developed, qualified and delivered. The following paper presents the design concept and the components used to realize this design, the development and verification logic as well as the lessons learned throughout the complete development and verification of the MHS Scan Mechanisms. The Microwave Humidity Sounder Instrument is being developed under contract to EUMETSAT.

Introduction

The MHS Instrument is a five-channel self-calibrating microwave radiometer to be flown on METOP and NOAA. It utilizes an offset paraboloid reflector that is mechanically scanned to provide earth scene, on-board target, and cold space views. The associated angular sectors are passed at low speed for optimum radiometric performance, the remaining angles of the full rotation are passed by acceleration and deceleration each for minimum time consumption. The momentum of the reflector scan motion is fully compensated by a counter rotating flywheel. Control of the scan profile is implemented within the electronic equipment of the Instrument which interfaces with the motors and sensors of the Scan Mechanism.

The Scan Mechanism described in this paper is one of the MHS components. The configuration of the MHS Instrument is presented in Figure 1.

Design Concept

Main Requirements
The main requirements for the MHS Scan Mechanism are as follows:
- The Scan Mechanism shall rotate the MHS reflector and shroud according to a scan profile as presented in Figure 2.
- The Scan Mechanism shall provide a torque / momentum compensation for the Instrument by driving a flywheel synchronised with, but in the opposite direction to, the reflector.

The main mechanical interface requirements are the total length of 180 mm and the diameter of 200 mm at the central mounting flange. The mass is limited to 7.85 kg.

---

* Dornier Satellitensysteme GmbH, Friedrichshafen, Germany
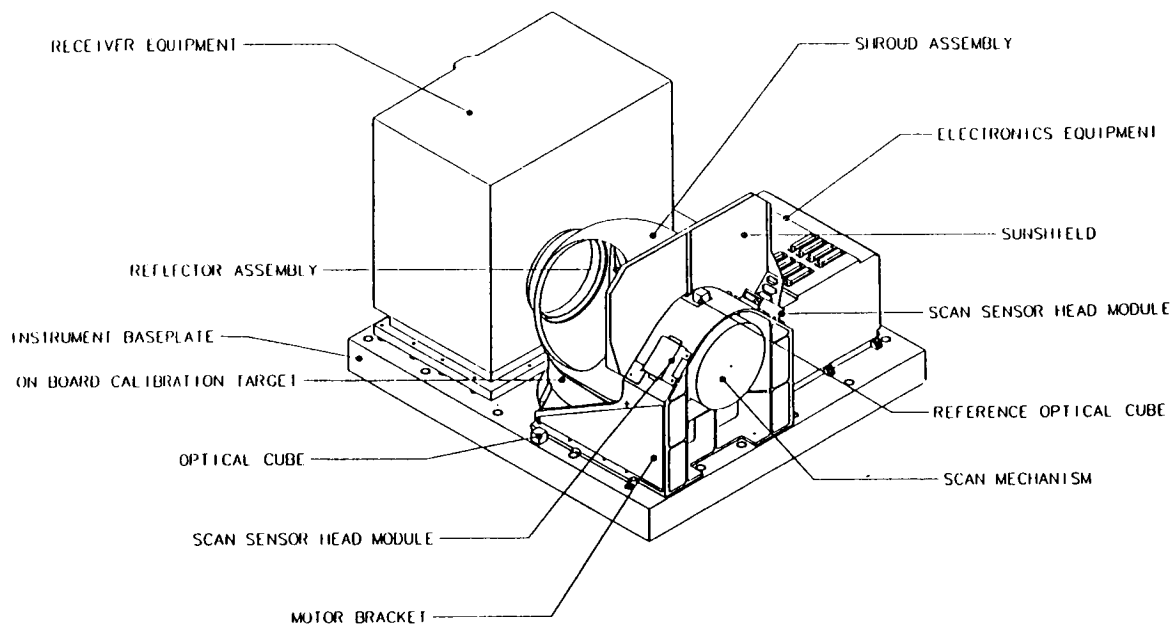
Figure 1. Typical MHS Instrument Configuration
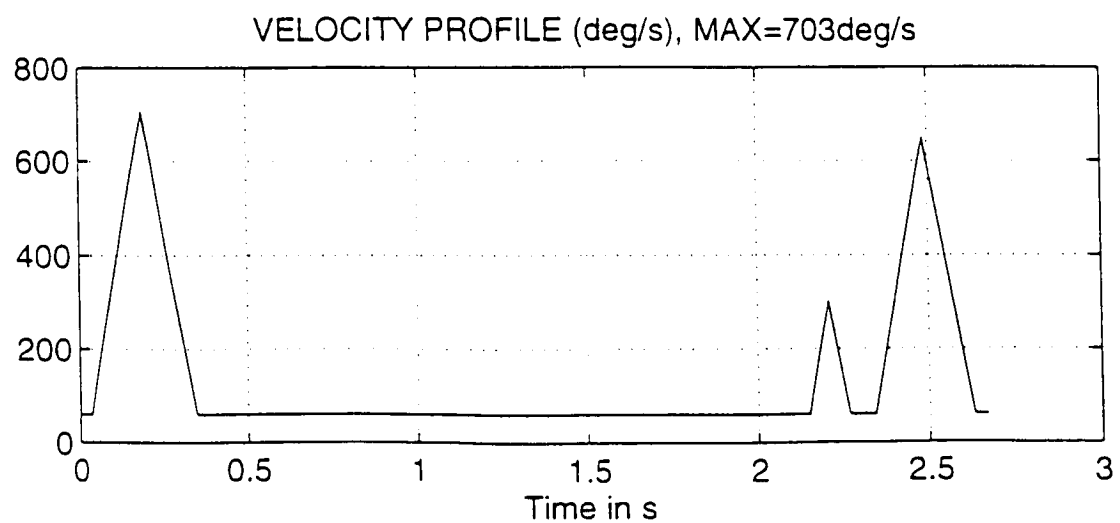
Figure 2. Scan Profile of MHS Scan Mechanism

The scan requirement is to rotate the reflector in a defined manner in response to the selected mode of operation. Within the 360° rotation, the reflector will rotate uniformly during the Earth Scan, will allow a Cold Calibration by pointing to cold space, and will allow a Hot Calibration by pointing to an On-board Calibration Target. Figure 2 presents a typical angular velocity profile for the performance of the required scan profile.

Design Description
The Scan Mechanism consists of four modules, namely the Reflector Drive Module (RDM), the Flywheel Drive Module (FDM) and two Scan Sensor Head Modules (SSHM). The Reflector Drive Module and the Flywheel Drive Module are mounted in a common structure. The Flywheel Drive Module has the task of rotating a flywheel opposite to the reflector rotation in order to compensate for the momentum of the Reflector Drive Module to the maximum extent possible.

The Scan Sensor Head Modules are self-contained small electronics boxes that amplify the low-level signals of the position sensors of both the RDM and the FDM.

Figure 3 presents a sketch of the Scan Mechanism together with its main components.
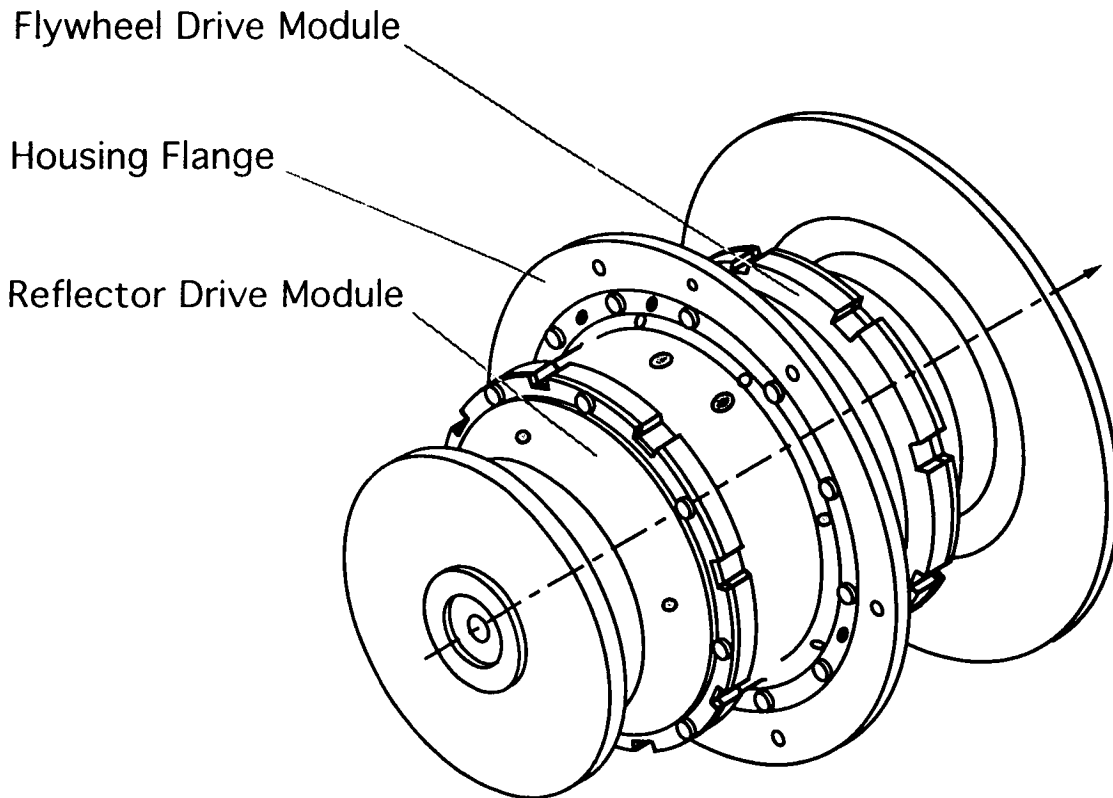
Figure 3.   MHS Scan Mechanism

The RDM and the FDM are identical. Each module contains two bearings which support the shaft, one motor, one position sensor and a set of two switches that can be used to trigger the position zero reference logic of the drive electronic. The two modules RDM and FDM are electrically connected to two independent control loops. In accordance with the scan speed profile, the control loops generate motor current to accelerate, decelerate and rotate the shafts at constant speed. The motor currents are commutated upon output signals from Hall devices that are arranged on the motor windings. For redundancy, there are two sets of such Hall devices.

The position sensors are Inductosyns that possess an excitation pattern on the rotor and 50-speed sine and cosine patterns on the stator. These patterns are printed circuits, which, by the absence of iron, exhibit very low voltage transformation ratios. Therefore, it is necessary to amplify the sine and cosine signals in the Scan Sensor Head Modules that are to be located adjacent to the Scan Mechanism in order to minimize losses and electromagnetic interference. After the amplification, the inductosyn signals can be processed in high resolution A/D circuits, thus enabling the controller to control the speed very precisely. In order to avoid sliprings, the carrier frequency is transferred from the inductosyn stator to the rotor by rotary transformers which are incorporated into the inductosyns.

The zero reference position is triggered by redundant Hall devices in the inductosyns. Their signals only serve to identify the following zero crossover of sine and cosine as the reference.

In order to ensure adequate temperature conditions, two heaters are bonded to the housing surface. The survival heater is wired with a thermostat that triggers it on and off. The operational heater can be switched on and off at any temperature of the mechanism.

For temperature monitoring, the Scan Mechanism is equipped with five thermistors, three of them close to the housing flange, the other two in the central bore of the housing.

The flywheel forms part of the Scan Mechanism. It is composed of a flange ring that contributes the basic inertia and an extra ring that allows adjustment of the actual reflector and shroud inertia. There are 16 equispaced threads in the flange ring that can accept bolts with washers as necessary to dynamically balance the flywheel. Balancing is done in the fully assembled state in the course of the formal test program.

Scan Mechanism Components

Motor

The motors used for the Scan Mechanism are modified RBE 0300 type from Inland. The modifications are the use of space-rated materials, the implementation of redundant Hall sensor for commutation, and the change of lead wire gauges to improve the assembly. The redundant Hall sensors are located on top of the main Hall sensors to yield the same switching position. Winding redundancy is not considered necessary because the average power during nominal operation of about 1 W is low compared to the power at stall of about 16 to 20 W.

Position Sensors

The sensors used for the Scan Mechanism are modified Inductosyn 21910 type from Farrand / Inductosyn International. The modifications are the use of space-rated materials, the implementation of redundant Hall sensors for commutation, and the change of lead wire gauges to improve the assembly. The sensor is composed of a stator part and a rotor part. Two sensors are used in the Scan Mechanism, one for the RDM side, the other for the FDM side. For the detection of the zero position, main and redundant Hall sensors are incorporated 180° apart in the Inductosyn stator. They are triggered by a magnet in the Inductosyn rotor. The Hall sensors used are a space version of a Hall sensor from Optec.

Bearings / Bearing Preload

Every orbit the MHS Instrument will experience a temperature cycle. It is anticipated that the cycling will introduce thermal gradients into the mechanism structure, which lead to differential expansions of housing and shaft. The common solution for space mechanisms to this problem is the choice of angular contact ball bearings with interference fits for all races and preload applied by an axially compliant structural element that is radially stiff. This solution prevents potential jamming of a sliding bearing fit. The elastic structural element is a pair of membranes in the bore of the bearing seating of the outboard bearing each. The preload level is chosen with the aim to prevent gapping of the bearing under quasi-static load condition (30 g). The preload level chosen on both the RDM side as well as on the FDM side leads to a nominal life of 9 years. Preload variations that result from differential thermal expansions of the housing and the shaft will be kept low by the use of an aluminium alloy with high contents of silicon that exhibits a low coefficient of thermal expansion and by limiting the heat flux by the choice of materials.

The bearings used are from UKF with an inner diameter of 35 mm, an outer diameter of 55 mm, and a width of 10 mm. The retainer material is cotton-phenolic. The contact angle is 21° and the load carrying capacity is more than 4000 N. The bearing races from standard bearing steel (100Cr6) are plated with 2.5 µm chrome in order to protect them against corrosion during ground life. The chrome plating process is widely used in the aerospace industry and in the power plant industry. Corrosion of the balls is overcome by the choice of balls made from hot isostatic pressed ceramic (Si_3N_4). Both

materials are well known from terrestrial applications as wear resistant materials that exhibit low friction. For the space application, it is important that they will not cold weld in high vacuum. The cotton-phenolic cage has been chosen in view of the adopted wet lubrication system.

Lubrication System

With respect to the lifetime of 5 years in orbit at an average speed of 22.5 rpm (yielding $59.2 \cdot 10^6$ revolutions) a liquid lubrication system is chosen for the bearings. This promises low average friction and low friction noise. The oil is impregnated in the porous bearing cages that are made from cotton-phenolic and in a reservoir made from sintered nylon arranged between the bearings. The races and balls are wetted by a few droplets of oil during assembly. The total amount of oil in the mechanism is about 3.3 gram.

Oil loss is limited to evaporation by the use of anti-creep barriers in the vicinity of the bearings. The anti-creep barriers, applied to all surfaces leading out of the bearing compartment, exhibit a lower surface tension than the oil, which means that oil creep is stopped at the edge of the barrier. The oil used for this application is Pennzane SHF X-2000.

Such lubrication systems have been used extensively with many different oils in the area of spin stabilized spacecraft in the despin mechanisms of Tiros, OSO, and Intelsat. The spin rates of these mechanisms ranged from 30 to 100 rpm and in orbit lives in excess of 7 years have been achieved. Another application of wet lubrication was with the Solar Array Drive Mechanism for the Hubble Space Telescope. One of these mechanisms has been returned from space in December 1993 and was dismantled and inspected for any signs of wear. The impression was that the bearings looked like new.

Structure Materials

The housing, housing flange and shafts are made from DISPAL S225, an aluminium alloy with the following composition: Si 33 - 35%, Fe 1.8 - 2.2%, Ni 0.8 - 1.2% and Al remainder. It is produced by the "Osprey" process, in which the molten material is sprayed on a turntable where it solidifies instantaneously. By axial motion of the turntable, cylinders of the desired length are grown. Compacting the cylinders by hot pressing is the final production step. As a result of the shock cooling, the alloy exhibits unusual characteristics like a coefficient of thermal expansion of $10.2 \cdot 10^{-6}$ 1/K and a Young´s Modulus which is about 30% higher than for standard aluminium. Since the CTE of the bearing steel of $11.6 \cdot 10^{-6}$ 1/K is almost equal, interference fits for the whole temperature range are possible with very moderate interferences. The shaft flanges and the housing flanges are made from an aluminium alloy and the surfaces are treated with Alodine 1200. The bearing preload membranes are made from a titanium alloy. The tapered intermediate flanges of the shafts are made from stainless steel.

Heaters and Thermostats

Thermofoil heaters from Minco and a thermostat from Elmwood are used. The heaters exhibt a resistance of 135 Ohm. The thermostat switches the survival heater on at -47.2°C ± 2.8 K and opens at -40.0 °C ± 2.8 K.

Scan Sensor Head Modules

The Scan Sensor Head Modules (SSHM) amplify the sine and cosine signals from the inductosyns of the drive modules. The amplifier circuitry uses two operational amplifiers in series per channel. The overall amplification is 1687.5 ± 5%. EMC tests have shown that the sine and cosine signals have to be filtered. Therefore, filter conectors are used.

Figure 4 presents a photo of the PFM Scan Mechanism together with the Scan Sensor Head Modules.

Development Logic

Hardware Breakdown

The design, development and qualification of the MHS Scan Mechanism was performed by the following hardware models of the Scan Mechanism:
- one Breadboard Model Scan Mechanism (BBM)
- one Engineering Model Scan Mechanism (EM)
- one Life Test Model Scan Mechanism (LTM)
- one Protoflight Model Scan Mechanism (PFM)
- three Flight Models Scan Mechanism (FM)

and the following hardware models of the Scan Sensor Head Modules:
- four Engineering Model SSHM (EM)
- two Protoflight Model SSHM (PFM)
- six Flight Models SSHM (FM)

Development Basis

The design of the Scan Mechanism is based on a design concept developed during a Phase B study. It employs an Inland brushless DC motor with Hall effect sensors for commutation control and an inductosyn for position measurement, which is also equipped with Hall effect devices to trigger the zero reference. Both components were determined by the control loop design.

For the Breadboard Model, a master slave drive concept was foreseen. The reflector drive control loop containing the inductosyn was the master that generated the motor drive signal for both reflector drive motor and flywheel drive motor.
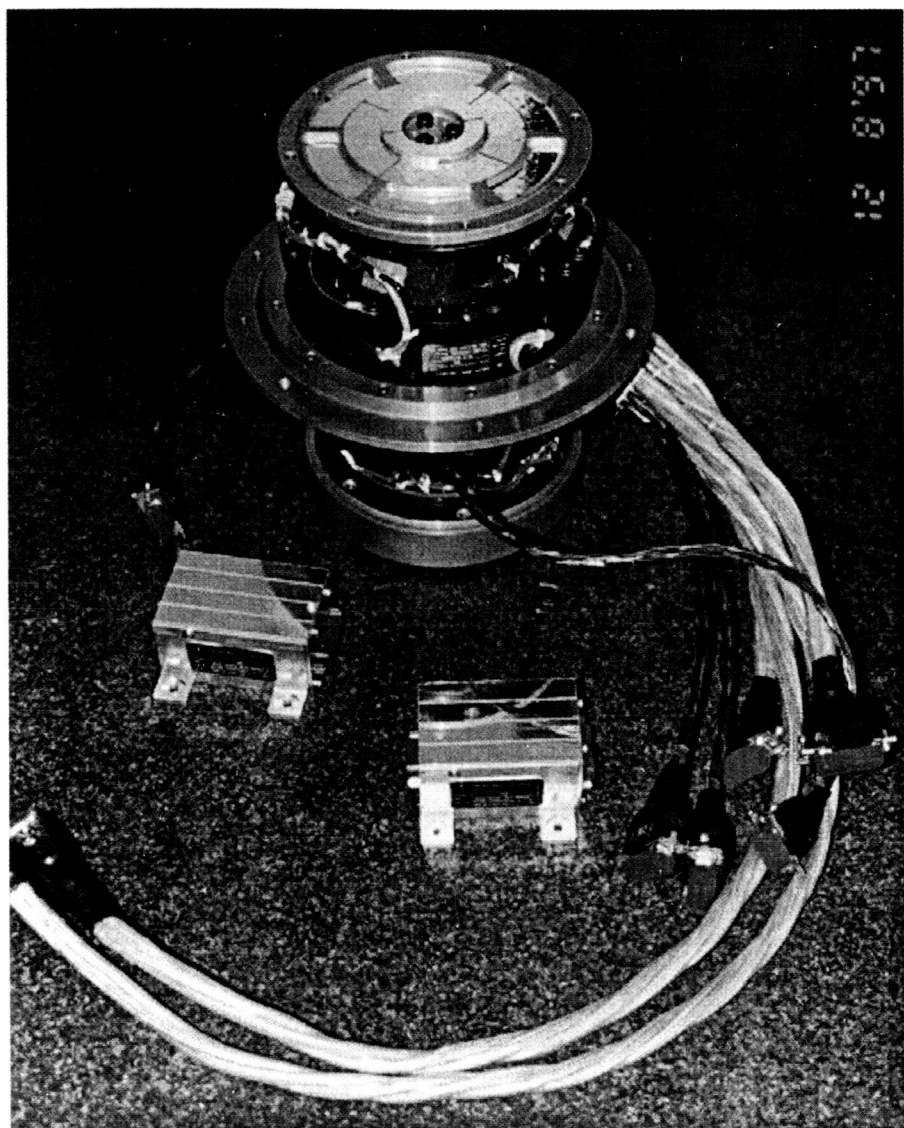
Figure 4.   MHS PFM Scan Mechanism

In order to ensure the correct distance and concentricity of stator and rotor of the inductosyn, this unit was placed next to the reflector flange such that these dimensions could be verified even after completion of assembly of the mechanism.

In the breadboard phase, no vibration test loads nor static loads had been defined. In order to avoid a separate off-load device, rather large bearings with high load carrying capacity were chosen. The large inner diameter of the bearings lead to a large central bore of the structure, which was necessary to provide clearance for the wrench nut during insertion and tightening of the reflector fixation bolt in the original concept. The temperatures assumed in this early phase ranged between 15°C and 35°C. Therefore, a solid preload was considered adequate with the expectation that the change in average friction could be accepted by the control system. Since wet lubrication was not allowed for the Breadboard Model, dry lubricated bearings were installed in the mechanism. The bearings that were actually installed had races from standard bearing steel (100Cr6) with chrome plating, ceramic balls (Si_3N_4) and a Duroid cage. This bearing design features all characteristics necessary for a space mechanism.

The structure of the Breadboard Model was manufactured mainly from aluminium alloy. In view of the moderate temperature range and associated variation of the interference fits of the bearings, this was acceptable. The mass target of 6 kg for the Breadboard Model was met with this structure.

The essential changes for the following models (Engineering Models and Flight Models) with respect to the Breadboard Model are:
- The introduction of a separate inductosyn for the Flywheel Drive Module.
  The Flywheel Drive Module is controlled by a dedicated controller that follows the same nominal speed profile as the Reflector Drive Module. A significant improvement of momentum compensation was realized with this change because differences in friction and motor characteristics are now compensated by the individual control loops.
- The choice of liquid instead of dry lubrication.
  The repeated accelerations and decelerations of the shaft mean cyclic loads at the contacts of balls and retainer that are much higher than in a bearing under uniform rotation and there is concern that excessive wear could result from this in a dry lubricated bearing. Even with boundary lubrication there is separation of the contact surface by the oil film which minimizes wear. Furthermore, the heat transport capability of the oil prevents the formation of hot spots at the cage. Thus wet lubrication is preferred for its higher probability to meet the 5 year life requirement.
- Elastic instead of hard preloading of the bearings.
  The predicted qualification temperatures called for elastic preload to prevent preload variations

- New structural material with low coefficient of thermal expansion.
  The CTE of $10.2 \cdot 10^{-6}$ 1/K of the used DISPAL S225 almost matches the CTE of the bearing steel. Hence interference fits over the temperature range can be achieved with minimum interference and the tensions introduced by temperature gradients between housing and shaft become low. Finally preload variations due to the temperature fluctuations are reduced to 40% of what could occur with standard aluminium alloy.
- New interfaces for reflector and reflector shroud.
- Separate Scan Sensor Head Modules forming part of the Scan Mechanism.

The Engineering Model and Life Test Model Scan Mechanisms and Scan Sensor Head Modules were produced fully representative of the Flight Models (including PFM) in order to ensure a successful pre-qualification of the MHS Scan Mechanism. This means specifically materials and processes, manufacturing activities, test equipment and facilities as well as test procedures. The MIL-STD parts used in the EM and LTM instead of the hi-rel parts of the Flight Models are the same generic parts as the hi-rel version, procured from the same supplier as the hi-rel parts and have the same performances.

The special aim of the Life Test Model is to verify the lifetime requirement of 5 years of the MHS Scan Mechanism and SSHMs including all components. For this, the LTM has performed an Abbreviated Life Test for five months with following dismantling and inspection of the main components such as the bearings and motor. The LTM then was reassembled and its build state was revalidated by dedicated tests. The LTM now is subjected to an Extended Life Test in vacuum conditions lasting until August 2002. There the Scan Mechanism is slewed according to the nominal speed profile.

Verification Philosophy
The Scan Mechanism design was verified by means of the following methods:
- Analysis (budgets, stress, reliability)
- Demonstration and/or design documents (references, interfaces)
- Similarity assessment (parts, material, processes)
- Inspection (mechanical interfaces, marking, surfaces, workmanship)
- Functional test (operation by test electronic)
- Environmental test (vibration, static load, function in thermal vacuum, temperature cycling)
- Validation of records (components traceability, transfer of exemplary test results)

The main contributors therefore are the tests perfomed for qualification and acceptance of the Scan Mechanism design.

40

Qualification Logic

Qualification

The qualification of the Scan Mechanism for its tasks in the MHS Instrument is achieved by the presented design that conforms to the functional requirements, by the selection of components like motor and inductosyn that have been used successfully in other space programs, and last but not least, by the choice of materials and processes that are suited both for space application and pre-orbital life and that are compatible amongst each other and with interfacing hardware.

Though there is no special Qualification Model of the Scan Mechanism, there was qualification level testing on the Engineering Model, the Life Test Model, and the Protoflight Model. Qualification level means quasi-static loads corresponding to 30 g, qualification level vibration and durations, and a thermal vacuum test temperature range widened by 10 K beyond the predicted worst case flight temperature range.

The qualification of the Scan Sensor Head Modules was verified with the PFM modules. However, there were pre-qualification tests with the Engineering Models which are equipped with commercial amplifiers and accompany the EM and LTM Scan Mechanisms. For the Extended Life Test, one Scan Sensor Head Module is equipped with commercial amplifiers while the other one uses the same hi-rel components as the Flight Models.

Acceptance

The Flight Models were manufactured and assembled in accordance with the materials and processes requirements and exposed to the acceptance level test program.

Test Program

During the qualification and acceptance of the Scan Mechanism and the Scan Sensor Head Modules, a complete test program has been performed containing the following tests:

- Scan Mechanism Electrical Properties Test to verify the properties of the Scan Mechanism components at the beginning of life. The main aspects of this test are the measurement of the thermistor resistance values at the actual Scan Mechanism temperatures, the verification of the switching function of the Hall sensors of motors and zero reference, the measurement of resistance values of motors and inductosyns, and the measurement of insulation resistances.
- Scan Sensor Head Module Electrical Function Test to prove the proper function of the electronic boxes prior to the use with the Scan Mechanism.
- Scan Mechanism and Scan Sensor Head Module Mechanical Inspection to verify the mechanical interfaces and physical properties of the mechanism and the electronic boxes.

- Functional Tests to verify the operation of the mechanism together with the Scan Sensor Head Modules at the specified scan profile and the proper function of all main and redundant components before entering the environmental tests.
- Scan Mechanism Torque over Angular Range Tests to verify the overall resistive torque of the Reflector Drive Module and the Flywheel Drive Module at three different speeds. The test is performed prior and post the environmental tests in order to make sure that the bearings did not suffer damage from the environmental test loads.
- Vibration Tests in three axes first to verify the capability of the Scan Mechanism and the Scan Sensor Head Modules to survive random vibration environments and sine burst on qualification and acceptance level and secondly to verify the Scan Mechanism resonance frequency.
- Thermal Vacuum Test on qualification and acceptance level to demonstrate that the Scan Mechanism is capable to start operation after exposure to hot and cold survival temperature conditions and to function properly throughout the specified temperature range. Furthermore, survival of a stall condition was demonstrated with the EM.
- Electro Magnetic Compatibility Test of the Scan Mechanism and SSHMs at standstill and during nominal operation.

To complete the qualification of the Scan Mechanism for life-related aspects, the following additional tests have been performed on the LTM:
- Abbreviated Life Test to prove that there is no degradation of the lubrication system under qualification temperature conditions and nominal scan operation. A decomposition of the oil by temperature effects and/or high pressure and/or shear forces would result in catastrophic wear of the bearings, shown by a significant increase of average torque and torque noise.
- Extended Life Test to demonstrate that the lubrication prevents wear of the bearings beyond the nominal life of five years. By not influencing the mechanism temperature from outside, a stable track of the balls on the races shall be achieved thus maximizing the wear travel. Like in the Abbreviated Life Test, wear would be detected by a rise of average torque and torque noise. The Extended Life Test was started in August 1997 and will last until August 2002.

Lessons Learned

During the development and qualification program the following aspects lead to extensive experiences:
- During qualification level random vibration serious problems with the stiffness of the Scan Mechanism have been encountered, which lead to a redesign of the bearing support concept of the Scan Mechanism.

- During vibration, a problem with the position sensor occurred. In favor of the output level, the gap between the stator and the rotor of the inductosyn had been chosen too close to prevent the parts from harmful contact. This problem lead to a wider gap and to the introduction of additional endstops.
- After the Abbreviated Life Test, the Scan Mechanism was disassembled and thoroughly investigated. No damage was detected during this inspection and the proper function of the lubrication system including the anti-creep barrier was confirmed.
- During the Instrument test preparation at the customer's site, an anomaly was detected on the PFM Scan Mechanism inductosyn. The inductosyn was repaired and additionally qualified. The remaining inductosyns for the other Flight Models were screened and another anomaly was detected on a sensor.

Redesign of Bearing Support Concept
During the qualification level vibration tests of the EM Scan Mechanism it was detected that the stiffness of the bearing was not as high as necessary. This was a result of the bearing support by a single membrane. To reach the required stiffness of the bearing, a double membrane was implemented into the design. With this solution the required stiffness was reached.

Endstop for Inductosyn
During the visual inspection of the EM Scan Mechanism after the qualification level vibration test, particles adhering to the inductosyn housing were detected. After removal of the shaft flange, a damaged area on the inductosyn was detected coming from a harmful contact between the stator and the rotor part of the inductosyn. To enlarge the signal output of the sensor, the gap between the stator and the rotor was chosen too tight. To prevent both parts of the inductosyn from further contact, the gap was enlarged and an endstop made of Vespel was implemented into the design. With this endstop, a contact between stator and rotor is impossible. The design of this endstop is verified by vibration tests performed on the other models up to now.

Abbreviated Life Test
The Abbreviated Life Test was performed in the period November 1996 to May 1997. The aim of the test was to prove that there is no degradation of the lubrication system which could lead to excessive wear of bearing components when the Scan Mechanism is operated at the nominal speed profile under qualification temperatures in vacuum.

The Abbreviated Life Test is followed by dismantling and inspecting the Scan Mechanism. The aim was to prove that there was no degradation of the lubrication system under the aspects
- discoloration of oil
- grease or resin-like deposits next to the ball tracks on the races
- cage material on balls and/or ball tracks

- leakage paths for the oil
- residual amount of oil in the reservoirs
- signs of wear like debris of cage material.

The inspection shows that the lubrication system was all right under the described aspects.

Inductosyn Anomalies

During the electrical integration of the PFM Scan Mechanism to the MHS Instrument, an anomaly was found with the inductosyn output of the RDM side. An isolation check between the Scan Mechanism chassis and the cosine pattern of the inductosyn failed as there was detected a short circuit with approximately 4 Ω. The cause of this short circuit was found to be debris of unknown source that lead to a contact between the printed cosine pattern and the gold layer of the inductosyn. The inductosyn was repaired by removing parts of the gold layer arround the damaged areas, removing the isolating Perylane layer and overcoating these areas with an epoxy adhesive. To verify the qualification of this repair action an additional test program was done on the PFM Scan Mechanism. This test program contains isolation tests of the sensor with 50 volts, vacuum testing and thermal cycling containing ten cycles between -50°C and +70°C. To stress the remaining inductosyns, foreseen for the assembly to the Flight Models FM2 to FM4, the test program containing the isolation tests, the vaccum test and the thermal cycling was initiated on these sensors. During performance of the thermal cycling, an anomaly was detected on another sensor in the way that after performance of about five thermal cycles the resistance of a pattern was floating to open circuit. This sensor is at the time being under investigation at the manufacturer.

Conclusion

The paper has presented details of the design, development and verification of the Scan Mechanisms for the Microwave Humidity Sounder (MHS) Instrument. Up to now the Engineering Model, the Protoflight Model as well as Flight Model 2 have been delivered to the customer. The first launch of a MHS Instrument together with the Scan Mechanism is foreseen for 2002.

Acknowledgement

Cryogenic Scan Mirror Mechanism for SIRTF/MIPS

Robert M. Warden* and Gerald B. Heim*

S4-19
168089
141.
336849

Abstract

A Cryogenic Scan Mirror Mechanism (CSMM) has been developed for the Multi-band Imaging Photometer for SIRTF (MIPS) which is one of three scientific instruments in the focal plane of the Space Infrared Telescope Facility (SIRTF). The design of this scan mirror is based on a mirror mechanism which is currently in operation onboard the Infrared Space Observatory (ISO) Short Wave Spectrometer (SWS). The SWS team provided this design through the University of Arizona, to Ball Aerospace, where it was modified to satisfy the requirements for MIPS. A brassboard unit (figure 1), built to the new design, has been fabricated and tested. This unit is the predecessor to the flight unit and the subject of the testing. This paper summarizes the modifications made to the mechanism, the subsequent testing, and describes the flight design of the MIPS cryogenic scan mirror mechanism.

Background

The design of the SIRTF MIPS instrument[1] incorporates a single axis scan mirror to direct the optical path. Because SIRTF is a far infrared observatory, it must operate at cryogenic temperatures. All instruments and mechanisms within the Multiple Instrument Chamber (MIC) will be launched and operated at about 1.5 Kelvin.

The CSMM is the only moving part in the MIPS instrument and it serves three basic functions. First, it allows for mapping a region of sky by compensating for the SIRTF scan motion with a corresponding mirror motion. Second, it performs "beam switching" to move the MIPS instrument FOV between the desired celestial source and nearby "blank" sky. Third, it is used to move and hold the mirror in one of several specified positions to direct light into the appropriate optics for each MIPS observing mode.
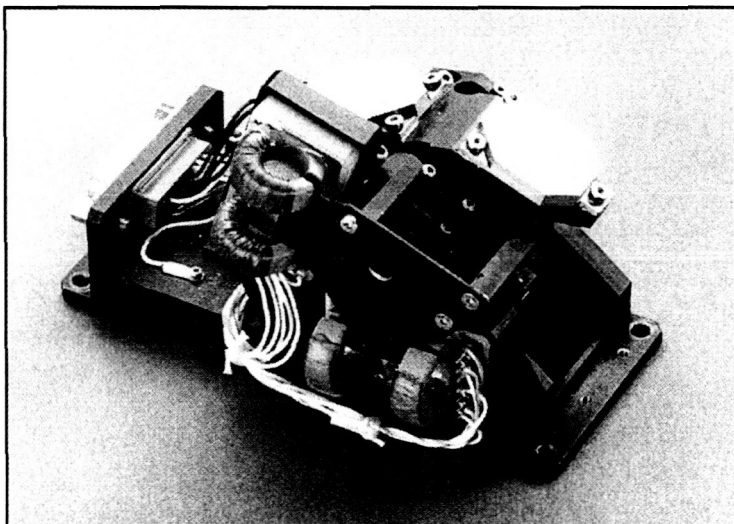
Figure 1. CSMM Brassboard Unit

*Ball Aerospace and Technologies, Boulder, Colorado

The CSMM is a limited angle rotation device (±7.5 degrees) which uses steel flexures to support the mirror while allowing it to rotate without wear or friction. A linear voice coil motor is offset from the center of rotation to provide the actuation force needed to rotate the mirror. Stable and accurate position sensing is obtained by means of redundant differential impedance coils. This scan mirror is not a fast steering mirror; the MIPS requirement for closed loop bandwidth is only about 10Hz.
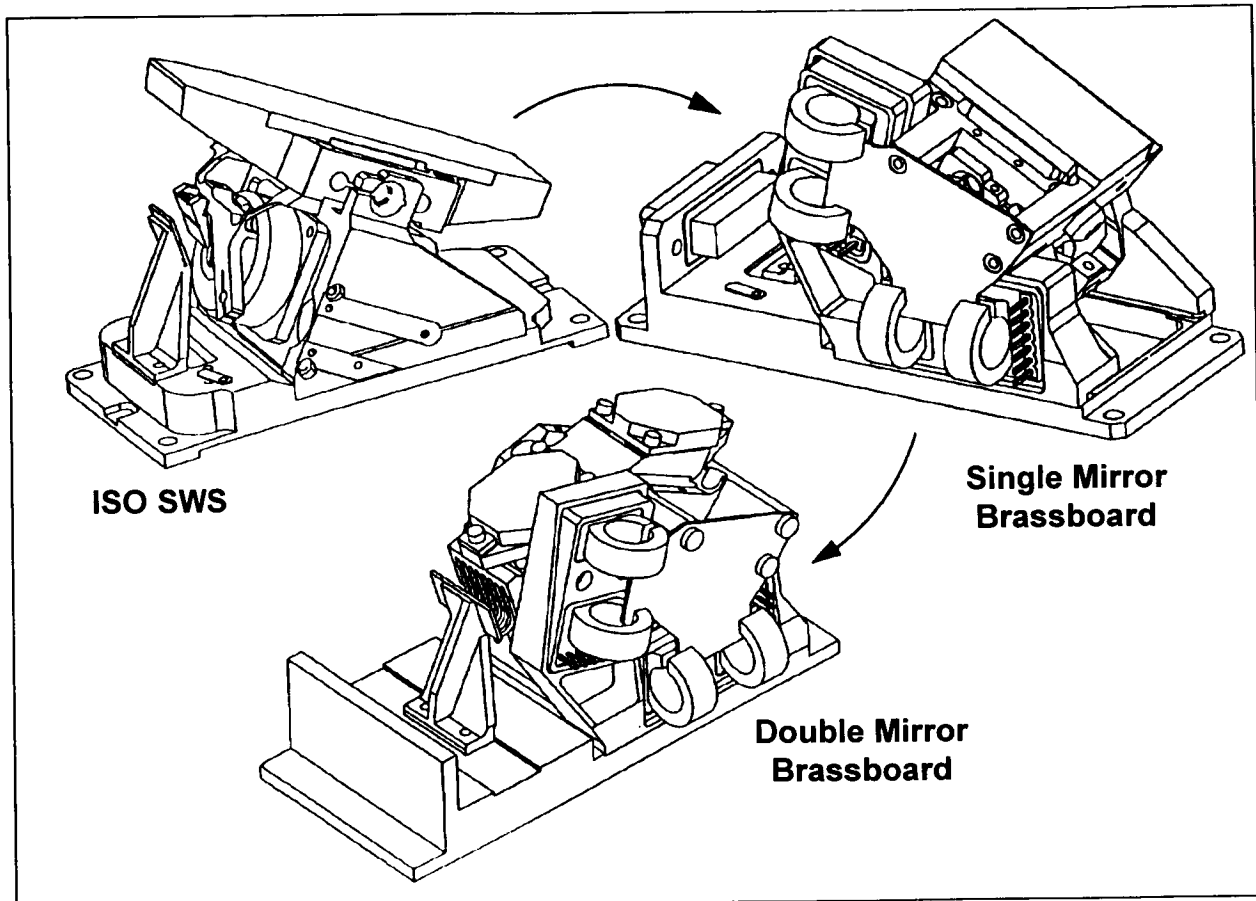
Figure 2. Scan Mirror Evolution

The scan mirror assembly consists of two main sub-assemblies. The fixed portion is made up of the base, frame, magnet and housings. The rotating portion is made up of the mirror carrier, the two mirrors and the coil assembly. Figure 2 shows the evolution of the scan mirror design. The original ISO SWS scan mirror[3,4] is shown in the upper left hand corner. This design was modified at Ball by incorporating a new position sensor in the first MIPS brassboard unit as shown in the upper right hand corner of Figure 2. This unit was later modified to support two mirror surfaces resulting in the brassboard unit shown in Figure 1 and the lower drawing in Figure 2. The brassboard design was further modified to produce the flight CSMM design shown at the end of the paper.

46

Problem Statement

The purpose of this design effort was to adapt the ISO SWS scan mirror design to satisfy the requirements for MIPS. To this end, four separate tasks were identified.

1. Reduce power dissipation at cryogenic temperature.
2. Assess the reliability of the flexural elements in the CSMM.
3. Mechanical redesign to satisfy optical requirements.
4. Develop and verify a mathematical model of the mechanism.

Following the description of these tasks is a summary of the flight CSMM.

Design Solution

1. Reduce power dissipation

The operational lifetime of the SIRTF instrument is closely related to the power dissipation in each instrument and, therefore, much emphasis is placed on minimizing the power dissipation in all of the cryogenic elements in the instruments. In addition, power dissipated in the CSMM could raise its temperature and result in excess background flux in the MIPS instrument. To reduce the power dissipation of the CSMM, the MIPS team modified the ISO design by substituting superconducting wire for the copper wire used in the voice coil actuator (Figure 3) and by redesigning the position sensor.

Figure 3. Cross Section View of CSMM

The ISO scan mirror uses standard copper wire in the voice coil actuator. This coil dissipates 0.65mW at the maximum deflection of 7 degrees. The MIPS design team investigated several alternatives for a lower power substitute for the copper actuator wire before settling on a superconducting wire manufactured by Supercon. This wire is made up of 54 filaments of a niobium titanium alloy which is supported in a copper matrix. The critical temperature for this wire is about 9.5 Kelvin.

The copper in the wire allows the mechanism to be operational at ambient temperature, although the resistance of the coil at this temperature is about 400Ω. Using this wire, power dissipation in the mechanism at maximum deflection when operated below the critical temperature is so small that it is practically unmeasureable. When making the voice coil actuator, two coils are wound on the coil former to provide redundancy in case one of the coils should fail in operation.

The ISO SWS scan mirror uses a linear variable displacement transducer (LVDT) to provide position feedback information. The ISO LVDT power dissipation is about $350\mu W$. The MIPS team replaced the LVDT with a new position sensor which is based on a sensor design developed at Ball for another application[2]. The new

Figure 4. CSMM Position Sensor

sensor, a differential impedance transducer, provides slightly reduced position accuracy when compared with the LVDT but with much lower power dissipation. The CSMM position sensor relies on a pair of transformers, each wound on a slotted torroid. Both transformer primaries are fed by a constant amplitude 10KHz sine wave. An aluminum vane, which is attached to the rotating scan mirror, moves in the slots cut in the torroid as shown in Figure 4. The vane is designed such that as the mirror rotates in one direction, the amount of aluminum in the slot for one transformer increases while it decreases for the second transformer. Eddy currents in the aluminum vane cause the coupling between the primary and secondary of the transformer to change relative to the amount of aluminum in the slot. Both of the transformer secondaries are fed to a differential amplifier in the electronics and then demodulated and filtered to produce a signal which is directly proportional to the scan mirror angle. The power dissipation of this position sensor is less than $100\mu W$. Two sets of position sensors are included in the flight CSMM design for redundancy.

48

2. Flexural Elements

Functional Description

The CSMM has only two moving parts and both are flexural by design. In this way, all of the friction and debris problems associated with sliding surfaces are avoided. The two parts are the mechanical support flexures and the electrical contact flexures. This design was originally used in the ISO SWS mechanism, but further understanding of the operation was needed for the SIRTF program.

The mechanical flexures are used to support the rotating part of the mirror. For both MIPS and SWS, two 3/16 inch diameter Lucas Flex Pivots are used. The rotating mass is subject to three forms of loading. First is simple launch vibration. The flex pivot is rated at about ten times the estimated launch load so this requirement was satisfied by analysis. Second is life or fatigue. Again, analysis showed that the pivot should survive ten times longer than the required life. The CSMM was also life tested to verify that the pivots would survive. The third load case is impact loading due to the rotating mass hitting the end of travel stops. This is important because the steel used in the flex pivot has decreased impact strength at cryogenic temperatures. Analysis and testing have confirmed that impact loading is not an issue. Provided the rotating mass is well balanced, it will not hit the end of travel stops during launch.

The electrical flexures are used to electrically connect power to the voice coil. A simple service loop allows the mirror to rotate (see Figure 3) but this loop must survive the launch vibration as well as the millions of cycles expected over the mission. The SWS mechanism used 0.01 mm stainless steel for the electrical flexure. This material, however, did not satisfy the MIPS life requirements, so there was a need to increase the life of the flexure, while maintaining the flight heritage.

The solution was to change the material to Beryllium Copper which has much greater fatigue strength but otherwise has similar mechanical properties. This material is also easier to solder to and is a well understood spring material. Analysis showed infinite life for this material in this application.

Testing of Flexural Elements

An analysis of the MIPS instrument operation predicted that the CSMM will need to survive approximately 3 million cycles during its 2.6 year lifetime. 100,000 of these cycles are large scale deflection angle changes on the order of 7.5 degrees. The remaining 2.9 million cycles are small angle operations, ±1 degree. A safety factor of 2x was applied to this lifetime estimate for the CSMM operational lifetime requirement.

In order to verify that the CSMM flex pivots and electrical flexures would survive over this lifetime a number of tests were performed:

1) Five pairs of flex pivots were cycled end to end (±7.5 degrees) 1 million times in the engineering brassboard CSMM at ambient temperature
2) A sixth pair of flex pivots was installed in the brassboard, cycled end to end (±7.5 degrees) 1 million times at ambient temperature plus 800,000 cycles at 77K plus 440,000 cycles at 4K.
3) This same set of flex pivots was then subjected to a two minute long 77K random vibration test which simulated the expected launch load on the mechanism (see vibration test description below).
4) Finally, this same set of flex pivots was cycled ±1 degree for 6 million cycles at room ambient temperature.

The same electrical flexures were used throughout tests 2, 3 and 4. Not a single flex pivot or electrical flexure failed or showed any signs of degradation during this testing.

As mentioned before, there was a concern that the rotating mirror would hit the stops during vibration. Analysis showed that this would not happen, but a simple cryogenic vibration test was performed on the brassboard CSMM to verify this analysis before proceeding with the design of the flight unit. The mechanism was vibrated at 77K instead of 1.5K because Liquid Nitrogen could then be used to cool the mechanism. Material properties of the structural elements are similar enough between these two temperatures.

Figure 5. Cryogenic Vibration Test

During launch, the SIRTF instruments will be held at cryogenic temperature. The purpose of the vibration test was to simulate the expected mechanism launch load and temperature. The test setup for the cryogenic vibration test is shown in Figure 5. In this test, an insulating box was used to cover the head of the vibration table. Liquid Nitrogen was used to cool a cold plate and also to purge the box.

Once temperature was reached, the vibration test was performed. The CSMM was vibrated for 2 minutes to the PSD level shown in Figure 6. During launch, the drive electronics will not be powered and therefore during this test the CSMM actuator drive current was disabled. The CSMM position sensor output was monitored and the maximum CSMM deflection angle measured during this vibration test was only 0.2 degrees.
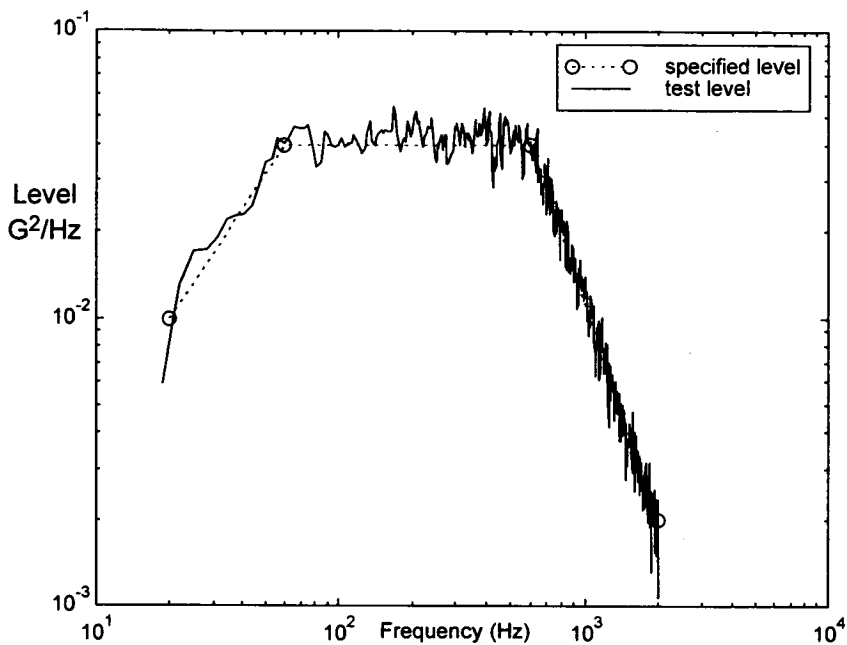
Figure 6. CSMM Random Vibration Test Level

At the conclusion of this test the flex pivots and the CSMM were visually inspected under a microscope and no signs of degradation were found.

3. Mechanical Redesign

The scan mirror used in the ISO SWS instrument was close to what was needed for the MIPS program, but several modifications were necessary to satisfy all the requirements. Mechanical redesign was needed to accommodate the new position sensor, but there were two changes that were needed to satisfy the optical requirements.

First of all, travel of the CSMM needed to be increased from ± 7.0° to ± 7.5°. To achieve this, material needed to be removed from the voice coil core without significantly modifying the properties of the motor. This modification proved to be fairly straight forward, but a detailed tolerance analysis was necessary to ensure that the operation of the mirror would not be degraded by variations in the machining or assembly of the unit. Intermediate dimension checks were used on sub-assemblies to monitor tolerance build-ups.

A magnetic analysis was also performed to verify that changes in the shape of the core and housing would not affect the magnetic flux of the motor.

The second change was to redesign the mirror to incorporate two mirror surfaces which could be individually removable. To do this, a new mirror carrier was designed to replace the old mirror. The new mirror carrier is based on the geometry of the ISO SWS mirror body with features added to attach the two mirrors. Raised pads enable the interface surface on the carrier to be diamond turned. The total mass and static balance was maintained so as to preserve as much of the previous design as possible.
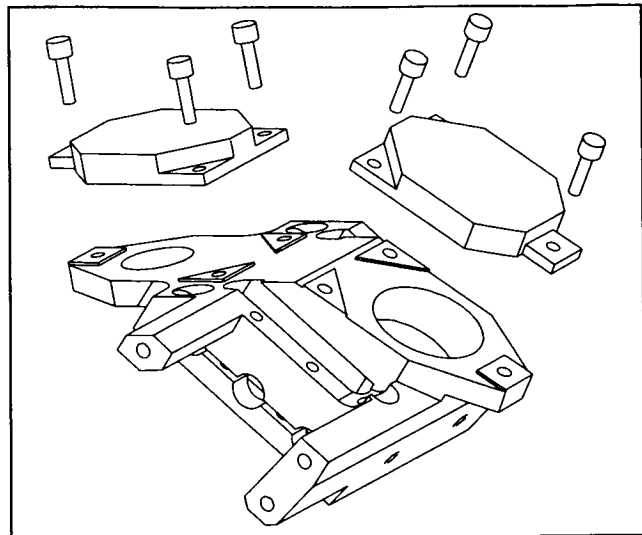
Figure 7. Removable Mirror Config.

The new mirror design was performed on I-Deas Master Series CAD Software. Using this tool, the parts could be modified so as to shift the center of mass of the rotating mirror assembly to line up with the center of rotation. Balance weights were incorporated to accommodate variations in machining.

Magnetic Analysis

The CSMM is powered by a linear voice coil motor but instead of a linear travel, the coil is mounted on a pivoting carrier which is supported by two flexures. The philosophy of the motor design was to make the stationary parts heavier in order to make the rotating parts lighter. This reduces the moving mass and therefore allows the system to respond faster. Also, the power required by the electronics to position the motor is reduced. The magnet is made of Samarium Cobalt and the core and housing are made of a high permeability steel. The design is such that minor changes in the core and housing do not change the properties of the motor. This also makes the motor very stable over a broad temperature range which is desirable for a cryogenic mechanism.
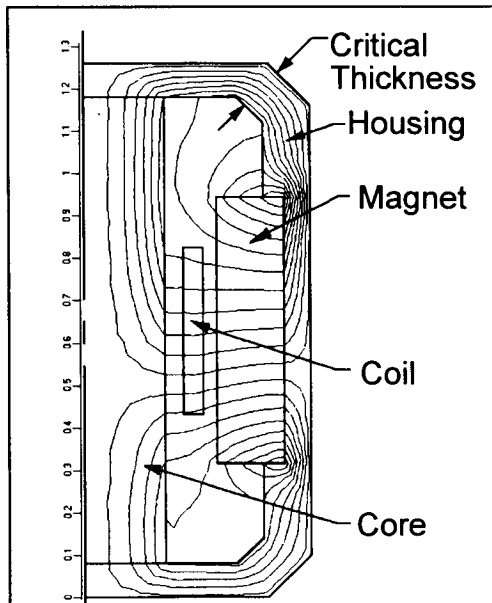
Figure 8. Magnetic Diagram

The original configuration of the CSMM brassboard model fit fairly well into the MIPS flight envelope but some mechanical redesign was needed to satisfy the optical and packaging requirements. This redesign required that the motor housing be modified and there was concern that the redesign would change the properties of the motor.

In the magnetic analysis of the motor system, it was found that certain thicknesses in the motor housing were critical to the flux path. The outer corner of the motor was chamfered in order to package the CSMM in the specified volume. To maintain the flux path, the inner radius was increased. Magnetic analysis of the two configurations were compared and found to have similar flux paths.

4. Mathematical Model

A model was developed for the CSMM in order to predict the reaction of the CSMM when deliberately unbalanced and subjected to a vibration sine sweep. The complete model for the unbalanced mechanism is shown in Figure 9. In the model, the unbalanced mass produces a torque input to the CSMM. The model for the mechanism is a simple, damped spring mass system. The position sensor is modeled as a second order low-pass filter.

Torque Input

Mechanism Deflection Angle

$$w \times a \times l$$

Unbalanced Mass

$$\frac{1}{Js^2 + D_m s + K_f}$$

Mechanism

$$\frac{K_s \omega_n^2}{s^2 + 2\omega_n D_s s + \omega_n^2}$$

Position Sensor

Voltage Out

Where:
- w = weight of unbalancing mass (oz)
- a = acceleration due to vibration (g)
- l = moment arm length (inches)
- J = moment of inertia of mechanism (oz-in-sec^2)
- D_m = mechanism damping (oz-in-sec/radian)
- K_f = spring constant of both flex pivots (oz-in/radian)
- K_s = position sensor gain (volts/radian)
- ω_n = position sensor cutoff frequency (radians/sec)
- D_s = position sensor damping (dimensionless)

Figure 9. CSMM Mathematical Model

When a force (torque) is applied to the mechanism, it rotates and eddy currents are induced in the aluminum coil former. These eddy currents induce a magnetic field which produces a force in opposition to the applied force. Thus, the eddy currents provide a damping force for the mechanism. This damping will help stabilize the mechanism during launch.

Test data from the original ISO SWS mechanism showed that the mechanical damping of the mechanism (D_m) actually increased at cryogenic temperatures by a factor of 2.86 over the room temperature. This increased damping is due to the increase in the eddy currents flowing in the aluminum coil former caused by a reduction in the electrical resistance in the aluminum at the cryogenic temperature.

The model was used to predict the vibration test results using the following parameters:

w	= 0.028 oz
a	= 0.7g peak
l	= 0.76 inches
J	= 3.4 oz-in-sec^2
D_m	= 0.1797 oz-in-sec/radian (@300K)
D_m	= 0.1797 * 2.86 = 0.5139 oz-in-sec/radian (@77K)
K_f	= 11.29 oz-in/radian
K_s	= 88.54 volts/radian
ω_n	= 2*pi*200 radians/sec (200Hz bandwidth)
D_s	= 0.707

The moment arm of the unbalance weight (l) and the moment of inertia (J) of the mechanism were measured using the I-DEAS mechanical model. The damping at 300K and the spring force of the flex pivots was taken from data provided for the original ISO SWS mechanism. The position sensor is designed for a bandwidth of 200Hz.

Using these parameter values, a Matlab model was used to determine the response of the deliberately unbalanced mechanism vs. frequency for both the 300K and 77K temperature. The results of this model are shown in Figure 10. The voltage output of the model was multiplied by a gain of 1.5 volts/degree to produce the plot shown in this Figure.

As Figure 10 shows, the model predicts a slight resonant peak at about 7Hz at 300K. The 77K data in Figure 10 shows that the increased damping has eliminated the resonant peak.

Also note in Figure 10 that the response of the mechanism is quite small beyond 100Hz and therefore the position sensor bandwidth of 200Hz does not affect the modeled or measured data.

54

CSMM Mathematical Model Verification test

The brassboard CSMM was artificially unbalanced using a simple washer which was attached to the side of the scan mirror with a screw. This configuration was then subjected to a sine sweep from 4Hz to 200Hz both at 300K and 77K (using the same cryogenic vibration test setup as was used in the random vibration test shown in Figure 5). The test results are shown in Figure 10 along with the predicted results. Figure 10 shows that the model agrees quite well with the actual values. Again, the voltage output of the position sensor was multiplied by the transfer gain of 1.5 volts/degree to produce this plot. Testing at these low frequencies and low temperatures is difficult. However, the test data does show that the model accurately predicts the response of the CSMM to the unbalanced vibration input at both 300K and 77K.
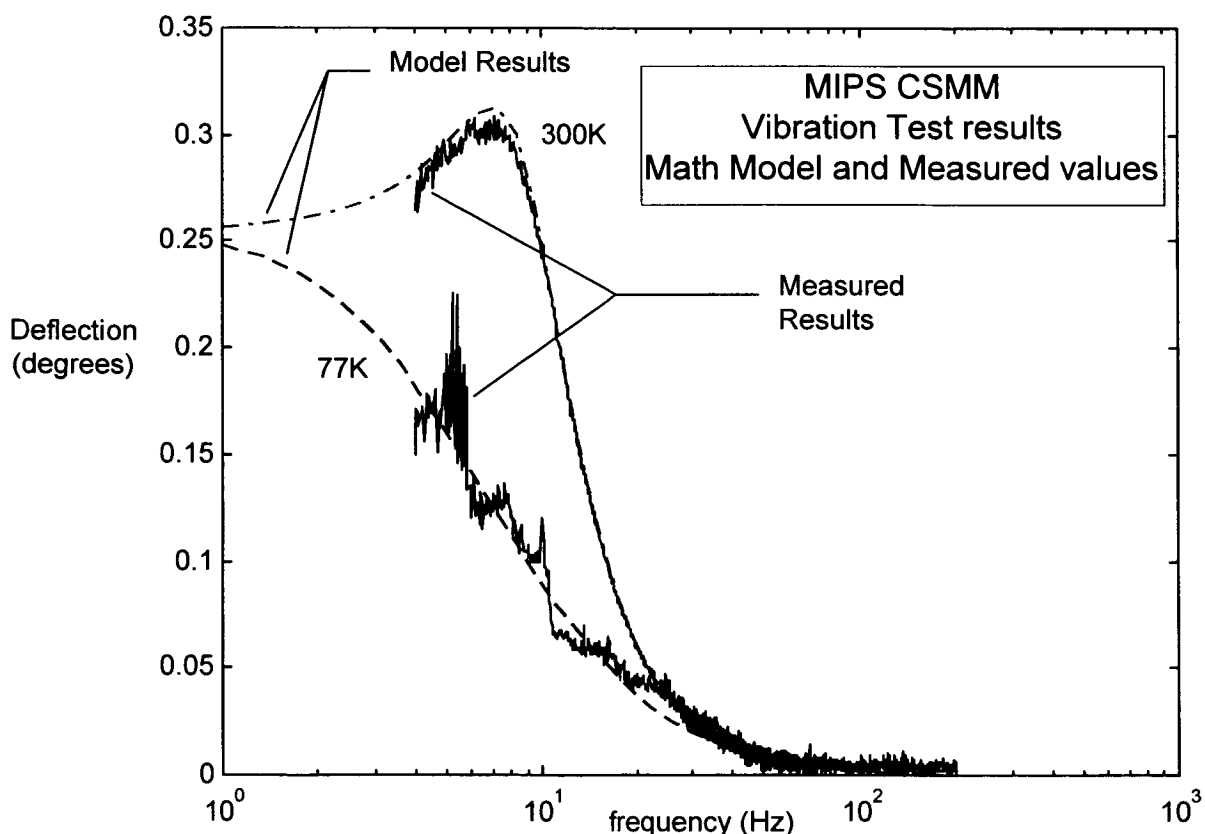
Figure 10. 300K & 77K Vibration Test Data and Model Results

Description of the Flight CSMM

Figure 11. CSMM Flight Configuration

Summary of properties
Flight CSMM

- Single Axis Rotation
- Operating Temp. <2K to 300K
- Scan Angle: +/- 7.5°
- Weight: 362 grams
- Size: 63 x 61 x 120mm
- Power Dissipation:
    <0.5mW at 2°K
- 1° Step & Settle < 0.2 sec
- Precision: < 2 arcsec RMS
- Removable mirror facets
- Redundant Actuator Windings
- Redundant Position Sensors
- Linear Voice Coil Actuation
- Position Sensor Mode:
    Differential Impedance
- Structure: 6061-T651
- Insulation: G-10 Fiberglass
- Connector Interface: MDM-25
- Precision Mirror Lyot Stop
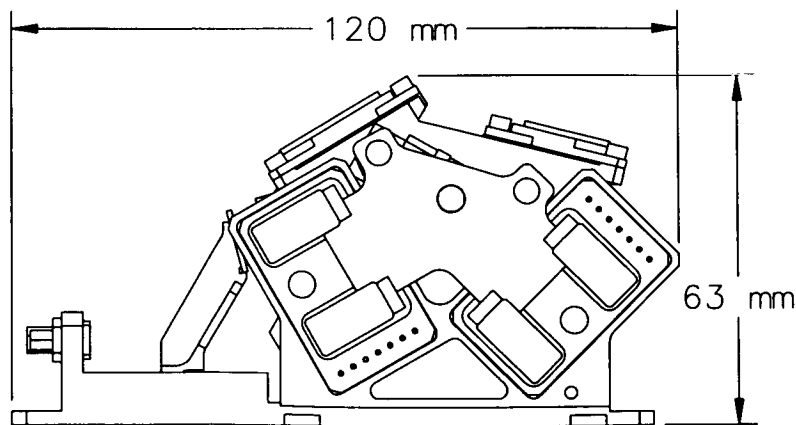
Figure 12. Physical Dimensions

56

Conclusion

Ball Aerospace has constructed an engineering brassboard model of the CSMM to test the performance of the mechanism, motor, and position sensors at ambient and cryogenic temperatures. The results of this testing show that the design meets all requirements of the MIPS instrument. Preparation is now underway to construct, test and integrate the flight unit in anticipation of a SIRTF launch in 2001.

Acknowledgments

References

1. Thompson, C.L., Rieke, G.H. and Young, E.T. "Compact and Versatile Far-Infrared Imager for SIRTF" *SPIE Proceedings* Vol 2475, April, 1995, 449-455

2. Downey, C.H., Houck, J.R., Kubitsckek, M.J., and Tarde, R.W. "Arcsecond Grating Drive Mechanism" *Cryogenics* Vol 31, December, 1991, 1030-1037

3. Aalders, J.W.G., Wildeman, K.J., Ploeger, G.R. and Van Der Meij, Z.N. "New Developments with the Cryogenic Grating Drive Mechanisms for the ISO Spectrometers" *Cryogenics* Vol 29, May, 1989, 550-552

4. Wilkeman, K.J., Beintema, D.A., Ploeger, G.R., Snel, D. and Wijnbergen, J.J. "Grating Drive for the Short Wavelength Spectrometer in ISO" *Cryogenics* Vol 27, February, 1987, 68-72

Development of a Mirror Pointing Mechanism for an Atmospheric Gas Measurement Instrument

Michael Graham* Adel Belous*,
Jeff Brown** Dr. James Podolske**

Abstract

Development of the Open Path Tunable Infrared Monitor of the Atmosphere (OPTIMA) instrument involved designing a pair of motion systems that could maintain a precise alignment and spatial distance between two mirrors installed on the NASA DC-8 research laboratory aircraft. This is the first airborne optical instrument that allows direct measurement of the gases in the freestream airflow on the exterior of the aircraft. One mirror is mounted within a specially constructed open port cavity in the cabin of the aircraft and the second is mounted 6 meters away on top of the inboard port side (number 2) engine pylon. Three co-aligned laser beams are reflected between the two mirrors 64 times in a Herriott pattern. The resulting sample path length of 384 meters is used to perform a spectral absorption analysis of the airflow between the mirrors. To compensate for normal wing movement and engine oscillations both mirrors were designed as continuously driven mechanisms to maintain alignment within allowable limits. The motion systems of the two mirror assemblies provide five degrees of freedom and are designed to maintain a pointing accuracy within seven arc-sec with a response frequency in excess of 10 Hz. The pylon motion system incorporates controlled pitch and yaw movement. The fuselage motion system compensates for pitch variation as well as linear translation for focal length and vertical aiming of the laser beam via a controlled beam guidance mechanism.

Introduction

The OPTIMA instrument was designed to make direct in-situ measurements of nitric acid and nitrogen dioxide. The previous methods used to determine the quantities of these gases have yielded results of doubtful accuracy. Generally, measurements of these gases have been derived from theoretical relationships to other compounds being measured. On the occasions where actual measurements were made they did not correlate to the theoretically derived quantities.

To obtain appropriate sensitivity and accuracy the operation of the OPTIMA instrument is based on differential absorption of tunable infrared (IR) lasers, a proven technique used on various instruments developed over the last 20 years. To minimize the effects of water absorption and atmospheric pressure, measurements are made in the upper troposphere and lower stratosphere (6-12 km). OPTIMA provides an optical path through which two infrared laser beams are directed. As the beams travel this path,

* Sverdrup Technology, Ames Division, NASA Ames Research Center
** NASA Ames Research Center

they encounter molecules of the target gases that absorb a portion of the light energy. Analysis of the signal difference at the start and end of the optical path indicates the quantity of the gases encountered. In order to get the resolution down to 3 to 16 parts per trillion of volume, the optical path includes a Herriott pattern.

Generally, Herriott patterns are generated in a Herriott cell, a cylinder with two fixed spherical mirrors at either end. One of the end mirrors has an optical opening through which a laser is directed to strike the reflective surface of the opposite mirror. The beam reflects between the two mirrors a prescribed number of times before it exits the opening through which it entered and is directed to a detector for analysis. The path the light takes within the cylinder is called a Herriott pattern and the number of passes produced is determined by the relationship of the spherical radii to the distance between the mirrors. By using a Herriott cell a relatively long path length can be generated in a small physical space.

When a Herriott cell is used the sample has to be ducted into the cylinder for evaluation. The OPTIMA instrument removes the cylinder walls and creates the first known actively aligned multipass Herriott "cell" with an open absorption path that allows the direct detection and measurement of the target gases in the airflow between the two mirrors.

General Description (Figure 1)

A Fuselage Pressure Box is attached at a modified window opening on the interior of the aircraft to provide an open port cavity to the exterior of the aircraft. An optics table is attached to the top of the Fuselage Pressure Box where two specially selected and tuned infrared lasers are co-aligned with a visible laser into a single beam. This single combined beam is directed via fixed turning mirrors through an optical window into the Fuselage Pressure Box and onto the surface of the Beam Guidance Mirror Assembly (BGMA). The beam then passes through an opening in the Fuselage Pitch Motion Base (FPMB) and on to the Pylon Mirror Motion Base (PMMB). The reflective angle of the BGMA is constantly adjusted over a 3 degree range to compensate for vertical motions of the wing at the number 2 engine pylon. The beam is then reflected between the mirrors of the PMMB and FPMB in a 64 pass Herriott pattern in the airflow between these two locations. The mirrors are kept face to face by pitch mechanisms in both the PMMB and the FPMB that respond to vertical wing movement, while rotational motions of the engine pylon are compensated for by the yaw mechanism of the PMMB. This alignment is maintained by feedback from a pair of visible lasers set to strike two position sensing detectors (PSDs). The vertical motion of the pylon also affects the distance between the two reflective surfaces. This focal length is held constant by attaching the FPMB to a linear translation stage. As the beam completes the Herriott pattern, it returns to the BGMA where it is reflected out of the Fuselage Pressure Box and back onto the optics table. The combined beam is separated into the three component beams with the visible beam directed to a third PSD to provide positioning feedback for the adjustment of the BGMA angle and the focal length of the Herriott

60

pattern. The infrared beams are then guided to detectors where the remaining signal is analyzed.
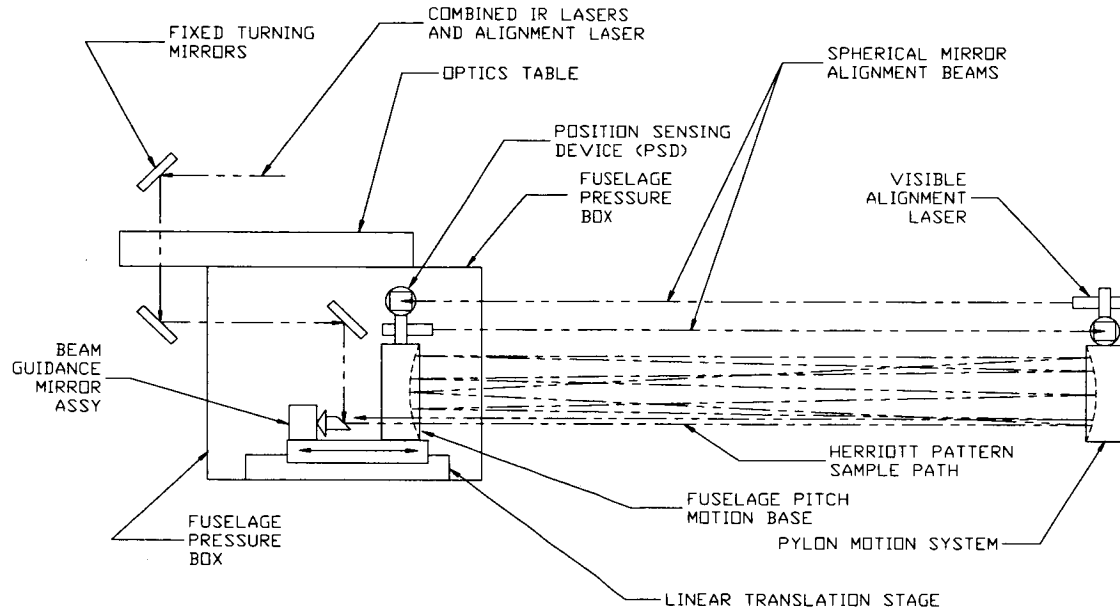
Figure 1. General layout of OPTIMA instrument

<u>Design Considerations</u>

The initial concept was to have a fixed mirror mounted on top of an inboard engine pylon of the NASA DC-8 aircraft. At the fuselage, near the leading edge of the wing, a window would be removed and a structural box attached to the window frame on the interior of the fuselage wall **(Figure 2)**. The cavity of this Fuselage Pressure Box would house a special mirror mounted to a pointing mechanism that would compensate for the expected movement of the mirror placed on the pylon. Pitch rotation, vertical translation and focal length translation would be the only motions required and that these could be incorporated into the fuselage mechanism.

A series of measurements of the DC-8 aircraft were made to determine the relationship of the component locations. These included static ground measurements with and without fuel loads as well as in-flight measurements to quantify the relative displacements at the proposed locations of the OPTIMA components. Analysis of these results indicated that 5 degrees of freedom would be required to accommodate the measured deflections. Pylon motions were more complex than anticipated and would require inclusion of a yaw motion and a second pitch motion. Provisions for accommodating the tracking system components would have to be made. All of the

61

exterior components would have to be protected during ascent, descent and ground activities. The inboard unit would be enclosed in its cavity, but a special housing would have to be built for the pylon module. Both the cavity and the pylon housing would incorporate shutter mechanisms for protection of the optical surfaces and mechanisms within.

Figure 2. OPTIMA Fuselage Pressure Box / Optics Table installed on fuselage wall of DC-8 with the No. 2 engine pylon and pylon mirror / fairing visible out the exit door.

Size would have to be minimized to simplify packaging. Any additions to the exterior of the aircraft had to be evaluated for its aerodynamic impact. This was particularly true at the engine pylon unit as it sat immediately in front of the leading edge of the wing and just aft of the engine intake. A special fairing was required to minimize airflow disturbance. There was a possibility that the mirrors themselves would be subjected to buffeting from impingement of the freestream airflow while the shutters were open during operation as well as the chance of acoustic effects. Provisions for mounting fences to deflect airflow "over" the openings were therefore incorporated into the design.

The mechanisms also have to be able to operate under severe environmental conditions. Temperature excursions of the ambient air in excess of 80 degrees C are not unusual. Thermal stability of the materials selected would be important to maintain critical optical alignments and mechanical tolerances. The temperature excursions would also lead to severe condensation of water on the instrument. This could lead to corrosion of mechanical components, water damage to the mirror surfaces and effects on the electronics.

62

Mechanism Description

The OPTIMA mirror alignment mechanism can be broken into two main component systems: the Pylon Mirror Motion Base (PMMB) and the Fuselage Mirror Motion Base (FMMB). The FMMB consists of three main subassemblies: the Fuselage Pitch Motion Base (FPMB), the Beam Guidance Mirror Assembly (BGMA) and a linear translation stage.

Spherical Mirror Assemblies

Both the PMMB and the FPMB contain spherical Mirror Assemblies, consisting of a specially shaped block of dimensionally stable glass, 4 cm X 10 cm X 30 cm (1.5 in X 4 in X 12 in) and approximately 3 kg (6.6 lb). The mirrors are bonded into 0.7 kg (1.5 lb) four sided frames made of Invar which have flanges to allow fastening to their respective motion base inner housings. This arrangement allows for easy change out of the mirrors with relatively minor adjustments to reestablish the proper position. The fuselage mirror has a small notch along one long edge as a pass through hole for the entrance and exit of the Herriott pattern laser beam.

Mirror Pointing

Mirror pointing is accomplished using accurately controlled limited rotation torque motors to drive specially designed ramped motion cams. The PMMB, FPMB and the BGMA all use the same basic method but the smaller overall size of the BGMA requires the downsizing of the components used in the other units. This method converts the relatively large rotation of a controlled servo motor into small and very precise mirror motions.

The torque motors are the key to a reliable, accurate and responsive positioning system **(Figure 3)**. They consist of a wound stator ring which is installed in recesses in the motion base housings and clamped into position. A magnetic rotor is inserted into the interior of this ring and by providing current through the stator ring, the rotor is driven through a 120 degree range of motion (±60 degrees from a central position). The rotor has a hole at its center through which the stem of the motion cam is inserted to provide a fixed rotating axis to maintain concentricity of the stator and the rotor. The cam disc is oriented onto the rotor to allow full range of motion and fastened to it maintain that position. The rotor is supported by a needle thrust bearing placed between two thrust washers. To prevent rocking of the rotor cam assembly and maintain concentricity between the rotor and stator, the motion cam stem spins in a shouldered radial ball bearing and bushing arrangement where the stem passes through the housing body. A radial resolver is used on the back side of the housing to provide positioning data for the control system.
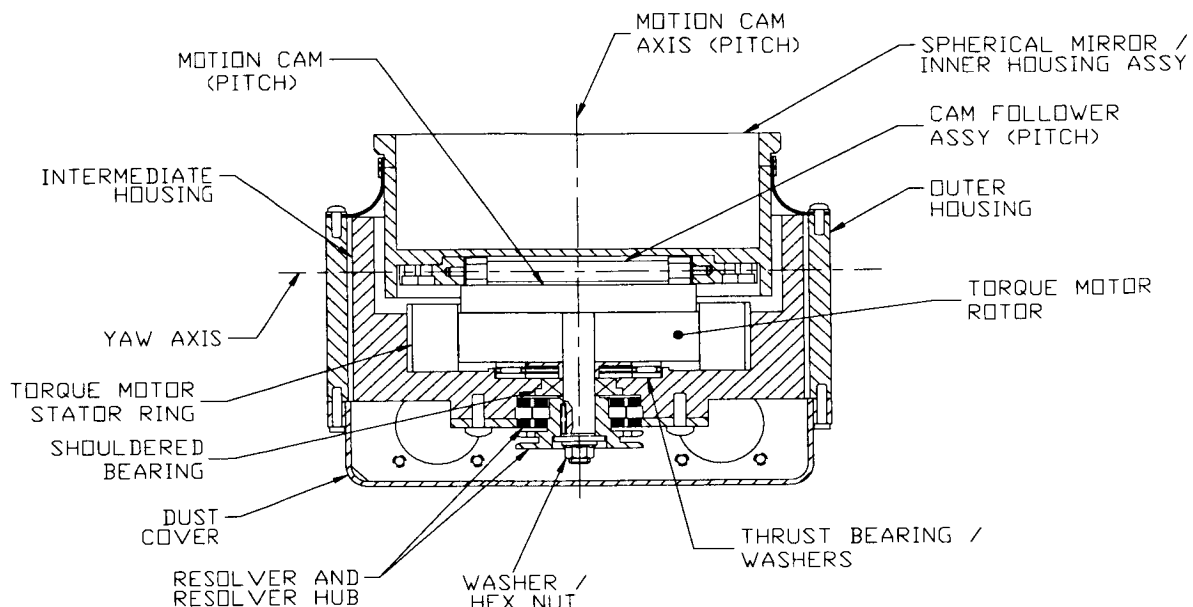
Figure 3. Motion System in section showing Pylon Mirror Motion Base pitch axis.

The resolver provides rotational position information to a control computer that compares this information with the linear displacement of a laser striking the surface of a position sensing device (PSD). As the impact point of the laser moves on the 360 mm^2 (.56 in^2) sensing surface of the PSD, the control system sends positioning commands to the torque motor to maintain the strike point near the center of the PSD.

Motion Cams

There are four motion actuating cams (three large and one small) in the OPTIMA instrument, each made of 17-4PH stainless steel **(Figure 4)**. The PMMB contains two large cams, one for inducing a ±1 degree yaw motion of the mirror, the other for inducing a ±2 degree pitch motion. The FPMB uses a ±2 degree cam identical to the PMMB cam. The BGMA uses a scaled down cam that produces ±1.5 degrees of deflection. Each cam consists of a flat disc with an inclined track around the perimeter of the top surface and a stem extending from the bottom surface. When assembled into the motion bases and the BGMA, cam followers on the driven components come into contact with the track. As the torque motor rotates the cam through its range of motion, the cam followers ride along the inclined track and cause their respective housings and mirrors to be pivoted.
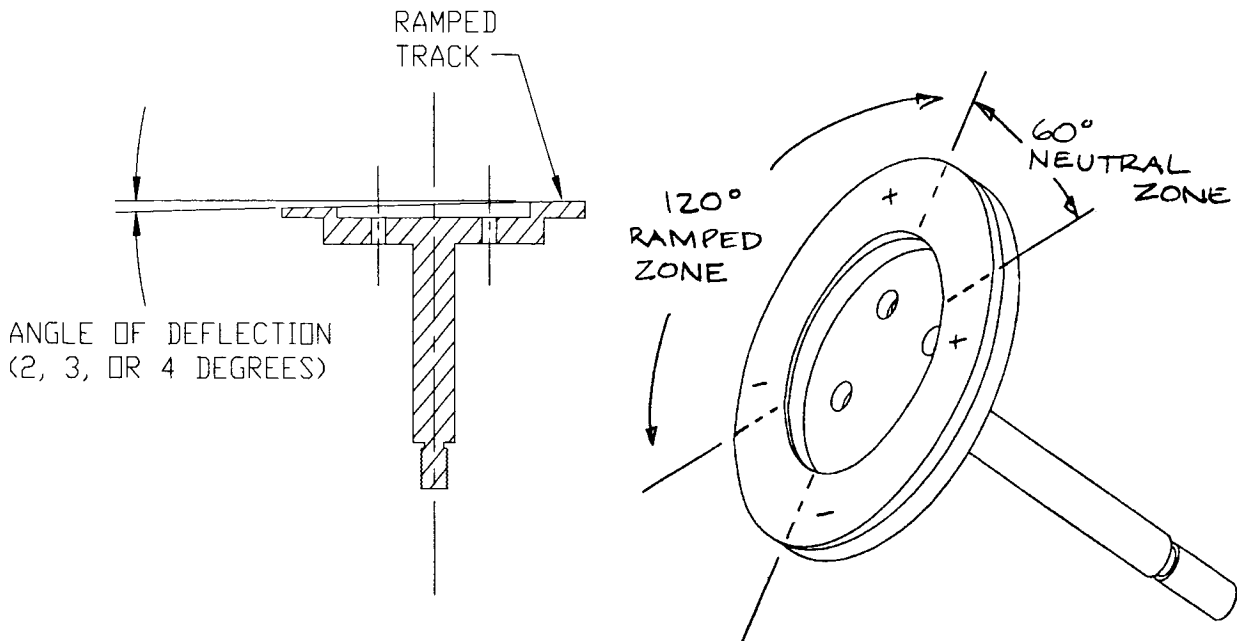
Figure 4. Detail of Motion Cam showing ramped track rising in (+) direction and dropping in (–) direction. Neutral zone is beyond torque motor's range of motion and is not used.

Pylon Mirror Motion Base

The PMMB provides 2 of the 5 degrees of freedom (pitch and yaw) with a nested series of rectangular housings arranged in a gimbal like configuration **(Figure 5)**. The outer housing is an open top box of 17-4 stainless steel and approximately 9cm X 15cm X 40cm (3.5in X 6in X 16in) and contains the yaw drive motion system. The intermediate housing is suspended from this via bearing supports, one fixed and the other a pillow block style flexure arm that provides the yaw axis pivot. The intermediate housing is also made of 17-4PH stainless steel, houses the pitch drive motion system and contains a similar bearing support system to provide a pitch axis (@ 90 to the yaw axis) for the suspension of the inner housing. The inner housing is a five sided box made of Invar to minimize the differential thermal expansion between it and the Spherical Mirror Assembly which nests inside. A module containing a position sensing device and an alignment laser is installed at one end of the inner housing to provide positioning feedback.
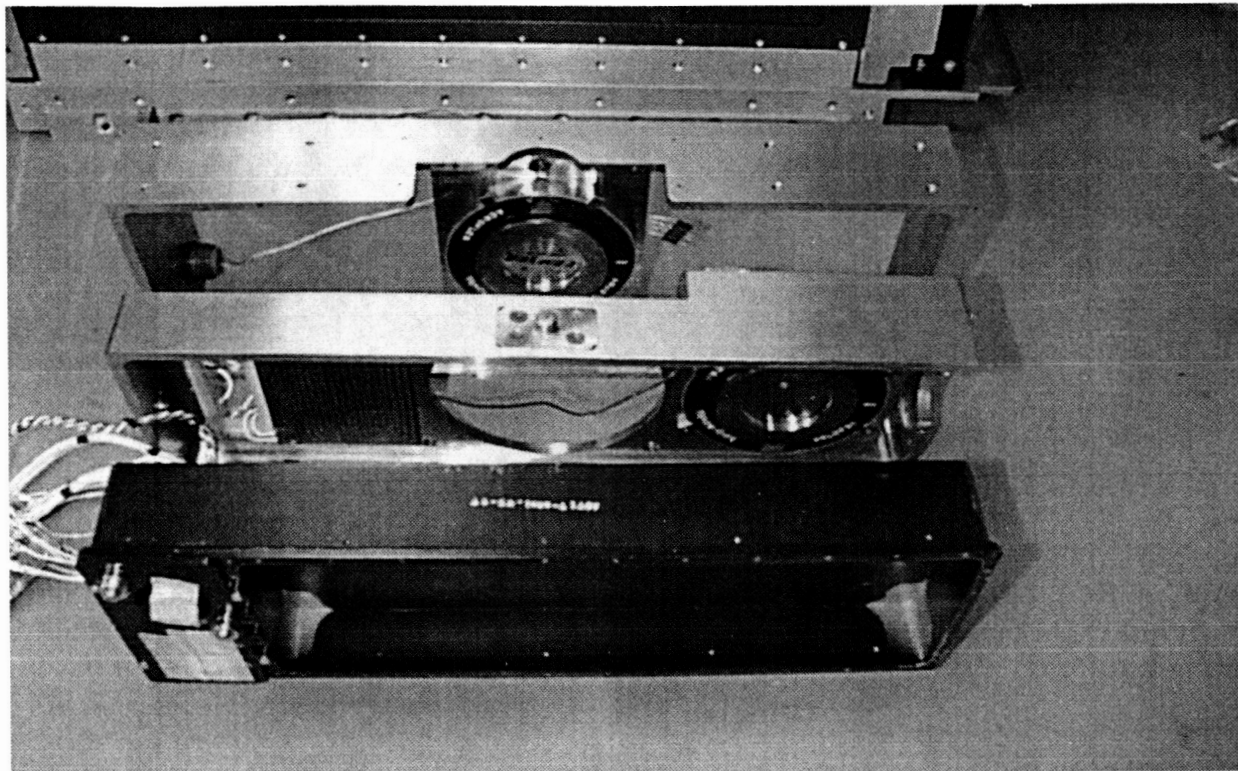
Figure 5. Nested housing arrangement of Pylon Mirror Motion Base assembly with torque motors and motion cams installed.

When assembled, roller bearings of two cam follower assemblies on the bottom of the Inner Housing fit against the motion cams of the pitch and yaw drive systems. The flexure arms of the bearing support systems are shimmed to provide a small preload of the motion system against the cams yet allow compliance to compensate for surface imperfections of the cam drive surface.

Fuselage Mirror Motion Base

The FMMB provides the remaining three degrees of freedom of the OPTIMA mirror alignment system **(Figure 6)**. Where the PMMB is designed to provide two degrees of freedom in one assembly the FMMB requires three distinct subassemblies and an integrating structure. The FMMB is installed into an open cavity created in the side of the aircraft by the installation of the Fuselage Pressure Box. A window above the leading edge of the wing is removed and replaced by an aluminum window blank with an integral shutter mechanism. The Fuselage Pressure Box is suspended off the interior surface of the window blank to provide a solid foundation for the FMMB and maintain a barrier between the pressurized cabin and the exterior test environment.
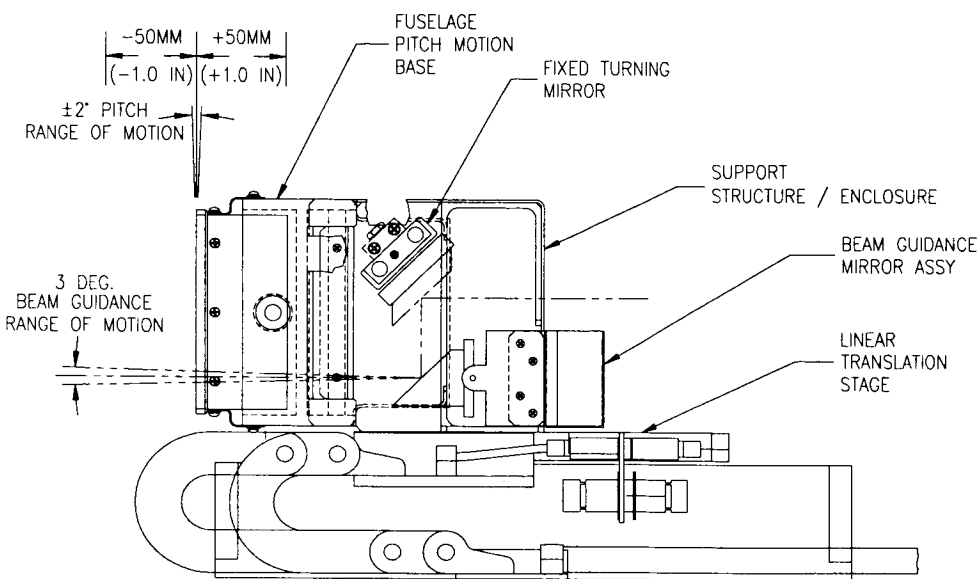
Figure 6. Assembly of the Fuselage Pitch Motion Base, Beam Guidance Mirror Assembly and linear translation stage into the Fuselage Mirror Motion Base.

The Fuselage Pitch Motion Base (FPMB) is essentially a PMMB with one less nested housing and one less torque motor / drive assembly, which was possible because no yaw motion was needed. The pitch motion of the FPMB allows the two spherical mirrors to maintain face to face alignment throughout the full range of vertical pylon movement.

The inner housing of the FPMB also includes an alignment module with a visible pointing laser and PSD to correspond with the arrangement on the PMMB. The laser of each motion base is aimed to strike the PSD on the opposite motion base. Initial alignment of these lasers is performed on the ground and must be adjusted to place the mechanisms in the center of their range of motion during flight. These two complementary laser / PSD modules provide the positioning feedback needed to maintain the relationship between the two spherical mirror surfaces.

Focal length is also affected by the wing movement and must be controlled to maintain the integrity of the Herriott pattern. It is controlled by mounting the FPMB onto a linear translation stage (a commercial linear slide table) that is able to maintain a constant distance between the mirrors by using 10 cm (4 in) of controlled travel.

The final component of the FMMB is the Beam Guidance Mirror Assembly (BGMA) **(Figure 7)**. This unit provides the initial aiming of the laser into the Herriott pattern and guides the returning beam back to the optics table area. This is critical to positioning the Herriott pattern onto the spherical mirrors and ensuring that the beam travels through the entire optical path.
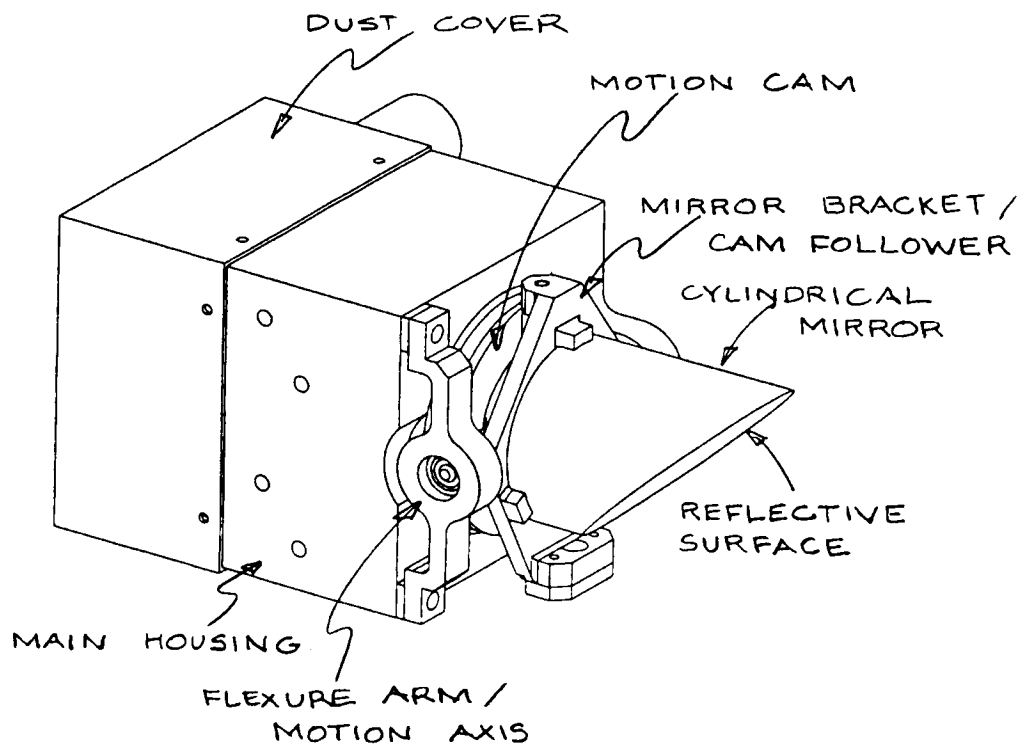
Figure 7. Beam Guidance Mirror Assembly

The mirror of the BGMA is a solid glass cylinder 25 mm (1 in) in diameter and 32 mm (1.25 in) in length and one end cut at 45 degrees with the resulting surface coated with protected silver. The end opposite the mirrored end is bonded to a plate assembly that includes radial bearing pivots to allow rotation and has a miniature cam follower assembly on the backside. The plate installs onto a single housing which incorporates a smaller limited rotation torque motor with a scaled down motion cam. This system is much smaller in overall size at 6 cm X 6 cm X 12 cm (2.25 in X 2.25 in X 4.75 in), as the size and weight of the mirror assembly it drives is considerably less than those in the PMMB and FPMB.

A third PSD and visible laser, which are integral to the IR laser system, determine the focal length and the aiming of the BGMA. The visible laser is co-aligned with the IR lasers and travels the entire Herriott pattern length and returns to the optics table. It is

68

separated from the IR beams and guided to a third PSD. Vertical motion on the PSD surface indicates the need for focal length adjustment while horizontal movement indicates a correction is necessary in the beam guidance angle.

Testing and Operational Development

Due to the compressed schedule, testing was organized into two phases. First, each unique subsystem was assembled and tested for function and performance characteristics. During this phase of testing any operational deficiencies were addressed and experiments to optimize performance were conducted. The second phase was an integrated system test. The subassemblies were brought together into their final configuration and tested as a complete system to verify that mirror alignment could be maintained in a laboratory setting.

Subsystem Testing

The first phase of testing was to connect the control system to an individual motion system and verify that the unit could be moved through its full range of motion with controlled velocity and position. The second phase required reflecting a beam off of the controlled surface onto a PSD and verifying that the strike position of the beam could be maintained on the PSD as it was moved through the mechanism's range of motion. The unit undergoing testing was closely observed for opportunities to improve operational characteristics via mechanical modifications or revised assembly techniques.

The Beam Guidance Mirror Assembly was the first major subsystem available for testing. The BGMA was placed on a flat table and lightly clamped in place. An alignment laser was then mounted in a fixed stand and pointed at the BGMA from a distance of approximately one meter. The mirror position of the BGMA was set to the middle of its 3 degree range of motion. The laser was turned on and bounced off the BGMA and onto a PSD that was set into the laser's path. By driving the mirror through its full range of motion, the extreme positions of the beam deflection were noted. The PSD was then moved along the surface of the table between the extreme positions at various rates as the position of the beam strike on the PSD was monitored. This allowed the initial evaluations and refinement of the velocity control, positioning and feedback software. During this phase of testing, it became apparent that proper assembly of the mirror pointing assembly was critical to minimize friction of the motion system while eliminating backlash and freeplay.

While the BGMA was undergoing testing the PMMB was in final assembly. During this assembly a design deficiency was discovered during installation of the Spherical Mirror Assembly onto the pitch and yaw motion cams. When assembled as intended the stack-up of components was designed to deflect the bearing flexure arms slightly, producing a preload of the cam followers against the motion cams at the bottom of the mirror housing. As both cams were acting against the same surface, only one could be tensioned properly at a time, which would produce an excessive clearance at the

second cam. As a result, the PMMB bearing flexure arms were modified so that when they were installed, the amount of displacement would be at a minimum.

The PMMB subsystem was then subjected to the same two phase test. At first the pitch and yaw axes were tested separately to verify control across the full range of motion of each axis. A flat mirror was bonded to the mass substitute and a test setup very similar to that used for the BGMA test was prepared. The area over which the beam could be controlled was determined. Testing and software development continued until the PSD could be moved within this two dimensional area while maintaining the laser on the center of the PSD.

Testing of the PMMB revealed several unforeseen complications. The large mass of the Intermediate Housing, Inner Housing and Spherical Mirror Assembly was all suspended and moved during yaw corrections. This arrangement generated high inertial loads and limited the yaw response performance. Additionally, the Inner Housing and Spherical Mirror Assembly are mounted in an unbalanced fashion with the majority of the mass cantilevered off to one side of the pitch pivot axis, which also required compromises in the control system that would limit performance. Despite these compromises, the functional requirements for overall system performance were still met.

Both the Linear Translation Stage and the FPMB testing were uneventful. Testing of the Linear Translation Stage was more of a characterization of a commercial assembly. The lessons learned during PMMB assembly, testing and development helped to expedite the process for the FPMB. The single axis could be centered in the housing and resulted in a better balance of the articulated mass. Also, with less suspended weight, the high inertial loads experienced in the PMMB did not occur in the FPMB.

By the end of this process, all subsystems were operating within parameters that indicated the completed system would perform as required. The subsystem testing and development had effectively refined each of the individual subassembly mechanisms.

Integrated System Testing

Once the testing of the subsystems was completed and all were determined to be operating properly, they were assembled into a laboratory simulation of the OPTIMA installation onto the DC-8. Mirror mass substitutes were replaced with the actual Spherical Mirror Assemblies and physical spatial relationships were approximated. A "floating" base for the PMMB was improvised to allow simulation of the motion of the PMMB during flight, as the results of the subsystem testing had indicated the integrated system could be made to track all 5 degrees of freedom fairly easily. Once this was accomplished the testing program involved further development and refinement of the control software and troubleshooting of the electronics.

70

Problems

Some of the difficulties encountered during the development of this device were:

Selection Materials

Invar was selected as the material for several major components. It has a rate of thermal expansion (one tenth that of carbon steel) which is very similar to the glass spherical mirrors. This dimensional stability would help minimize structural stresses due to differential expansion rates and maintain the critical optical alignments.

These advantages are somewhat negated by the difficulties Invar presents when machining. The processes of annealing, machining and heat treatment cause the accumulation and relief of internal stresses, resulting in distortions in the finished part. The warpage in some of these parts was occasionally much greater than the movement expected from differential thermal expansion.

All external components of the OPTIMA instrument would be exposed to considerable condensation. The system would be primarily operated at altitudes above 20,000 ft where ambient temperatures would cold soak the metal housings. While Invar is dimensionally very stable, it is very susceptible to corrosion. The method selected to control corrosion was to plate the Invar with a black chrome process per Mil-C-14538. This required a preplating with nickel (QQ-N-290, class 1, grade G). The combination of the movement of the Invar during manufacturing and the dimensional changes due to the plating process resulted in several key components not meeting drawing dimensional requirements.

In retrospect, it appears that the Invar could be replaced by 17-4PH stainless steel with little negative consequence. The stainless steel has superior machining characteristics, would not require plating and its thermal expansion rate could be accommodated.

Torque Motor Performance

17-4PH stainless steel was selected for the main housings and motion cams to take advantage of its strength, hardness, machinability, and corrosion resistance and was utilized where thermal stability was not a paramount concern.

The housings were designed and made with cup like depressions to hold the limited rotation torque motors. Initial consultations with the manufacturers of the motors did not reveal a cause for concern. The motors were installed into the housings and tests conducted to characterize performance and measure actual output. The results indicated an output torque less than 40% of the manufacturer specification. After consultation with the motor vendor, it was concluded that the close proximity of the magnetic material of the housings, cams and bearing was short circuiting the permanent

71

magnet rotor and reducing the flux through the motor stator. The vendor suggested substituting newly developed rare earth magnets or changing the material the cams were made of to a non-magnetic material. Long lead times for the new rotors dictated a search for a suitable material to make replacement motion cams. 300 series stainless steels and hard anodized aluminum alloys were investigated and rejected due to strength and durability concerns. To match existing geometric constraints, the cams had to have thin cross sections in an area that created significant stresses within the cam. In addition the contact stresses between the cam and the cam follower bearings are high enough to create local deformation in the cams. As these problems could not be resolved, the decision was made to procure the new, stronger rare earth rotors.

After the new rotors were installed and tested the results showed an improvement to only 45% of rated torque. Experiments replacing the magnetic 17-4PH housings with aluminum test housings demonstrated the need to remove as much magnetic material as possible from direct contact with the stators. This improved measured output to about 60% of rated torque which was considered to be adequate for the instrument.

The lack of power contributed to difficulties during testing and continues to compromise the performance of the PMMB and FPMA. The BGMA did not suffer as much from this effect; even though it was less powerful, it moved a much smaller and lighter mirror assembly.

Mirror Pointing Assembly

During evaluating and troubleshooting of the torque motor problem, it became apparent that considerable attention would be required during the assembly of the torque motor / motion cam stack-up. The initial attempts to assemble the BGMA confirmed this conclusion. The assembly and operation of the motion drive mechanism revealed that the preload of the component stack-up was critical. The ideal amount of torque took up all of the slop in the drive system but added very little friction to the system. Additionally, when originally assembled the cam could "rock" in the housing, even when preloaded. The original radial bearings were replaced with a shouldered bearing capable of both radial and thrust loads. Using this new type of bearing, preload could be applied to the cam to prevent rocking without the need of high contact forces between the cam and the cam followers.

During initial testing of the BGMA it was not possible to control the torque motor over 100% of its motion. Characteristics of the resolver and motor caused the control system to overdrive at the extreme end of each direction of travel. This necessitated the installation of mechanical stops that would restrict travel to approximately ±58 degrees from the center point. Without the stops it would be possible to over-rotate the rotor, resulting in damage to the resolver wiring and prevent any further control over the pointing of the mirrors. Similar stops were also incorporated into the PMMB and FPMB motors.

The type and quantity of grease was determined to be important at this point as well. Grease with very low friction and low start torque as well as the ability to maintain these properties throughout the expected operating temperature range was located and used with excellent results.

The most critical aspect of the mechanism proved to be loading the cam followers against the motion cams as mentioned in the previous **Testing and Operational Development** section. No free play could be tolerated yet even slightly excessive preloads would cause binding due to small irregularities in the surface of the tracks of the motion cams. The control system was extremely sensitive to these conditions. Ideally the force required to rotate the cam would be consistent or at least linear in quality to allow optimal tuning of the control system.

Conclusion

The OPTIMA instrument was successfully installed onto the NASA DC-8 research platform during September 1997. After local checkout flights it was deployed for a period of one month to Shannon, Ireland, the Azores Islands and Bangor, Maine. Despite the difficulties discussed above, the instrument performed as intended during all flight conditions encountered. Mirror alignment was easily obtained once in flight and tracking was only infrequently interrupted, and then only for periods of 5 to 10 seconds. These interruptions were primarily due to PSD saturation by ambient lighting or the requirement to open control loops for beam guidance and focal length due to degradation of spherical mirror reflectivity. Some flight operations, such as descending with reduced engine power, produced conditions where control of the PMMB yaw axis became difficult. This may be a result of the displacement frequency of the engine changing to a natural frequency of the motion system.

No mechanical failures were experienced during the 3 checkout or the 14 mission flights. The trouble free operation of the mechanical mirror alignment system and the outstanding performance of the control system allowed full concentration on the refinement of the science portion of the instrument during deployment.

THE FAST BOOM MECHANISMS
Magnetometer Booms, Radial Wire Booms, & Axial Booms

D. Pankow[*] (systems engineering), R. Wilkes[**] (radial
wire booms), R. Besuner[*] (magnetometer booms), and R.
Ullrich[*] (axial booms)

Abstract

The Fast Auroral SnapshoT (FAST) satellite was launched on a Pegasus XL on August 21, 1996. This was the second launch in the NASA SMall EXplorers (SMEX) program, often heralded as the new NASA model of smaller, faster, cheaper science returns. Early in the mission planning it was decided that the University of California at Berkeley (UCB) mechanical engineering staff would provide all of the spacecraft appendages, in order to meet the short development schedule, and to insure their compatibility. This paper describes the design, development, fabrication, testing and on-orbit deployment of these boom systems.

Mission Background

The scientific objective of this magnetospheric physics mission was a detailed investigation of the Aurora Borealis, or "Northern Lights". The fields experiments (electric and magnetic) were constructed by the University of California at Berkeley (UCB) and Los Angeles (UCLA), respectively. The particles instruments were constructed by UCB, and the University of New Hampshire in collaboration with Lockheed Palo Alto Research Laboratory. The instrument data processing unit was provided by UCB. The spacecraft bus, communications, and launch services were provided by the NASA Goddard Space Flight Center SMEX office. The science principal investigator is Dr. C.W. Carlson of UCB, and the program is managed by the SMEX office.

Introduction

Three orthogonal dipoles with six tip mounted sensors are needed for a vector measurement of the DC and AC electric fields in the plasma. Sounding rocket and early satellite experiments used stiff deployable booms for the dipoles. Solar-thermal bending and vehicle dynamics severely limit these stiff booms to lengths of several meters, far short of those lengths desired for meaningful physical measurements. In the evolution of instruments, the preferred practical configuration was found to be a spinning vehicle with four limp wires in the "spin plane" and two stiff axial booms along the spin axis. The limp wires can be precisely positioned by centripetal acceleration, and are immune to the bending and buckling concerns in stiff booms. These

---

[*] Samuel Silver Space Sciences Laboratory, University of California At Berkeley
[**] Lockheed Martin Space Mission Systems & Services, Houston, Texas

lightweight wires allowed about a tenfold increase in the practical radial boom dipole lengths.
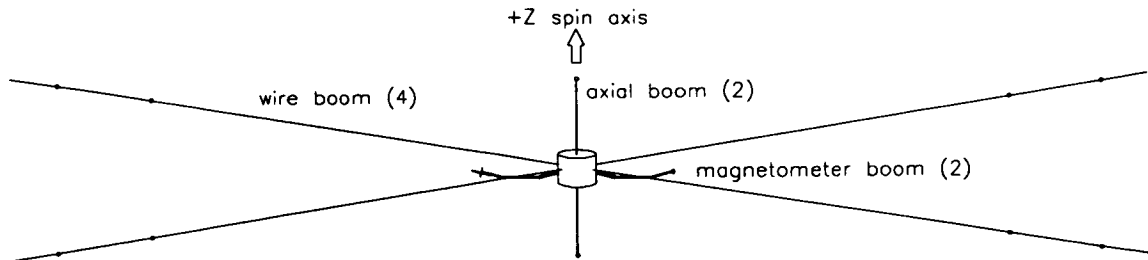
Figure. 1 FAST spacecraft

In practice, boom lengths are determined by the need for a spin stable vehicle. Briefly stated, a spinning body will be stable about the principal axis having the largest second mass moment, based in conservation of angular momentum and body-flexing dissipation of energy to a rotational energy minimum [1]. The spin stability ratio (>1) is defined as the ratio of the second mass moment about the spin axis to the larger of the two transverse axes (I_S/I_T) , while the so called stability margin is this ratio minus one. This means the spin plane wire booms improve stability and can be quite long, while the spin axis booms are length limited because they reduce the stability margin.

The wire boom cables are essentially limp, such that transient motion, or oscillations are dictated by spacecraft maneuvers. The pendulum behavior is dependent on the wire root or hinge attachment radius, the distance from the spin axis to the wire attachment (or exit point). On FAST, the spin induced wire boom stiffness was enhanced by providing trap doors at the vehicle skin, which increase this hinge radius. There is a practical (ACS stability based) bound on wire length, which is the geometry in which the spin plane torsional resonance equals the spin. This mode may be envisioned as a spin "flutter" with all wires swinging in phase and a 180° phase shift for the center body [2]. The FAST boom geometry approaches this limit, with a wire boom second mass moment that is 24 times that of the vehicle. The deployed wire boom plane was located close to the spacecraft Z axis center of mass, in order to avoid spin axis tilt caused by wire boom mass moment asymmetries.

The axial booms must be rigid to avoid elastic instability and subsequent collapse. Additionally, the vehicle stability issue severely limits the boom length. In the mission planning stages, we decided to include the stabilizing effect of wire booms, to increase the allowed axial boom length. In practice this increased the boom length from 2.6 m to 3.8 m each, which is a very significant improvement with respect to the emission of vehicle photo-electrons. Conventional wisdom would suggest that boom length might be increased by decreasing the boom mass, which will also decreases the stiffness. However, spin induced boom flexing amplifies the "effective" boom second mass moment [1]. A boom cantilever resonance of four times the spin (as compared to a customary requirement of two) was selected to maximize boom length.

The FAST Boom Mechanisms

The deployment sequence for FAST releases the magnetometer booms, the radial wire booms, then the axial booms. For both enhanced reliability and simplicity, these boom mechanisms are purposely designed without a retraction capability. The boom systems are manually rewound and reset after ground testing, and on-orbit retraction is neither possible nor necessary.

The UCB design philosophy emphasizes the demonstration of design margins set by peer review. As a result, each boom system was extensively tested at a prototype level (class 3) before the flight units were manufactured. Additionally, the design, assembly and testing of each boom mechanism was conducted by a single engineer solely responsible for its success.

The Magnetometer Booms

System constraints imposed on the magnetometer booms are straightforward. They must be stiff compared to the other booms (to avoid dynamic interactions), as well as thermally stable to maintain sensor alignment. A two meter distance from the spacecraft was determined to be adequate to avoid false signals related to spacecraft current loops and digital circuitry. Perhaps the greatest challenge in the design of these booms was the geometric constraint of their location, within the 2" irregular annulus between the solar array and the launch vehicle fairing.

Magnetometer Boom Configuration

Fluxgate, search coil, and attitude control system (ACS) magnetometers are installed on two deployable, articulated, carbon-fiber booms, approximately two meters in length. Novel features of the magnetometer booms include latchless hinges, low mass, and an innovative carbon-fiber/epoxy fabrication technique.
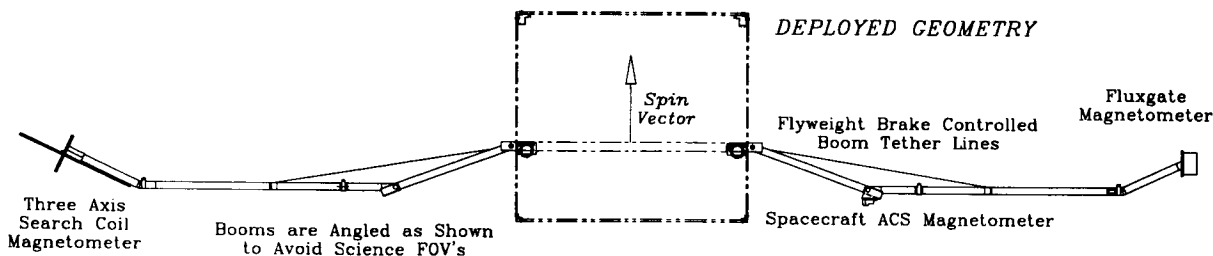
Figure 2. Magnetometer booms: deployed configuration

Each magnetometer boom assembly consists of a base assembly, dual inner boom segments, an outer boom segment, and saddles at the upper and lower corners of the spacecraft solar arrays. The base assembly includes a centrifugal brake to control deployment velocities, a restraint/deployment assist system, electrical connectors for spacecraft housekeeping and magnetometer data, and a "shoulder hinge". The inner

boom segment is composed of two carbon-fiber tubes, side by side, separated by a gap in which the outer boom segment nests. The outer boom segment is hinged to the inner segment and is comprised of carbon-fiber tubes with aluminum "hard points" which restrain the boom for launch dynamics. The outer boom elements are angled to clear the launch fairing of the Pegasus XL. The science magnetometers (fluxgate and search coils) are mounted at the ends of the booms. The ACS magnetometer is located on the elbow hinge of the fluxgate magnetometer boom.

The booms are mounted to the deck on opposite sides of the spacecraft. During launch, the booms were stowed against saddles on the sides of the spacecraft solar arrays, restrained by stainless steel cables at the spacecraft deck and by beryllium-copper rods at the upper array corners. The booms were preloaded against the deck and solar array edges to reduce the launched induced vibration amplitudes. This three-point bending geometry bows the middle of the booms toward the spacecraft with a force at the deck of ~450 N. High force, short travel spring based deployment assist plungers were incorporated in the deck mounts, to overcome any binding forces that might develop in the mounts. These plungers also freed the centrifugal brakes, which were pin locked for launch.
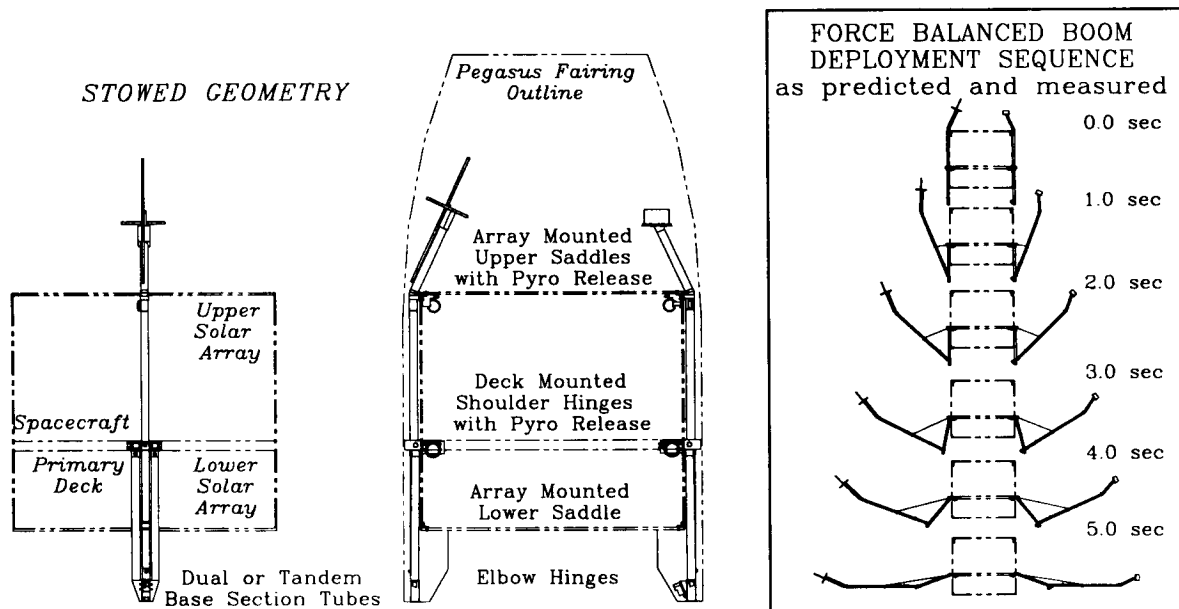
Figure 3. Magnetometer booms deployment sequence

Magnetometer Boom Deployment

Once the spacecraft was in orbit and spinning at 20 rpm, the magnetometer booms were deployed by firing pyrotechnic cable cutters at the upper saddles and shoulder hinges. Centrifugal force motivated the deployment. The speed of deployment was controlled by a tether attached to the outer boom segment which spun a centrifugal (flyweight) brake in the base hinge assembly. The function of this brake was to provide a force balanced boom deployment environment, so that the booms could be deployed

over a wide range of spin rates. Analysis and test set this range at 12 to 60 RPM. The final deployed position of the booms was determined by hard stops in the hinges. These hard stops consist of v-blocks into which the round boom nests. No latching mechanism is used. The position along the spin (Z) axis of the line of force due to centripetal acceleration of each boom/magnetometer assembly is between the Z positions of the shoulder and elbow hinges. This causes the shoulder hinge to try to rotate in the spacecraft up direction and the elbow hinge to try to rotate in the spacecraft down direction, into their respective V-block stops. Torsion springs in each hinge assured deployment and increased loads on the stops. Normal spring end and coil forces push each hinge pin against its clevis holes to prevent hinge rattle. Deployment testing and flight deployments showed that the final position of the magnetometers were repeatable to ~1 mm, while the science magnetometer orientation was repeatable to ~3 arc minutes, and deployed boom resonance was above 2 Hz. The unequal weights of the three magnetometers led to concerns of spacecraft balance. Balance weights were added such that that the spacecraft was dynamically balanced with the booms removed, or deployed. As a result, FAST was launched with an intentional one degree tilt of the spin axis, which went to zero when the booms were deployed shortly after separation.

Magnetometer Boom Design

Carbon fiber/epoxy was chosen as the primary structure of the booms due mainly to its very high stiffness and strength to weight ratio, as well as the low thermal expansion coefficient. The magnetometer signal and power wires were routed inside the boom tubes and hinges using coaxial cables. Each boom also included an outboard connector, so that the magnetometers could easily be removed for testing. Harnessing was reduced to about 40% of the customary weight by using Goretex dielectric and helically served foil coaxial shields with six drain wires. Served shield coax is not only lighter and more flexible than the braided shield option, but also provides better electrical coverage. In spite of these weight saving measures, the electrical harness remained 25% heavier than the composite boom tubes. The total mass of the two booms, including the restraint mechanisms, saddles, tubes, balancing mass, and interfaces to the magnetometers is 3.5 kg. The total mass of the three magnetometers is 1.8 kg.

The carbon fiber/epoxy tubes were constructed from 5 layers of woven prepreg material. The 0.14 mm thick layers were laid out with 0/90° orientation for the outer, inner, and middle layers, and +/-45° orientation for the other two layers. The finished tubes have an outside diameter of 32 mm and a wall thickness of 0.7 mm. The tubes were fabricated by SSL personnel in the Composite Materials Laboratory of the UCB Mechanical Engineering Department, directed by Prof. Hari Dharan. The prepreg layers were laid by hand on a polished aluminum mandrel, then wrapped with a film of PTFE Teflon. Instead of using an autoclave or vacuum bagging, a length of thick-walled neoprene heat shrink tube was placed around the uncured tube. The shrink temperature of the tubing is the same as the cure temperature of the epoxy in the prepreg (175°C). The entire assembly was baked for two hours and cooled. The shrink

tube was carefully sliced off, and the aluminum mandrel thermally contracted to release the finished tube. Avoiding the use of vacuum bags or autoclaves significantly reduced labor and expense and produced uniform, high quality tubes. The metal to composite tube joints used thin aluminum sleeves bonded with structural epoxy (both internal and external) to minimize both distortions and stresses. Alternating bands of aluminum tape and conductive black tape were chosen by the SMEX office for the thermal control, so as to minimize the temperature excursions in shadow.

Magnetometer Boom Testing

Testing of the boom systems included vibration and deployment testing. Deployment tests were conducted in two configurations: ceiling drops and spin tests. For ceiling drop tests, a boom with magnetometer mass dummy was installed on a fixture simulating the side of the spacecraft mounted to the ceiling of the test facility. The fixture was tilted about the spin axis to approximate tangential corriolis accelerations of the actual deployment. The boom was released, and the boom segment positions were measured using potentiometers at the hinges. Overload tests were conducted using oversized instrument mass dummies. Spin tests were conducted on a spin table with a fixture simulating two sides of the spacecraft. Also mounted to the table was an overhead track on which rode trolleys carrying constant-force springs. The springs were fastened to key points on the magnetometer booms to counter the effects of gravity. The table was spun at various speeds, and the booms were deployed to verify computer simulations. Numerical prediction of the deployment environment was a vital part of the design process to establish the needed strength and stiffness margins.

The Electric Fields Experiment

The Sensors

The primary sensing elements for the FAST vector electric fields experiment are ten 8 cm spherical sensors. Each axial boom has one sensor, while each of the four 30 m wire booms has two sensors, separated by five meters. Each of the sensors contains a pre-amplifier, which uses a variety of active feedback schemes to achieve an ultra-high impedance measurement of the local plasma potential, while also minimizing the local disturbances of the plasma. The preamps are housed in 1 mm thick aluminum shells, which are coated with electrically conductive DAG-213 (an epoxy based paint doped with fine carbon particles).

The $\varnothing$ 2.5 mm electrical cable used for wire booms is an advanced construction, designed at UCB/SSL and fabricated by W.L.Gore, Inc. This cable includes two $\varnothing$ 0.6 mm fifty Ohm coax cables and eight AWG #36 conductors. The central wire bundle is jacketed with a Kevlar braid, an aluminized Kapton conductive foil, and a silver plated copper outer braid. With Kevlar as the internal strength member of the cable, we were able to cut and electrically isolate the outer braid, as desired. In fact, each boom cable is divided into eight surfaces that are electrically biased to minimize the disturbances of this conductor in the local plasma. Special attention to design and fabrication details ultimately provided a very flexible cable, which was shown to deviate less than a cm

80

from the desired limp wire radial line. Another formidable engineering tasks was to also produce a very low thermal expansion cable, so as to avoid "wind-up" effects of the rapidly cooled and reheated cable each time the satellite traverses the earth's shadow. The Kevlar braiding could not alone provide the desired low expansion cable. We utilize the fact that the cable core is mostly Teflon insulation (by volume) covered with a helical wrap. This results in an apparent negative expansion as the helical path length increases (when the cable warms in sunlight) due to an expanding Teflon core diameter. The sphere connections provide a "plug & play" design, wherein any of the cables, sensors, or preamps could be rapidly swapped out (as needed), without mechanism tear down or cable de-soldering. The $\emptyset 10$ mm x 15 mm miniature boom cable connectors for each cable end were also a custom UCB design using developmental pins and sockets provided by Hypertronics, Inc.
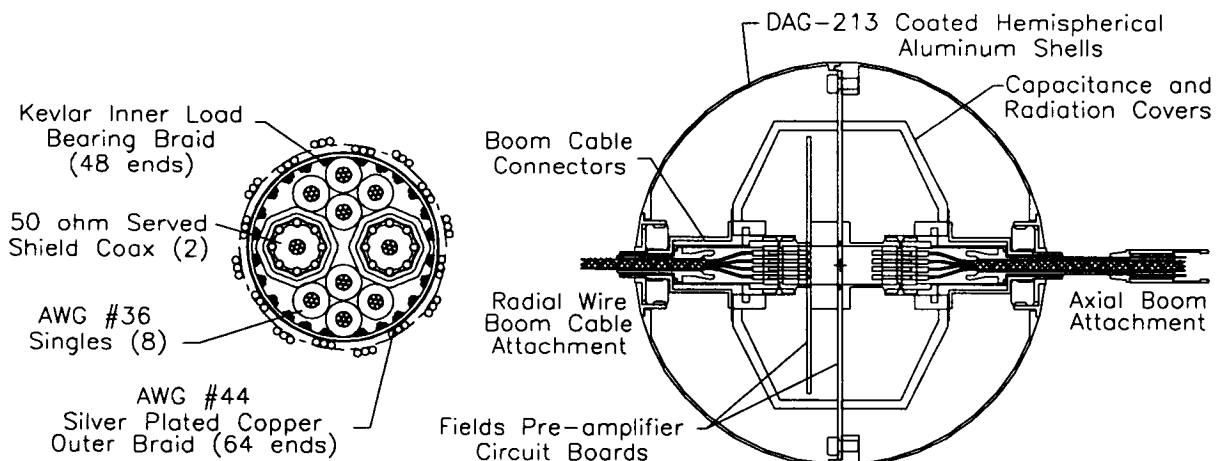

Figure 4. FAST wire boom cable & electric fields sensors

A major boom mechanism design challenge was the proper handling of the spheres. Since the painted surfaces of the spheres are the primary science sensing surfaces, blemishes or abrasions simply could not be tolerated. No contact of the sphere surface could occur during ground handling, launch, or deployment. Small $\emptyset$ 4 mm stubs protrude from either side of each sphere, and these alone could be used to support the sensors.

Wire Boom Deployed Configuration
Each radial wire boom has two spherical sensors and three cable assemblies; a 23m inner cable, a 5m sphere to sphere cable, and a 2½m "tail wire" (extending beyond the outer sphere to provide electrical and mechanical symmetry about the sensor).

A mechanism design issue was the on-orbit activities needed to deploy this rather complex wire geometry, without impacting the delicate body mounted solar array, touching the surfaces of the spheres, or tangling the cables on the magnetometer booms. The deployment of the wire boom is broken up into three events corresponding

to each cable assembly. The three cable assemblies are each deployed by a different method.
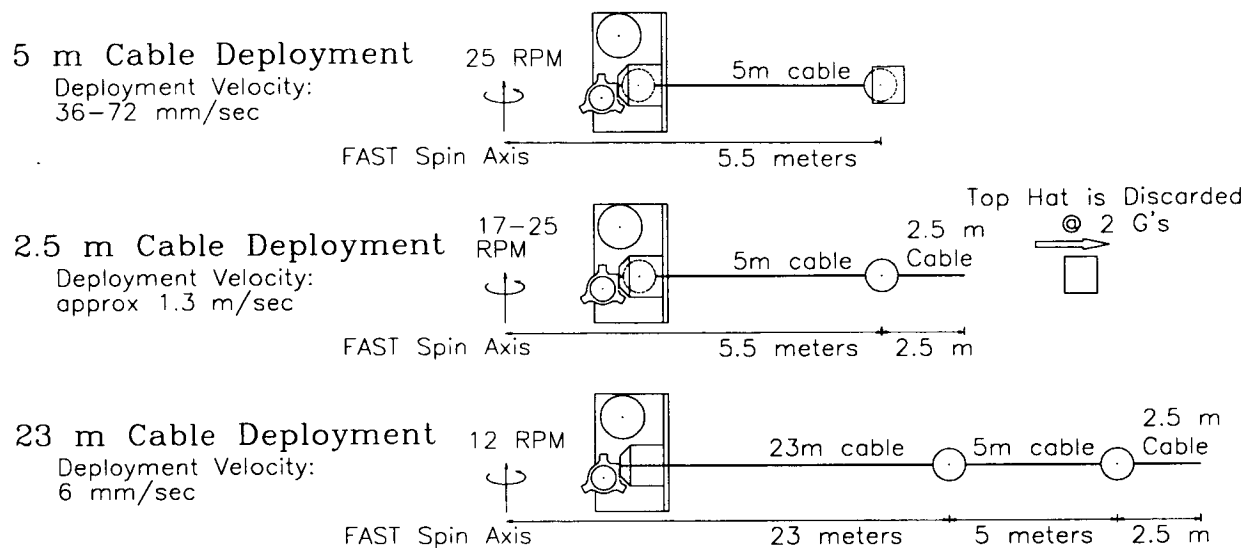
Figure 5. Spin plane wire boom deployment

REAR VIEW   SECTION SIDE VIEW   FRONT VIEW
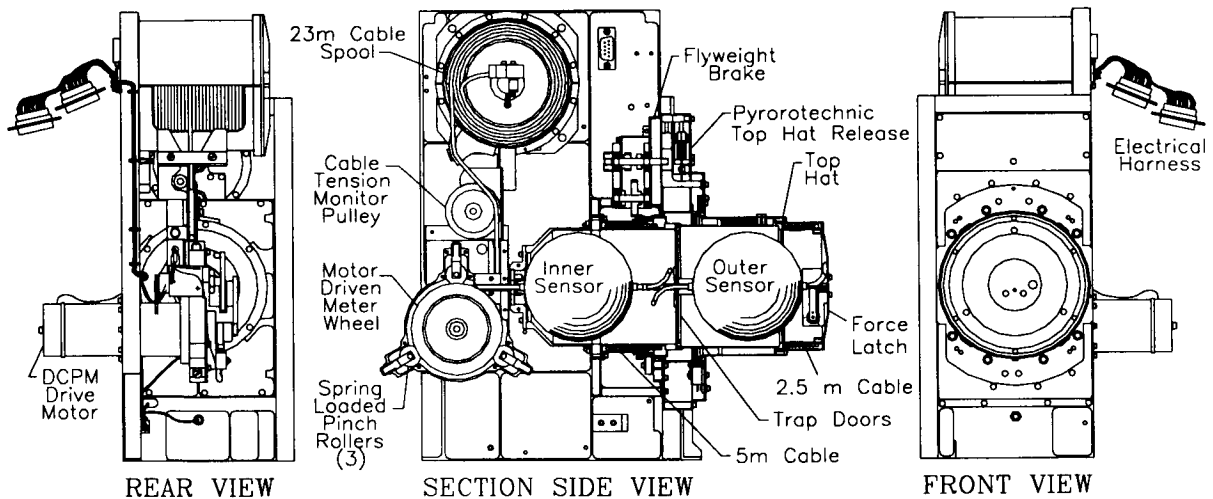
Figure 6. Wire boom deployment mechanism

5m Cable Deployment
The outer sphere and a covering "Top Hat" are released, and are pulled outward by an initial centripetal acceleration of .3 G. The centripetal acceleration varies as the outer sphere travels away from the spacecraft, increasing to over 1.5 G. This first deployment of a pair of booms also slows the spin of the spacecraft from 25 to 17 rpm, within approximately 60 seconds. A centrifugal brake on the deploying cable was sized to limit the cable feed rate to below 0.08 m/s, in order to keep the corriolis induced wire boom

82

offsets to less than 10° from true radial, well away from the magnetometer booms, which are at 45° from the wire booms.

FAST WIRE BOOM
5m CABLE PAYOUT

ACCELERATION (G)   SPEED (m/s)
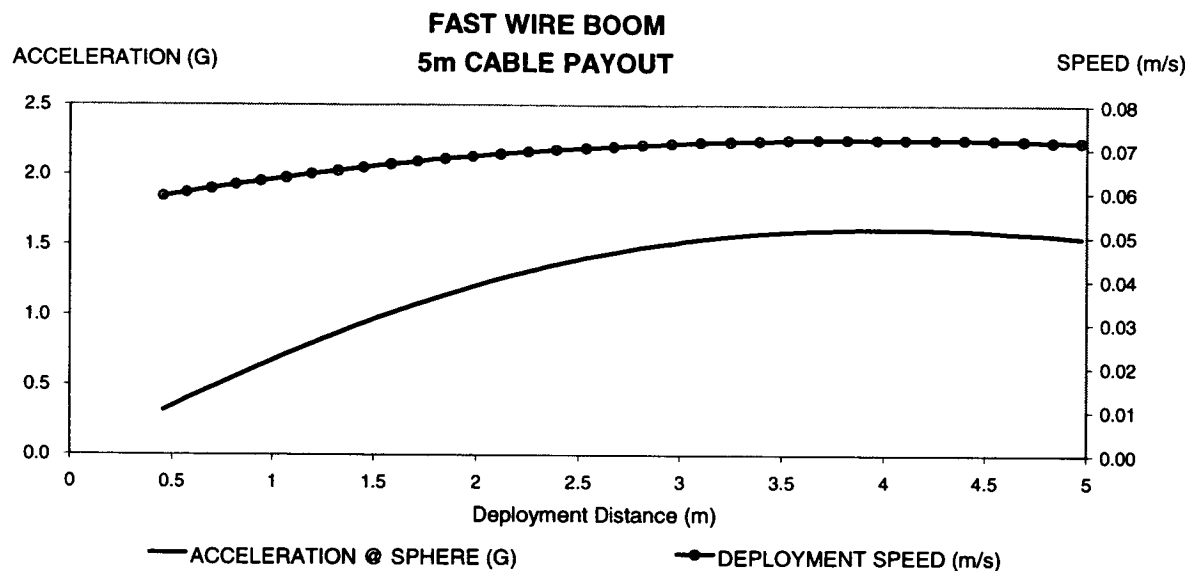
Figure 7. On-orbit deployment environment

Tail Wire and 23m Cable Deployment

After a pair of 5m sphere to sphere cables are deployed, the spacecraft is spun back up to 25 RPM to release the Top Hats. The Top Hats are held to the outer sphere by a force latch that releases at ~2 G's. Release of the Top Hats rapidly unfurls the 2½ m tail wire, well away from the spacecraft.

With the outer sensors and cables deployed, the wire booms are ready for the third event, metered deployment of the 23m main cable. On-orbit, this stage is done in two meter increments, with constant ACS spin-up torquing, in order to maintain 12 RPM spin for continuous science data.

Deployment Mechanisms: Hat Release

For launch, the inner sphere is housed in a Spool within the body of the boom mechanism. The outer sphere is housed in the Top Hat, which is held against the boom housing by four latches. A ⌀ .61 mm hat retention cable circles the Top Hat, and holds the latches against the Top Hat with a noose-like action. The cable circle changes diameter, and correspondingly drives in or releases the latches, with the position of a tension arm. The tension arm position is also used to simultaneously lock and unlock the centrifugal brake mechanism. The tension in the hat retention cable is maintained with a pair of redundant springs, which are tied to the tension arm by a pair of ⌀ .46 mm cables. Release of the Top Hat and flyweight brake occurs with the firing of a pair of redundant pyro operated cable cutters (each severing the pair of ⌀ .46 mm cables), freeing the tension arm and allowing the hat retention cable circle to expand,

83

thereby releasing the latches. Confirmation of Top Hat release is provided by a microswitch acting directly on the edge of the Hat. The pyrotechnics are ICI Americas type 192Y subminiature wire cutters. They are ∅ 4.8 mm x 27 mm and contain a 25 milligram charge.

Deployment Mechanisms: 5m Cable Payout

The sphere stubs between sensors are supported by a pair of spring loaded trap doors. The outer 2½ m tail wire is wrapped into an annulus in the Top Hat. The 5m sphere to sphere cable is routed to the exterior of the Spool, and wrapped into an annulus around it. The cable is held in place simply by fixing the cable endpoints. A rotating "bale" that later allows the cable to peel out from the end of the Spool, one coil at a time, lies at the external edge of the Spool. This bale operates analogous to, but opposite of, the bale on a spin casting fishing reel: In the wire boom, a rotation of the bale is required to remove cable from the Spool, with the fishing reel, the bale rotation acts to wind fishing line onto the reel.

The bale is linked to a centrifugal (flyweight) brake through a 20:1 step up gear train, to control the speed of cable pay out. The flyweight brake uses spring loaded PEEK friction pads, acting against an aluminum housing. The entire gear train is supported by Barden dry film lubricated ball bearings. No preload of the bearings can be tolerated, as the bale must function with only a 5 gram tangential input. All gear and bearing spacing requirements are therefore controlled by shims. This was the most critical aspect of the mechanism, as even a light preload from wavy washers allowed undetected imperfections or perhaps dry film particulate in the bearings to produce unacceptable spikes in the rotating torque. The brake mechanism maintains a payout speed of .06-.08 m/s, despite variations in the wire tension of over a factor of 5.

Deployment mechanisms: 2.5 m Cable Payout

The release of the Top Hat by the latches frees the Hat, which contains a spring loaded Acetal (Delrin) sleeve. This sleeve pushes the Top Hat away from the spacecraft, and simultaneously opens the end of the annulus containing the 2.5 m cable. Constraint of this cable is required for launch, and the sleeve motion allows it to peel out of the annulus freely, upon separation of the sphere from the Top Hat.

The force latch which controls the separation of the sphere from the Top Hat consists of a torsion spring acting on an arm, which engages the sphere stub through a small hole in the stub. The preload of the torsion spring is set such that a 2 G load on the Top Hat will begin to allow arm rotation, which releases the sphere.

Deployment Mechanisms: 25m Cable Payout

The 23m cable deployment mechanism contains a rotating cable storage drum, a metering wheel based cable deployment assembly, a vacuum service brush DC gear motor, over-tension and end-of-cable indicators, analog and digital cable length indicators and redundant gold alloy slip ring electrical contacts on the inboard end. The mechanism deploys cable at a nominal rate of 8 mm/sec with tension ranging from 0 to

100 N. The drive motor is magnetically and EMI shielded. The meter wheel cable grip is enhanced by three equally spaced spring loaded pinch rollers. The meter wheel and pinch rollers have fluorocarbon (Viton) surfaces to avoid damaging the cable braid. The internal cable over-tension indicator prevents breaking and "discarding" the cable, should a malfunction occur.

Wire Boom Testing

Both horizontal and vertical deployments were used to test the wire boom deployment, most testing focusing on the dynamics of the 5 m cable segment. Vertical deployments downward were used with varying masses at the sphere / Top Hat location to verify margins and to allow 3 dimensional dynamics. Deployment was demonstrated with a mass of 39, 119, 350, 606, 2270 and 3180 gram. This demonstrates a .11-9 G range, simulating a range of spacecraft RPM of 15-135. The predicted 8° corriolis angle was simulated by tilting the boom housing during these deployments.

Horizontal tests both in air and in thermal vacuum were conducted by constraining the sphere / Top Hat to a linear track, and allowing the boom to pivot freely about it's center of gravity. This only provides one plane of motion for the deployment dynamics, but it is sufficient for acceptance testing of the flight units, allowing operation through the range of -40°C to +60°C to be demonstrated. All horizontal testing employed a continuously variable clutch to provide a tensile force on the Top Hat in place of the corriolis force. This force could be changed during the deployment to match the force profile that would be encountered on-orbit, but in practice, the lowest level initial force was retained throughout the deployment as a worst case. The subsequent spin up and Top Hat separation force were verified by increasing the tensile force on the Top Hat with the variable clutch until separation occurred. Each boom was deployed horizontally after vibration testing in 3 axis, and thermal cycling in a vacuum.

The Axial Booms

The FAST spin axis sensors use a boom commercially known as the "Stacer", a proprietary concept developed by the Hunter Spring Co. The deployed boom is a gently tapered hollow tube, in its stowed state, it fits within a short cylinder. This boom geometry resembles the "chinese yo-yo" sometimes used as birthday party favors. The Stacer element is cold formed using 0.004" x 5" Elgiloy strip material. The strip is formed with a constant (or fixed) free coil diameter and helix angle. The preferred forming geometry involves significant coil overlap, such that two layers of strip material would be found at any point along the length of the extended Stacer element. The outermost coil cinches on a cylindrical tip piece and the subsequent coils of an extended boom element "stack" on the previous coils producing the characteristic taper. Typical deployed coil diameters are appreciably larger than the free coil diameter, which means that normal forces exist between coils due to this "stacking" process. These intercoil forces in turn produce intercoil friction forces that prevent gross coil slippage. The resulting boom has bending stiffness and strength which compare favorably with the equivalent solid thin walled tube.
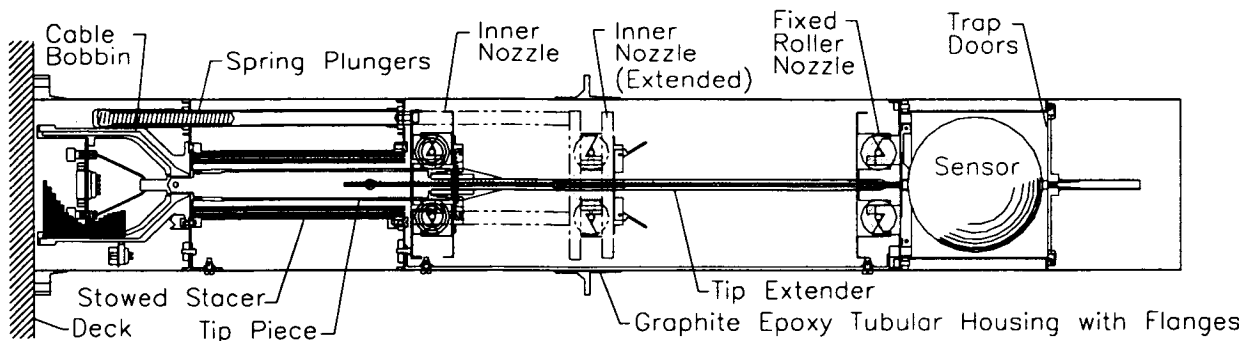
Figure 8. Stowed axial Boom

For pre-launch storage, the element is elastically compressed into a canister whose length is only the strip width. The Stacer will then rapidly self extend by the spring energy as a one shot device. The spring force is due to the release of strain energy as the larger diameter stowed coils "collapse" onto the previously formed boom coils within a single coil transition zone. The boom element thus has full cantilever stiffness, but the base end represents only a pinned joint. Two nozzles positioned beyond the canister and separated by a grip length of several boom diameters provide a rigid pinned-pinned base support. The expanding roller nozzle has been developed to accommodate the changing boom diameter, while also minimizing friction. Axles of the four rollers are held between the base and wedge plates by spring loaded guide posts. The resulting geometry allows concentric outward movement of all rollers, but produces a friction lock when only one roller is loaded by cantilever boom bending. The inner roller nozzle is held against the canister for launch, and then pushed beyond the coil transition zone by spring loaded plungers when the boom is released. These plungers also provide an initial kick force to provide cinching of the first coil on the tip piece, and a robust deployment of the remaining coils.
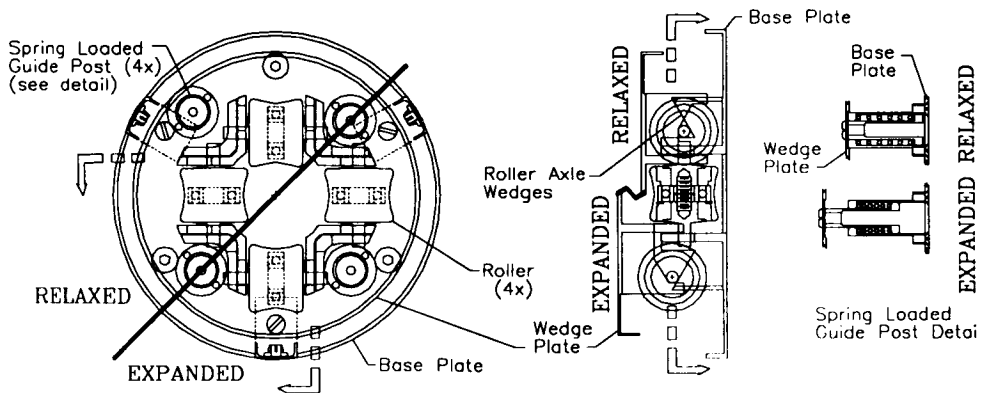

Figure 9. Axial boom roller nozzle

A primary advantage of the Stacer element, as compared to other stiff boom geometries, is its thermal symmetry. The often used alternative uses two longitudinal cambered (>180°) strips that overlap lengthwise to form a tube. The low thermal

86

conduction between strips can produce significant thermal bowing [4], which has been known to cause thermal pumping on slow spinning spacecraft. The helical overlap of the single Stacer strip, by contrast, is axi-symmetric for circumferential heat flow. Other advantages of the Stacer are that it does not need a motor driven deploy mechanism, and the fact that a cable may easily be fed up the center of the boom.

The axial boom electrical cable is stored for launch on a bobbin inboard of the boom canister. The bobbin annulus is sized to prevent crossing and subsequent tangling of the cable coils. The cable is pulled from the end of the bobbin, up the center of the boom element as it deploys, and also aids in stopping the element at its desired final length. The spherical sensor is mounted on a $\varnothing$ 6 mm x 250 mm tip piece extender which also provides the electrical "guard and stub" segments. A UCB designed electrical connector between tip and extender allows swapping of the sensors without disturbing the boom. Inboard and outboard passive "trap doors" support the sphere for launch. The boom is restrained for launch by a "fishhook" geometry on the rear of the tip piece. This hook is held with an aircraft cable loop that is cut by pyro activated cable cutters to release the boom. Each boom assembly is mounted in a $\varnothing$ 100 mm x 670 mm thin wall graphite epoxy tube. The upper tube was extended to 800 mm in order to support the S-band antenna well away from spacecraft. Deployed boom straightness was found to be the order of ±1 cm at 3.8 m length, and the cantilever resonance was above 1 Hz. In this free-pop configuration, the extension velocity reaches ~ six meters per second. As such, it is prudent to include some form of extension restraint in order to reduce the shock forces at the end of the extension stroke. This is achieved by sheathing the last bobbin coil with PTFE shrink tube. The tight fit within the bobbin annulus provides the needed retarding force as the boom reaches full length.

On-orbit Deployment

The FAST spacecraft was launched on a Pegasus XL on August 21, 1996. Within one week, the spacecraft was turned on, and the magnetometer booms deployed at a spin rate of 20 rpm. After a spin up to 25 rpm, the deployment sequence was begun on the first pair of wire booms.

One of this first pair of wire booms, boom #2, stopped after 25 cm of deployment, boom #4 deployed out to 5m. In an attempt to free the stuck boom and to release the Top Hat from the sphere, the spacecraft was spun up to 40 rpm. Subsequently, the spacecraft was slowed down, then "kicked" with the highest impulse available with the spacecraft torque coil. None of these maneuvers were able to move the boom any farther out. The second pair of wire booms was then deployed, both extending to 5m. Top Hat separation occurred during the 5m deployment.

The three of four wire booms deployed to 5 m were then extended out to their full 23 m length. Because the booms do not deploy from exactly the CG of the spacecraft, the asymmetric load due to the partially deployed boom causes the spacecraft to tilt. Deployment of the +Z axis axial boom shifted the spacecraft CG upward, and

decreased the tilt to .4°. Because deployment of the -Z axis boom would increase the tilt substantially, to about 1.6°, it was decided not to deploy this boom.

The on-orbit deployment failure in wire boom #2, most likely due to the 5m cable crossing over itself during launch was unfortunate, and may have been avoided by additional testing. The location of this boom during the horizontal Pegasus launch was down, superimposing a DC acceleration during the launch and pull-up, which would tend to bias any cable motion to the edge of the Spool, where the cable crossover would have occurred. This has moved the composite center of mass ~5 cm from the spacecraft axis, causing the two adjacent wires to shift 6° in the spin plane, toward the missing boom. This somewhat triangular wire boom orientation still provides excellent planar components of the vector fields measurement. The vehicle spin axis has only a 0.4° tilt from the geometric axis, well within the established science tolerances. This is also flight verification of the widely held opinion that vehicle dynamic balance takes precedence over the static balance.

The unprecedented scientific data is a tribute to the robust nature of this system architecture. On-orbit, the FAST vehicle has been found to have excellent attitude stability and spin axis maneuverability. Eclipse spin up, caused by rapidly cooling wires, has been found to be only one part in several thousand. The "negative orbit normal cartwheel" orientation of spin to orbit makes the vehicle relatively immune to gravity gradient disturbances.

Summary

The FAST boom mechanisms designs have evolved over a period of twenty years, from a series of successful satellite instruments flown on S3-3, ISEE, Viking, Freja, CRRES, Polar, and Cluster. This FAST mission was a unique opportunity to advance the state of the art of the three boom systems it employed. It was predicated as a higher risk mission with a short development and fabrication cycle. Nevertheless, new systems were designed for all three booms, each extending the limits of what had been done before. The spacecraft's' subsequent science success provides validation for the engineering mission as well, and development history for future missions to call upon.

References

1. Meirovitch, L. and R. E. Calico, "The Stability of Motion of Satellites with Flexible Appendages," NASA CR-1978, 1972.
2. Lai, S. T. and K. H. Bhavnani, "Dynamics of Satellite Wire Boom Systems," AFCRL-TR-75-0220, 1975.
3. Thomson, W. T., Introduction to Space Dynamics, J. Wiley, 1961.
4. Staugaitis, C. L. and R. E. Predmore, "Thermal Static Bending of Deployable Interlocked Booms," NASA TN D-7243, 1973.

Thermal Vacuum Deployment and Retraction Testing of the Photovoltaic Radiator

Ron B. Hofstad[*]

Abstract

The Photovoltaic Radiator (PVR) is a structural element of the International Space Station (ISS) designed to reject the waste heat of the Photovoltaic Power Generation and Storage System. The requirement for the PVR to be deployable once on orbit necessitates the design of a structural deployment and retraction mechanism. This paper describes the PVR design with emphasis on the deployment and retraction mechanism and discusses operational verification testing of the mechanism in both ambient and thermal vacuum environments.

Introduction

The ISS PVR design was initiated in 1990 and is being designed and fabricated by Lockheed Martin Vought Systems under contract to the Rocketdyne Division of Boeing North American. Four PVR units will ultimately be furnished to NASA for usage on the final ISS configuration currently scheduled to be complete in June 2002. Due to a requirement for heat rejection during the early mission phases, three PVR units will be utilized on the Flight 4A launch package currently scheduled for launch in April 1999. Figure 1 shows three PVR units deployed on an early mission configuration. Thermal and modal tests have been conducted on a single radiator panel and an acoustic test was performed on the Flight 4A launch package. Planned testing includes a stowed acoustic test, electromagnetic interference test, heater system qualification test, modal survey test, and a flex hose bending stiffness test. All testing is currently scheduled to be completed by July 1998.

Operation of the PVR uses a combination of Extravehicular Activity (EVA) and automatic features. Once in orbit, EVA is required to prepare the PVR for deployment and is ultimately used for deployment and retraction tasks if the automatic feature fails to operate. Two series of neutral buoyancy tests have been successfully conducted at the NASA Marshall Space Flight facility. These tests demonstrated the accessibility of the EVA operation points and the feasibility of accomplishing the activities. Further testing is planned at the Johnson Space Center facility in 1998.

PVR Design Summary

The PVR design consists of seven lightweight panels hinged together forming a folded array. The panel stack attaches to a structural torque panel and torque arm that mount to a skin stringer box-like base structure. A stowed and deployed configuration of the

---

[*] Lockheed Martin Vought Systems, Dallas, TX

PVR assembly is shown in Figures 2 and 3 respectively. Each panel is approximately 1.8m by 3.3m in size and consists of 24 inconel flow tubes surrounded by an aluminum extrusion and variable density aluminum honeycomb core. The flow tubes terminate in pairs of enclosed manifold tubes located on the outboard sides of the panel. Outboard of the manifold tube enclosures, scissors beams are attached at the center with a pin and bushing arrangement. This combination provides a rotational element allowing the enclosure and beam to pivot relative to each other during the deployment and retraction motion. During mechanism operation, the panel array and adjacent scissors beams fold outward or inward forming the extended or retracted position. Attachment of the hinges for the adjacent panels and scissors beams is accomplished using structural pins coated with Everlube 620C. This dry film lubricant is necessary to assist the array motion and prevent binding. The working fluid (ammonia) is transferred between adjacent panels through sets of flexible metal hoses. During operation in orbit, each panel provides 11 m^2 of radiating area and rejects approximately 1.5 kW.

The torque panel and torque arm are key structural elements of the design that "drive" the panel array during operation of the deployment and retraction mechanism. Both elements consist of tubular and sheet metal structure made from aluminum material. On the outboard sides, the torque panel attaches to hinges on the manifold tube enclosures of the first radiator panel. The torque arm attaches to hinges located on the first scissors beams. The inboard sides of both the torque panel and the torque arm attach to and pivot about hinges located on the upper surface of the base structure. Likewise, the rotational element in all hinges consists of pins coated with Everlube 620C. At two places on each of these two elements, torque is applied by the mechanism forcing the radiator panel and scissors beam assemblies to assume their extended or retracted state.

The base structure assembly is an aluminum sheet metal structure approximately 1.8m by 3.6m by 0.13m in size and houses the electrical, mechanical, and fluid ISS interface points. Riveted skins are attached to the upper surface while the lower surface is equipped with removable doors in order to allow access to the interior. The majority of the interior is comprised of fluid lines, electrical components, and the deployment and retraction mechanism.

Deployment and Retraction Mechanism

The PVR is required to deploy and retract in the on orbit thermal environments. Deployment must be accomplished with an ammonia system pressure of 1,724 kPa in a period of 10 minutes using no more than 20 watts of power. A life cycle of 120 cycles of deployment and retraction is specified.

The PVR uses an electric motor-gearbox, drums, wire ropes, and pulleys to actuate the scissors-type deployment and retraction mechanism. The PVR deployment and retraction mechanism is shown in Figures 4 & 5. A wire rope mechanism is employed

due to its inherent simplicity, good mechanical efficiency, and reliability. The electrical motor drives a five-stage planetary gearbox with a 9255:1 reduction ratio. A spring-applied, electromagnetically released brake is present on the motor to prevent unwanted motion. A differential gear arrangement permits a back-up manual input (activated by EVA on orbit), and a spring-loaded mechanical lock is present to prevent back driving of the manual drive shaft. The motor-gearbox is connected through a splined shaft to a tubular shaft with drum sets on either end. Each drum is grooved to retain the stainless steel wire rope during rotation. Pulleys redirect the wire ropes to the ends of the base support structure and terminate at the drive pulleys on the torque panel and torque arm. Torque from the motor is transferred to the torque panel and torque arm drive pulleys allowing 98° of rotation. This rotation accomplishes the deployment and retraction motion.

Wire Rope System and Tensioning

The wire rope and drum extension system consist of four driving drums and four driven pulleys with connecting wire ropes. Each drum has two wire ropes anchored at one end and wrapped such that tension in the rope produces torque in the drum shaft. The ropes are directed such that when the motor or manual input rotates the four driving drums, all four of the driven pulleys are turned to extend or retract the torque panel and torque arm simultaneously and at the same angular rate. The wire rope pairs on each drum are wrapped such that during rotation, the ropes move in opposite directions. Each pair operates a driven pulley at one of the two ends of either the torque panel or torque arm.

An initial tension at 16° to 32°C (with no operating load in the wire ropes) of 2,780 ± 111 N in each wire rope is required to assure correct positioning of the array at the temperatures and loads expected on orbit. The initial tension assures that no wire rope will go slack. Another factor must be accounted for when the eight wire ropes are adjusted to the initial tension at assembly. It is structurally necessary to have a nearly equal load on the mechanism extend stops when the torque panel and torque arm are fully extended and the motor-gearbox is supplying full torque (> 452 N•m). Analysis of the mechanism upon completion of array deployment indicated the existence of a "soft side" in the design due to the presence of the torque shaft between the two drive drum sets. Rigging adjustments for the eight wire ropes were necessary to achieve equivalent loading on the extend stops. This results in the best resistance to loads expected on the radiator panels when deployed on orbit. The ropes are, therefore, adjusted while two conditions are maintained. First, no friction, weight, or other factors are allowed to load the movable parts. Secondly, the torque panel and torque arm are held in a specific relationship to each other during adjustment. This relationship exists when the torque arm is 1.62° of arm angle farther toward full extension than the torque panel. This is accomplished by inserting spacers between the torque arm and the retracted position stops on the base structure while adjusting the tension on each wire rope to the initial specified tension of 2,780 ± 111 N. To assure that the torque panel or torque arm is not loaded against their respective mating stops during tensioning, a

0.005 - 0.076 cm clearance is maintained. At any point in the deployment and retraction process, static loads in the wire ropes can be measured using a calibrated mechanical tension gage. The measured loads will certainly be altered from the initial tension setting because of the effect of residual friction resistance or other loads on the mechanism. Initial tension can always be determined however, as it is the average of the two tensions of a wire rope pair, loaded or not loaded. This rigging process has shown satisfactory results within acceptable limits.

Operational Verification Testing

Verification of the key PVR requirements is accomplished by a combination of testing and analysis. As is the case for most spacecraft, exact simulation of operating conditions in space is not possible. A process of creating analytical models, verifying them through ground testing, and then using these models to predict on orbit performance is used. Verification testing of the PVR operational requirements has been accomplished in both an ambient and thermal vacuum environment.

Ambient Environment

Ambient operation of the PVR has been demonstrated on an Engineering Model and on the first two Flight Units using a low friction deployment fixture. The fixture provides a smooth, lubricated, hard steel track that supports the weight of the PVR in a vertical position. A low-friction, dry film lubricated spherical roller is attached to each scissors beam and manifold enclosure pivot pin in order to allow deployment and retraction along the track. Figure 3 shows the PVR mounted on a similar track used during thermal vacuum tests. Usage of spherical roller bearings provides a conservative test as the applied frictional forces that act against deployment are absent on orbit. Counterweight mechanisms were considered but ruled out due to the greater complexity in design and alignment procedures.

Ambient testing of the Engineering Model revealed the importance of vertical alignment of the spherical roller bearings and the engagement of the adjacent panel array cinch fittings and scissors beams. A laser transit was used to establish an axis through the adjacent fittings so that vertical adjustments could be made. Alignment of the adjacent pins and receptacles posed interesting challenges. The adjacent panel to panel pins and receptacles are required such that when in the retracted position, the PVR launch package is rigid. Six cinching mechanisms restrain the panel array against the base structure to maintain a stiff PVR assembly. Each cinching mechanism consists of a wire rope, nut, and bolt combination. When the cinching mechanism is employed, launch modal frequencies are satisfied and array movement during on orbit operations is minimized. The cinch fitting and scissors beam pins engage in their mating receptacles on adjacent panels and eventually engage receptacles on parts located on the base structure assembly. This structure transfers launch loads and must remain rigid. Thermal environments that impart large temperature differences between the mating pins and receptacles are possible. This requires adequate

clearances between each pin and receptacle in order to prevent binding during deployment or retraction.

Thermal Vacuum Environment

Thermal vacuum testing of the PVR was successfully demonstrated at the NASA Lewis Research Center Plum Brook Station Space Power Facility in March and April of 1997. All tests were conducted at the required pressure of 1,724 kPa using both the electric motor and the motor's manual back-up mode. The result of each test condition is summarized in Table 1.

The Plum Brook chamber is approximately 30 m in diameter and provides thermally conditioned cold wall shrouds to emulate the low temperatures. The PVR assembly was surrounded by an array of infrared lamps in order to provide temperature control. Mechanism operation was demonstrated in a vacuum at cold temperatures of -87°C and hot temperatures of 52°C, including thermal gradients across the PVR assembly from top to bottom (Z-axis) and front to back (X-axis).

Instrumentation was mounted on several elements in order to measure panel to panel angles, wire rope loads, and motor power expelled during deployment and retraction mechanism testing. Angular potentiometers measured deployment angles of the pivoting joints across the top and bottom of the array. Of the conditions tested, the cold soak deployment test shows the most severe angular displacement. A graph of the angular displacement for the cold soak test is presented in Figure 6. During deployment, a slight hesitation occurs when the hinge position between the torque panel and the first radiator panel is at approximately 30°. This hesitation is the result of frictional forces between the spherical rollers and the steel track in the 1g environment. The remaining test conditions revealed that the frictional forces had a negligible impact on both deployment and retraction.

Electric Motor

During deployment and retraction, the power required from the electric motor was measured for each test condition. The results were predictable and well within the allowable limit of 20 watts. Figure 7 shows measurements of a typical deployment and retraction cycle. Power requirements are greatest at the onset of the deployment and retraction motion as the initial inertia of the assembly is overcome. Measurement of the elapsed time for both array deployment and retraction is also presented in Figure 7. Each test condition exhibited satisfactory deployment and retraction durations within the 10 minute requirement.

For each test condition, the total wire rope resistance load was determined in order to calculate the motor output torque during the deployment and retraction cycle. The minimum available motor output torque is 259 N•m. To determine the wire rope resistance load, strain gauge pairs were mounted on the turnbuckle of each of the eight wire ropes. Strain measurements were recorded throughout the cycle. The differential strain, wire rope modulus, and wire rope geometry are used to calculate the

individual wire rope resistance load. The motor output torque is simply the product of the sum of the resistance load of all eight wire ropes and the drum radius. Results indicated that the Z-axis gradient test required the greatest amount of torque to operate the mechanism (187 N•m). Compared to the minimum available motor torque (259 N•m), a sufficient margin of 28% exists.

EVA Drive Motor

Deployment and retraction tests at the thermal extremes were also performed using a EVA drive motor coupled with the motor's manual back-up system. The EVA drive motor, supplied by NASA, emulates the torque and speed available for operations performed on orbit during EVA tasks. The available drive motor torque and speed is variable and is limited to 11 - 20 N•m and 0 - 20 RPM. The purpose of the tests is to determine the minimum applied torque and speed required to satisfactorily deploy and retract the array. Monitoring of the elapsed time for the cycle was not a requirement.

The EVA drive motor was attached to the PVR assembly at the EVA manual back-up actuation point located on the base structure assembly. Due to the selected location of the drive motor for the tests, a series of interconnecting shafts and couplings between the drive motor and base assembly was required. Instrumentation used to measure output torque and speed of the drive motor during operation was secured to the interconnecting shaft nearest to the base assembly.

A pretest checkout of the cycle was accomplished using the drive motor in order to verify operation and to provide preliminary torque and speed requirements. This test was performed at ambient temperature. During the initial deployment operation, the drive motor torque and speed was set at 11 N•m and 15 RPM. At a point approximately halfway through deployment, the drive motor stalled. At this time, the torque was raised to 14 N•m and the deployment operation was completed. Since the drive motor lacks sufficient power to fully retract the array, the torque was increased for the retraction operation. For the retraction operation, the torque and speed were set at 16 N•m and 8 RPM, and retraction was accomplished satisfactorily without hesitation.

A summary of the EVA drive motor test results during the thermal extremes is also presented in Table 1. During the cold soak test deployment, the drive motor stalled with the output torque and speed setting at 14 N•m and 15 RPM. Adjustments to the torque and speed (16 N•m and 10 RPM) were required to complete the deployment operation. Measurements during retraction were not recorded due to the expiration of the data set; however, normal retraction without hesitation was observed. The torque and speed required for the hot soak deployment matched the cold soak identically while the retraction motion required 18 N•m of input torque. Results for the gradient tests were undetermined due to a failure in the drive motor-to-base assembly shaft system. Investigation revealed that a decoupling occurred between two shafts on the drive motor side. With the instrumentation located on a base assembly side interconnecting shaft, the feedback showed an unresponsive drive motor. After repairs, the gradient test points were not repeated, and verification of the EVA drive

motor was accomplished during the thermal cycling tests. Figure 8 shows torque and speed requirements for a deployment and retraction cycle using the EVA drive motor.

Conclusions

During ambient condition testing, the importance of adjacent member pin and receptacle fit and alignment was realized due to several deployment failures. Investigation revealed that binding between a single pin and receptacle was enough to stall the electric motor, thus preventing deployment. Additional analysis was required to determine differential thermal expansion between the adjacent panels. Consequently, the receptacle holes were modified to increase clearances while maintaining a structural positive margin. When the PVR was initially installed on the low-friction deployment fixture, panel-to-panel alignment was accomplished using a complex spherical roller bearing adjustment procedure. This procedure proved unsuccessful because the individual panel tolerance accumulation was not taken into account. Therefore, the laser transit was employed to control the alignment.

The initial tensioning of the wire ropes is designed to be completed during integration of the torque panel and torque arm without attachment of the panel array. When the PVR assembly was installed at the thermal vacuum facility, tension adjustments to the eight wire ropes to the specified 2,780 ± 111 N were required. This task proved to be quite challenging. The added panel array weight coupled with vacuum chamber temperature, test fixture drag, and tensiometer tolerance added enormous complexity to the mechanism rigging. Several hours were expended adjusting, measuring, and cycling the array to arrive at the desired wire rope tension.

Large space structures designed to deploy and retract on orbit require careful design and analysis of all components. The results of the thermal vacuum tests matched the predicted behavior satisfactorily and confirmed the design of the deployment and retraction mechanism. Operation and performance of the electric motor and manual back-up mode were also successfully verified.

Table 1. Thermal Vacuum Test Results

| TEST COND	TEMPERATURE ENV (°C)	TEMPERATURE PVR (°C)	ELECTRIC MOTOR							EVA DRIVE MOTOR			
			ANGULAR DISPLACEMENT	MOTOR POWER (WATTS)	DEPLOY/RETRACT DURATION (MIN-SEC)		CABLE LOAD (N)	CABLE TORQUE REQ'D (N m)	TORQUE SETTING		MOTOR SPEED (RPM)	
					DEPLOY	RETRACT			DEPLOY	RETRACT	DEPLOY	RETRACT
COLD SOAK	-87	-87	161.1° - 161.9°	< 9	7 - 22	5 - 7	4066	163	16	N/A	10	N/A
HOT SOAK	+52	+52	161.0° - 161.7°	< 9	7 - 52	5 - 0	3768	151	16	18	10	10
Z - AXIS GRADIENT	-87	-87 BOT +52 TOP	160.8° - 162.5°	< 9	7 - 29	5 - 14	4631	187	N/A	N/A	N/A	N/A
X - AXIS GRADIENT	-87	-87 PAN 7 +52 BASE	161.0° - 161.7°	< 9	7 - 17	5 - 6	4315	173	N/A	N/A	N/A	N/A

PVR
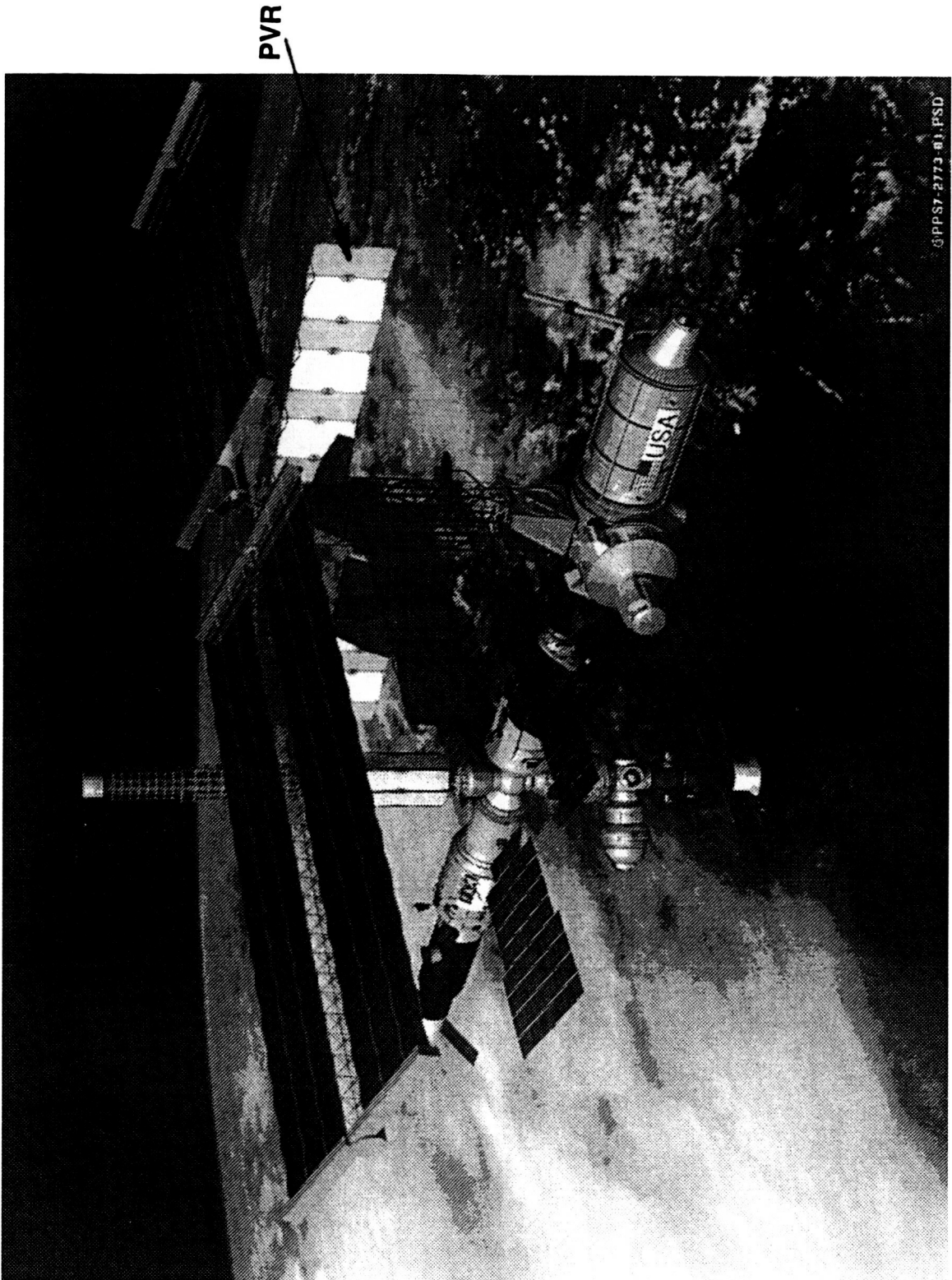
Figure 1. Deployed PVR Units on Early Mission Configuration

97
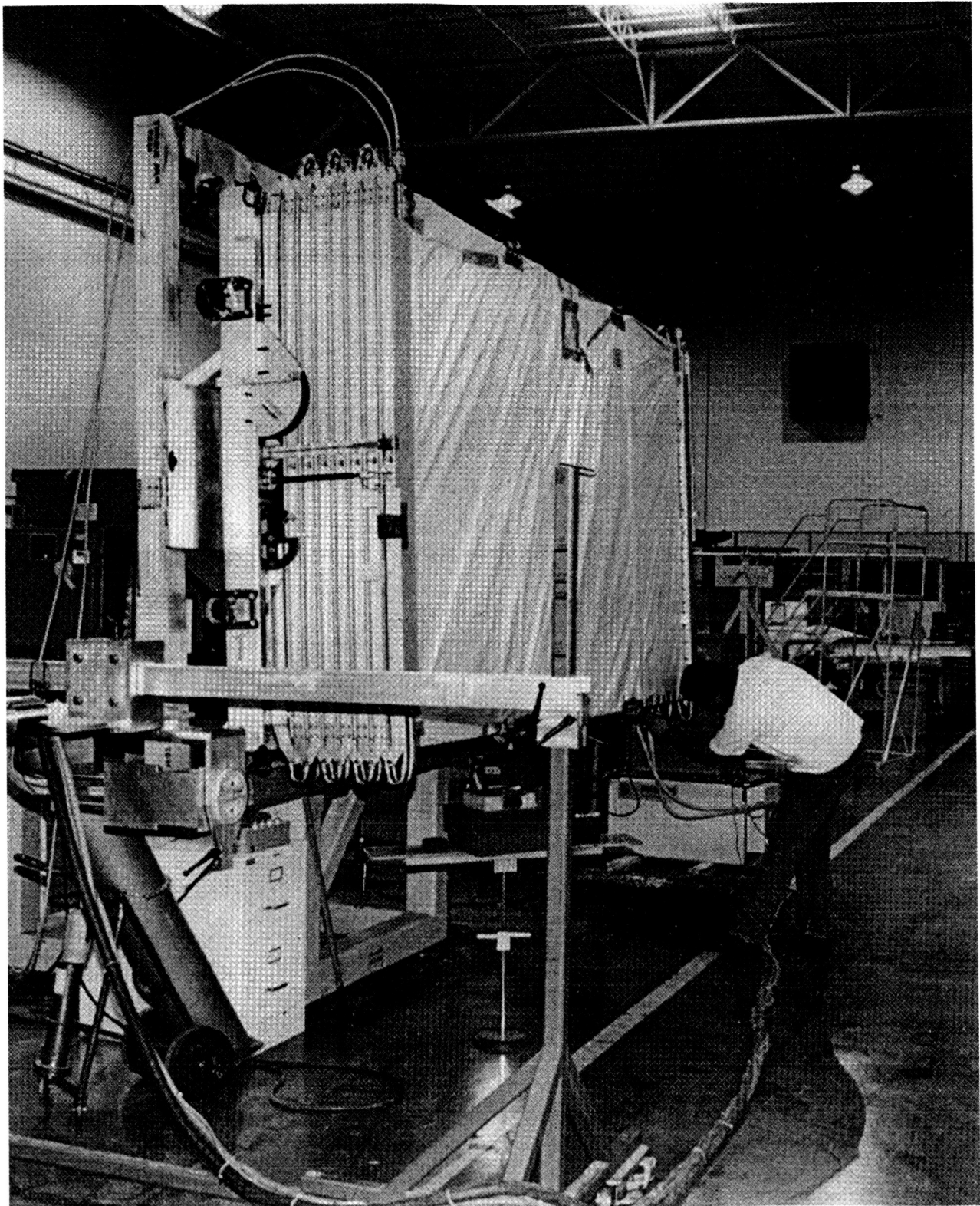
Figure 2. PVR Retracted Position

Figure 3. PVR Deployed Position

99
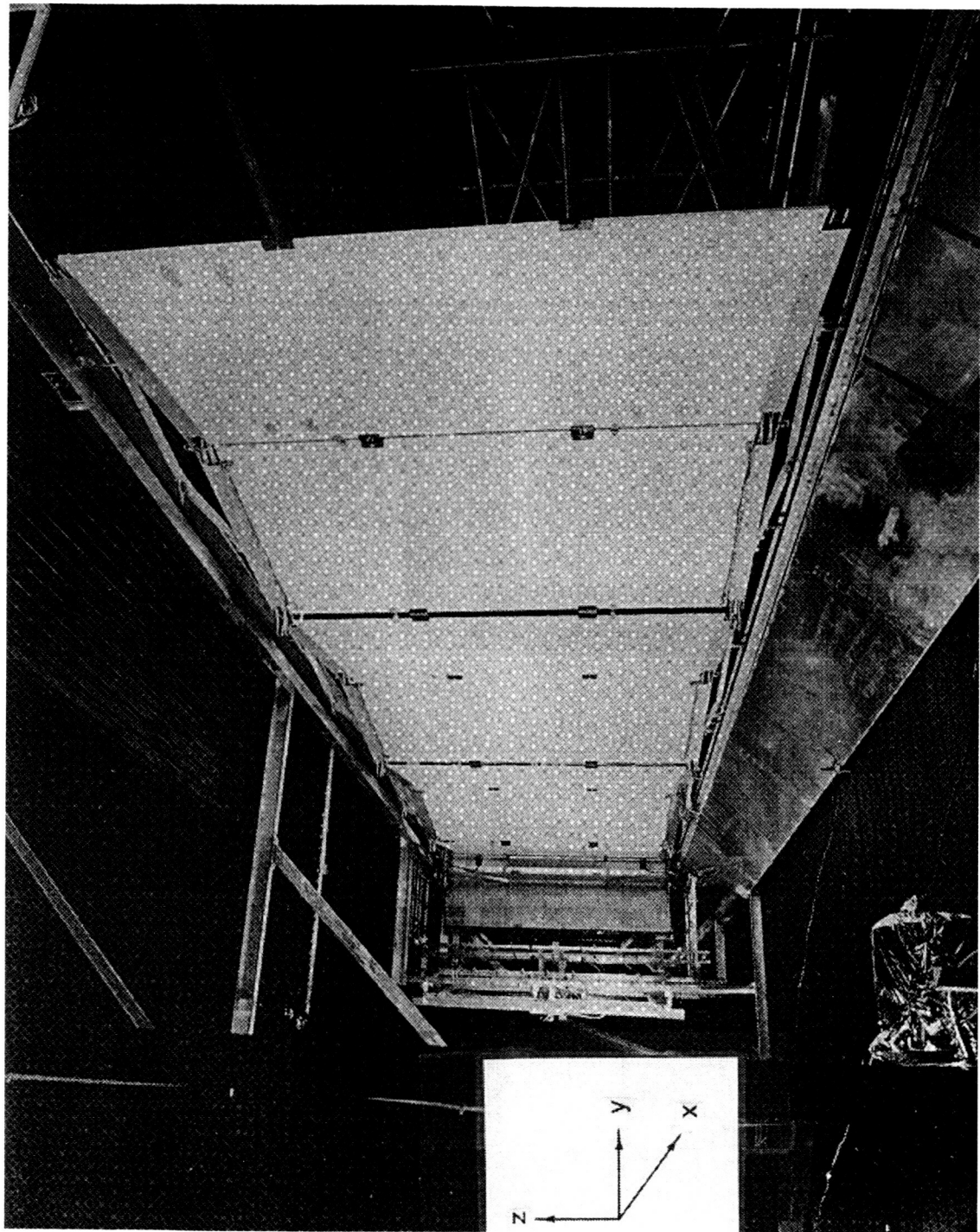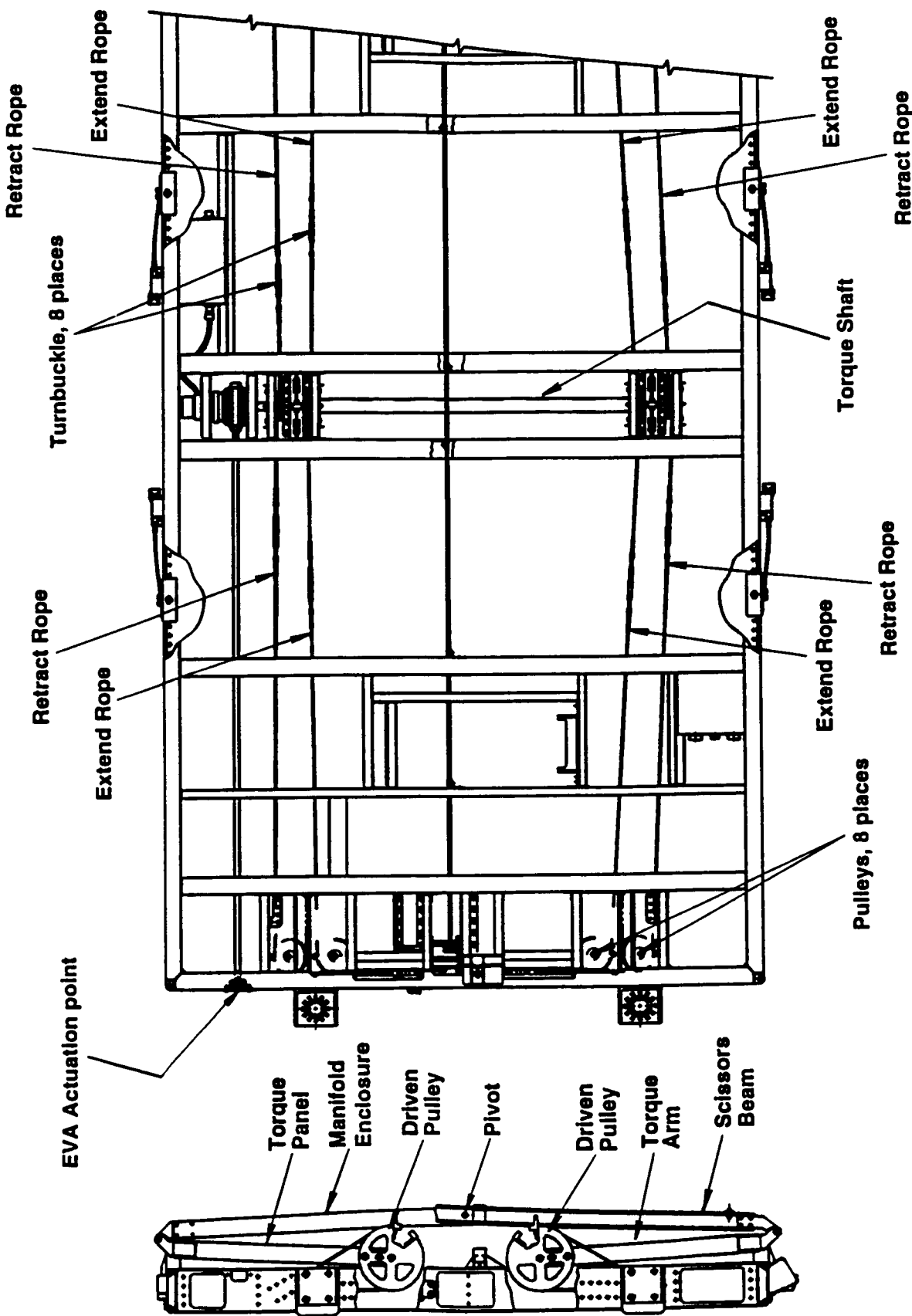
Figure 4. PVR Deployment and Retraction Mechanism

Extend Rope
Retract Rope
Extend Rope
Retract Rope
Turnbuckle, 8 places
Torque Shaft
Retract Rope
Extend Rope
Retract Rope
Extend Rope
EVA Actuation point
Pulleys, 8 places

Torque Panel
Manifold Enclosure
Driven Pulley
Pivot
Driven Pulley
Torque Arm
Scissors Beam

100
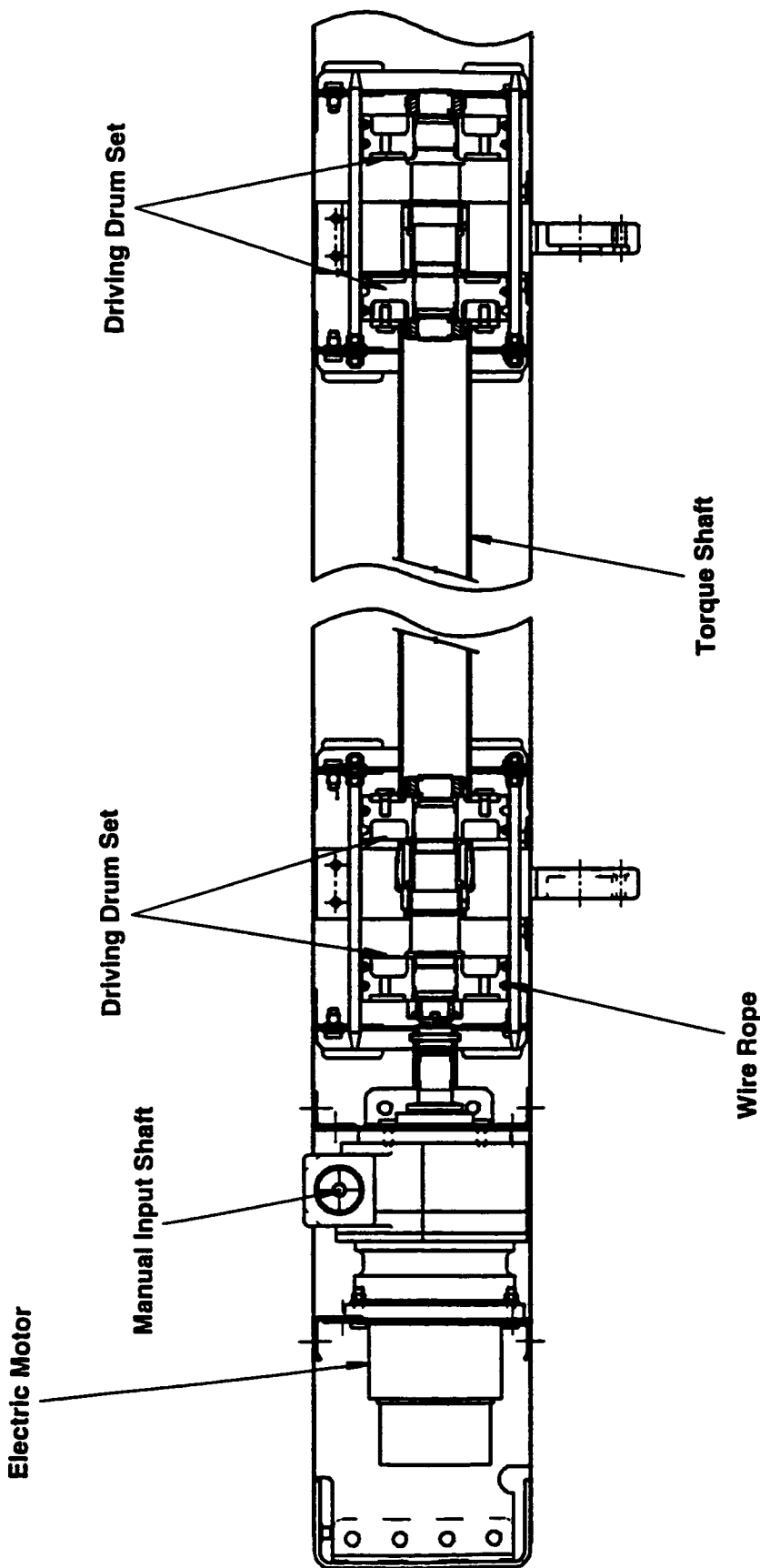
Figure 5. PVR Deployment and Retraction Mechanism
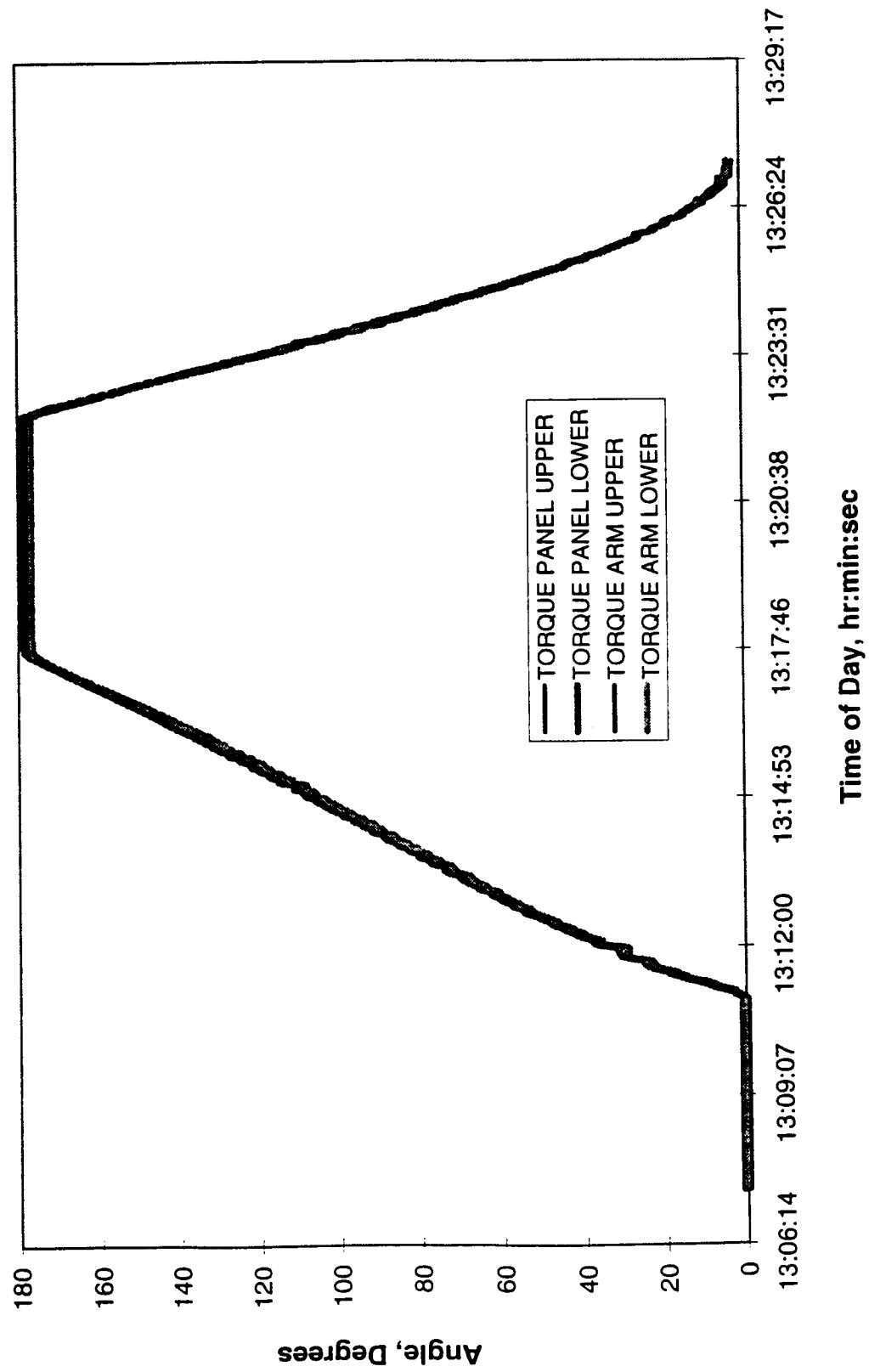
Figure 6. Deployment and Retraction Angular Displacements

102
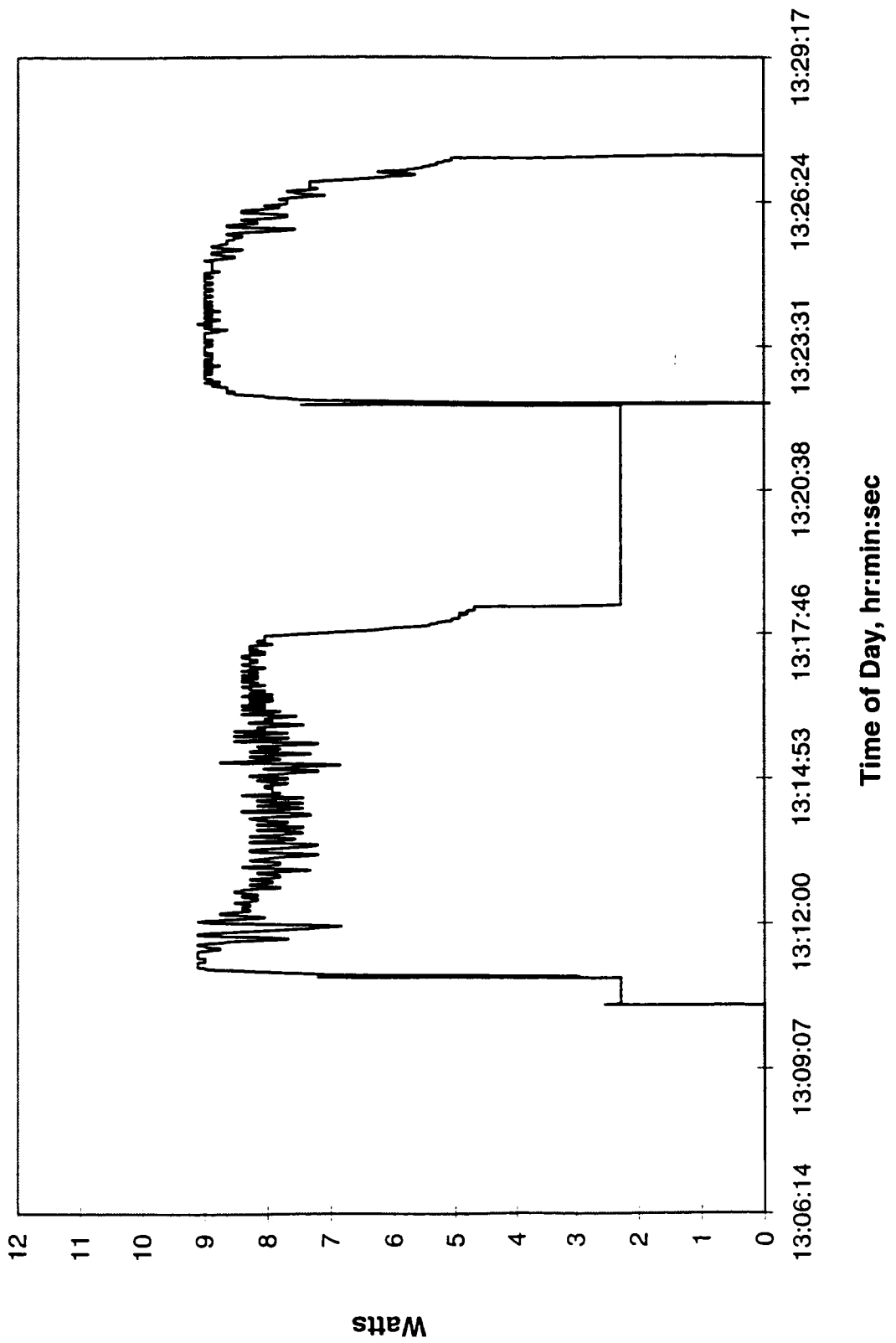
Figure 7. Motor Power Requirements During Deployment and Retraction
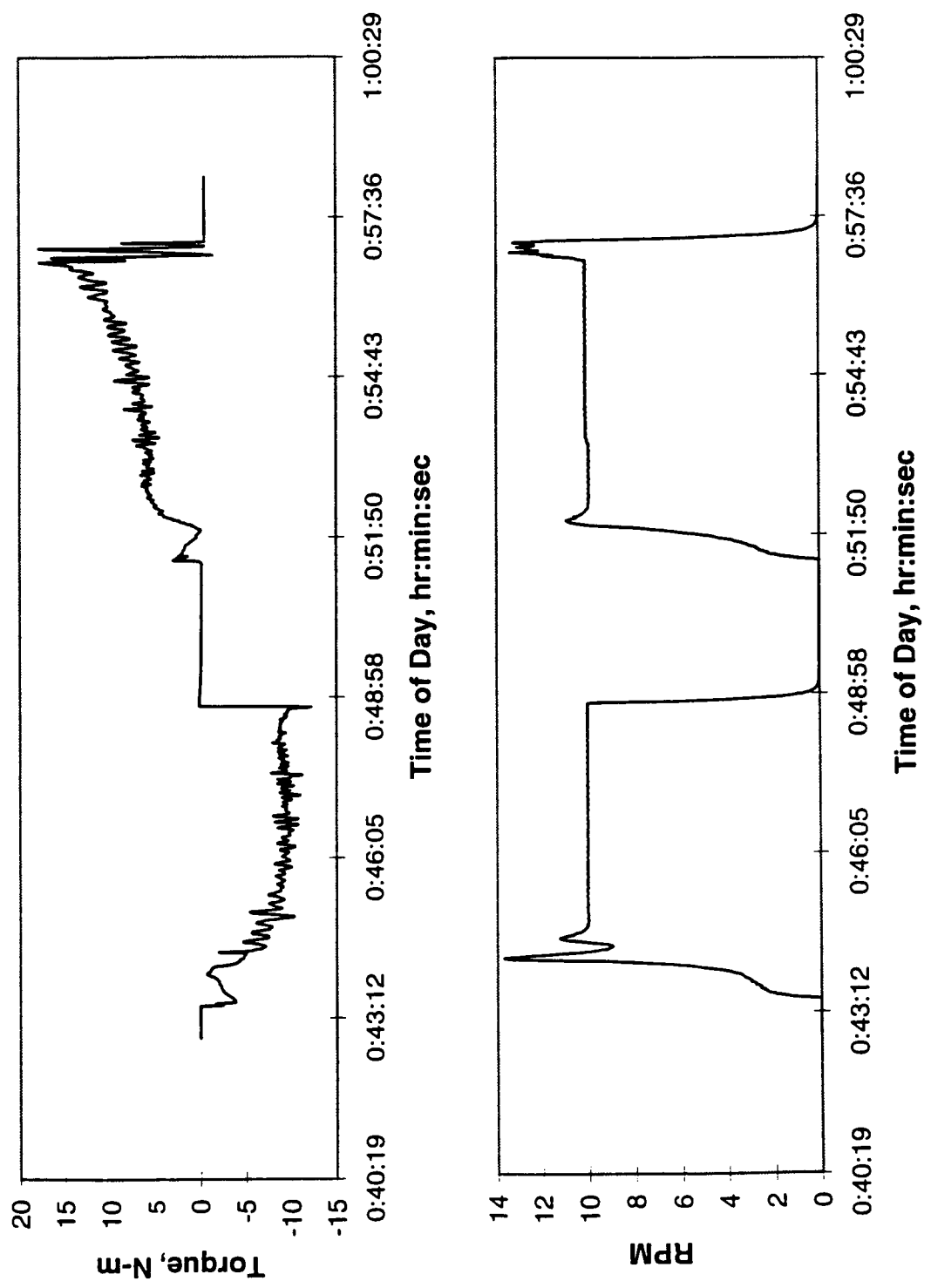
Figure 8. EVA Drive Motor Input Torque and Speed

Non-Explosive Pinpuller and Rotary Actuators

Michael Bokaie* and Kevin Barajas*

Abstract

Development of a line of high performance Pinpullers and Rotary actuators for aerospace applications has recently been concluded by TiNi Aerospace. Pin retraction or rotation is achieved by coupling the recovery characteristics of Shape Memory Alloy (SMA) material with a specially designed ball detent mechanism. In each case, Nitinol wire is used to trigger the release of stored energy in a preloaded spring (compression or torque, respectively). Key to the uniqueness of the actuators is fast actuation time, simple operation, and small size. Design, performance, and qualification considerations are presented.

Introduction

Pinpullers and rotary actuators serve as a common means for deployment of low force appendages such as optic and instrument cover doors, solar antennas, and other remote release applications. Among the devices currently available to the aerospace community are actuators which incorporate pyrotechnic, electromagnetic, fusewire, or paraffin as the means for actuation. In each case, however, certain disadvantages such as poor reliability, large size, excessive cost, and slow actuation time make each technology less than ideal for many applications. In particular, the recent trend away from pyrotechnic actuators aboard spacecraft due to concerns over safety, shock, and outgassing, has triggered research and development of a host of alternative technologies including Shape Memory Alloys (SMAs).

SMAs refer to a group of materials that have the ability to return to a predetermined shape when heated. The shape memory effect is caused by a temperature-dependent crystal structure. When an SMA is below its phase transformation temperature, it possesses a low yield strength crystallography referred to as Martensite. While in this state, the material can be deformed into other shapes with relatively little force. The new shape is retained provided the material is kept below its transformation temperature. However, if it is heated above this temperature, the material reverts to its parent structure known as Austenite causing it to return to its original shape. This phenomenon can be harnessed to provide a unique and powerful actuator.

The SMA actuators were developed under a NASA Small Business Innovation Research contract entitled, "A Low Cost, Compact Non-Explosive Pinpuller for Aerospace Applications" [1]. The pinpuller and rotary actuators developed can be operated with a wide range of power, cycled hundreds of times, and are reset by simply re-extending or counter rotating the output shaft, respectively. Furthermore, the

---

* TiNi Aerospace Inc., San Leandro, CA

105

SMA actuators consume relatively little power, are fast acting and do not pose any safety or outgassing concerns.

Discussion

Actuator Design:

Pin retraction or rotation is achieved by coupling the recovery characteristics of the Nitinol SMA with a detent mechanism that can support and release energy stored in a compression or torque spring, respectively. The detent is designed such that manual re-extension or counter-rotation of the pin automatically locks it back into the reset position, while simultaneously re-enabling the Nitinol wire for another actuation cycle. Further, to increase reliability, the SMA actuators incorporate a redundant Nitinol element capable of independently functioning the actuator.

Figures 1 and 2 represent a cross-sectional view of the mechanism used in the pinpuller and rotary embodiments, respectively. In each case, joule heating of the Nitinol wire causes it to shrink in length, thereby pulling "up" on the detent latch. This in-turn allows the detent balls to roll inward, allowing the pin to translate or rotate under the forces of the drive spring (compression or torque, respectively). Reset of the mechanism is achieved by manually bringing the pin back into alignment with the detent lock (i.e. back to original position). This allows the reset spring to drive the latch "downward" thereby re-engaging the detent balls with the base of the pin.
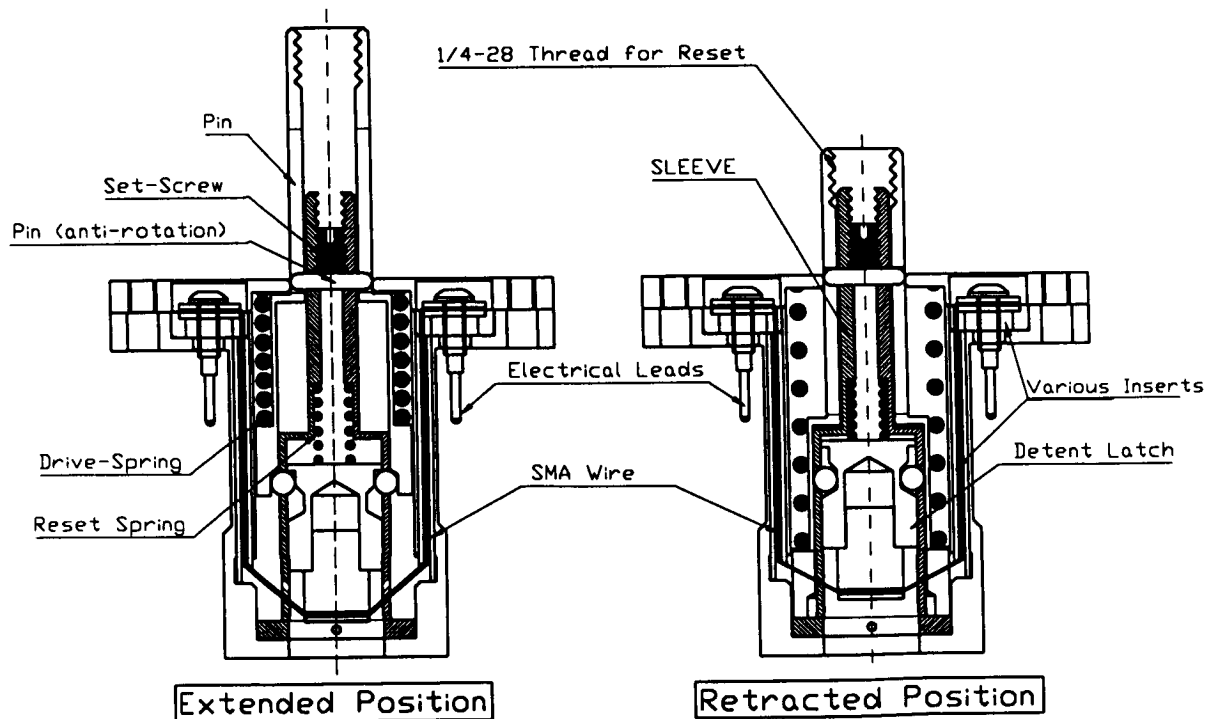

Figure 1   Pinpuller Cross Section (P25-8VS-1.2R)

Note that the Rotary embodiment of Figure 2 also incorporates an Auto Shut Off Switch which interrupts power to the Nitinol as soon as the actuator functions. This greatly increases the versatility of the actuator with respect to limitations on applied power (voltage and duration) and starting temperature. Without the switch, the Nitinol wire is prone to overheating if powered for too long. Experiments showed that for a given size Nitinol, applied power longer than 2 times the duration needed to function the actuator leads to premature Nitinol failure. Such levels of overheating result in the partial or full annealing of the Nitinol wire, causing Reset and or Actuation difficulties. Table 1 illustrates the basic performance specification corresponding to each of the actuators shown.
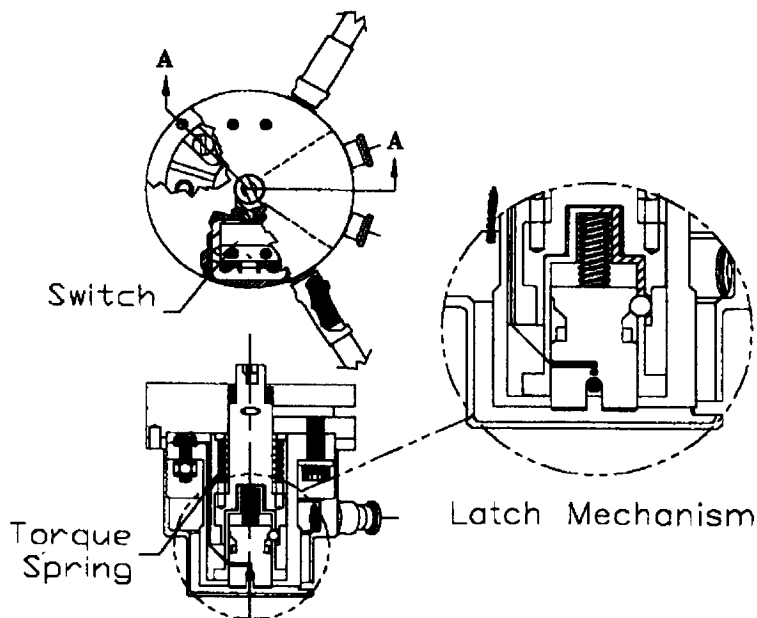

Figure 2   Rotary Actuator Cross Section (R4-45VSE-3.6R)

Table 1: Performance Specification

	Pinpuller P25-8VS-1.2R			Rotary R4-45VSE-3.6R		
Drive Force or Torque	110	N	25	lb	0.45	N-m	4	in-lb
Drive Stroke or Angle	1.27	cm	0.50	in	> 45	deg	> 45	deg
Resistance Primary Ckt.	1.2	ohms	1.2	ohms	3.6	ohms	3.6	ohms
Resistance Secondary Ckt.	1.2	ohms	1.2	ohms	3.6	ohms	3.6	ohms
Max Operating Temp.	70	°C	158	°F	70	°C	158	°F
Min Operating Temp	< -50	°C	< -58	°F	< -50	°C	< -58	°F
Mass	120	gm	4.23	oz	135	gm	4.76	oz

SMA Technology

The SMA material used is an alloy of Nickel and Titanium called Nitinol. This particular alloy has excellent electrical and mechanical properties, long fatigue life, and high corrosion resistance. In wire form, it has been found capable of up to 4% strain and greater than 400 MPa (57 ksi) stress recovery, resulting in ~1 Joule/g of work output. For engineering purposes, the Shape Memory phenomena can be best modeled using the material stress-strain curve. Figure 3 is such an illustration [2].
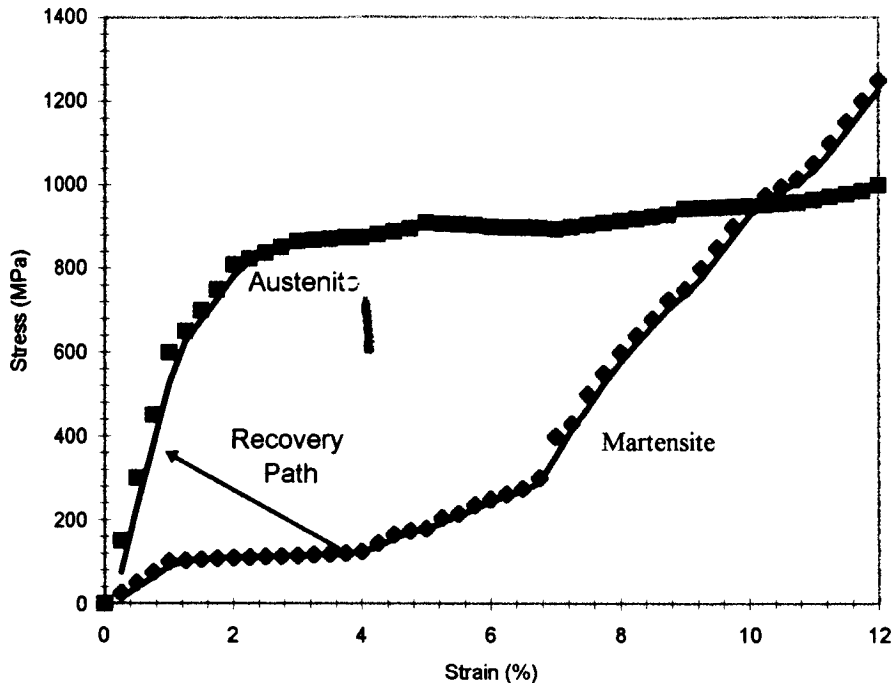

Figure 3:   Typical Stress-Strain Curve(s) for Nitinol

Note that 4% strain and 400 MPa are the points of intersection between the recovery path, and the corresponding martensitic and austenitic curves. The slope of the recovery line represents the external load applied to the Nitinol element. In the case of the actuators developed, this is a sum of the following:

- Ball Detent Forces
- Opposing Reset Spring
- Other Frictional Forces
- Dynamic Forces

As such, the steeper the recovery path (i.e., the higher the loads) the less stroke effectively recovered, and vice versa. Furthermore, the total amount of work performed by the Nitinol can be estimated to be the area under the stress/strain recovery path. Note that this path may be non-linear (Fig. 5).

108

Ball Detent Mechanism

The primary focus of the development effort was to optimize the latch trigger
mechanism. Although the ball detent had proved from the onset to be a reliable method
of securing and releasing shaft loads, many different iterations had to be designed,
manufactured and tested before the optimum configuration could be derived. The
challenge was to converge on a design that demonstrated the proper balance between
the following key requirements:

1) Maximize the reduction ratio between force applied to the output shaft/pin (i.e.,
   from the compression or torque springs, respectively) to the force needed to
   release the latch (i.e., from the Nitinol wire).

2) Minimize the stroke needed from the Nitinol wire to reliably release the latch.

3) Ensure that the design is fully stable in the latched position so as to be capable of
   enduring launch shock and vibration.

4) Design sufficient margin into the SMA force and stroke as to meet aerospace
   requirements.

Figure 4 represents the basic design evolved. Note that the directions of the particular
vectors shown is more representative of the loading for the pinpuller configuration. The
rotary actuator is designed to mimic the same load distribution with the forces rotated 90
degrees about the vector F_{latch}.
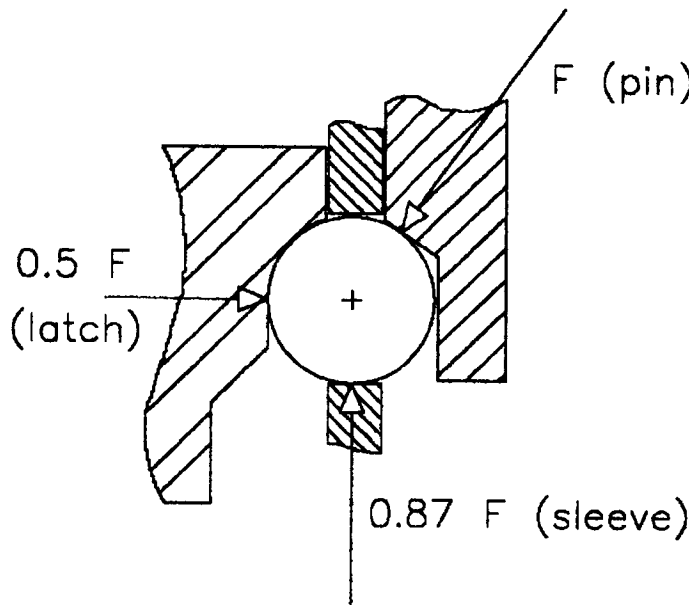
Figure 4 Ball Detent Force Balance

Figure 5 represents a characteristic latch release force profile. Note that since this test was performed with a relatively slow moving latch, it does not take into account the dynamic forces that are developed during a typical 10 msec actuation cycle. Under such conditions, the latch is accelerated sufficiently fast such that its mass contributes significantly to the total load applied to the Nitinol wire. The trigger force vs. stroke data is shown as a function of various input forces from the drive spring (Fpin) to determine susceptibility to overloading. The trend suggests that the latch configuration is inherently forgiving to higher forces applied (i.e. a 200% increase in drive spring force (from 20 to 40 lbf) increased the maximum release force by ~50% (from 2 to 3 lbf)).
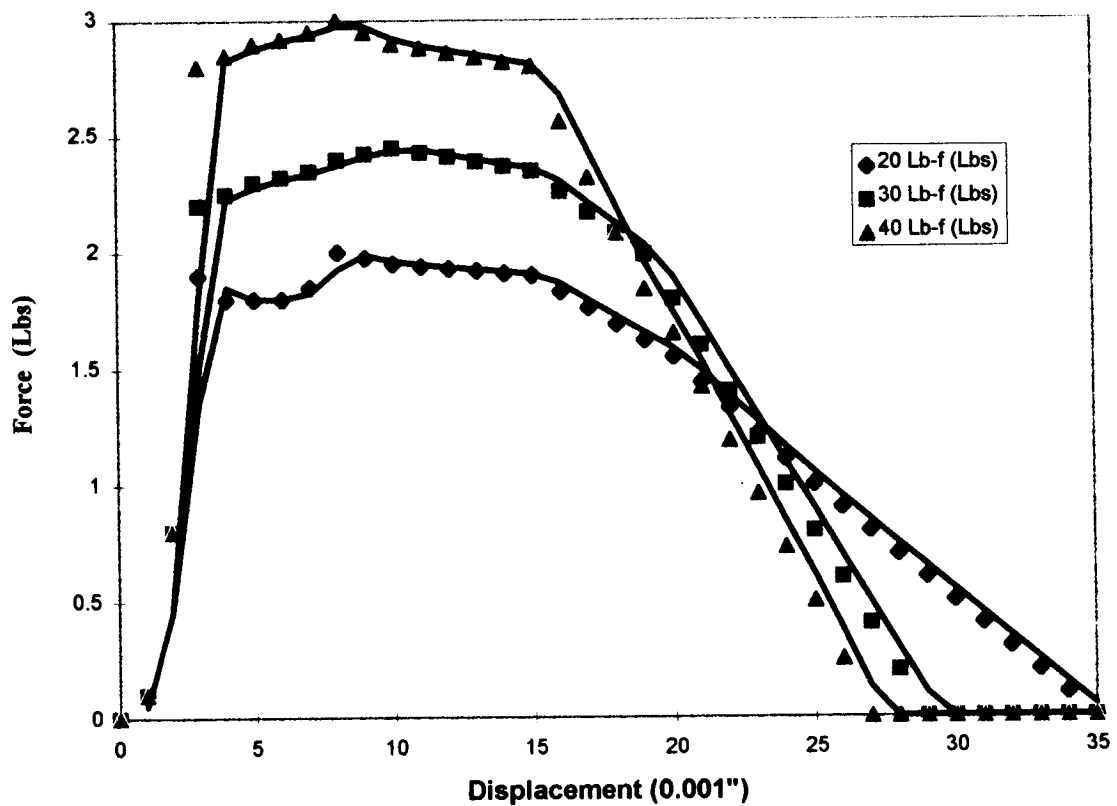

Figure 5   Latch Release Force Profile

The rapidly increasing force during the first 0.13 mm (5 mils) of latch travel is attributed to higher initial frictional loads potentially causing the detent ball to slide rather than roll. Note that theoretically there should be no latch movement until a force equal to the reset spring preload (~1.0 lbf) is applied. The gradual decrease in release force, after ~0.38 mm (15 mils) of travel, is attributed to the vector component which begins to help push the latch to the release position.

110

Actuator Function Time

One of the primary attributes of the technology developed is that the actuators may be functioned in milli-second time frame. Figure 6 represents a typical function time curve for a Rotary embodiment. Note that as with other thermal actuators, the function time of the SMA is dependent on applied current and starting temperature.
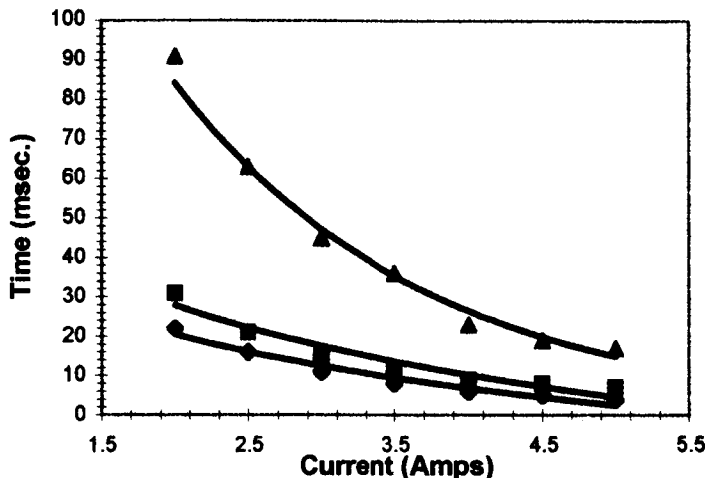

Figure 6 Actuation Time as a Function of Applied Current

The following equations govern the function time of SMA actuators [3].

$$T \quad = \quad Q_T / P \quad = \quad Q_T / R^* I^2 \qquad \textbf{(Equation 1)}$$

where;

T	=	Actuation Time	(sec)
Q_T	=	Total Energy Needed	(Joules)
P	=	Power Applied	(Watts)
R	=	Nitinol Resistance	(ohms)
I	=	Applied Current	(amps)

$$Q_T \quad = \quad Q_{1\,(to\,heat)} + Q_{2\,(transformation)} + Q_{3\,(Work\,Performed)} + Q_{4\,(Lost)} \qquad \textbf{(Equation 2)}$$

where;

Q_1	=	(m) * (Cp) * (T_{finish} - T_{start})	(J)	(Equation 2.1)
Q_2	=	(m) * (lt)	(J)	(Equation 2.2)
Q_3	=	(F) * (d)	(J)	(Equation 2.3)
Q_4	=	Heat Lost (minimal <10%)	(J)	

where;

m	=	Actuator Mass	(gms)
Cp	=	Specific Heat Capacity of Nitinol = 322	(J/kg°K)
T_{finish} - T_{start}	=	Temperature Delta	(°K)
lt	=	Latent Heat of Transformation = 24200	(J/kg)
F	=	Recovery Force Exerted by the Nitinol	(N)
d	=	Recovery Stroke Distance	(m)

SMA Margin

During the course of developing and qualifying the actuators, the force and stoke margin placed on the Nitinol wire was found to be key to proper operation of the mechanism. Safety margins placed on the Nitinol wire must take into account the dependency of recovery force vs. stroke. Namely, as the applied load goes up, the recovered stroke goes down. <u>Furthermore, the failure mode will always present itself as lack of available stroke</u>. Such a failure was observed during the qualification of the Rotary Actuator (model R4-45VSE-3.6R).

The Nitinol wire used has a maximum recoverable strain of only 4%. This calculates to ~2.5 mm (100 mils) of stroke at the latch for the particular actuator configuration of Figure 2. Under ideal conditions, this represents a greater than 3X margin on the 0.71-mm (0.028-in) stroke needed to release the latch. However, through an exhaustive qualification test program, it was discovered that each of the following items helped sufficiently reduce the net stroke available, as to cause a random failure under cold test (-15°C) conditions.

1. Excessively stiff reset spring significantly increased the stress placed on the Nitinol wire. This had two side effects. First, this reduced the overall stoke capability of the Nitinol wire. Second, the higher stress caused the Nitinol strain recovery to decay at a much faster rate. This caused the problems to appear not during the 18-cycle acceptance test, but during qualification and system-level tests.

2. Additional torque (load) applied to the output shaft (due to an interface problem), caused significantly increased loads to be transmitted through the ball lock. Figure 5 shows the ball lock to be generally forgiving to force fluctuations. However, if the applied load is increased dramatically (several times), then the latch release force can grow beyond the capability of the Nitinol wire.

3. Differences in material CTE (Coefficient of Thermal Expansion) caused the Nitinol wire to effectively become slack under cold temperature conditions. The housing and latch are made from SP1 Vespel (CTE of 30×10^{-6}), resulting in an overall Nitinol path length shrinkage of 0.076 mm (3 mils). This was sufficient as to surface the overall lack of margin problem under cold temperature conditions.

4. Dynamic effects significantly increased the overall force which the Nitinol had to overcome. Throughout development the benchmark test for latch release force, was a manual release using a force gage through an access hole in the back of the actuator. Although this proved invaluable at determining the general "health" of the mechanism, it did not register the acceleration forces which are developed during fast actuation (<10 msec). This further reduced the Nitinol stroke margins.

For the particular program, the fix was achieved through a correction of items 1 and 2, above. Note, however, that if the application is not sensitive to actuation time, more

112

force margin can be obtained by simply increasing the size of the Nitinol wire diameter (F= Stress•Area). This of course has the primary negative consequence of reducing the function time and or requiring higher power consumption.

Conclusion

Lessons Learned

As with most things, ultimately it is the end user which has the fortune of uncovering design weaknesses which, when corrected, transforms the prototype into working hardware. Development of the SMA actuators was no exception. During the course of flight qualification, the following key lessons were learned:

1) SMAs have two primary failure modes: Over-Heating and Over-Stressing.

2) Integration of a shut off switch is invaluable in eliminating the risk of overheating the Nitinol wire. This is especially critical when the application must endure a wide range of operating voltage and starting temperature.

3) Margins on SMA work output (stroke recovery) must take into account performance degradation over the life of the actuator under worst-case operating conditions, including maximum applied loads, high acceleration forces, and temperature effects.

Current State of Development

Since its introduction in early 1996, the SMA actuators have gained increasing popularity as demonstrated by the following product heritage.

Organization	Project	Embodiment	Status
AeroAstro	Terriers	Pinpuller	Qualified
Space Sciences Lab.	MARS Global Srvyr	Pinpuller	Flown
NASA Wallops Flight Cntr.	Sounding Rocket	Pinpuller	Flown
Naval Research Lab.	ATEX	Pinpuller	Qualified
Space Sciences Lab.	Lunar Prospector	Pinpuller	Flown
NASA Wallops Flight Cntr.	Sounding Rocket	Pinpuller	Qualified
NASA Marshall	IMAGE (WIC.)	Rotary	Qualified
Space Sciences Lab.	IMABE (SI.)	Rotary	Qualified
Naval Research Lab.	ARTS II	Rotary	Qualified
Lockheed Martin	Classified	Rotary	Qualified

References

1. Michael D. Bokaie: "A Low Cost, Compact Non-Explosive Pinpuller for Aerospace Applications", NASA Small Business Innovation Research (SBIR) contract NAS3-27292 final report, February 1996. NASA Lewis Research Center, Cleveland Ohio.
2. Tom Waram: "Actuator Design Using Shape Memory Alloys", second edition ©1993.

John D. Busch and Michael D. Bokaie: "Implementation of Heaters on Thermally Actuated Spacecraft Mechanisms" 28th Aerospace Mechanism Symposium, NASA Lewis Research Center, May 18-20 1994, page 379-393.

Improvements for Rotary Viscous Dampers used in Spacecraft Deployment Mechanisms

Alphonso Stewart*, Charles Powers* and Ron Lyons**

Abstract

During component level thermal-vacuum deployment testing of eight rotary viscous dampers for the Tropical Rainfall Measuring Mission (TRMM) satellite, all the dampers failed to provide damping during a region of the deployment. Radiographic examination showed that air in the damping fluid caused the undamped motion when the dampers were operated in a vacuum environment. Improvements in the procedure used to fill the dampers with damping fluid, the installation of a Viton vacuum seal in the damper cover, and improved screening techniques eliminated the problem.

Introduction

The Tropical Rainfall Measuring Mission is a joint mission between NASA and the National Space Development Agency of Japan designed to monitor and study tropical rainfall. The TRMM spacecraft structure was built by the NASA Goddard Space Flight Center (GSFC) in Greenbelt, Maryland. The TRMM spacecraft carries five instruments and is powered by two solar arrays. Communication with ground stations is through a high gain antenna (HGA).

Rotary viscous dampers have been successfully used in hundreds of deployment mechanisms for satellites, and were therefore selected for the TRMM solar arrays and HGA deployment. The dampers are used in tandem with springs which supply the deployment energy. Without properly functioning dampers, the solar arrays and HGA would deploy at abnormally fast rates which would result in excessively high impact loads at the end of travel. The damper controls the deployment velocity and the end of travel impact loads. This approach is typical of spacecraft deployment mechanisms used to deploy solar arrays, antennas and instrument booms.

Initially, the dampers were deployed in an ambient environment and operated nominally. As part of acceptance and qualification testing, the dampers are subjected to a component level thermal-vacuum deployment test. When this test was performed on a group of eight dampers for TRMM, none of the dampers provided adequate damping during deployment. An investigation of the damper failures identified the cause and led to improvements to resolve the problem.

After the TRMM spacecraft was successfully launched on November 27, 1997, all the dampers performed nominally during the deployment of the solar arrays and HGA.

---

* NASA Goddard Space Flight Center, Greenbelt, MD
** DEB Manufacturing Inc., LakeWood, NJ

Discussion & Analysis

TRMM Damper Description

Rotary viscous dampers are used in deployment mechanisms to control the rate of deployment. The basic internal components of the damper used in the deployment of the TRMM solar arrays and HGA is shown in Figure 1 (DEB Manufacturing Inc. p/n 1025-9370). The damper is comprised of a rotating paddle or vane in a (primary) chamber of high viscosity fluid. There is a secondary (fluid expansion) chamber which allows the fluid in the primary chamber to expand due to changing thermal conditions. Between the primary and secondary chambers is a check valve system. The check valve allows the expanding fluid in the primary chamber to flow into the secondary chamber during thermal expansion. During damper actuation the check value closes, which keeps the fluid in the primary chamber. An adjustment screw in the center of the rotating shaft allows the damping rate to be controlled by adjusting the size of an orifice in the shaft. Prior to resolving the TRMM damper problem, the Viton seal was not included in the damper.
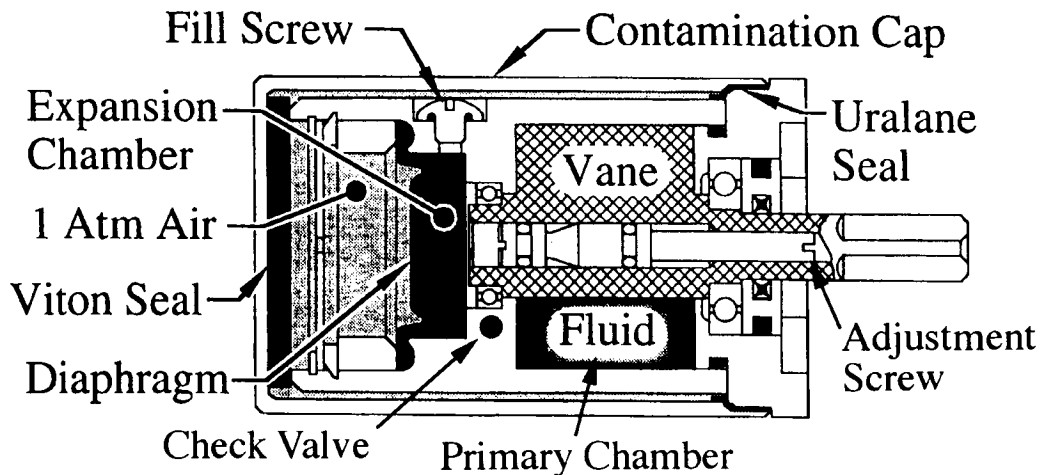

Figure 1. Internal View of TRMM Damper

When torque is applied to the damper, the paddle forces viscous fluid through an orifice to the back side of the paddle in the primary chamber. The viscous fluid flow through the small clearances in the primary chamber also adds to the damping. This design allows the adjustment screw to control the fluid flow through the orifice until its resistance becomes greater than the resistance of fluid flow between the paddle and the chamber walls.

The damper is mounted along the hinge line of the deployment mechanism such that pure torsional loading is applied. There are no side (moment) loads on the shaft and there is a flexible coupling between the damper and rotating shaft to prevent axial loads from transmitting into the damper.

116

Original Fabrication and Testing

Following assembly of the damper components, each damper is filled with degassed silicone damping fluid. A cup filled with the damping fluid is attached to the damper at the fill hole (see Figure 2). The cup and damper are then placed into a vacuum chamber that achieves a pressure of about 1.3 Pa (10^{-2} torr). This setup requires any air in the damper to exit through the damping fluid in the cup. The damper is also heated to help the flow of the damping fluid. The cup and damper remain in the vacuum chamber until no bubbles are observed coming from the damping fluid in the fill cup (usually 2 to 4 days). After being removed from the vacuum chamber, the cup is removed from the damper and a screw is put in the fill hole of the damper to seal in the damping fluid.
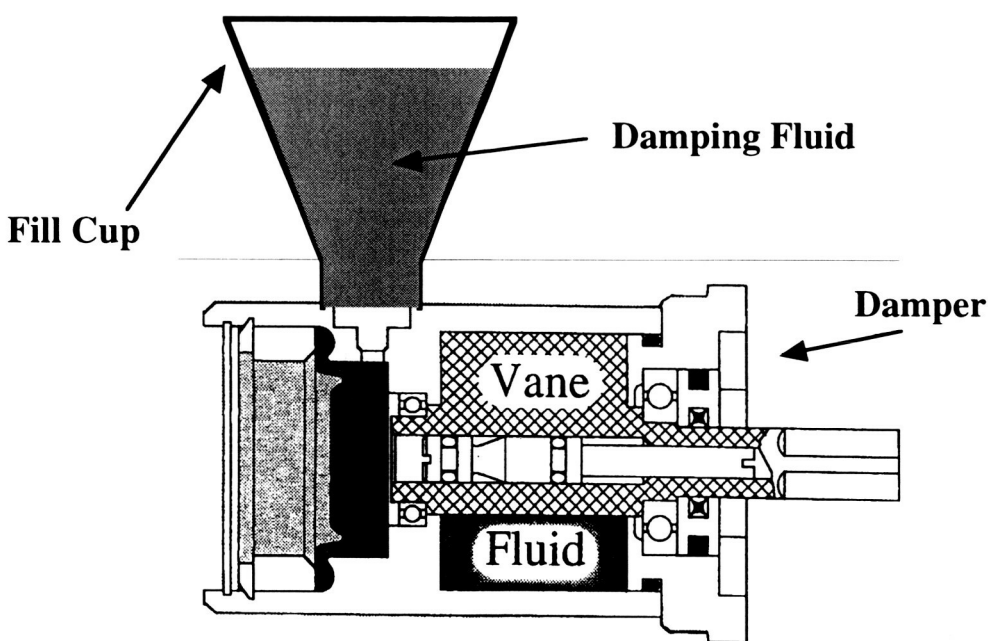

Figure 2. Original Damper Filling Setup

Each damper is then placed into a test fixture to measure and adjust the damping rate to meet specifications. A radiograph of each damper is taken at ambient pressure to examine the internal condition of the damper. After delivery to GSFC, the dampers are subjected to a random vibration test and inspected for damping fluid leaks. Further deployment tests at hot and cold temperatures (in air) are performed at GSFC to adjust the final setting of the damping rate for each damper. A contamination cap is then screwed on to each damper. Epoxy or uralane is applied to the threads connecting the cap and damper to seal the damper against vacuum exposure. The potential problem of air bubbles developing in the damping fluid during vacuum exposure was known at this time.

TRMM Deployment Anomaly

There were a total of 8 hinge mechanisms and 16 dampers. Each damper was mounted to a hinge assembly and deployed at +30°C at ambient pressure prior to a thermal-vacuum deployment test. Undamped motion was not observed during this test. Eight dampers and hinge mechanisms were then placed in a thermal-vacuum chamber and cycled 4 times between -20°C to +50°C before being deploying at -20°C. The mechanisms were restowed and the test continued. After four more cycles the dampers and hinge mechanisms were deployed at +50°C.

Figure 3. Radiographic Image of Air Bubble

During the thermal-vacuum deployment test, the hinge mechanism for each damper "jumped" a portion of their travel. There was no apparent damping for this portion of the travel. All the hinge mechanisms exhibited some undamped motion. The hinge mechanisms were removed from the thermal-vacuum chamber and an ambient deployment test was performed. Undamped motion was again noted with some of the dampers. The dampers were removed from the mechanisms and examined using digital radiography in an ambient environment. This examination revealed that 2 of the 8 dampers had air bubbles in the damping fluid as well as extended diaphragms. Figure 3 is a radiographic image of a damper tilted at a 45 degree angle, showing an air bubble in the damping fluid in the expansion chamber. The diaphragm should

118

normally be just above and parallel to the white band running across the image. The diaphragm in the other 6 dampers were also extended from their nominal "as delivered" position. Several days later, radiographic examination found that the six dampers that did not have visible air bubbles had recovered back to their "as delivered" condition. The other two dampers still had a visible air bubble in the damping fluid.

To further investigate the vacuum effect on damper behavior, a small glass vacuum jar was added to the digital radiography facility in the Materials Engineering Branch. This setup allowed the development of an air bubble under vacuum conditions to be observed radiographically in real time. This setup later became a tool to screen dampers before going through a thermal-vacuum deployment test. Figures 4 and 5 show the condition of a damper before and during vacuum exposure. In this particular damper, a visible air bubble existed in the damping fluid at ambient conditions. When the damper was exposed to a vacuum, the bubble expanded which also caused the diaphragm in the damper to extend from its normal shape. After the vacuum exposure, the damper returned to its pre-vacuum condition. Shown in these figures is a pin that was allowed to rest on the diaphragm to measure diaphragm extension. In the case of the 6 dampers that did not have a visible bubble at ambient conditions, a bubble was seen when they were exposed to a vacuum and examined with radiography.

This behavior explained how a damper could perform nominally in an ambient environment, but not in a vacuum. A small amount of air in the damping fluid does not effect the performance of the damper under ambient conditions. This air expands to fill a larger volume under vacuum conditions, which causes a dead band (region of no damping) during deployment. For this to occur, air must be present in the damping fluid and the damper must have a poor seal against vacuum.

The Fixes
Initially, it was determined that inadequate epoxy adhesive was applied in the threads between the damper and contamination cap to vacuum seal the damper. To repair the vacuum seal, the contamination caps were removed from the dampers, a generous amount of uralane was applied to the threads and the caps were screwed back on to the dampers. All 16 TRMM dampers were retested with a thermal-vacuum deployment test and performed nominally. However, during a post thermal-vacuum deployment test, one of the dampers provided no damping for a portion of the deployment. Radiographic examination determined that the failed damper had a bubble in the damping fluid.

With the failure of this one damper to operate properly, an effort was undertaken to eliminate all air bubbles in the damping fluid by improving the fill process performed by the vendor. This included adding a step to the fill process to first evacuate the inside of the damper before adding the damping fluid and by lowering the vacuum pressure in which the fill process was performed. An inspection step was also added by the vendor to help determine if there was any air left in the damper after filling.
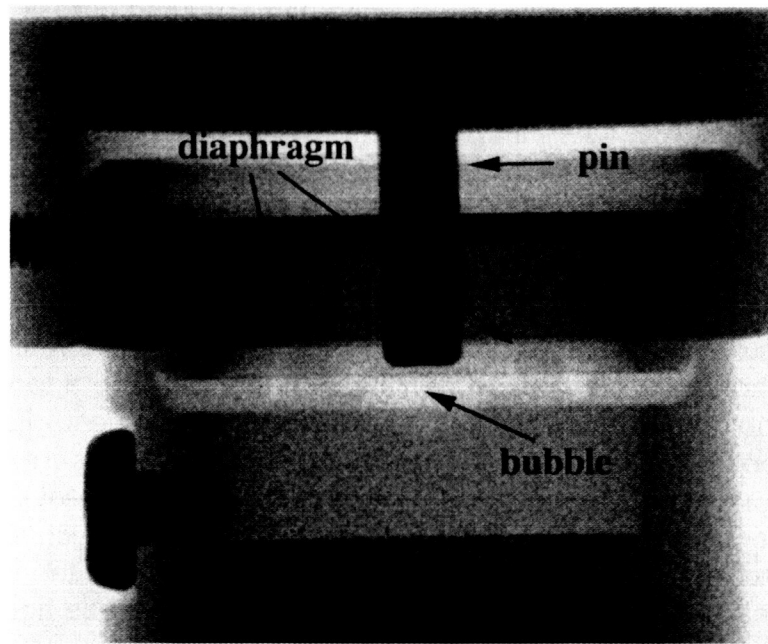
Figure 4. Radiograph of Damper at Ambient Conditions
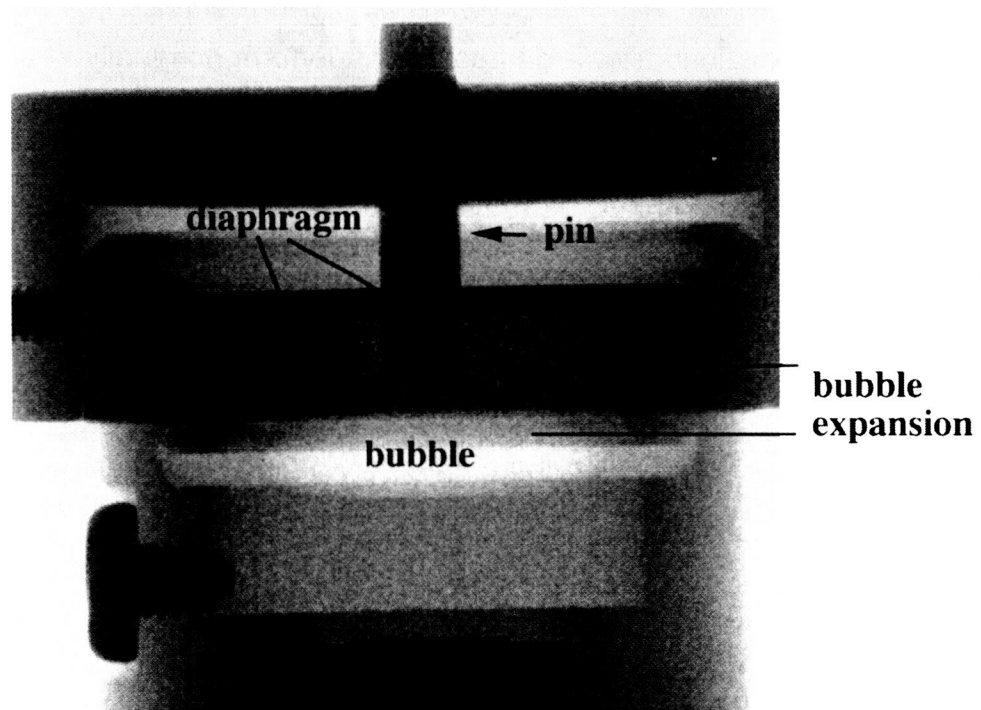

Figure 5. Radiograph of Damper During Vacuum Exposure

The original fill process for these dampers was performed in a vacuum chamber that was evacuated using a mechanical pump. This setup could achieve a vacuum pressure of about 1.3 Pa (10^{-2} torr). For the new fill process, a diffusion pump attached to the vacuum chamber was refurbished. With the diffusion pump now operational, a vacuum pressure of 1.3×10^{-3} Pa (10^{-5} torr) could be achieved.
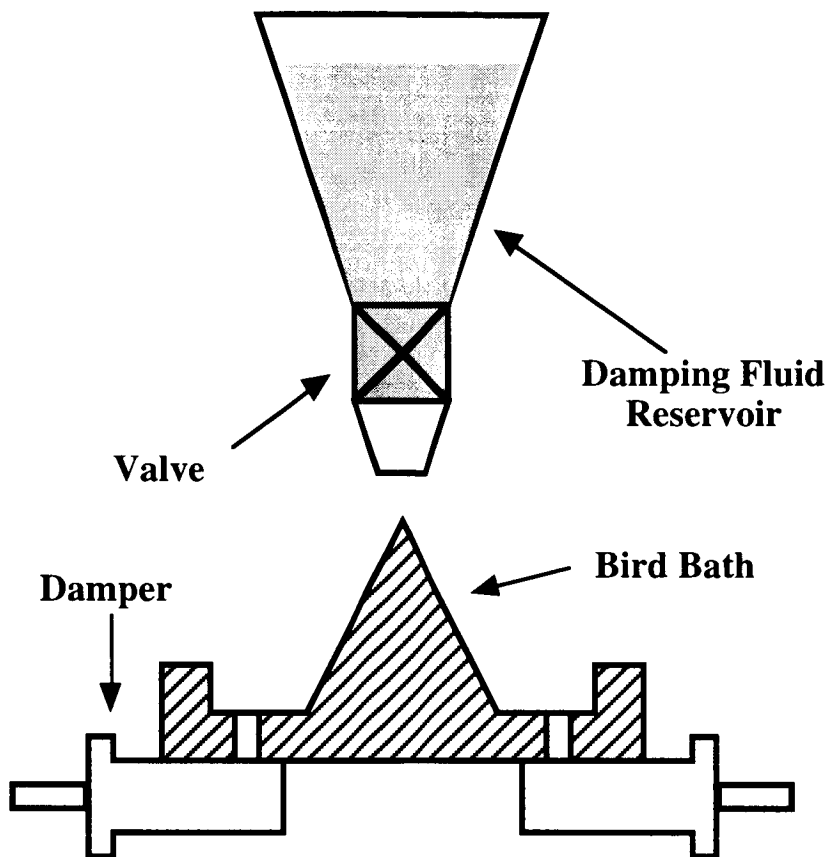

Figure 6. New Evacuation/Fill Fixture for the TRMM Dampers

A new fixture was also fabricated that would allow air in the dampers to be evacuated before the damping fluid was added. The design of this fixture was based on another fixture used by the vendor to fill a smaller damper. The dampers would be attached to the bottom part of the fixture (called the "bird bath") and the reservoir was mounted above the bird bath to fill the dampers (Figure 6). The reservoir has a valve attached at the bottom that was used to release the damping fluid into the bird bath and into the dampers. The fixture was placed into the vacuum chamber for several hours to evacuate the dampers before the valve was opened. This allowed air in the damper to be evacuated before the damper was filled. Once the damping fluid was allowed to flow, the bird bath filled with damping fluid which flowed into the dampers. The apparatus remained in the vacuum chamber until bubbles stopped coming out of the dampers through the fluid in the bath. Once the dampers were filled, the vacuum was

released and the fill screw was installed while the fill hole of the damper was still submerged.

Following the fill process, the dampers were tested for air bubbles using a "pin" test. A small dowel pin was allowed to rest on top of the diaphragm in the damper. The pin and damper was placed back in the vacuum chamber. If a bubble formed in the damping fluid, it caused the diaphragm to extend which would cause the pin to rise. This is illustrated in Figures 4 and 5. If the pin rose more than 1.3 mm (0.050 inch), the damper would go through an additional fill step. The additional fill step required the damper to be returned to the bird bath fixture without draining the damping fluid, and the fill process repeated. Ideally, the fill process was repeated until the damper passed the pin test. The criteria was set at 1.3 mm (0.050 inch) because this volume was estimated to be equivalent to a bubble volume that would produce a 10 degree loss of damping during deployment. A 10 degree loss of damping was acceptable for the TRMM spacecraft. Testing of the new multiple fill process revealed that some dampers could be filled to a point that they would pass the pin test and others could not.

Since the new fill process alone did not completely guarantee that a damper would be bubble-free when exposed to a vacuum, the possibility of improving the seal against vacuum exposure was further pursued. This effort found that a disk shaped Viton seal placed between the contamination cap and the damper would provide the needed seal against vacuum exposure (see Figure 1). The Viton seal was rigorously tested in over 20 dampers and always provided a seal against vacuum-induced bubbles.

With the success of the Viton seal, the requirements of the pin test were relaxed provided a bubble was not visible in the radiograph of the Viton sealed damper taken in a vacuum. The digital radiography system with the vacuum jar was used to verify that all the TRMM dampers met this requirement. After the dampers were refilled, a Viton seal was installed in each damper (without the application of uralane to the threads). To verify that the seal was working, the damper would be examined for bubbles with the radiography system under vacuum conditions. After the Viton seal was found to be acceptable, final installation of the contamination cap on to the damper was performed with uralane applied to the threads.

The final fix used for the TRMM dampers included the new fill process, the Viton seal, the application of uralane on the threads of the contamination cap and damper, and examination of the damper under both ambient and vacuum conditions using digital radiography. None of the reworked TRMM dampers developed a visible bubble during radiographic screening in vacuum and all the reworked dampers operated nominally (no loss of damping) during thermal-vacuum deployment testing.

Lessons Learned

1. In general, some air will remain in the damping fluid after the damper is filled. The new fill process developed for the TRMM dampers reduced the amount of trapped air, but did not completely eliminate it in every damper.

2. A fill verification must be performed prior to installation of the contamination cap on to the damper, either before delivery by the manufacturer or upon receipt of the damper by the customer. This will help discover any bubbles early on. For the manufacturer, the pin test is the easiest method of verification. At GSFC, a verification of the fill process is done with radiography at ambient conditions.

3. A reliable seal, such as the Viton seal used for TRMM, must be added to the damper to prevent a vacuum environment from effecting the diaphragm. Our testing has shown that a damper with no detectable bubble at ambient conditions can develop a bubble under vacuum conditions if it does not have a good seal. Radiographic examination of a sealed damper under vacuum conditions is the best method for verifying that the damper is bubble-free. Identical deployment test behavior of a damper under ambient and vacuum conditions can also be used to assure the integrity of the seal.

4. Typically, the performance of a damper is checked by deploying it in air and in vacuum, and then comparing the deployment times. Our testing has shown that this will not always reveal the presence of a bubble or dead band in the damper. Typically, a dead band during deployment (due to a bubble) does not greatly effect total deployment time because the deployment mechanism provides little inertial load. To identify a bubble in the damper, the deployment angle versus time must plotted. If sudden jumps or dead bands are observed, the damper contains an air bubble.

5. The effect of a bubble in a damper during a deployment test was generally not repeatable. In a damper with a bubble and a bad seal, there was a large test to test dead band variation under vacuum test conditions. This was probably due to bubble size variations from vacuum test to vacuum test. In a damper with a bubble but with a good seal, the variation in dead band was less. This was probably because the size of the bubble was not changed by vacuum exposure.

6. Gravity affects the location of a bubble in the damper. During our grounding testing of the dampers, the dead band due to a bubble always occurred at the beginning of a deployment test. It is not known whether this behavior will be the same in the "zero-G" environment of actual space flight use.

Conclusions

1. The improved fill process, the addition of a Viton vacuum seal, and radiographic screening provided reliable dampers for the TRMM program. All the reworked dampers went through deployment testing under ambient and vacuum conditions without developing a measurable dead band (loss of damping) due to air in the damping fluid. This method of filling, sealing, and testing the dampers can produce dampers with no detectable bubble in the damping fluid.

2. More recent work on 1025-series dampers for another program showed that a damper containing a bubble in the damping fluid but with a good vacuum seal is acceptable for space flight use provided the deployment mechanism can tolerate a small stable bubble-induced dead band when deployed.

Acknowledgments

Stress Relaxation of Spring Materials

W. David Hanna, Dick J. Chang and Gary L. Steckel

Abstract

Stress relaxation behavior is presented for five spacecraft spring alloys. Data were obtained as a function of initial stress for 0.51 and 1.27 mm (0.02 and 0.05 in) wires in uniaxial tension at ambient temperature. Elgiloy and 17-7 PH were the most resistant, followed by 302 stainless steel and music wire. Be-Cu alloy 25 was the least resistant. An analytical technique to predict stress relaxation of springs, based on the uniaxial wire data, is presented.

Introduction

Deployable space hardware, such as solar panels and booms that depend on spring energy for deployment forces, may be compromised by loss of energy in the spring due to stress relaxation during long-term storage. As a result, either a pre-storage or post-storage analysis is required whenever critical hardware having stressed springs is placed in long-term storage. A major obstacle to these analyses is the lack of information available in the literature for predicting stress relaxation of the high-strength alloys used in the manufacture of spacecraft and satellite springs.[1,2] Much of the stress relaxation data available are for short times, typically up to 100 h, relative to the multi-year storage durations anticipated for many of the current space systems. This often leads to an undesirable circumstance in which extrapolation of sparse data over several orders of magnitude is required for the analysis.

To aid this situation, a test program was instituted to generate longer-term stress relaxation data for several alloys commonly used in spacecraft springs. Because it would be impractical to test the myriad types and sizes of springs used for spacecraft hardware, a more general approach was taken. A database of stress relaxation behavior was generated by testing wires in tension, and an analytic method was developed to apply this database of uniform tensile behavior to the more complex, non-uniform stress states that exist within the cross section of springs.

Important material considerations affecting the stress relaxation behavior of metals are alloy composition, strength level, heat treatment, degree of cold work, and residual stresses. Significant test parameters to consider are the stress field, the initial stress level, time, and temperature. In this study, an effort was made to address all of these factors, either through material selection or test planning. However, it is worthwhile to note that residual stresses, which are the result of non-uniform plastic yielding of a

---

* All authors: The Aerospace Corporation, El Segundo, CA

125

spring cross section, cannot be generated in a uniform tensile stress field. For this reason, they were considered in the analytical, rather than the experimental portion of the study. An understanding of the existence and magnitude of residual stresses is needed for modeling, but experimental determination can only be made using the springs themselves.

Temperature excursions encountered during normal storage would have a slight effect on the stress relaxation behavior of spring alloys. However, maintaining a constant temperature during testing is important to eliminate complicating effects arising from differential thermal expansion between the sample and the testing apparatus. For this reason, all stress relaxation testing was done in a constant temperature environment, controlled to within $21° \pm 1.5°C$.

Materials

Five alloys were selected for testing in this program: 302 and 17-7 PH stainless steels; steel music wire; beryllium-copper alloy 25; and Elgiloy, a cobalt alloy. These are common alloys in general use for spacecraft springs and also represent a wide variety of compositions, strength levels, heat treatments, and cold-worked conditions. Details of the tested alloys are listed in Table 1.

The 17-7 PH stainless steel and Elgiloy are high-strength, precipitation-hardening alloys. Wire of these alloys intended for spring fabrication is supplied in the solution-annealed condition, requiring an age-hardening heat treatment to develop final properties of the solution treated and aged (STA) condition. Aging would normally be done after spring fabrication, but for the uniaxial wire tests, was done beforehand. The other alloys were supplied in their final conditions, requiring no additional heat treatment, except for a limited number of music wire and 302 stainless-steel samples that were tempered at either 260 or 366°C. For three of the alloys, two diameters of wire were tested in order to investigate the effect of cold work and strength level. Compared to larger-diameter wires, smaller wires require additional cold work during manufacture and are generally at higher strength levels.

Table 1. Alloys Tested for Stress Relaxation in Uniaxial Tension

Alloy	Specification	Tested Condition	Wire Diameter mm	Wire Diameter in
Be-Cu Alloy #25	ASTM B197-91	Tempered, 1/2H	0.51 & 1.27	0.02 & 0.05
Steel Music Wire	ASTM A228-91	As-Drawn	0.51 & 1.27	0.02 & 0.05
Steel Music Wire	ASTM A228-91	Drawn and Tempered	0.51	0.02
302 Stainless Steel	ASTM 313-91	As-Drawn	0.51 & 1.27	0.02 & 0.05
302 Stainless Steel	ASTM 313-91	Drawn and Tempered	0.51	0.02
17-7 PH Stainless Steel	AMS 5678B	Solution Treated & Aged	1.27	0.05
Elgiloy	AMS 5833	Solution Treated & Aged	1.27	0.05

Tensile properties were determined for 0.51 mm (0.02 in) diameter wires of Be-Cu, music wire, and 302 stainless steel, and for 1.27 mm (0.05 in) diameter wires of all of the alloys, by uniaxial tensile testing of three replicate samples. The results of these tests are given in Table 2, where F_{TU} is the ultimate tensile strength, F_{TY} is the 0.2% off-

126

set tensile yield strength, and F_{PL} is the tensile proportional limit stress of the wire.[3] The proportional limit stress is a rough measure of the elastic limit strength of a material and has been defined in various ways. For present purposes, F_{PL} is taken to be the stress at 100 microstrain (0.01%) offset.

Stress relaxation of several compression springs of 17-7 PH and 302 stainless steel from actual space hardware were also tested during this study. This was done primarily to provide needed data for the springs, but it also allowed for comparison of the torsional stress data from the springs with the tension data from the wire tests.

Table 2. Tensile Properties of the Tested Alloys

Alloy	Condition	Wire Diameter mm (in)	F_{TU} MPa (ksi)	F_{TY} MPa (ksi)	F_{PL} MPa (ksi)
Music Wire	As Drawn	1.27 (0.05)	2270 (326)	1970 (282)	1150 (164)
		0.51 (0.02)	2750 (393)	2640 (378)	1730 (248)
Music Wire	Tempered 260°C	0.51 (0.02)	2650 (379)	2620 (375)	2160 (310)
Music Wire	Tempered 366°C	0.51 (0.02)	2310 (331)	2060 (295)	1690 (242)
Be-Cu Alloy 25	1/2 Hard	1.27 (0.05)	1330 (191)	1180 (170)	683 (98)
		0.51 (0.02)	1300 (186)	1220 (175)	712 (102)
302 SS	As Drawn	1.27 (0.05)	1930 (277)	1730 (247)	944 (135)
		0.51 (0.02)	2330 (333)	2020 (289)	1260 (181)
302 SS	Tempered 366°C	0.51 (0.02)	2520 (361)	2280 (326)	1480 (213)
17-7 PH SS	STA	1.27 (0.05)	2190 (313)	2030 (291)	1190 (171)
Elgiloy	STA	1.27 (0.05)	2210 (317)	1960 (280)	955 (137)

Experimental Procedures for Wire Testing

The stress relaxation data were obtained at constant temperature by measuring the time-dependent decrease in stress in the wires while they were constrained at a constant displacement. All testing equipment and measurement procedures met or exceeded ASTM requirements for stress relaxation testing.[4] The wires were mounted and held in one of twelve identical test fixtures located in the constant temperature facility. A schematic of the fixture is shown in Figure 1.

Each fixture consists of two square base plates separated by four cylindrical posts. There are two capstan-type gripping devices, one to hold each end of the wire. The upper grip is attached to a load cell, while the lower one is attached to the bottom base plate. The load cell is affixed to a threaded rod that passes through a hole in the center of the upper base plate. Load is applied to the wire by tightening a tensioning nut, which is screwed onto the threaded rod and bears against a precision washer atop the upper base plate.

127
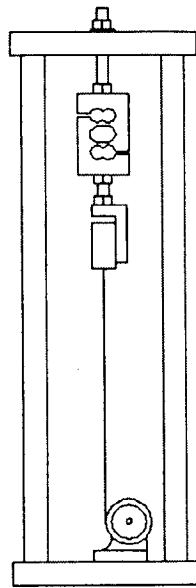
Figure 1. Fixture for stress relaxation testing of wire. A wire sample is shown between the capstan grips, which are rotated 90° with respect to each other here to provide a more detailed view.

To ensure that all of the stress relaxation occurs in the sample rather than the fixture, it is important that the fixture be rigid compared to the wire. Thus all the components were fabricated from steel. The cylindrical posts are 2.5 cm (1.0 in) in diameter, and the base plates are 2.5 cm (1.0 in) thick by 20.3 cm (8.0 in) on a side. The 1.3 cm (0.5 in) diameter bolts and threaded rods are used to attach the capstan grips and the load cell. The capstan grips are 5.1 cm (2.0 in) in diameter. The overall dimensions of the fixture are 91.4 cm (36.0 in) high by 20.3 cm (8.0 in) on a side. Nominal gauge length of the tested wires is 61 cm (24.0 in). Maximum force rating of the load cell is 2.2 kN (500 lb).

The tests are conducted by carefully attaching each end of the wire to one of the capstan grips, then wrapping three times around by rotating the capstan so as not to twist the wire. After tightening down the capstans, the tensioning nut is screwed down to apply just enough force on the wire to hold it in place. Next, the slack is removed from the wire wraps while maintaining the slight tension. The wire is then loaded to a pre-selected value and placed aside with no further disturbance. Load, time, and temperature are monitored continuously throughout the tests using analog strain-gauge signal conditioners and computer-controlled digital data logging equipment.

Stability of the load monitoring instrumentation is important when conducting long-term tests. To investigate stability of the equipment, a weight of 2.1 kN (483 lb) was applied to one of the 2.2 kN (500 lb) load cells for a period of almost 2,000 h. The results of that test are shown in Figure 2, where the stability of the reading is seen to be a near perfect 0.007% per log hour.

128
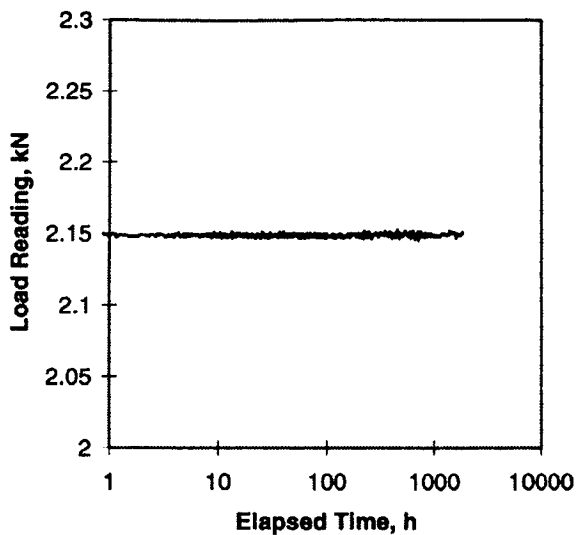
Figure 2. Stability of a 2.2 kN (500 lb) load cell and instrumentation with a hanging load. Error = 0.007 % per log hour.
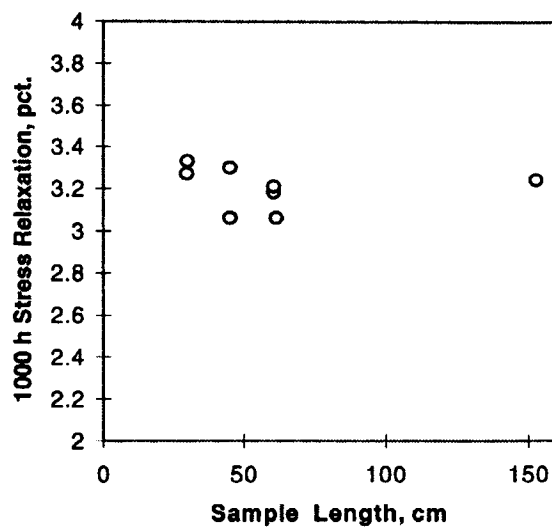
Figure 3. Stress relaxation after 1,000 hours for 1.27 mm (0.05 in) 302 SS samples. Nominal initial stress = 0.64 ± 0.01 F_{TU}.

A major concern was that some slippage of the wire on the grips would occur during the test. Any slippage would result in extraneous deformation of the wires, thus introducing errors into the data. Slippage would be independent of the wire length, and so would be expected to affect the stress relaxation data more severely for shorter wires. To settle this question, long-term tests were performed on eight wires of 302 stainless steel. Sample lengths were either 31, 46, 61, or 152 cm (8, 18, 24, or 60 in). The longest sample was accommodated by stringing it between two test fixtures that had been clamped tightly together, end to end. Nominal test durations were 8,000 h. Results of these tests are presented in Figure 3, where the percentage of stress relaxation after 1,000 h is plotted versus gauge length. The graph shows that there is no significant effect of sample length on the stress relaxation. This is strong evidence that no slippage is occurring in the grip ends of the wires and that the stress relaxation data obtained by using this fixture are valid.

Another possible source of error during long-term testing is equipment breakdown or power failure. During the course of this test program, which lasted approximately four years, there were several electrical power interruptions. Each time, the facility was restarted, and temperature stability was re-established to within 21° ± 1.5°C. In some cases, particularly for samples in which little time had been invested at that point, tests were simply aborted. On most occasions, data logging was resumed after restoration of the power with no harmful consequences. However, in a few instances where data gathering continued on existing samples, a small shift in the curve was noted. An example is shown in Figure 4a. Clearly, such an abrupt shift represents a slight

129
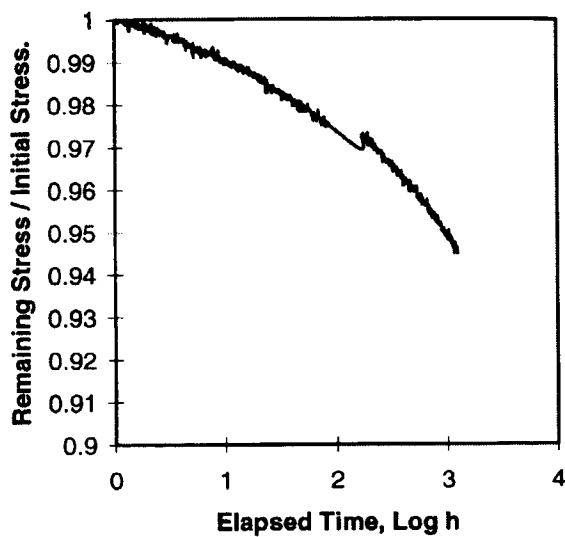
Figure 4a. Stress relaxation of a Be-Cu wire sample showing data shift upon restarting after a power outage.
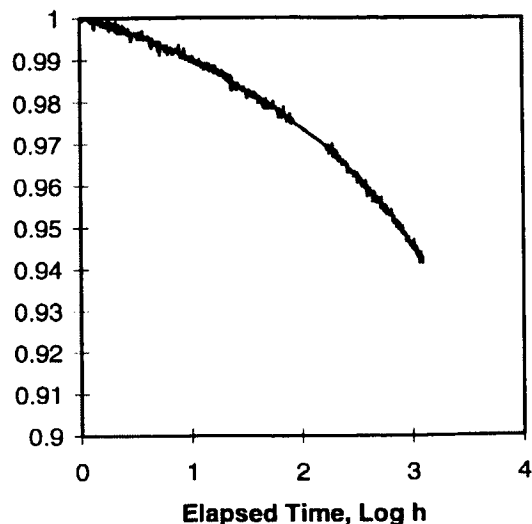
Figure 4b. Curve of Figure 4a after correction for the data shift.

change in the electrical balance point of the instrumentation, rather than an actual change in the stress relaxation behavior of the sample. Following this reasoning, these data shifts were corrected, as necessary, by superimposing a constant correction factor on the remaining portion of the data. The correction was made by curve-fitting the existing data, extrapolating to the restarting point, then applying the appropriate correction factor from that point onward. Figure 4b shows the correction of the data of Figure 4a.

Experimental Results of Wire Testing

A total of 94 wire samples was studied for periods ranging from 1,000 to 10,000 h. Representative stress relaxation data for the different alloys are plotted in Figure 5, where the fractional reduction of initial stress is plotted versus the logarithm of elapsed time. Because the initial stress at time zero is undefined for a logarithmic plot, a suitable value had to be selected. Although stress reduction begins immediately upon loading, the initial decline is somewhat variable, depending on loading rate. For all samples tested, this transient behavior, as observed on a semi-logarithmic plot, was completely attenuated after approximately 0.5 h. Therefore, for purposes of this study, initial stress is defined as the stress remaining after 1 h of testing.

The slope of a straight line drawn from the origin through the 1,000-h point in each curve of Figure 5 would represent the 1,000-h stress relaxation rate. The curves of Figure 5 show that the wires of all alloys, except music wire and the Be-Cu alloy,
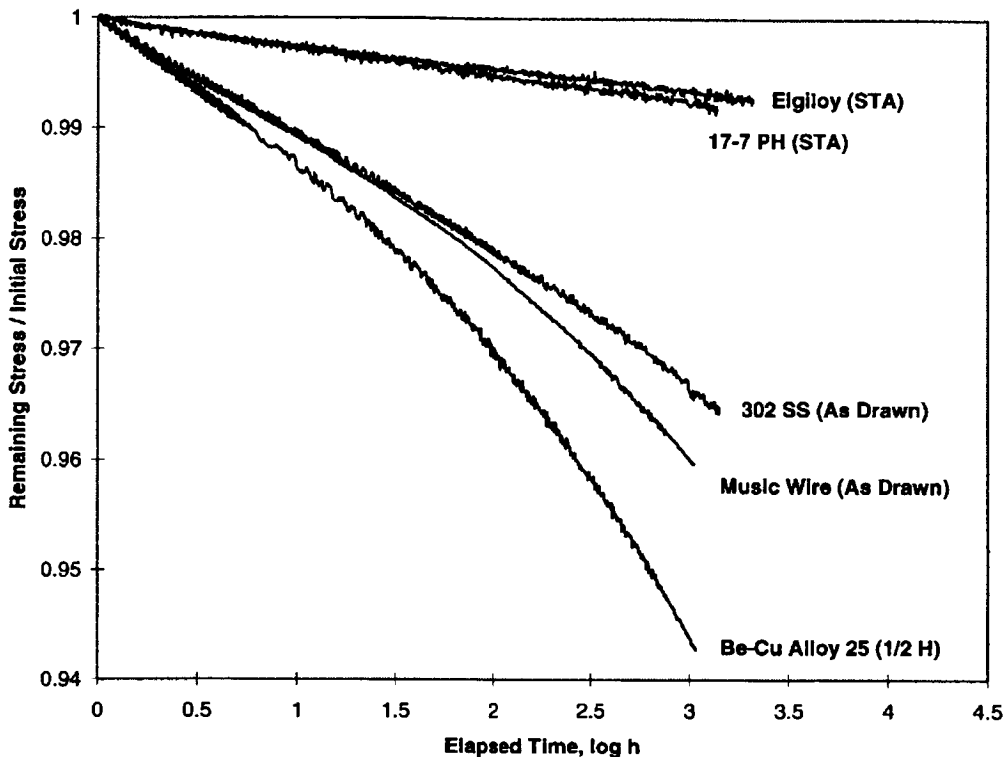
Figure 5. Stress relaxation of five 1.27 mm (0.05 in) diameter, high-strength spring alloy wires. Nominal initial stress = 0.66 ± 0.02 F_{TU}.

exhibit reasonably linear behavior on this semi-logarithmic plot, and so can be characterized by this rate. Analysis of long-term (8,000 h) 302 stainless-steel data has revealed that the slight nonlinearity evident in these data results in an insignificant error (less than 1%) when extrapolated from 1,000 to 8,000 h. Further linear extrapolation to periods of up to three years (approximately 26,000 h) is reasonable. Because of the convex curvature of Be-Cu and music wire data, linear extrapolation beyond 1,000 h may not be warranted. This is especially noteworthy since the extrapolation would be non-conservative, which illustrates the danger of linear extrapolation of short-term (≤100 h) stress relaxation data to predict stress relaxation during long-term spacecraft storage.

A number of mathematical functions were investigated in an effort to establish a viable technique to extrapolate the nonlinear music wire and Be-Cu data. Empirical curve fitting by a third-order polynomial was found to provide an excellent correlation, as illustrated in Figure 6, where the Be-Cu data of Figure 5 are re-plotted. In this figure, only the data up to 1,000 h were used for the curve fit. The curve beyond 3 log hours represents an extrapolation. It is clear that for these data, the polynomial representation is much more conservative than the linear one, and turns out to be surprisingly accurate in predicting the stress relaxation behavior beyond 1,000 h. Although not shown here, this technique produces excellent extrapolations for the nonlinear music

131
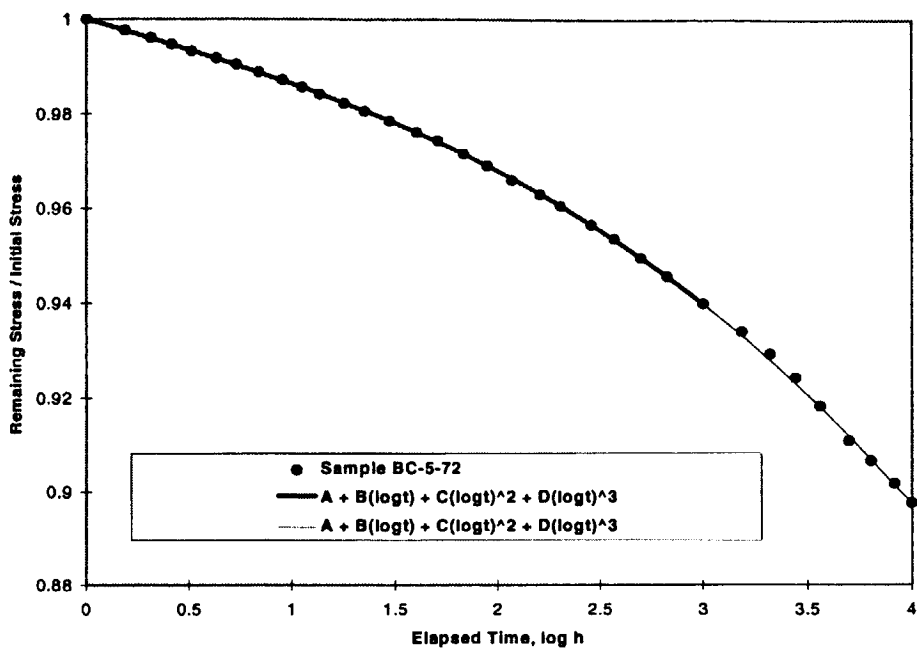
Figure 6. Third-order polynomial curve-fit of data for the Be-
Cu wire sample of Figure 5. Only the data from 0 to
3 log hours were used for the analysis. The curve
beyond 3 log hours is an extrapolation.

wire data as well. There is no known physical justification for this polynomial repre-
sentation, however. It is presented here as an empirical finding only.

A few of the 0.51 mm (0.02 in) diameter music wire and 302 stainless-steel samples
were tempered before being tested to investigate possible beneficial effects on the
stress relaxation behavior. Figure 7 shows the results of those tests. In each case, it is
seen that tempering does reduce the stress relaxation rate compared to the as-drawn
wire, probably by rearranging the dislocation structure into a more favorable state.
This may also be the case for 17-7 PH and Elgiloy, whose aging treatments could well
provide a similar annealing effect. The stress relaxation behavior of these alloys is far
superior to the other alloys tested, as evident in Figure 5.

Data from the 0.51 mm (0.02 in) wires of Figure 7 appear noisier than those from the
1.27 mm (0.05 in) diameter wires of Figure 5. The noise is due to minor temperature
fluctuations of the constant temperature laboratory ($\pm 1.5°C$), which cause differential
expansion between the fixture and the sample. It is more noticeable for the smaller
wires because the lower loads from these tests require higher amplification. The noise
does not affect the outcome of the tests because it tends to average out.

A summary of the stress relaxation after 1,000 hours as a function of initial stress ratio
for all 94 samples tested in this study is shown in Figure 8. Most of the data are from
1.27 mm (0.05 in) diameter wires, but about 50% of the music wire, 302 stainless steel,

132
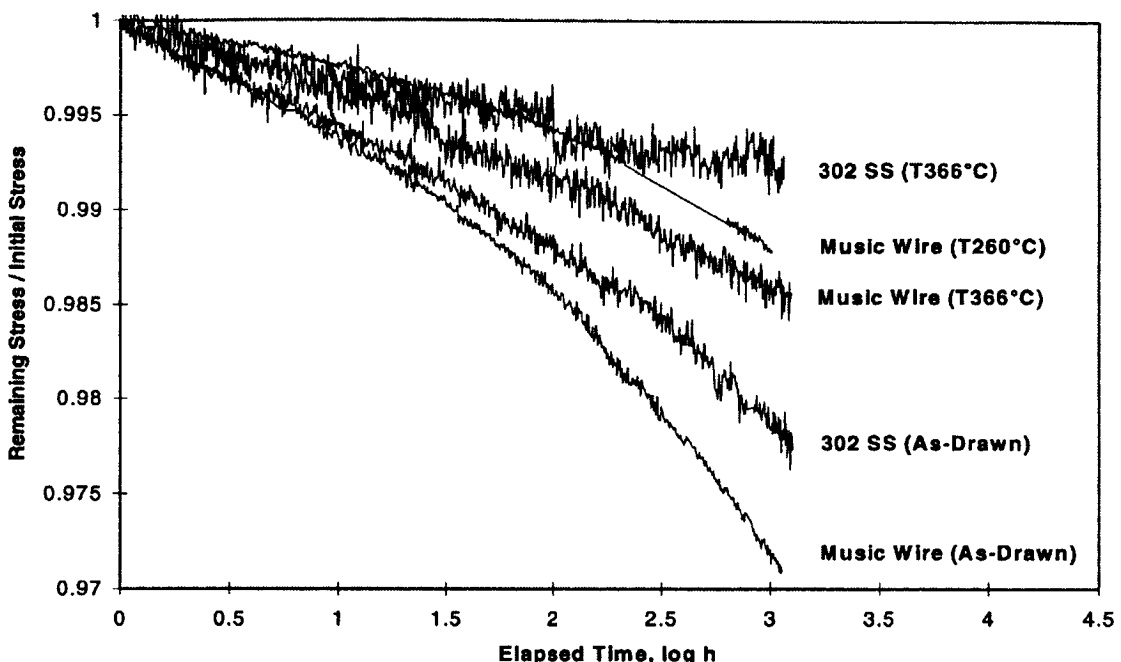
Figure 7. Data curves showing the effect of tempering on the stress relaxation behavior of 0.51 mm (0.02 in) diameter music wire and 302 stainless steel samples. Nominal initial stress = 0.44 ± 0.03 F_{TU}.
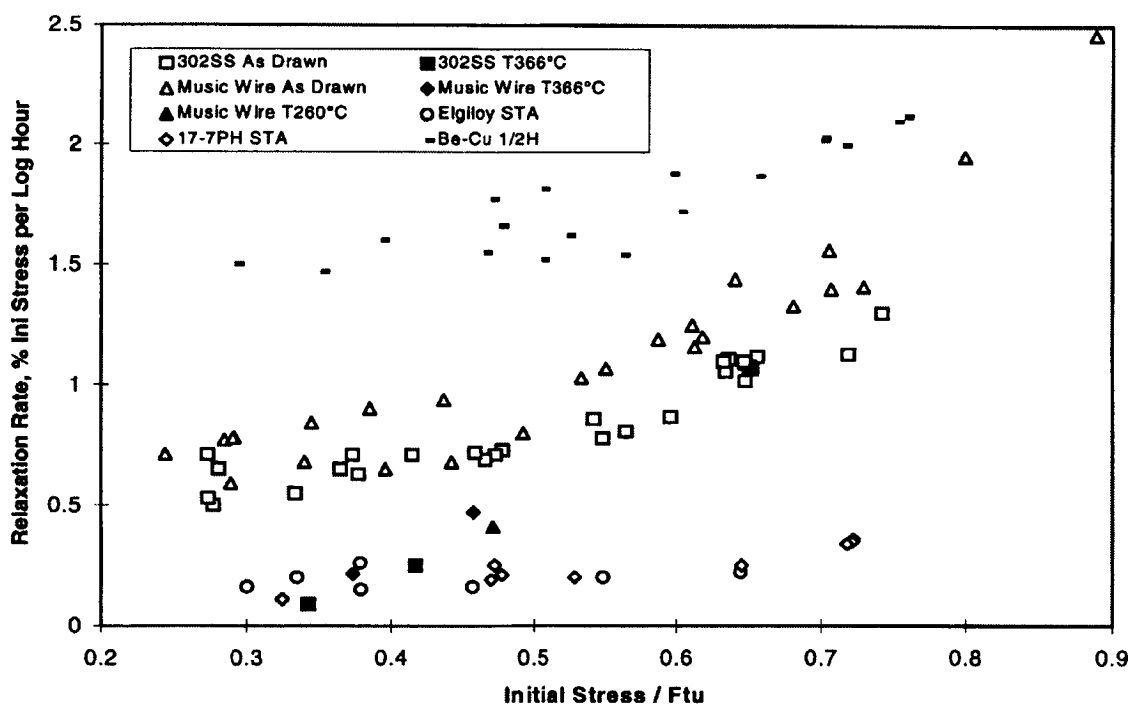

Figure 8. Stress relaxation after 1000 hours for five high-strength spring alloys.

133

and Be-Cu tests were done on 0.51 mm (0.02 in) diameter wire. The data from both sample sizes are intermixed in Figure 8 because there is no discernible effect of wire size on the results.

Figure 8 shows again that Elgiloy and 17-7 PH stainless steel are highly resistant to stress relaxation compared to the other alloys, although the limited data of the tempered music wire and 302 stainless steel appear nearly comparable. The stress relaxation rate of Be-Cu alloy 25 is almost an order of magnitude higher than the best materials here. Another interesting observation from Figure 8 is that, at high values of initial stress, the stress relaxation rate increases rapidly as the initial stress ratio increases. However, below a stress ratio of approximately 0.5, the rate tends to become constant. Since the conservative design of spacecraft hardware generally calls for stresses in this lower regime, analysis of stress relaxation in spacecraft springs can be greatly simplified by assuming the stress relaxation rate, expressed as a ratio of the initial stress, to be independent of the initial stress level.

Analytical Modeling

Basic Theories

Tension/compression and torsional springs are the two most common springs used in storing energy. Tension/compression springs are normally made from constant cross-sectional wires wound in helical shapes. Depending upon the direction of the applied force, the overall length of the spring will either extend or contract. Because of the fabrication of these springs, the wire itself is subject to a combination of shear force and torsion about the center of the cross-section. The applied torsion is the dominate stress source. Torsion springs, on the other hand, are designed to store energy generated from torsional moment. The wire is under axial force with bending as the primary source of stress. Moreover, either type of stress is non-uniform. Because of the stress non-uniformity, the stress relaxation of the spring assembly is difficult to assess experimentally. Therefore, an analytical prediction for the spring assembly is necessary.

In attempting to apply the tension stress-relaxation data to shear stressed conditions, a shear stress-strain curve from a tensile stress-strain curve was constructed based on the following two facts:[5]

1. Plastic strain is caused solely by shear strain;
2. Maximum shear stress is one-half of the tensile stress in a uniaxial tensile specimen.

For simplicity, it is assumed that the uniaxial stress-strain curve is bilinear, as shown in Figure 9a. The modulus of elasticity is E, and the elastic limit stress and strain are σ_o
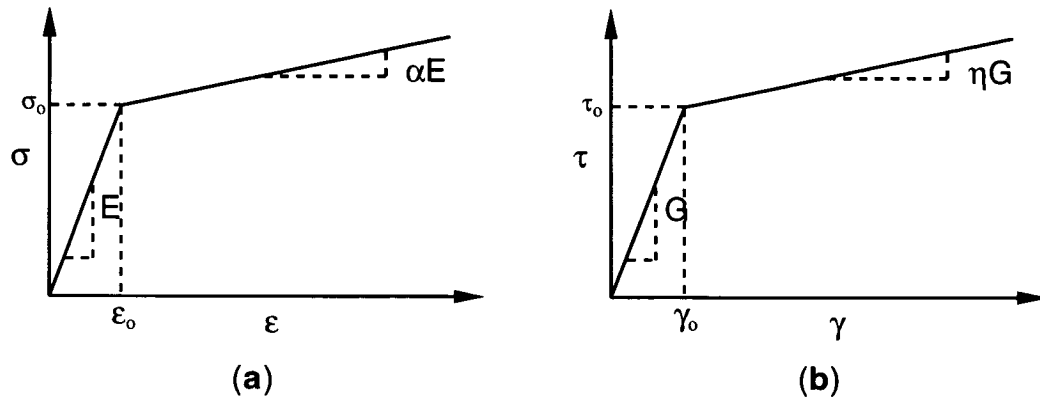
Figure 9. Uniaxial and shear bilinear stress-strain curves. (a) Bilinear uniaxial tensile stress-strain curve; (b) bilinear shear stress-strain curve.

and ε_o, respectively. The modulus in the inelastic portion of the curve is αE. Similarly, a shear stress-strain curve is constructed as shown in Figure 9b. The elastic limit stress and strain are τ_o and γ_o, respectively. The shear modulus in the elastic region is G, and that in the inelastic region is ηG. We shall establish the value of η in terms of α and other material constants.

Let us define (σ, ε) and (τ, γ) to be two points on the tensile and shear stress-strain curves, respectively. The slope of the inelastic portion of the tensile curve is

$$(\sigma - \sigma_o)/(\varepsilon - \varepsilon_o) = \alpha E. \tag{1}$$

Similarly, the slope of the inelastic portion of the shear curve is

$$(\tau - \tau_o)/(\gamma - \gamma_o) = \eta G. \tag{2}$$

From fact 2, above,

$$\tau = \sigma/2, \qquad \tau_o = \sigma_o/2$$
$$\gamma = 3\varepsilon/2, \qquad \gamma_o = \tau_o/G,$$

and taking into account the fact that Poisson's ratio in the inelastic region is 1/2, we have

$$(\tau - \tau_o)/(\gamma - \gamma_o) = [(\sigma - \sigma_o)/2]/(3\varepsilon/2 - \tau_o/G) \approx [(\sigma - \sigma_o)/2]/(3\varepsilon/2 - 3\varepsilon_o/2)$$
$$= \alpha E/3.$$

$$\eta = \alpha. \tag{3}$$

This means that the ratio of the inelastic shear modulus to elastic shear modulus in a shear stress-strain curve is equal to the ratio of the inelastic modulus to elastic Young's modulus in a uniaxial stress-strain curve.

Relation Between Tensile and Shear Stress Relaxation

Let $F(\sigma_o, t, M, T)$ and $G(\tau_o, t, M, T)$ be the stress-relaxation functions associated with tension and shear modes, respectively. Then we have

$$\sigma = \sigma_o \, F(\sigma_o, t, M, T) \text{ for tension} \qquad (4)$$

and

$$\tau = \tau_o \, G(\tau_o, t, M, T) \text{ for shear}, \qquad (5)$$

where σ and τ are the stresses at time t, σ_o and τ_o are the initially applied stresses, M represents the materials and specimen structure parameters, and T is the temperature. Based on facts 1 and 2 in the Basic Theory section, together with the fact that part of the elastic strain is converted into plastic strain during stress relaxation, it is concluded that

$$G(2\tau_o, t, M, T) = F(\sigma_o, t, M, T), \qquad (6)$$

and that the uniaxial tension stress-relaxation data can be applied to shear loaded cases.

Relaxation Test Data for 302 Stainless Steel

Data from a 302 stainless-steel V-band spring can be used to validate the model. The relaxation function $F(\sigma_o, t, M, T)$ for this case is independent of M and T. From the uniaxial test data, the tension relaxation function was expressed as

$$F(\sigma_o, t, M, T) = 1 - S \log(t), \qquad (7)$$

where t is in hours. The S is expressed as a linear function of the applied initial stress, S_o, i.e.,

$$S = S_o + \kappa \, \sigma_o.$$

$$\sigma_o = 903 \text{ MPa (131 ksi)}, \quad S = 0.0065$$

and $\sigma_o = 1234$ MPa (179 ksi), $S = 0.0116$,

gives $S_o = -0.0074$, and $\kappa = 1.537 \times 10^{-8}$ $((MPa)^{-1})(0.000106(ksi)^{-1})$.

The above-established values for S_o and κ, as well as Eq. (7), were applied to a 302 stainless-steel tension/compression spring. The spring is used in a satellite program. The dimensions of the spring, the applied initial load, the moment, and the load relaxation are listed as follows:

Spring diam	= 19.76 mm (0.778 in)	Wire diam	= 1.78 mm (0.07 in)
Initial load	= 72.1 N (16.2 lb)	Final load	= 70.5 N (15.86 lb)
Test time	= 1000 h (extrapolated)	Percentage of load relaxation	= 2.1%.

136

We now predict the torque relaxation in a compression spring by the use of Eq. (6) and compare the prediction with the actual experimental observation. Consider a compression spring of circular cross-sectioned wires. We designate:

M = the applied torque equal to PD/2; P = applied compression load;
D = spring diam; and d = wire diam.

The shear stress in the wire is expressed as

$$\tau = (16PDr/\pi d^4)K, \tag{8}$$

with a maximum value of

$$\tau_{max} = (8PD/\pi d^3)K,$$

where r is the radial location from center of the wire where the shear stress is calculated, K is a stress concentration factor equal to $(4C-1)/(4C-4) + 0.615/C$, and C is equal to D/d.

To determine the torque relaxation in the spring, we use Eqs. (6), (7), and (8) in the following torque equation for the wire cross section:

$$\tau/\tau_o = 1 - (S_o + 2\kappa\tau_o)\log(t) \tag{9}$$

$$M_t = 2\pi \int_0^{d/2} \tau_o r^2 dr$$

which gives

$$M_t/M_o = 1 - S_o \log(t) - (128M_o/5\pi d^3)\kappa \log(t), \tag{10}$$

where

$$M_o = \tau_{max} \pi d^3/16PD.$$

A substitution of the S_o and κ values into Eq. (10) yields a M_t/M_o ratio of 0.974. In other words, the predicted load relaxation for this compression spring is 2.6%, which compares well with the 2.1% measured value. The difference is due to several possible reasons, including the bilinear stress-strain and linear S vs s_o assumptions used in the derivation.

Determination of Residual Stresses

Residual stresses are often generated in both compression and torsion springs by presetting the springs. The residual stresses occur as a result of the plastic yielding of the spring wires, followed by an unloading of the spring. The residual stresses always act in the opposite direction to the operating stresses, thus increasing the range of the operating stress without inducing further plastic yielding. As will be seen from the calculation, the residual stresses can be a significant portion of the yield strength and

may experience a relaxation themselves. The determination of the residual stresses becomes an important portion of the overall relaxation prediction.

Residual Stresses in a Compression Spring with a Circular Wire Cross Section

Assume that part of the wire cross section is plastically yielded due to the application of an external torque M_t, and that the stress distribution in the wire is bilinear, as shown in Figure 9b. At a distance aR from the center of the wire, the shear stress is τ_o. Therefore, the stress, τ, as a function of r is expressed as

$$\tau = \tau_o r/(aR) \quad 0 \leq r \leq aR; \quad \tau = [(1 - \alpha) + \alpha r/(aR)]\tau_o \quad aR \leq r \leq R. \tag{11}$$

The external M_t is expressed as

$$M_t/M_e = [a^3 + 4(1 - \alpha)(1 - a^3)/3 + \alpha(1 - a^4)/a], \tag{12}$$

where $M_e = \pi\tau_o R^3/2$ is the torque with a maximum shear stress equal to τ_o at r = R. For 302 stainless-steel wire, the value of τ_o is 741 MPa (107.5 ksi). For a given value of M_t/M_e, the corresponding value of a can be solved algebraically. The shear stress distribution in the wire can be then determined using Eq. (11). The residual stress following an elastic unloading is expressed as

$$\tau' = -2 M_t r/\pi R^4. \tag{13}$$

A combination of Eqs. (11) and (13) gives the distribution of the shear stresses for any given M_t/M_e. Figure 10 depicts the residual stress distribution for 302 stainless steel with a 1.27 mm (0.05 in) wire diameter and a M_t/M_e value of 2. The maximum residual stress is about 165 MPa (24 ksi), which is approximately 22% of the elastic limit stress of 302 stainless steel in shear.

Residual Stress Determination for a Torsion Spring with a Rectangular Wire Cross Section

Assume the wire has a width b (in the direction parallel to the axis of the spring) and a depth of 2D (in the direction parallel to the radius of the spring). Again, assume the cross section is partly yielded plastically due to the application of an external bending moment, M_b. The bilinear stress-strain curve is as shown in Figure 9a. The elastic stress, s_o, is 1482 MPa (215 ksi). Similar to the distributions in the shear, the elastic and inelastic stress distributions in the cross section are expressed as

$$\sigma = \sigma_o x/(aD) \quad 0 \leq x \leq aD; \quad \sigma = [(1 - \alpha) + \alpha x/(aD)]\sigma_o \quad aD \leq x \leq D. \tag{14}$$

The bending moment, M_b, is

$$M_b/M_{be} = [a^2 + 3(1 - \alpha)(1 - a^2)/2 + (1 - a^3)\alpha/a] \tag{15}$$

where

$$M_{be} = 2\sigma_o bD^2/3.$$

138
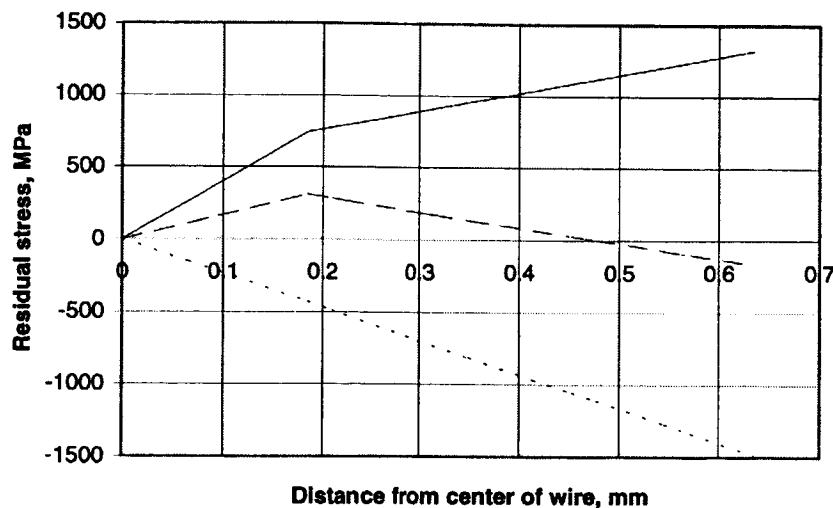
Figure 10. Residual shear stress for 302 stainless steel 1.27 mm (0.05 in) diameter wire (M_t/M_e ratio = 2.0). Solid line is nonlinear loading; dotted line, linear unloading; dash-dotted line, residual stress.
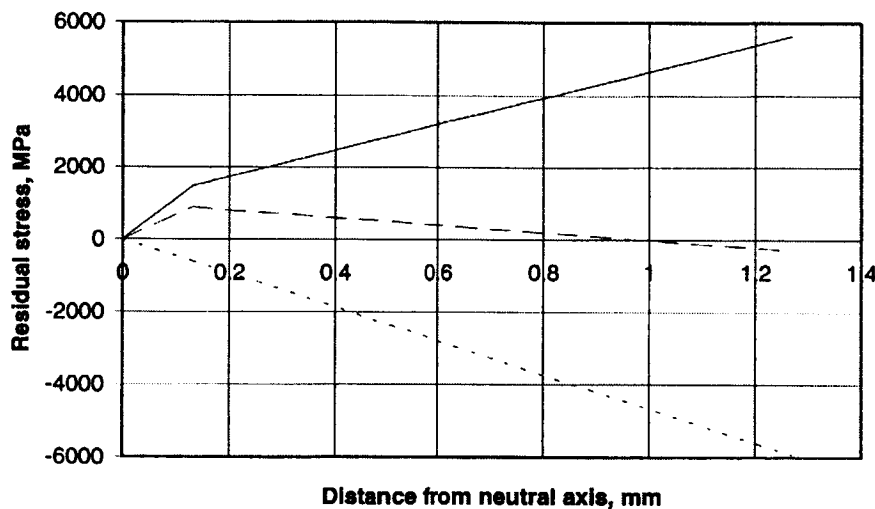

Figure 11. Residual bending stress for 302 stainless steel 1.27 mm (0.05 in) wide and 2.54 mm (0.10 in) rectangular cross sectioned wire (M_b/M_{be} ratio = 2.0). Solid line is nonlinear loading; dotted line, linear unloading; dashed line, residual stress.

For unloading elastically, the stress distribution for the moment, M_b, is expressed as

$$\sigma_o' = -3M_b x/(2bD^3).$$ (16)

A combination of Eqs. (14) and (16) gives the residual stresses in the cross section. A case with M_b/M_{be} of 2 was calculated for b = D = 1.27 mm (0.05 in). The residual stress distribution is depicted in Figure 11. A residual compressive stress of 296 MPa (43 ksi) corresponding to 20% of the elastic limit stress is obtained.

Summary

Stress relaxation testing results for 0.51 and 1.27 mm (0.02 and 0.05 in) wires of 302 stainless steel, music wire, and Be-Cu, and for 1.27 mm (0.05 in) wires of Elgiloy and 17-7 PH stainless can be used for predicting the stress relaxation behavior of springs made from these alloys. Linear extrapolation of the 1000-h data has been shown to be reasonable for the 302 stainless steel, 17-7 PH stainless steel, and Elgiloy. It was shown that the high-strength, precipitation-hardening alloys, 17-7 PH stainless steel and Elgiloy, are by far the best choice for alloy selection when stress relaxation of springs is a major concern. However, tempering of cold-worked music wire and 302 stainless steel imparted significant improvements and stress relaxation resistance of these materials.

An analytical technique was developed to predict the stress relaxation for compression and torsion springs based on the uniaxial wire data. In this technique, the tensile stress relaxation function for 302 stainless-steel wires has been used successfully to predict the torque reduction for a 302 stainless-steel V-band compression spring. The predicted 2.6% load reduction after 1000 h compares well with the 2.1% load reduction obtained from tests.

Residual stress prediction for both compression and torsion indicate that the residual stresses can be significant portions of the elastic-limit stress and are beneficial in actual satellite or launch operations.

References

1. S. U. V. Idermark and E. R. Johansson, "Room-Temperature Stress Relaxation of High-Strength Strip and Wire Spring Steels—Procedures and Data," *Stress Relaxation Testing*, ASTM STP 676, Alfred Fox, ed., American Society for Testing and Materials, 1979.

2. M. J. Manjoine and H. R. Voorhees, *Compilation of Stress-Relaxation Data for Engineering Alloys,* ASTM Data Series Publication No. DS 60, American Society for Testing and Materials, 1982.

3. C. W. Marschall and R. E. Maringer, *Dimensional Instability*, Pergamon Press, 1977.

4. "Standard Methods for Stress Relaxation Tests for Materials and Structures," ASTM E 328-86, *1990 Annual Book of ASTM Standards*, Vol. 3.01, American Society for Testing and Materials.

5. T. H. Lin, *Theory of Inelastic Structures*, John Wiley and Sons, Inc. 1968.

Compact Drilling and Sample System

Greg R Gillis-Smith[*] and Doug Petercsak[**]

Abstract

The Compact Drilling and Sample System (CDSS) was developed to drill into terrestrial, cometary, and asteroid material in a cryogenic, vacuum environment in order to acquire subsurface samples. Although drills were used by the Apollo astronauts some 20 years ago, this drill is a fraction the mass and power and operates completely autonomously, able to drill, acquire, transport, dock, and release sample containers in science instruments. The CDSS has incorporated into its control system the ability to gather science data about the material being drilled by measuring drilling rate per force applied and torque. This drill will be able to optimize rotation and thrust in order to achieve the highest drilling rate possible in any given sample. The drill can be commanded to drill at a specified force, so that force imparted on the rover or lander is limited. This paper will discuss the cryo dc brush motors, carbide gears, cryogenic lubrication, quick-release interchangeable sampling drill bits, percussion drilling and the control system developed to achieve autonomous, cryogenic, vacuum, lightweight drilling.

Introduction

The goal that initially began the development of the CDSS was to obtain a subsurface sample from up to 1 meter deep, without mixing with the material along the hole, and place that sample in a science instrument onboard the lander, without letting the sample warm up at all. Originally this mechanism was developed to drill into cometary materials in a microgravity environment where a controlled maximum drilling force was critical. Cryogenic and vacuum operation, small mass, and low power requirements were the primary design requirements. As this drill became a candidate for Mars sampling, operation requirements became easier to meet with an increase in temperature and atmosphere.

In order to not thermally alter the sample, the CDSS was designed such that all components would operate at the bulk temperature of the sample. For comets this meant as cold as -165°C and for Mars it is closer to -100°C. The motors, lubricants, and materials had to be developed to meet these requirements. Following is a summary of the operation of the CDSS and then a discussion about each of the major components of the mechanism.

---

[*] Mars Exploration Engineering, Caltech, Jet Propulsion Lab, 4800 Oak Grove Dr, Pasadena, CA 91109
[**] American Technology Consortium, 2510-G Las Posas Rd, Suite 201 Camarillo, CA 93010

141

Basic Design

The basic design of the drill mechanism uses a keyed acme lead screw that is rotated by one motor/gearbox and a nut driven by a second motor/gearbox to provide thrust. (Figure 1) Since the nut and keys can drive the screw from anywhere along its length, this design allows the drill to be longer than its current 1.2 m screw by adding screw segments. It does not require a drill tower equal in height to the desired drill depth. The mass of the drill mechanism without indexing arm is 2.0 kg. Maximum electrical power to drive the mechanism is below 25 W. The current drill diameter is about 15 mm and sample volume is about 400 mm^3.
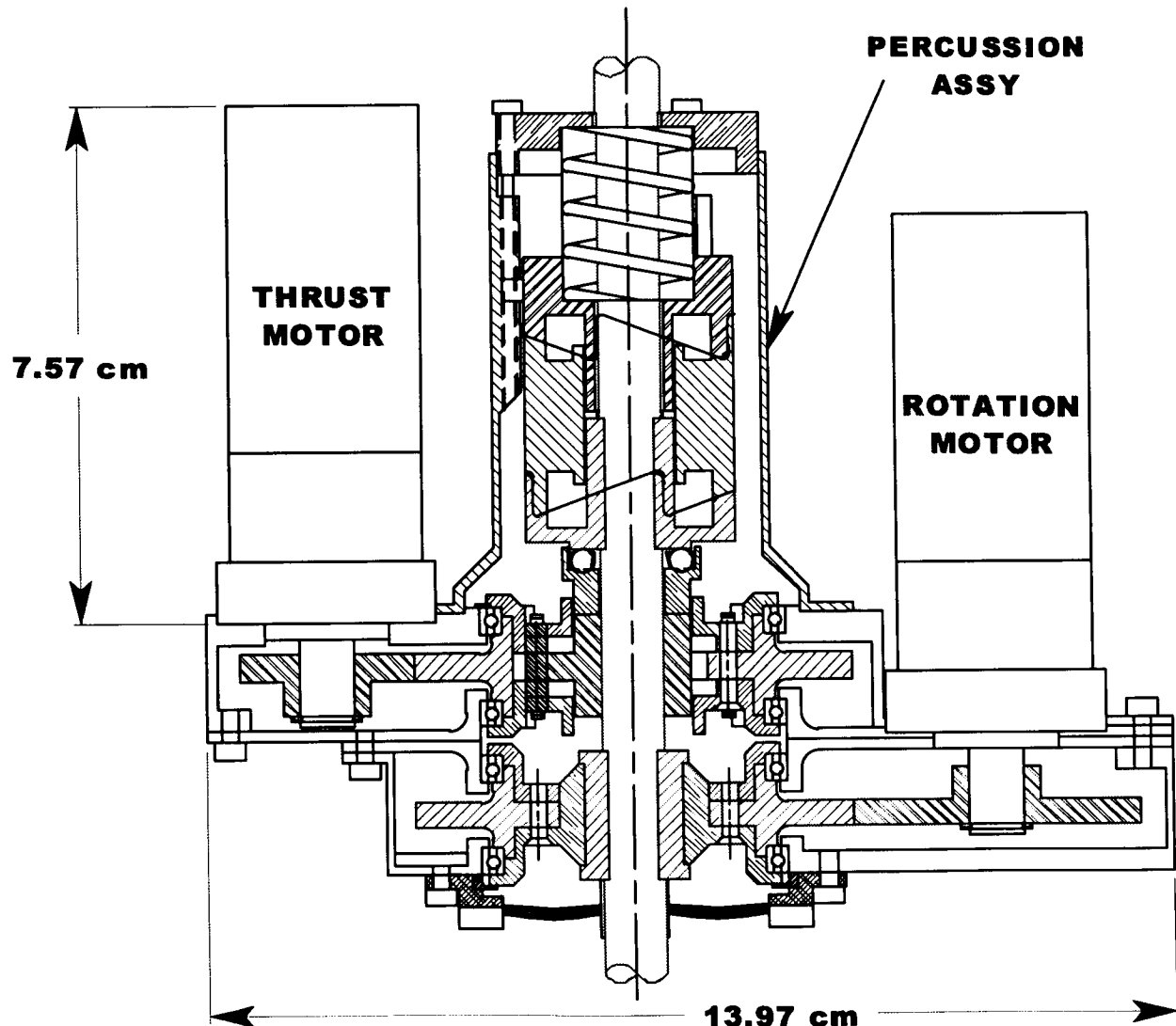
Figure 1. Compact Drill Mechanism Cross-Section

Operation

The drill is commanded to rotate clockwise (CW) and plunge until the surface is encountered. Software controls the speeds and feeds to optimize power and drilling speed. A discrete sample may be taken at any depth by opening the sample door in the end of the bit at that location. The sample door is opened by turning the drill in reverse (CCW) while plunging. Once the sample is acquired, the drill in driven CW while plunging to close the door. The sample and bit is extracted from the hole while rotating forward and withdrawing the drill bit.

The drill is launched with one drill bit attached to the end of the drill rod, but after capturing the first sample, the drill deposits the drill bit with sample enclosed into the science instrument. The drill then attaches to the next drill bit with a positive latch mechanism. Further drilling and sampling is done with the second bit, which is deposited in the second instrument. A third bit is picked up and drilling is continued.

Some advantages of such a removable bit design include the ability to have no contamination of samples. Also, removal of the bit, which is the crucible, removes the thermal mass from instrument. The bits are always sharp and failure of one bit would not impact the success of the mission. For future sample return projects, the multiple bits would allow for easy storage and return of multiple samples. The design of the removable bit drill eliminates the need for a secondary delicate and precise sample ejection system. Disadvantages include the challenge of autonomously picking up and putting down small mechanical parts.
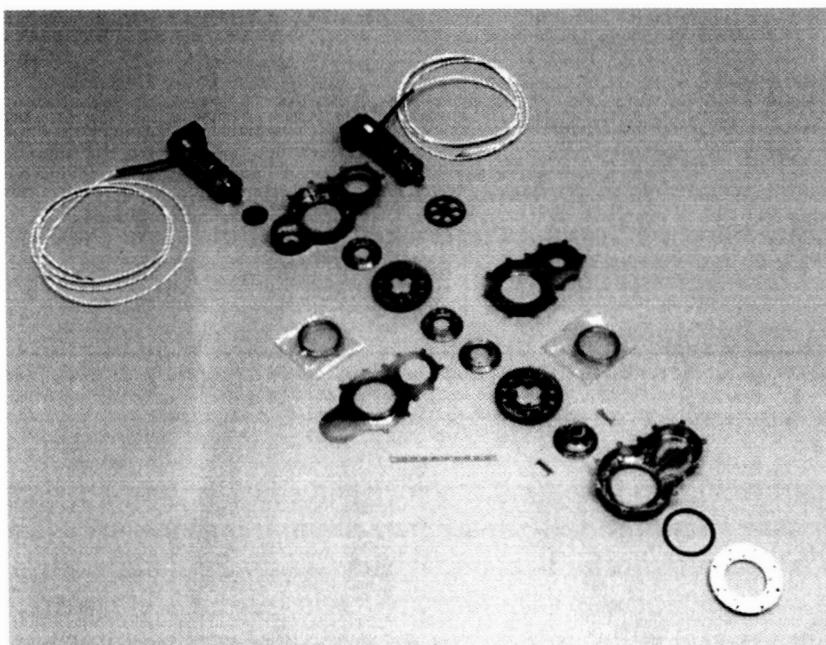

Figure 2. Compact Drill Mechanism Exploded View

Compact Drill Mechanism Components

Motors
In order to minimize mass and power, a dc brush motor needed to be developed for this limited-life application that could survive the −165°C vacuum environment. (Figure 3)

Motor Trades
The extremely low operating temperature requirement warranted a conservative approach with respect to internal torque margins and demands on the lubricant scheme. To this end, a low speed high torque brush motor was developed to work in concert with a relatively low gain two stage planetary gearbox. This resulted in a slightly heavier motor than optimum with very high margins over internal frictional losses. Frictional losses were a major concern in the design since the characteristics of the lubricants were not well understood at the operating temperature. The brush DC motor was

Figure 3. Cryogenic DC Brush Motors

of a conventional wound armature laminated core design with a pair of permanent magnets attached to a stationary backiron that also acted as the motor housing.

Motor Brush Design
Based on previous experience with vacuum brush motor design silver graphite was chosen as the brush material. Since brush wear at the extreme low temperatures was also an unknown inspection ports were provided to allow for easy brush inspection. The silver graphite brushes transfer current to the rotor through a silver bar commutator.

Brush DC motors are wear limited devices, consequently reducing the rate of brush wear is almost always of paramount concern. There are two basic mechanisms of brush wear, mechanical wear and electrical wear.

Mechanical brush wear can be caused by excessive brush preload, high commutator surface speed, commutator runout, and/or bar to bar misalignment. Each of these contributors to excessive mechanical brush wear was addressed by the motor design. The size of the commutator was minimized to minimize the surface speed of the commutator with respect to the brush. By reducing the commutator surface speed brush life is enhanced considerably. The reduced commutator size also has the added benefit of making additional room for extra brush material again increasing the potential life of the brushes. The increased brush length reduces the reaction loads reacted into

144

the brush holder from the brush as it resists the drag force generated at the brush/commutator interface. Reduced reactions forces improve the brush's ability to maintain contact with the commutator even under adverse conditions of commutator runout and bar to bar misalignment. Commutator runout and bar to bar misalignment were controlled by final machining of the commutator at the rotor assembly level using diamond tip tools. Dynamic models of the brush holder assembly and commutator were developed to simulate the behavior of the brush as it reacted against the commutator with manufacturing tolerances for worst case runout and bar to bar misalignment. The models were used to optimize the brush holder design and the brush spring force required. Originally the design of the brush holder included negator springs to provide near constant force brush pressure over brush life. Schedule constraints and long lead times conspired to force revisions to the brush holder to also allow the use of torsion springs. The completed units used torsion springs for providing brush preload. The torsion springs were designed to have a very low spring constant to minimize the change in preload as the brushes wore in and the initial preload was set to be on the high end of the brush pressure envelope.

Inadequate brush preload, excessive current density, and/or electrical arcing can cause electrical brush wear. Designing the brush with a large enough cross section to prevent excessive current densities eliminated problems due to improper current density. Electrical arcing, another significant contributor to electrical wear can be controlled through several different approaches. The right brush material for the operating environment is crucial. Standard graphite brushes that operate acceptably at sea level provide very poor performance in low pressure and vacuum conditions. This is because of the lack of humidity and atmosphere that supports the development of an oxide layer on the commutator, this film reduces both the mechanical and electrical wear of the brush.

Another contributor to electrical arcing is the inductive energy stored in the coil. This form of electrical arcing was controlled by increasing the number of commutator bars as high as possible. The maximum number of commutator bars feasible in the application was eleven. The higher number of commutator bars the less inductance and hence less inductive energy. This reduces the electrical stress on the brush.

Brush arcing was then further reduced by the addition of a ceramic capacitor in parallel with the brush assemblies. The ceramic capacitor acts to suppress arcing of the brushes by reducing the effective source impedance at high frequencies.

Armature
Wire EDM was used to manufacture the armature core from a bonded laminated stack of M19 steel. The wire EDM process is ideal for low volume motor development applications since it allows design iterations to be incorporated without expensive and time consuming tooling changes. Kapton insulation was used to insulate the rotor core slots in-place of a typical electrostatic coating over concerns that the electrostatic insulation might crack and flake off at low temperatures. The trade-off for using the Kapton insulation is that the rotor end-turns are slightly longer thus increasing the motor size.

Magnetic Design
Magnetic models of the motor were developed to predict the motor performance and size the motor for the application. The magnetic analysis allowed optimization of the motor backiron, magnet, and rotor core geometry for reduced weight. Neodymium-iron-boron rare earth magnets provided additional weight savings through increased energy densities over alnico and samarium based magnets. Initial testing with the motor control system indicated that motor detent would need to be reduced to improve the low speed controllability of the units. Since both the armature core and magnets were manufactured using the wire EDM process it was relatively easy to manufacture new skewed magnets to replace the original straight magnets and achieve the desired reduction in motor detent.

Temperature Performance
Due to the extremely low operating temperature of the motor the winding resistance drops significantly at -165°C. Consequently the current draw increases at the reduced temperatures and performance is actually enhanced over ambient performance considerably. The predicted motor performance over the extremes of applied voltage and environment temperature is presented in Figure 4. Notice how the motor stall torque becomes very large at the maximum voltage and minimum temperature (upper line). The maximum voltage and minimum temperature scenario drove the requirements for the planetary gearbox design.

146
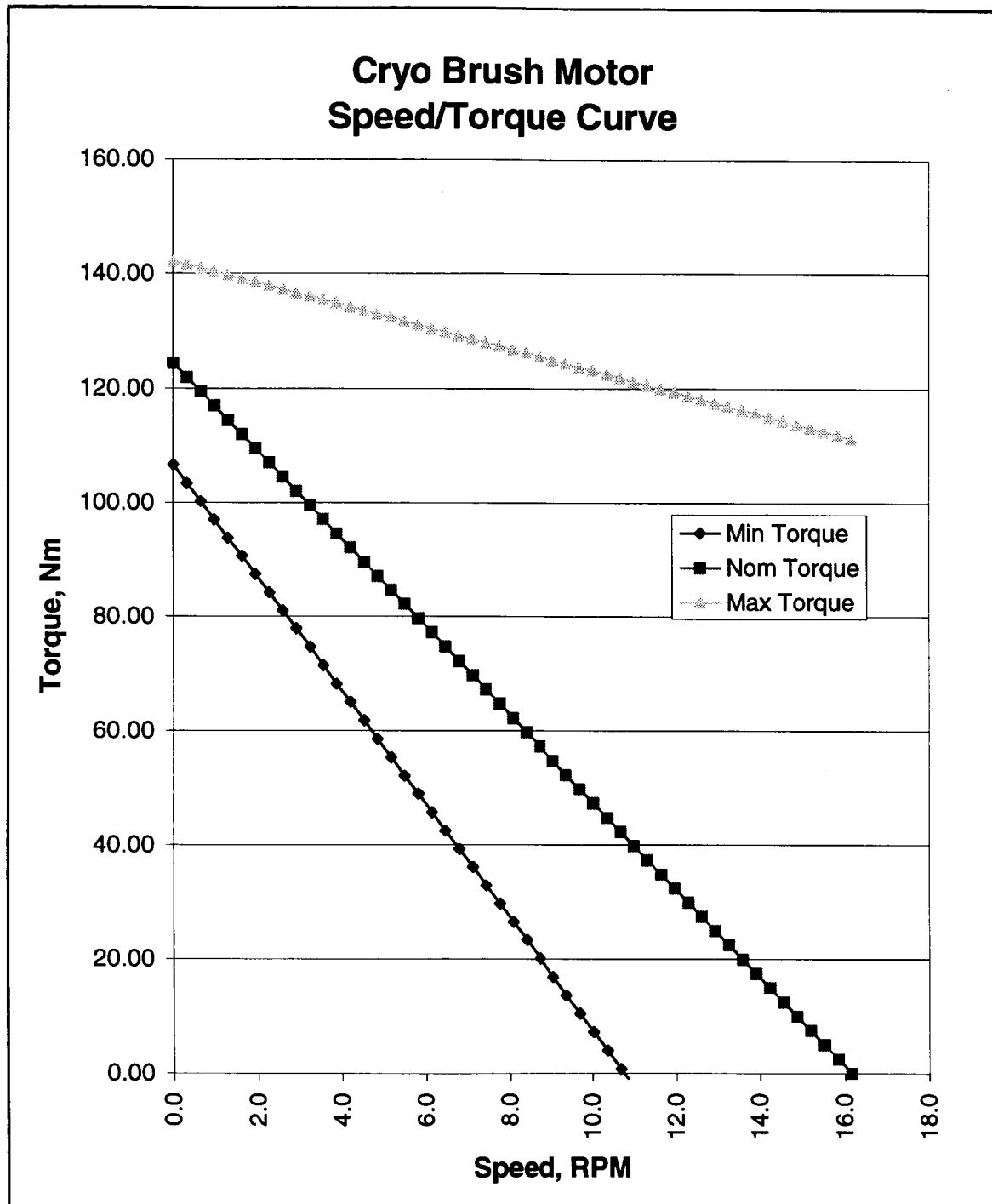
Figure 4. Nominal, Minimum and Maximum Motor Torque/Speed Profiles

Planetary Gear Box

The planetary gearbox and secondary spur gears, with associated bearings and lubricants needed to be developed to function in this challenging environment. The planets and sun gears in the two-stage planetary gearbox are made out of maraging Vascomax C250 steel and lubricated with a tungsten-disulfide molecular coating. The bearings in the first stage are modified 440C bearings with ceramic balls and lubricated with retainers made out of bearium, a copper, lead and tin alloy. The second stage planets are simply bushing supported. The tungsten-disulfide coating performed well in ambient conditions, but failed after one and a half hours at cryo/vac. The failure appeared to be wearing of the lubricant and subsequent galling of the maraging steel.

Ferro-Tic pins and bushings were installed which resulted in galling failure in one and a half minutes. (Figures 5-6) Ferrotic is a metal matrix composite that contains hard rounded titanium carbide grains in a steel matrix. Notice in the micrographs the visible Tic grains that appear as gray dots. For this material to perform well, one must polish the parts such that the matrix is worn down enough to expose the TiC grains but not so much that they fall out. Our parts had not been polished enough, so the matrix material was able to contact the matrix material of the contacting part. Although this material shows promise of performing well, it was abandoned due to its process sensitivity.
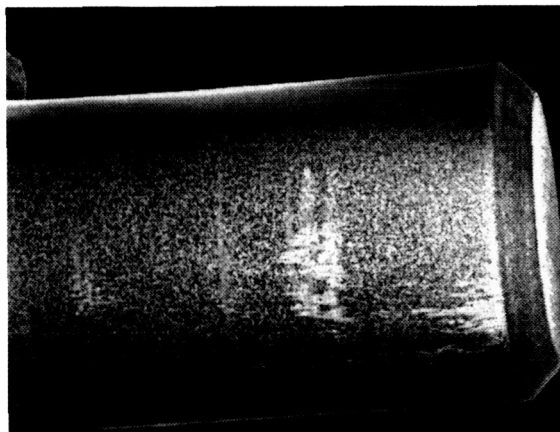

Figure 5. Ferro-Tic Pin with Galling   **Figure 6. Ferro-Tic Pin with Galling**
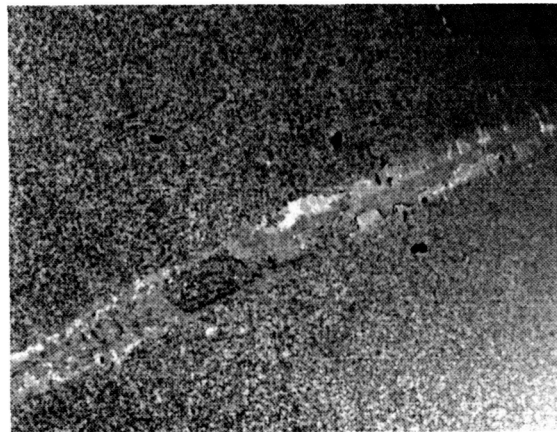
Nitronic 60 pins and bearium bushings were installed and tested and failed in air due to bearium galling. Although bearium is good as a bushing material when wet lubed, it tended to gall under dry operation. Due to this failure, the bearium retainers in the large bearings were inspected for wear. The retainers were slightly misshapen and the holes elongated. Applying a small amount of Bray 602 grease to the large bearings reduced the loud squealing that had been present with the dry bearium retainers.

Secondary Gears

Tungsten carbide was chosen for the secondary spur gears to eliminate galling and need for lubrication. Wire EDM was used to cut these gears to a AGMA class 14 quality. While these gears have good anti-gall properties and high rupture strength, they are more than twice as heavy as steel. These gears performed well under ambient conditions. These were later changed to Titanium Carbo-Nitride to save weight. (Figure 7) These performed well both at room temperature and -165°C. During FY98, the bearings in the motors and large bearings that support the secondary gears will be made entirely out of Titanium Carbo-Nitride.

Figure 7. Titanium Carbo-Nitride Gears

The drive nut was originally made out of tungsten carbide too, but fracturing of the thread surfaces required a change in materials. Due to the cryo/vac environment, bare Nitronic 60 was selected and has been performing well under ambient conditions and at -165°C and will be tested at cryo/vac soon.

Lubrication

Lubrication for cryogenic, vacuum operation has long been a design challenge, which has usually been solved by isolating the friction components, lubricating them with grease, and heating them. In the new age of smaller, lower power spacecraft, the luxury of heating mechanical components will soon disappear. To prepare for this, the hybrid ceramic/stainless steel bearings with bearium retainers that were developed this year will be further improved to decrease friction and increase life. All titanium carbo-nitride bearings have been fabricated and tested at Mecanex S.A. in Switzerland by Dr. Volker Gass. These bearings have superior friction properties and still have high toughness properties at cryo temperatures. No liquid or dry lubrication is used, thus eliminating the problems of grease viscosity and dry lube buildup. Having had positive results with the titanium carbo-nitride secondary gears, it is anticipated that this will be a worthwhile study.

Several of most significant failures in this mechanism were due to incorrect lubrication. As discussed in the Planetary Gearbox section, the tungsten-disulfide molecular coating wore off and allowed the 440C and maraging steels to gall. Also, dry bearium retainers and bushings galled.

The higher speed, low load bearings in the motor were also lubricated with bearium retainers. These seemed to perform without galling, but were rather noisy.

Percussion

Drilling in hard, brittle materials is usually assisted by using percussion. Percussion has been incorporated into the drilling mechanism by using axial toothed cams that load a compression spring which then accelerates a large mass. To make the percussion system more mass efficient, the accelerated mass is made up of the three cam pieces. (Figure 8) Most of the mass is accelerated for CW rotation, while CCW rotation only accelerates the small cam. Bare 440C and

Figure 8. Cams

Nitronic 60 have been used for the cams with good results. In order to decrease the friction that the small motors had to overcome for the ambient tests, some Bray 602 was added.
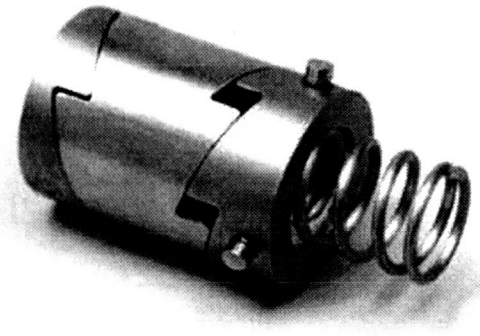
The percussion cams operate at 5 strikes per revolution in the CW drilling direction. When storing samples and rotating in the CCW direction, the drill still strikes at 5 hits per revolution, but with reduced energy due to the mass division.

It was found that percussion generated by this spring-cam system did not improve drilling performance in most materials. It is believed that the arm is not stiff enough and that the energy imparted is not high enough to yield the typical drilling improvement that is seen in commercial hammer drills.

150

Drill Bits

There are two features that make these drill bits unique and elegant. The sample chambers are inside the bit and the bits are interchangeable. (Figure 9) The swivel-head bit was developed to eliminate the need for an additional motor to be able to drill to any depth, take a sample at that depth, and reduce sample mixing with material along the depth of the hole. The swivel-head is passive and only requires counterclockwise rotation of the bit to open the chambers. Once the sample is acquired with multiple CCW revolutions, the head is swiveled closed with multiple CW rotations. The sample is fully contained in the bit. By making the bit removable the sample could stay in the bit and the bit used as the crucible for science experiments.
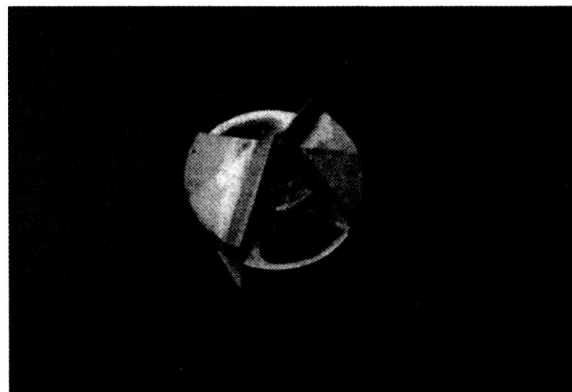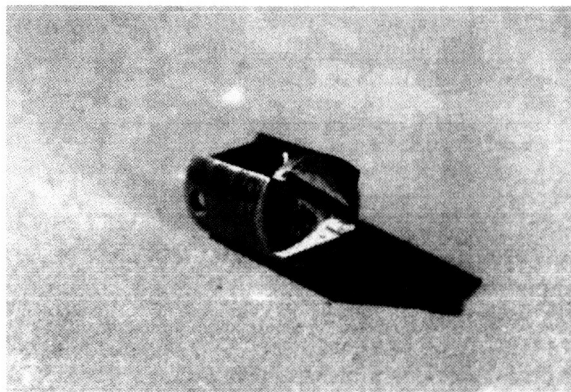

Figure 9. Drill Bit with Head Swiveled Open

Past designs of the drill had some type of sample acquisition area that would be filled in some way and then emptied by some mechanical means into a science instrument. The advantages of interchangeable bits was soon discovered. Interchangeable bits allow the use of different types of bits depending on sample type, the use of the bit as the crucible, the acquisition of several discreet samples for a sample return mission, the elimination of a secondary mechanism to extract the sample, and the ability to replace a damaged bit.

The current drill bit was custom designed to have high strength, low wear, and high sample volume. Eight different bit styles were tested in six different material at different drilling forces and rotation rates. (Figure 10) It was found that a split tip design worked best, with a 15° rake angle and 10° relief angle. The notches seen in the rear row of bits did not seem to affect drilling performance.
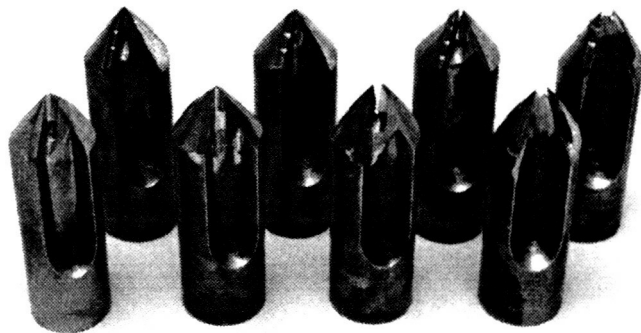

Figure 10. Test Drill Bits

Quick Release

The quick release is composed of two button bars separated by a compression spring. (Figure 11) By pressing in on the upper buttons, the lower ones retract to allow engagement with the bit. Knife-edge pivots are used to make it more tolerant to debris.

The quick release design functions well, but accurate placement and repeatability are required. Testing has been completed that autonomously dropped off a bit in the right hand port and picked up a new bit from the left port and then continued drilling. It was found that a mechanical indexing feature is necessary to ensure alignment between the bit and the bit pick-up device.

UNLATCHED   LATCHED

BUTTONS   BUTTONS
DEPRESSED   ENGAGED

2.37 cm
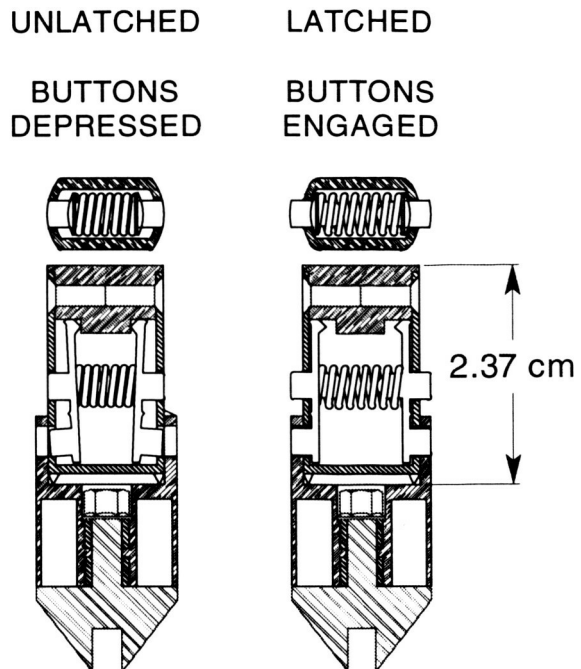
Figure 11. Drill Bits Cross-Section

Mechanical Testing

Mechanical testing of six different materials has been completed. Both bending/shear and compression tests have been done in order to determine a correlation between drilling rate and mechanical properties. From the hundreds of drilling tests using eight different bits at three rotational speeds with and without percussion at two different forces it has been determined what are the most significant factors in drilling.

By measuring the thrust and torque imparted on the drill bit while drilling, substantial data was collected and processed for each material and bit. What was found was a signature for each material that could be related to the 3-point bend data. The drilling rate was inversely proportional to the 3-point bend strengths, but unrelated to the compression strengths. (Figure 13)
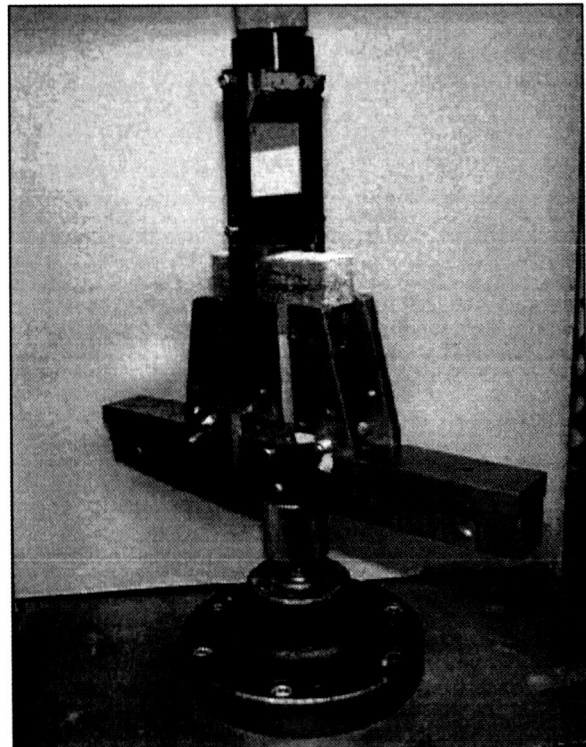

**Figure 12. 3-Point Bend Test**

152

Material Test Data
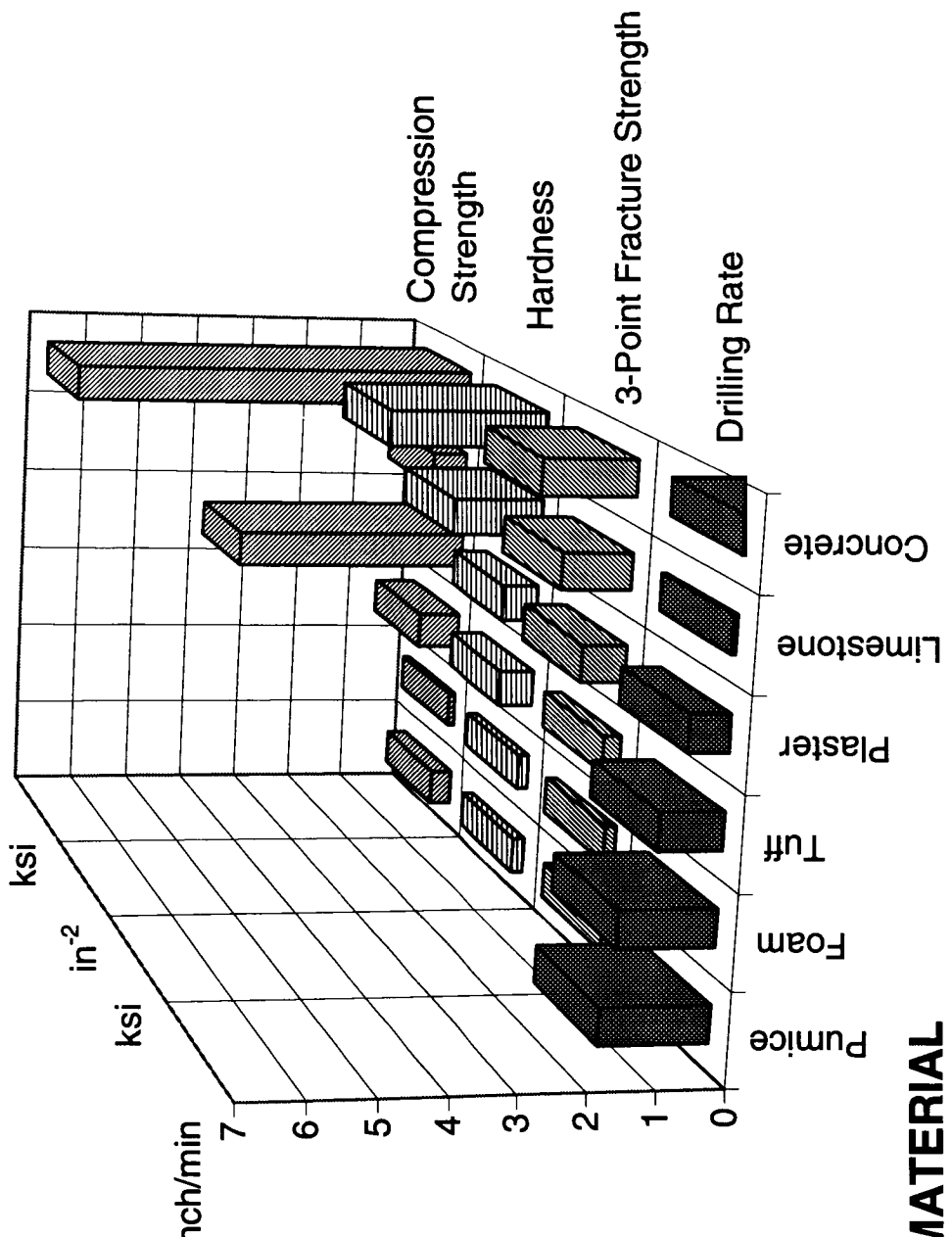
Figure 13.

153

Control System

The control system can command the drill at a specified force or rate using a six-axis force transducer to determine thrust, lateral forces, and torque. The software and motor control system is designed to be able to drill any sample by either manually specifying drill thrust velocity and rotation speed or using force control mode which automatically modulates the speed and feeds to maintain the optimal or highest drilling rate. These control sequences have been integrated into a single autonomous sequence that will undock, index, drill, acquire, transport, deposit, and pick up new drill bits. Since by measuring speeds and feed rates and doing force versus deflection testing will determine the material characteristics, more analog materials will be tested and cataloged. These cataloged data will enable the flight drilling instrument to make comparisons to earth analogs and customize its drilling.

It is planned for future drilling software development to create look-up tables from the terrestrial analogs so that the drill may autonomously adapt its drilling speeds and feeds to optimize drilling.

For microgravity landing environments found on asteroids and comets, drilling thrust loads must be controlled under the holding abilities of the anchoring system and yet high enough to provide efficient drilling. There are maximum rotation and thrust rates above which power efficiency is diminished, so the drill is able to recognize this and control to lower rates.

154

Conclusions

While the new colder, high vacuum and dusty environments will pose a host of new challenges to mechanism design there will be many possible solutions. Several were attempted in this task that had higher risk, but great reward if they succeeded.

DC brush motors have great potential for this application where lightweight, limited-life actuation is required. Brush wear continues to be the area of greatest concern, but the Martian environment appears to be a fairly benign environment compared to high vacuum.

The elimination of lubrication seems to be a reliable way to design mechanisms of the future for cryogenic, vacuum environments. The way to eliminate lubrication is to use harder, durable materials that can be formed using the advanced machining processes available now. Without liquid or grease lubrication, mechanisms are no longer restricted to operation above -70° C. Since motors run more efficiently at lower temperatures anyway, heaters can be eliminated resulting in more robust, efficient actuators.

It is apparent that drilling will continue to be a study of interest into the next millennium in order to understand more about the planets around us. Bit design and software development will be enhanced and optimized as we learn more about the environments that we desire to explore. By using the operation of the drill to gather scientific data about the material being drilled, the drilling mechanism becomes an instrument of sorts. This enables the scientists to learn about the mechanical properties of the rocks being sampled many years before those samples can be returned to Earth.

Acknowledgments

References

Dr. Volker Gass at Mecanex S.A., Switzerland
Jim Sprunk at American Technology Consortium
Shenandoah Wang at Bearing Technology
Web site for Exploration of Small Bodies Task: http://esb.jpl.nasa.gov/
Web site for American Technology Consortium: www.consortium.com

Active Sample Acquisition System for Micro-Penetrators

Chris Voorhees* and Benjamin Potsaid*

Abstract

This paper summarizes the design and development of a sub-surface sample acquisition system for use in micro-penetrators. The system was developed for flight use under NASA's New Millennium Program, Deep Space 2 project. The system goal is to acquire approximately 100 mg of Martian sub-surface soil and return it to the inside of the micro-penetrator for analysis to determine the presence of water. Various passive and active sampling techniques that were tested during the development cycle are described. After significant testing, a side bore drill mechanism was chosen to be developed for use in the flight penetrators. The design, development, and testing of mechanism element are outlined, with particular emphasis placed on actuator development, drill stem design, impact testing, and mechanism testing in various soil types. The other system elements, a pyrotechnically actuated door mechanism to seal the sample and an impact restraint mechanism, are also described.

Introduction

The goal of obtaining a sub-surface soil sample is widely regarded in the scientific community as critical to unlocking the mysteries of the Martian past. This is because, planetary scientists argue, most of the evidence of the planet's geologic history is obscured on the surface by a layer of younger material – dust that has been distributed relatively uniformly around the planet. In order to reach conclusions about Mars' past, a sample of material must be obtained undisturbed from beneath the surface. One of the most straightforward methods of getting to this sub-surface material is through the use of a soil penetrator, a simple device that uses its own kinetic energy to bury itself upon impact with the surface. This type of spacecraft is currently being developed as a part of the NASA New Millennium Program, which is managed by the Jet Propulsion Laboratory. The program goal is the flight demonstration and validation of new technologies and techniques needed for the next century's robotic explorers [1]. The second of these missions, Deep Space 2 (DS-2), or Mars Microprobe, will deliver two micro-penetrators to the surface of Mars. Scheduled for launch in January of 1999, the basketball-sized crafts will piggy-back to Mars aboard the Mars Surveyor '98 Lander cruise stage. The probes consist of three major parts: aeroshell, forebody, and aftbody. The aeroshell protects and orients the rest of the probe during entry into the Martian atmosphere. Instead of separating from the rest of the craft, the aeroshell stays attached to the rest of the probe until impact. The aeroshell is made of a brittle

---

* Jet Propulsion Laboratory, Pasadena, CA

ceramic material which allows the probe to punch through when it reaches the surface. Upon impact at an estimated velocity of 200 m/s, the probe separates into two main sections, shown in Figure 1. The aftbody stays on the surface, housing batteries and telecommunications assemblies for transmission to the Mars Global Surveyor spacecraft. The bullet-shaped forebody, containing the sample acquisition system and science experiment, penetrates and descends into the sub-surface. The forebody and aftbody remain connected through a flex umbilical that provides power to the forebody and data transfer to the aftbody for communication to Earth. Once a sample has been collected, it is sealed in a ceramic chamber and heated. Any water vapor that is created is evacuated through small holes in the bottom of the chamber and into an analysis chamber, where a tunable diode laser detects the water vapor. The data is then transmitted, along with temperature and pressure information, which will be collected throughout the 14-day mission length [2]. The remainder of this paper describes the design, development, and testing of the system used on DS-2 to acquire the sub-surface sample, starting first with a discussion of the various sampling techniques tested, as well as the reasons for the selection of the technique used on DS-2.

Sampling Techniques

In using a micro-penetrator as the platform, several techniques can be implemented to acquire a sub-surface soil sample. These techniques can be separated into two broad categories: passive and active. Passive systems simply use the kinetic energy of the penetrator impact itself and/or gravity to collect the sample. This approach is desirable, since the sample is collected without the addition of another mechanism, making the system more robust. Active systems wait until after impact and penetration has occurred and use an additional action to obtain the soil sample. This avenue is not as desirable as the passive technique, since additional complexity must be added to the probe in order to accomplish the task.

To experiment with various passive and active concepts, prototypes of each technique were fabricated and impact tested. Penetrator testing was carried out in an air gun, owned by Sandia National Labs and operated by the New Mexico Institute of Mining and Technology's Energetic Materials Research and Test Center EMRTC [3]. Each prototype was fired into a clay and/or sand matrix target which was coated with colored chalk so that surface material was discernible. Passive sampling techniques included: a rear sampler, where the soil sample was collected from material that fell into the back of the probe; a side sampler, where the sample fell into twelve holes angled 45 degrees from vertical; a digestive tract sampler, where the sample passes through a tapered hole along the penetration axis of the forebody. As explained in [3], the results of the passive acquisition tests were unfavorable. In each case, surface soil was found mixed in with the rest of the sample, indicating that the sample did not wholly originate from the final rest position of the forebody. It was also impossible to determine from what depth the rest of the sample had been taken. In addition, a boundary layer of surface material averaging 1 mm thick was seen to surround the

158

outside surface of the forebody. This boundary layer would have to be cleared in order to reach uncontaminated sub-surface soil. In light of this information, it was decided that an active sampling technique would have to be employed in order to obtain a sub-surface sample accurately. After initial testing, a compact drill mechanism seemed the most viable option. In addition, the drill axis could be oriented to drill out the side of the forebody, where the surface contamination would be minimized.

The DS-2 Drill Mechanism

For DS-2, an active side bore drill mechanism was selected as the baseline configuration for flight. The mechanism consists of three sub-components: drill tip/auger, torque/axial force transfer, and drill motor. To capture a sample, the mechanism drills out the side of the forebody. Material is then transported back into the forebody by means of the auger flutes. The collected soil then falls through a 7-mm hole into the sample chamber. A pyrotechnically activated door mechanism then closes over the sample, sealing it from the rest of the forebody. The sample is then heated and analyzed for the presence of water.

The constraints and design criteria that the mechanism needed to fulfill were significant. The forebody internal cavity, where the mechanism must reside, is a cylinder measuring only 36 mm in diameter by 83.5 mm in length. Along with the mechanism, the volume must also contain the probe microcontroller and electronics, water detection experiment and electronics, temperature sensors, impact accelerometer, flex umbilical connecting forebody to aftbody, heating chamber, and a chamber door mechanism to isolate the collected sample. In addition to the significant packaging challenges, the mechanism also faced considerable environmental and performance issues. First, the probe's impact velocity is estimated to be 200 m/s. This corresponds to a worst-case loading of the forebody of 30,000 G axially. The variance in angle of attack and angle of incidence of the probe creates the possibility of a worst-case lateral load of 15,000 G in the forebody. Second, the mechanism must survive impact at a temperature of -40 °C. Third, the mechanism must operate several hours after impact, which gives the forebody time to cool down to sub-surface temperatures. Because of this, a worst-case operating temperature of -125 °C at a pressure of 0.8 kPa (6 torr) CO_2 was imposed on the mechanism. Fourth, because the probe must use on-board power sparingly, the mechanism was allotted only 5 minutes to obtain the required 100 mg of sub-surface soil. Fifth, the mechanism must be able to keep itself closed during launch, cruise and impact, and open itself up during sample collection. This requirement keeps the drill mechanism isolated and free of surface contamination caused by soil entering the sample collection chamber simply by the force of impact. The mechanism then opens itself when ready to collect a sample. Sixth, the stroke of the drill must be great enough to extend past the boundary layer of surface soil surrounding the forebody and far enough into the undisturbed sub-surface soil that a good sample can be taken. Seventh, the characteristics of the soil to be

drilled are unknown. Because of the limited knowledge about the nature of the impact area, the soil encountered upon impact could be anything from dry sand to solid ice. An exploded view of drill mechanism elements is shown in Figure 2. A cross-sectional view of the forebody, showing drill mechanism elements, is shown in Figure 3. In the sections that follow, the design and development of the mechanism sub-assemblies will be discussed.

<u>Drill Tip/Auger</u>

The drill tip/auger sub-assembly of the mechanism needed to be one of the most robust. Because of the wide variety of soils possible at the impact site, the drill tip/auger must be designed to drill through the strongest soils while still being able to transport the weakest, most granular media. In addition, the design was driven to a two-part configuration because of the desire for the mechanism to be self-closing.

The drilling of frozen media is of considerable terrestrial importance. Oil and well drilling, in addition to mining applications, must understand how the properties of frozen ground will affect the ability to penetrate and transport the media. Unfortunately, frozen soil properties are not homogeneous and vary wildly with water content. At one extreme, dry frozen soil has no shear strength whatsoever and can be quite difficult to transport in the flutes of a drill. At the other extreme, saturated frozen soil is analogous to rock, with relatively high strength in shear, and can be quite difficult to penetrate [4]. In many terrestrial applications, brute force is used to solve penetration difficulties [5]. Of course, this was not a possibility for the DS-2 drill mechanism application. In any drilling application, three main factors affect successful drilling performance: one, having adequate available torque to continue the cutting action; two, having adequate axial force to continue penetration; and three, having the correct cutter geometry for the material being penetrated. The balance between these three factors is critical to the performance of the drill. This was no different for the DS-2 drilling application. As a starting point for the mechanism design, the torque and axial force requirements for drilling into various frozen soil samples were first determined, which was accomplished through the use of a custom test apparatus. The apparatus used compression springs to provide axial force on a conventional 9.53-mm (0.375-in) high-speed steel drill bit, while an Instron machine was set to spin a frozen soil sample at a constant rate of 0.838 rad/s (8 rpm). The drill bit was put into contact with soil and allowed to penetrate for 5 minutes. Torque and axial force levels were recorded throughout the test. The soil samples used to perform the tests were a hybrid mix of frozen sand and water at varying % H_2O by weight. The sand was a mix of grain sizes, with a nominal grain size around 150 μm. The sand was saturated at 20% by weight H_2O, and this was considered to be the worst-case soil sample. At worst case, an initial axial spring force of 44.5 N (10 lbf) allowed for continuous penetration. The torque required to cut the material averaged between 0.226 and 0.282 N-m (2 and 2.5 in-lbf). The average penetration into the worst case material after 5 minutes was 5.08 - 6.35 mm (0.20 - 0.25 in).

160

Once the torque and force requirements were determined, the cutter geometry needed to be defined. This was accomplished through the use of another custom test apparatus, shown in Figure 4. This drill test rig allowed the user to swap in and out custom and commercial drill tips of differing diameters and cutting geometries and to vary the amount of initial axial spring force that was applied. The test rig also allowed different actuators and gear reductions to be tested. In addition, the feasibility of the sampling technique was itself tested. A 7-mm hole was bored from the bottom up into the drill bore to mimic the hole the sample would fall through to get to the sample heating chamber. Various soil samples could be placed into and removed from a square housing in the front of the test rig. Over 60 trials using various custom and commercial drill bits, coring bits, end mills, and reamers were completed, with torque and axial force data being recorded. In addition, total drill extension and sample acquired were also measured. The following general trends seemed to follow true throughout the testing: one, because the total extension of the drill during the 5-minute cycle was quite small, drills with flatter point angles tended to yield a greater sample size; two, an increase in relief angle, the angle between the cutting edge and the material, tended to increase penetration rate; three, a higher helix angle (~60 deg.) tended to provide better material transportation in both dry and saturated soils; four, because of the short operating time, larger bit sizes (~9.53 mm (0.375 in)) tended to acquire the required 100 mg soil sample more effectively in the allotted operating time; and five, because of the short operating time, carbide or nitride coatings did little to improve the cutting performance over standard high-speed steel bits.

Using the results obtained from the drill tests, a hybrid tip and auger were created. The tip was fabricated from T1 high speed tool steel. The tip had a flat point angle, an 8-degree relief angle, and a 13-degree rake. During testing, this combination of cutting angles seemed to yield the best overall cutting performance for the widest range of materials. The auger was fabricated from titanium, essentially for its high strength to weight ratio, with a 60-degree double helix material transport. This unit was then tested in various frozen soil samples. The results, shown in Table 1, show favorable performance for a wide variety of different frozen soil types.

In addition to being optimized to drill into frozen soil, the drill tip/auger sub-assembly is also designed to shutter itself open and closed. This feature allows the drill mechanism to remain closed during impact and then open up during the first few degrees of rotation upon start of the drilling sequence. This is accomplished by designing the drill tip with two pockets machined in its back face. These pockets accept mating nubs on the front face of the auger. The shaft of the drill tip also runs down a mating hole in the auger and is shoulder bolted at its end, permitting the drill tip to rotate but not to be moved axially. This design allows the drill tip to be shuttered open and closed on hard stops, as the nubs hit the ends of their respective pockets. A representation of this design is shown in Figure 5.

Torque/Axial Force Transfer

This sub-assembly purpose is to provide to the drill tip/auger sub-assembly the necessary torque and axial force to drill successfully into the frozen media. The sub-assembly consists of a 2.5:1, 90-degree bevel gear set, nested compression springs, and a spline. The external spline is directly fastened to the back end of the auger, while the mating geometry is machined directly into the hub of the bevel gear. The spline uses flat tooth geometry and is fabricated out of Nitronic 60, taking advantage of the alloy's anti-galling characteristics. Two compression springs in parallel provide the 44.5 N (10 lbf) of initial axial force required for drilling. The springs are nested together and housed in a cavity in the hub of the bevel gear.

The 90-degree bevel gear set is designed under an interesting set of constraints and criteria. First, the bevel gear itself is the keystone of the entire drill assembly. Its structure must support the impact loads of the auger/drill tip sub-assembly, the spline, the compression springs, as well as itself. Under a combined 30,000 G axial load and a 15,000 G lateral load, the forces on the bevel gear structure could become severe. Therefore, the bevel gear is fabricated from titanium, which gives it high strength characteristics while its relative low mass (~2 g) lessens the overall impact load. The pinion's primary design characteristic is its own mass. As can be seen in Figure 3, the pinion resides directly in line with the motor shaft. On impact, the load of the pinion is offset from the motor shaft by means of a small ball bearing, residing directly below the pinion. However, if the impact load of the mass of the pinion is too great, significant Brinell damage of the bearing could occur. Because of this, the pinion mass had to be minimized. Therefore, the pinion is fabricated from Aluminum 7075-T6. This ensures that the pinion can support stall loading of the geartrain while imparting as little impact load into its ball bearing as possible.

Another problem is created by the selection of these two gear materials. Titanium and aluminum are both materials that are highly susceptible to galling and cold welding in a vacuum. There is considerable risk to mechanism performance if there is no barrier between the two materials. A solid film lubricant, Lub-Lok 4306, is therefore employed to act as a barrier material between the two materials. As an added safety, the aluminum pinion is also hard anodized. The combination of these two barrier materials, in addition to the low number of cycles (~100 for pinion, 40 for gear), ensures successful operation of the mechanism.

Figure 6 shows the drill stem assembly. This assembly packages the drill tip/auger and torque/axial force transfer sub-assemblies into one assembly that can be inserted directly into the forebody. The drill stem assembly also includes an integral ball thrust bearing that the bevel gear rides on during operation. The bearing consists of ~30 Delrin 100 balls, 1.59 mm (0.063 in) in diameter riding in their own grooved retainer. There is a 0.127-mm (0.005-in) nominal riding clearance between the bevel gear and the retainer. Upon impact, the balls elastically deform until the bevel gear hard stops against the retainer. This allows the impact load to be taken through the retainer and

not the balls, which are unable to support a dynamic loading of that level. As can be seen in Figure 6, a restraint nut is used to keep the assembly together during launch, cruise, and impact. Upon operation of the drill mechanism, the auger turns itself out of the restraint nut in the first three rotations.

Drill Motor

The workhorse of the DS-2 drill mechanism is the drill motor, providing the necessary torque to drill into the frozen soil. As shown in Figure 3, the motor is mounted down the axis of the forebody, nested inside of the probe electronics. The motor in and of itself presents a full set of design constraints and criteria. The motor must operate at worst-case Mars temperature and pressure, -125 °C and 0.8 kPa (6 torr) CO_2, respectively. In addition, the orientation of the motor is such that it takes the full force of the axial impact load. The motor must also be able to provide the necessary 0.113 N-m (1 in-lbf) of torque required to drill the worst case saturated frozen soil. One positive design criteria, however, was that the motor had a one-time operating length of only 5 minutes.

It was decided early on in the mechanism development cycle that a stock motor would be used and modified if necessary to work under the above conditions. A 10-mm Micro-Mo DC brushed motor was selected as the baseline design. The motor also included a 5-stage, 1024:1 planetary gear reduction and precious metal brushes. The motor was of a coreless rotor design.

Initial impact testing of the stock motor and gearhead revealed significant problems in its impact survivability. First, the rotor coil of the motor was pulling away from the commutator plate, causing an open motor circuit. This problem was remedied with the addition of a cyanoacrylate adhesive to strengthen the interface. Second, the magnet post, while successfully impacted at ambient temperatures, was failing when impacted at the expected Mars impact temperature of -40 °C. This problem was due to a brittle transformation occurring in the polyamide material of the post. To solve the problem, the plastic post was replaced with a titanium one, greatly increasing overall strength with no undesirable temperature effects. Third, the magnet itself was shattering on impact. The stock magnet was Samarium Cobalt, a highly brittle magnet material. This magnet was replaced with a Neodymium Iron Boron (NdFeB) magnet of similar magnetic field strength. The NdFeB magnet had a much more rugged magnet material and survived subsequent impact tests with no deleterious effects. Fourth, the magnet was found to slip on the magnet post, causing interference between the rotor and the magnet. This problem was remedied by bonding the magnet to the magnet post using EA9309 structural epoxy.

In addition to problems encountered due to impact, temperature concerns also caused modifications to be made to the stock motor and gearhead. First, the motor was shipped with sintered bronze bushings, which seized during initial tests at

approximately -50 °C. The bushings were replaced with unlubricated ball bearings, which ran favorably at -125 °C. Second, the lubrication on the brushes caused them to lift away from contact with the commutator at -125 °C, which resulted in an open circuit. The lubrication was removed from the commutator and brushes to remedy this problem. Lubrication was also removed from the ball bearings and planetary geartrain of the gearhead. The planetary gears were then lubricated with finely ground MoS_2 powder. Once the gearhead lubrication was removed, additional play was found between each of the planetary stages. The additional play was a cause for concern over possible recoil in the gearhead at impact. Two additional stage dividing washers were added to take up the excess play.

The majority of the modifications to the drill motor are ones that affect the overall motor life in a negative way. Removal of lubrication in both the bearings and between the commutator and brushes dramatically reduces the operating life of the motor. The granular MoS_2 solid lubricant could become abrasive and life-limiting after prolonged use. However, because of the small operation length of 5 minutes, these modifications were acceptable. Under a worst-case load of 0.113 N-m (1 in-lbf), flight-like motors have run without substantial current increase for an average of 27 minutes. This value represents a significant ~5.5:1 life factor of safety over the nominal 5-minute operation.

Overall Mechanism Performance

A fully functional drill mechanism has a nominal drilling speed of 0.628 to 0.838 rad /s (6-8 rpm) with a maximum drill extension of 9.53 mm (0.375 in). The expected operating torque is 0.113 to 0.141 N-m (1 to 1.25 in-lbf) and a stall torque of 0.509 N-m (4.5 in-lbf). Motor operating current averages between 40 and 70 mA, with a stall current of greater than 300 mA. The mechanism has an operating time of 5 minutes at an unregulated voltage averaging ~10 V. To date, a fully functional drill mechanism has successfully completed a full mission sequence during two separate tests. The mechanism has survived impact at -40 °C. During the first test, it successfully demonstrated in-situ drilling and sample acquisition, acquiring 104 mg of soil sample from the impact target. In both tests, the forebody was removed from the target and brought back to JPL, where drilling tests were successfully completed at expected worst-case Mars temperature and pressure, -125 °C and 0.8 kPa (6 torr) CO_2, respectively. The sequence will be tested once again in late May, 1998, at EMRTC during the DS-2 System Qualification Impact Test.

Other System Elements

The DS-2 sample acquisition system includes two other elements without which a sub-surface sample could not be successfully acquired and analyzed. First, although the auger/drill tip sub-assembly allows the drill tip to shutter open and closed, it does not lock the tip into position. This is required so that launch or impact does not jar the tip open, causing surface soil contamination. This requirement is fulfilled with the drill

shutter restraint mechanism. Shown in Figure 7, this mechanism consists of a pin with a hook-shaped end and a compression spring. During launch, cruise, and impact, this spring-loaded pin is nested into a mating pocket machined into the back face of the drill tip. The hook feature keeps the drill tip from rotating in one direction, while the non-back-driveable geartrain keeps the mechanism from rotating in the opposite direction. Upon operation, the drill tip turns away from the restraint. When it clears the pocket in the drill tip, it springs up and out of the way of the drill stem.

The second additional mechanism in the sample acquisition system is a pyrotechnically activated door closure mechanism. After a soil sample is successfully acquired, a miniature piston actuator is fired, pushing a titanium guillotine "door" over the top of the sample chamber, sealing the sample inside for analysis. The door is held in the open position during launch and impact through the use of two 0.5-mm diameter 303 CRES shear pins. These pins are sheared when the actuator is initiated. The miniature piston actuator is commercially available from Eagle Picher Industries, and measures 3.43 mm (0.135 in) in diameter by 9.32 mm (0.367 in) in length. The mechanism, shown in Figure 8, has been operated successfully at -125 °C and 0.8 kPa (6 torr) CO_2.

Conclusion

The design, development, and testing of the DS-2 sample acquisition system have been discussed. Various active and passive sampling techniques tested during development have been described, along with the rationale of the selection for flight of the side-bore drilling method. A detailed description of the DS-2 drill mechanism and its performance has been presented, and the design of the mechanism sub-assemblies has been discussed in detail. Problems encountered through engineering tests have been outlined, and the solutions to those problems discussed. The resultant mechanism has been shown to operate successfully through a full mission sequence during two separate engineering tests. Finally, the design of related elements, the drill shutter restraint and pyrotechnically actuated door mechanism, has been presented.

Acknowledgments

Reference herein to any specific commercial product, process or service by trade name, trademark, manufacturer, or otherwise does not constitute or imply its endorsement by the United States Government or the Jet Propulsion Laboratory.

References

1. Casani, E. and Wilson, B., "The New Millennium Program: Technology Development for the 21st Century", AIAA Paper 96-0696, Jan. 1996

2. Gavit, S. and Powell, G., "The New Millennium Program's Mars Microrobe Misson", Proc. 2nd IAA International Conference on Low-Cost Planetary Missions, Johns Hopkins University Applied Physics Laboratory, April 16-19, 1996, Paper # IAA-L-0906

3. Bickler, D., Slimko, E., and Stone, J., "Sub-Surface Sampling with Penetrators", Proc. 4th International Symposium on Artificial Intelligence, Robotics, and Automation in Space, Tokyo, Japan, July 14-16, 1997, Ref. # U-12

4. Mellor, M. and Sellmann, P, "Drill Bits for Frozen Fine-grained Soils", USA Cold Regions Research and Engineering Laboratory, Special Report 86-27, Aug. 1986

5. Mellor, M., "Introduction to Drilling Technology", Proc. International Workshop on Physics and Mechanics of Cometary Materials, Munster, FRG, Oct. 9-11, 1989, ESA SP-302

Table 1: Flight Drill Tip/Auger Test (5 min. Duration)

Soil Type	Soil Temp.	Avg. Current	Sample Collected
Loose Sand, 120 μ	-85 deg C	26 mA	104 mg
Loose Sand, 120 μ	-82 deg C	27 mA	95 mg
8% H$_2$0, 120 μ	-75 deg C	40 mA	124 mg
8% H$_2$0, 120 μ	-78 deg C	37 mA	116 mg
8% H$_2$0, 120 μ	-80 deg C	42 mA	110 mg
10% H$_2$0, 120 μ	-79 deg C	55 mA	101 mg
10% H$_2$0, 120 μ	-82 deg C	52 mA	120 mg
12% H$_2$0, 120 μ	-80 deg C	64 mA	113 mg
13% H$_2$0, 120 μ	-76 deg C	62 mA	100 mg
15% H$_2$0, 120 μ	-80 deg C	67 mA	105 mg
15% H$_2$0, 120 μ	-74 deg C	70 mA	95 mg
20% H$_2$0, 120 μ	-75 deg C	82 mA	80 mg
20% H$_2$0, 120 μ	-77 deg C	80 mA	86 mg
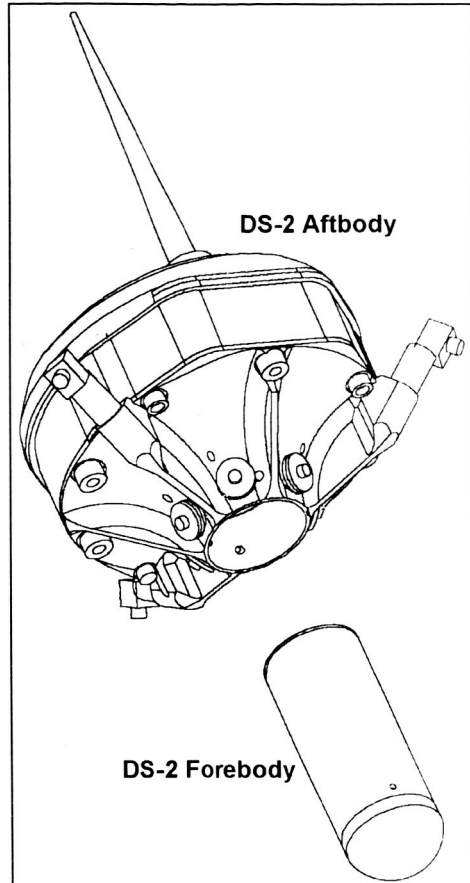
Figure 1: Deep Space 2 Forebody and Aftbody
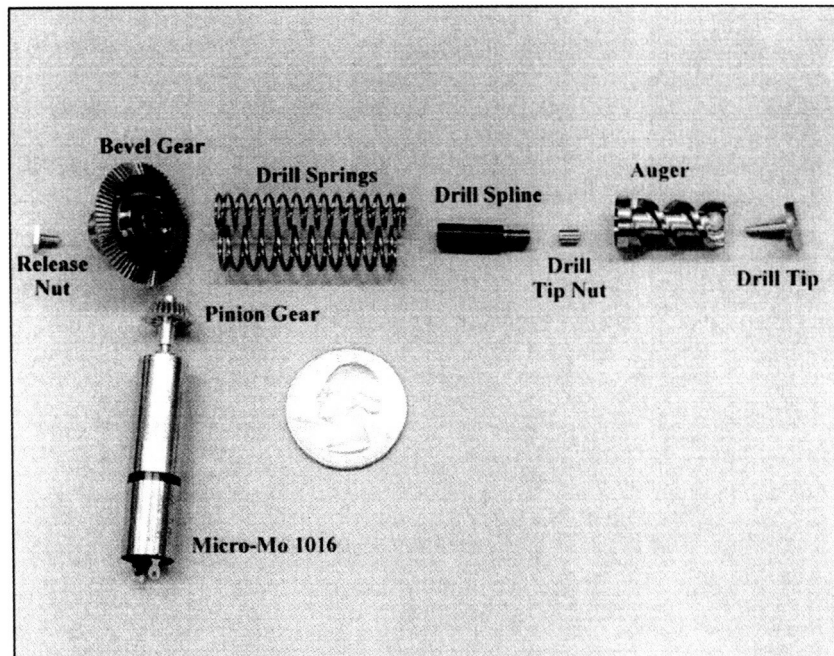
**Figure 2: Exploded view of drill mechanism elements**

168
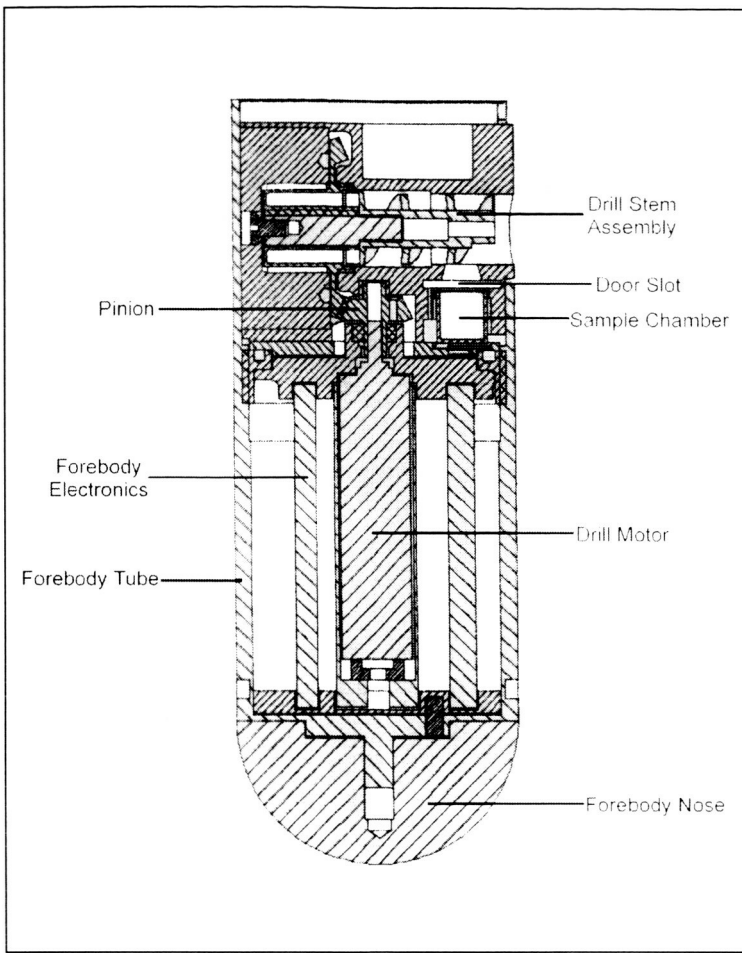
Figure 3: Cross Section of DS-2 Forebody
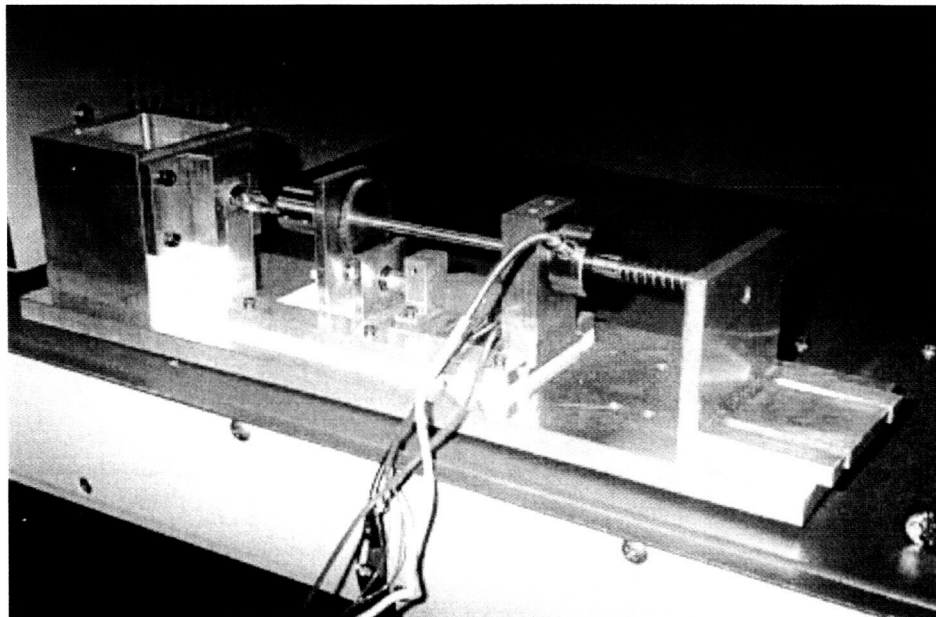

Figure 4: Drill Testing Apparatus

169
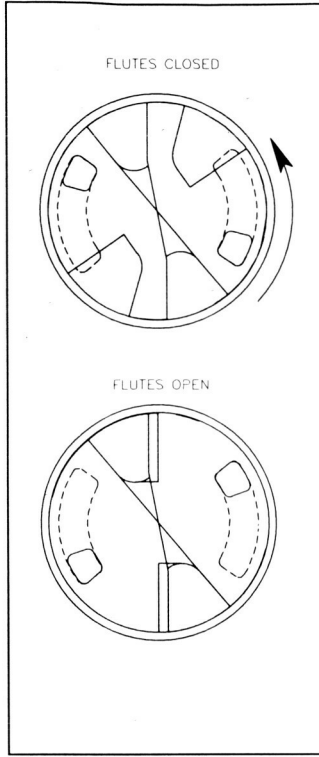
**Figure 5: Auger/Drill Tip Shuttering Action**
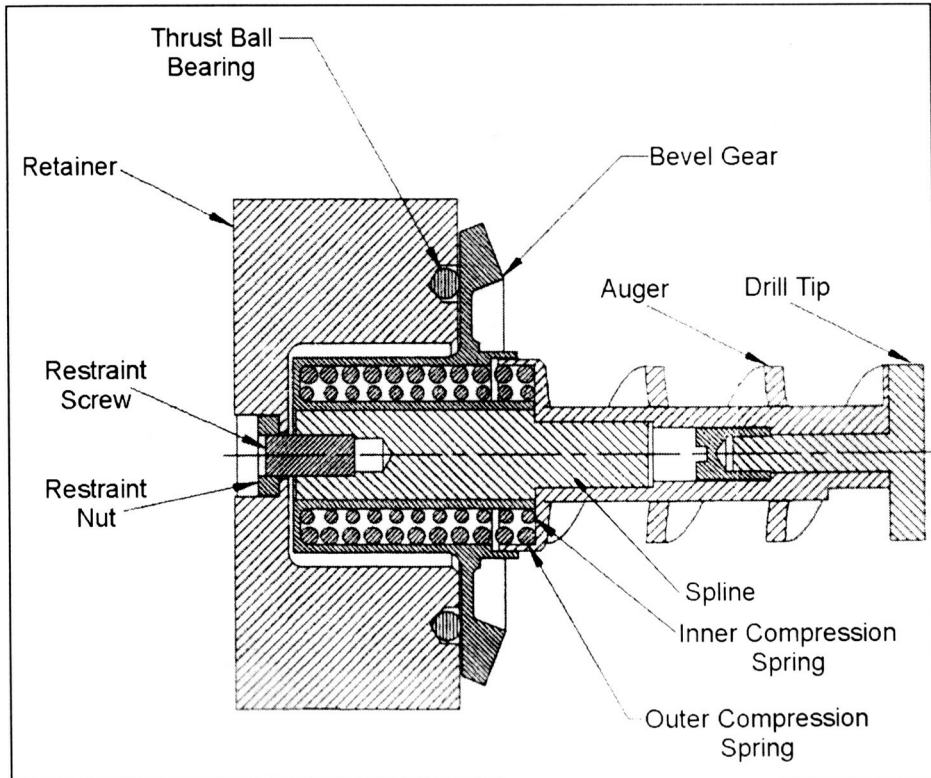
Figure 6: Cross-sectional view of Drill Stem Assembly

170
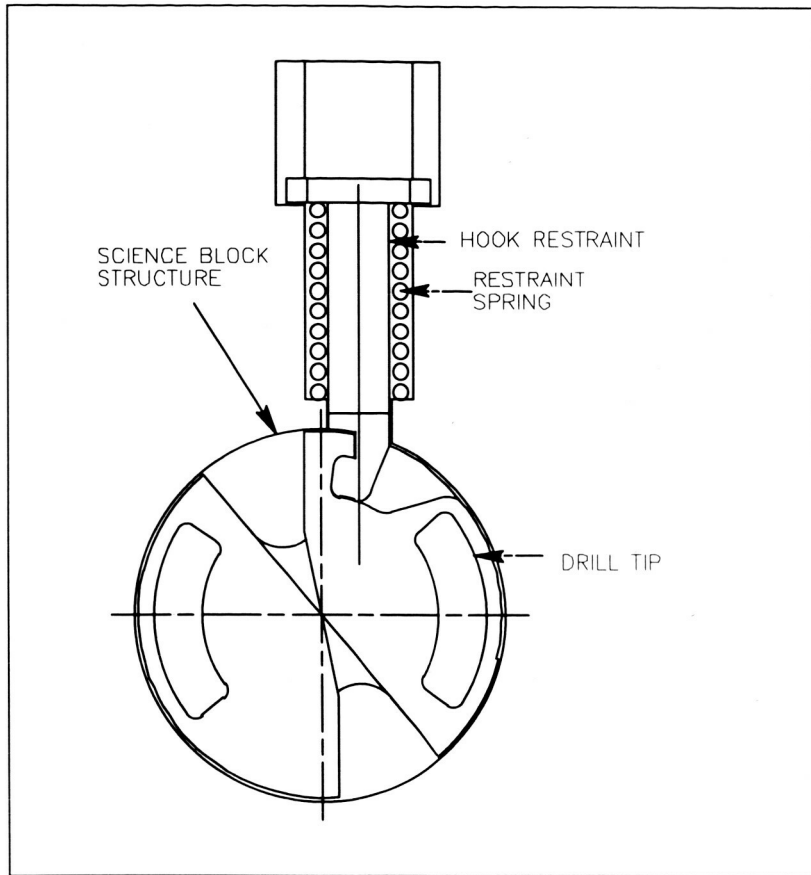
Figure 7: Drill shutter restraint mechanism
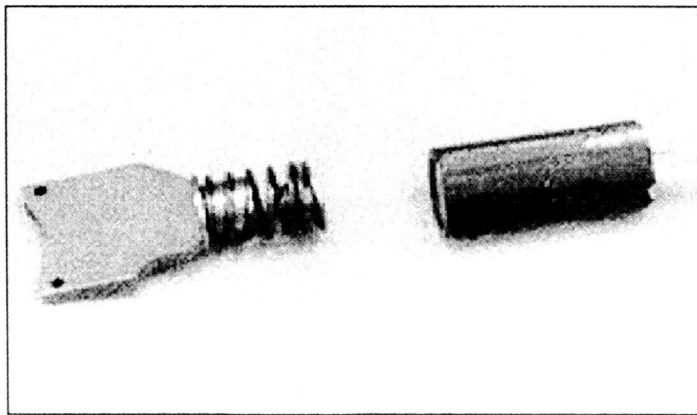
Figure 8: Pyrotechnically activated door mechanism
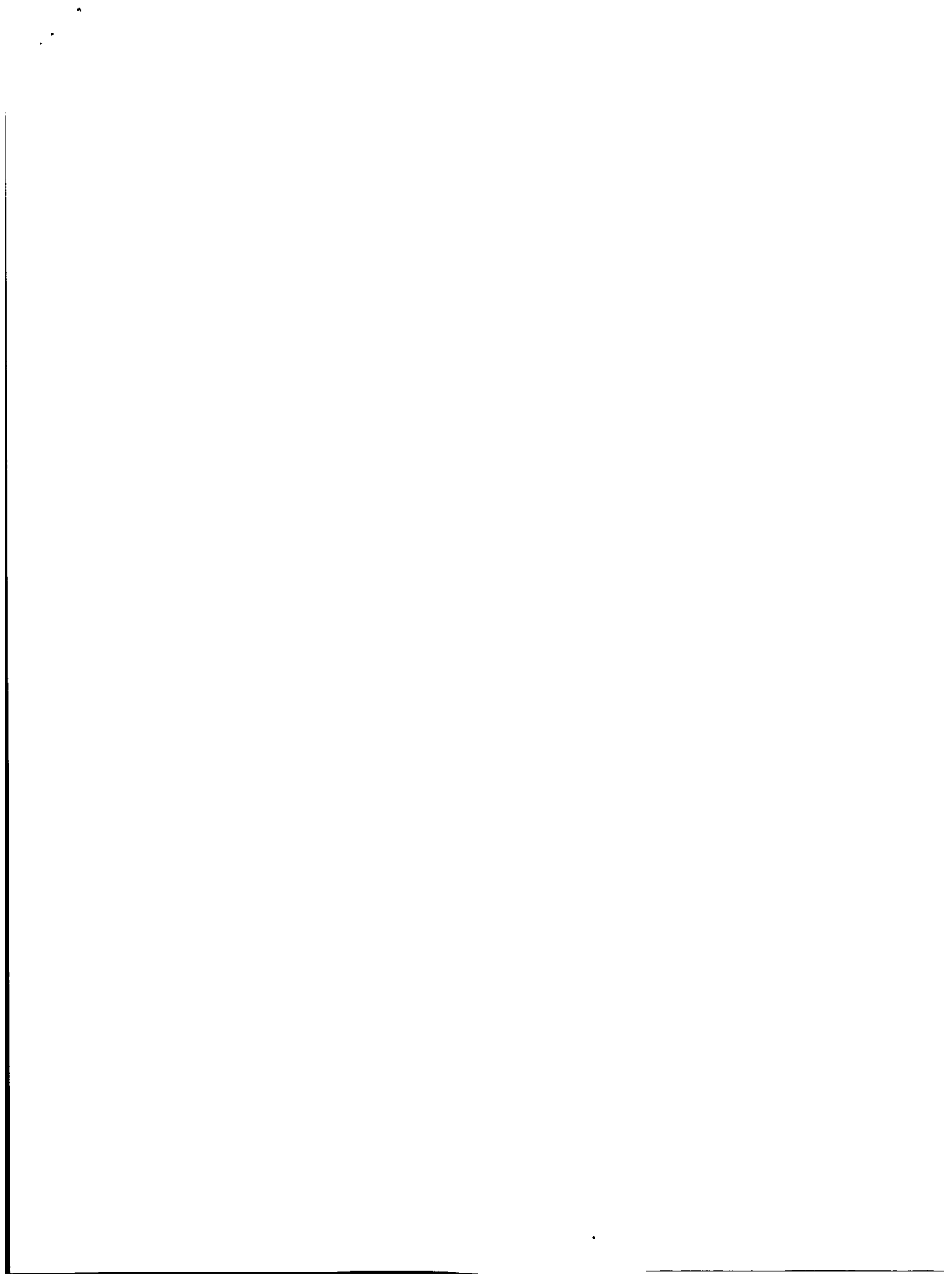
Thermal and Evolved Gas Analyzer

M.S. Williams, W.V. Boynton, R.L. James, W.T. Verts, S. H. Bailey and D.K. Hamara[*]

Abstract

The Thermal and Evolved Gas Analyzer (TEGA) instrument will perform calorimetry and evolved gas analysis on soil samples collected from the Martian surface. TEGA is one of three instruments, along with a robotic arm, that form the Mars Volatile and Climate Survey (MVACS) payload. The other instruments are a stereo surface imager, built by Peter Smith of the University of Arizona and a meteorological station, built by JPL. The MVACS lander will investigate a Martian landing site at approximately 70° south latitude. Launch will take place from Kennedy Space Center in January, 1999.

The TEGA project started in February, 1996. In the intervening 24 months, a flight instrument concept has been designed, prototyped, built as an engineering model and flight model, and tested. The instrument performs laboratory-quality differential-scanning calorimetry (DSC) over the temperature range of Mars ambient to 1400K. Low-temperature volatiles (water and carbon dioxide ices) and the carbonates will be analyzed in this temperature range. Carbonates melt and evolve carbon dioxide at temperatures above 600°C. Evolved oxygen (down to a concentration of 1 ppm) is detected, and CO_2 and water vapor and the isotopic variations of CO_2 and water vapor are detected and their concentrations measured. The isotopic composition provides important tests of the theory of solar system formation.

Discussion

TEGA is comprised of eight thermal analyzer modules (Figure 1), an oxygen sensor, and a carbon dioxide and water vapor sensor. The detection of carbon dioxide and water vapor is accomplished with a tunable diode laser built by the Jet Propulsion Lab [1]. Each thermal analyzer module (Figure 2) incorporates doors to prevent contamination of the module from inadvertent loading of soil, a soil processing system, a reference and sample calorimetry oven, oven closure mechanisms, and a plumbing system. A gas handling system stores and controls the release of purge gas and calibration gas, regulates the pressure and flow of the selected gas, distributes the gas to the selected thermal analyzer module, and directs evolved gases to the evolved gas analyzers.

Doors are necessary to prevent dust-borne soil, or soils loaded into adjacent thermal analyzer modules, from contaminating a module not in use. Each module has two doors attached by spring-loaded hinges to the sides of the module. When closed, the

---

[*] University of Arizona, Tucson, AZ

doors overlap slightly to create a seal against particulate contamination. The doors are closed until a particular analyzer is selected whereupon the doors are opened, on command, under the action of a solenoid.
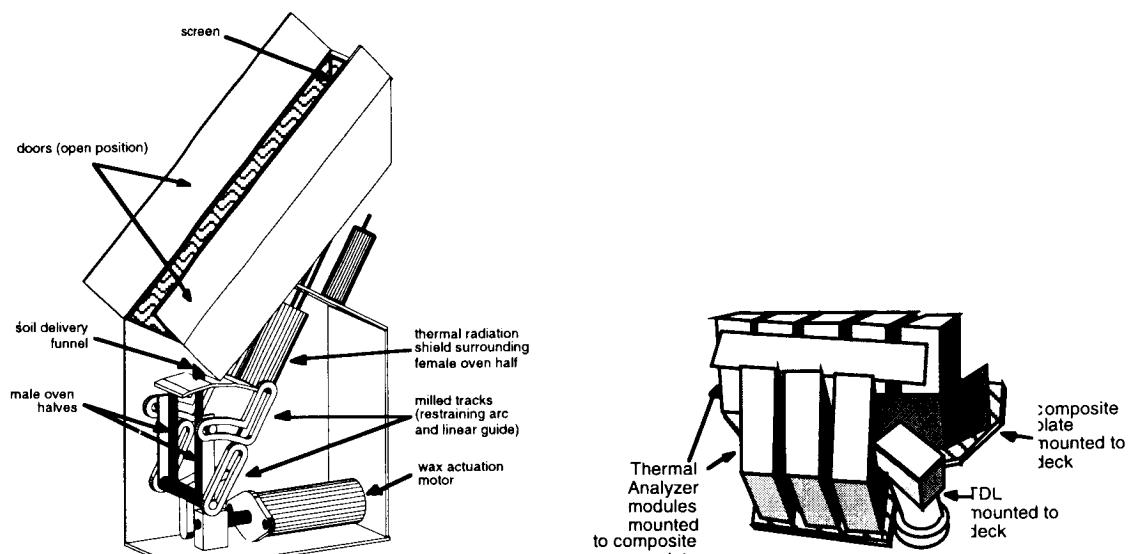

Figure 1—Thermal analyzer module (left), configuration on deck (right)
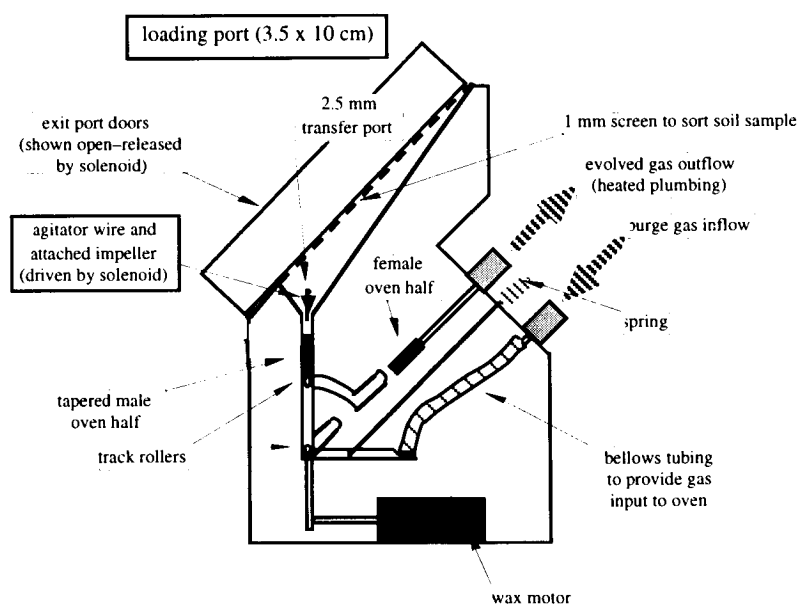

Figure 2—Thermal analyzer module schematic

An extension of the open door forms a dam to hold back the flow of soil (Figure 5). The doors are restrained in the closed position by a latch. The latch is driven to release the doors by a clutched axle attached to the solenoid. The solenoid also drives a soil impeller, and imparts a vibration to the module chassis to encourage soil to advance

toward the soil loading port. The clutch requires the axle to advance 40, 10° strokes before the door will open to reduce the chance of accidental door opening.
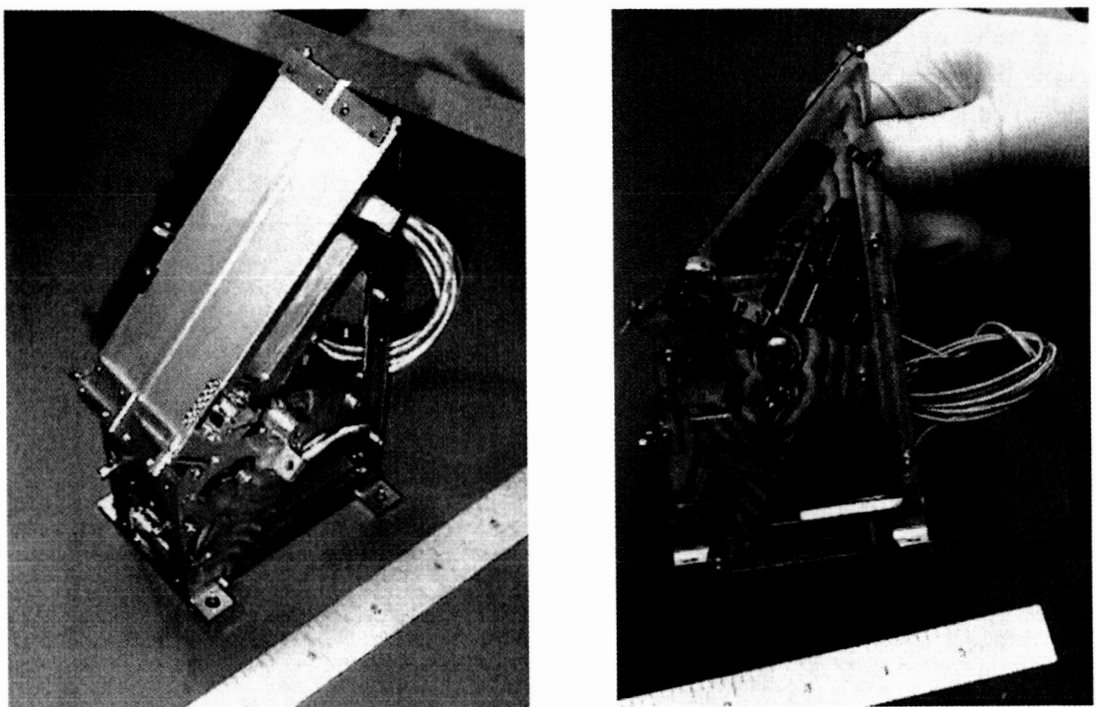

**Figure 3—Flight thermal analyzer module (doors closed)**
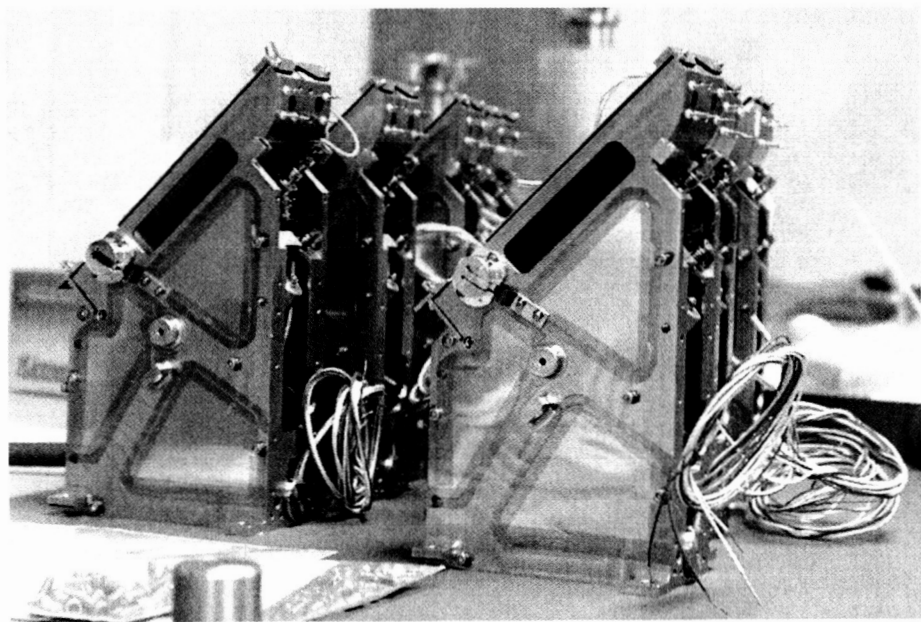
Figure 4—Assembled flight thermal analyzer modules ready for integration

In addition, a memory metal release inhibits the clutch from any advance until a release temperature is achieved. This feature was included to prevent the doors from inadvertently opening as the result of vibration experienced during the launch of the spacecraft. Each memory-metal release was individually tested in the fully assembled thermal analyzer module to guarantee that actuation would be inhibited at the lowest anticipated temperatures prior to launch. A nickel-titanium alloy (Nitinol) was used for fabrication of the memory metal component (Figure 5).
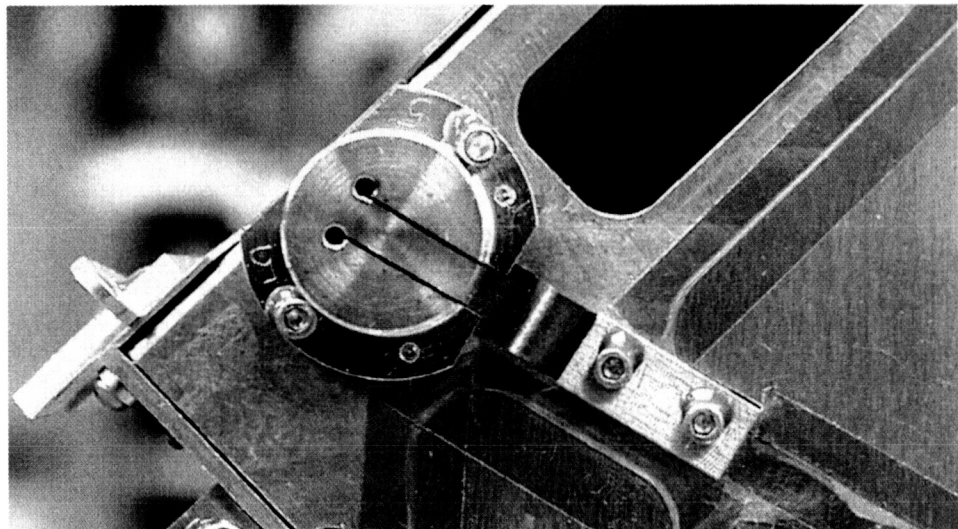
memory metal release mechanism
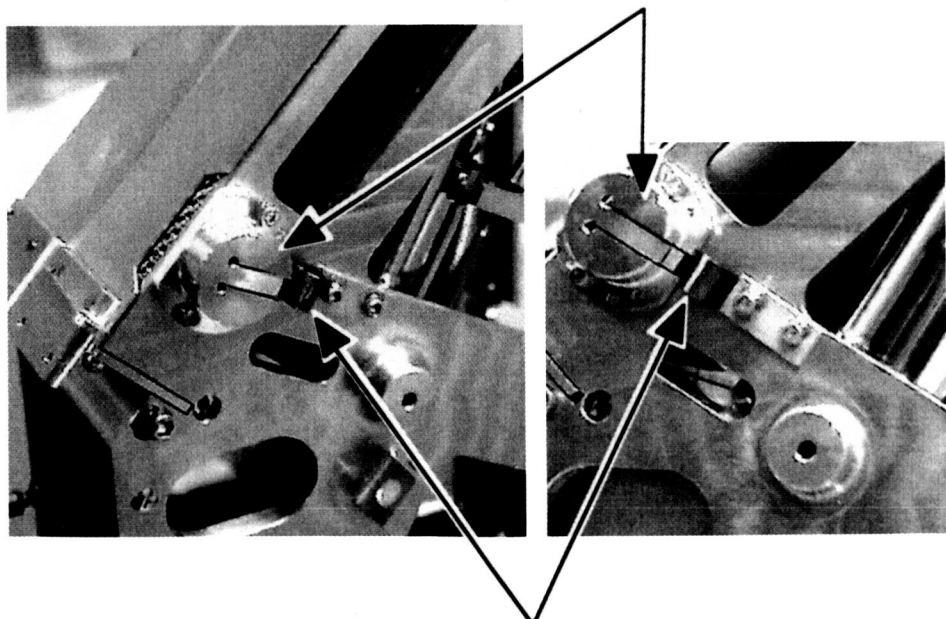
memory metal release

Figure 5—Memory metal release mechanism view from above (left), and below (right)

The soil processing system transports unprocessed soil delivered to the unit from the scoop of the MVACS robotic arm. Soil will fall under the influence of Mars gravity onto a slanted screen with a 1 mm grid. 1 mm fines falling through the grid enter a funneled path leading to a 2.5 mm loading port. Astride the port is a three-bladed miniature soil impeller mounted on a wire (Figure 6). The wire is driven by a solenoid that is excited at a ramped frequency causing the impeller to spin. As it spins, the impeller sweeps particles to the hole.

Soil impeller

Dams
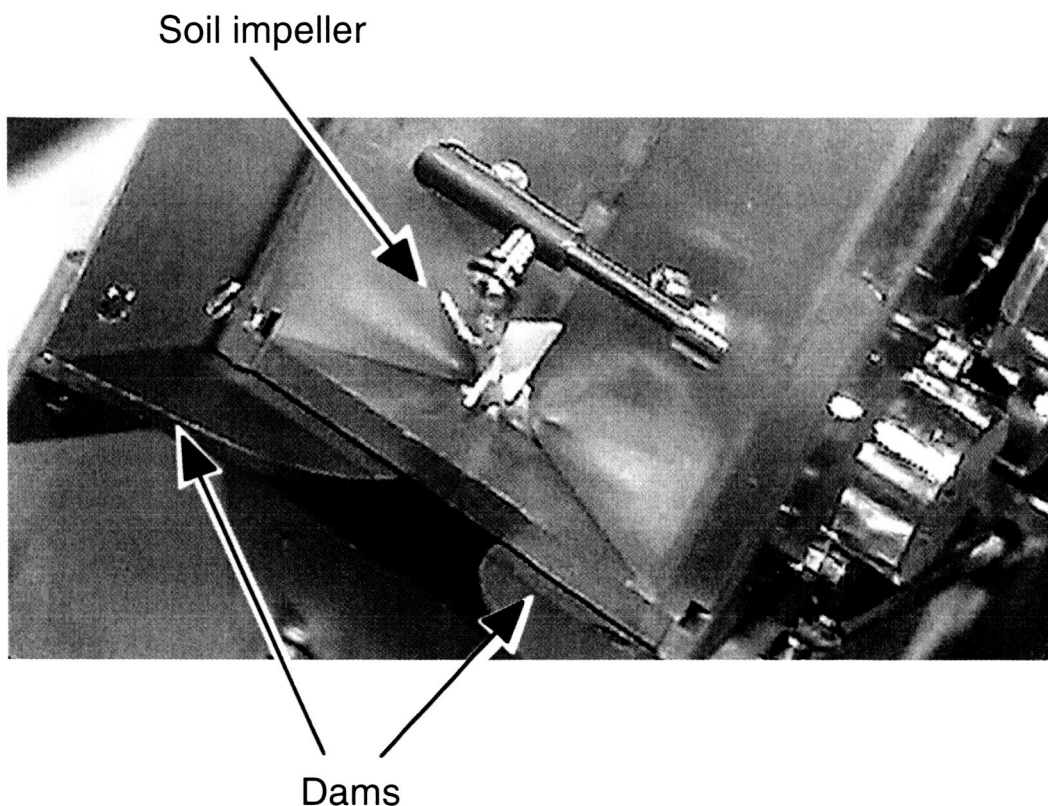
Figure 6—Soil impeller (doors open, screen removed)

The wire extends into the hole agitating particles and preventing bridging by the soil particles. The solenoid is mechanically coupled to the housing and the screen of the thermal analyzer so that the imparted vibrations shake particles through the screen, as well as those in the funnel area, and work them towards the hole. This simple concept has proven to be highly effective in transporting a large variety of Mars simulant soils from the screen into the oven. Testing was done using samples that ranged in water ice content from dry to about 50% ice by mass. The test samples for each of these soils were deposited into test thermal analyzer modules by prototype MVACS Robotic Arm scoops. The scoop has been designed to effectively collect soils ranging from loose dust to hard frozen aggregate. In all cases, the TEGA soil handling system was highly effective. A light-emitting diode and receiver pair are located across the throat of the soil loading hole. Particles falling through the hole are detected as they occlude

the light. When the oven is full, the light becomes completely blocked thereby giving a positive indication of a successful soil load. At the exit of the hole, the male half of the sample calorimeter oven is stationed.

The male half of the oven consists of a tapered nickel cylinder supported by a thin-walled stainless purge-gas inlet plumbing line. Nickel was chosen for its freedom from corrosion and its relatively high thermal conductivity. Thin-walled stainless tubing was selected to reduce the conductive heat loss to a minimum. The female counterpart is mounted to the housing at an angle to receive the male taper and includes heating and temperature sensing windings. The mating of the taper creates a reliable gas-tight seal even in the presence of particulates on the taper.

Heating and temperature sensing oven windings are 0.05 inch and 0.075-mm platinum wires solenoidally bi-filar wound about the female body. The temperature sensing wire is wound closest to the nickel oven body to reduce the gradient between the sample in the oven and the measured temperature. The temperature is determined from a measurement of the resistance of the platinum wire and reference to a platinum resistance temperature calibration. The heater wire is wound over the temperature sensing wire.

To prevent electrical contact between the nickel body and the temperature sensor wire, a thin (0.025-0.050 mm) layer of ultra-pure alumina is plasma coated onto the nickel prior to the winding of the wire (Figure 7). After this wire is wound onto the oven body, another ultra-pure alumina coating is applied to electrically isolate the temperature sensing and heater wire. A final coat of ultra-pure alumina is applied to the heater wire. The alumina affords good thermal contact between the heater wire and the nickel to transport effective heat transfer. The use of ultra-pure alumina is required to avoid ceramic electro-chemical activity at temperatures above 500° C that would otherwise interfere with the measurement of temperature. Application of alumina by the plasma coating permitted a highly controlled thickness of fully sintered ceramic to be bonded with sufficient mechanical strength to withstand the forces generated by the thermal expansion of the underlying nickel oven body.

The heater and temperature sensing windings are restrained at each end of the ovens by custom, press-mold, ultra-pure alumina end pieces. One of the end pieces supports the four electrical connections that must be made. The electrical connections must be able to sustain the launch loads and the highest temperatures the oven will achieve. This was accomplished by gold bonding the electrical connections to a platinum-iridium tube that offered sufficient strength and reduced thermal conductivity so that the temperature at the site of the gold bond was sufficiently lower than the oven. This is a critical connection because the 2-mil platinum heater wire must be in good thermal contact everywhere along its length to avoid developing a hot spot and melting in a fuse-like fashion. The connection is completed by gold bonding to thicker platinum pigtails. The other end piece offers a place to reverse the winding direction of the wire to complete the bi-filar solenoid thereby canceling the electrical inductance

178

that would otherwise be created. Careful reduction of all heat loss mechanisms was necessary to permit calorimetry to be possible with the limited power and energy available from the lander.


platinum sense wire   platinum heater wire
second ceramic coat
outer ceramic coat
first ceramic coat
threaded nickel oven body
turnaround end-piece
end-piece   platinum-iridium tubing
male oven half
.81 "
female oven half
.27 "
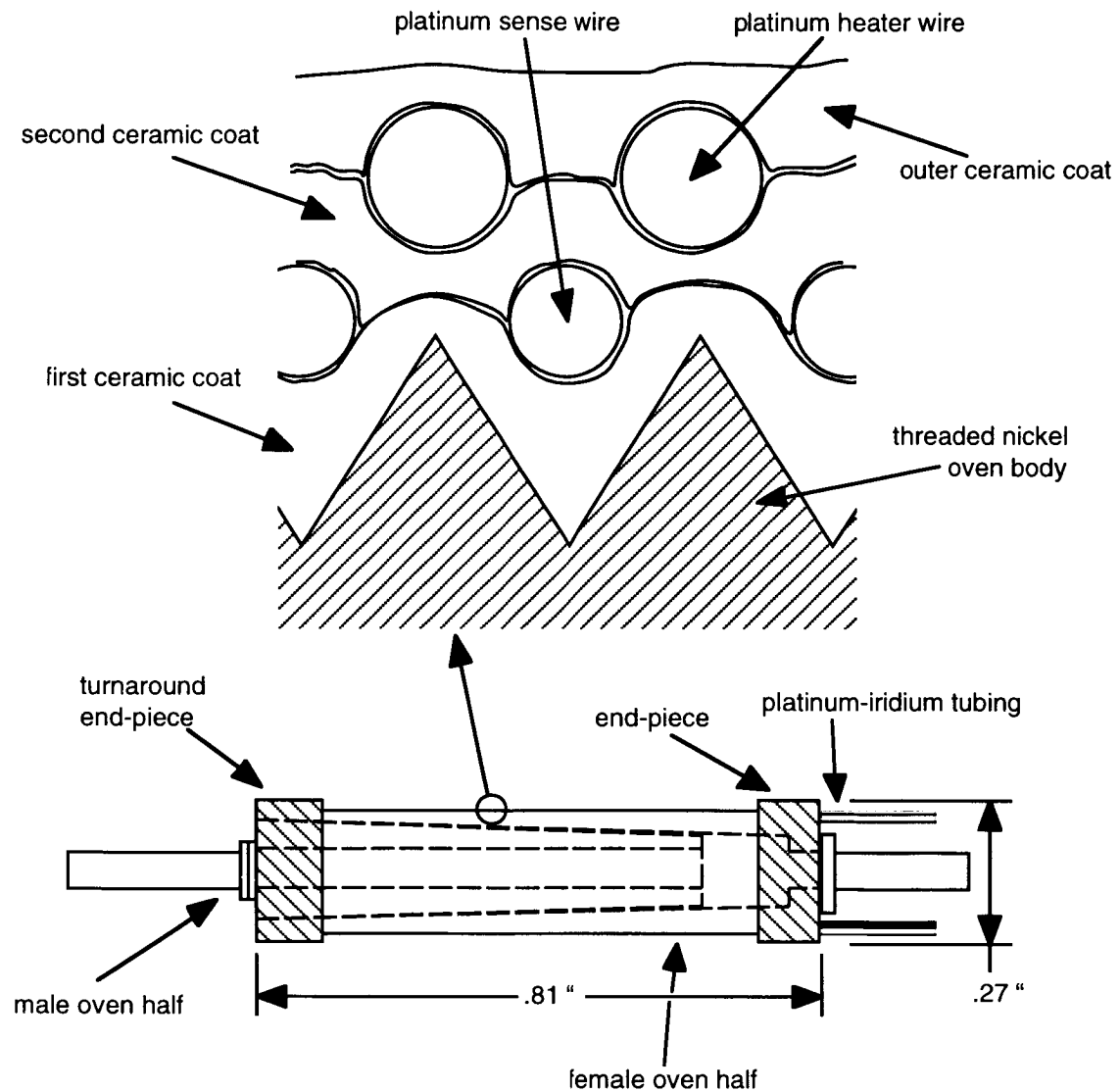
Figure 7—Oven coatings and windings

Two thermal radiation shields surround the ovens. One of these is a multiple layer nickel sheet wrapped around each oven. This also serves to almost eliminate the gas conduction of heat in the 6 mbar atmosphere of Mars because the interlayer distance is less than the mean free path of the atmospheric molecules. The second radiation shield surrounds both ovens and also includes a multiple layer nickel sheet (Figure 8).

179

inner radiation
shield material

female oven half

male oven half

outer radiation shield
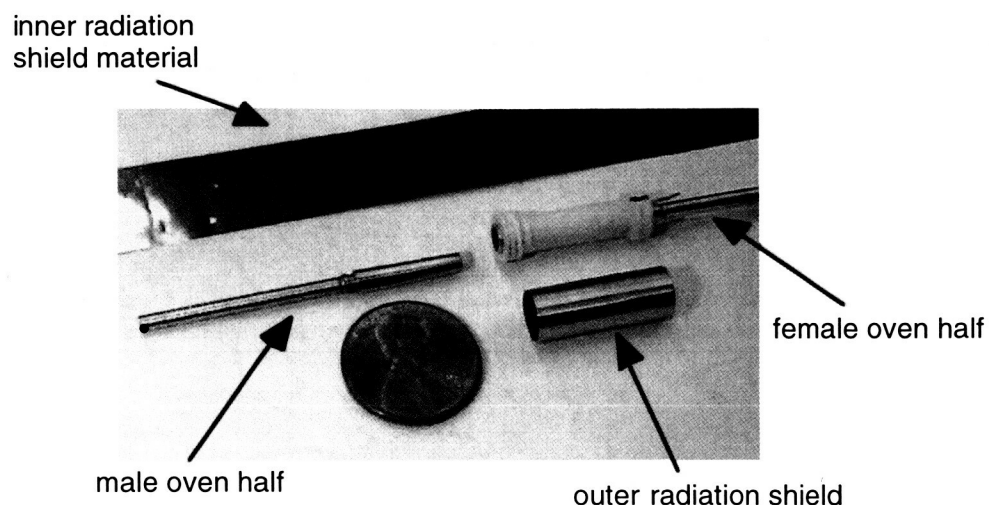
Figure 8—Oven components

The development and testing of the manufacturing process of the laboratory-quality ovens for TEGA was a singular challenge accomplished on a tight schedule concurrently with the other parts of the instrument.
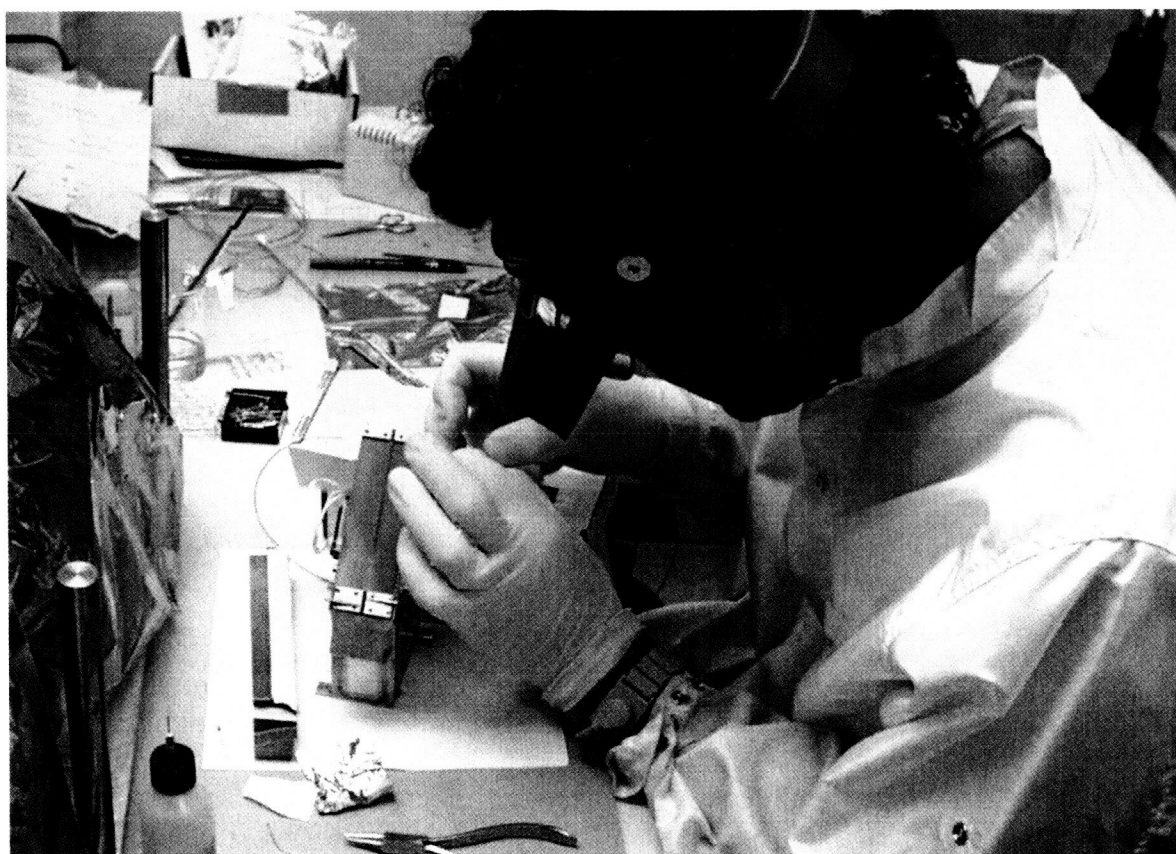

Figure 9—Thermal analyzer construction in the clean room

Each male oven pair is mounted on a Nickel 200 yoke attached to flexible bellows that receives purge or calibration gas from an inlet plumbing line. The bellows is restrained during the vibration of launch by a capture device that is released when the oven is closed. The yoke also supports the reference oven. The yoke is attached to the wall of the thermal analyzer housing by two bearings. One of these is free to rotate; the other moves in a milled arc (Figure 1). Under the influence of a drive rod from a wax motor the yoke is forced to rotate until the bearing in the arc reaches a linear track whereupon it is driven by a spring to mate the male and female oven halves. This action takes place with sufficient force to cause the male taper to form a gas-tight seal with its female counterpart. Oven mating is detected by the change in specific heat of the composite oven. Flashing is provided to protect the bearings from the intrusion of foreign materials such as dust from interfering with their function.

Once the sample is loaded and the ovens are closed, the calorimetry run may begin. TEGA performs differential scanning calorimetry. The DSC method is effected by forcing the sample and reference ovens to follow a pre-programmed temperature ramp. The TEGA microprocessor measures the temperature of the sample and reference ovens approximately 4,000 times every second. At each measurement, the microprocessor determines whether the oven is above or below a commanded temperature. If the oven is below temperature, the microprocessor increases the amount of power delivered to the oven in that cycle. If the oven is above the commanded temperature, the power is decreased. The commanded temperature follows a ramp with time. By determining difference, in power, between the reference and sample oven, the differential power is determined. The differential power is a sensitive measure of the specific heat and latent heat of the sample because the sample and reference ovens are essentially identical.

During a DSC run, a nitrogen purge gas flows through the sample and reference ovens. As the purge gas passes through the oven pair, the gases evolved from the samples are swept to the oxygen sensor and the water and carbon dioxide sensor and are then vented to Mars atmosphere. A calibration gas consisting of water vapor, carbon dioxide, and nitrogen is also provided to calibrate the gas sensors between DSC runs. A TEGA block diagram can been seen in Figure 10.

The TEGA gas handling system distributes purge gas to the cell under test and regulates the pressure in the system. Purge gas is transported in a stainless tank pressurized to 65 psia. It has sufficient capacity to handle all eight DSC runs with a margin of about 100%. Due to mass and volume constraints, elastimer-seat, normally-closed solenoid valves were selected and qualified for TEGA. During the 8-month cruise period to Mars, the leak integrity of the gas is maintained by a nickel foil that is punctured by a wax motor mechanism just prior to the first operation on the surface. The master valve is used to regulate the pressure of the tank even as pressure declines as the gas in the tank is consumed to about 20 mbar.
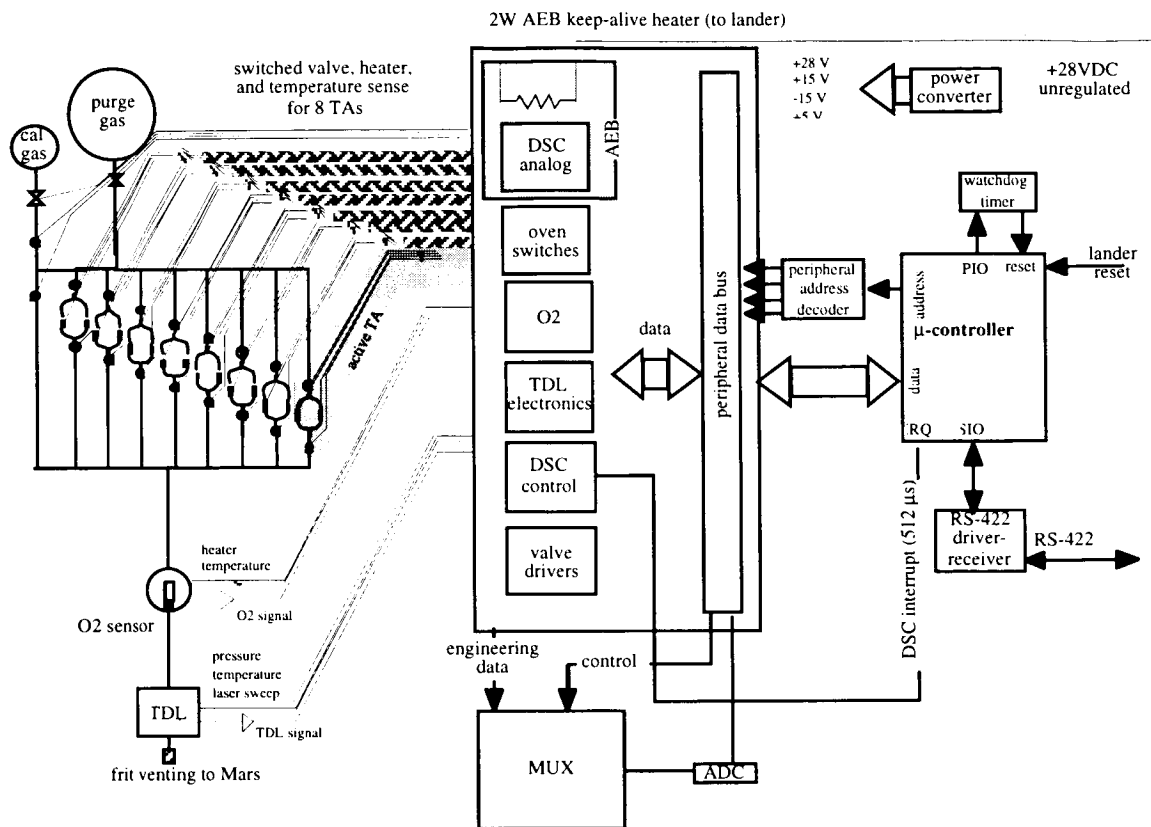
Figure 10—TEGA block diagram
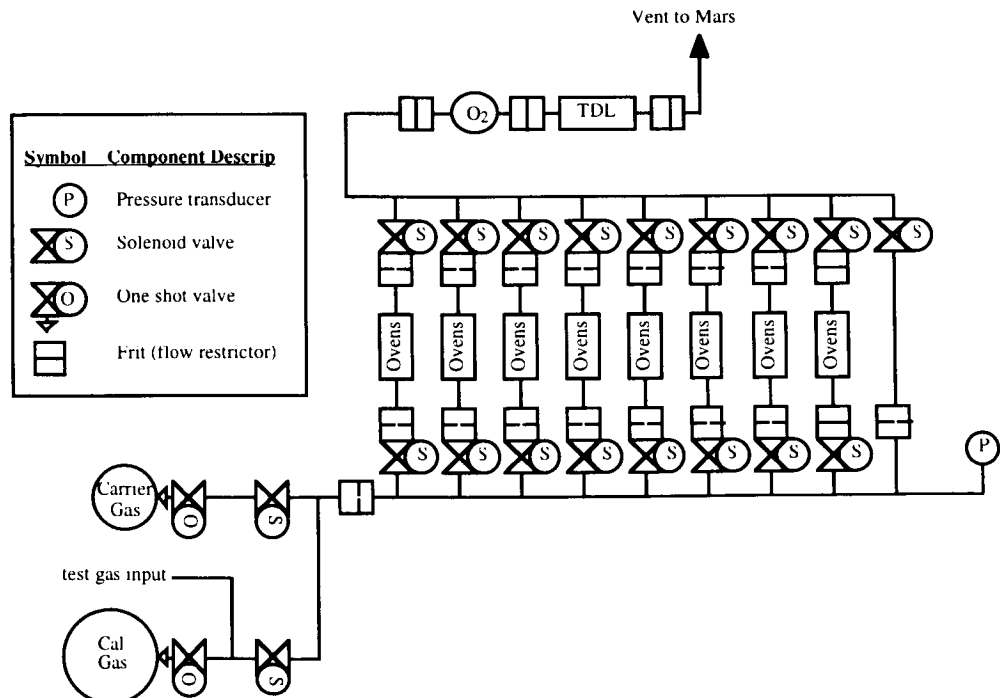
Figure 11—plumbing diagram

182

This is done by designing the gas system with appropriate flow restriction and chamber sizes so that opening and closing the master valve can effect adequate regulation with an acceptable pressure fluctuation. A similar arrangement is provided for the calibration gas including a by-pass valve and plumbing to flow gas directly to the gas sensors.

Severe constraints were imposed on the accommodation of the TEGA instrument on the lander deck that affected the design and assembly. Constraints on mass forced all components to be lightened as much as possible. Volume became the most severe constraint, however, and this had serious consequences during the assembly of the instrument.

baseplate with deck mounting holes   baseplate with TEGA instrument installed
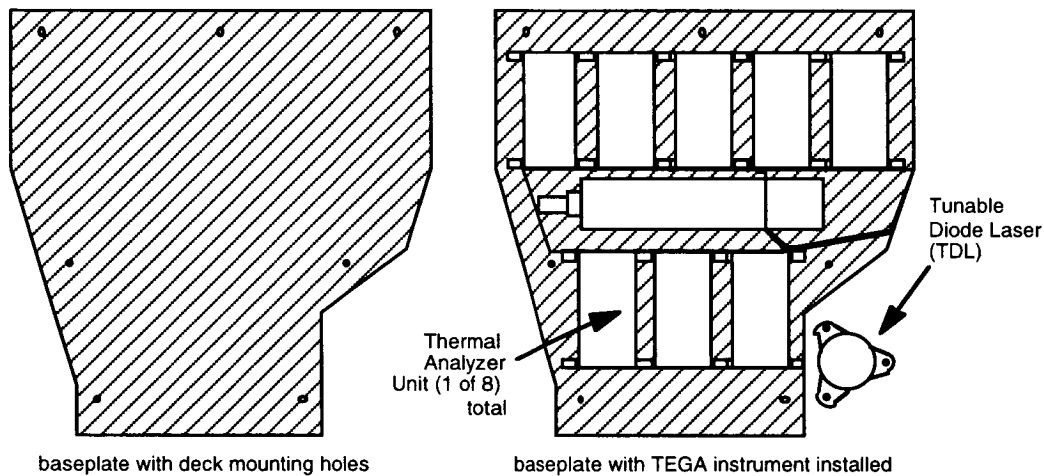
Figure 12—Carbon-epoxy aluminum honeycomb composite base plate

A titanium wedge (Figure 13) serves as a junction for the cable from the common payload electronics box, the eight thermal analyzer modules plus oxygen sensor, a small auxiliary electronics box housing noise-sensitive electronics, and the tunable diode laser. The connector junction area was forced to be reduced in size because of a potential interference with one of the aeroshell release struts. The reduction of the junction area created a challenging assembly problem that propagated through the entire instrument.

Acknowledgments

References

1. R.D. May, et al, Data Processing and Calibration for Tunable Diode Laser Harmonic Absorption Spectrometers, J. Quantitative Spectroscopy Radiative Transfer, 49, 4, pp 335-347, 1993
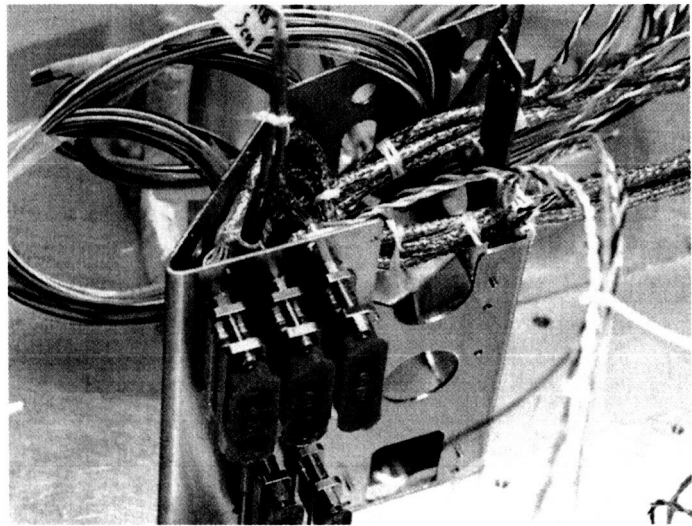
Figure 13—Titanium wedge junction
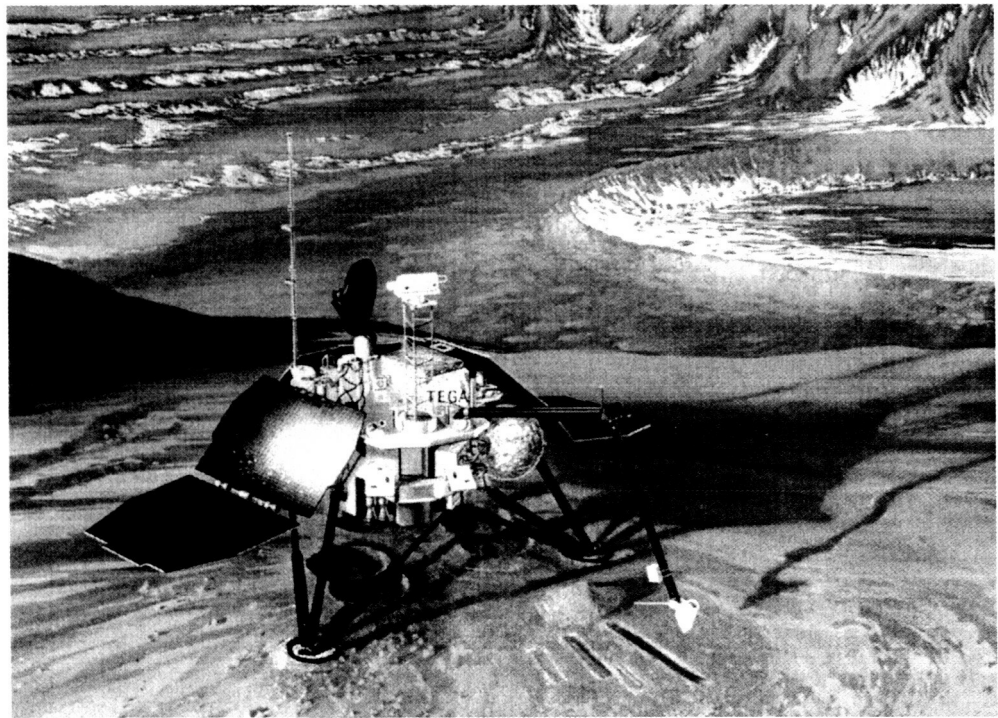
Figure 14—Lander with TEGA on the deck

184

"Long Life" DC brush motor for use on the Mars Surveyor Program

David Braun[*] and Don Noon[*]

Abstract

DC brush motors have several qualities which make them very attractive for space flight applications. Their mechanical commutation is simple and lightweight, requiring no external sensing and control in order to function properly. They are extremely efficient in converting electrical energy into mechanical energy. Efficiencies over 80% are not uncommon, resulting in high power throughput to weight ratios. However, the inherent unreliability and short life of sliding electrical contacts, especially in vacuum, have driven previous programs to utilize complex brushless DC or the less efficient stepper motors. The Mars Surveyor Program (MSP'98) and the Shuttle Radar Topography Mission (SRTM) have developed a reliable "long life" brush type DC motor for operation in low temperature, low pressure CO_2 and N_2, utilizing silver-graphite brushes. The original intent was to utilize this same motor for SRTM's space operation, but the results thus far have been unsatisfactory in vacuum. This paper describes the design, test, and results of this development.

Introduction

The Robotic Arm is part of the scientific and engineering payload for the Mars Surveyor Program (MSP'98) mission which will explore the South Pole of the Martian surface. It is a 2 meter long, semi-autonomous, 4 degree of freedom arm designed to dig in very hard soil of the seasonally receded CO_2 polar cap. The flight Robotic Arm is shown in Figure 1. The mission is scheduled for launch in January, 1999, and will land on Mars in December, 1999.

Environments

During assembly, test, and flight of the Robotic Arm, the motors are subjected to a number of environmental conditions:

1. Operate in ambient air, up to 55% relative humidity (clean room functional checks).
2. Operate in 8 Torr N_2 from -80°C to -10°C (system level testing).
3. Survive in vacuum (flight; cruise phase)
4. Operate in 8 Torr CO_2 from -80°C to -10°C (on Mars).

For SRTM, the main environmental challenge is to operate in a vacuum.

[*] Jet Propulsion Laboratory, Pasadena, CA

Background

The initial motor choice for the Robotic Arm was the Maxon RE016 motor which had been used successfully on the Mars Sojourner Rover. This 38-gram motor was an ironless core brush type DC with precious metal brushes, Neodymium-Boron-Iron magnets, oil-impregnated bronze bushings, and rotor-mounted capacitor for arc suppression and long brush life. Maxon specifies a minimum operating temperature of -20 ºC for this motor, which was not sufficient for the -80 ºC Mars Sojourner Rover environment. The main modification was to delete the grease normally applied to the commutator. At temperatures below -60 ºC, the grease could bond the delicate motor brushes to the commutator, resulting in a permanent failure due to bent motor brushes. A secondary problem was the loss of effectiveness for bushing oil below -40 ºC, resulting in increased wear and current draw which reduced bushing life. The wear was judged to be acceptable, so no modifications were made to the bushings. Since the ironless core rotor has no inherent detent torque, an external magnetic detent had to be added in order to hold position when unpowered.

The Sojourner Rover primary mission required 100 meters of travel on Mars, in addition to 100 meters of testing. That amount of travel equals approximately 1 million motor revolutions. The "extended" mission of up to 1 km on Mars would require a total of 5.4 million motor revolutions. Two motors were tested to 40 million revolutions (no-load, +20 ºC , low pressure air) without failure, and two complete actuators were tested under load and start-stop conditions to 30 - 40 million revolutions at failure. Part of the testing was conducted at -70 ºC in low pressure CO_2. Primary failure mode was conductive debris bridging the gaps in the commutator. These tests showed adequate life margin for the Sojourner mission.

Testing Maxon RE016 Motors for the Robotic Arm

Although the Maxon RE016 motors chosen for the Robotic Arm were nearly identical to the Sojourner motors, there were sufficient differences in the design and operating conditions which warranted further testing. The main difference was the requirement to operate the motors at their full rated 30 volts, as opposed to Sojourner's conservative 15.5 volts. In addition, SRTM was required to operated at 28 volts in a vacuum, as opposed to the 8 Torr CO_2 environment of Mars. Also, in the 2 years between the Sojourner and Robotic Arm programs, Maxon began offering ball bearings and a double-ended shaft on the RE016 motors. The ball bearings greatly improved performance below -40 ºC (when lubricated with Braycote 604 for low temperature operation), and the double-ended shaft simplified the incorporation of the magnetic detent and encoder.

<u>RE016 Test Results</u>
Twenty-nine Maxon RE016 motors were tested under various conditions of air, vacuum, low-pressure CO_2, low-pressure N_2, and several methods of commutator lubrication. All of the testing was done between -70 ºC and -80 ºC. The new testing

resulted in much lower life times (less than 10 million revolutions average) than was experienced in the earlier Sojourner Rover tests. Three separate failure modes were observed. The most common, which was also observed on the Sojourner tests, was rotor shorting due to conductive debris in the commutator slots. The second common failure mode was motor brush damage. The motor brushes and commutator would gall or micro-weld together, bending the delicate brushes out of contact with the commutator or breaking the brushes off entirely. The least observed (one or two times) failure was physical contact between the rotor and motor casing, resulting in an open circuit in the rotor winding. It is possible that operating the motors well outside of the limits specified by the manufacturer could have warped the rotor, or that these motors were built with slightly smaller (but within tolerance) clearances which were not enough for our temperature range.

Motor life versus life tests. The chart only shows how long the motors lasted until failure, but does not indicate what type of failures were observed. Of the 5 motors in vacuum with unlubricated commutators, 100% exhibited damaged motor brushes. Of the 10 motors in CO_2 with unlubricated commutators, 60% had damaged brushes. Of the 5 motors in vacuum with lubricated commutators, 20% had damaged brushes. And of the 10 motors in CO_2 with lubricated commutators, there were no damaged brushes.

Figure 3 shows motor life versus voltage. There is no clearly visible influence of voltage on motor life (with "life" given in terms of motor revolutions). Due to the large number of variables included in the testing, there is a large variation in the results which could easily mask any effects due to voltage. A factor of 2 or 3 difference could be hidden by the noise.

The Sojourner Rover Team, only a few weeks from launch, was somewhat alarmed by the new test results, but life looked adequate for at least completing the primary mission. With 6 wheels, the mission could even be accomplished if one motor failed. It was not practical at this late stage of the program to make any changes to Sojourners motors*.

Requirements Re-Examined
The life requirements for the Robotic Arm had been stated only in terms of the need to be able to dig a trench in Mars up to 0.5 m deep. This was converted into an equivalent life requirement in motor revolutions by looking at scoop volume and how many movements it would take to dig the required trench. The result was 10 million revolutions. The motor life should therefore be in the 30- to 100-million revolution range in order to have a comfortable margin. There was a definite mismatch between the required life and the test results. (In fairness to Maxon, it should be remembered

---

* The Sojourner Rover was still running with no indication of motor problems when the Lander communication link failed to transmit to Earth. Total travel on the surface of Mars was approximately 100 meters.

that this motor was designed for atmospheric operation above -20 ºC, and we were trying to make it run at -80 ºC in vacuum and 8 Torr CO_2).

Decision to Use a Larger Motor

Early in the RE016 testing program, when the first indications of a problem were becoming apparent, an effort was launched to identify alternative motor designs and suppliers. The Cassini program had developed and qualified a brush-type DC motor for the engine gimbal actuator, which operated in vacuum. Although the size and configuration of the motor was not directly applicable to the Robotic Arm or SRTM, the success with silver-graphite motor brushes (SG54-27 from Superior Carbon) running on a copper commutator was encouraging.

A slightly larger motor was desirable from several standpoints. The higher torque would allow us to use a smaller gear ratio, thus reducing the number of motor revolutions needed to accomplish the mission. Higher power could also be utilized, allowing the mission to be completed in less time (the lander had more power available than the RE016 motors could use). A larger motor would have more room internally for larger motor brushes, increasing potential life. The only technical drawback was the increased mass (initially, the Robotic Arm mass budget was too tight to baseline heavier motors).

<u>New Motor Options</u>
The MVACS project evaluated the reliability and lifetime issues for the Robotic Arm. In addition to the requirement for longer life, the motors on the Robotic Arm represented single point failures, where failure of any one of the motors would result in total loss of the arm's capability to complete its tasks. Because of these critical issues, 0.3 kg of project contingency mass was added to the Robotic Arm mass budget so that the larger motors could be accommodated. Gear ratios on the elbow and shoulder elevation actuators were reduced by a factor of 5 by simply shortening the gearcase and omitting one stage of the planetary gearbox.

After the approval for the change, the effort was then focused on the formidable task of getting the motors delivered on time. We had only 3-4 months until the new motors were needed. The American Technology Consortium (ATC) proposed a custom designed 100-gram motor using a conventional iron-core rotor which would also provide inherent magnetic detent torque. With ATC's good record of extremely rapid delivery on a Mars Pathfinder actuator, this became the new baseline approach. As a backup option, JPL purchased stock Maxon RE025 graphite brush motors (130 grams) with an ironless rotor, which would have to be retrofitted with SG54-27 brushes, re-lubricated bearings, and external magnetic detent assembly.

ATC Motor Development Lessons Learned and Good Design Practice

There were many lessons learned during the development of the ATC motors. For a schedule-critical program, such as the Robotic Arm, it is important to identify any long lead-time items which may need design iteration, and try to develop a selection of designs in parallel instead of in series. One example is ordering and processing several candidate brush materials concurrently. Another example is the rotor core design, which is critical in obtaining the desired magnetic detent torque. The original design did not have enough detent, and several weeks could have been saved by fabricating two or three core designs simultaneously, and selecting the one that best met the requirements.

Late in the program, we experienced an open circuit motor failure. Disassembly and inspection of the motor revealed a manufacturing defect. A service loop between the rotor windings and the commutator had inadvertently been potted tautly against the windings; subsequent thermal expansions and vibrations had eventually broken the wire. To assure that this situation did not cause a flight failure, the flight mechanisms (which had passed acceptance tests at the time) had to be disassembled for inspection. Significant time and effort could have been saved if we had carefully inspected all rotors before assembly.

Unlike precious metal brushes, graphite brushes generate significant quantities of conductive debris, and the motors must be designed to accommodate it. Electrically conductive surfaces internal to the motor should be conformal coated wherever possible to minimize the possibility of shorting or grounding, and space should be provided within the endbell for the debris to accumulate safely.

Predictions of motor brush wear rate are not very accurate, and it is best to provide as much motor brush length as possible. A cantilevered leaf spring design was used for the MVACS motor. While this provided adequate life, a cartridge-type brush design would improve motor life significantly.

Testing the ATC Motors

Screening Tests

All motors were put through a screening test to check for early failures or defects. After two cycles between +80°C and -125°C (non-operating), the motors were run at various speeds at +80°C and -90°C. Motor current was charted whenever the motors were operated.

A variety of other tests were conducted to characterize the motors and provide data for selecting the best ones for flight. Magnetic detent torque and no-load speed were measured, minimum running voltage was tested, and friction torque was estimated from the measurements. Many of these measurements were made by both ATC and JPL. After the flight and spare motors were selected, dynamometer tests were

conducted at JPL (also a duplicate of the ATC testing). Plots of current versus torque and speed versus torque for motor S/N 0039 (used for the flight shoulder elevation actuator) are given in Figures 4 and 5, respectively.

Life Testing
No-load tests of both the ATC and modified Maxon motors in air and 8 Torr CO_2 showed excellent life and reliability, in excess of 100 million revolutions with no failure. Extrapolating from the measured brush wear, it is estimated that the motors would last 300 to 500 million revolutions under no-load conditions. Complete mechanisms with ATC motors were cycled under high load in -70 ºC, 8 Torr CO_2, resulting in lifetimes of 102 million, 62 million revolutions in ambient air, and 36 million revolutions at -70°C in 8 Torr nitrogen before the motor brushes wore out. There were some differences in the loading conditions of the tests, but they do not appear to be large enough to account for the factor of 3 difference between the CO_2 and nitrogen lifetimes. Although we tentatively attribute the life difference to the gas, we cannot come to any solid conclusions on the basis of only one test.

Vacuum test results (for SRTM) were far less satisfactory. Only no-load tests were conducted at JPL. Results are generally described by several minutes to hours of smooth operation, followed by a sudden transition to high and variable current draw and motor brush wear-out after as little as 3 million revolutions. An alternative motor brush material (Superior Carbon SG59) appeared to perform somewhat better, with over 5 million revolutions of smooth operation before the high current phase, and wear-out in the 20-million revolution range. Interestingly, 3 completely stock RE025 motors with lubricated precious metal brushes were run for 21 million revolutions in vacuum at +20 ºC without any problems.

Summary and Discussion

The fundamental limitation of lifetime for brush-type DC motors is due to wear and lubrication at the brush/commutator interface. The materials for brushes, commutators and lubrication must be electrically conductive and be compatible with its intended environment (temperature and atmosphere).

Precious metal brushes require a wet lubricant to function properly. The usual lubricants developed for sliding electrical contacts cannot function below -60 ºC and have high outgassing rates in vacuum. Without wet lubrication, lifetime is severely reduced, but adequate, for the Sojourner Rover program. The presence of even a small amount of atmosphere was found to be extremely important to avoid immediate catastrophic failure of unlubricated precious metal brushes. It is possible that lubricants could be found or developed for precious metal brushes that would be compatible with low temperature and vacuum applications.

"Graphite" brushes are a sintered mixture of a conductive medium (copper or silver) and lubricating materials, such as graphite, molybdenum disulfide, and a number of

190

other proprietary compounds. One major advantage of this material is that it does not require a wet lubricant, and therefore can operate very cold. Conventional wisdom states that graphite needs moisture in order to function as a lubricant. Our testing showed that 8 Torr of dry CO_2 allowed the motor brushes to perform about as well as in moist air and one or two orders of magnitude better than in vacuum. These results are good news for Mars missions, such as MVACS, but not so good for SRTM which must operate in a vacuum. SRTM decided that the best solution for their program is to seal the actuators in an atmospheric environment.

Several other motor contact materials and processes are available. Unfortunately, our testing program could not be comprehensive due to schedule and cost pressures. Claims have been made for wear rates of one material in vacuum that are two or three orders of magnitude better than the test results at JPL. JPL plans to continue testing of this material and others in the next few months to determine the best material for Mars and space missions.

Figure 1. 1998 Mars Surveyor Program Robotic Arm.
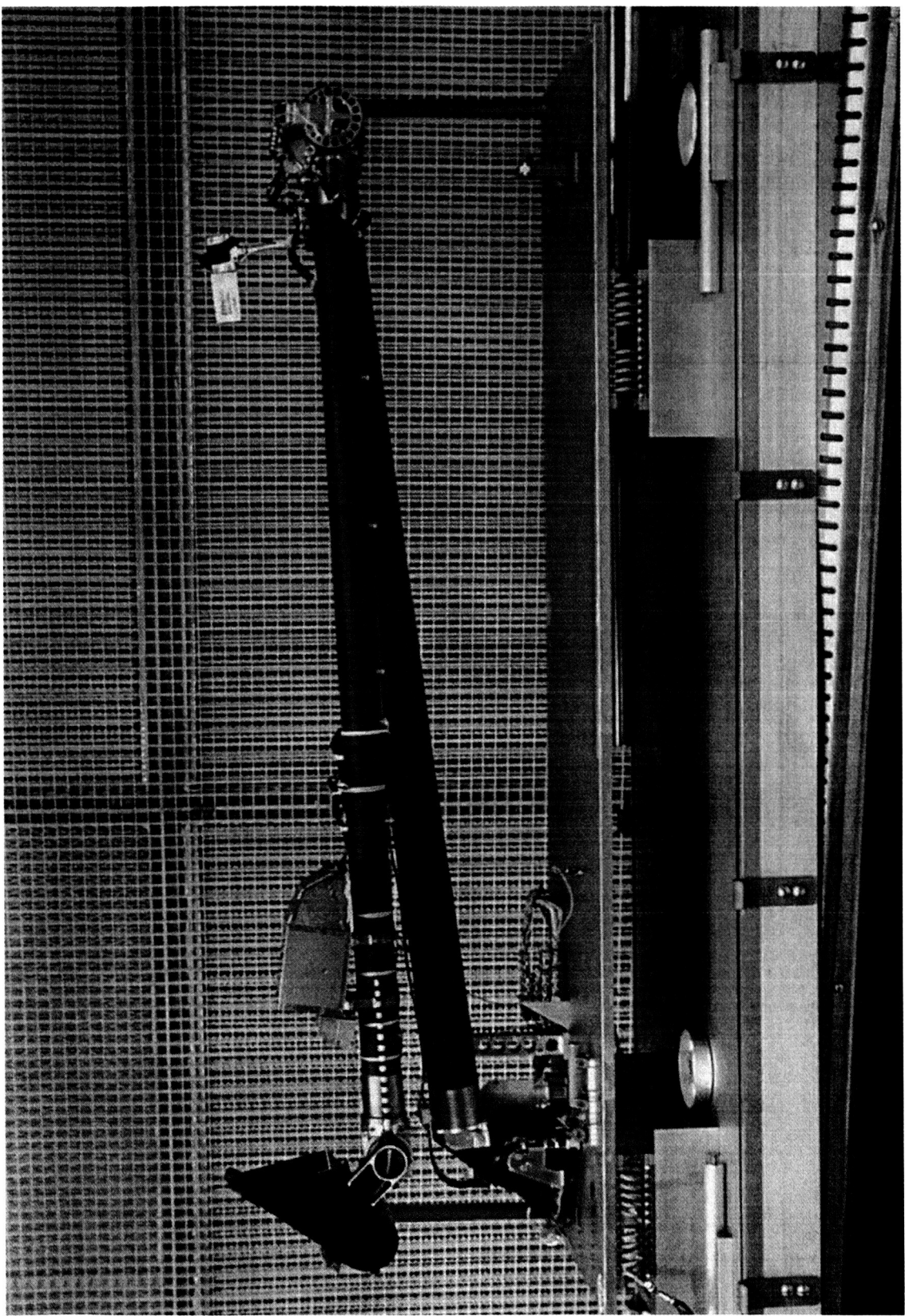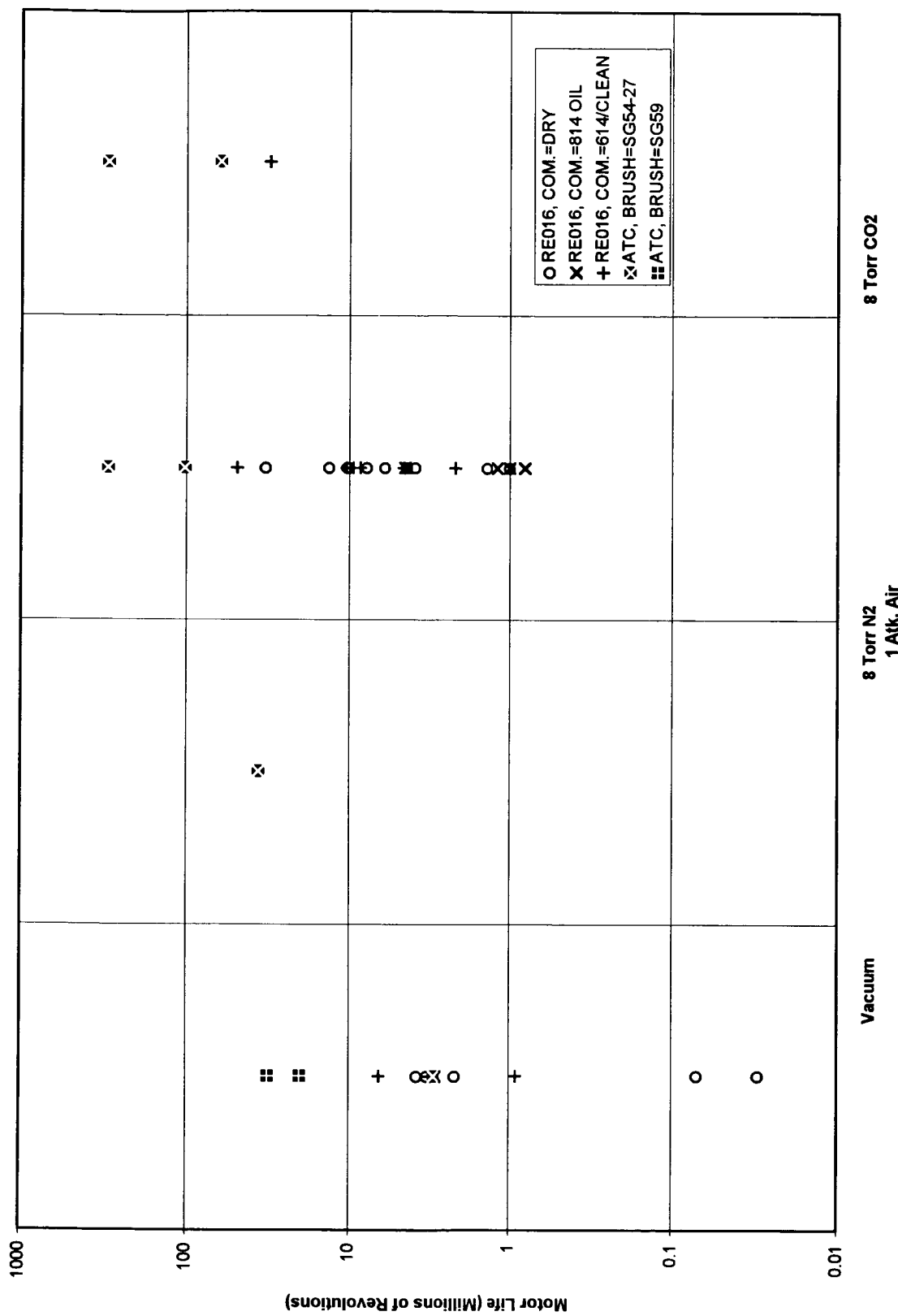
Figure 2. Motor Life vs. Atmosphere

193

Figure 3. Maxon RE016 Motor Life vs. Voltage

194

Figure 4. ATC Motor S/N 0039 Current vs. Torque @ 28 Volts

195

Figure 5. ATC Motor S/N 0039 Speed vs. Torque @ 28 Volts

Liquid Hydrogen Testing of Silicon Nitride Bearings for Use in High Speed Turbomachinery

Chip Moore*, Howard Gibson* and Dr. Robert Thom*

Abstract

Hybrid ceramic rolling element bearings are being tested in liquid hydrogen at Marshall Space Flight Center. The testing will evaluate their long term durability for use at high speeds in cryogenic rocket engine turbomachinery. The use of hybrid ceramic bearings in liquid hydrogen follows successful development and flight in liquid oxygen turbopumps.

Introduction

Hybrid ceramic rolling element bearings promise significant benefits for use in high speed, rocket engine turbomachinery. The primary benefits of ceramic rolling elements over steel include increased rotor dynamic stiffness and lower centrifugal loads due to less mass. Silicon nitride is the best suited ceramic for rolling element bearing applications and is presently flying on the newer liquid oxygen, high pressure oxidizer turbopumps of the Space Shuttle Main Engine (SSME) [1]. Similar hybrid ceramic bearings will also be used in the new liquid hydrogen, high pressure fuel turbopumps [2]. For the liquid oxygen pumps, extensive ground testing of the bearings was conducted in test rigs. This was followed by use in pumps on ground test engines then use on flight engines. Based on the success in the liquid oxygen pumps, no preliminary bearing rig tests were planned for the new fuel pump bearings prior to insertion into pumps on ground test engines. During these hot-fire engine tests, unique surface anomalies were observed on the silicon nitride rolling elements. The surface anomalies resembled fine, hairline cracks which were dubbed "river marks" (Figure 1). These river marks raised initial fracture concerns. In response, a rigorous ground test program was implemented at Marshall Space Flight Center to investigate the effect of these river marks. This testing continues a history of leading edge, high speed, cryogenic tests of rolling element bearings, including hybrid ceramics, for rocket engine applications [3,4].

Summary

Two hybrid ceramic ball bearings were rig tested in liquid hydrogen for the equivalent of sixty mission cycles (flights) of an SSME fuel pump. This is about six times the service life of a fuel pump and three times the certification life. Prior to the rig tests, one of the bearings had developed extensive river marks on its balls during use in a development fuel pump. The other bearing had no river marks on its balls prior to this particular test series. These balls did develop river marks during the course of the

---

* NASA Marshall Space Flight Center, Huntsville, AL

testing. Thus, the rig testing demonstrated two important points: 1) that the rig could produce the river mark phenomenon; and 2) that the river marks had no significant impact on life or performance of the bearing in long term use for this application.

Experimental Procedure

<u>The Bearings</u>
The bearings (Figure 2) used in this rig are the same bearings as used in development and certification fuel pumps. In fact, most bearings have had some previous use in a development pump, thus are very high fidelity specimens. The sixty-millimeter bore, angular-contact ball bearings are designed for high speed operation in excess of two million DN (bore diameter, D, in millimeters times shaft speed, N, in revolutions per minute). The rings are of Cronidur 30, a relatively new nitrogen alloyed, stainless bearing steel [5]. The cage is of a wound fiberglass cloth structure impregnated with polytetrafluoroethylene (PTFE). The cage also incorporates pocket inserts of bronze/PTFE composite and is outer race piloted. The eleven balls are hot isostatic pressed, silicon nitride with a 20.59 mm nominal diameter.

For the series of tests covered by this report, the bearings had a previous test history. For identification purposes, the bearings were identified as the "reaction" bearing and the "load" bearing, referring to their position relative to the applied radial load. The reaction bearing had previously run in a development pump on a ground test engine for 3 starts and 1594 seconds. During its last engine test, an incident occurred in the turbine section of the pump where some turbine blade tips were broken. The resulting rotor dynamic imbalance caused radial loads that exceeded the design load of the bearing. At the subsequent disassembly inspection, all of the balls had extensive river marking. It is not known if river marks were caused or exacerbated by the turbine imbalance. Wear of the raceways, balls (apart form the river marks), and cage was negligible. Thus the reaction bearing was an excellent specimen for endurance testing of a bearing with river marked balls.

The load bearing ran in a separate development pump for 5 starts and 932 seconds without any significant events. The load bearing had also previously run time in the test rig for 7 starts and 2,441 seconds during proof tests. This bearing had no visually discernible river marks at 30x magnification. Thus, the load bearing was an excellent example to see if river marks would form on balls in the rig.

<u>The Tester</u>
The liquid hydrogen bearing rig (Figure 3) is a modified fluid film bearing test rig. Using liquid hydrogen, the rig is located on a test stand in a hazardous test area. The rig can accommodate two rolling element bearings mounted on a common shaft in either ball-ball or ball-roller bearing configurations. Radial load can be applied directly to the central (load) bearing. This radial load is then reacted by the upper ball (reaction) bearing and the lower hydrostatic bearing. Axial pre-load is applied by a beam spring on top of the reaction bearing outer race. The axial load can be

198

controlled during test by varying internal operating pressures. Liquid hydrogen is the coolant and flows through the rolling element bearings in series from top to bottom. Liquid hydrogen is also the working fluid for the hydrostatic bearing, though from a separate feed than the bearings. The shaft is turned by a gaseous nitrogen impinging on a terry turbine machined into the bottom of the shaft. A helium buffer seal prevents leakage of the hydrogen from the hydrostatic bearing into the turbine section.

Test Series Objectives

The main objectives of the test series were to determine 1) if the rig would produce river marks on previously unmarked bearing balls and 2) what affect river marks would have on life or performance of a bearing.

To achieve those objectives, the bearings were tested for the equivalent design life of a fuel pump. The primary parameters to measure this goal were total run time, high speed run time, and transient axial loads. A fuel pump is designed for sixty missions, however it is planned to only fly them for about ten missions with certification units ground tested for about twenty missions. During a typical 520 second flight profile, the engines will throttle to various power levels, spending about 420 seconds at 100% rated power level (RPL) or above. Since the engines may be required to operate at up to 109% RPL, the corresponding shaft speed of 35,000 rpm, was chosen for the high speed endurance portion of the tests. During the engine start up and shut down, the bearings in the fuel pump react a significant transient axial load, up to 22,200 N, before a balance piston can compensate. Thus, 120 high, transient axial loads would be applied to the bearings during the tests. This sixty mission goal translated into 31,200 seconds of total run time; 25,600 seconds at 35,000 rpm; and 120 transient axial load cycles of 22,200 N.

Test Profiles

To keep control of the tester simple, duplication of the actual flight power level profile was not attempted. Rather a simplified profile was chosen: ramp up to 20,000 rpm; apply nominal radial load of 780 N; apply a brief series of 22,200 N transient axial loads; then ramp up to 35,000 rpm and run until depletion of hydrogen. Total rotation time for a nominal test was from 900 to 1100 seconds. Nominal steady state conditions during test included: 0.25 kg/sec of liquid hydrogen coolant flow through the bearings; 8.1 MPa bearing cavity pressure; and 3560 N axial preload.

A vast array of instrumentation was connected to the test rig for performance monitoring, recording, and control. Of primary concern were the bearing cavity pressure, differential axial pressures, axial preload spring strain gages, coolant inlet and outlet temperatures, turbine inlet pressure and shaft speed. This performance data was reviewed after every test to ensure proper rig control and that the bearings were operated within the test objectives.

<u>Bearing Metrology</u>
Several high precision bearing dimensional and surface texture measurements were made before and after a series of tests to quantify any consequences of extended operation. Such measurements included diameter, roundness, surface texture, and cross race curvature, and cage wear. Stylus profilometry was used to statistically characterize width and depth of the river marks on the silicon nitride balls.

Results

From October 1996 to March 1997, a total of 31,207 seconds of total run time was accumulated on the two bearings. Of that time 26,407 seconds were at 35,000 rpm, which again represents approximately 109% RPL of a flight engine. There were also 120 transient axial load cycles of 22,200 N applied to the load bearing during the later half of the test series. Keep in mind that these bearings previously accumulated run time in development pumps and previous rig tests. Table 1 shows a summary of their starts and total run time.

<u>Bearing Metrology: Ball Diameter</u>
To assess overall wear of the balls, their diameters were measured before and after test with a device similar to those used to measure gage blocks. The device was a comparator type measuring instrument using opposing anvils and a reed spring gauging transducer. A master ball was placed between the anvils and the instrument zeroed on the master. Subsequent measurement of test balls were then compared to this zero. With care, repeatability in the 0.050 μm range was possible. While diameter variation was measured for each ball, for brevity, this paper reports the set diameter variation and the set mean diameter for each bearing ball set at each time interval. These definitions are similar to Anti-Friction Bearing Manufacturer Association (AFBMA) definitions for lot diameter variation and lot mean diameter [6].

The set diameter variation is the difference between the mean diameter of the largest ball and that of the smallest ball in each bearing. Table 2 lists the set diameter variation for each measurement interval. Note that the maximum allowable for these bearings when new is 0.5 μm and this value was not exceeded by either bearing at either measurement interval.

Next an estimate of ball wear within a bearing was made considering the set mean diameters. The set mean diameter being defined as the arithmetic mean of the mean diameter of the largest ball and that of the smallest ball in the bearing set. Figure 4 shows the change in the set mean diameters from the beginning of the test series. The vertical axis is normalized to show zero wear at the start of the rig test series covered in this report. While the intermediate data points are within the repeatability error range of the instrument, the end data point is not and thus has a greater degree of credibility. A 0.16 micrometer amount of wear for each bearing ball set is still less than one tenth of their design tolerance. Thus, ball wear was considered insignificant.

Ball Weights

Only after testing was a sensitive balance scale found that might be able to indicate ball wear as a function of mass loss. For a new 20.587 mm diameter ball of 3.243 gm/cm^3 density silicon nitride, a uniform wear of 0.5 μm would result in a mass loss of approximately 1 mg. Considering the diametric wear stated previously of about 0.16 μm, a measurable mass loss of about 0.3 mg would be expected. Future tests will include precision weighing of the balls before and after test.

Ball Roundness

A high precision roundness machine was used to make three orthogonal roundness traces of each ball. The values of out of roundness were skewed however by the river marks. These would appear as deep valleys on the traces, with the remainder of the trace being similar to an unused ball. Thus, out of roundness was not a particularly useful measurement for these tests. Depth information on the river marks from the roundness traces was not useful as the stylus tip radius was much too large to accurately follow the cross section of the river mark. A separate effort, discussed next, was made to determine the width and depth of the river marks. Though not the same as equatorial roundness traces, the previous diameter measurements still give some insight to the roundness of the balls.

River Mark Width and Depth

A stylus profilometer was used to measure the width and depth of the river marks at somewhat random locations. The profilometer was equipped with a diamond tipped stylus of 2 μm radius. Using laser interferometry, the profilometer could resolve 0.01 μm vertical surface features over a vertical range of 6 mm. The horizontal sampling interval was 0.25 μm. While the physical size of the stylus, its traverse speed, and sampling intervals will cause some distortion when tracing across a river mark, it was the best method available to assess their physical dimensions. Non contact, surface area profiling machines using laser scanning or white light interferometry are being investigated for three dimensional characterization of the river marks. Trial measurements have been made on candidate three dimensional topographic systems which corroborate the two dimensional stylus measurements. Such a system is planned to be procured for future tests.

To assess any change in the river marks, the following strategy was adopted. Each ball had ten traces made across its river marks at various locations. While it was virtually impossible to place the stylus at the same locations before and after tests, the effort was made to trace the larger areas of the river marks. The traces were distributed evenly among the main channels on a ball. That is if a ball had two main river mark channels, five traces would be made on each one. If a tributary appeared similar in size to a main channel, it too would be traced. Simple statistics were used to assess growth.

Traces were made for the reaction bearing before, midway through, and at the end of testing. Traces were made of the load bearing balls midway through and at the end. Recall that the load bearing balls did not have river marks prior to testing. The average and maximum values for width and depth were calculated for all traces of a bearing ball set at each interval. Figures 5 and 6 show the statistical results of the cross sectional traces. Values for the reaction bearing happen to lie above the load bearing on all curves. This is not particularly relevant as the variation is small, though river marks had existed longer on the reaction bearing.

In Figure 5, the average width of the main channel of the river marks appeared to be stable at about 0.140 mm. The main channels seem to form at a nominal width and depth and did not appear to increase significantly after formation. The number of the finer tributaries increased with time. A few maximum widths were observed in the 0.5 to 1.0 millimeter range. Note that the chart may suggest that the maximum dimensions of the river marks decreased during the end of testing. This is not so. This merely indicates that the maximum dimension traced at the end of testing was less than the maximum dimension traced at the midway point. The traces were also not at the exact same point. The maximum values charted are a single value of 110 traces and represent a magnitude, not the actual change in dimension of one specific river mark. The average values more accurately reflect the trend as each point is a summary statistic for 110 traces.

In Figure 6, the average depths of the main channels also seemed stable and were about 0.004 to 0.005 mm deep. While a wide stylus tip can span a narrow crevasse, thus missing the maximum depths, these river marks are wide (0.140 mm average) with respect to the stylus tip (0.002 mm radius). Thus the depths do not appear to be significantly clipped. Optical microscopy also did not reveal any narrower crevasses in the bottom of the river marks. A few maximum depths were found to be in the 0.014 to 0.027 mm range. These are 0.07% to 0.13% of the ball diameter.

A low aspect ratio (width/depth) would suggest a sharper profile and might be of more concern as a crack initiation site. Aspect ratios followed a similar trend averaging 24 to 30 times wider than deep. The lowest aspect ratios measured were 4 to 5 times wider than deep. Sample images from optical interferometry area profiling instruments revealed that while the marks are much wider than deep, they can still have steep walls. This shape was also seen in several stylus traces, but was difficult to summarize statistically.

Cage Imbalance
The cages are outer race piloted, i.e. they contact the outer race rather than inner race during operation. This can be beneficial for minor cases of cage imbalance. That is, if the cage has an imbalance, it will tend to rub against the outer race in the vicinity of the imbalance. Wearing away of material in that region then will reduce the imbalance. The static imbalance of the load bearing cage was reported to be 50% greater than the design limit at the time. The effect of the imbalance was visually evident on the outer

diameter of the cage where it would touch down on the outer ring land. The touch down rub patterns were concentrated to one portion of the outer diameter, covering six of the ball pockets. The touch down marks appeared to be more of a burnishing or compressing of the fiber matrix rather than material loss. A future build of the test rig will include a cage with additional static imbalance.

Cage Pocket Wear

In high speed bearings, rubbing of the ball against the cage pocket is a significant source of friction due to the pure sliding motion. The bronze/PTFE inserts are intended to reduce this sliding friction and provide transfer film lubrication to the balls and races. The inside of the bronze/PTFE cage pocket inserts were traced with the stylus profilometer to measure wear due to ball rub. Traces were made to measure fore and aft wear, and lateral wear upstream and downstream of the coolant flow. Figures 7 and 8 show the wear was greater in the fore direction for all pockets in each bearing. This indicates good stability as all the balls are driving the cage. The wear was slightly more overall for the reaction bearing cage. Also the location of heaviest wear in the reaction bearing cage pockets was closer to the centerline than in the load bearing. The heaviest wear for the load bearing cage pockets was slightly on the upstream side.

The wear was also measured in the axial position of the cage pockets (Figures 9 and 10). The magnitude, as expected, was less than in the fore and aft sides. Typically, the force of the coolant flow through the bearing will push the cage against the balls and cause more wear to occur on the upstream side as seen in Figure 10 for the load bearing. However, when the flow enters the bearing on the same side as the load is applied to the outer ring, the motion of the balls and outer ring piloting design leads to pumping of the coolant. This pumping of the coolant then "pulls" the cage in the direction against the flow. Thus, slightly more wear was experienced on the downstream side of the reaction bearing cage (Figure 9).

Cross Race Wear

Stylus profilometry was used to measure wear of the races. Cross race traces were made on each ring in three places, 120 degrees apart around the circumference. Maximum depth values were averaged from the three traces and are presented in Table 3. Due to time constraints, these traces were made only at the conclusion of the tests. With the slight amount of wear detected, loss of the mid time data point is a minor concern.

The bearings are angular contact and thus have load paths on opposite axial sides of the races for the inner and outer raceways. In the rig, the bearings are loaded in the opposite axial direction than when installed in development and flight pumps. The races are axially symmetric, so this load inversion is not a concern regarding race to ball contact. Since these bearings were previously run in development fuel pumps, this inversion provides a new surface for the inner race when used in the rig. However, for the outer race there is some load path overlap.

As seen in Table 3, the wear depth was greater in the outer raceway for each bearing. Although accurate determination of the width of the wear track is more difficult for the outer raceway due to the overlap from pump operation, its wear depth can clearly be measured from the rig side of operation. The 0.3 to 0.9 μm values can easily be discerned with the 0.010 μm resolution of the stylus profilometer. This is a very small amount of wear for these bearings, especially considering the testing represents approximately six times the expected service life.

<u>Raceway Brinell Marks</u>
In a previous test series, the outer race of the load bearing had been inadvertently brinelled, or dented by the balls due to a high static axial load. Although the high static axial load pushed the balls up the raceway shoulder, placing the center of the brinell marks just outside of the normal load path, a portion of the brinell marks remained in the load path. A roundness trace, made in the center of the visible load path, shows eleven brinell marks clearly visible ranging in depth from 0.0006 mm to 0.0011 mm. This is less than the AFBMA depth for the basic static load limit, defined as 0.0001 times the ball diameter [7]. For this bearing, the deepest allowable brinell mark would be 0.002 mm. The maximum depths of the brinell marks, just outside the load path, were at this limit. The balls likely rolled through the maximum depths during the transient axial load cycles. This brinell tolerance demonstrates additional proof of the robustness of this bearing design.

Conclusions

This test series was very successful in demonstrating the ability to rig test high speed, hybrid ceramic ball bearings in a high fidelity, liquid hydrogen environment. More importantly, it has helped alleviate concerns for the long term affects of the river mark surface distress. These river marks thus far are unique to certain cryogenic applications and have not been mentioned as failure modes in other published research on failure modes for ceramic bearings or in failure atlases for bearings in general [8,9]. Although the exact cause of the river marks has yet to be determined, rig testing has done much to assess their potential. Summarizing:

1) The test rig did produced river marks on previously unmarked balls. Although the specific cause and time of formation could not be determined.
2) River marks did not affect long term life or performance of bearings in the rig.
3) The main channels of the river marks did not appear to change appreciably in width, depth, or aspect ratio with increasing run time. There was an increase in the number of finer tributaries.
4) Brinell markings (at the static load limit) on one of the bearing raceways, did not impact performance.
5) The rig has demonstrated that these hybrid ceramic bearings are very robust.

204

References

1. Bursey, Roger W., David L. Haluck and Robert L. Thom; "Incorporation of Silicon Nitride Rolling Elements into the Pratt and Whitney High Pressure Oxidizer Turbopump for the Space Shuttle Main Engine;" Proceedings of the *Advanced Earth-To-Orbit Propulsion Technology Conference-1994*, NASA CP-3282 Vol. II, pp. 365-374.

2. Bursey, Roger W., Herb Chin, et al; "Advanced Hybrid Rolling Element Bearings for the Space Shuttle Main Engine High Pressure Alternate Turbopumps;" 32nd AIAA/ASME/SAE/ASEE Joint Propulsion Conference, Lake Buena Vista, Florida; July 1996.

3. Gibson, Howard G. and Shawn D. Fears; "Bearing Tests Performed in Liquid Oxygen;" Proceedings of the *Advanced Earth-To-Orbit Propulsion Technology Conference-1992*, NASA CP-3174, Vol. II., pp. 417-423.

4. Gibson, Howard G. and Fred J. Dolan; "Overview of Bearing Testing at Marshall Space Flight Center; Past, Present, and Future;" Proceedings of the *Advanced Earth-To-Orbit Propulsion Technology Conference-1994*, NASA CP-3282 Vol. II, pp. 361-365.

5. Chin, Herbert A., Roger W. Bursey, et al; "Cronidur 30 - An Advanced Nitrogen Alloyed Stainless Steel for Advanced Corrosion Resistant Fracture Tough Cryogenic Bearings;" Proceedings of the *Advanced Earth-To-Orbit Propulsion Technology Conference-1994*, NASA CP-3282 Vol. II, pp. 321-330.

6. American National Standard/AFBMA Standard 10-1989 - "Metal Balls," p. 2.

7. American National Standard/AFBMA Standard 9-1990 - "Load Ratings and Fatigue Life For Ball Bearings," p. 2.

8. Hadfield, M., T.A. Stolarski, and R.T. Cundhill; "Delamination of Ceramic Balls in Rolling Contact;" *Ceramics International*, 19, 1993, pp. 151-158.

9. Tallian, T.E.; *Failure Atlas for Hertz Contact Machine Elements*, ASME Press, New York, 1992

Table 1. Bearing Test History

	Reaction Bearing	Load Bearing
	Starts; seconds	Starts; seconds
Development Pumps	3; 1,594	5; 932
Previous Rig Builds	0	7; 2,441
Rig Build for This Report	38; 31,207	38; 31,207
Grand Totals	41; 32,801	50; 34,580

Table 2. Ball Diameter Variation

Bearing	Before Test Series	Mid Series	Post Series
Reaction	0.12 μm	0.19	0.33
Load	0.17	0.33	0.25

Table 3. Raceway Wear Depths, Average Values

| Raceway	Reaction	Load
Outer	0.65 μm	0.89
Inner	0.49	0.31

206
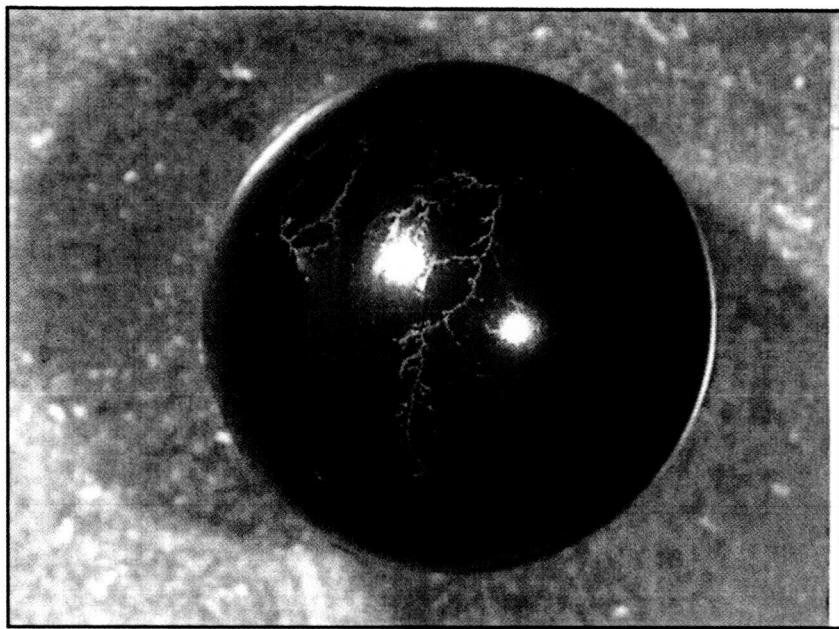
Figure 1. Ceramic Ball With "River Mark" Surface Distress (20.59 mm diameter)
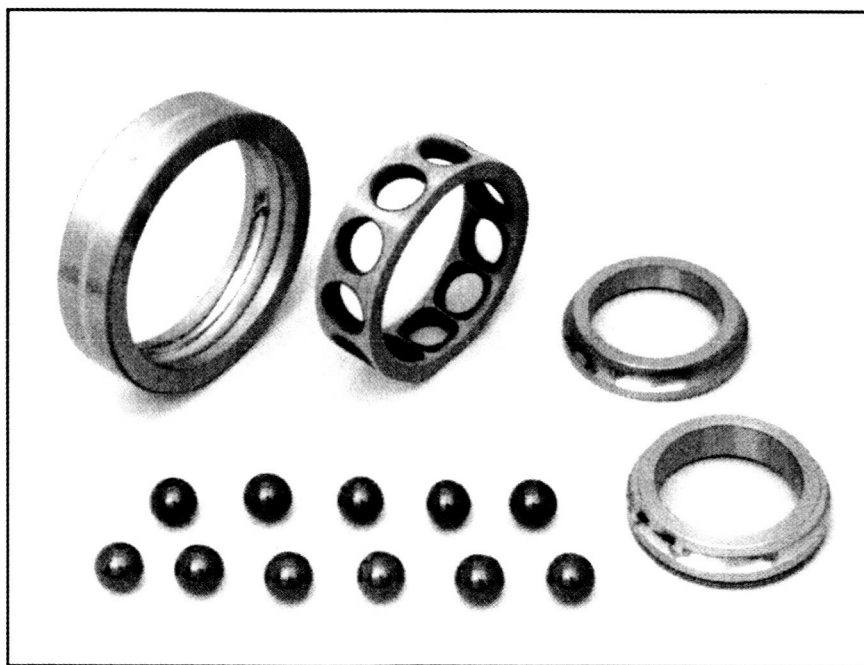
**Figure 2. Hybrid Ceramic, Angular Contact Ball Bearing, 60 mm Bore**
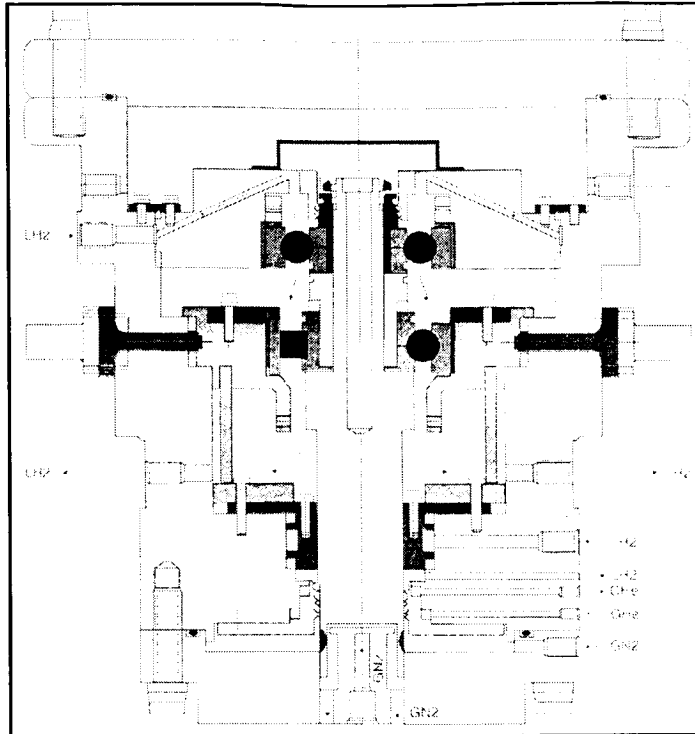
Figure 3. Cross Section Of Liquid Hydrogen Bearing Test Rig. Note that the left half of the sketch depicts the ball-roller bearing configuration and the right half the ball-ball bearing configuration. Only one configuration is possible during a test!
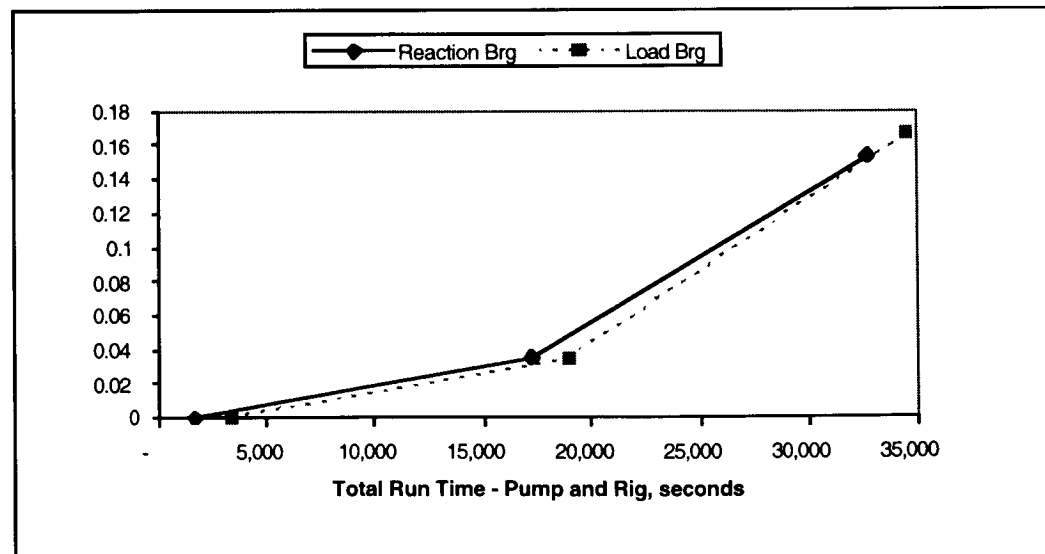

Figure 4. Ball Wear Versus Run Time.
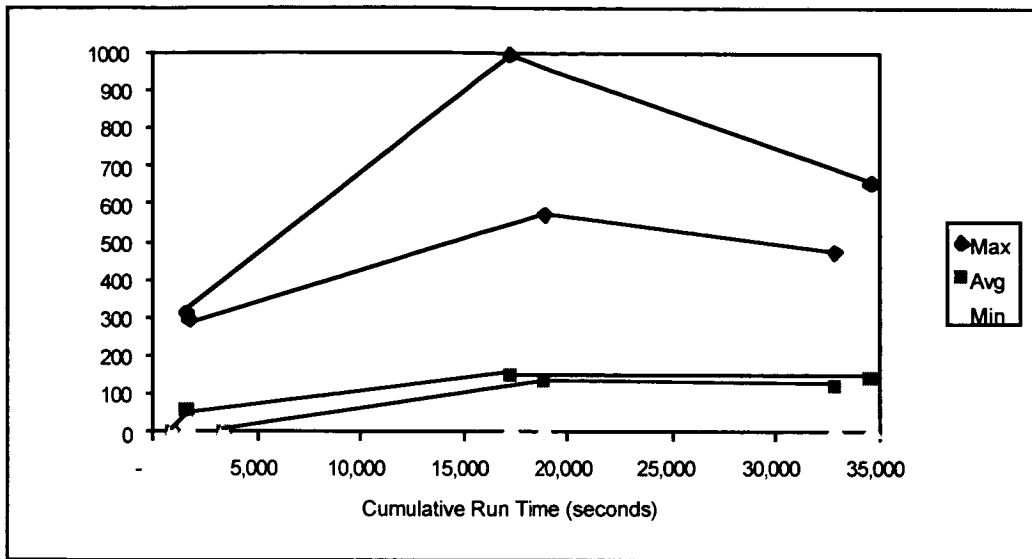
Figure 5. Widths Of River Marks From Stylus Profilometry.
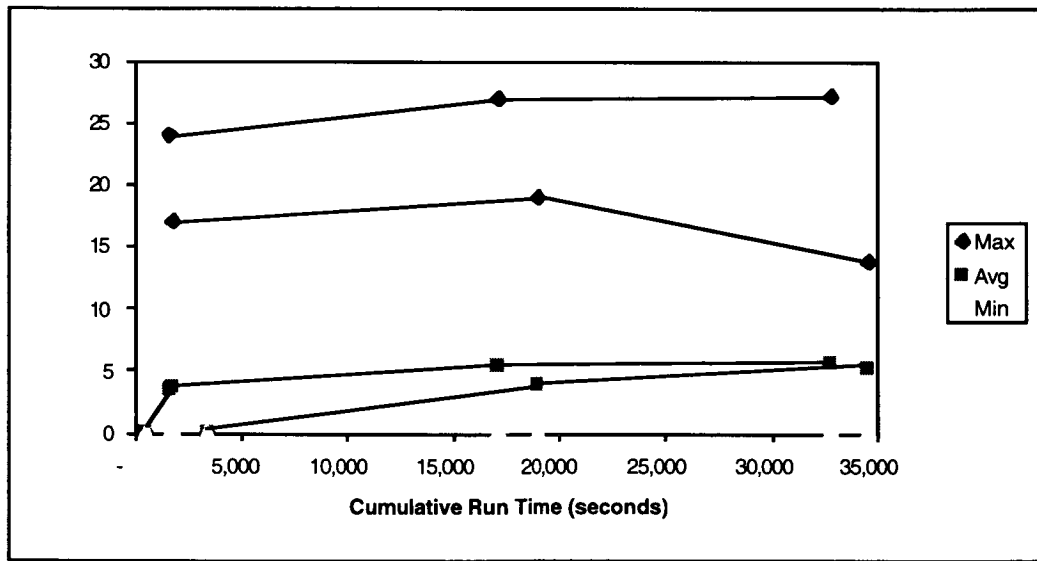
Figure 6. Depths Of River Marks From Stylus Profilometry.
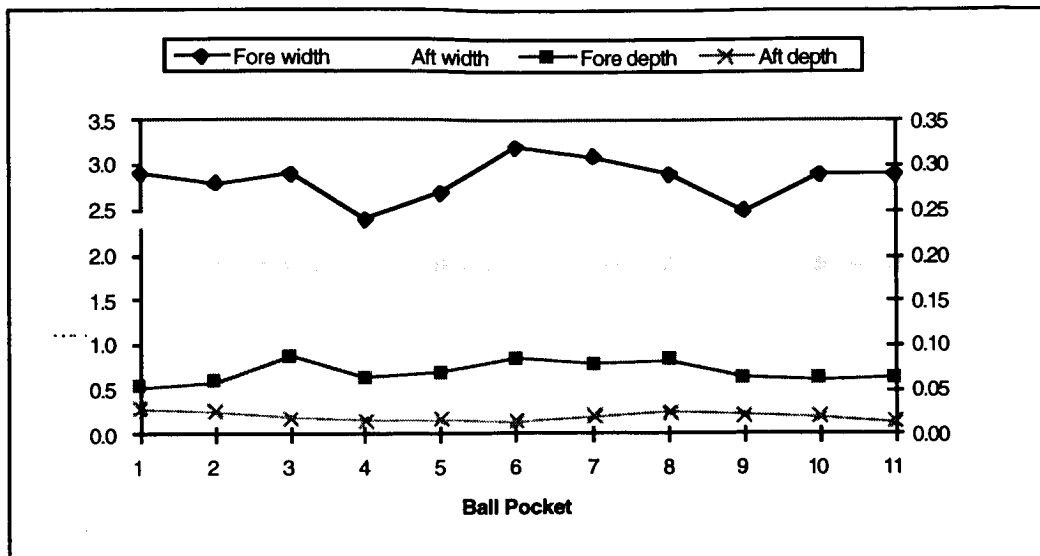
Figure 7. Wear of Cage Pocket Inserts Due to Ball Rub In Circumferential Direction (Reaction Bearing).
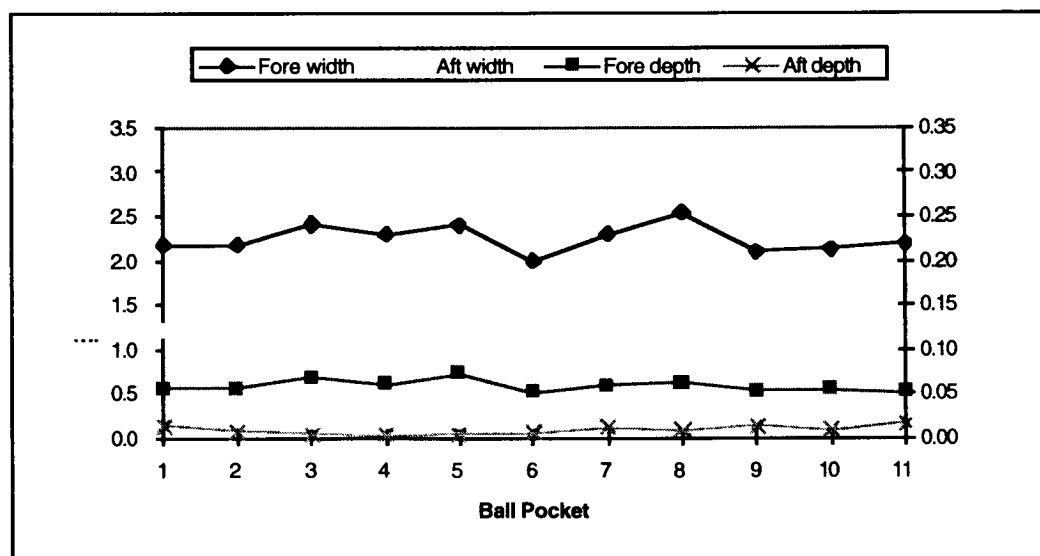
Figure 8. Wear of Cage Pocket Inserts Due to Ball Rub In Circumferential Direction (Load Bearing).

210
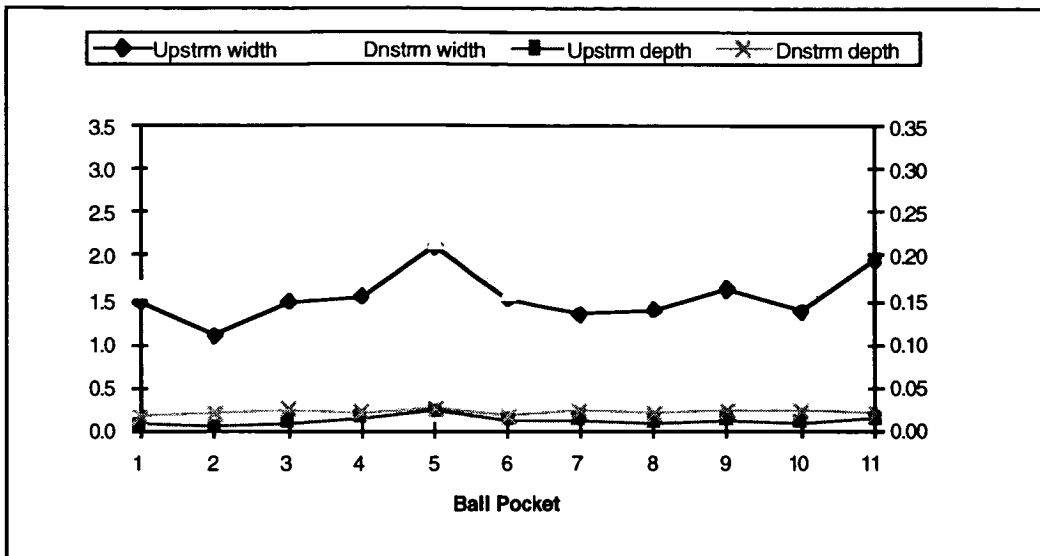
**Figure 9. Wear of Cage Pocket Inserts Due to Ball Rub In Axial Direction (Reaction Bearing).**
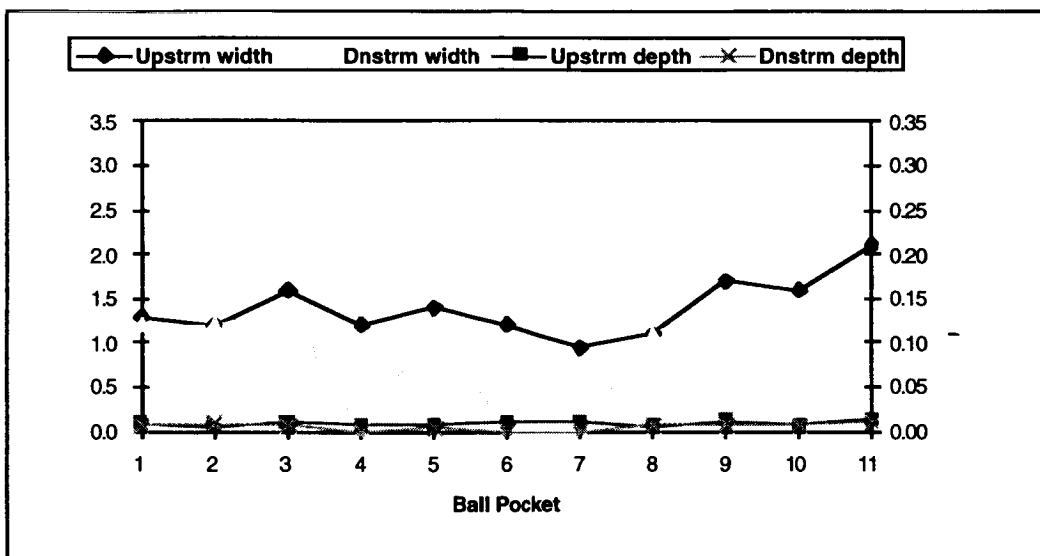
Figure 10. Wear of Cage Pocket Inserts Due to Ball Rub In Axial Direction (Load Bearing).
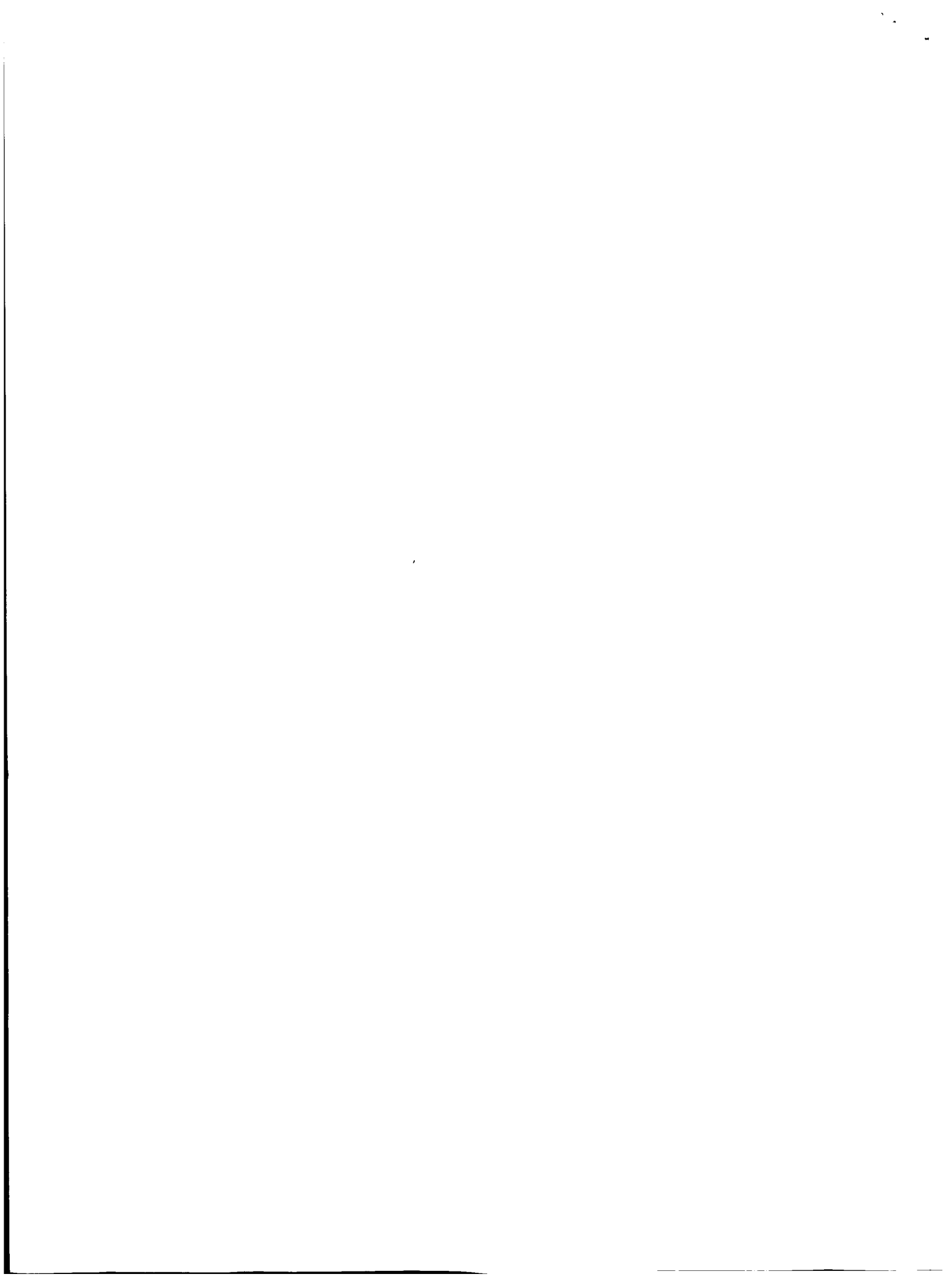
Experiences with Differentiating Ball Bearing Retainer Instabilities

Bill Bialke*

Abstract

Ball bearing retainer instability can be a problem for rotating mechanisms such as reaction wheels, momentum wheels, and gyroscopes. Some types of retainer instability can lead to catastrophic bearing failure, while other types can be merely an indicator of an ample lubricant supply. This paper focuses on experience with differentiating the detrimental types of retainer instability from other similar, but benign, symptoms, particularly in reaction wheel applications with phenolic retainers.

Introduction

Classical retainer instability has been observed frequently and modeled extensively, with a general consensus that it is the result of an increase in retainer friction above an inherent threshold for a given retainer design. The instability is typically characterized by audible noise, torque increase and vibration. This type of retainer instability can be detrimental and potentially catastrophic if it is allowed to continue for long periods of time, and is generally the result of lubricant depletion and/or deterioration. Improper lubricant impregnation of phenolic retainers has also been suspected to be a cause for the initiation of instability. This 'bad' instability can occur naturally, but can also be initiated by high frequency vibration excitation.

Another type of retainer resonance has been observed on several occasions which exhibits behavior consisting of a narrow band, high pitch audible noise and decreased torque. This has been determined to be caused by the retainer hula-hooping on its guiding land. In this type of retainer motion, the viscous friction of the retainer with the land initiates hula-hooping, or 'whirling', of the retainer. The torque decreases as the retainer enters this mode, due to the reduction in retainer sliding friction. This 'good' instability is not undesirable from a tribological standpoint, as it exhibits nearly pure rolling retainer motion, which results in lower torque and less wear. It is also evidence of ample lubrication, as opposed to other retainer instabilities which are typically caused by insufficient lubrication.

The objective of this paper is to aid in the discrimination between these 'good' and 'bad' forms of cage instability with anecdotes of first-hand experience with both types. In addition, some general guidelines for designing bearings in order to minimize the potential for catastrophic retainer instability will be presented, based on lessons learned during the previously mentioned experiences.

---

* ITHACO Space Systems, Inc., Ithaca, NY

Classical Retainer Instability

Classical retainer instability, sometimes referred to as 'cage squeal' due to the high-pitched noise it makes, has long been a serious problem in rotating mechanisms. As a result it has prompted considerable research. In precision spaceflight mechanisms such as gyroscopes, reaction wheels and momentum wheels, retainer instability is not only a source of undesirable noise and jitter, but can ultimately lead to catastrophic bearing failure.

The instability is typically initiated by a lubrication-starved condition, where the frictional coefficient of the retainer in the ball pocket and/or the guiding land increases beyond a threshold for a given bearing design. When unstable, the retainer motion is no longer simply rotational, but has erratic, high-frequency motion radially and/or axially. The unstable modes can be very energetic, in which case the heat dissipation can increase the bearing temperature and drive off the remaining lubricant, which compounds the problem and eventually leads to retainer failure. The bearing does not normally go to catastrophic failure with the first occurrence of instability. Rather, instabilities are followed by periods of recovery because the excessive motion and temperature are believed to acquire some additional lubricant from adjacent areas. Eventually, there is no longer a supply of additional oil to halt the instability and it then leads to runaway thermals and forces, and eventually failure.

Tests at Aerospace Corporation[1] demonstrated that instability can be initiated in the lab by intentionally starting with lubricant-starved bearings. This is useful for those studying unstable retainer behavior by providing a repeatable test specimen, and also supports a generic claim that retainer instability is the result of insufficient lubrication. It was also demonstrated in many cases that addition of oil to bearings during a period of instability resulted in an immediate return to stable operation.

Since the lubrication in question is on the surface of the retainer, vacuum impregnation of phenolic retainers is critical in order to ensure that the contacting surfaces of the retainer do not dry out and increase friction. Bertrand[2] has shown that proper vacuum impregnation of phenolic retainers requires a high temperature bake-out and a lengthy soak time. Without these measures, the interior of the retainer will eventually rob the exterior surfaces of oil, resulting in the dry, high friction contacting surfaces which tend to be ripe for occurrences of retainer instability.

Vibration Induced Instability

Retainer instability was observed during initial operation of a prototype reaction wheel. The instability was consistent whenever the wheel speed was increased above 3000 rpm. This was considered to be out-of-the-ordinary, since the bearings were pristine and well lubricated. The instability was characterized by a squealing noise and increased bearing drag torque.

After a considerable amount of time was spent focusing on the bearings as the source of the problem, it was eventually learned that an induced vibration from the reaction wheel motor was the real culprit. This was revealed by accelerometer measurements taken near the bearing, and processed with a dynamic signal analyzer.

Figure 1 shows a waterfall chart during a run-up from 0 rpm to 3600 rpm, with spectral data sampled every 200 rpm. A structural resonance at 1800 Hz is discernible, but a 36x per revolution disturbance dominates the plot. The retainer instability is clearly visible in the 1 kHz range above 3000 rpm, which is the exact speed at which the 36x per revolution disturbance intercepts the 1800 Hz resonance.

The source of the 36x per revolution disturbance was the prototype motor used to drive the reaction wheel. Circulating currents in the armature were caused by amplitude modulation of the magnetic flux density in the motor gap. To prove this, the motor was rewired without potential circulating current loops, and the waterfall measurement was immediately retaken. The results are shown in Figure 2, which clearly shows elimination of the 36x per revolution disturbance, and no signs of retainer instability. The modified motor winding was the only change to the reaction wheel between the data taken in Figures 1 and 2.

A potential vibration forcing function should always be considered when reviewing the causes of a retainer instability problem. This experience also demonstrates the value of having clear disturbance data from a tool such a dynamic signal analyzer.

Retainer Hula-Hooping

During subsequent acceptance testing of the same reaction wheel design, a narrow-band, high-pitched audible noise was noted at high speeds. The phenomenon was most often noted during cold temperature testing, and early in the acceptance test program when run-in time on the bearings was low.

The noise was similar to the vibration-induced retainer instability, but it was almost a pure tone, or hum, rather than a squeal, which tends to be more choppy and broader band. It also typically started with a low amplitude and gradually increased in intensity, rather than intermittently or discretely occurring. The musical note quality of the noise was not the strangest observation. The most puzzling characteristic was that the noise was coincident with a significant reduction in bearing drag torque. How a noise can be generated, dissipating energy, yet simultaneously requiring less power to operate is difficult to explain.
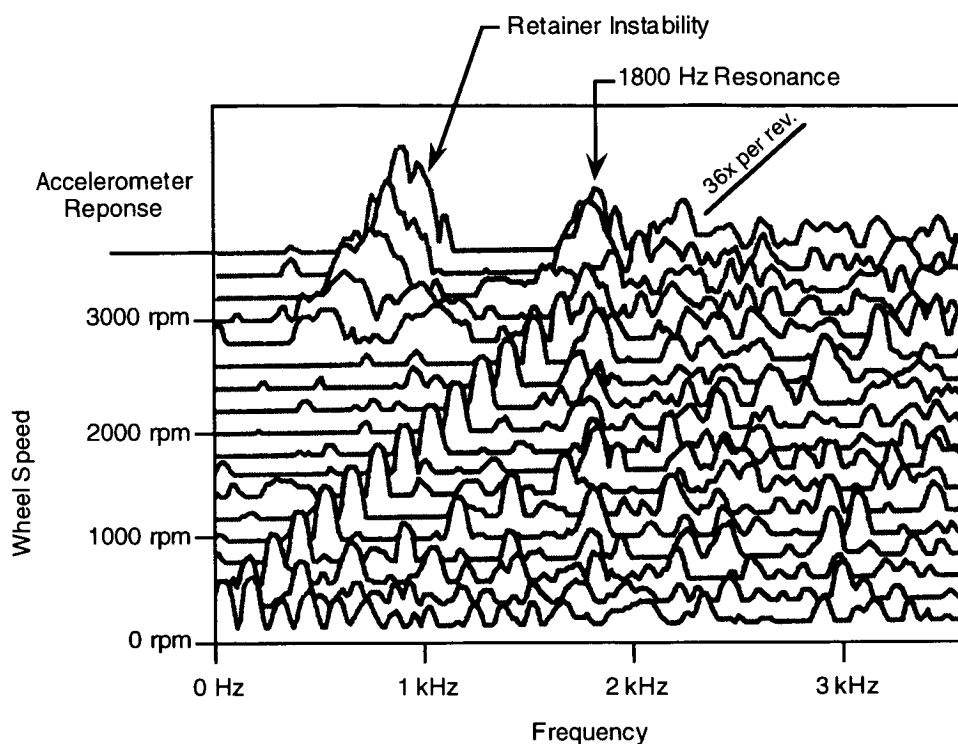
**Figure 1. Run-up with 36x per Revolution Motor Disturbance**
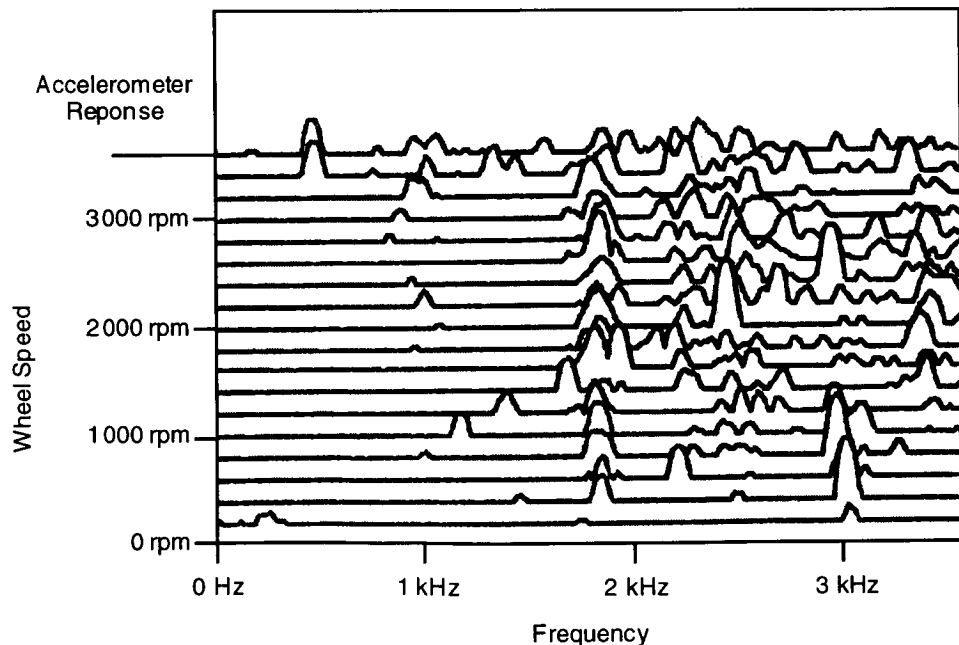
Figure 2. Run-up with Motor Disturbance Removed

216

Stevens[3] observed similar phenomenon during extensive studies of retainer instabilities. He found one unstable mode which resulted in a slight decrease in torque in cases of flooded lubrication, and speculated that it could be due to the retainer vibration disrupting the lubricant film established between the retainer and the outer race.

In Draper Lab's *Guide for Selection and Application of Precision Instrument Bearings*[4] a possible retainer mode is described where a retainer hula-hoops on its guiding land, as shown in Figure 3. The retainer rolls on its guiding land, rather than sliding as the usual retainer motion. This would conceivably allow a pure rolling bearing, with no sliding surfaces which are inevitable with a typical bearing retainer.

Outer Race
Rotation

Motion of a Point
on ID of Retainer

Whirl Motion
of Retainer
Ceter of Gravity

Average Rotation
of Retainer

Retainer Rolls
Without Slipping
on Guiding Land
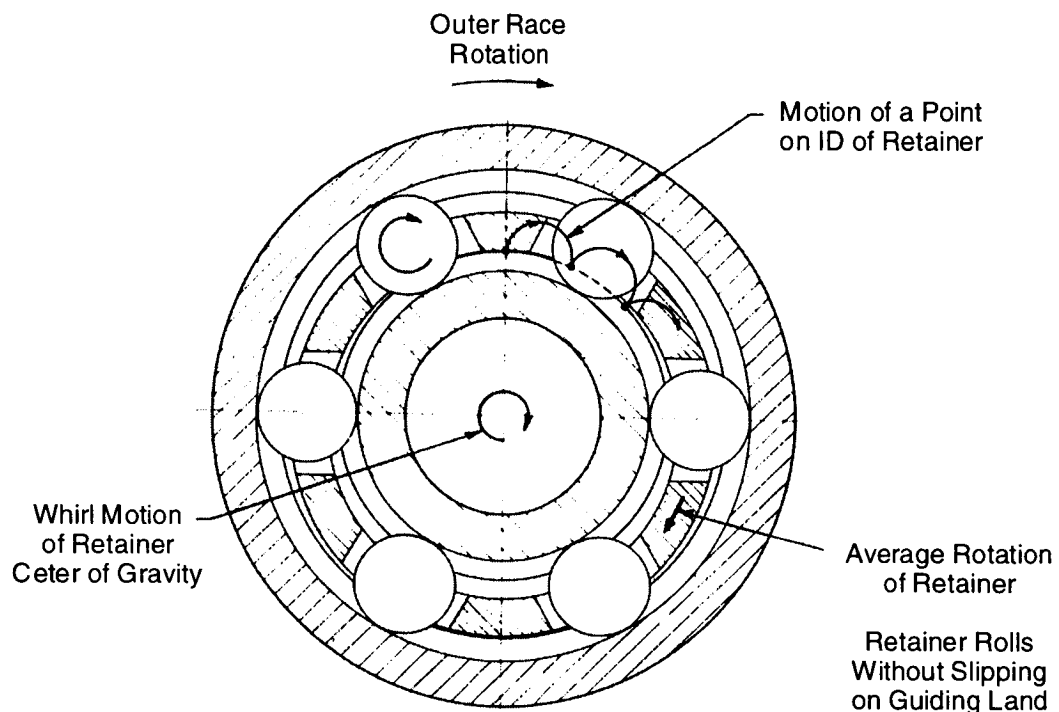
**Figure 3. Retainer Hula-Hooping Mode**

The reaction wheel bearings where the hum was observed were well-lubricated with a low vapor pressure grease and assembled with properly impregnated phenolic retainers. This led to suspicion that hula-hooping was occurring. In the case of the reaction wheel, the retainer is outer race guided, so a harmonic drive is an alternate analogy to a hula-hoop.

217

If the traction between the retainer and its riding land were perfect with no slippage, the disturbance would be at a whirl frequency corresponding to:

$$\text{Whirl Speed ratio} = \frac{\text{land circumference}}{\text{Distance of each hula-hoop step}} \tag{1}$$

$$= \frac{d\pi}{\Delta d\pi} = \frac{1.05"\pi}{0.012"\pi} = 87 \text{ x per retainer revolution}$$

where d = guiding land diameter
       Δd = land diametral clearance

In one case, the hum started at a wheel speed of 2500 rpm. At this speed, the no-slip retainer resonant frequency would be approximately 1400 Hz, using a 2.5 shaft/retainer revolution ratio. The resonance appearing at 700 Hz would require 50% slippage, which is not unreasonable for the low amplitude of the measured disturbance.

On this reaction wheel, drag torque was measured while simultaneously monitoring the unit with an accelerometer. The accelerometer showed the resonance appearing at 2500 rpm, and gradually reaching peak amplitude at 4000 rpm. Figure 4 shows the amplitude of the resonance and the drag torque during the measurement. In addition, the drag torque is included from a measurement taken one day earlier when no resonance, or hum, was present. The results show clearly that the resonance results in a net reduction in drag torque from the previous test.
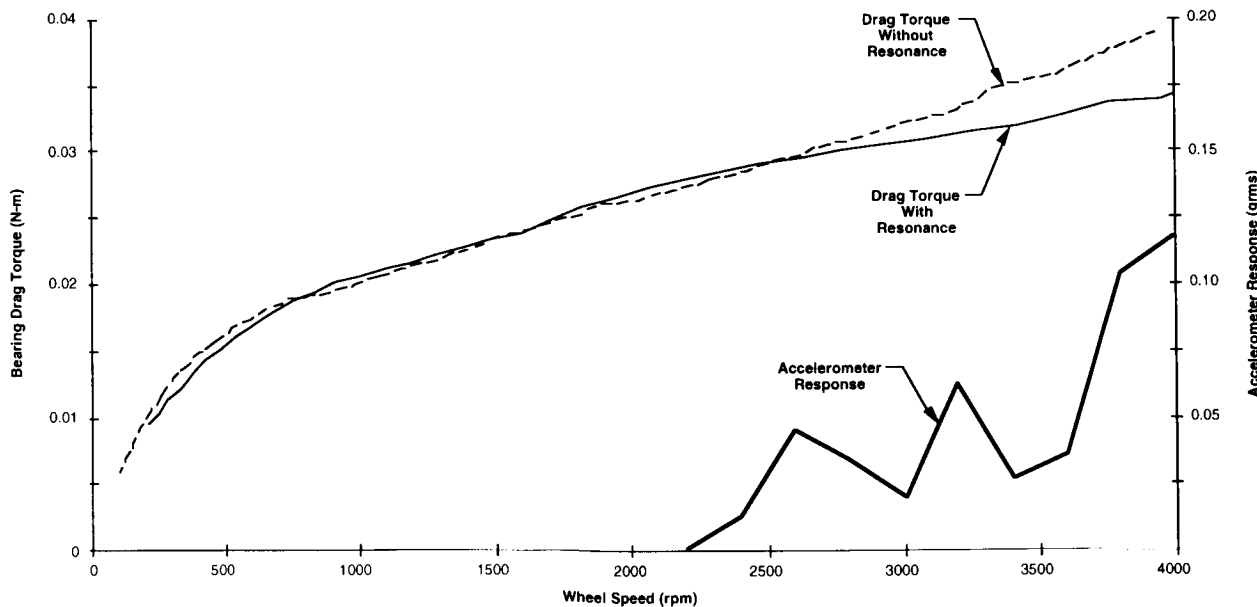

Figure 4. Bearing Drag Torque and Accelerometer
Response vs. Wheel Speed

218

It should be noted that the bearing drag torque in Figure 4 is the combined torque from four bearings. The drag torque reduction during the resonance is roughly 50% at 4000 rpm if it is assumed that only one of the bearings is resonating.

Figure 5 shows the waterfall data on a different unit, where a divergence of the hum frequency from the theoretical whirl speed ratio can be seen as the speed is increased. This would be expected as the slip increases with speed and the resulting increase in bearing temperature.
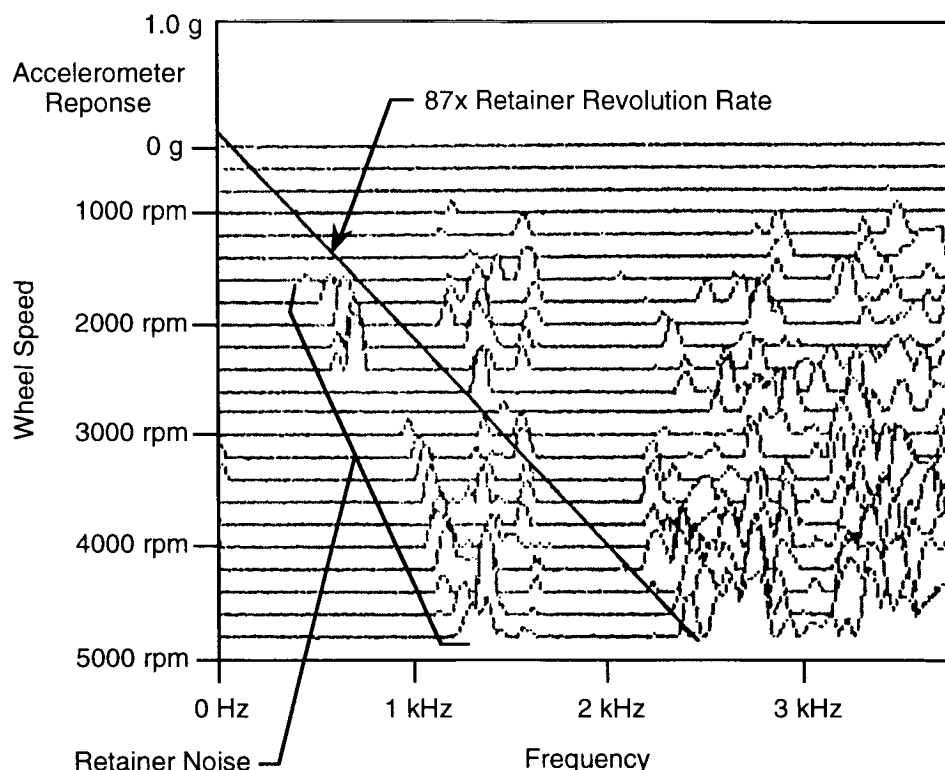
Figure 5.   Coast-Down With Hula-Hooping Retainer

The hula-hooping can be caused by a temporary excess of lubricant at the retainer/land interface. It was observed during testing that after minimal run-in, the resonance would disappear. It was also much more likely at cold temperatures, where the lubricant viscosity increases and results in higher traction between the retainer and land. This would also suggest that hula-hooping is primarily an indication of lubricant distribution and/or ample lubricant quantity.

Thus, this dynamic mode need not be considered detrimental. It will typically exist only during the initial run-in of the bearings, or at extremely cold temperatures. The reaction wheel design on which it was observed has been operating successfully on life test for over four years without anomaly, and numerous flight units, which initially demonstrated hula-hooping during acceptance testing, have performed flawlessly on-orbit for over two and a half years.

Designing for Retainer Stability

Many different approaches have been taken to solving the problem of retainer instability. In general, the solutions involve incorporating some form of asymmetry to the bearing. A bearing manufacturer's primary objective is to fabricate a perfect bearing, which inherently drives the components towards perfect symmetry. A low threshold for retainer instability is sometimes blamed on this ideal goal, given that a perfect retainer in a perfect bearing will maximize the retainer free play, or deadband. An asymmetry is assumed to be required to bias the retainer to a stable position and keep it there. This theory has been used successfully in many applications. Draper's guide[4] lists the following such variations which have been used successfully:

Variation of ball diameters, which results in different ball speeds and lead or lag positions of balls in retainer pockets.

Static or dynamic unbalance of retainer to provide stability to particularly eccentric or cocked positions of the retainer.

Variation of clearance, ball-to-pocket and retainer-to-guiding land, which can favor or inhibit whirl modes.

Variation in retainer-pocket geometry, including round, square, diamond or oval and variation from pocket to pocket in size or location.

Variation in land-guiding diameters - guiding on inner or outer race, or on one land or two.

Of these suggestions, ball diameter variation was tried as an attempt to solve the vibration-induced retainer instability previously discussed, prior to the discovery of the anomalous motor excitation. In this case, it was observed that incorporating two undersized balls in each bearing did reduce the occurrences of retainer instability, but it was also noted that the instability which did occur was more energetic than observed with a symmetric ball compliment.

When designing for retainer stability, it is probably more effective in the long run to ensure the retainer's coefficient of friction is maintained below a modest threshold. If, instead, the threshold is increased, it could contribute to additional retainer wear. This ignores the true source of the problem, which is lack of lubrication.

There are several important design features which can be employed to ensure adequate lubricant on the surface of the retainer. The most important, when dealing with phenolic retainers, is to properly impregnate them. As previously mentioned, insufficient impregnation will eventually leave the retainer exterior dry. Ensure that the vacuum bakeout and soak times incorporate Bertrand's conclusions.

Use of a low vapor pressure lubricant when operating in vacuum is also important. Volatile lubricants can deplete easily from a retainer. Because of its thermal isolation, the retainer will be the warmest component in a bearing. A significant portion of the

viscous friction is generated between the retainer and the steel bearing parts. As a result of this high relative temperature, the retainer will experience a net evaporative lubricant loss over time. The lower the vapor pressure of the lubricant, the lower the loss rate. In addition, testing performed at Aerospace Corporation[1] concluded that synthetic hydrocarbons, typically created for low vapor pressure characteristics, tend to be less susceptible to retainer instability when compared to higher vapor pressure mineral oils.

Inner race rotation is preferred over outer race rotation, since it is not conducive to the centrifuging of lubricant out of the bearing. Instead, the inner race rotation merely circulates the lubricant. Maintaining a sufficient quantity of lubricant in the bearing is obviously the best way to keep the retainer surfaces lubricated. Using grease lubrication, rather than merely oil, is an excellent way to minimize lubricant depletion from the bearing due to surface migration.

With inner race rotation bearings, guiding the retainer on the outer race land is preferred over the inner race, because any centrifuging of the lubricant in the retainer itself will relubricate the guiding surface, rather than deplete it. In addition, the retainer is thermally coupled with the fixed bearing race and will thereby operate cooler. This will minimize depletion of lubricant from the retainer due to evaporation.

For long-term missions where retainer instability is potentially a single point failure, a means of lubricant replenishment should be provided. It has been frequently demonstrated that adding lubricant directly to a squealing bearing will result in immediate recovery and a significant amount of extended operation. Tungseth[5] recommended that, for a DSP (Defense Support Program) momentum wheel which had periods of retainer instability, a relubrication system which would channel lubricant to the guide surface of the retainer would improve performance and increase mission life.

An active lubrication system is currently being developed for the GPS (Global Positioning System) IIF reaction wheels, which has the capability to add grease to the retainer guiding land of the bearing on command. The patented device, shown in Figure 6, is a simple concept. It utilizes a grease filled cartridge which is heated on command. The high thermal expansion coefficient of the grease forces a controlled amount of grease past a check valve and directly into the bearing. It is included only as a contingency, to be used in the event that on-orbit data show signs of lubricant depletion or retainer instability.

Conclusions

Experiences with several forms of retainer instability support the notion that adequate lubrication is the primary key to preventing it. Over-lubrication can result in a form of instability which is characterized by a subtle reduction in bearing torque, but this is not considered to be detrimental. Cases of potentially catastrophic retainer instability can be identified by periodic step increases in bearing torque. Conventional bearing retainer designs maintaining symmetry can be used successfully when they are properly impregnated with oil and sufficient lubrication is provided.
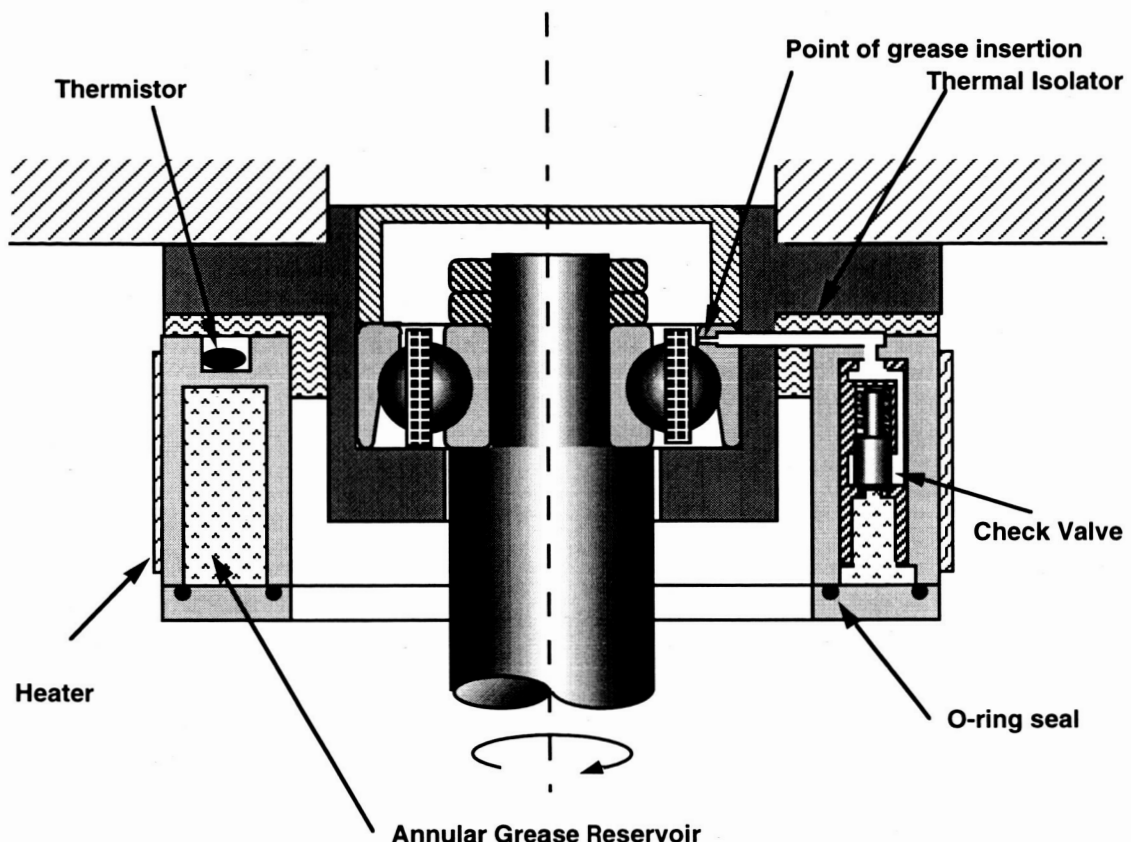
Figure 6.   Active Lubrication System Layout

Acknowledgment

The author would like to thank Alan Leveille of Aerospace Corporation for his guidance during the experiences discussed, and his helpful critique of this paper.

References

1. Carré, D. J., Kalogeras, C. G., Didziulis, S. V., Fleischauer, P. D., Bauer, R., "Recent Experience with Synthetic Hydrocarbon Lubricants for Spacecraft Applications," *Sixth European Space Mechanisms & Tribology Symposium*, 1995.
2. Bertrand, P. A., "Oil Absorption into Cotton-Phenolic Material," *Journal of Material Research*, Vol. 8, No.7, July 1993.
3. Stevens, K. T., "Experimental Observations on Torque Variation Caused by Bearing Cage Instabilities," *Proceedings of the Second Space Tribology Workshop*, 1980.
4. The Charles Stark Draper Laboratory Report R-1010, *A Guide for Selection and Application of Precision Instrument Ball Bearings*, October 1976.
5. Tungseth, Allen E., "DSP Wheel Recent Experience," *17th Annual AAS Guidance and Control Conference*, 1994.

Rex 20/Si₃N₄ Control Moment Gyroscope Bearing Development

D.W. Smith*, A. R. Leveille**, M.R. Hilton**, P.C. Ward+

Abstract

In order to build larger momentum wheels, the capacity of the spin bearings had to be increased to handle launch loads. This could be done by building larger bearings or making current size bearings of stronger materials. Larger bearings require a great deal of development, are heavier, and have significantly more drag torque, which increases operating temperatures and reduces lubricant life. Making an advanced material bearing similar in design to the current bearing provides increased capacity without increasing weight and power.

This paper describes the selection of material candidates, as well as the designing, testing, and ultimately down-selecting to a single candidate to be life tested. Details of high pre-load, short-duration tests will be presented. Design analysis, load capacity, and fatigue testing details are presented in other papers.

A natural adaptation of this technology is high-speed bearing applications. The high-speed thermal characteristics will be discussed.

Introduction

Load capacity requirements for spin bearings in a space application are dictated by launch loads defined by the rotor mass and vibration environment. The required bearing size is determined by this load capacity and by the endurance of both the bearing and its lubrication system for the required life. The largest current Control Moment Gyroscopes (CMG) use two duplexed pairs of 305 size angular contact ball bearings to support the spin axis. A new application was envisioned that would require a CMG with 50% more output torque, 75% more momentum, and double the life. These requirement demanded a larger rotor and, subsequently, a significant increase in spin bearing capacity. Even without considering the load capacity limits of the current 52100 305 size bearings, the combination of rotor speed, gambling profile, and long life put these bearings beyond fatigue endurance limits.

The only two solutions were to use larger bearings, probably a 306 size, or make the current bearings of materials that would provide substantial increases in load capacity and fatigue limit. Previous experience developing a larger bearing for this type of application made an alternative material approach attractive. In addition, larger bearings have higher drag torque. This increase in drag torque means higher operating temperatures that reduce lubricant life. If the new materials have similar enough

* Honeywell Inc., Glendale, AZ
** Aerospace Corp., El Segundo, CA
+ MPB Corp., Keene, NH

properties, the dynamic development history can be transferred to the new bearing intact. In addition, the energy dissipated in the bearing will be similar for like loads, speeds, and environmental conditions. The chances for success were greatest if new materials could be found that provide the needed increase in load capacity and fatigue resistance.

In order to achieve the higher capacity, materials with substantially higher stress limits were required. The mean Hertzian stress limit of 52100 is about 2551 MPa (370 kpsi) when the hardness is Rc 62. This is about as high as any of the conventional through-hardening bearing steel, so surface hardening and particle metallurgy materials were considered. Heritage was also desirable, so materials used in other bearing applications were considered first.

The material candidate that merged was Crucible Steels' Rex 20. This material is used in X-ray tube bearings that operate under high-speed, high-temperature and high-vacuum conditions. The material has a hardness of Rc 66-67 compared to Rc 60-62 for 52100. The projected mean Hertzian stress limit was at least 2965 MPa (430 kpsi). In fact, there was some evidence that the stress limit might be significantly higher than that. This limit was explored by Hilton and Ward (reference 1) and found to be closer to 3790 MPa (550 kpsi). The material is a powder metallurgy product and has very even distribution of carbides throughout the matrix, providing consistent properties and good surface finishes.

Approach

Having chosen to use advanced materials in the same size bearing, a plan was developed to down-select to the final material combination and qualify that selection for flight use. Three material candidates were selected for testing: a 52100 baseline, a Rex 20 bearing with Si_3N_4 balls, and a Rex 20 bearing with TiC-coated Rex 20 balls. The down-select and qualification plan consisted of the following:

1. **Optimize bearing design for new materials.** Details may be found in "Contact Angle Optimization for Variable Load Applications" by Smith [2].
2. **Build examples** of the three candidate bearings to flight-bearing standards to prove the new materials can be produced at that quality level. Previous bearings made of Rex 20 have been much smaller (outside diameters of 25 mm instead of the 100 mm required for this application).
3. **Conduct high-load, short duration tests** to detect infant mortality problems and rank the candidates on performance. This testing is discussed in the subsequent paragraphs.
4. **Perform rolling element fatigue tests** on candidate material combinations to determine their respective limits. Details of this testing may be found in load and fatigue properties of Rex 20 by Hilton and Ward [1].

5. **Perform load capacity tests** to determine the limiting mean Hertzian stress limit. Details of this testing may be found in load and fatigue properties of Rex 20 by Hilton and Ward [1].
6. **Perform high-radial load cycling test** to verify the ability of each candidate to survive the required high-load environment.
7. **Perform a real-time life test** on the winning candidate material.

High-load, Short Duration Testing

A series of high-load, short duration tests were performed to provide insight of the early life performance of new materials. Tests of three candidate bearings designs, including the current baseline, Rex 20/TiC, and Rex 20/Si_3N_4, were conducted with axial preloads simulating the normal mean Hertzian stress in the 4068 N-m-s (3000 ft-lbf-s) CMG gimballing at 0.5 rad/s. All tests were conducted at 6000 rpm in dry nitrogen for 63 days, using Rheolube 2000 grease. Torque data obtained during the test and post-test examination were used to evaluate the relative performance of the three candidates.

Description of Test Equipment
The four spindle fixtures with associated temperature baths and motor controllers are illustrated in Figure 1, along with the data acquisition system to the right of the photo. A cross-section of the test spindle is illustrated in Figure 2.
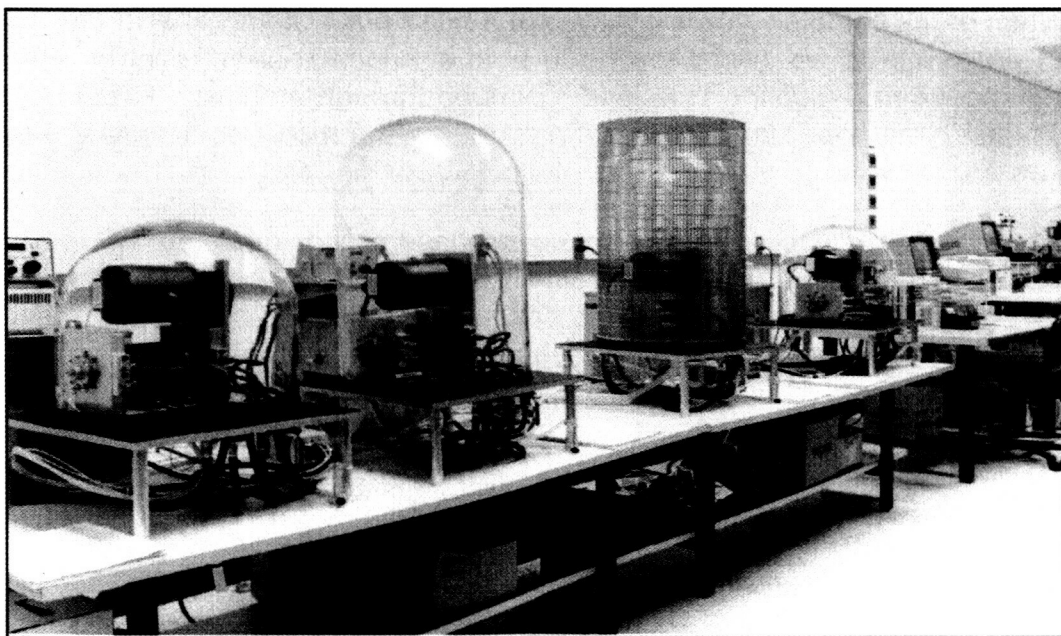

Figure 1. Spindle Test Fixture
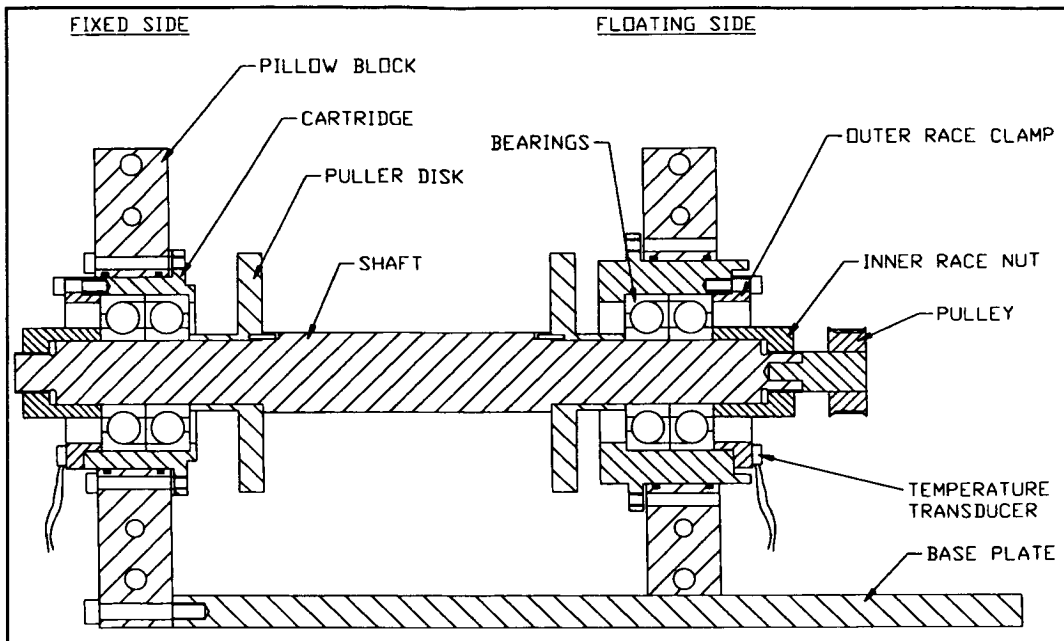
Figure 2. Spindle Cross-section

Test Fixtures

The spindle fixtures were designed and built to perform numerous accelerated bearing tests. Each of the spindle fixtures consists of a base plate, spindle, and bell jar. A dry nitrogen environment was used for the tests to enhance thermal control and provide an inert atmosphere. Cooling fluid was circulated through a shroud that surrounds the shaft. In the dry nitrogen atmosphere, circulated by the motor cooling fan, this proved quite effective.

Mounted to the base plates are the spindle subassemblies, depicted in Figure 2. The left pillow block and bearing/cartridge assembly represents the fixed side of a CMG, while the right pillow block arrangement simulates the floating side. Pinned and bolted to a base plate, the pillow blocks are line-bored to provide mounting tolerances similar to a CMG. Outer-ring clamps, similar to flight configuration, were used on both cartridges. Clamp screws and inner-ring nuts were torqued to flight values.

Running the tests in a dry nitrogen atmosphere enabled the use of brush-type DC motors with a timing belt/pulley arrangement to achieve the 6000-rpm operating speed. After the first test, a very high belt wear rate was observed. Some of the belt dust generated during the test made its way into the floating bearing cartridge, so slinger disks were added to the shaft, inboard of the pulley.

Temperatures were monitored using integrated circuit temperature transducers epoxied to each bearing cartridge and the motor (Figure 2). A Hewlett-Packard data

226

acquisition control and buffer unit collected the data and passed it to a computer for storage, and was monitored using a program written for this test. These data were used for trend analysis and reporting. Motor current was monitored as an indication of spindle drag torque using a current sense device on the motor leads, and motor speed was monitored using the digital tachometer signal.

Test Specimens

The test bearings were mounted into the fixture as DF-duplexed pairs. The bearing preloads were ground to simulate the operating stress seen by each of the candidate bearings during a 0.5 rad/s gimbal rate of a 4068 N-m-s (3000 ft-lbf-s) CMG. The differences in preload required by each of the bearings (Table 1) is a function of the material for that bearing, as well as its specific internal geometry. One set of bearings (two duplexed pairs) from each candidate was run on each fixture, ensuring each candidate was equally subjected to any fixture idiosyncrasies.

Table 1. Preload Determination

Candidate	Radial Load N (lbf)	Average Load N (lbf)	Normal Stress MPa (kpsi)	Equivalent Preload N (lbf)	Calculated Torque N-m (in-oz)	Measured Torque N-m (in-oz)
Baseline	3874 (871)	503 (113)	1055 (153)	1446 (325)	0.26 (37)	0.22-0.24 (31-34)
Rex 20/TiC	3874 (871)	503 (113)	1110 (161)	1432 (322)	0.25 (35)	0.27-0.29 (38-41)
Rex 20/Si$_3$N$_4$	3874 (871)	512 (115)	1241 (180)	1779 (400)	0.24 (34)	0.18-0.19 (26-27)

The bearing bores were sized to provide a slip fit with the shaft. This makes the bearing less sensitive to differential thermal growths which can cause significant changes in preload. Another benefit is in the mounting and dismounting of the bearings to the shaft. A drawback to the loose fit is that it decreases the thermal path from the bearing inner race to the shaft, making it harder for the heat generated at the inner race to be transferred to the shaft. However, this was mitigated by the nitrogen atmosphere and cooling shroud.

The bearings were lubricated with Rheolube 2000. All the bearings were lubricated with the same lot number and quantity of grease, so any differences observed in test life was attributable to the bearing materials/geometry.

<u>Failure Criteria and Follow-up Inspection</u>
A particular test was to be terminated if the average drag torque increased 50% higher than the beginning average drag torque of, or if the temperature of either bearing cartridge exceeded 76.67 °C (170 °F). Upon exceeding these criteria, the test was stopped and the bearings removed from the spindles to conduct a post-test disassembly and inspection of bearings and lubricant. In addition to the visual inspection, lubricant samples were sent to Dr. David Carre for analysis.

Tests not failing prematurely were run for 63 days and terminated. Post-test examinations were identical to those conducted on units that did not complete the planned test period.

Results

The following are summaries of the results of the individual tests: baseline, four Rex 20/Si$_3$N$_4$,and four Rex 20/TiC. Torque and temperature traces are provided for one test in each series. Data from fixture 2 is shown in each case for consistency.

<u>Baseline Test Results</u>
In the first baseline test, the drag torque gradually increased from the 0.20 N-m (28 in-oz) range to near 0.35 N-m (50 in-oz) over a period of about 23 days when the temperature exceeded the 76.67 °C (170 °F) limit. Aluminum particles were found during the post-test examination, suggesting that this failure may have been caused by the contamination, rather than the design or materials. Consequently, the results were dismissed. The second test completed the prescribed 63-day test with only a couple of torque excursions. Figure 3 illustrates the torque and temperature history of the test. Post-test examination revealed heavy wear tracks and darkened grease.

Drag torques were more erratic in the third test, but temperatures were not. The test easily reached the planned 63-day period. In the fourth test, the torque ran a steady 0.21 N-m (30 in-oz) for the entire test, but the temperatures became somewhat erratic about 25 days into testing. Post-test examination of both the third and fourth tests revealed heavy wear tracks and darkened grease.

228
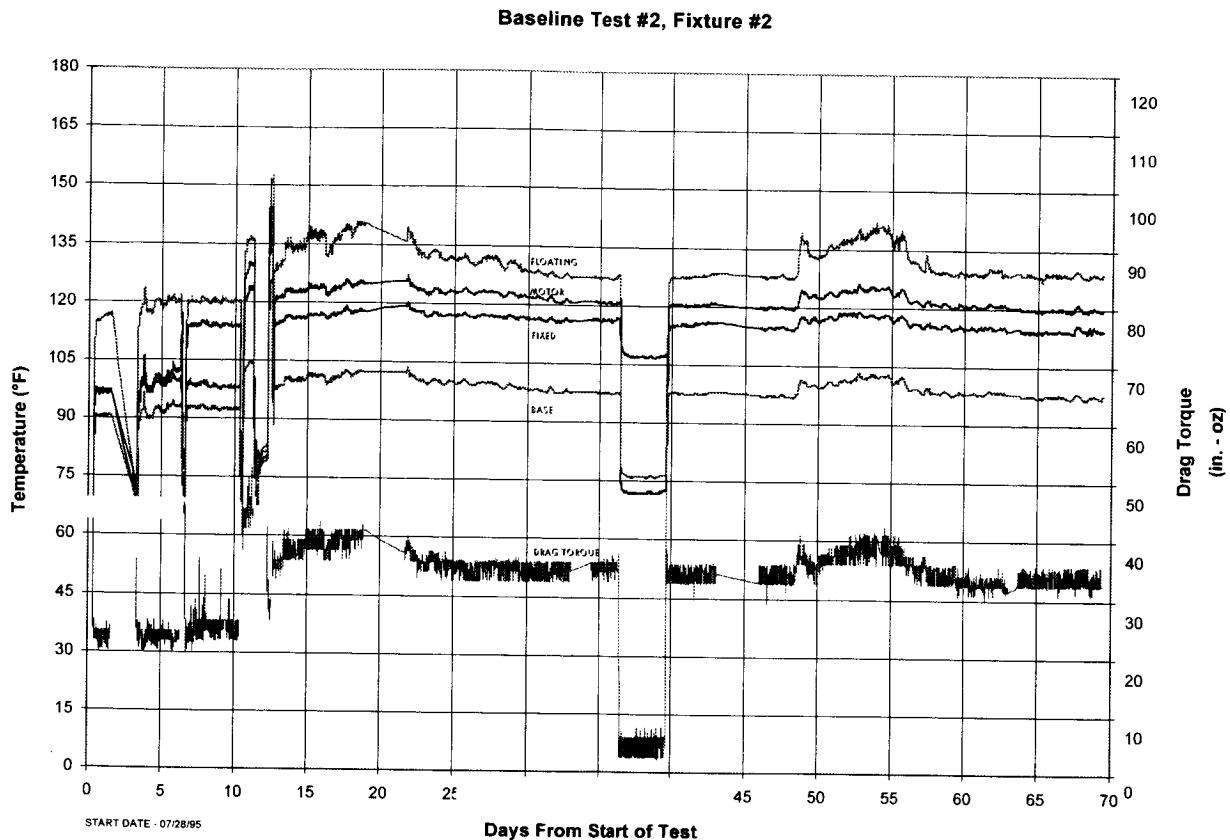
Figure 3. Baseline Test Torque and Temperature History

Rex 20/Si₃N₄ Tests Results

Drag torque began in the 0.18 N-m (25 in-oz) range, and was relatively steady except for a short time when the drive belt had worn to a degree that it required replacement. In the second test, the drag torque and all of the temperatures remained very steady during the entire test period. Post-test examination of both tests showed like-new components with scarcely visible running tracks and new, moist-looking grease. The grease on the floating side contained some black specks, believed to have been belt wear debris. Figure 4 depicts torque and temperature history of the test.

Just as in test #2, test #3 results showed little change in either the drag torque or temperature readings for the duration of the test period. Again, some black belt debris was observed in the floating side grease. The fourth Rex 20/Si₃N₄ test operated in the 0.19 to 0.21 N-m (27 to 30 in-oz) range, except for a short period just before the belt was changed, as seen in test #1. As with all of the Rex 20/Si₃N₄ tests, it easily ran the planned 63 days of testing. Post-test examination of tests #3 and #4 revealed like-new components with scarcely visible running tracks and new, moist-looking grease.
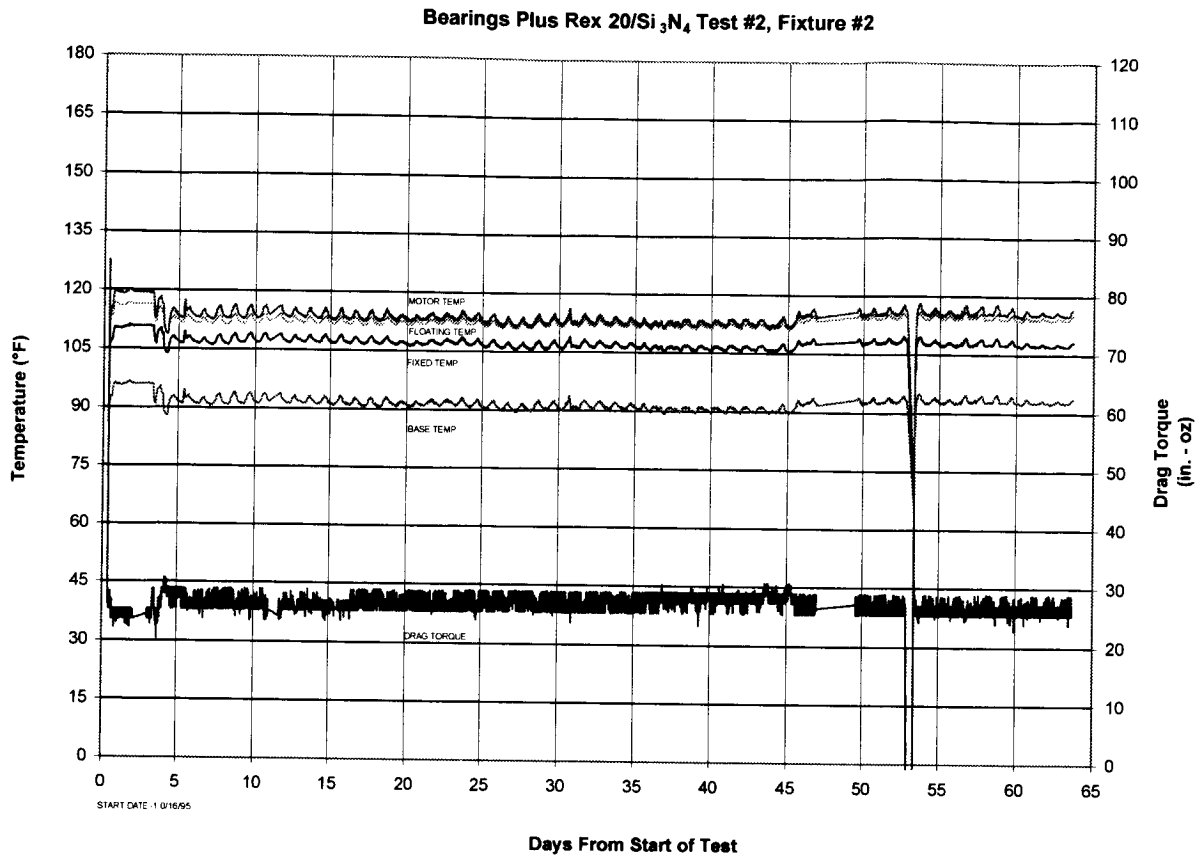
Figure 4. Rex 20/Si$_3$N$_4$ Test Torque and Temperature History

Rex 20/TiC Test Results

Beginning at 0.26 N-m (37 in-oz), the drag torque increased to the 0.35 to 0.39 N-m (50 to 55 in-oz) range, where it remained for the duration of test #1. The second test showed steady torque and temperatures for the remainder of the test period. The recorded torques, however, were considerably higher than expected, remaining in the 0.35 to 0.39 N-m (50 to 55 in-oz) range for the entire test. However, temperatures of the bearing cartridges and motor were at normal levels, leading to the conclusion that the amplitude of the torque readout was not accurate. Figure 5 shows the torque and temperature history of the test. Post-test examination for the first two tests revealed like-new components with very light running tracks and new, moist-looking grease. Some balls in each test had small areas of pitting in the TiC coating.

Bearings Plus Rex 20/TiC Test #2, Fixture #2

Temperature (°F)

Drag Torque (In. - oz)

FLOATING TEMP

FIXED TEMP

MOTOR TEMP

BASE TEMP

DRAG TORQUE

START DATE 11/3/96

Days From Start of Test
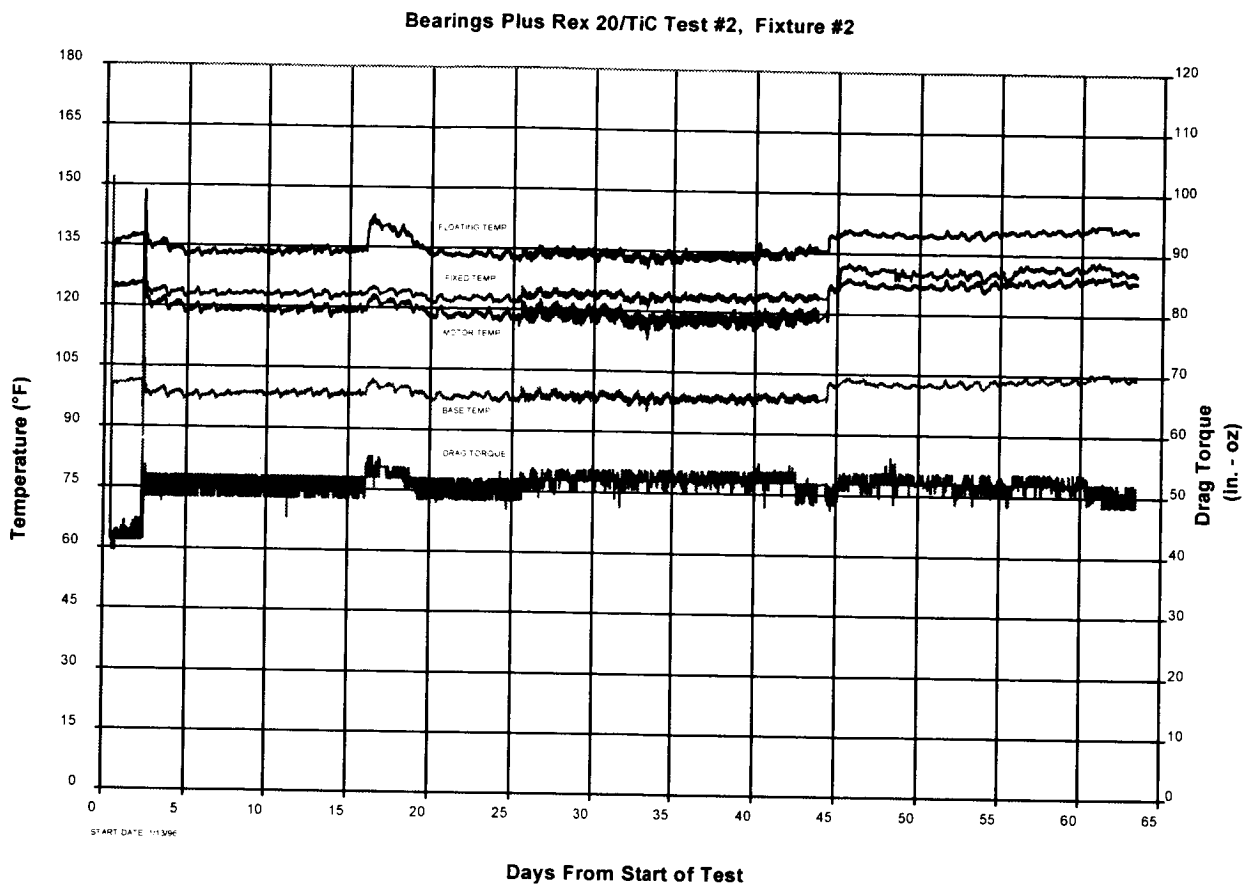
Figure 5. Rex 20/TiC Test Torque and Temperature History

In test #3, as in test #2, the torque, though steady, was considerably higher than expected, given the normal bearing and motor temperatures. In the post-test examinations, evidence of damage to some of the TiC coated balls was observed. As in the first two tests, there were a number of small pitted areas, but three of the balls had significant areas where the coating was removed. Energy-dispersive X-ray analysis results in the damaged area showed a large Fe peak and a very small Ti peak, suggesting that the majority of the TiC was removed. Dr. Mike Hilton sectioned one of the balls through the large damaged area and showed that the TiC coating had fractured and that the edges of the damaged area were continuing to fracture and flake off. It was concluded that pitted areas on the balls, attributed to incomplete polishing, acted as initiation sights for fatigue cracks in the TiC coating, resulting in pieces of coating being dislodged. The incomplete polish was due to sphericity changes caused by the high temperatures encountered during the coating and post-coating heat treatment. Subsequent changes in the processing of the balls, suggested by Dr. Mike Hilton, Dr. Winsup Park, Peter Ward, and Dennis Smith, allow Rex 20 balls of this size, 12 mm (15/32 in), to be coated with less change in sphericity, thus allowing a better finish on the TiC coating without sacrificing coating thickness.

Torques and temperatures were more controlled in test #4. Torques were in the 0.26 to 0.30 N-m (37 to 42 in-oz) range for the duration of the test and were quite constant. Temperatures tracked the torque signature well. Again, TiC coating damage was observed on several of the balls, but raceways showed only extremely light wear tracks. More pitted areas were observed on the balls of these bearings; however, the nature of the pits and areas of coating damage were similar.

Thermal Sensitivity Analysis

Because of the very low Coefficient of Thermal Expansion (CTE) of the Si_3N_4, a bearing with Si_3N_4 balls has greater sensitivity to temperature than does a bearing made of one steel. Two quantitative comparisons will be shown using a medium-series spindle bearing with a 25-mm bore having 10-12 mm (15/32 inch) balls. The first comparison will be the change in preload over a temperature range. The second comparison will be the difference in self-induced temperatures at high speeds. For space applications, conduction is the primary means of heat transfer, and self-induced runaway temperatures would generally limit how fast the bearings may operate.

Comparison #1 - Preload Sensitivity to Temperature

A hybrid bearing, using Si_3N_4 balls, introduces the possible loss of preload as temperatures rise because the Si_3N_4 grows less with temperature; hence, preload becomes less at higher temperatures. Conversely, preload would increase as temperatures reduce. The preload sensitivity analysis used the material properties of Table 2.

Table 2. Material Properties Used

	Modulus Pa (lb_f/in^2)	Poisson Ratio	CTE cm/cm/°C (in/in/°F)
Shaft	179E9 (26.0E6)	0.31	3.3 E-6 (5.9E-6)
Rex20	234E9 (34.0E6)	0.30	3.8 E-6 (6.8E-6)
52100	206E9 (30.0E6)	0.30	3.8 E-6 (6.8E-6)
Si_3N_4	317E9 (46.0E6)	0.26	0.9 E-6 (1.6E-6)

The Si_3N_4 density is 3.32 g/cc (0.12 lb_m/in^3). The density of 52100 and REX20 is 7.84 g/cc (0.283 lb_m/in^3).

The preload analysis was done using the Beta Gimbal Roll Ring Subsystem (BGRRS) program [2], developed by A.R. Leveille over the years.

Figure 6 compares an all Rex 20 bearing with the hybrid bearing for the case of a 178-N (40lb$_f$) room temperature mounted preload. For the monolithic Rex 20 bearing, as temperature increases, preload decreases at the slow rate of approximately 1.04 N per °C (0.13 lb$_f$ per °F). The hybrid bearing preload decreases at about **10X** the 1.04 N per °C (0.13 lb$_f$ per °F) rate, or about 10.4 N per °C (1.3 lb$_f$ per °F). The much steeper loss of preload with temperature does have a possible advantage in that the rapid fall-off of preload would tend to be more stabilizing and may prevent a runaway thermal condition.

Figure 6 also includes the effects of an inner race hotter than the outer race by 1.7 °C (3 °F) (3-DT), as well as the effect of an elastohydrodynamic (EHD) film thickness of 0.25μm (10 micro-inches) (10 EHD). This condition of EHD film and temperature difference is typical of the 6000-rpm operation of the 305 bearing application that is the basis for the study. Figure 6 illustrates that the influence of a 1.7 °C (3 °F) temperature difference across the bearing and the 0.25μm (10 micro-inch) film are both in the range of 13 to 22 N (3 to 5 lb$_f$).
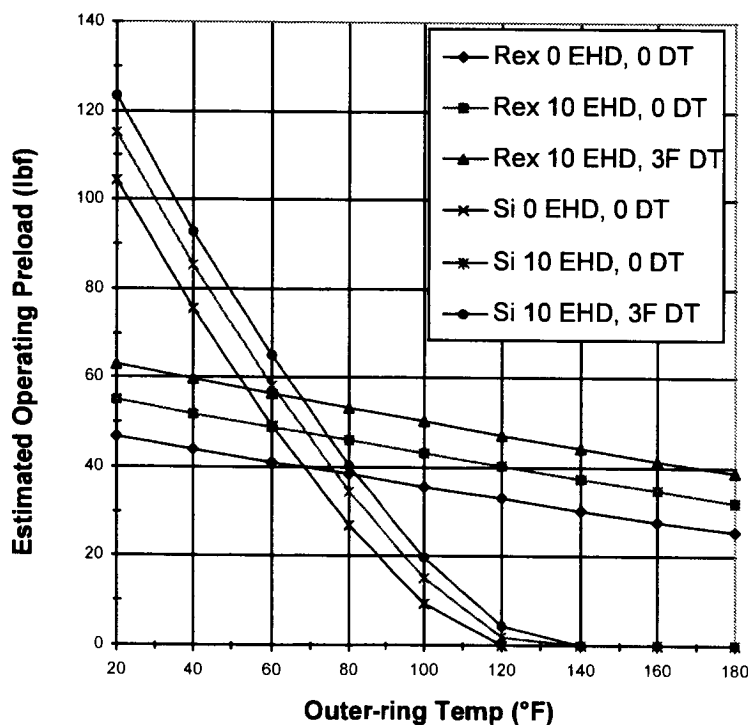

Figure 6. Preload Sensitivity Comparison

Comparison #2 - Self-induced Temperatures at High Speeds

Operating temperatures and temperature rise factors due to bearing friction losses were assumed based on application experience for a 305 size bearing made of 52100 steel. The point of these assumptions is to illustrate the thermal sensitivities for a range of operation that is realistic but not necessarily exact.

Figure 7 illustrates the drastic reduction that occurs with the use of the Si_3N_4 balls as speed increases. A significant driver is the reduced centrifugal ball forces that occur. In addition, the reduced size of contact area results in lower micro-slip friction.

The analytical tools used to perform the analysis of Figure 7 is beyond the scope of this paper and may be presented at a later date. The solution approach is simple enough. A set of operating temperatures are assumed. These assumptions then are fed into the BGRRS program that predicts total friction torque. The torque prediction is then applied to the temperature rise factors to predict temperatures. The process is repeated until the assumed conditions match the predicted.
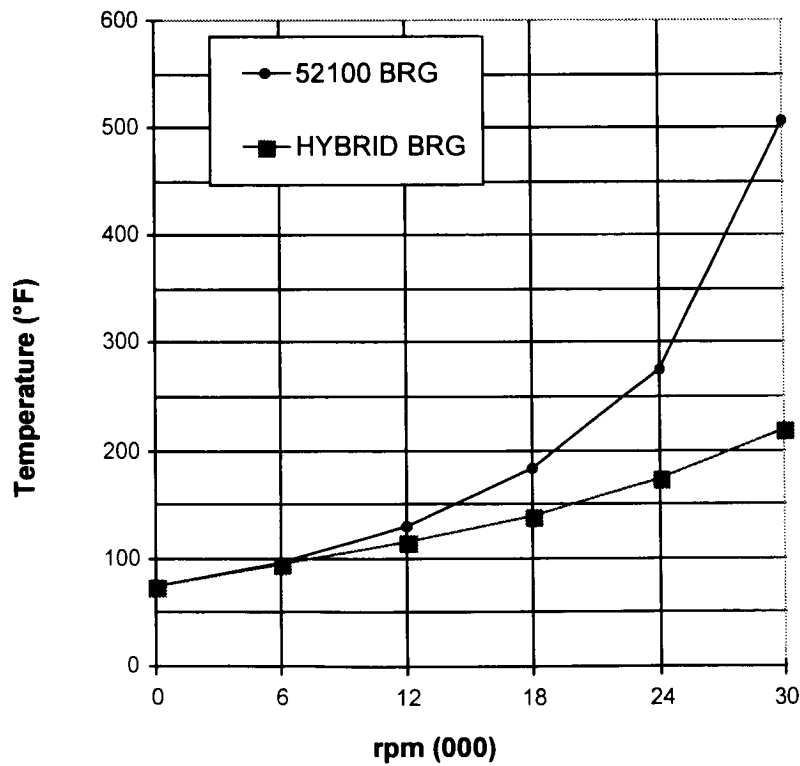

Figure 7. Comparison of Self-induced Temperatures at High Speed

Conclusions and Recommendations

Analysis Conclusions

- The baseline candidate had just enough capacity to support the 4068 N-m-s (3000 ft-lbf-s), 6509 N-m (4800 ft-lbf), CMG launch loads, but the reliability of 0.86 is unacceptable.

- Rex 20 bearings with TiC-coated Rex 20 balls have plenty of load capacity and high enough reliability to be considered for a 10-year mission.

- Rex 20 bearings with Si_3N_4 balls have slightly less capacity then the TiC-coated ball candidate, but it still has plenty of margin. The reliability of a 10-year mission is similar to the Rex 20/TiC, making it a close second choice.

- By selecting an appropriate preload at room temperature, it is possible to retain adequate preload at the highest temperatures without having an unacceptably high preload at the lowest operating temperatures when using Si_3N_4 balls. This is true even though the change in temperature preload is considerably more than with an all-steel bearing.

- At substantially higher speeds, the use of Si_3N_4 balls dramatically reduces the operating temperature with a commensurate extension of lubricant life.

Test Conclusions

- Rex 20/Si_3N_4 tests had the most consistent torques and temperatures during the 63-day tests. They also had the best-looking balls and raceways in the post-test examination.

- Rex 20/TiC tests were the next most consistent, once allowance was made for instrumentation noise. The Rex 20 raceways from these bearings were a close second; the raceways run with Si_3N_4 balls. However, some of the balls had evidence of coating loss in spots that were in the running tracks.

- The coating damage observed on the TiC balls was believed to have been caused by imperfections that resulted from incomplete finishing of the coating due to sphericity change during the post-coating heat treatment.

- 52100 bearings produced significant track wear and darkened grease during the same test duration.

Down Select Conclusion

Rex 20/Si_3N_4 was selected as the life test candidate.

References

1. Hilton, M.R, Ward, P.C., Leveille, A.R., Park, W., M.cClintock, D.A., Smith, D.W. "Rolling Contact Fatigue and Load Capacity Test is of M62 Bearing Steel," 32nd Aerospace Mechanisms Symposium, 13-15 May 1998.
2. Smith, D.W. "Contact Angle Optimization for Variable Load Applications," Rolling Element Bearing Symposium, 30 Apr 1997.
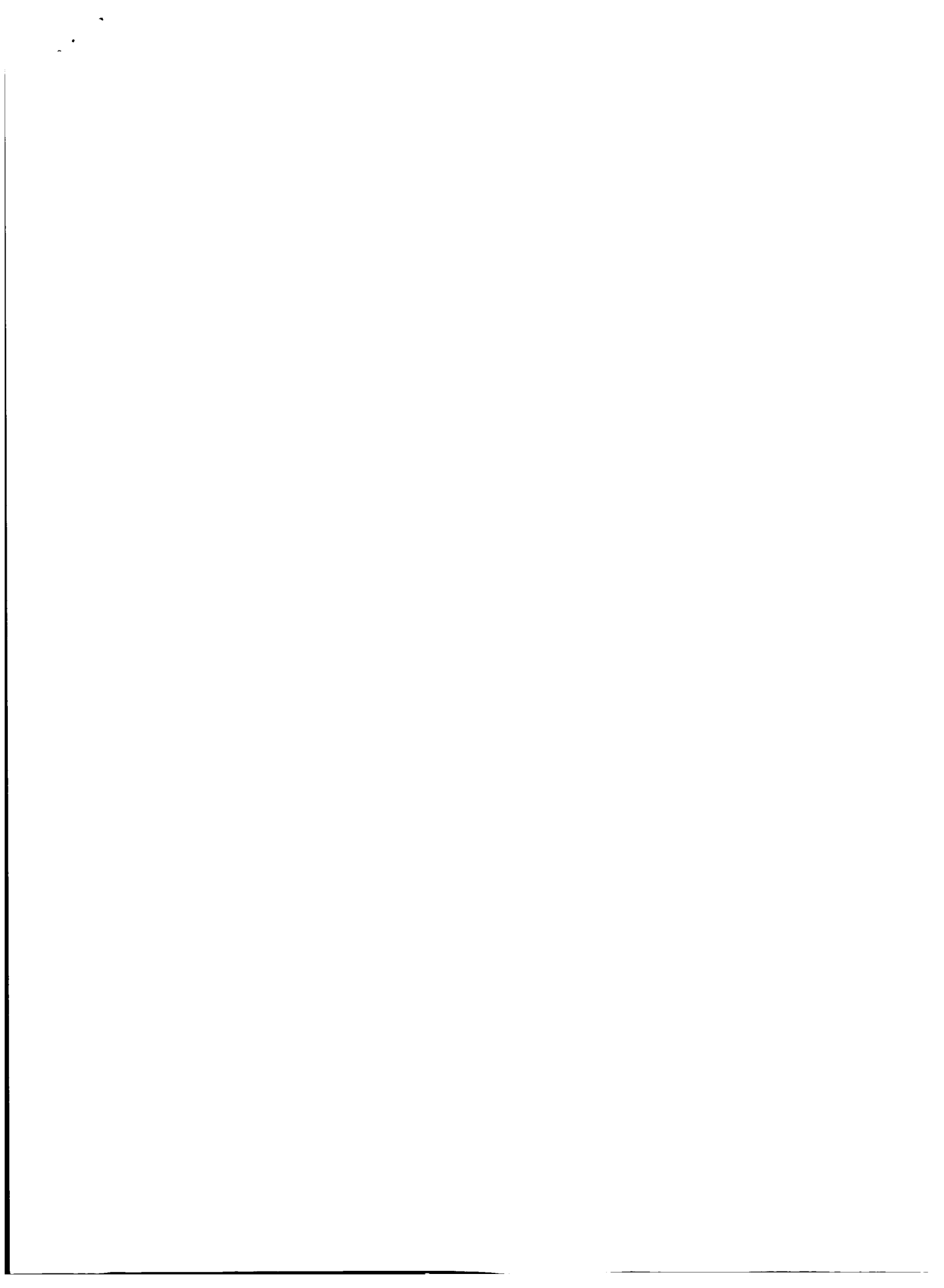
Rolling Contact Fatigue and Load Capacity Tests of M62 Bearing Steel

W. Park,* M. R. Hilton,* P. C. Ward,** G. W. Henderson,* A. R. Leveille,*
D. A. McClintock,+ D. W. Smith++

Abstract

A series of tests were conducted to determine the dynamic fatigue properties and static load capacity of M62 steel (Rockwell C hardness, HRC 66-67). Rolling contact fatigue tests used 207-size bearings having raceways made with the air-melted powder metallurgy version of M62 steel (aka REX20) and balls of Si_3N_4. The tests were conducted at 565.5 rad/s (5400 rpm) and 1882 MPa (273 ksi) with a lambda of 1. The tests showed that hybrid bearings had excellent fatigue resistance relative to all vacuum induction melted-vacuum arc remelted (VIM-VAR) 52100 steel bearings. Under the conditions run, the 52100 bearings had an L15.69 life of 181 h, while the hybrid bearings ran to 2600 h suspension without failures. The static load capacity was determined by conducting careful brinelling tests over a range below and above the compressive yield strength of the steel, which was measured for the first time. The data indicate that the static load capacity of REX20 at HRC 66-67 is between 3790 and 4140 MPa (550 and 600 ksi) mean contact stress. Separate launch vibration tests of a reaction wheel incorporating these hybrid bearings revealed no damage after the bearings were subjected to a stress level of 3780 MPa.

Introduction

The successful design of a high-cycle spacecraft mechanism that employs bearings requires that the bearing materials have at least two properties: high rolling contact fatigue (RCF) resistance to meet operational dynamic cycling requirements, and adequate static load capacity to survive launch loads. In recent years, test results have been reported for hybrid bearings consisting of Si_3N_4 balls and steel raceways in commercial machine tool spindles, in military bearing applications,[1] and in the Space Shuttle main engine liquid oxygen and fuel turbopumps.[2] Such hybrid bearings appear to provide good fatigue performance and to avoid metal-to-metal contact, which, in turn, retards the onset of lubricant degradation. Most of the hybrid bearing results reported to date use existing bearing steels (52100, 440C, M50, M50Nil), although Cronidur 30 steel is planned for use in the Space Shuttle fuel turbopump bearings.[3] However, bearing materials are of interest that can operate under higher stress with longer life. Recently, a powder-metallurgy high speed M62 tool steel, called VIM REX20, or CRU20, has emerged as a good candidate for improved bearings due to its high hardness (HRC 66-67) and wear resistance, fine carbide structure, and improved RCF performance. Early ball-on-rod fatigue tests have been

* The Aerospace Corporation, El Segundo, CA
** MPB Corp., Keene, NH
+ Timken Co., Canton, OH
++ Honeywell Inc., Phoenix, AZ

reported that indicate that this steel has very high fatigue resistance compared to either 52100 and M50 steels.[4]

In order to survive launch loads, the spacecraft mechanism designer must select a bearing size such that the static load capacity of the bearing material exceeds the stress levels expected during launch, to avoid brinelling damage. Such brinelling damage could generate torque noise in precision, torque-sensitive mechanisms. If the brinells are deep, the damage could also reduce fatigue life. Indeed, for spacecraft mechanisms, it is the launch loads that generally define the size of a bearing. The operational stresses are usually significantly lower, such that without the launch load requirements, a smaller bearing could be used to meet operational stress and fatigue requirements. Since bearing torque scales with bearing size, the need for a larger bearing to survive launch incurs a penalty of greater torque, and therefore greater power consumption, during the life of spacecraft vehicle. A larger bearing also incurs a weight penalty, both directly, in terms of the size of the bearing itself, and indirectly, in terms of the size of the surrounding support structure. When the higher modulus of Si_3N_4 relative to most steels is considered, it is realized that the incorporation of Si_3N_4 balls reduces the load capacity of the bearing system. This reduction occurs because higher Hertzian contact stresses develop in the steel raceway, with Si_3N_4 balls at a lower load compared to an all-steel system. Thus, if hybrid bearings are considered as a design option, it is desirable to incorporate another steel that has a higher static load capacity relative to baseline 440C and 52100 steels. In terms of potential load capacity, M62 steel is an attractive candidate as a ring material because of its high hardness (HRC 66-67).[5]

The spin bearings of momentum and reaction wheels, control moment gyroscopes, and related flywheels could benefit from hybrid bearing materials technology. However, fatigue data from full-scale bearing tests, and precise load capacity data for these newer materials, are sparse[6] or, in some cases, nonexistent. In order to obtain more information for design options, a series of tests and experiments were executed. In this paper, we report, for the first time, RCF data derived from full-scale bearing tests of Si_3N_4 balls with M62 steel raceways. Precise brinelling experiments were conducted on M62 steel plates which, combined with the first-ever obtained compressive yield tests of M62 at bearing-level hardness, were used to estimate the static load capacity of this steel.

Experimental Procedures

The Si_3N_4 ball material used in this study was an MgO-doped, hot isostatically pressed version of the ceramic.[7] Grade 3 balls were used. The balls were inspected by the supplier under 3x magnification using fluorescent dye penetrant. The M62 steel used in this study was primarily the Crucible Steel REX20 version of this material. REX20 is a powder metallurgy product–air-melted, gas-atomized powders, hot isostatically pressed into 100% dense billets, and subsequently forged to bar stocks. For RCF tests, a vacuum induction melted (VIM) version of REX20 steel, known as CRU20 (i.e.,

VIM REX20), was used to make the outer raceways, due to material availability issues for this bar stock size. The M62 steels were quenched and triple tempered to achieve a Rockwell hardness of HRC 66-67, with a retained austenite of less than 5 vol% as measured by x-ray diffraction. VIM-vacuum arc remelted (VAR) 52100 (HRC 61) and 440C (HRC 57) steels were used as baseline comparison materials in the indentation and compressive yield tests. Cold stabilization procedures were executed to minimize retained austenite content in these steels. For the RCF studies, only the VIM-VAR 52100 steel was used as a baseline. Additional hardness levels were prepared of 52100 and 440C steels for the indentation and compressive yield tests by adjusting the tempering of the steels. In the case of 52100 steel prepared at HRC 65, untempered 52100 was used. For 52100 at HRC 61, steel lots with varying retained austenite levels (as measured by x-ray diffraction) were prepared by adjusting the austenitization temperatures preceding quenching.

RCF tests were executed at the Timken Research Facility using 207-size bearings run at 565.5 rad/s (5400 rpm). The RCF fixture can test four bearings, as shown in Figure 1. The bearings were thrust loaded to a mean Hertzian contact stress of 1882 MPa. MIL-L-7808 lubricant, filtered to 3 µm, was used at a flow rate of 0.95 l/min/bearing. The lubricant inlet temperature was 71°C. These test conditions resulted in a lambda of 1. (Lambda is the ratio of the calculated lubricant film thickness divided by the average of the surface roughness). Twenty-four bearings were tested per material type, in six groups with four bearings in each group. A "first-in-four" sudden-death protocol was used for each group. That is, when one of the four bearings failed by spallation, the other three bearings were suspended. Weibull analysis of the six failures would lead to an estimate of an L15.91 life with 65% confidence bands. Bearings were run to failure or to 2600 h suspension. The following materials groups were tested: (1) all 52100 bearings; (2) Si_3N_4 balls/REX20 inner raceways/ CRU20 outer raceways.

Ball-on-plate indentation tests of REX20, 52100, and 440C steels at various hardness levels were performed. A ball of 11.93 mm diameter, made of either Si_3N_4 or TiC-coated REX20, was used as the indenter to investigate the load-bearing capacity of these bearing steels in more detail. The test specimens were steel disks of 12.7 mm diameter and 6.4 mm thickness. The following hardness levels were tested: for the REX20 material–HRC 57, 61, 67; for 52100–HRC 61, 63, 65; and for 440C–HRC 57, 60, 60, 61. The disks were polished to a mirror finish using 1 µm diamond paste. A loading fixture to hold the balls was built of 17-4 steel, as shown in Figure 2. The fixture has a spherical seat with a small hole at the center to prevent single-point loading of the ball. A brass ring was used to retain the ball. A mating sample holder for the disks was also made. The ball fixture was attached under the cross-head of an Instron universal test frame, and the disk holder was attached to the top of a 4448 N (1000 lb) compression load cell.
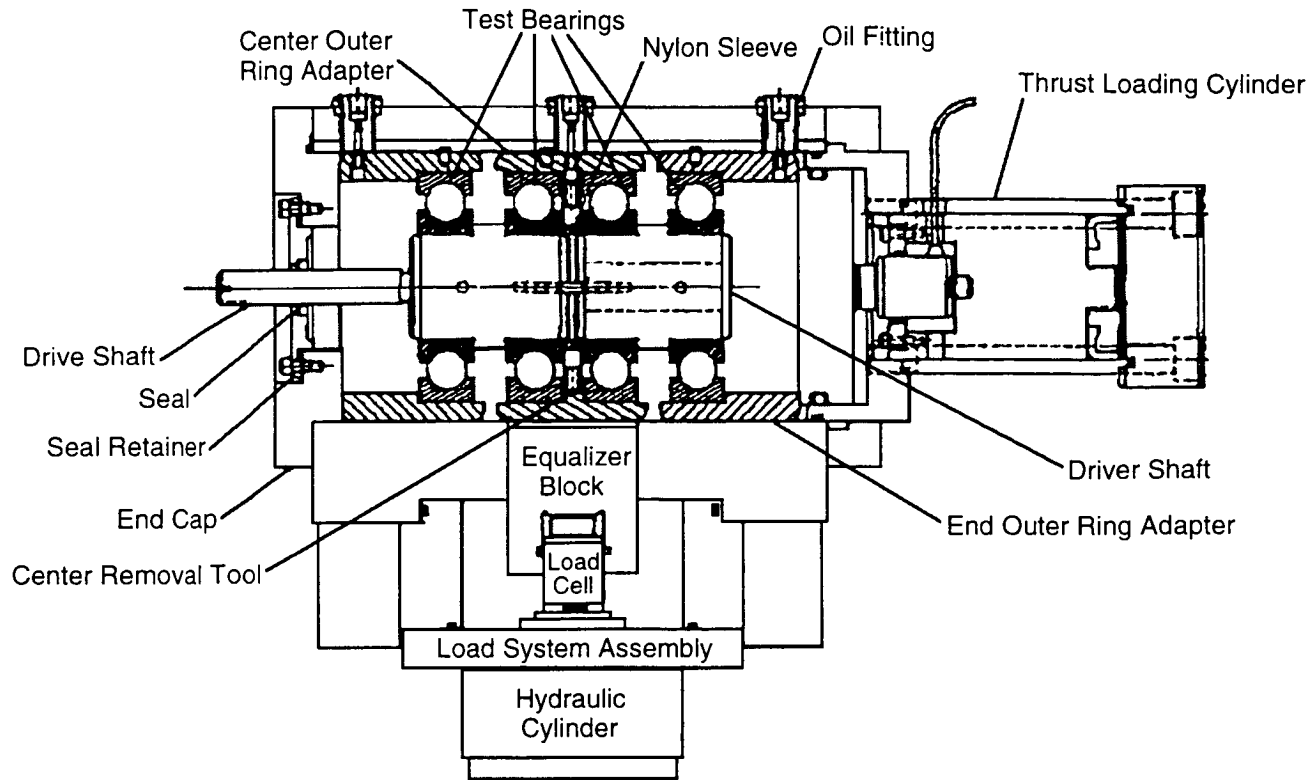
Figure 1. Sketch of the RCF fixture

Indent tests were performed on the Instron load frame in the compression test mode. The range of the loads for each hardness level of these steels was selected to ensure the formation of a sizable plastic brinell mark at the highest load for each material condition. Prior to the tests, the fixture was subjected to a higher load (4450 N) than loads of the test series. This higher load allowed the ball to seat by localized yielding of the 17-4 steel, which had a hardness of HRC 52 due to aging at 480°C. During the tests, the sample disks were wiped with a cotton swab that had been wet with methanol just prior to loading. The disks were then put into the sample holder. The indentations were made by manually moving the indenter fixture–which was attached to the cross-head of the test frame–very slowly to the steel sample disk, until the desired load was reached. The load was measured by the load cell, which was calibrated with 10 4.54 kg (10 lb) precision weights before the test. The load was released by lifting the cross-head at a rate of 0.5 mm/min after holding it for 5 min. The load relaxation during the hold time was minimal, usually in the range of 22 to 44 N. Multiple indentations were made for a given loading condition. For each indentation, a mean Hertzian contact stress was calculated, based on elasticity. Actual mean contact stresses were somewhat lower than the elastic Hertzian stresses at higher loads due to plastic brinelling. However, the difference was negligible in the load range of interest. The modulus and Poisson's ratio values used for the Hertzian equation are listed in Table 1.

240

17-4 PH Loading Fixture

Indenting Ball (15/32 inch)

Brass Retainer Ring

17-4 PH Sample Holder
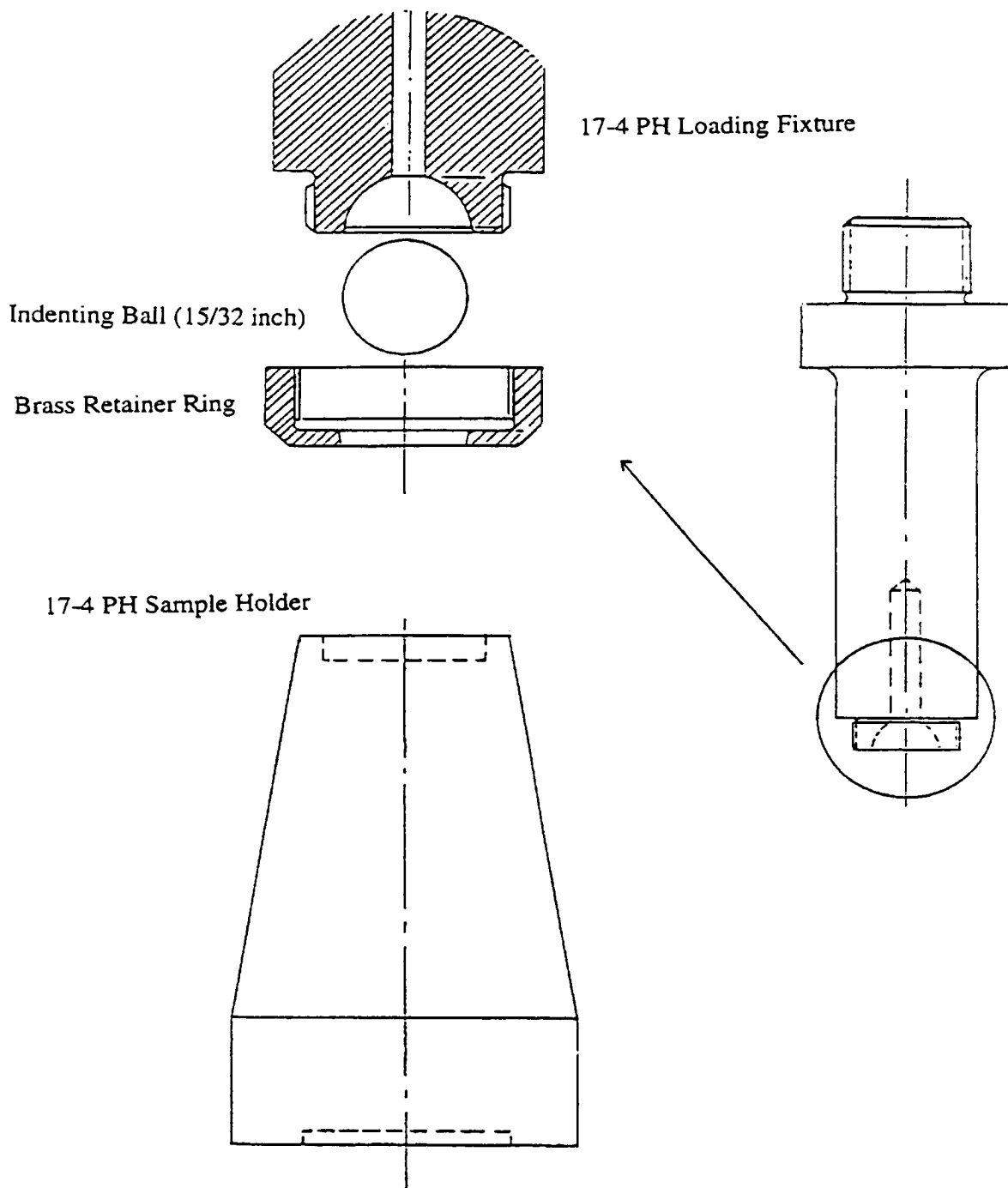
Figure 2.   Sketch of the indentation test fixture

Indentation depths were measured on a Dektak 3030 Surface Profile Measuring System using a 12.5 μm radius diamond-tipped stylus loaded to 30 mg. Scanning was done at medium speed, with a scanning width of 2 mm at a resolution of 4 μm. Scans were made in one direction until the dead bottom was found and recorded. The sample was then rotated 90°, and the process was repeated. The larger of the two depth values measured in this way was selected for the indentation depth.

241

Table 1.   Materials values used for Hertzian contact equations

Material	Modulus	Poisson's Ratio
Si_3N_4	310.3 GPa	0.26
REX20	234.4 GPa	0.29
52100	206.8 GPa	0.29
440C	200.0 GPa	0.284

The compressive yield strength tests of these steels were performed with a Riehle test machine using cylindrical specimens of 25.4 mm length and 12.7 mm diameter, following ASTM Test Standard Procedure E9.[8]

To verify the estimates of load capacity using indentation and yield strength results, a confirmation test was executed. During this test, a minimum load capacity was verified by exposing bearings to random vibration loads to simulate launch load requirements. Hybrid 101-size bearings of Si_3N_4 with REX20 raceways were prepared and installed in a 81.36 N-m-s (60 ft-lbf-s) reaction wheel. This wheel type has been extensively tested and analyzed over the years. A previbration induced vibration (IV) test was conducted to characterize the torque performance of the bearings. The reaction wheel was shaken to achieve maximum expected vibration loading on the bearings, simulating launch loads with margin. A postvibration IV test was performed. The bearings were disassembled and then inspected visually.

Results

The RCF tests of VIM-VAR 52100 steel bearings resulted in predominantly inner raceway failures. Failure times and modes are listed in Table 2. Typical fatigue spalls are shown in Figure 3. The L15.6 lifetime (58.7 million cycles, 181 h) is consistent with estimates of expected lifetime using procedures and materials factors published in the literature for the bearing stress level and speeds employed.[9] Thus, it can be concluded that the current tests provide a direct relative factor assessment of RCF performance of the hybrid bearings as compared to 52100 steel used in the industry. Figure 4 shows the relative lifetimes of the all-52100 steel bearings vs the Si_3N_4-REX20 bearings, including 65% Weibull confidence bands.

The hybrid bearings of NBD-200 Si_3N_4 balls with REX20 raceways ran to ~2600 h (846 million cycles) without failure. Since there were no failures, an absolute relative materials factor cannot be determined. However, a minimum value of the relative materials factor can be estimated by assuming that failures would occur just beyond the suspension time and conservative Weibull slope of 1.5. Based on the existing data, it can be expected that the hybrid bearing (Group B in Figure 4) has a relative improvement factor of 5, with a 90% confidence over the all VIM-VAR 52100 bearings (Group A in Figure 4).

242

Table 2. Fatigue lifetimes and observed failure modes

Bearing Group	All 52100 Steel Bearings			Hybrid Bearings: REX20 Inner Raceways, Si$_3$N$_4$ Balls, CRU20 Outer Raceways		
	Revs 10^6	Hours	Failure Mode	Revs 10^6	Hours	Failure Mode
1-4	5.626	17	IR-Inclusion	852	2630	Suspension
5-8	41.094	127	OR-Inclusion+ Ball-PSO	902	2784	Suspension
9-12	109.877	339	IR-Inclusion	852	2630	Suspension
13-16	15.118	47	IR-PSO	846	2611	Suspension
17-20	117.969	364	Ball-Inclusion	846	2611	Suspension
21-24	294.918	910	IR-Inclusion	846	2611	Suspension
L15.91	58.747	181		857	2611	
Slope	0.716					

Failure location: Ball, inner raceway (IR) or outer raceway (OR)
Failure mode: Inclusion or point source origin (PSO)
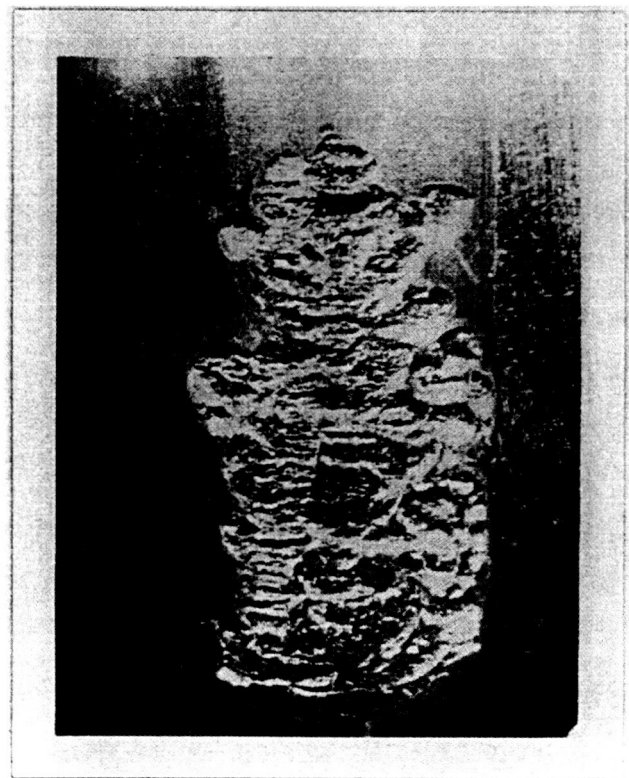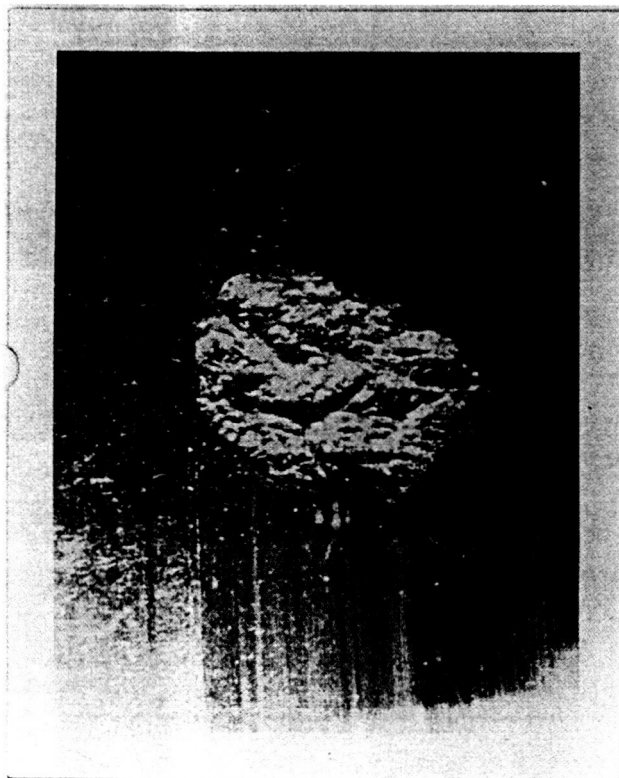


Figure 3. Typical micrographs of 52100 race spalls
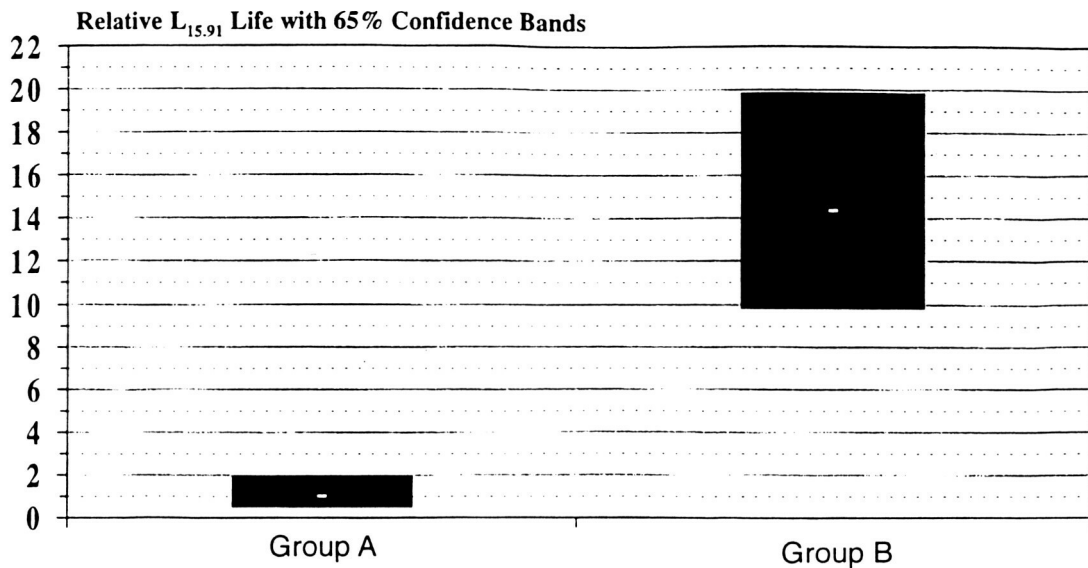
Figure 4. Relative L15.91 fatigue life of all-VIM-VAR 52100 (Group A) and Si$_3$N$_4$-REX20 hybrid (Group B)

Indentation test results of REX20 with different hardnesses are shown in Figure 5 as a plot of dp/D vs mean contact stress. A normalized depth parameter, dp/D, is used, where dp represents the deepest indentation depth measured by profilometer, and D represents the ball diameter. The data, as expected, show an increase with hardness in the contact stress required to create an indentation of a particular depth. These particular data show the importance of requiring a high hardness for M62 steel. As the hardness decreases from HRC 67 to HRC 60, the resistance to brinelling decreases by approximately 690 MPa (100 ksi) or more.

Bearings engineers generally use a dp/D value of 0.0001 to define the static load capacity. This is a fatigue-driven definition, with an understanding that brinelling damage greater than a dp/D of 0.0001 is believed to degrade fatigue life. However, a study by Leveille and Murphy[10] has shown that a more stringent requirement is advisable for torque-noise-sensitive applications, such as instrument bearings. In that study, the low speed torque signatures of 440C and 52100 bearings were measured before and after increasing the levels of static loading. Torque disturbances became apparent after static loading that created calculated dp/D values between 0.00003 and 0.00005. If we use a dp/D of 5 x 10^{-5}, the static load capacity of REX20 at HRC 67 is given by the mean contact stress of 4033 MPa (585 ksi).

In Figure 6, the dp/D vs mean contact stress plots for REX20, 52100, and 440C steels are compared at their typical usage hardness for bearing applications. The mean contact stresses for an indentation size of dp/D = 5x10^{-5} are 4033 MPa (585 ksi) for REX20-67, 3343 MPa (484 ksi) for 52100-61, and 2620 MPa (380 ksi) for 440C-57. These results show that the load-bearing capacity of REX20 is clearly higher than the

244

capacities of 52100 and 440C steels. It is also noted that the load-bearing capacities of 440C and 52100 steels are higher than those previously accepted for these steels (2275 MPa–2550 MPa [330–370 ksi]). The cold stabilization procecures used on these steels resulted in a lower retained austenite content than was typical of circa 1970 specimens. A lower reatined austenite content would account for higher yield strengths and load-bearing capacities.
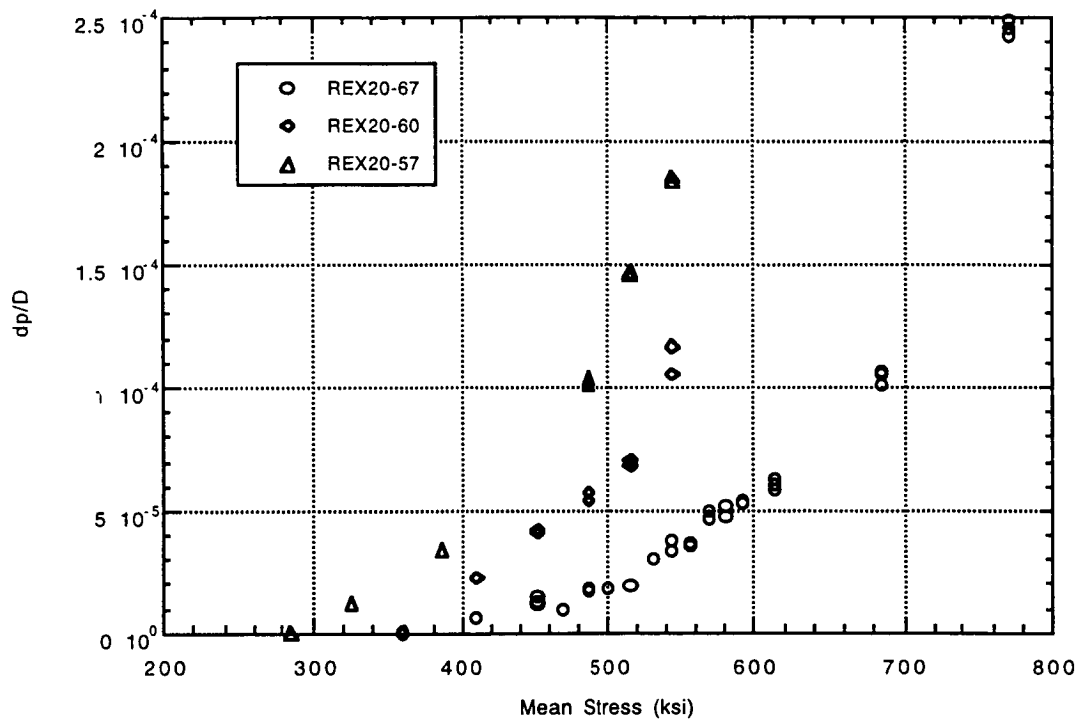

Figure 5. dp/D plot vs mean contact stress for silicon nitride ball indentations on REX20 steel plates of three conditions, with hardness ranges from HRC 57 to HRC 67. HRC 67 represents the typical heat treatment condition used for bearing applications.

Figure 7 shows the dp/D vs mean contact stress for 52100 steel of different hardness levels (HRC 61, 63, and 65). HRC 61 represents the normal hardened and tempered condition used for bearing applications. HRC 65 samples were in "as-quenched" condition, and HRC 63 samples were produced by under-tempering the HRC 65 samples at 175°C. Unlike the REX20 plots in Figure 5, the increase in the hardness over HRC 61 does not result in corresponding increase in the load-bearing capacity in 52100 steel.

The results of the compression tests are shown in Figure 8. The compressive yield strengths as a function of the Rockwell C hardness are plotted for REX20, 440C, and 52100 steels. REX20 specimens with HRC 63 and 60 were prepared by over-tempering the fully hardened and tempered REX20 (HRC 66-67). The 440C steel at HRC 58 and the 52100 steel at HRC 61 represent the typical hardened and tempered conditions for bearing applications. Lower hardness specimens (440C at HRC 55 and 52100 at HRC 57) were prepared by over-tempering, while higher hardness specimens went through no tempering (440C at HRC 61) or under-tempering (52100 at HRC 63). Some of the 52100 specimens (denoted as 52100-HT1 and 52100-HT2) were heat treated differently compared to the standard bearing steel, but at comparable hardness levels of HRC 61 to 63.
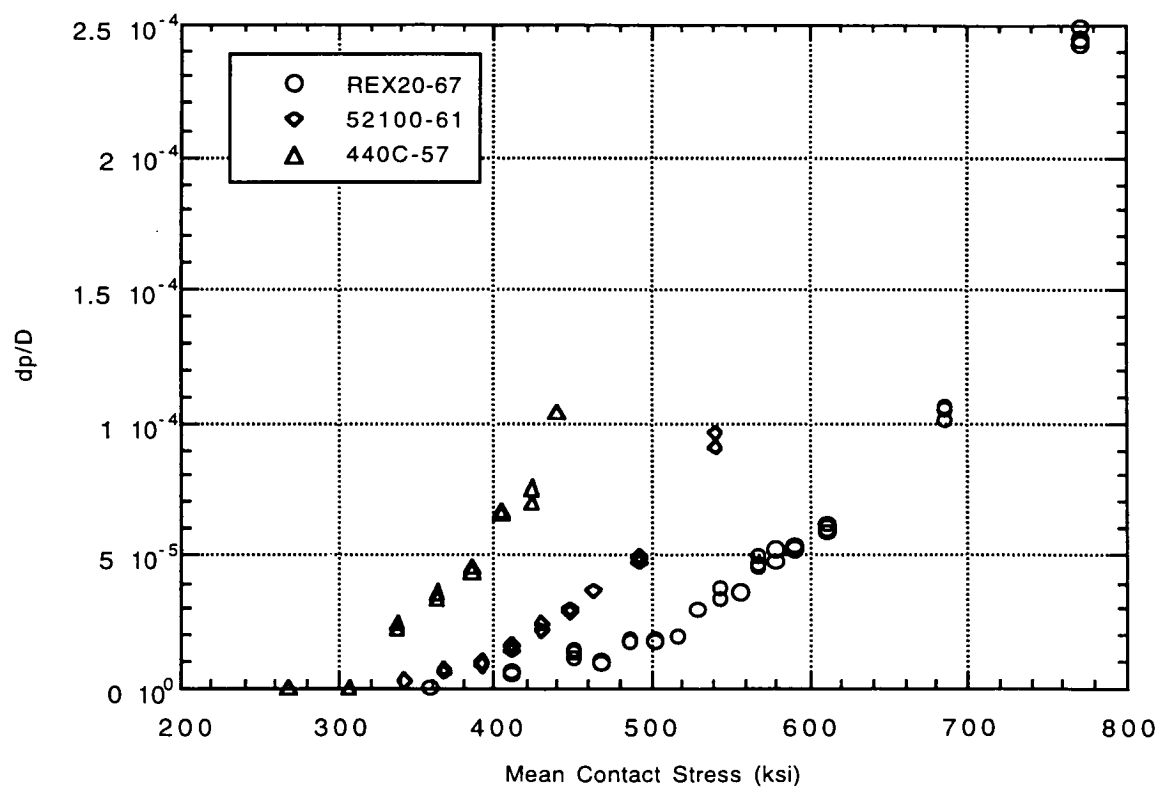

Figure 6. dp/D vs mean contact stress plot for silicon nitride ball indentations on steel plates to compare the performance of three steels at typical usage hardness levels and heat treatments: 440C at HRC 57, 52100 at HRC 61, and REX20 at HRC 67.

The compressive yield strength values of REX20 fit into the straight line that represents the linear relationship experimentally established for high speed tool steels.[11] At fully hardened and tempered conditions of HRC 66-67, REX20 has compressive yield

246

strengths ranging from 3344 to 3500 MPa (485–508 ksi). The 52100 and 440C steels also show linear relationships between the compressive yield strength and the hardness, but the slopes are lower than the slope of the high speed tool steels. The compressive yield strength of 440C at HRC 58 is about 2068 MPa (300 ksi), which agrees with published data.[12]
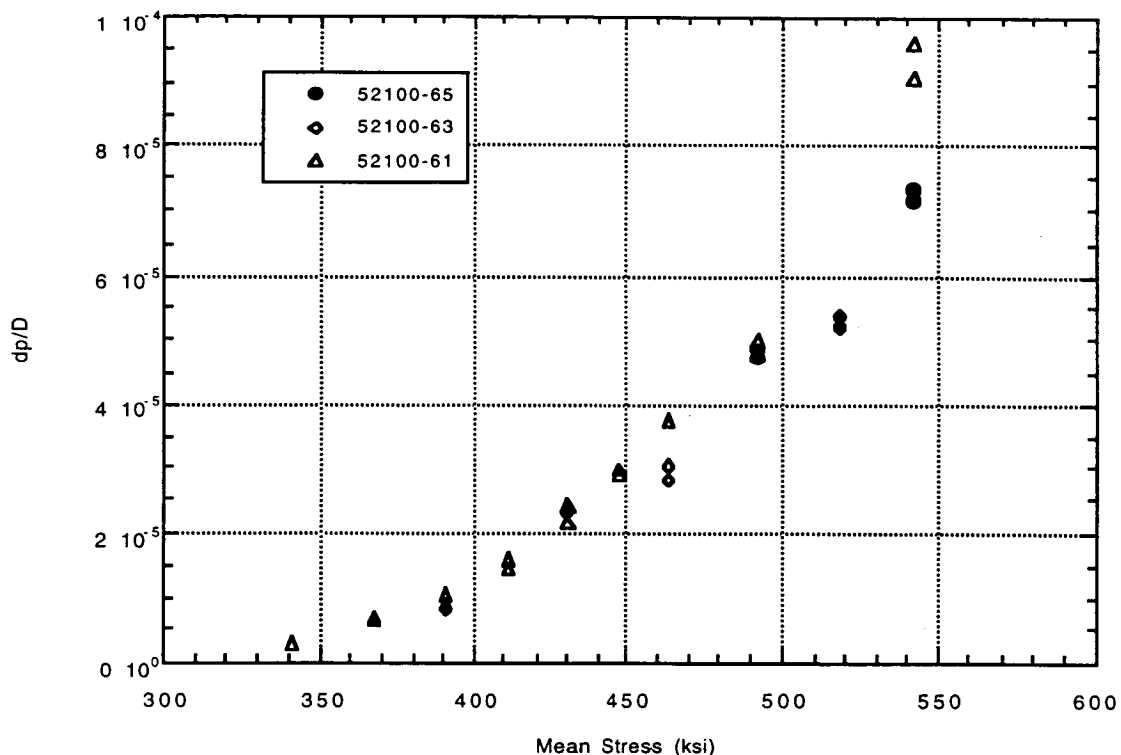

Figure 7. dp/D vs mean contact stress plot for silicon nitride ball indentation on 52100 steel plates at three hardness levels: HRC 65, 63, and 61

The 52100 steel heat treated according to the standard bearing application has a compressive yield strength of 2275 MPa (330 ksi) at HRC 61. It should be noted that substantially different compressive yield strengths can be obtained in 52100 steel at the hardness range of HRC 61 to 63 (as low as 1586 MPa) due to different microstructures that resulted from different heat treatments. When the steel contains a large amount of retained austenite that is softer than the martensite phase, the austenite phase starts to yield at a lower stress level. It then transforms into a hard martensite phase as it deforms, resulting in rapid strain hardening. Published data on the compressive yield strength of 52100 steel are very limited, with poor correlation to the hardness and the microstructure, making the comparison of our data to the literature not feasible.

The hybrid 101-size bearings inserted in the reaction wheel were subjected to vibration tests that resulted in a calculated mean contact stress of 3778 MPa (548 ksi). The bearings did not exhibit increased torque in postvibration IV tests. Inspection of the disassembled bearings did not reveal damage.
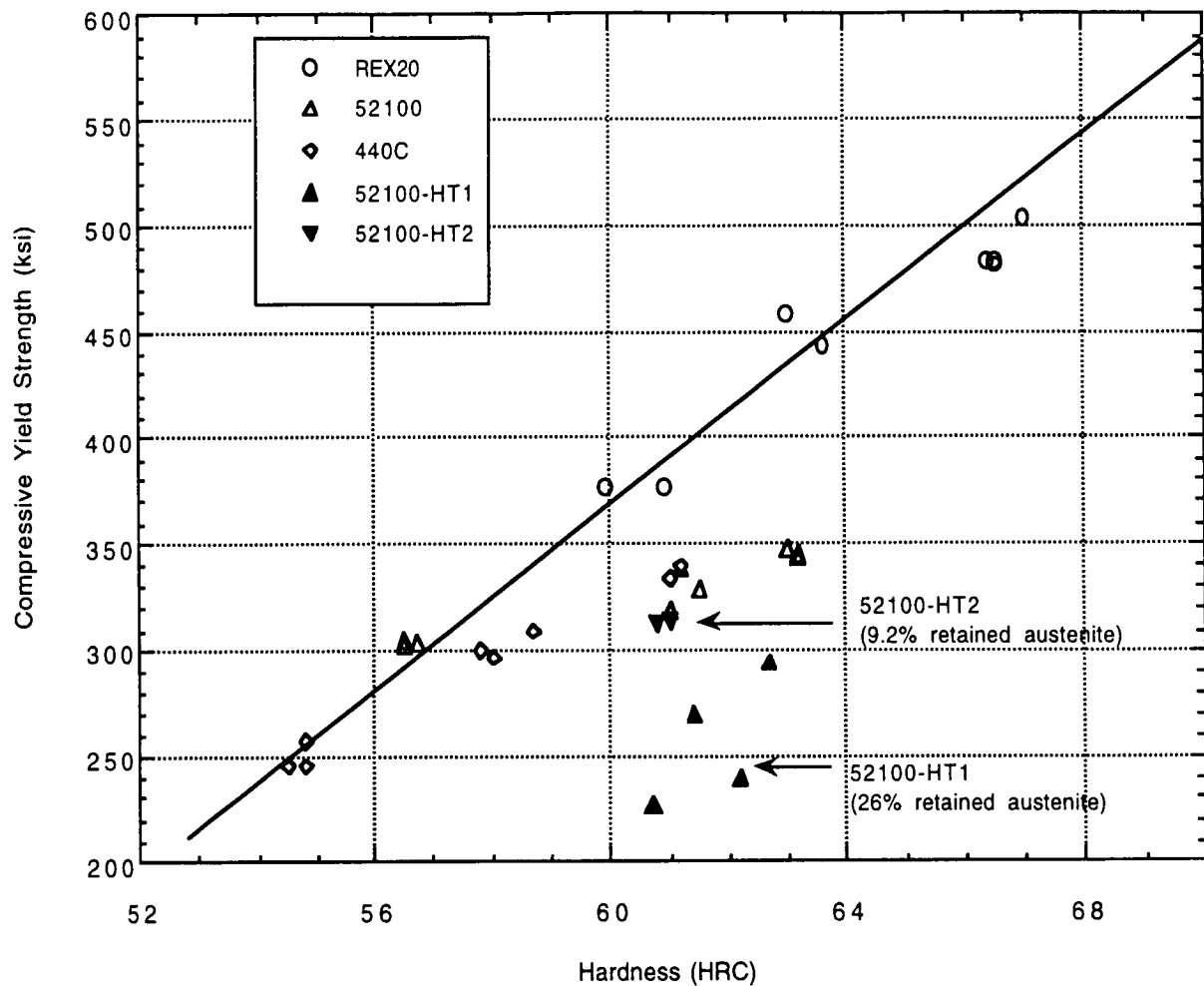

Figure 8. Compressive 0.2% offset yield strength of 440C, 52100, and REX20 steels at various hardness levels, and also, in the case of 52100 steel, different retained austenite volume percentages at the same hardness

Discussion

The bearing-level RCF tests qualitatively reaffirm improved performance of REX20 steel that has been reported in ball-on-rod tests.[4] For the stress level tested, the REX20 has a life improvement factor of 5 with statistical confidence. It is hypothesized that the superior fatigue life observed for REX20 is due to the high hardness of the material, particularly of the martensitic matrix, combined with the fine carbide size and narrow carbide size distribution that is achieved with hot isostatically pressed powder metallurgy material. It is anticipated that the VIM CRU20 version of the M62 steel may have superior fatigue life in terms of the low-end tail of the life distribution. Since the present REX20 tests were run to suspension, we do not know the characteristics of the low-end tail of the life distribution.

The Si_3N_4 balls ran without failure in the test conditions studied. This result is consistent with other full-scale bearing studies of Si_3N_4 with other steels such as 52100 steel.[6] At a mean contact stress of ~1965 MPa (285 ksi), inner raceway failures were observed in those studies. However, at higher mean stress levels, i.e., 2413 MPa (350 ksi), some studies have reported occasional ball failures. Tests are planned that will evaluate the performance of Si_3N_4 balls with REX20 steel raceways at 2310 MPa. These tests are important, because 2310 MPa (335 ksi) in this hybrid bearing represents an equivalent load condition to an all-52100 bearing tested at 1882 MPa (273 ksi).

Ball-on-plate indentation test results show that the static load-bearing capacity of REX20 at HRC 67 is about 100 ksi higher than that of 52100 steel at HRC 61. It is possible to harden 52100 steel to HRC 65 by introducing a high carbon untempered martensite microstructure. However, our indentation tests show that there is no increase in the load capacity of 52100 at HRC 65 compared to 52100 at HRC 61. It is believed that the untempered martensite structure of 52100 at HRC 65 contains higher retained austenite compared to fully tempered 52100 at HRC 61. Precision retained austenite measurements are planned to elucidate this hypothesis further. The untempered martensite phase in 52100-65 is harder than tempered martensite in 52100-61, but the presence of the soft retained austenite phase makes it yield at a comparable stress level compared to that of 52100-61.

For REX20 steel of HRC 67, values of dp/D between 3 and 5 x 10^{-5} were obtained in a mean Hertzian contact stress range in excess of 3450 MPa (500 ksi). A prior study has shown that these values of dp/D can be sufficient to cause torque noise, as opposed to the classical definition of the static capacity limit of dp/D = 1 x 10^{-4}, which defines the level of damage that is believed to degrade fatigue life.[10] In our study, independent ball-on-plate experiments were also conducted in which visual measurements of indent width instead of depth were obtained. These experiments, conducted in a separate facility of the authors, agreed with the aforementioned test results. In addition, vibration tests of a reaction wheel using REX20 bearings were performed. The vibration tests subjected the bearings to a calculated stress of 3778 MPa (548 ksi). Post-test analyses revealed no damage.

The compressive yield strength data of REX20 steels at HRC 66-67 agree with data on similar tool steels. The values obtained for 440C steel also agree with published data. As a function of hardness, these differing steels follow different linear relations. These steels are, in fact, different classes of steel, so this result should not be surprising. The influence of retained austenite content on the yield strength, typified by the data obtained for 52100, has been noted before, but its meaning is worth reemphasizing: specifying hardness to achieve desired static load capacity and fatigue performance is not enough. One has to specify a maximum allowable retained austenite content to be assured that the necessary static load capacity will be achieved by the steel of a particular Rockwell hardness.

Conclusions

A series of tests have been conducted to determine the dynamic fatigue properties and static load capacity of M62 steel. The high hardness (HRC 66-67) of the steel makes it an attractive candidate as a raceway material in hybrid bearings using Si_3N_4 balls. RCF tests with 207-size bearings showed that hybrid bearings using raceways of the air-melted powder metallurgy version of M62 steel (aka REX20) with Si_3N_4 balls had excellent fatigue resistance relative to all VIM-VAR 52100 steel bearings. Under the conditions run, the 52100 bearings had an L15.91 life of 181 h, while the hybrid bearings ran to 2600 h suspension without failures. The static load capacity was determined by conducting careful brinelling tests over a range below and above the compressive yield strength of the steel (~3450 Mpa [~500 ksi]), which was measured for the first time in compression tests. The data indicate that the static load capacity of REX20 at HRC 66 is between 3790 and 4140 MPa mean contact stress (550–600 ksi), assuming a torque-noise-sensitive criterion. The brinelling data are consistent with the compressive yield data via a von Mises criterion that predicts the onset of deformation under Hertzian contact to occur at 1.1 times the yield strength. Separate launch vibration tests of a reaction wheel incorporating these hybrid bearings revealed no damage after subjecting the bearings to a stress level of 3778 Mpa (548 ksi). The compressive yield data also reaffirmed the importance of specifying and minimizing the retained austenite values of the steels–hardness alone is not sufficient.

Acknowledgments

References

1. ARPA Ceramic Technology Insertion Program, ACTIP Annual Review, Aug 25-26, 1997, Annapolis, MD. Program Manager: Dr. Bill Coblenz, Tel: 703-696-2288.
2. R. W. Bursey, "Space Shuttle Main Engine Turbopump Applications", ACTIP Annual Review, Aug 28-29, 1995, Annapolis, MD.
3. H. A. Chin, R. W. Bursey, D. D. Ehlert, R. Biroscak, E. Streit, and W. Trojahn, "Cronidur 30 – An Advanced Nitrogen Alloyed Stainless Steel for Advanced Corrosion Resistant Fracture Tough Cryogenic Bearings", 1994 Earth-to-Orbit Conference, Univ. of Huntsville and NASA MSFC, pp 321-330.
4. P. K. Pearson, J. H. Moll, C. J. Hannigan, D. R. Atwell, "Evaluation of P/M Tool Steels for Bearing Aplications", 1994 Int. Conf. & Exposition on Powder Metallurgy & Particulate Materials, 8-11 May, 1994, Toronto, CA MPIF, Princeton, NJ.
5. Crucible Data Sheet, Issue #3 on CPM REX20, Crucible Specialty Metals, Syracuse, NY.
6. (A) Y. P. Chiu The Torrington Company, "Rotating Beam Fatigue Testing and Hybrid Ceramic Bearings", Air Force Wright Laboratory Technical Report, WL-TR-95-4088, July 1994. (B) M. M. Dezzani, P. K. Pearson, The Torrington Company, "Improved Hybrid Bearings", Air Force Wright Laboratory Technical Report, WL-TR-95-4084, Dec 1994. (C) H. I. Burrier Jr., C. Burk, Norton Advanced Ceramics, "Ceramic Bearing Developemnt—Vol.1: Fatigue and Wear Testing of NBD-200 Silicon Nitride Balls", Air Force Wright Laboratory Technical Report, WL-TR-96-4015, March 1995.
7. Cerbec NBD-200 material, Norton Advance Ceramics, East Granby, CT 06026. Tel: 860-653-8071.
8. ASTM, "E 9: Standard Test Methods of Compression Testing of Metallic Materials at Room temperature", Annual Book of ASTM Standards, Vol. 03.01.
9. STLE Life Factors for Rolling Bearings, E. V. Zaretsky, Ed., STLE, Park Ridge, IL, (1992).
10. A. R. Leveille and J. J. Murphy, "Determination of the Influence of Static Loads on the Output Torque of Instrument Ball Bearings", presented at the Charles Stark Draper Laboratory International Ball Bearings Symposium, June 5 1973.
11. P. Bleiss and R. Wähling, "Toughness Comparison between Vacuum Sintered Plus Forges PMS T15 and Conventional Tool Steels", Metal Powder Report, Nov. 1989, p 740.
12. ASM International, Metals Handbook, 10th Ed. Vol. 1, 1990, Materials Park, OH.
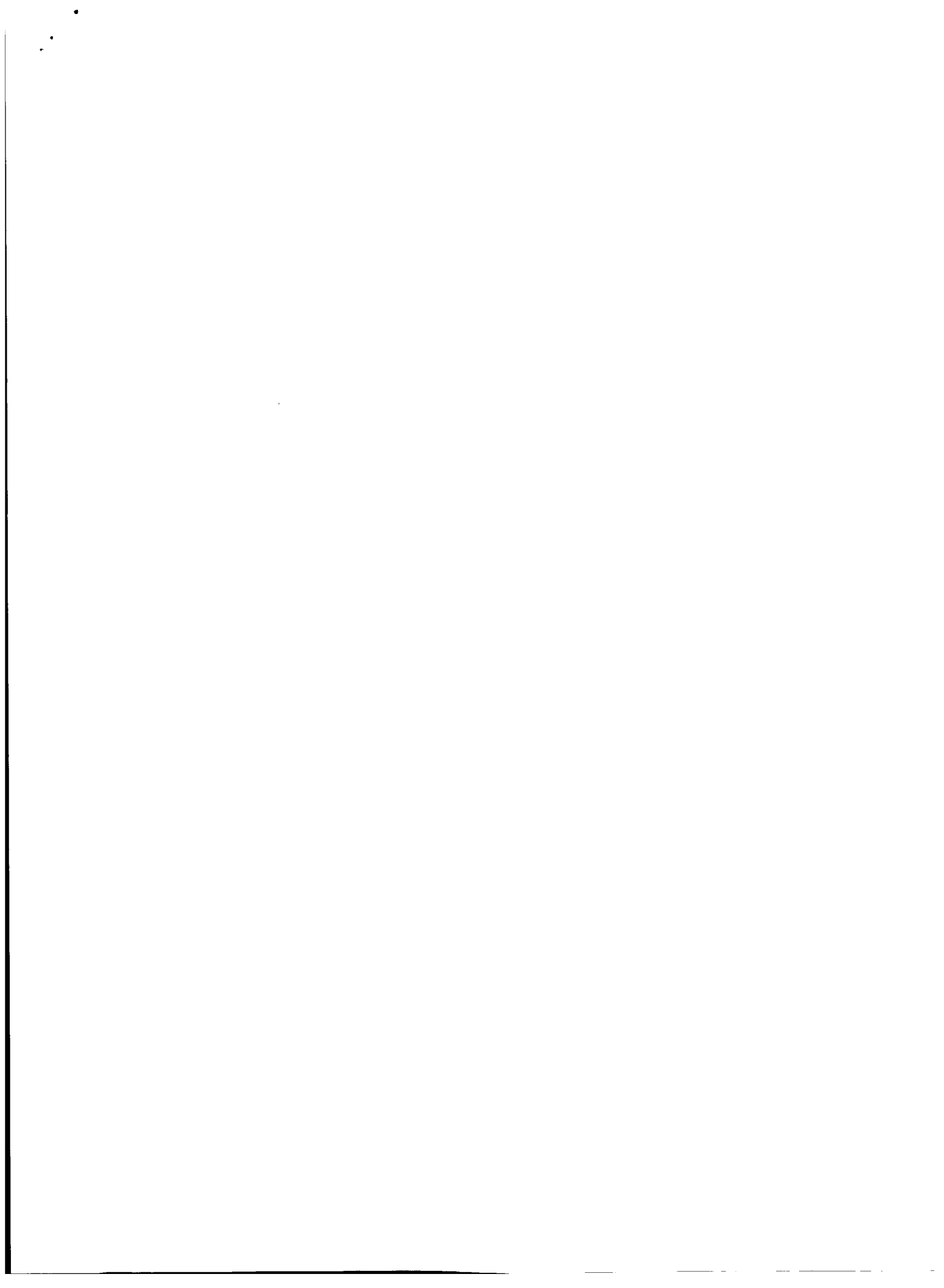
Development of a Large Rotary Positioning Mechanism

Edwin Joscelyn*, Richard Casper*, Heinz Rott* and Alexander A. Solla*

Abstract

The ultimate function and sponsoring program for this aerospace mechanism is proprietary. This unknown, however, does not detract from the interesting challenges this mechanism presented to the designers. The task was to build a mechanism which would structurally support (in a 1 "G" environment) a 227 kg cantilevered disc-shaped load with a moment of inertia of 30 kg•m^2 and to be able to rotate it to one of 24 pre-determined and equally spaced clocking positions to within an accuracy of ±1.5 arc min (±436 μrad) with a 34 Nm load imbalance. Additionally, the mechanism must have the ability of holding this position when power is removed in the presence of shock and vibration. Some of the defining ground rules which made this task challenging were that the rotary mechanism shall:

- not have a mass more than 30.5 kg (excluding load)

- have a fundamental resonance of > 60 Hz (including load)

- have a 100-mm-diameter bore hole completely through and concentric with the axis of rotation

- have an O.D. no greater than 236 mm with the length not exceeding 279 mm.

To help orient the reader, a description of the mechanism's components is discussed. (Figure 1 is a photograph of the Rotary Positioning Mechanism). The device consists of a fixed base from which everything is cantilevered, the rotating portion is captured by a set of 4 tandem duplex bearings and a set of 2 duplex bearings, which are spaced as far apart as possible to give the greatest possible radial stiffness. The load is driven by a three-phase pancake brushless DC motor through a unique 10:1 planetary gear train. There is also a brushless pancake tachometer and a resolver which are used for control and positioning feedback. The unpowered holding torque is provided by a unique toothed brake consisting of opposing gear teeth that are disengaged by a set of 6 solenoids.

* Aeroflex Laboratories Inc., Farmingdale, NY

Introduction

In order to accomplish the goals of rotating a large inertial load accurately, several aspects of the design had to be established early within the rigorous constraints of time and budget. Those design aspects needing answers were: 1) What is the basic mechanical configuration which would provide support and allow rotation of the load while satisfying the mass and resonance requirements for the mechanism? 2) What method could be used to insure the ±1.5 arc min positioning accuracy could be maintained even with the power removed? 3) What materials will best help achieve the goals of weight, stiffness and temperature?

In order to answer Question 1, design concepts were drawn and modeled using FEA techniques to establish weight, deflection and resonance results. It took many iterations to arrive at a viable approach without resorting to Beryllium Albemet, or other expensive, unpalatable or exotic approaches. The lessons learned here are to use FEA models early, even if some of the structure is only an approximation of the final form factor. Areas of critical cross-section become apparent early on and are helpful in forming the final cross-section of the mechanism.

The answer to Question 2 centered on the concept of using a special profile and accurately cut gear toothed brake to provide the positioning and holding accuracy. The servo system would align the brake teeth in the proper clocking position and the subsequent engagement of the brake would perform the final accurate nesting of the load into position. The challenge was to design a method of allowing the fixed gear to engage and disengage the rotating gear with no possibility of jamming while maintaining a backlash that would not exceed the ±1.5 arc min positioning accuracy requirement. Pins were considered to be a liability because the tight tolerances required for the rotational positioning accuracy could introduce the possibility of jamming due to cocking or torsion from imbalanced loads. Again, it took several iterations before a gear system would hold the ±1.5 arc min accuracy with a 34 Nm torque applied. The lessons learned here were that frictional systems, no matter how simple in construction, seem almost never to obey the friction coefficients given in the texts. Surface finish, ramp shape, material heat treat condition, and contaminants all play a part in the brake's performance.

The answer to Question 3 involved the investigation of all types of materials including Beryllium and Albemet. It was an ever-evolving task. Titanium and steel ultimately filtered out as the best compromises to achieve weight, cost and timely completion goals.

The servo electronics were also part of this design effort but will not be discussed in detail herein. The system uses custom DSP-based full mil electronics with custom Aeroflex hybrids for power control. A block diagram of the servo is shown in Appendix A for those interested in this aspect of the design.
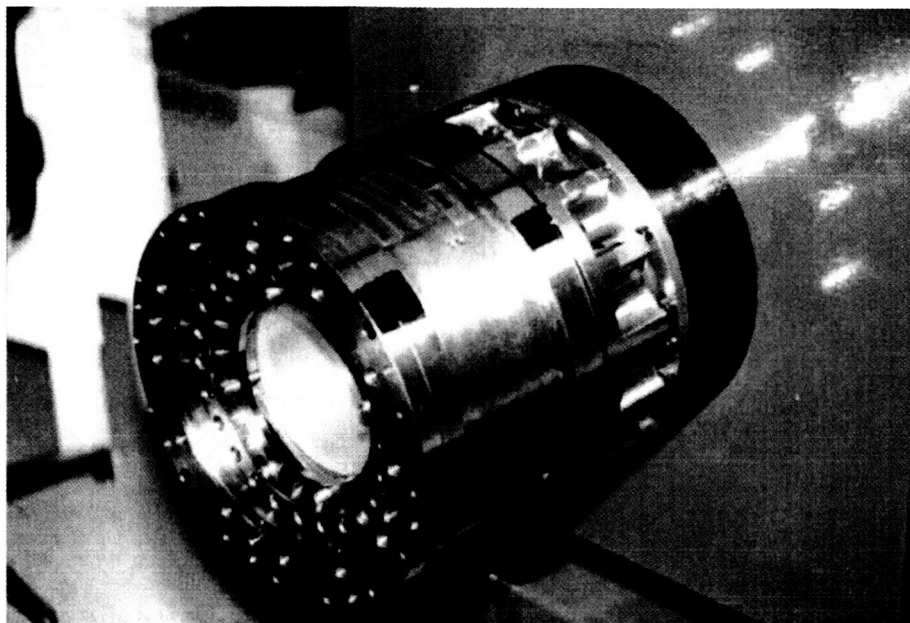

Figure 1. Photograph of Mechanism without load

Basic Mechanical Approach

Figure 2 shows a cross section of the mechanical approach.
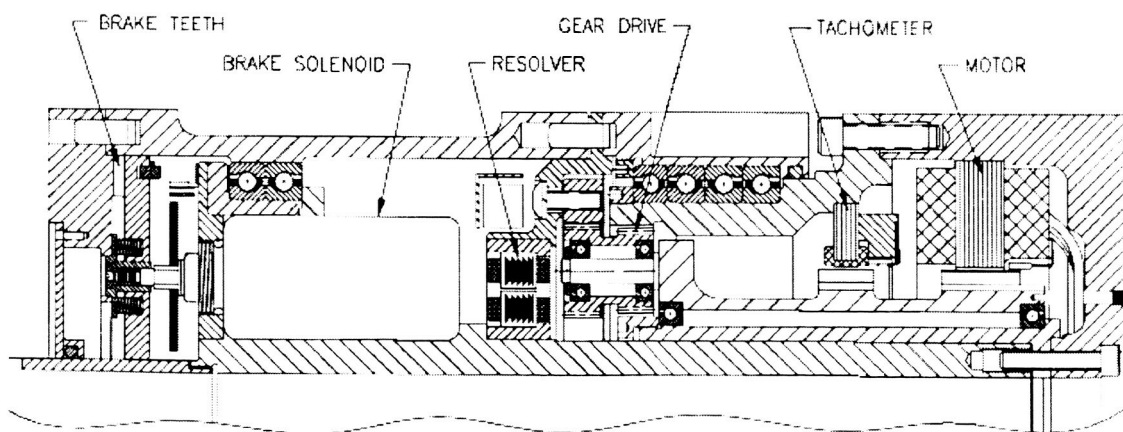
Figure 2. Cross-section of mechanism design

<u>Bearings</u> The bearings are placed as far apart as possible to equally share the weight of the load. Sizing and preload for the bearings was facilitated with the very responsive and professional aide of the Kaydon engineering people. Preloading considerations were adjusted to provide the maximum stiffness for structurally supporting the load while considering the impact of the resulting torque resistance. The preload values were set at 133 N for the set of 4 bearings and 45 N for the set of 2 bearings. The bearing fits to the housing were also designed to stay within the torque budget established with the considerations of internal friction and drag over the entire operating range of -25C to +70C. The bearing nearest the fixed flange is a four bearing Duplex Tandem set and the other bearing is a Duplex set of two.

The rotating flange provides 12 threaded holes and four dowel pin holes for mounting the load. Runout of the load was less than 25 μm.

<u>Motor Drive</u> The motor is a three-phase, 32 pole brushless dc motor with a non-integer slot to pole ratio to minimize cogging torque. Commutation is provided using ceramic B level Hall effect devices. A 32-pole brushless tachometer rotates with the motor to provide damping information to smooth servo performance. A resolver is coupled to the load side of the gear train for position information. The servo system positions the load so that the proper alignment of gear teeth is allowed to engage and settle in one of the 24 selected positions. The accuracy of the positioning system is approximately 2 arc minutes. The brake has 120 teeth. The motor and tachometer are Aeroflex custom designs. The total rotational travel of the mechanism is 345 degrees. This eliminated the need for slip rings. The resolver is fed by a 6-mm-wide Kapton flex circuit which folds back on itself and is constrained to run in a specially designed Teflon-coated toroidal channel to bring the excitation power to the resolver. Several wooden mockups of the channel were made to ensure the flex circuit would fold and ride correctly.

The drive profile needed to move the load from any position to any other position in 10 sec or less was determined to be as shown in Figure 3.
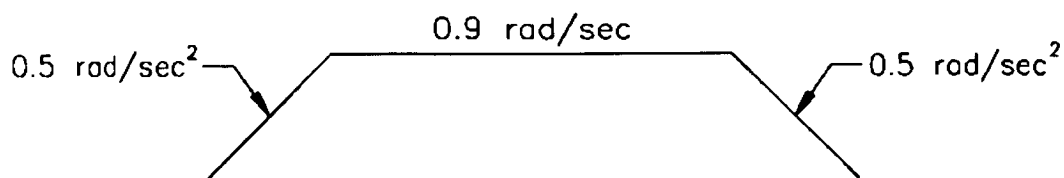

Figure 3.   Drive profile for load

Gear Train The gear train is particularly interesting in that the 100-mm hole in the center of the mechanism presented a challenge as to how to fit a gear train within the "tube" space available. The answer came in the form of an epicyclic fixed differential drive. This gear train employs two internal tooth ring gears and 4 cluster gears. A schematic of the gear drive is shown in Figure 4 and a photograph in Figure 5.
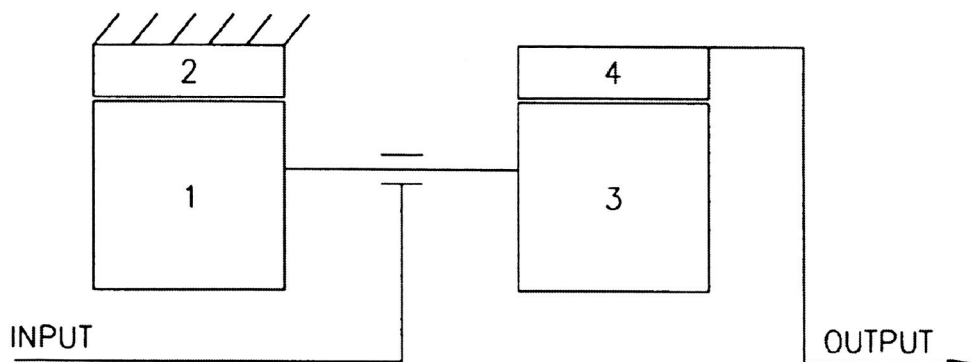

Figure 4.   Gear train schematic
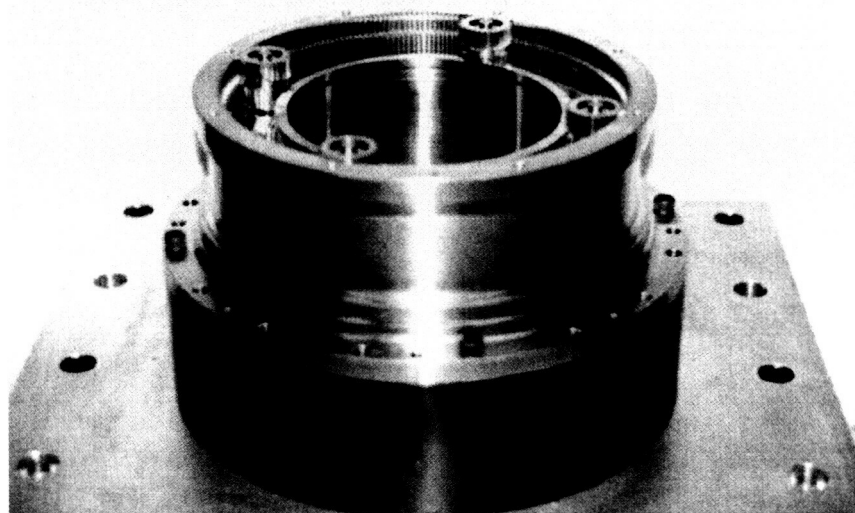
Figure 5.   Photograph of gear arrangement

A single rotor contains the magnets for the tachometer and the motor and has four drive fingers extending axially as shown in Figure 5. These drive fingers engage each of the four cluster planet gears placed symmetrically around the circumference of the mechanism. Each cluster gear drives against the fixed internal tooth gear with one end while the other end of the cluster gear drives the output rotating ring gear. If the planet gear is driven CW, the output gear follows CCW.

The maximum output torque needed to meet the speed profile was determined to be approximately 20 Nm at a speed of 0.9 rad/sec. This dictated a gear ratio of approximately 10:1 given the motor parameters constrained by the size and weight criteria. In order to understand the ratio, one can take the formula offered in the literature

$$R = 1/ (1 - ((N_3 N_2)/(N_4 N_1)) \qquad \text{(equation 1)}$$

or the system can also be viewed as a double lever system which can be represented schematically as shown in Figure 6. The number of teeth or the respective radii can be used as representative of the ratios.
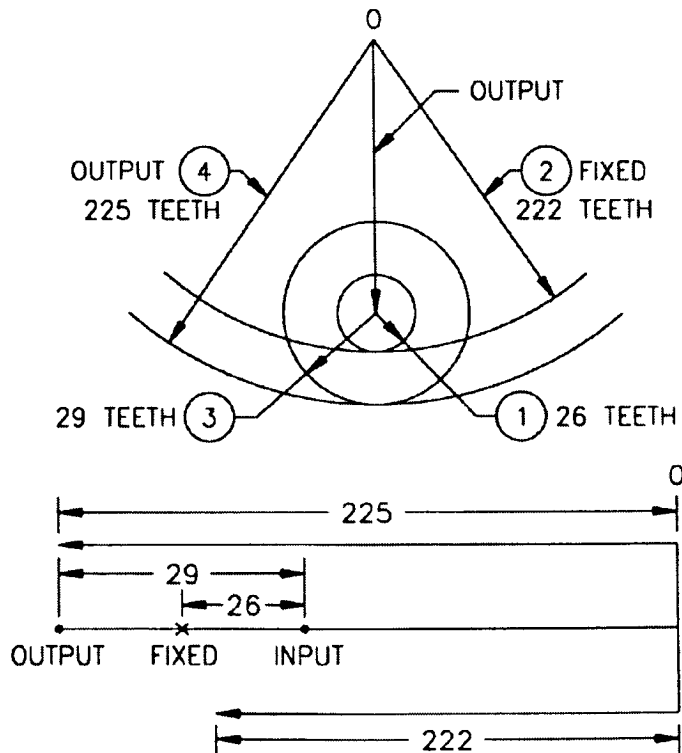

Figure 6. Gear Train Lever Schematic

258

The input arm is (222-26); the output arm is (225). Referencing the input and output arms to the fixed gear gives:

$$\text{input } (222\text{-}26)/26 = \text{output } (225)/(29\text{-}26)$$

$$\text{output/input} = ((222\text{-}26)/26)((29\text{-}26)/225) = 0.1005$$

$$\text{or input/output} = 9.948\text{:}1$$

or by equation 1

$$R = 1/(1 - ((29)(222))/((225)(26))) = \text{-}9.948\text{:}1$$

The diametrical pitch of the gears is 32 and the material is 17-4 PH stainless steel. The AGMA quality number is 10. The mounting of the internal toothed gears are adjusted until the mesh with the planet gears is smooth and the train is easily rotated by hand before the hardware fixing the internal tooth gears is tightened.

The gear life requirement is approximately 10,000 rotations over 6 years. The lubrication is molybdenum disulfide.

Brake/positioning mechanism The design using a brake to guarantee positioning eliminated the need for fine electrical positioning as well as solving the problem of holding position with the power removed in the presence of shock and vibration. A photograph of the brake mechanism is shown in Figure 7.
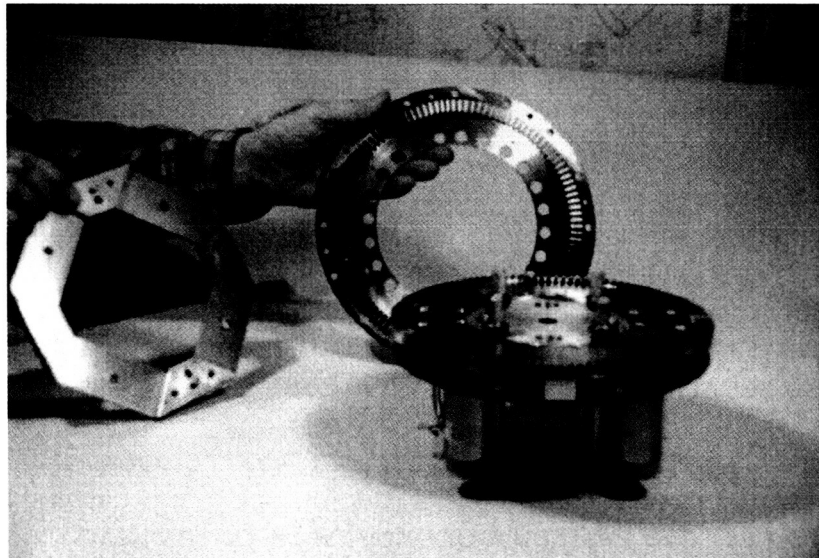

Figure 7. Brake Mechanism Details

259

The challenge here was to design a brake spring that was very compliant in the axial direction but very stiff in the torsional direction. This torsional stiffness must provide a positioning accuracy of ±1.5 minute of arc with a offset load of 34 Nm. A unique 8-sided stainless steel "leaf" spring approach was conceived. Two opposing sides of the leaf would engage the fixed gear and the 90 degree leaves would engage the stationary side of the mechanism. A representation of the leaf is shown in Figure 8.
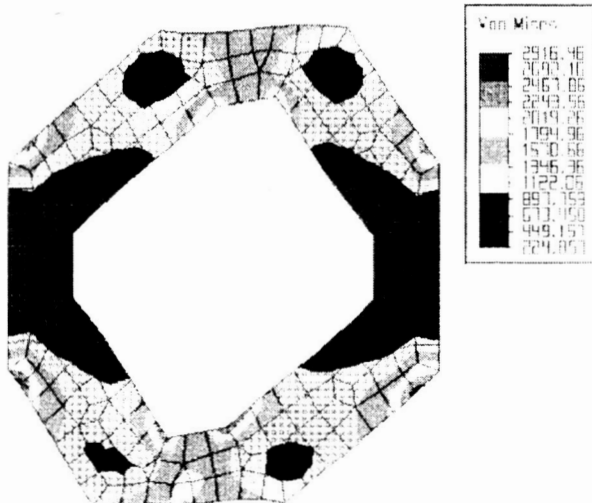

Figure 8.   Leaf Spring for Brake

A FEA for the leaf spring showed it to be of adequate stiffness for a single leaf. The concern was, however, for buckling of the leaf because there was nothing to keep it in a plane when torsional forces were applied. This problem was solved by making a sandwich using 7 leaves. This was still compliant in the axial direction (needs to move approximately 3 millimeters to disengage the brake) while making it torsionally rigid. The edges of the leaves were welded to ensure they would not slip one over the other. This method can never "hang up" or cock as a pin in a hole might do.

The stationary brake disc is driven to engage the rotational brake disc with eight compression springs set at a value of 45 N each. This keeps the brake engaged with power removed. The 360 N (plus) force necessary to disengage the brake to allow rotation was initially provided by 4 solenoids. An electronic interlock using four solid state Hall switches to monitor brake position is also provided to ensure that the brake is fully disengaged before the motor is allowed to start.

As simple as this leaf spring device appears, it took three iterations involving state of the art welding, accurate positioning, control of tolerancing and careful analysis of kinematic centers to achieve the required performance. In fact, it was necessary to develop a special tool to allow the compression spring, leaf spring and gear tooth assembly to be tested using a large torque wrench to simulate the imbalance. This same test fixture was used to ascertain the holding and slipping amount for the brake

teeth. The brake material was eventually changed from steel to titanium to increase friction and reduce weight.

The brake, in addition to holding the ±1.5 arc min with a 34 Nm imbalance, had to resist an 8.7 "G" shock load without slipping a tooth. The initial brake pair selection was for a rack-generated couploid with crown faces. The material was initially chosen as 17-4PH stainless steel. This was unsuccessful. The crowned tooth "point contact" of the gear teeth together with the coefficient of friction of steel against steel allowed the teeth to ride up and rotate more than the desired ±1.5 arc min for the 34 Nm of torque applied.

The next iteration was to change the tooth design to a "Hirth" tooth using titanium in place of steel. The coefficient of titanium on titanium was listed as two times that of steel on steel. One must be careful as to what coefficient of friction to use as there are many experimenters and many sources for friction ...all seemingly listing different numbers. We opted for early definitive testing rather than relying on analysis in this instance and avoided having to back track at a more advanced stage of development.

The titanium showed a marked improvement with the displacement meeting the requirements most of the time. Still not there. The final and successful step came with decreasing the pressure angle from 20° to 14.5° and the increasing of the compression spring forces offset by using 6 solenoids in place of 4. A small mass penalty, but a necessary one.

As a safety factor, since we could not guarantee nor test the ability of the unit to not skip a tooth during shock, pins with 3 arc min clearance holes were installed which paralleled the brake teeth. These pins would prevent disengagement if the teeth began to rotate and separate by coupling the two brake discs together. With the solenoids activated the pins are retracted first, well clear of the locking holes allowing rotation. There is no chance of cocking or hang-up due to the large clearances.

System Performance

Positioning The system required that the load must be positioned from any position to any other position in 10 sec or less from command to command. In order to test system accuracy, a precision indexing mirror was affixed to the load and the position measured using an optical collimator to determine deviations. The results are shown in Figure 9.

The effect of the load unbalance can be seen as the dotted line represents the neutral position of the imbalance. The system does make the specification at the greatest imbalance positions but illustrates the difficulty in achieving this goal.
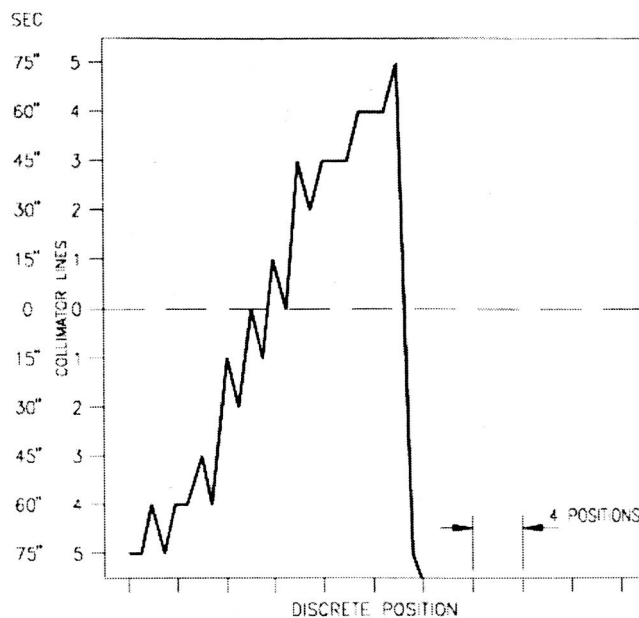
Figure 9.   True Position Relative to Index Position

System Resonance: FEA analysis using Algor was performed to judge the resonance performance of the system relative to resonance. Figure 10 shows the FEA model of the mechanism and the simulated load.
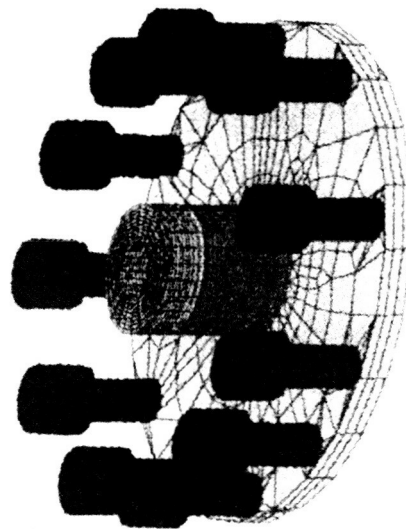

Figure 10.   FEA model of the mechanism and Load

262

The bearings were modeled as rings with equivalent Young's modulus to give the radial and axial displacements published by Kaydon. Since these curves are not linear displacement values near the 227 kg load were chosen. Figure 11 shows a bearing model with the expected displacement. The load was equally divided and applied uniformly to all nodes around the inner ring.
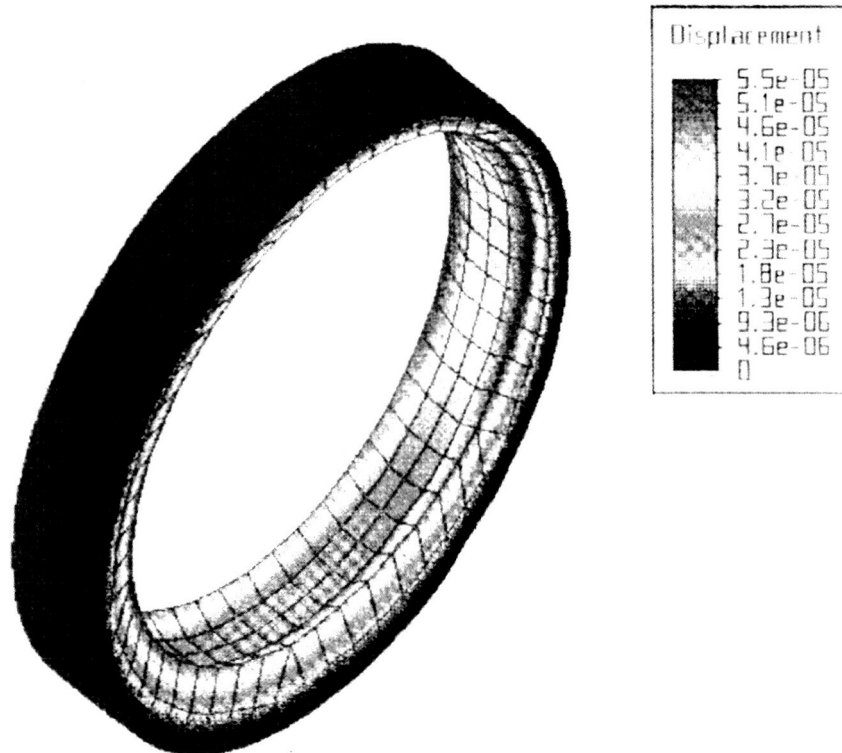

Figure 11. Bearing model

An FEA cross-section of the mechanism is shown in Figure 12. This cross section is then rotated 360 degrees and mated to the load model to generate Figure 10. Early resonant frequency analysis showed that the fundamental resonance was below the required 60 Hz and several design iterations were necessary to bring the mechanism into compliance. These design iterations mainly involved redistribution of cross-section thickness and bearing placement. The FEA model predicted that the fundamental resonant frequency of 75 Hz would occur. Actual resonance test data is shown in Figure 13 verifying FE predictions. The accelerometer for this particular run was placed on the edge of the load with the vibration input perpendicular to the axis of rotation. There were dozens of runs and the data from 5 accelerometers were simultaneously recorded. Figure 13 is a typical result.

Figure 12. FEA Cross-Section of Mechanism

1: Freq = 76.52 Hz   Trans. = 7.09

Frequency in Hz
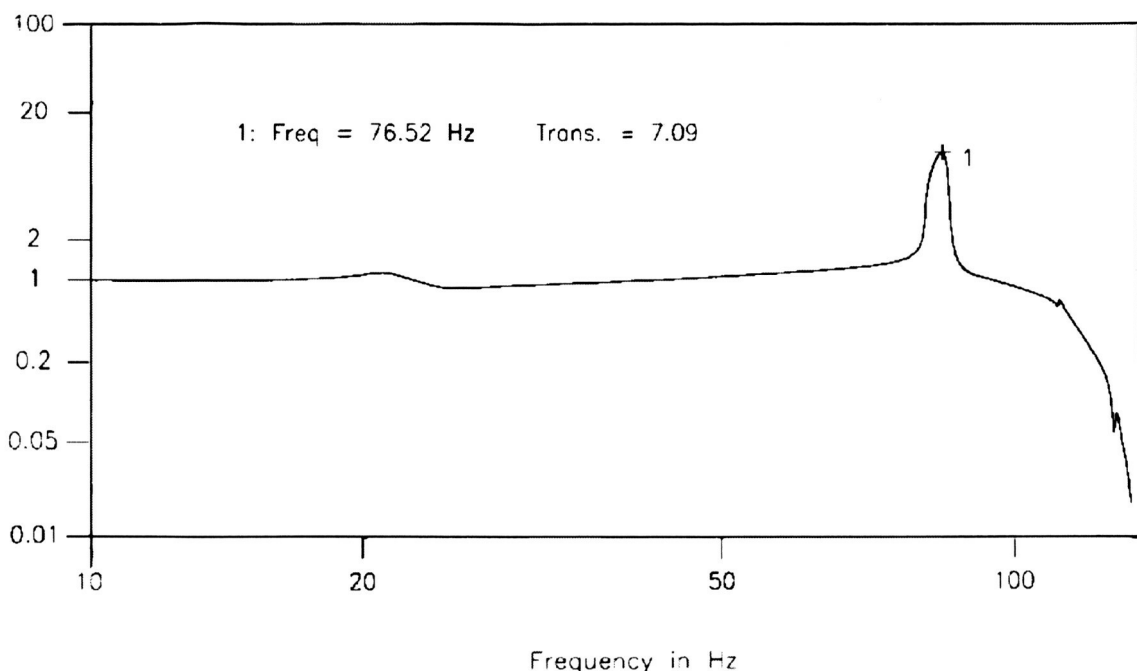
Figure 13. Resonance Test Data

Conclusion

Unique and different design solutions to difficult problems can be successful if approached cautiously and interspersed with as much interim testing and design verification exercises as practical. The lack of twisting stability of the initial 8-sided brake springs, the lack of sufficient friction of the brake teeth, and the low resonance of the initial designs were all obstacles to overcome. Fortunately, these were identified early enough in the program to allow for corrective action to occur.

Several systems have been delivered and have met customer expectations.

References

1. Ronald A Walsh <u>McGraw-Hill Machining and Metalworking Handbook,</u> McGraw-Hill, 1994

<u>Appendix A</u>
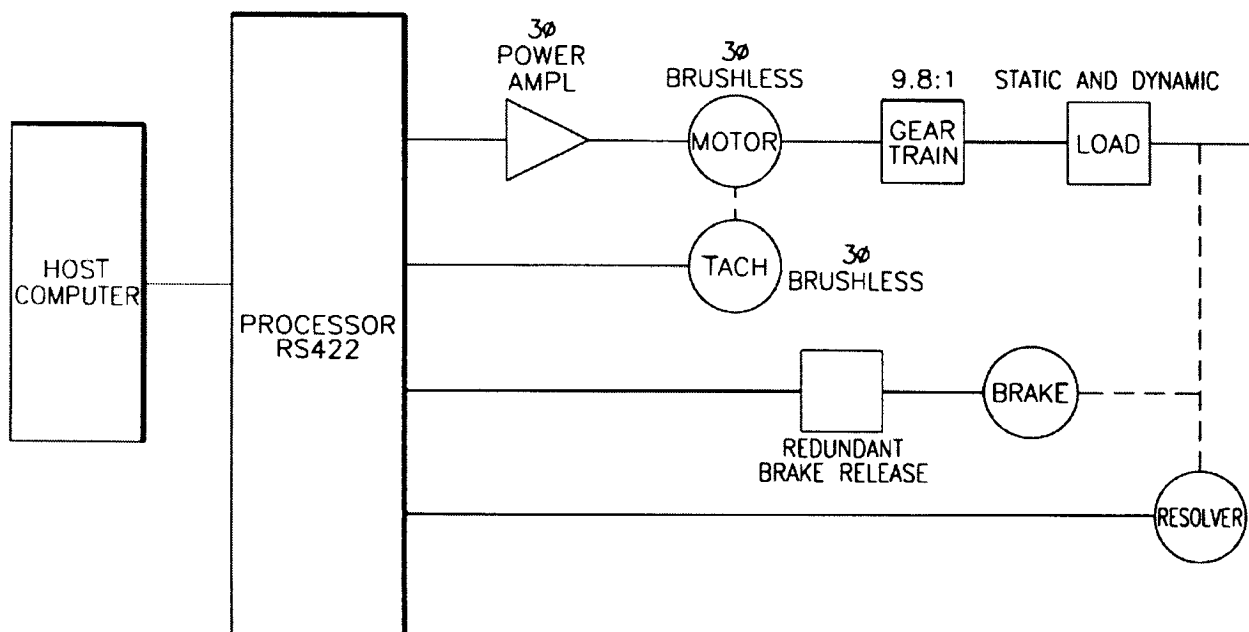
<u>SERVO SYSTEM BLOCK DIAGRAM</u>

High-Precision Pointing Gimbal Development

$S_{20}-37$

168112

336879
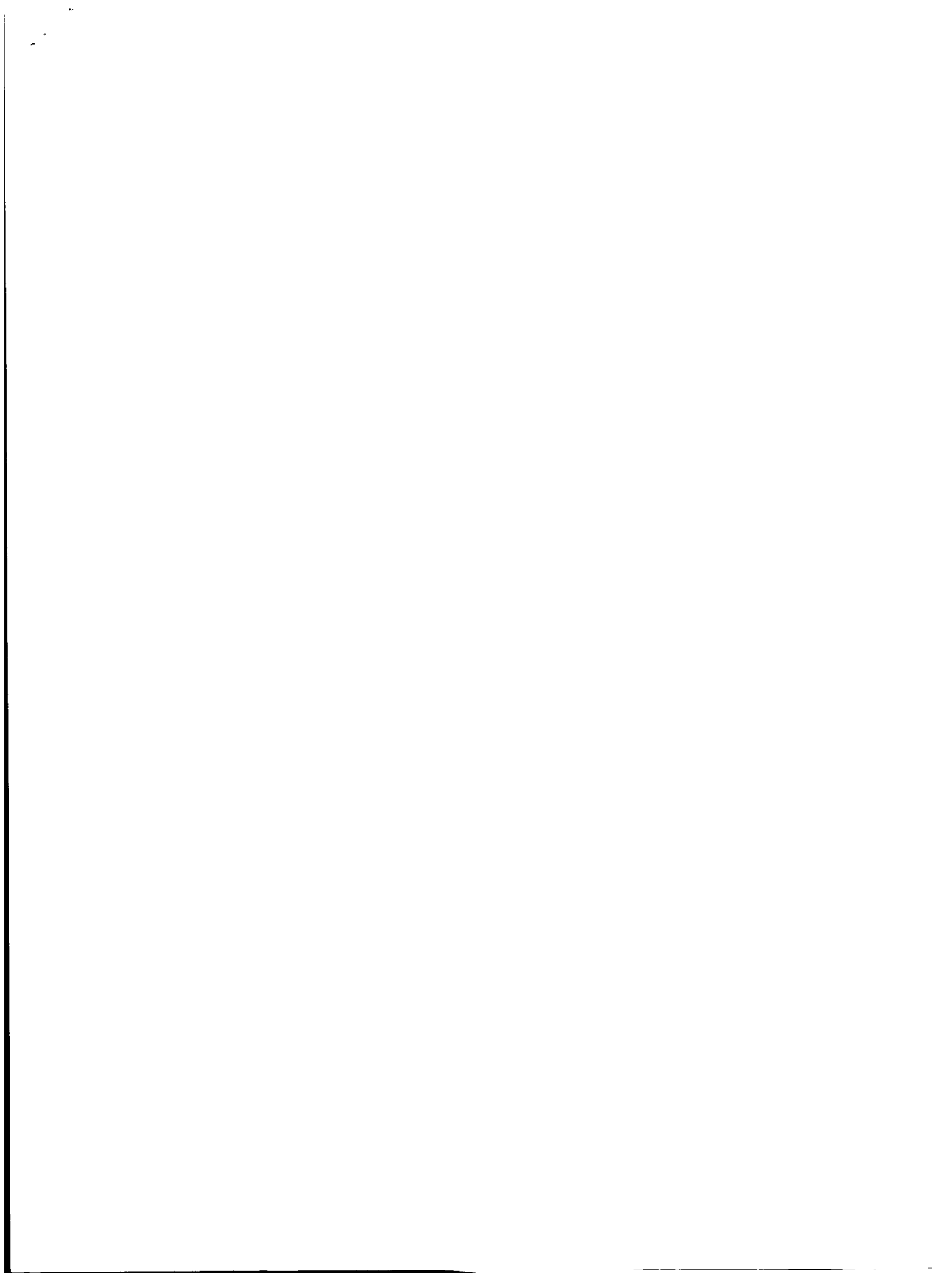
D. Hobson Lane[*] and Mark A. Carroll[*]

16 p.

Abstract

The goal of the High-Precision Pointing Gimbal (HPPG) development project was to demonstrate a lightweight, high-accuracy pointing mechanism. Presented here are test results which confirm a single axis pointing repeatability of better than 2.6 µrad (1.5×10^{-4} deg). In addition to sharing high-precision pointing results, this paper will also describe the unique mechanical design approaches employed along with the lessons learned for control and modeling of high-precision actuated mechanisms.

Introduction

Space applications for precision pointing mechanisms are numerous. Previous gimbal design efforts often resulted in massive mechanisms whose performance lagged behind the design requirements. The design challenge for HPPG was to develop a lightweight, low-profile, high-stiffness, thermally stable pointing mechanism with a minimum 178 mm (7.0 in) diameter clear aperture through the center of the drive module. Recent advances in composite materials, encoder optics, bearing, and motor technology have provided the components of a mechanism design to meet stringent precision pointing requirements while also achieving significant reductions in weight and overall profile. In addition to combining the various technologies required to meet ambitious performance goals, the HPPG program also produced an effective controller for exploiting the favorable characteristics of the new gimbal design.

Mechanical Design

Unique design features of the HPPG that contributed to its light weight and precise pointing capability include a direct-drive constant-reluctance motor, a high resolution optical interferometric encoder, a low wire count flat-flex cable within a lightweight, "clock-spring" type cablewrap, and a graphite-epoxy elbow with titanium end fittings. This was achieved while also maintaining a very low profile drive module and a large clear aperture. A cross section of the drive module is shown in Figure 1. One key weight saving feature of the HPPG is the use of a titanium shaft or sleeve that is bonded over the top of the graphite-epoxy cylinder section. In this way, the gimbal housing takes advantage of the light weight of composite materials and the precise alignment of titanium end fittings. Special assembly tooling was utilized for precise alignment of the shaft to the bearings and the composite. A flight-qualified adhesive was used for the titanium to graphite bond. Composite materials were chosen for the design of the majority of the mechanism because of the high stiffness-to-weight ratio of

---

composites and also because the lamina can be oriented to produce a thermal expansion coefficient of approximately zero.
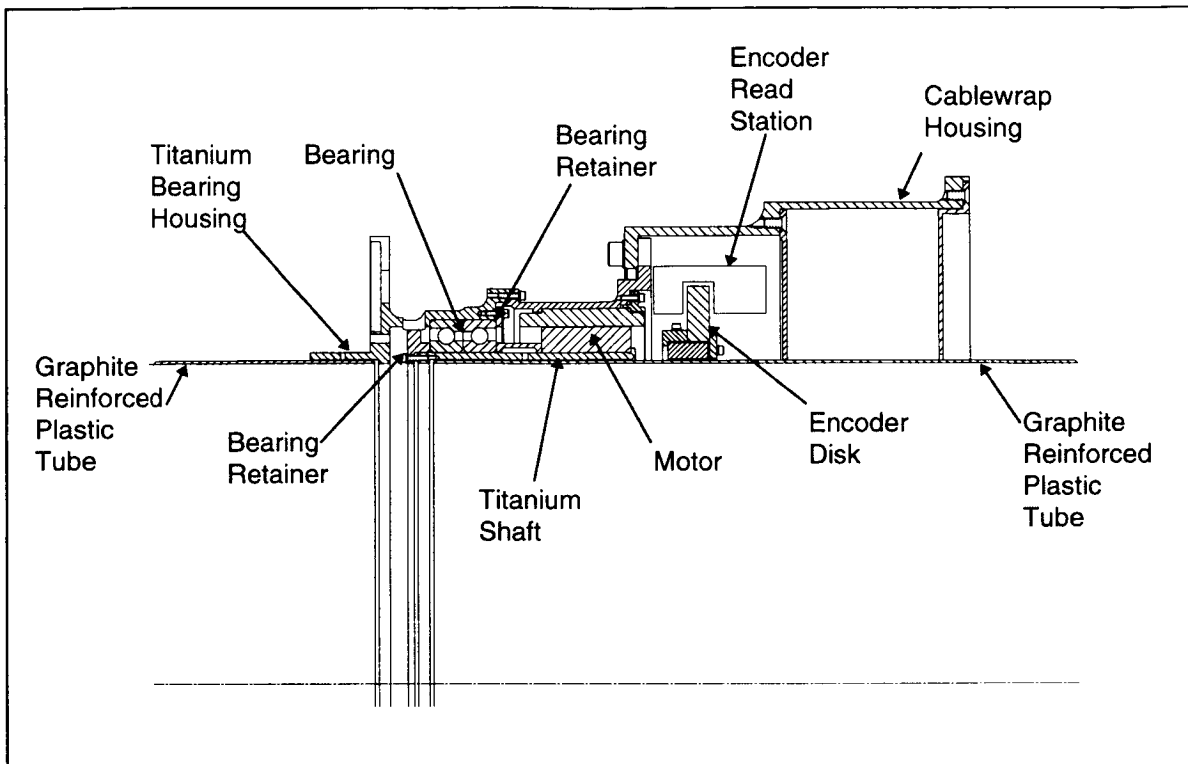

Figure 1: Drive-Module Cross Section

Duplex Bearing
Many mechanisms that have included large diameter bearings have used a phenolic laminate retainer and have often experienced disturbance torques which degrade pointing performance. They have also typically utilized fairly high preloads to maximize stiffness and load capacity. For the HPPG, the large pitch diameter achieves the desired stiffness while the external caging and the extremely light structure enable a light preload. Because of schedule and cost constraints during development of the HPPG, an "off-the-shelf" bearing was selected. The HPPG bearing differs from past designs in that it has Teflon toroid separators and a light ground-in preload. Consistent with the low profile, the HPPG bearing takes advantage of a thin-section angular-contact duplex-pair bearing in a back-to-back configuration. The bearing was cleaned and lubricated with Penzane with lead additive prior to assembly and test. Testing to date has not shown any disturbance torque problems with this large diameter, thin annulus bearing.

Direct-Drive Motor
In order to achieve a low profile drive module with minimal cogging, a direct-drive, surface-wound motor was selected for the HPPG with air-stabilized neodymium iron

268

boron magnets on the rotor. This design is scaled up in diameter from an existing flight design and exhibits a torque constant, K_t, of 2.54 N·m/A (360 in·oz/A). Its large diameter, high energy-product magnets, and thin cross-section enable its exceptional specific motor constant of 0.433 N·m/W$^{\frac{1}{2}}$/kg (1.74 in·oz/W$^{\frac{1}{2}}$/oz).

Cablewrap

The HPPG cablewrap is a "clock-spring" type cablewrap with a graphite-epoxy cylinder for the inner diameter and an aluminum cablewrap housing. A flat-flex cable was selected for low overall volume, low stiffness, and low friction. Because the wire count requirement was low, the cable consists of only two layers of a Kapton sandwich flat-flex cable, each with a thickness of 0.457 mm (0.018 in), and a width of 5.08 cm (2.00 in). Approximately 3.1 turns or 2.258 m (88.88 in) of cable were wrapped around the inner diameter and clamped to the inside of the cablewrap housing which has a diameter of 27.305 cm (10.75 in). This configuration provided more than 360 deg of total travel. Mechanical stops were installed to limit travel to 340 deg and preclude cable damage.

Interferometric Encoder

The challenge of the encoder development project was to produce a high-resolution encoder with an exceptionally large (19.685 cm diameter) through hole, while confining the encoder hardware to a small annulus and minimizing the on-board encoder inertia and as well as the total encoder weight. The brass board configuration included an offset interferometric encoder with a pinion gear coupled to a large ring gear, which also acted as a bearing retainer. This design allowed gimbal travel verification and validation of the encoder interface. For the engineering model this design evolved into a direct drive interferometric device consisting of a glass code disk, two read stations, two amplifier boards, and a single Digital Signal Processing (DSP) board.

The components of the HPPG encoder are shown in Figure 2. The 180 g (6.3 oz) soda lime glass code disk was designed with a 22.86 cm (9 in) outer diameter and a 19.685 cm (7.75 in) inner diameter. The disk was etched to produce 72,000 grating lines per revolution with a spacing of approximately 10 μm. Because of cost and schedule constraints, a photo-resist process was utilized to generate the grating pattern on the code disk. An ion-beam etching process would be implemented in a flight design. The resulting interference pattern consisted of 144,000 optical fringes per revolution. The two read stations were designed to be installed diametrically opposed so as to average out any concentricity errors between the encoder optical axis and the mechanical axis of the HPPG. A read station along with its amplifier board has a mass of only 35 g (1.2 oz), which brings the total on-board encoder mass to 250 g (8.8 oz) for two read stations, two amplifier boards, and one grating disk. A bench mounted DSP board was used to interpolate the optical fringes to 4096 counts per optical fringe at a rate of 40 kHz. This produced a total encoder resolution of 6.1×10^{-7} deg (0.0022 arcsec). The DSP is capable of maintaining its incremental fringe count up to a maximum rotation rate of 500 deg/s and can sustain full resolution at rates up to 25 deg/s. Once the

269

encoder was installed in the HPPG and held stationary, the resulting output remained stable up to the three least significant bits.
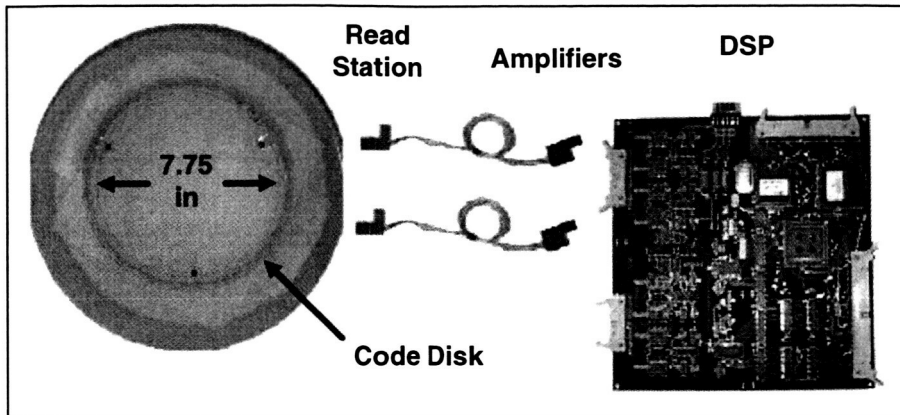

Figure 2: Encoder Components

Component Testing

Duplex Bearings

The duplex bearing pair was preloaded to approximately 35.1 N (7.9 lbf) while mounted on an air bearing. The resulting friction torque was measured versus angular position. Figure 7, in the Controller Design section, shows a plot of torque versus angle for 10 cycles of approximately ±0.01 deg. This plot reveals the hysteretic behavior of the bearing and indicates a maximum friction torque of 21 mN·m (3 in·oz) for this particular angular excursion.

Interferometric Encoder

In order to bound the worst case accuracy of the HPPG encoder it was coupled to a Heidenhain encoder (Model No. ROD 800) with a reported accuracy of $\pm 2.78 \times 10^{-4}$ deg (±1 arcsec). Both encoders were aligned and mounted on an air bearing and then rotated with an HPPG motor. Angle measurements from both encoders were acquired at increments of 0.0439 deg. The Heidenhain encoder was taken as the truth standard and the difference between the HPPG encoder and the Heidenhain encoder readings was utilized to estimate the HPPG encoder error. A plot of the encoder error is shown in Figure 3. Fourier analysis of the data indicated several low frequency, angular periodicities in the error signal. This suggested that the discrepancy between the two encoder readings was largely due to imperfect mechanical alignment of the encoders and elasticity of the Heidenhain spring-loaded coupler, which is rated at $\pm 2.78 \times 10^{-4}$ deg (±1 arcsec). In addition, residual vibration of the shaft during the delay (< 1 ms) between acquisition of the two measurements may have also contributed significant error. Nonetheless, the data acquired indicate an encoder accuracy of better than $\pm 5 \times 10^{-4}$ deg (±1.8 arcsec), three sigma (3σ).
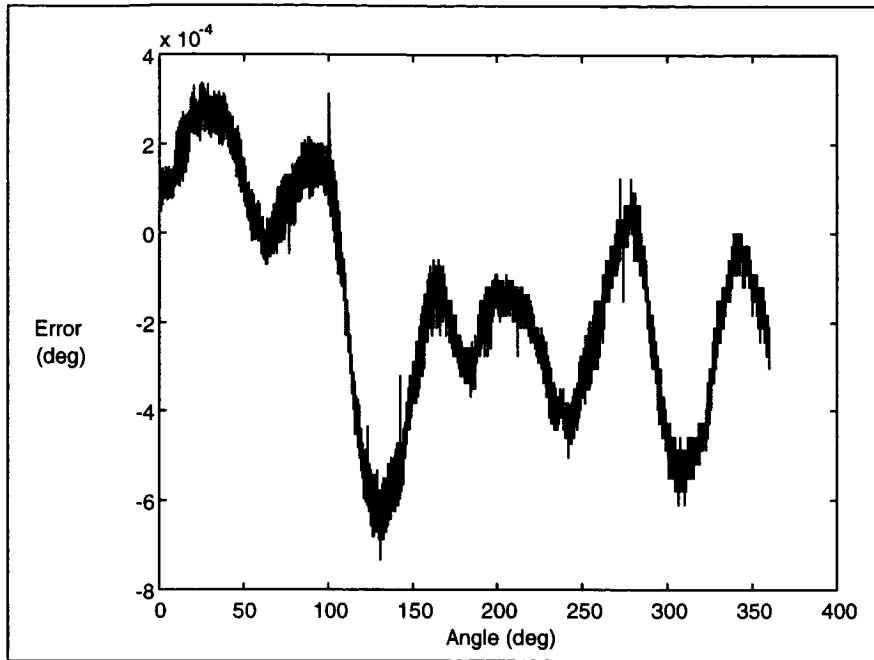
Figure 3: Encoder Accuracy, Test Data

Motor

The HPPG motor was tested for ripple error by coupling it to the HPPG encoder and mounting both on an air bearing. The difference between the commanded motor position and the measured encoder position was taken every 0.0439 deg. The motor ripple error is plotted in Figure 4. A frequency response plot of the motor error versus angle is provided in Figure 5. At a frequency of 0.0028 1/deg (a period of 360 deg) there is an error of approximately 0.0089 deg. At a frequency of 0.0887 1/deg (a period of 11.28 deg) there is an error of approximately 0.0024 deg. At a frequency of 0.1774 1/deg (a period of 5.64 deg) there is an error of approximately 0.0041 deg. At a frequency of 0.3547 1/deg (a period of 2.82 deg) there is an error of approximately 0.0070 deg. At a frequency of 0.7122 1/deg (or a period of 1.40 deg) there is an error of approximately 0.0036 deg. The sum of these ripple error components is 0.026 deg (1.56 arcmin).
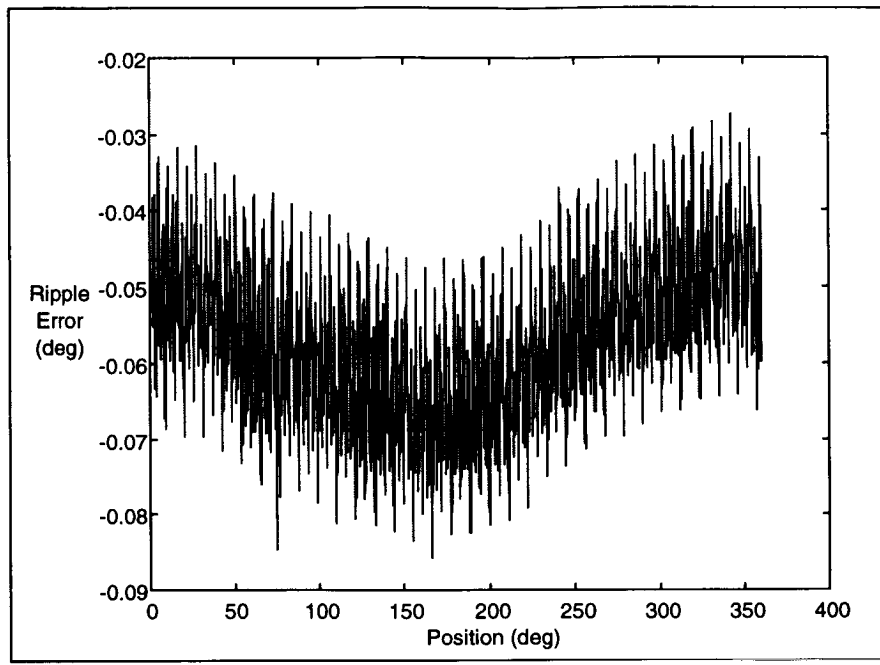
**Figure 4: Motor Ripple Error**
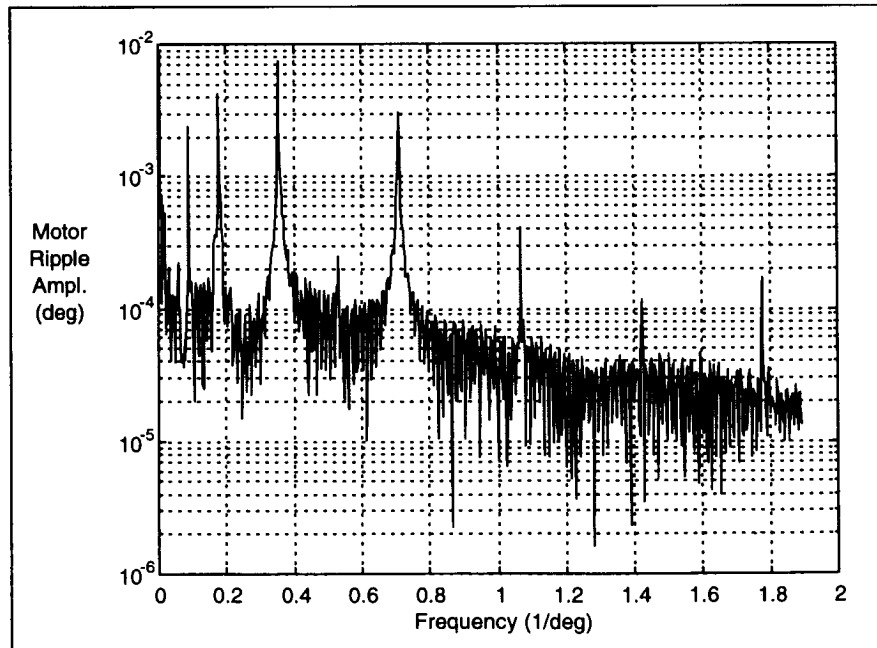
Figure 5: Motor Ripple Magnitude Spectrum

Cablewrap

The HPPG Cablewrap was tested to determine the friction torque behavior for both large and small rotations and at the "tight wrap", "center-of-travel", and the "fully unwrapped" positions.

Plots of torque versus angular position for the HPPG Cablewrap were obtained for travels of 170 deg ± 170 deg, 5 deg ± 5 deg, 335 deg ± 5 deg, 170 deg ± 5 deg, and 170 deg ± 30 deg. For reference, the "center-of-travel" position for the HPPG is located at 170 deg, whereas 0 deg represents the "tight-wrap" position, and 340 deg represents the "fully unwrapped" position. A representative plot for a travel of 170 deg ± 30 deg is shown in Figure 6. The open loop shape in Figure 6 reveals the hysteretic friction of the cables sliding against each other, against the inner shaft, and against the cablewrap housing. The estimated friction torque for all test runs is shown in Table 1.
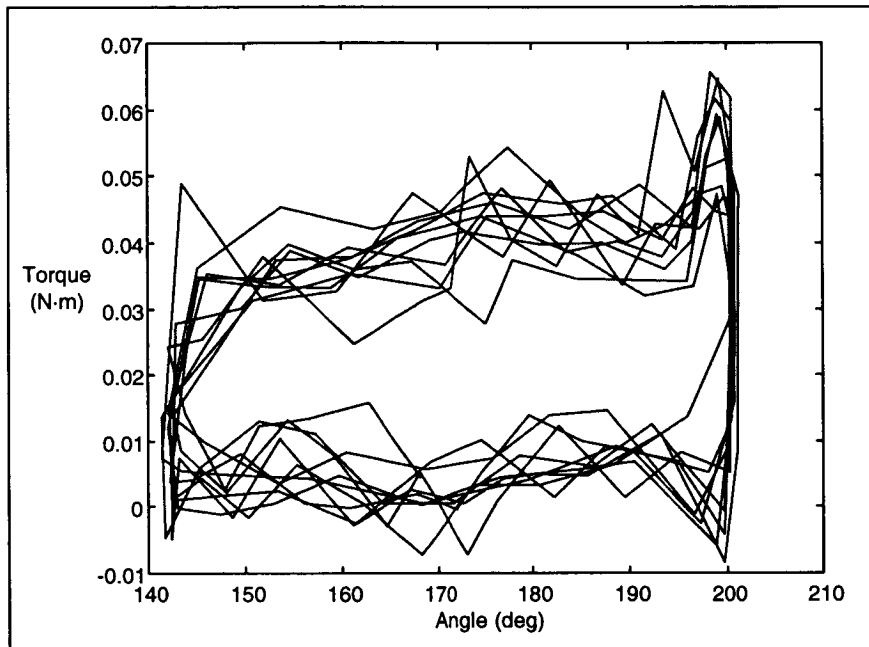

Figure 6: Cablewrap Friction Test #5 (170 deg ± 30 deg)

Table 1: Estimated Friction Torque

Data Case No.	Travel Range deg	Estimated Friction Torque mN·m (in·oz)
1	170 ± 170	162 (23.0)
2	5 ± 5	120 (17.0)
3	335 ± 5	120 (17.0)
4	170 ± 5	35 (5.0)
5	170 ± 30	53 (7.5)

Structural and Thermal Testing

Structural Testing

Structural testing of the HPPG included stiffness testing of the single-axis gimbal with and without the drive module as well as an ultimate strength test of the composite structure. The composite structure proved to be extremely stiff under pure moment loading. With the drive module integrated into the composite structure there was not a significant depreciation in the overall moment stiffness even with a very low bearing preload. The ultimate strength test of the composite structure consisted of loading the test unit with simultaneous moment and shear loads. The composite structure was accurately modeled using finite-element techniques and first-ply failure was predicted within 6% of the actual failure load. The ultimate failure load far exceeded the requirement for probable launch loads.

Thermal Distortion Testing

Thermal distortion testing of the HPPG composite structure was performed using videogrammetry techniques. No significant change in the pointing vector could be measured over the expected operational temperature range. Thus, the thermal distortion requirements for the HPPG were easily met.

Controller Design

In order to achieve the performance goals of the HPPG project, a classical PID control scheme was modified in two significant respects. First, nonlinear PD gains were implemented in order to partially compensate for friction effects. In addition, a low-saturation, high-gain, discrete Euler integrator was used to compensate for biasing torques such as cablewrap elasticity, unbalanced gravitational forces, and air current pressures. Likewise, this low-saturation integrator proved useful in combating friction because the friction torque was variable and its exact magnitude and profile were unknown. A block diagram of the modified PID controller is shown in Figure 8. This Simulink diagram was implemented directly on a TI TMS320-C40 DSP processor by utilizing "Real Time Workshop" software by Math Works, in conjunction with a dSpace software and hardware package.

The HPPG controller was designed with two different operating modes in mind. In what is termed "Internal Feedback Mode" the HPPG utilizes only encoder information for position feedback while executing a slew. After acquiring a reference signal from the autocollimator, feedback on the new signal is initiated in what is termed "External Feedback Mode."

The hyperbolic tangent function (tanh) was chosen as the nonlinear gain function for the proportional and derivative controller terms. It can be seen in Figure 7 that near zero the tanh function more closely matches bearing test data than a linear gain. For reference, the time order of the data points in Figure 7 indicates a clockwise encirclement of zero. The shape of the tanh function closely resembles the torque

274

profile of the Dahl friction model.[1] When compared to traditional PD control, this nonlinear scheme produces larger gains when the error signal is below a threshold, which is dependent on f_{tanh}. Because the hyperbolic tangent function has a maximum of one, its gain, K_{tanh}, could be estimated by equating it to the maximum friction torque in the axis. Similarly, f_{tanh} could be estimated as the inverse of K_{tanh}. This preliminary tuning technique allowed the linear gains to dominate only after friction was overcome. The resulting nonlinear gain scheme produced axis motion that resembled a device settling into a mechanical notch at the desired position. The "width" of the virtual notch was determined by the f_{tanh} value, while the "depth" was determined by the K_{tanh} gain.
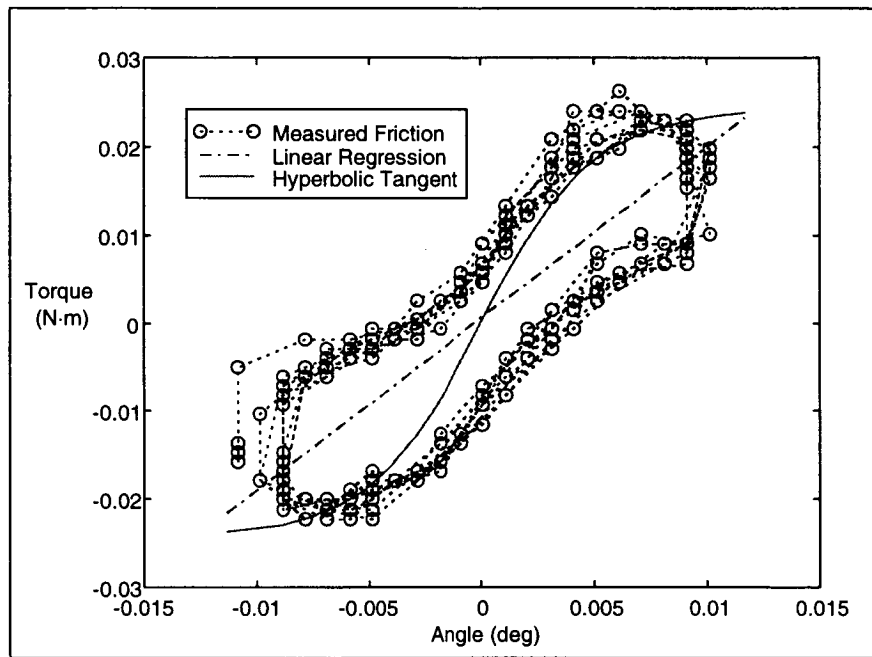
Figure 7: Bearing Friction

The gain (K_i) and limit (L_i) for the discrete integrator were chosen so that the integrator output at saturation would be enough to overcome all biasing torques including friction, unbalanced gravitational forces, and cablewrap elasticity. This defined the product L_i x K_i to be 0.7 N·m (100 in·oz) for this particular mechanism. K_i was then chosen to be as large as possible to produce the shortest possible settling time without exciting high frequency oscillations.

[1] Armstron-Helouvry, Brian; Dupont, Pierre; Canudas De Wit, Carlos; "A Survey of Models Analysis Tools and Compensation Methods for the Control of Machines with Friction," *Automatica*, Vol. 30, No. 7, 1994.
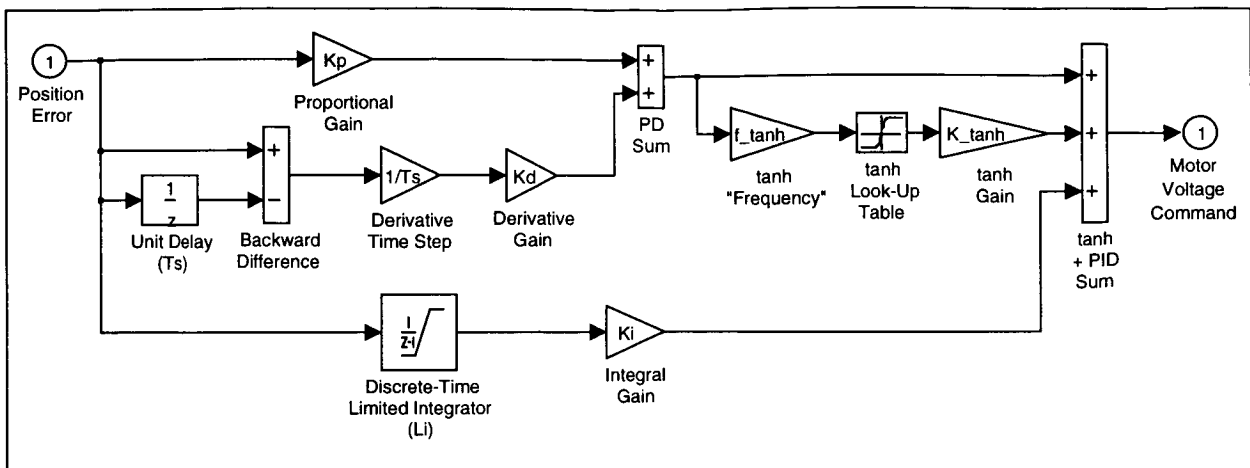
Figure 8: Controller Block Diagram

For the results discussed at the end of this paper, when "Internal Feedback Mode" is indicated, the controller gains employed were: a proportional gain of K_p = 12.6 V/deg = 1.55 N·m/deg (220 in·oz/deg), a derivative gain of K_d = 2.5 V·s/deg = 0.31 N·m·s/deg (44 in·oz·s/deg), an integral gain of K_i = 251 V/deg·s = 31 N·m/deg·s (280 in·lbf/deg·s), an integral saturation of L_i = 0.029 deg·s, and unitless hyperbolic tangent coefficients of f_{tanh} = 1 and K_{tanh} = 1. In order to improve the bandwidth of the controller during "External Feedback Mode" the integral gain was increased to 388 N·m/deg·s (55,000 in·oz/deg·s) and the integral saturation limit was decreased to 0.0029 deg·s. A controller sample time of 0.01 s was selected in order to avoid excitation of the mechanical resonances of the structure that exceed 150 Hz.

Test Setup

Figure 9 contains a picture of the equipment utilized for the experiments described in this paper. For scale, the distance between the autocollimator and the HPPG is 0.6 m (24 in). The HPPG assembly was mounted horizontally on a gimbal test stand. The test stand was equipped with a DC motor, flex pivot joints, and a travel reduction linkage. It was utilized for simulating the base motion that would be experienced by a gimbal mounted on a spacecraft. The test stand was capable of sinusoidal motions at frequencies from 0.01 Hz to 10 Hz and amplitudes of 0.001 deg to 0.5 deg.
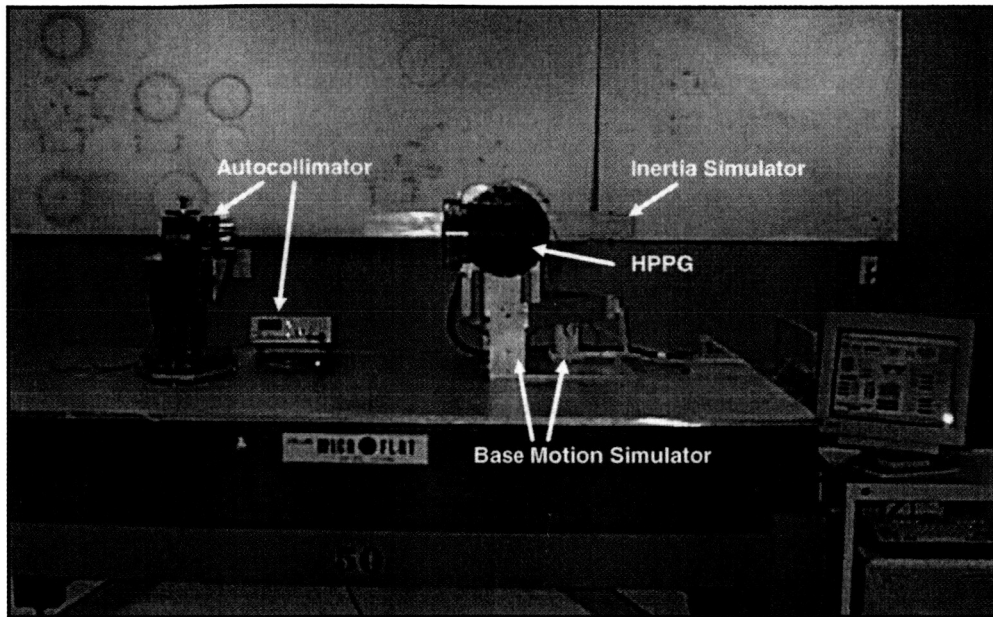
Figure 9: Test Setup
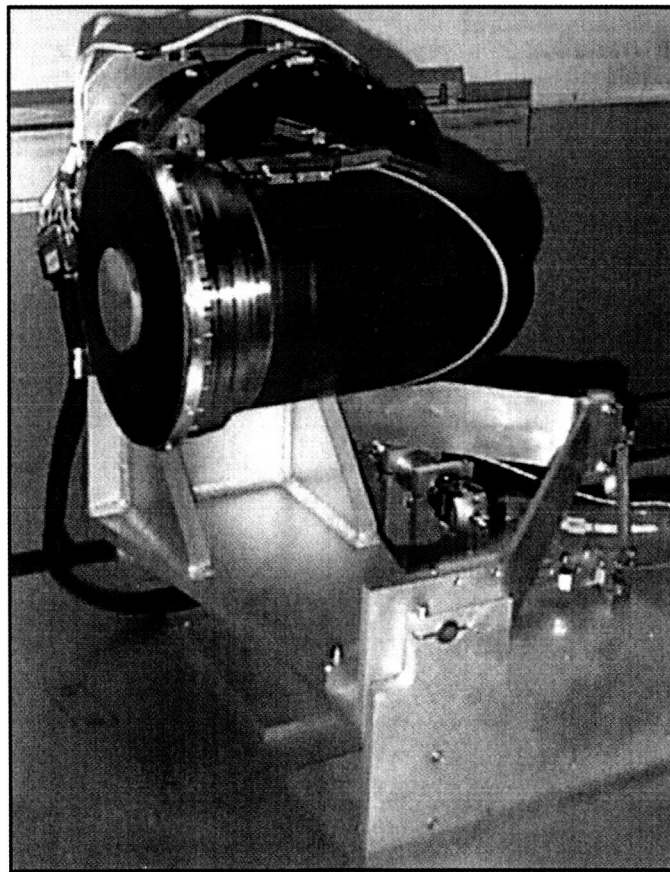
Figure 10: HPPG and Test Stand

Figure 10 shows a more detailed view of the HPPG. The diameter of the graphite epoxy elbow is approximately 19 cm (7.5 in). The front surface was capped and fitted with a 5 cm (2 in) mirror for use with the Micro-Radian Instruments autocollimator. The flat-flex cables along the top surface of the elbow are signal and power lines for any potential payload. The cablewrap housing is located at the base of the graphite-epoxy elbow. A flat-flex cable is draped over its top surface. An I-beam is attached to the rear of the shaft to effect an inertia load. With the I-beam installed, and only gravity-balancing weights attached, the HPPG baseline inertia in the test configuration was calculated to be 0.600 $N \cdot m \cdot s^2$ (84.9 $in \cdot oz \cdot s^2$). In some cases, an additional 1.0 kg (2.2 lb) of mass was distributed between the two outer mounting holes on the I-beam in order to increase the inertia to 0.763 $N \cdot m \cdot s^2$ (108 $in \cdot oz \cdot s^2$).

Results

Internal Feedback Mode
In order to evaluate controller performance several step responses about a nominal operating orientation (horizontal) were recorded. A typical step response for a 1.0 deg slew, and no added inertia is shown in Figure 11. Step response performance measures for additional step sizes and directions and two different inertia values are given in Table 2. In all cases the final orientation of the gimbal was as depicted in Figure 9 and Figure 10. The results for the larger inertias in Table 2 were obtained only after increasing the integral gain by a factor of 10 while reducing the integrator saturation limit by a factor of 10.

In order to obtain an estimate of the closed-loop transfer function, conventional and advanced techniques were combined. First, the estimate of the magnitude of the closed-loop transfer function in Figure 12 was obtained using classical methods—by performing numerical differentiation on multiple +1.0 deg step responses and averaging the Fourier transforms of the results. For the phase of the transfer function a less established technique was used—the Empirical Transfer Function Estimation method described by Tzes and Yurkovich[2] which can be summarized as taking the average of the quotients of the Fourier transform components of the input and output signals for multiple data ensembles. Each of these techniques alone can normally be employed to provide both the phase and the magnitude response. However, it was found that the variance in the resulting transfer function could be reduced if the relative strengths of each method were exploited separately.

---

[2] Tzes, A.; Yurkovich, S.; "A Frequency Domain Identification Scheme for Flexible Structure Control," *Transactions of ASME: Journal of Dynamics Measurement and Control,* Vol. 112, Sept. 1990
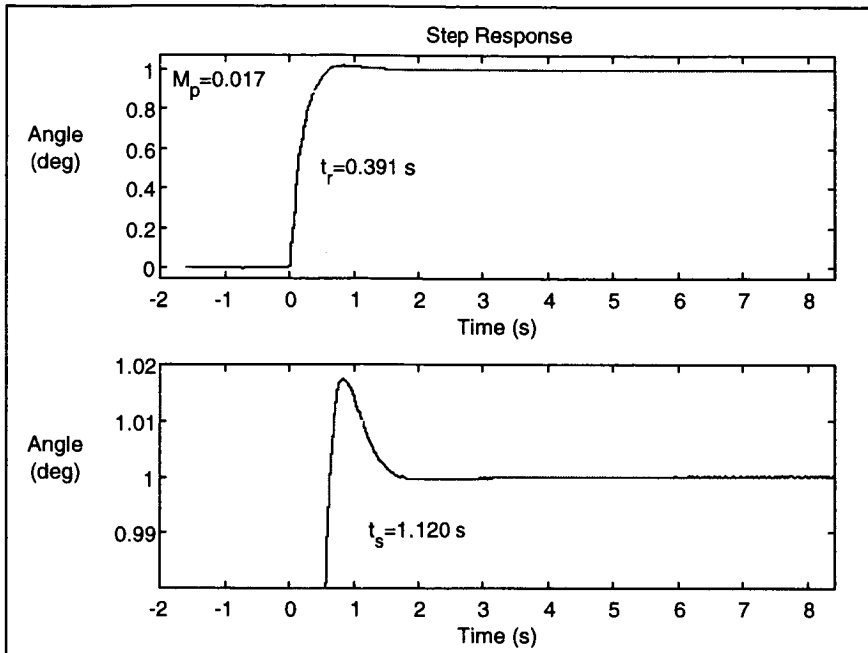
Figure 11: Internal Feedback Step Response (1.0 deg)

Table 2: Internal Feedback Step Response Performance

Inertia N·m·s² (in·oz·s²)	Step (deg)	Steady-State Error (10^{-6} deg)	1% Settling Time (s)	90% Rise Time (s)	Overshoot (%)
0.600 (84.9)	1	18	1.30	0.18	26.70%
	-1	13	1.12	0.40	-1.76%
	10	17	1.03	0.48	2.63%
	-10	16	0.89	0.50	-0.18%
	90	12	1.27	1.08	0.30%
	-90	12	1.33	1.16	-0.03%
0.763 (108)	1	22	1.12	0.13	59.59%
	-1	23	0.81	0.14	-23.24%
	10	19	1.03	0.33	13.07%
	-10	16	1.05	0.31	-16.02%
	90	19	2.48	0.98	23.16%
	-90	22	2.36	1.03	-23.15%

279
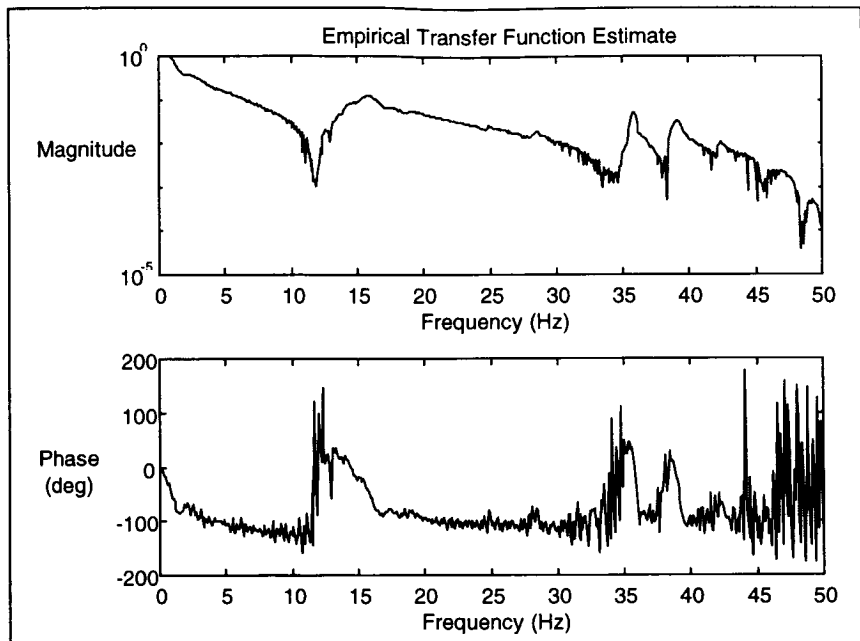
Figure 12: Closed-loop Transfer Function Estimate

External Feedback Mode

After the HPPG was transitioned to "External Feedback Mode", the base was excited with a sinusoidal motion at an amplitude of approximately 0.15 deg. Figure 13 shows the standard deviation (equivalent to the sinusoidal amplitude scaled by .707) of the autocollimator signal for the baseline HPPG inertia of 0.600 N·m·s^2 (84.9 in·oz·s^2) and base motion frequencies up to 2 Hz. Figure 14 shows the results of the same test after the HPPG inertia was increased to 0.763 N·m·s^2 (108 in·oz·s^2). For the larger inertia, proportional and derivative gains were doubled while the integral gain was increased 20 fold. The output at integrator saturation was held constant at 7 V.
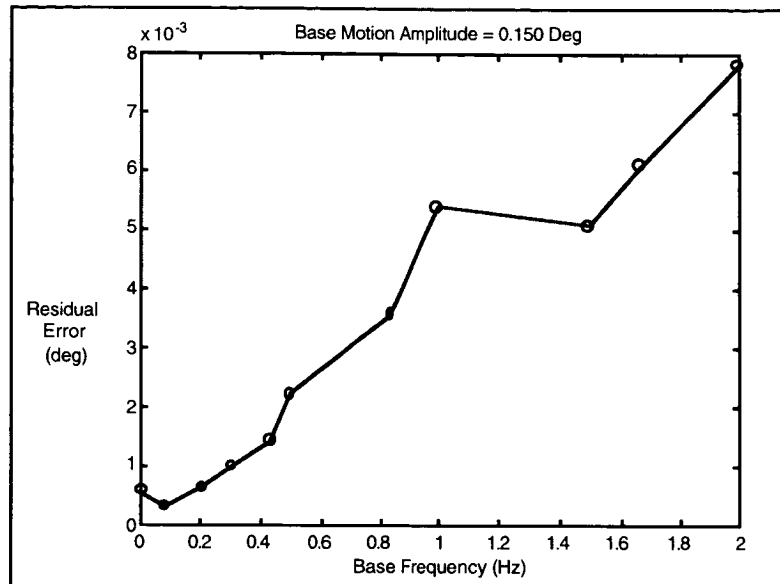
Figure 13: **External Feedback Sine Sweep, Baseline Inertia (0.600 N·m·s^2)**
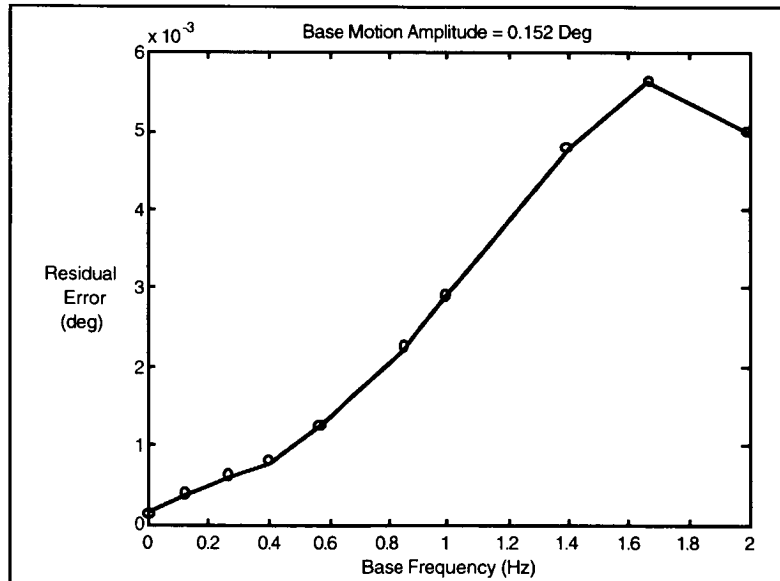
Figure 14: **External Feedback Sine Sweep, Larger Inertia (0.763 N·m·s^2)**

Conclusion

The results presented in this paper reveal that microradian positioning of a lightweight, low profile, single-axis gimbal with a large clear aperture can be achieved by combining a wide range of recent technological advances. This project also demonstrated the design and fabrication of a stiff, thermally stable, composite gimbal housing. A key design feature that enabled a composite structure to be integrated into a precision pointing mechanism was the bonding and alignment of the titanium end fittings.

Among the lessons learned from the HPPG effort is the fact that motor ripple error does not seriously limit the pointing accuracy of a gimbal. The results shown here also demonstrate that the destabilizing effects of noncollocated actuators and sensors can be eliminated by designing a structure with a much higher resonant frequency than the desired controller bandwidth. The two distinct problems of payload positioning and joint positioning pose different difficulties. It is well understood that structure rigidity and bearing stiffness are critical factors when accurate positioning of a payload is desired. The efforts of this project demonstrated that the driving factors limiting gimbal positioning accuracy are sensor resolution and accuracy. Future research will attempt to demonstrate similar pointing accuracies for multi-axis gimbals.

Acknowledgments

The Challenges of Designing a Retracting Tether for Space Applications

Jon R. Salton* and Frank W. James*

$S21-18$

168113

$164.$

336880

Abstract

An extensive development effort was conducted in an attempt to design a tool which would provide for the retention of an Orbital Replacement Unit (ORU) during maintenance operations on the International Space Station (ISS). Since ORUs come in various shapes, sizes, and masses, this tool was designed to be used in a large array of applications. The result of this effort was a retracting equipment tether mechanism capable of allowing an Extravehicular Activity (EVA) crew member to capture, retain, translate (if necessary), and release an ORU during such replacement operations.

Introduction

To aid in the construction and maintenance of ISS, the development of various different tools was necessary. Many of these tools were focused on the task of retaining either equipment (such as an ORU) or the EVA crew members themselves. In January of 1995, the development of a retracting tether that would retain an ORU during change-out operations began. Over the course of the next two years, the design was refined until the final ISS version was attained.

Numerous issues were addressed during the development process that helped to shape the fit, form, and function of the final design. Important knowledge was gained about materials, assembly techniques, visual markings, application of friction (both desirable and undesirable), and manufacturing concerns. Equally important in the development of the tool were the use of specific basic mechanisms such as ratchets, centrifugal brakes, clutches, and mating hardware interfaces. The final result was a robust design capable of operating in a broad range of applications with user-friendly features to suit a variety of operator preferences and needs.

With the initial design incorporating an EVA Equipment Hook nested inside of a small rectangular 'box', it was found that more control was needed in keeping the ORU stable. Without a large enough footprint to react against, the ORU was able to move around in too large of a volumetric envelope. This caused a separation of the retracting tether from the 'hoop' interface that maintained the orientation of the ORU. Essentially, it was found that a 'balloon-on-a-stick' type of interface was not acceptable while at the same time, precise control of the ORU was not necessary. Therefore, the interface was changed to a hoop with a larger circumference than the first design and it was separated from the retracting mechanism so that more flexibility in its orientation could be attained. This made the tool easier to use and kept the ORU more stable

---

* Lockheed Martin Space Mission Systems & Services, Houston, TX

while still not having to hold it rigidly. The final design to be used on the International Space Station was called the ORU Tether Assembly (Figure 1).

The first design effort for this retracting equipment tether mechanism was manufactured and flown on STS-72 (1/96) with mixed results. The second design effort was a reconfiguration of the first and flew on STS-80 (11/96). However, no EVA occurred on this flight due to an orbiter hatch malfunction. It successfully flew again on STS-87 (12/97). In addition to this, the certification testing and training that accompanied these flights produced a wealth of knowledge. This led to the design of the final version that will be used on the space station. Four prototype/trainer, one qualification, and two flight units were made in 1997 and eight more flight units were ordered for 1998 deliveries.

Tool Requirements

The initial requirements for this project were to produce an EVA tool for ISS that would retain a defective or worn out ORU during change-out operations. In addition, the tool was needed to retain ORUs without provisions for handling or interface with robotic devices. Initial scenarios used this tool in conjunction with other tools. With EVA compatible interfaces, the tool could be used as a type of end effector on various types of EVA crew member or structure-mounted hardware.

During the initial stages of the design, most of the features of the tool were defined by the basic operational requirements. For example, the fact that the 'old' ORU had to be retained within some defined area meant that the retracting tether needed a feature that would prevent the tether cord from extending freely. In addition to this, it had to allow a crew member to easily pull out the tether cord when retrieving an ORU. This immediately defined the need for at least two modes of operation: retention and free running. However, after initial design reviews and testing, features were added or modified that enhanced the use of the tool while in these modes of operation.

These additional features were added to broaden the functionality of the tool depending on the task to be performed and simplify operations for a wider variety of users. However, this is the point in every design process where extreme discretion is needed. It is often easy to add features that add too much complexity to the operation of the tool. Also, features that are seldom used should be avoided because they do not focus enough on the basic requirements of the design.

With this in mind, a brief summary of the operational features incorporated into the final ISS design can be explained. There are three basic modes of operation for the tether cord. These modes are as follows:

Free — allowing the tether cord to extend & retract freely
Lock-In — allowing the tether cord to retract freely, but not extend
Lock-Out — allowing the tether cord to extend, but not retract

Every EVA tool that is not hard mounted to structure must have a tether point. This is for translating to and from the worksites at which they will be used. To satisfy this requirement, the ORU Tether Assembly incorporated an integral tether point into its housing (Figure 1). Also, a clutch was needed for the 'Lock-In' mode of operation in order to protect the ORU tether point interface from damage. These core design features were able to accommodate all of the foreseeable uses and possible misuses of the tool and included the basic requirements needed to accomplish ORU change-out tethering operations.

Design Considerations

Visual Markings
Consideration was given to the visual markings or indicators that corresponded to each mode of operation. Initially, a color scheme of green, red, and yellow was used to indicate the 'Free', 'Lock-In', and 'Lock-Out' modes of operation, respectively. However, after preliminary evaluation, it was found that this was both too complex and not as contrasting as simply using white and black. In fact, this tool along with several other tools being developed at the same time showed that black and white visual indicators were preferred over any other color combinations. Our design team standardized on the procedure of using black-on-black to indicate locked and white-on-black to indicate unlocked or released. The text was engraved and back-filled with the appropriate color permanent ink. Another lesson learned was minimizing the number of words to read. All users would be trained to operate the mechanisms prior to flight. Therefore, just one or two words were sufficient to remind the user which way to turn the control lever for each function.

Lubricants
In the environments that ISS EVA tools will see, lubrication between moving parts can be critical. This is particularly true of the extreme cold environments, which can be as low as -100°C (-150°F). Even the best greases begin to freeze at just under -73°C (-100°F). In most cases, it is best to design key areas of a mechanism such that no secondarily applied lubrication is necessary. Quite frequently, this can be accomplished by using Teflon-impregnated hard coatings, dry film lubricants, or non-metallic bushings and spacers such as Vespel[1]. However, care must be exercised in using some of these techniques. For example, while graphite is a highly effective lubricant in the presence of water vapor, it can actually become abrasive in the absence of moisture (such as in the vacuum of space).

Another important facet to the lubrication problem is that of migration. There are certain aspects to every design that require friction. Therefore, it may be undesirable to have lubricant from one part of a mechanism migrate to other areas. This is especially important when using oils and greases. Even some non-metallic materials such as plastics with graphite additives can be detrimental if not used judiciously. This

---

[1] DuPont Engineering Polymers, Pencader Site, Newark, DE.

was of particular interest for this design in the area of the 'Lock-Out' brake and 'Lock-In' ratchet. These two features were in close proximity to one another within the mechanism. Therefore, it was important that the lubricant necessary to the function of the ratchet did not migrate to the 'Lock-Out' brake. If this were to happen, it could prevent the 'Lock-Out' brake from functioning properly. For this application, it was decided to use a dry film lubricant on each of the locking pawls. This enabled the 'Lock-In' ratchet to function properly throughout its temperature range without putting the 'Lock-Out' brake in jeopardy of failing.

Often times it is possible to make a mechanism work sufficiently without the application of any post-manufacturing lubricants. However, in some cases where alternative methods are not possible, the use of greases or oils may be necessary. This has been found to be true even when the temperatures go below the freezing point of the lubricant, provided that they have been applied properly. If used only in certain areas of a mechanism and if applied in a very thin layer, grease and oil have been found to be effective. However, if used too generously or in areas where very low motive forces are used to actuate mechanisms (such as with small springs), then grease or oil can cause failures to occur.

Constant-Force Spring Applications
While establishing the requirements for the tool, it was decided that a low, constant retracting force would be desirable. This would allow for a light and consistent manipulation of the tether cord. The logical way of accomplishing this was to use a Neg'ator constant-force spring. During the initial stages of the development, in an attempt to make the retracting mechanism as compact as possible, the design used a spring configuration with coaxial spool and spring arbor axes (Figure 2a).

In ambient conditions, using grease as a lubricant, this design had no problems. However, at cold temperatures, the grease drastically reduced the performance of the spring due to the large amount of inter-coil friction inherent with this spring configuration. Therefore, a low viscosity oil was used instead in an effort to minimize the impact of the inter-coil friction. During the certification testing of the first flight unit though, it was discovered that even with the oil, the inter-coil friction of the spring was too great. The tether cord had difficulty retracting at temperatures below approximately -46°C (-50°F).

Therefore, an alternate spring configuration was used with separate axes for the spool and spring arbor (Figure 2b). While this did cause the volumetric envelope of the tool to grow somewhat, it eliminated the inter-coil spring friction and allowed the retracting tether to function properly throughout its operating temperature range. This also had the added benefit of prolonging the life of the spring.

Ratchet - Lock-In Mode

During the design, certification, and fight testing of the retracting mechanism, several things were learned that were transferred directly into the final design. The first was the development of the ratchet layout used for the 'Lock-In' mode of operation. For safety reasons, it was decided to mechanically drive the locking pawls (Figure 3) to the unlocked or disengaged position. Springs were used to engage the pawls into the ratchet teeth. This layout ensured the pawls could be disengaged in the event of a spring failure. In order to minimize the amount of backlash in the retracting cord once the 'Lock-In' mode was selected, three out-of-phase pawls were used. They were sized to carry the load individually. This also allowed for the failure of all three pawl and spring combinations before the ratchet failed altogether. The lubricants chosen for the initial designs proved to be detrimental at approximately -46°C (-50°F). Therefore, the final design used a dry film lubricant rather than grease on the locking pawls.

The same control lever incorporated the cams for both the 'Lock-In' pawls and the 'Lock-Out' brake buttons. The two cams were combined on the same shaft as well as providing for a position in which both features were disengaged (the 'Free' mode). Ball plungers in the control lever were used for positive engagement of each operational mode and positive stops were positioned so that the control lever could not be assembled incorrectly. Finally, the surfaces of the control lever external to the assembly were designed with a profile that would interface with an EVA crew member's gloved hand. All of this made for a very complex part. Phasing of the cams, detents, ball plungers, stops and visual indicator markings all had to be carefully laid out allowing for machining and the ability to assemble the mechanism. On the other hand, making the control lever a single component allowed for a very compact retracting tether design with fewer fasteners and increased reliability.

Orbital Replaceable Unit Tether Point Loads

A load-limiting clutch is active when the pawls of the 'Lock-In' mode are engaged into the ratchet teeth. The purpose of the clutch was to limit the load transferred to the tether points to which the retracting tether was attached. This feature would allow the numerous providers of ORUs with tether points to design their products with a minimum load requirement regardless of the input loads. This minimum limit was set at 334 N (75 lbf) early in the development of the space station program and follows the established equipment tether ratings for the space shuttle[2]. The ORUs that require tether points for EVA handling scenarios range from less than 0.5 kg (1 lbm) to over 160 kg (350 lbm). Providing a load-limiting feature allows for much greater design flexibility and reduced development costs for all such ORU providers.

The clutch was comprised of a non-metallic composite material[3] sandwiched between the corrosion resistant steel component of the ratchet teeth and a hard anodized

---

[2] NASA JSC26626A, Generic Design Requirements Document.

[3] Universal Friction Composites company, M8351 graphite composite.

aluminum plate (Figure 4). The non-metallic clutch material was keyed to the spool that stores the tether cord. The load was applied to the clutch via two Belleville springs in series and a uniquely designed fine-pitch lock nut. It was discovered in the initial design of the clutch that its slipping force varied too much within the required temperature range of -87°C to 104°C (-125°F to 220°F). In this initial design, the Belleville springs were used in the 90% compressed range. With no development resources available to research the issue, it was speculated that the Belleville springs may have been the cause of the variations. The final design switched to Belleville springs that would produce the required load at approximately 35% of their total available deflection. This application of the Belleville springs proved to be capable of handling the temperature range required without undue variations in clutch performance.

Retraction Force Relief - Lock-Out Mode

Another design consideration was for the 'brake' incorporated into the 'Lock-Out' mode of operation. It was important that this aspect of the design work properly since it would eliminate the need for the user to have to think about the potential energy that was being stored as the cord was extended. The trick was to allow the cord to extend smoothly and consistently while at the same time, prevent it from retracting.

One option would have been to use detents with ball plungers. However, this would have made the extension of the cord fairly jerky. Therefore, it was decided to use spring-loaded buttons that would press against the braking surface when actuated by a cam. However, in order to make the brake work consistently throughout its entire life, the buttons were made from a non-metallic polyimide resin (Vespel SP-1)[4]. This would allow for much smoother extension of the cord.

In order to ensure that the brake would prevent the cord from inadvertently retracting while in the 'Lock-Out' mode, six small flats were added to the circular braking surface (Figure 5). Through development and training, it was also found that these flats had the additional effect of giving the user tactile feedback that they were indeed in the 'Lock-Out' mode while extending the cord. This proved to be quite beneficial in that it set the modes of operation apart from one another with tactile as well as visual feedback.

Centrifugal Brake

During the initial development of this tool, it was realized that some method would be needed to control the stored potential energy if the equipment hook was inadvertently released. This was clearly demonstrated during a development test on NASA's Zero G aircraft with the first development unit. When the tether cord was released after extending out 1.83 m (6 ft) and while in the 'Free' mode, the equipment hook was able to cause noticeable denting and scratching to anything that it impacted. To make

---

[4] DuPont Engineering Polymers, Pencader Site, Newark, DE, Type I, unfilled base resin per MIL-R-46198, Amendment 2, 20 September 1996.

288

matters worse, the ISS version of this tool was to have 3.66 m (12 ft) of tether cord. Both of these factors meant that logically there should be some way of controlling the retraction of the tether cord in the event of an inadvertent release while in the 'Free' mode of operation.

This was accomplished through the use of a centrifugal brake (Figure 6). However, the difficulty in designing a centrifugal brake is that the coefficient of friction can not be easily predicted. Also, depending on the materials used, the coefficient of friction can change with wear and/or changing environmental conditions. Therefore, it was decided to use non-metallic (Vespel SP-1) brake pellets in an attempt to eliminate the possibility of galling, reduce wear, and maintain braking characteristic consistency. For this particular application, it was desired to make the brake as effective as possible without making it self energizing. In other words, the tether cord should retract as slowly as possible without stopping.

Through the development of other ISS EVA tools, it was found that the coefficient of friction between hard anodized aluminum and Vespel SP-1 varied after being operated at elevated temperatures of 66°C (150°F) or more. This was accounted for during the development of the retracting tether by assuming a large range in the coefficient of friction, and the design turned out to be robust enough to work as desired. This emphasized the need to account for friction coefficient variations during the early stages of all designs.

Tether Cord
Another feature of the design that needed careful consideration was the tether cord itself. One of the most frequently made comments by EVA crew members concerning EVA operations is the large amount of time that is spent thinking about the location of their safety tether cord. Therefore, in developing any retracting tether, reducing the tether cord operational 'overhead' can be of paramount importance.

In addition to this, thought should be put into how the tool will be applied relative to its surroundings. For example, during an EVA it is not always possible to control what the tether cord rubs against. Therefore, in general, larger cords will do better than smaller ones. Not only will it be stronger, but it will also be less likely to get caught in cracks and crevices and it will be easier to see. Non-metallic cords tend to be preferred over metal cables since they are more easily manipulated. Metallic cables also have the potential to damage soft goods (such as the EVA Mobility Unit (EMU) i.e., space suit) when they become frayed. With all of this in mind, it was decided to use a non-metallic

liquid crystal polymer fiber material called Vectran[5]. The drawback of using this material is that it will have to be a limited life item for ISS[6].

Since the tether cord would need to meet its minimum breaking strength requirement at the end of its life, a study of the degradation factors for ultraviolet and atomic oxygen exposure, abrasion, temperature, and cord end termination was made. From all of this, an equation was used to help define what the strength of the tether cord would be as it degraded over time.

To begin with, the end of life strength (σ_{el}) of the cord was defined as:

$$\sigma_{el} = 1.5 \times \text{Maximum Operational Load} \qquad (1)$$

where the maximum operational load was the limit load of the ORU tether point of 334 N (75 lbf). Substituting this into Equation 1 gives the following:

$$\sigma_{el} = 1.5 \cdot (334 \text{ N})$$
$$= 501 \text{ N} (112 \text{ lbf})$$

The next step was to determine how the initial cord strength would degrade with use and exposure. Equation 2 below shows how this breaking strength (σ) as a function of time was calculated[7]:

$$\sigma(t) = K_{sp} \cdot K_{t,perm} \cdot K_t \cdot K_{uv}(t) \cdot [K_{ao}(t) + K_{abr}(t) - 1] \cdot B_{allowable} \qquad (2)$$

where

K_{sp} = degradation coefficient due to cord end termination (experimental)

$K_{t,perm}$ = degradation coefficient for one time permanent temperature exposure (manufacturer's data)

K_t = degradation coefficient for transient temperature exposure

K_{uv} = degradation coefficient for ultra violet exposure (experimental)[8]

K_{ao} = degradation coefficient for atomic oxygen exposure (experimental)[9]

K_{abr} = degradation coefficient for cyclic abrasion (experimental)

---

[5] Hoechst Celanese Corporation, Charlotte, NC. This material, configured into a hollow braided cord proved to be more resistive to ultraviolet light and atomic oxygen exposure than other non-metallic cord materials evaluated.

[6] Any item kept in orbit with an operational life of less than the ISS projected 15 years is considered to have a limited life.

[7] Bilateral Tools Critical Design Review #3, Johnson Space Center, May 8, 1996.

[8] Manufacturer's data for long term Florida coast exposure to approximate EVA ultraviolet exposure for ISS tools.

[9] Dosage based on expected atomic oxygen exposure of 5.0×10^{21} atoms/cm^2 per year per JSC26626A, Generic Design Requirements Document.

and $B_{allowable}$ is the experimentally derived strength of the raw cord using the statistical mean minus two standard deviations of a sample lot of 20 cords tested to failure. The results of this study are summarized in Figure 7 and show how the tether cord breaking strength degrades over time.

The end of life strength in combination with the degradation equation were then used to determine what life span particular size cords would have. The cord chosen for the final ISS design of the ORU Tether Assembly actually started its life with a breaking strength of over 2700 N (600 lbf) in ambient conditions. This information was then used in conjunction with information on all other limited life items in the assembly[10] (based on stowage location and projected amount of use while in orbit) to arrive at a 5 year limited life. From here, it was a simple matter to plug in all of the coefficients and $B_{allowable}$ into Equation 2 to calculate the cord breaking strength as a function of EVA time. When $\sigma_{el} = \sigma(t)$, the end of life limit had been reached. As Figure 7 shows, this occurred at approximately 1900 hours of EVA time which corresponded to approximately 5 years of ISS EVA usage[11].

Mounting Interfaces
One obvious consideration for the retracting mechanism was how it would be mounted to structure. An important element to all interfaces is versatility. A large part of this includes trying to establish all of the foreseeable uses of the tool. In this case, it was initially thought that the mechanism would mount to structure via an existing EVA quick connect mechanism, which would not require the use of tools for installation/removal. The downfall of this approach was that the quick connect required a lot of volumetric real-estate. This in turn located the retracting mechanism too far from the structure and into the working envelope of the EVA crew member. Real estate is at a premium when trying to operate at a work site in the EMU.

Through the evolution of the design (which included the separation of the ORU interface 'hoop' from the retracting mechanism), it was found that an alternate interface was needed. This alternate interface used the same six-bolt circular pattern as the existing quick connect mechanism while occupying far less volume. This allowed flexibility with future configurations of the tool. In addition, the hole pattern in the retracting mechanism was expanded to a 12 hole pattern for maximize mounting orientation options. The alternate design allowed the user to install the retracting mechanism without tools. To remove the unit, a simple 'probe', much like a flat-bladed screwdriver, could be inserted into a cavity thereby tripping a restraining latch. The unit would then be free from the structure to be moved to a new location or replaced at the end of its useful life.

---

[10] The marking ink for visual indicators and the Neg'ator spring were also determined to have approximately a 5 year life span.

[11] Only the EVA operational time was counted toward its life. During non-operational periods, the cord is protected inside of the retracting mechanism.

Manufacturing Issues

Another area of the design that needed to be considered was manufacturing processes. With all of the tight tolerances and exotic materials that are often called for with space application mechanisms, manufacturers have a challenging task to meet all of the requirements on the drawings. This, combined with the fact that only very limited quantities of each product are made, demands that special attention must be given to certain aspects of the manufacturing process.

One of these considerations was the sharp edge requirement that all EVA hardware is obligated to meet. The requirement states that any edge that can come into contact with an EVA crew member's gloved hand must have a minimum 1.5 mm (0.06 in) radius. If this is not possible for all of the exposed edges on a tool, then each discrepant edge must pass a certification test that proves that it will not cut the glove. In theory, this is not a difficult requirement to meet. In practice however, manufacturing vendors consistently provided discrepant hardware in this respect. Even with tailored notes on the drawings, it was found that the key to solving this problem was frequent communication with the vendors.

Another aspect of manufacturing that needed special attention was that of hard anodizing of aluminum parts. Although the anodizing specifications are clear on surface growth for finished dimensions, the tight tolerances sometimes required frequently resulted in discrepant parts. Ultimately, the best solution to this problem seemed to be ensuring up front that manufacturers had good communication with their anodizing vendors prior to beginning any machining processes. This allowed the anodizers to work in tandem with the people doing the machining to see that the finished product met its requirements. This approach has been the most effective in obtaining the desired results.

The post-fabrication inspection of parts was yet another manufacturing aspect that required careful consideration. For the most part, hardware designed for space applications is only manufactured in limited quantities. As a result, it is usually not practical to use gages or any other production run type of inspection equipment. This means that the post-manufacturing inspection of parts must be kept in mind during both the design and fabrication stages. Parts that are difficult to inspect can add both time and expense to the finished product. There are times when a simple change of an angle, a radius callout, a tolerance, or some other small modification can be made to greatly reduce the inspection effort. Asking for inspector's input during the design phase can also be helpful at times. Also, during the fabrication phase, particular features that are too difficult or costly to inspect may simply need to be verified by a fit check rather than dimensional inspection. However, this may only be done in cases where stress is not an issue. For example, the cam surfaces for the 'Lock-In' and 'Lock-Out' modes on the control lever were quite complex and difficult to inspect. Therefore, since there were no small stress margins on that part, the only mandatory inspection points in that area of the part were the major and minor diameters. All of the

other cam features (rising rate, angle of dwell, corner radii, etc.) were simply verified at assembly. This greatly helped to facilitate the inspection process.

Finally, there were important lessons learned during the development of this tool along with other ISS EVA tools concerning two particular manufacturing processes. The first was the application of polymer impregnated hard coatings. Through the development of the prototype, training, and flight hardware, it was found that General Magnaplate's[12] HRC and Tufram Teflon[13] impregnated hard anodizing were superior to any other processes that were used for this purpose. This was true for both performance and endurance. However, when using these coatings, it was crucial to contact General Magnaplate at the very beginning of a project. Whenever this was done, there was no impact to delivery schedule. However, if a manufacturer waited to contact General Magnaplate, then the backlog of work that they had would sometimes greatly impact the desired delivery dates. Again, good initial communication with the vendors (as well as the fabrication planners) was the key to solving this potential problem. The second manufacturing process of concern was the use of dry film lubricants. In cases where it was necessary to use dry film lubricants, it was determined that post application burnishing was crucial. Without this process, parts that sat for long periods of time with no use would tend to bond to adjoining surfaces. When properly burnished though, dry film lubricants can be used in limited applications.

Assembly Considerations

One final aspect of the design that did not receive enough initial attention was the assembly of the tool. On the first development unit, it was discovered by mistake that the control lever (Figure 1) could be inserted into the mechanism 180° out of phase. If this was done, the control lever would become locked into place and could not be removed without damaging the assembly. The final design was made so that it could not be assembled incorrectly by adding a boss to the control lever and a groove to its mating part that prevented the two pieces from being joined improperly.

In retrospect, the subtle nature of how this anomaly could occur proved to be an important lesson in how to approach assembly techniques and procedures during the early phases of the design. While an extensive effort was made to make the assembly of the tool possible, improper assembly was overlooked. It became obvious then that when contemplating the assembly of a mechanism, consideration should be given to improper, as well as proper, assembly procedure. Prevention of improper assembly turned out to be the best approach.

---

[12] General Magnaplate Corporation, Arlington, TX.
[13] E.I. du Pont de Nemours and Company, Wilmington, DE.

Conclusion

As stated earlier, the purpose for this tool was to retain a worn out or defective ORU during change-out operations. The development process of this tool proved to be quite beneficial for the knowledge and insight that was gained. A great deal was learned during every phase of the development. For visual markings and indicators it was found that it was best to use only black and white colors for contrast and simplicity. When dealing with lubricants, how and where they were used was sometimes just as important as what was used. While the application of constant-force Neg'ator springs for retracting tethers is common practice, it was learned that configurations that relied on inter-coil friction would not work in large temperature range environments. Although more complex, it was realized that offset phasing of the locking pawls for the ratchet design was necessary to minimize backlash. With the large temperature variances expected in the ISS EVA environment, it was learned that Belleville springs should be used near the middle of their load curve whenever possible in order to maintain their spring constant. It was found that tactile, as well as visual feedback can be beneficial in certain operational situations. The development of the centrifugal brake showed the importance of designing for a broad range of friction coefficients. For the tether cords, using as large of a cord as the design would allow proved to be wise in dealing with degradation. When contemplating mounting interfaces, looking at what was available and designing for present and possible future interfaces was found to be beneficial. It was determined that maintaining open communication with manufacturing vendors was crucial throughout the fabrication phase. Finally, it was also learned that keeping all aspects of the tool assembly in mind during the design phase was critical. In the end, the lessons that were learned during the extensive development time put into this tool can now be applied to the design of other EVA mechanisms for use in the shuttle program and on the International Space Station.

References

1. Adlis, David S., JSC 26626A, Generic Design Requirements Document, May, 1995.

2. Oceaneering Space Systems, Bilateral Tools Critical Design Review #3: Tether Cords, May 8, 1996, pp. 73-98.
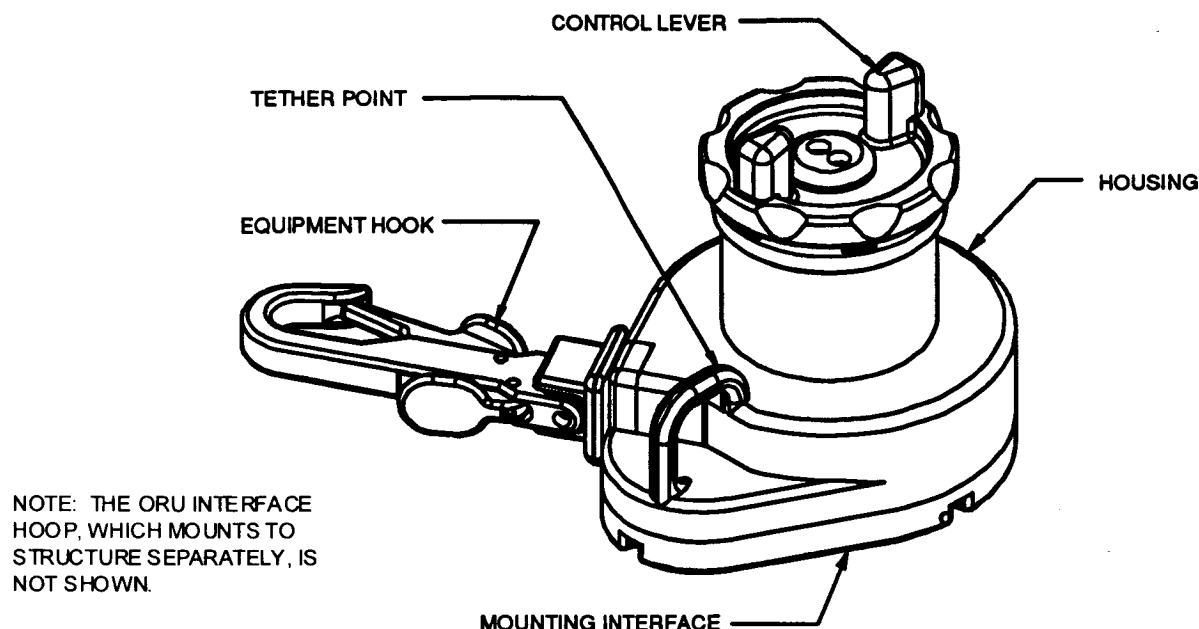
FIGURE 1: International Space Station ORU Tether Assembly

CONTROL LEVER

TETHER POINT

EQUIPMENT HOOK

HOUSING

NOTE: THE ORU INTERFACE HOOP, WHICH MOUNTS TO STRUCTURE SEPARATELY, IS NOT SHOWN.

MOUNTING INTERFACE

CORD SPOOL

ARBOR

NEG'ATOR SPRING
(REVERSE WOUND)

(a)

ARBOR

NEG'ATOR SPRING
(REVERSE WOUND)

NEG'ATOR SPRING
(FREE STATE)

CORD SPOOL

(b)
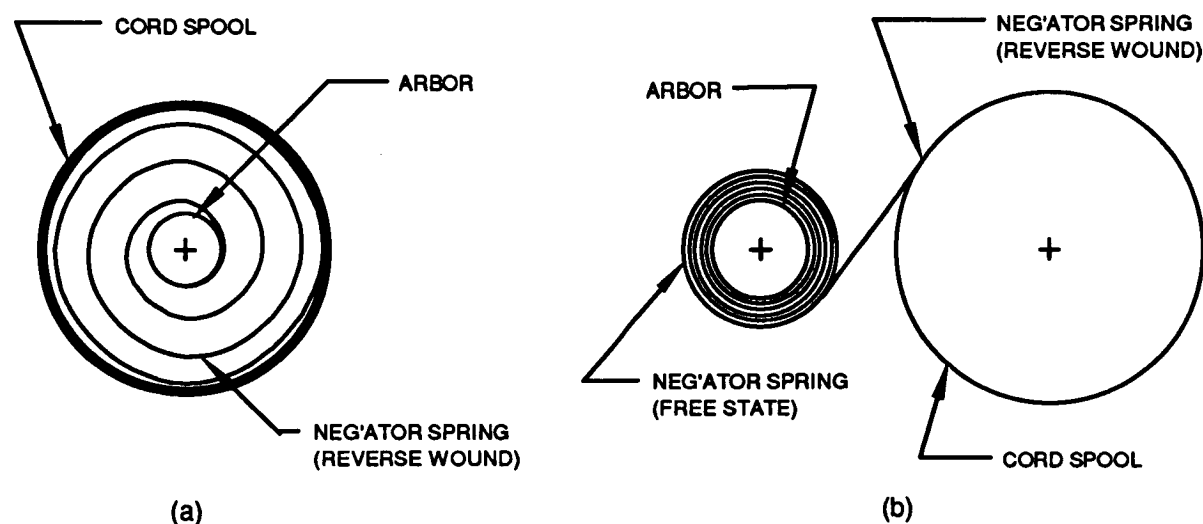
FIGURE 2: Constant Force Neg'ator Spring Configurations

295

RATCHET TEETH

CONTROL LEVER CAM
(LOCK-IN MODE)

ATTACHED TO
CORD SPOOL
THROUGH LOAD
LIMITING CLUTCH

LOCKING PAWL

LEAF SPRING
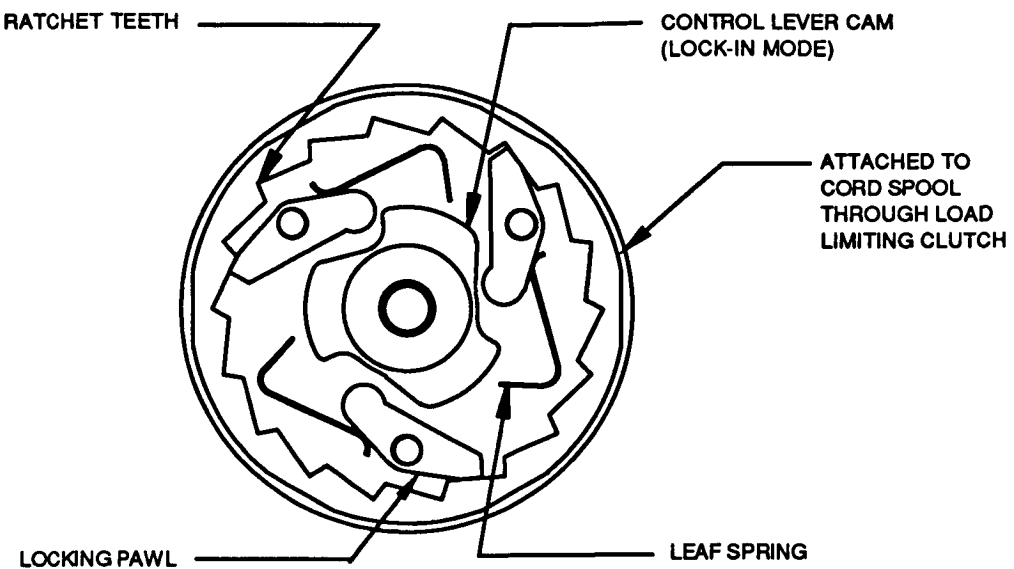
FIGURE 3: Lock-In Ratchet Layout

GEAR TEETH FOR RATCHET
LOCKING PAWL INTERFACE

GEAR RING

CLUTCH PLATE
(KEYED TO CORD SPOOL)

BELLEVILLE
SPRINGS

RETAINING PLATE
(KEYED TO GEAR RING)

LOCK NUT
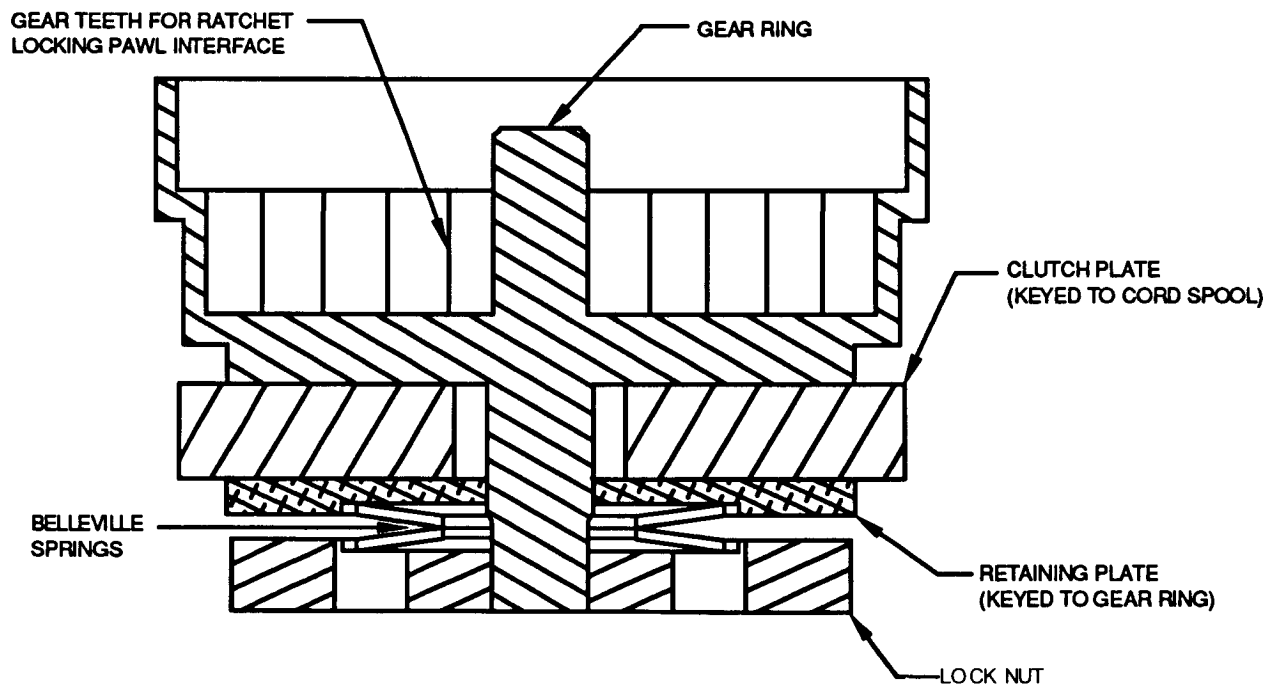
FIGURE 4: Load Limiting Clutch Layout

296

SPRING LOADED
BRAKING BUTTONS

CONTOL LEVER
CAM

ATTACHED TO
CORD SPOOL

BRAKING SURFACE 'FLATS' (6 PLACES)
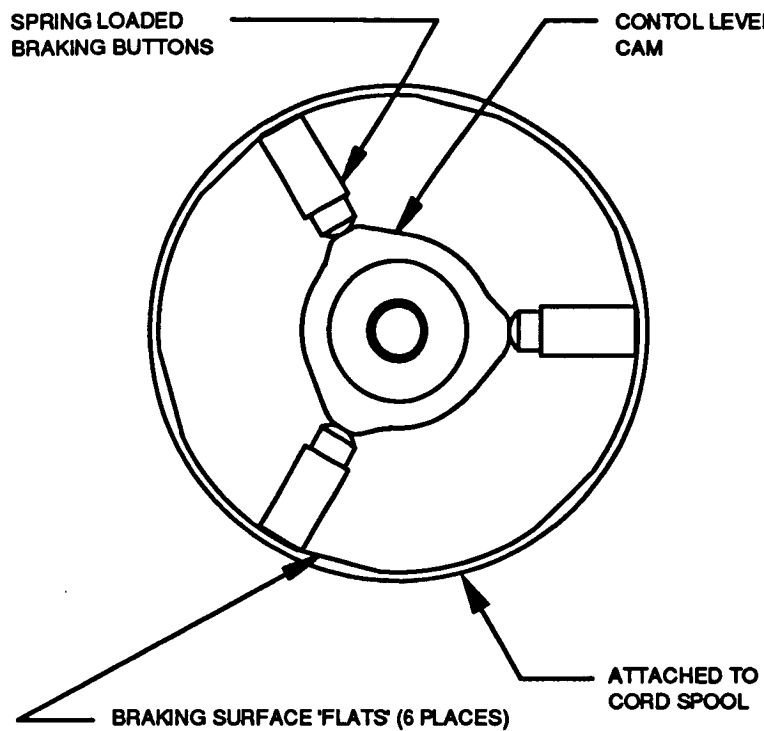
FIGURE 5: Lock-Out Brake Layout

BRAKE ARM

HOUSING

BRAKE PELLETS
(VESPEL SP-1)

CENTER OF
GRAVITY

ATTACHED TO
CORD SPOOL

RETRACT

EXTEND

CORD SPOOL ROTATION
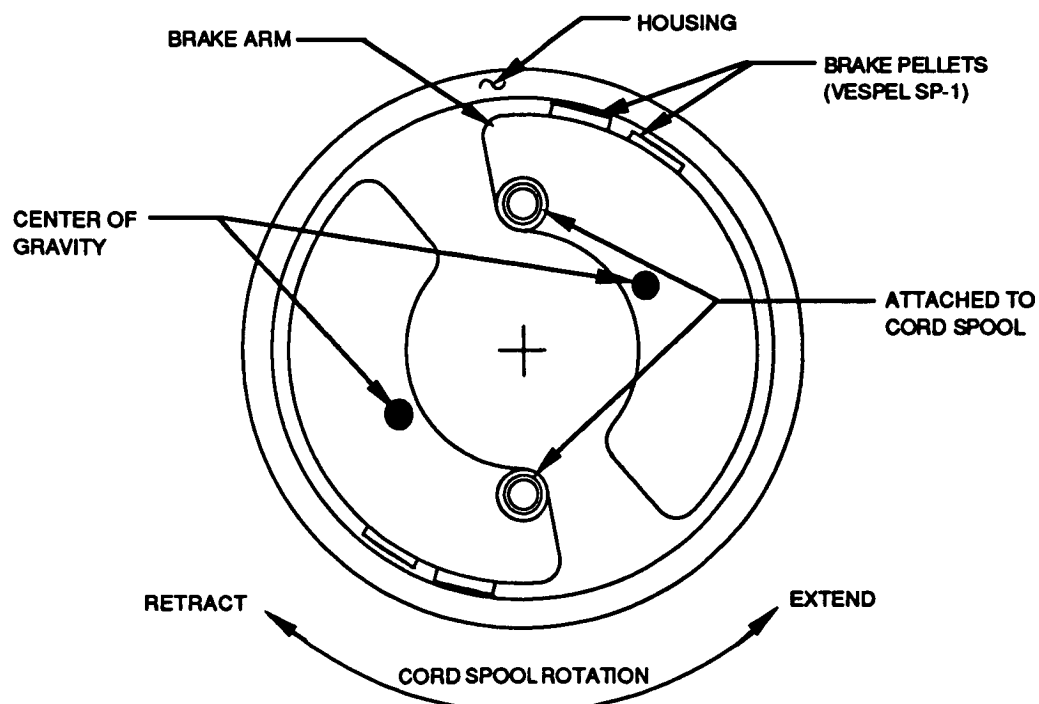
FIGURE 6: Centrifugal Speed Brake Layout

# Vectran Cord Strength vs EVA Time
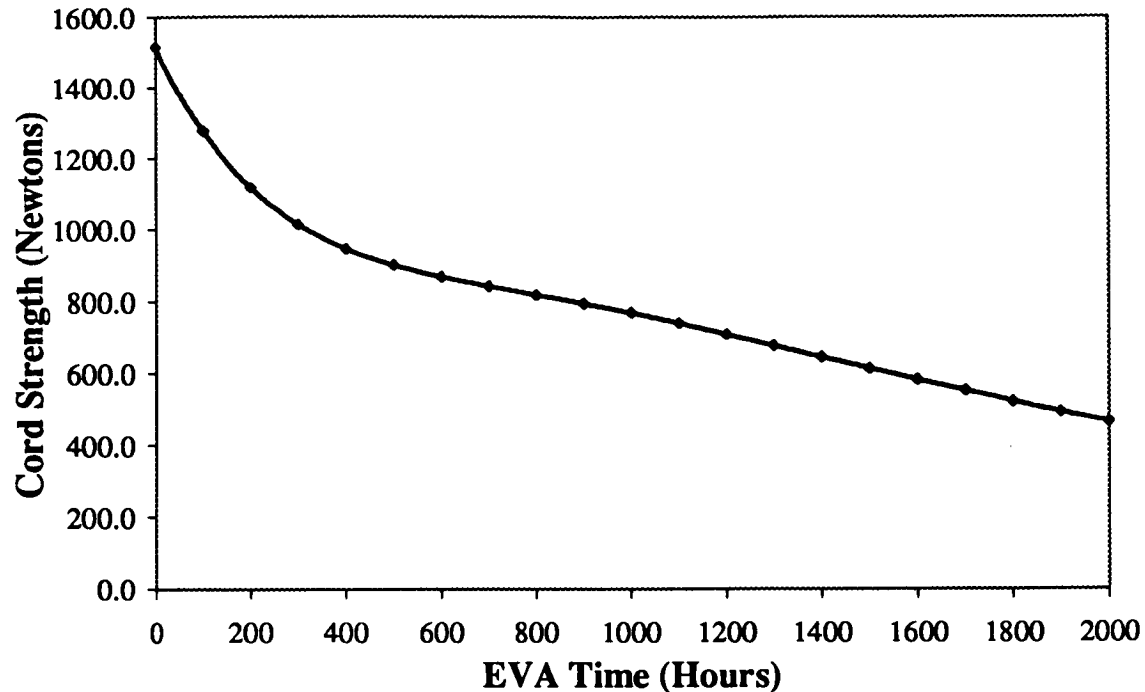
FIGURE 7: Tether Cord Degradation

298

Research on Liquid Lubricants for Space Mechanisms

William R. Jones, Jr.[*], Bradley A. Shogrin[**] and Mark J. Jansen[+]

Abstract

Four research areas at the NASA Lewis Research Center involving the tribology of space mechanisms are highlighted. These areas include: soluble boundary lubrication additives for perfluoropolyether liquid lubricants, a Pennzane dewetting phenomenon, the effect of ODC-free bearing cleaning processes on bearing lifetimes, and the development of a new class of liquid lubricants based on silahydrocarbons.

Introduction

Most moving mechanical assemblies for space mechanisms rely on liquid lubricants to provide reliable long-term performance. Historically, these materials have been based on mineral oils, polyol esters, perfluoropolyethers (PFPEs) or polyalphaolefins (PAOs) [1]. Recently, a new synthetic hydrocarbon, a multiply alkylated cyclopentane (Pennzane), has seen increased use [2]. However, all of these materials have disadvantages that can limit their lifetimes in a lubricated contact. The PFPEs [3] are poor boundary lubricants and will not solubilize conventional additives. They are also susceptible to autocatalytic degradation [4]. Mineral oils have wide molecular weight distributions and thus, volatility problems [5]. Recently, Pennzane dewetting problems have been reported [6].

In addition, with the phasing out of ozone-depleting chemicals (ODC), new concerns about bearing lifetimes have arisen due to the use of new, unqualified ODC-free cleaning techniques [7]. This paper reviews current research at NASA related to some of the above problem areas. These include: the development of a new series of soluble, low volatility, antiwear and anti-degradation additives for use in PFPEs, studies of the Pennzane dewetting phenomenon, and the use of the NASA ball-on-plate vacuum tribometer and parched EHL apparatus to study the effects of surface chemistry from ODC-free cleaning techniques on lubricated lifetimes. In addition, the development of a new class of synthetic space lubricants, based on the silahydrocarbons, is reported.

---

[*] NASA Lewis Research Center, Cleveland, OH
[**] Case Western Reserve University, Cleveland, OH
[+] AYT Corporation, Brookpark, OH

PFPE Boundary Lubrication Additives

Perfluoropolyethers (PFPEs) are widely employed as lubricants for space applications because of their excellent thermal and chemical stability, low volatility, spectral transparency and excellent EHL film forming characteristics [3]. However, when used as a boundary lubricant with steel surfaces, their performance is not always satisfactory [5, 8]. This is hampered further by the lack of soluble antiwear additives for this chemical class. Some soluble phosphorus based additives, carboxylic acids, esters and ketones have yielded mixed results in boundary lubrication experiments. For a more detailed discussion of these materials, see reference [9].

Tribological Tests

Recently, NASA has developed a vacuum four-ball apparatus and a test protocol for the evaluation of liquid lubricants and greases for space applications [10]. As part of an SBIR program with Exfluor Corporation, six additives were synthesized and evaluated as boundary lubrication enhancers for PFPEs [9]. These additives included: a phosphate, a thiophosphate, a β-diketone, a benzothiazole, an amide and a sulfite. Formulae appear in Table 1.

Table 1. Additive Formulae

Name	Formula
Phosphate	$O=P(OCH_2CF_2CF_2OCF_2CF_2OCF_2CF_2OCF_2CF_2OCF_2CF_2CF_2CF_3)_3$
Thiophosphate	$S=P(OCH_2CF_2CF_2OCF_2CF_2OCF_2CF_2OCF_2CF_2OCF_2CF_2CF_2CF_3)_3$
ß-Diketone	$CF_3CF_2CF_2CF_2OCF_2CF_2OCF_2CF_2OCF_2CF_2OCF_2CF_2COCH_2COCH_3)$
Benzothiazole	$CF_3CF_2CF_2CF_2CF_2CF_2OCF_2CF_2OCF_2CF_2OCF_2CF_2\text{-C}\overset{N}{\underset{S}{\rlap{\quad\text{I II}}}}$
Amide/Thiol	$CF_3CF_2CF_2CF_2CF_2CF_2OCF_2CF_2OCF_2CF_2OCF_2CF_2CONHCH_2CH_2SH$
Sulfite	$(CF_3CF(CF_3)CF_2CF_2CF_2CF(CF_3)CF_2CH_2O)_2S=O$

Additives were evaluated in a vacuum four-ball apparatus in a PFPE fluid (Krytox 143 AC) at an arbitrary one weight percent level. Tests were performed in vacuum (< 5.0 x 10^{-6} Torr), at room temperature, at an initial Hertzian stress of 3.5 GPa and a sliding velocity of 28.8 mm/sec. All additives yielded reductions in mean wear rates of at least 55 percent, with the exception of the benzothiazole which had no effect. Two of the additives, an amide-thiol and a sulfite, reduced the mean wear rate by at least 80 percent. This data is summarized in Figure 1.
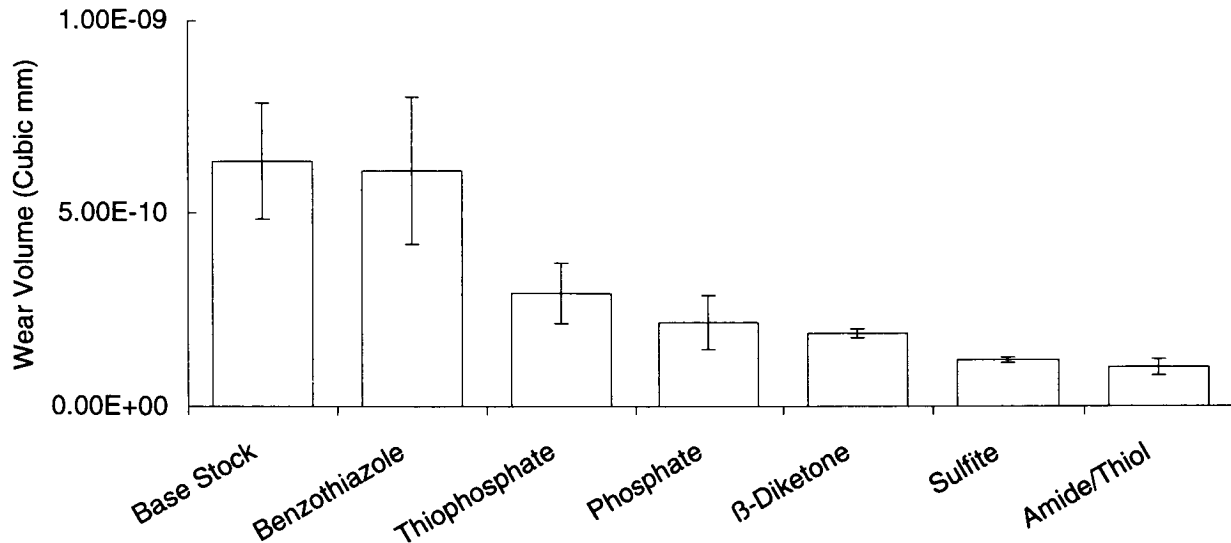
Figure 1. Mean wear rates from vacuum four-ball apparatus for Krytox 143AC and several additive formulations at one weight per cent. Error bars represent one standard deviation.
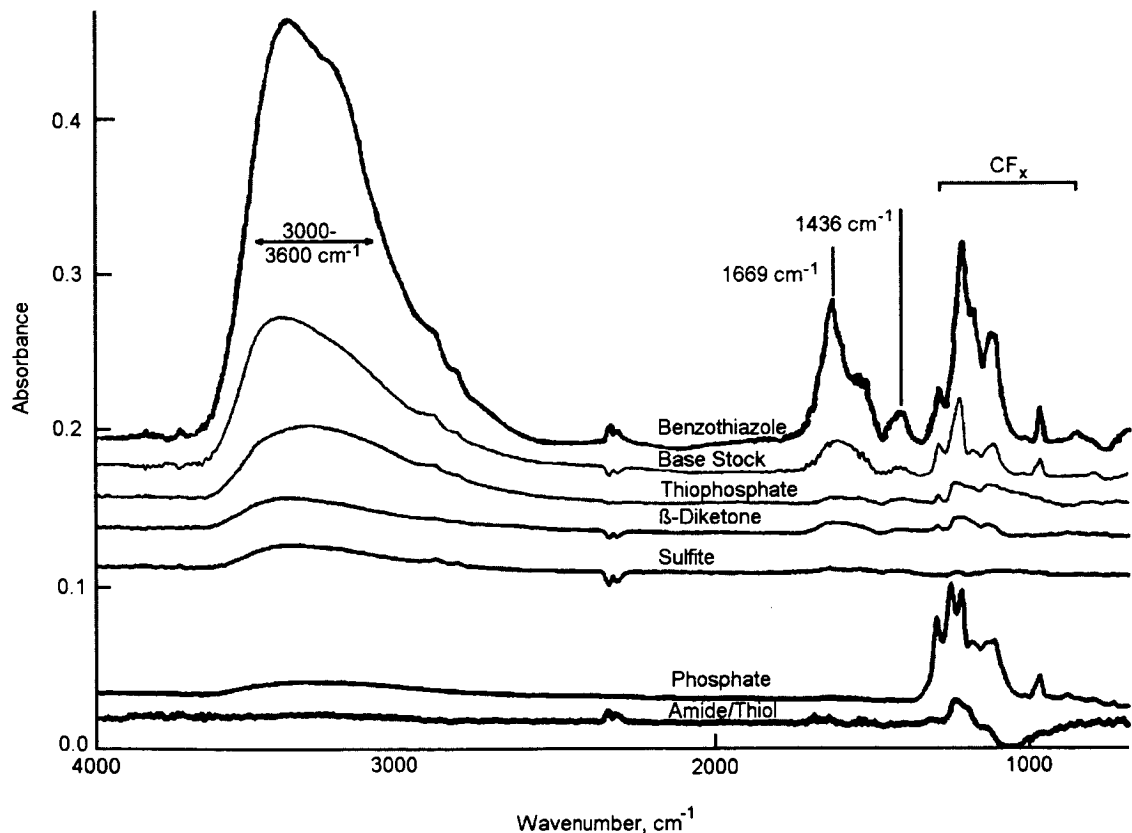

Figure 2. Infrared spectra of regions off the wear scar after solvent rinsing for formulated and unformulated tests

Surface Analysis

Infrared spectra of wear scars from each test were obtained using an IR microscope. This data appears in Figure 2 for the friction polymer region after solvent rinsing. In previous work, high wear with PFPEs have yielded IR peaks at 1436 and 1669 cm^{-1} and a broad band from 3000 to 3600 cm^{-1}. The broad band is associated with hydrogen bonded hydroxyl groups, while the other two bands are assigned to carboxylic acid species. In general, the greater the wear rate, the more pronounced are these bands. That is the case in Figure 2.

Pennzane Dewetting Phenomenon

For a lubricated contact, the supply of lubricant must be maintained throughout the life of the mechanism. If this supply is disrupted or reduced, the life of the mechanism may suffer. For elastohydrodynamic (EHL) contacts, the film thickness is determined by the EHL pressure generated in the convergent inlet region. If there is an insufficient supply of lubricant in this region, this pressure generation will be inhibited and the resulting film thickness will be diminished.

Effect of Dewetting on EHL Behavior

The inlet lubricant boundary is a function of several variables, including the quantity of lubricant, contact geometry, speed of the bearing surfaces, viscosity and surface tension. If the lubricant only partially wets the surfaces, this boundary can also be reduced, with an accompanying decrease in film thickness. If the contact is operating with a marginal film thickness, dewetting could drive the contact into the mixed or boundary film regime which would drastically affect bearing lifetime.

Dewetting Experiments

Researchers at INSA first reported on the phenomenon of Pennzane dewetting in vacuum in 1996 [11]. Since that time, detailed studies at NASA Lewis have verified this unusual behavior and have identified a possible mechanism. This dewetting behavior is illustrated in Figure 3. Dewetting was initiated by placing a few drops of neat Pennzane on a UV-ozone cleaned 440C surface. The specimen was then axially centered on the driving shaft of a centrifuge, covered and allowed to stand for several minutes. Then the specimen was spun at 5000 rpm for 30 minutes. The specimen was then covered and allowed to stand in room air for several hours. Over this time period, all lots of Pennzane dewetted to some extent.
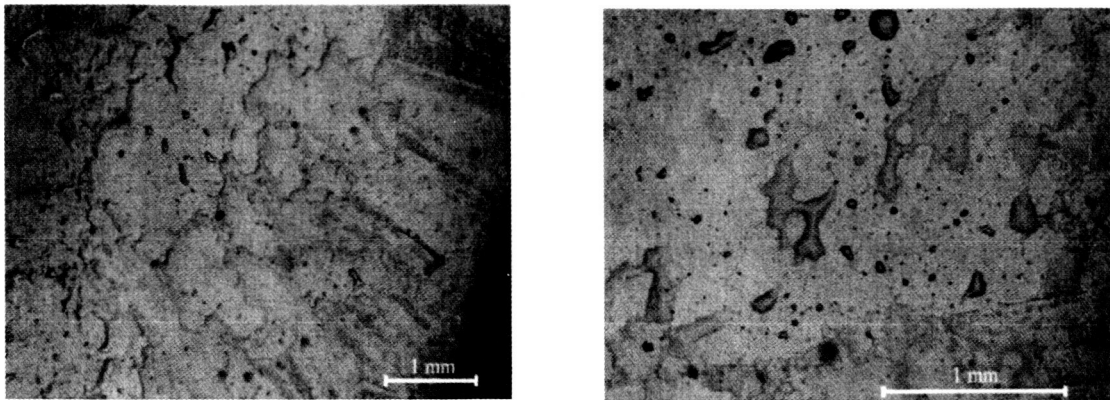
Figure 3. Dewetting of Pennzane on a clean 440C steel surface

Krytox Studies
Earlier studies [12] done on a particular lot of Krytox 143 AC yielded similar
behavior (Figure 4). In that study, only one lot of Krytox exhibited the dewetting
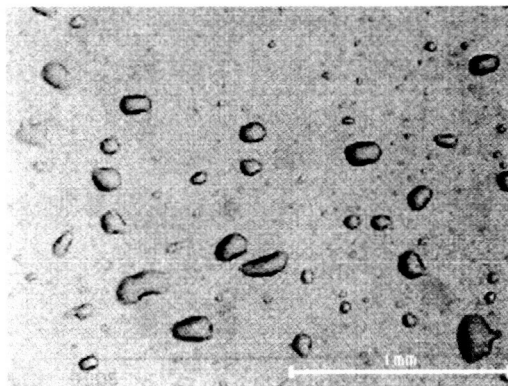
Figure 4. Dewetting of Krytox on a clean 440C steel surface

characteristics. In contrast, all Pennzane samples more or less exhibited
dewetting properties. By pretreating the Krytox at high temperature in oxygen or
filtering it through a silica or alumina column, the dewetting could be completely
eliminated. It was concluded that a low concentration of a surface active impurity
was present which caused the phenomenon, probably a carboxylic acid.

Possible Mechanism of Dewetting
In discussions with the developers of Pennzane at Pennzoil, it was determined
that a high molecular weight ester impurity is present in all samples at varying
concentrations. This ester is generated during synthesis when one of the
reactants, a C_{20} alcohol is partly oxidized to a C_{20} acid. The acid can then react
with the excess C_{20} alcohol to produce a C_{40} ester. Since esters have been
implicated in wettability problems in the past [13], it seems likely that this material
is responsible for the phenomenon. The ester being more surface active than
the hydrocarbon would adsorb at the metal interface. The ester would then

303

hydrolyze to form an acid, which in turn would react with the metal to form a soap of lower surface energy than the bulk surface tension of the fluid, thus causing partial dewetting.

Although there has been only anecdotal evidence of Pennzane dewetting in the field, it would seem prudent to carefully observe bearing performance in life tests under EHL conditions.

Effect of ODC-Free Cleaners on Bearing Life

Preliminary Tests in Air
The banning of the production of many ozone depleting chemicals (ODC) by the Montreal Protocol has resulted in many new bearing cleaning techniques including: super critical fluid (SCF) CO_2, various perfluorinated solvents, UV-ozone and many aqueous based systems. Some of these cleaners can decrease bearing lifetimes compared to the conventional CFC 113 (Freon) cleaning [14]. This is shown in Figure 5. These were from accelerated tests run in air with a parched EHL simulator. Both SCF CO_2 and UV-ozone cleaned bearings yielded reduced lifetimes compared to Freon.
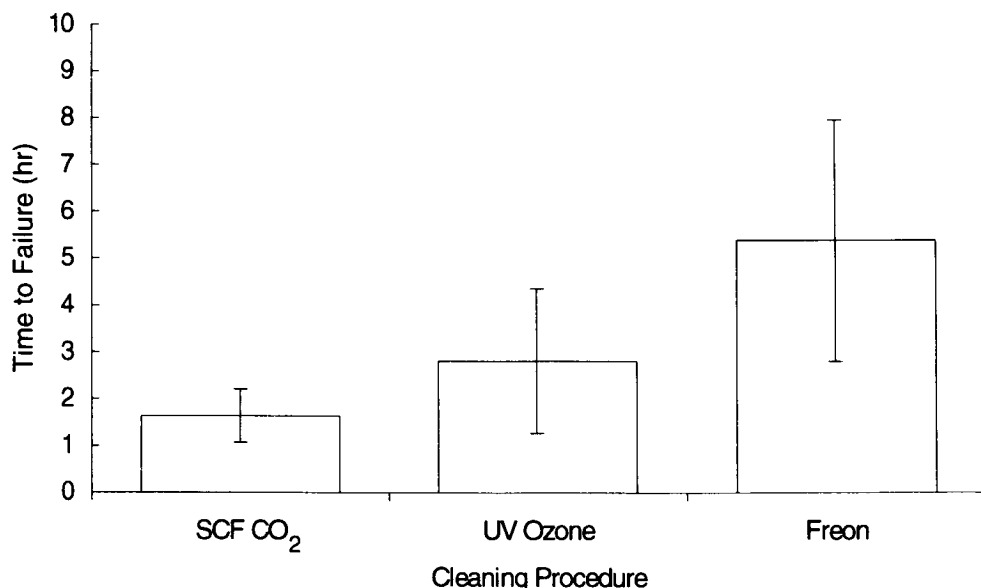
Figure 5. Effect of ODC-free cleaners on bearing lifetimes (Parched EHL apparatus, air, 4500 RPM, 23°C, Krytox 143AC)

Vacuum Tests
Recently, a new accelerated vacuum bearing apparatus, ball-on-plate (BOP) has been developed [15]. This device simulates an angular contact bearing by replacing the curved raceways with flat plates (Figure 6). The device operates in vacuum in the retainerless mode with a single bearing ball sandwiched between the plates. The test is accelerated by only lubricating the ball with microgram quantities of liquid lubricants. In the rolling and pivoting process, the lubricant is

304

transformed into a friction polymer or into low molecular weight products and is eventually consumed, at which time friction increases and the test is automatically terminated.
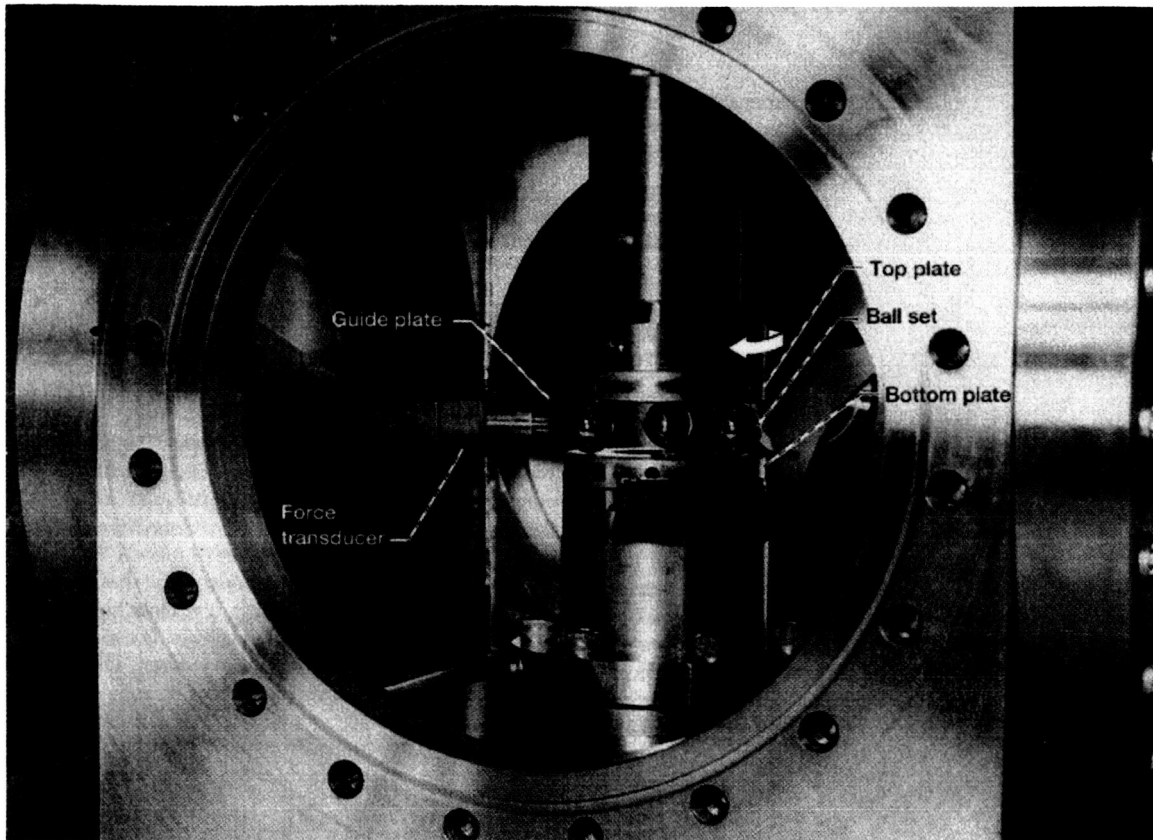
Figure 6. Ball on plate vacuum tribometer (Shown with three balls)

ODC-Free Cleaning Techniques
Four ODC-free bearing cleaning techniques were studied (levigated alumina, UV-ozone, SCF CO_2 and Brulin 815GD). These were compared to a standard Freon procedure. Lubricant lifetimes of a PFPE (Fomblin Z25), as a function of final specimen cleaning technique, appear in Figure 7. Two of the ODC-free processes, SCF CO_2 and aqueous Brulin 815GD, yielded longer lifetimes compared to the Freon standard. The UV-ozone and alumina results were comparable to Freon.

Comparison with Other Investigations
Preliminary data from accelerated bearing life tests at Lockheed Martin [16] showed that two ODC-free replacement cleaners (Vertrel XF, a perfluorinated solvent, and Brulin 815GD) yielded longer bearing lifetimes compared to Freon. The Brulin results correlate with the NASA results. In contrast, other accelerated bearing tests at Aerospace Corp. [17] have shown that Brulin cleaned bearings yielded lower lifetimes than the Freon standard. However, their Vertrel XF results do correlate with the Lockheed Martin data. The reasons for these discrepancies are not clear.

305
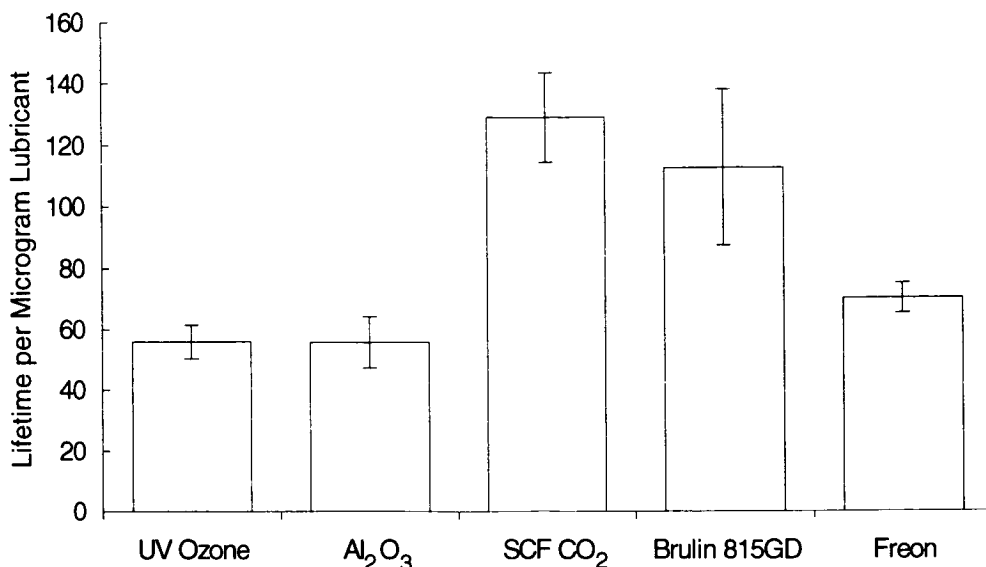
Figure 7. Lubricant lifetime for Fomblin Z25 from ball-on-plate apparatus for various cleaning techniques

Silahydrocarbons

Most liquid lubricants for space are either mineral oils, polyalphaolefins, PFPEs or synthetic hydrocarbons. Recently, a new class of lubricants containing only silicon, carbon and hydrogen (silahydrocarbons) have been developed [18]. These unimolecular materials have exceptionally low volatility and are available in a wide range of viscosities. There are three types based on the number of

Trisilahydrocarbon

$R_3Si(CH_2)_x - Si(R_2) - (CH_2)_x - SiR_3$
Where: $R = n\text{-}C_xH_y$
(a)

Pentasilahydrocarbon

$Si(CH_2CH_2CH_2SiR_3)_4$
Where: $R = n\text{-}C_xH_y$
(b)
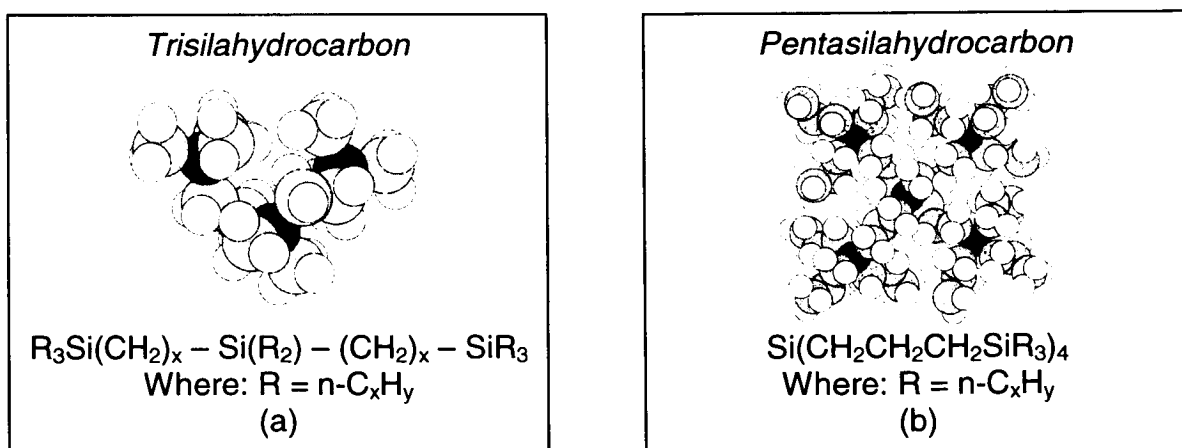
Figure 8. Structures for two silahydrocarbons (a) trisilahydrocarbon (b) pentasilahydrocarbon

silicon atoms present in the molecule (i.e., tri, tetra or penta). Examples of a tri and a pentasilahydrocarbon appear in Figure 8.

Viscosity Properties

A series of silahydrocarbons have been synthesized and their kinematic viscosities as a function of temperature have been measured (Figure 9). For comparison, a Pennzane plot has been included. As can be seen, the viscosity properties of the silahydrocarbons bracket the Pennzane data.
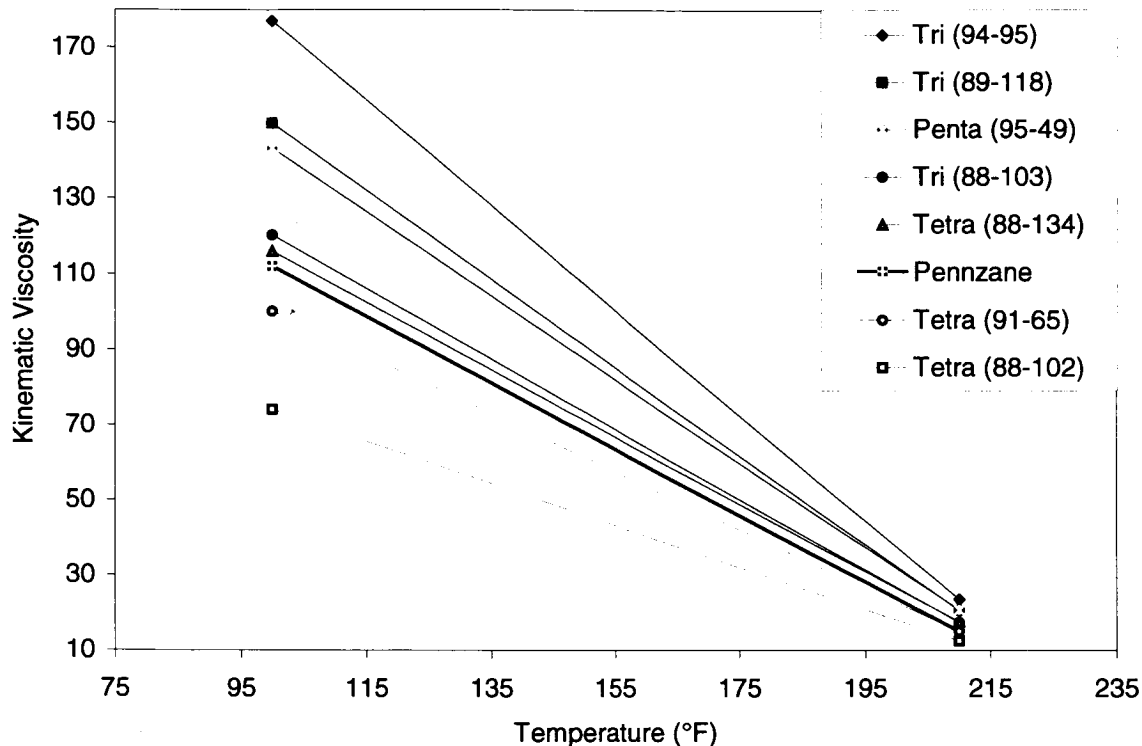
Figure 9. Kinematic viscosity as a function of temperature for a series of silahydrocarbons

EHL Properties

Elastohydrodynamic properties for two members of this class appear in Figure 10. This data was generated using a ball on plate optical EHL simulator [19]. Data is compared to a standard reference fluid of known pressure-viscosity properties. The trisilahydrocarbon has a pressure viscosity coefficient (α)of 16 GPa^{-1} ($\pm$ 0.3) at approximately 21 C, while the pentasilahydrocarbon has a value of 17 GPa^{-1} ($\pm$ 0.3). At 40 C, the trisilahydrocarbon has an α value of 11 GPa^{-1} ($\pm$ 1) and the penta, 13.5 GPa^{-1} ($\pm$ 1). For comparison, the α value for Pennzane at 30 C is 9.8 GPa^{-1} ($\pm$ 0.3), estimated by the same method.

Tribological Properties

Using the vacuum four-ball tribometer, the friction and wear characteristics of the neat pentasilahydrocarbon was compared to the three commercially available PFPEs and an unformulated Pennzane (Figure 11) [20]. As can be seen, this unformulated silahydrocarbon has wear rates comparable to Pennzane and superior to the PFPEs.
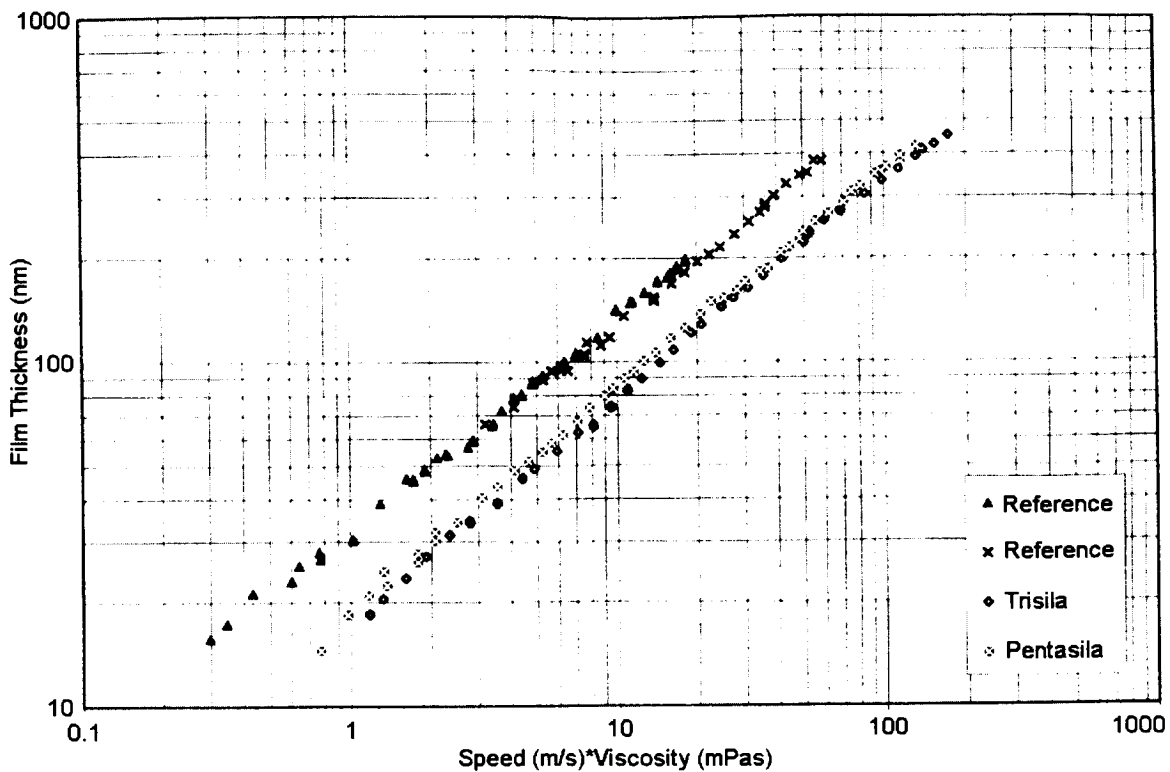
Figure 10. Elastohydrodynamic properties for a tri and a pentasilahydrocarbon
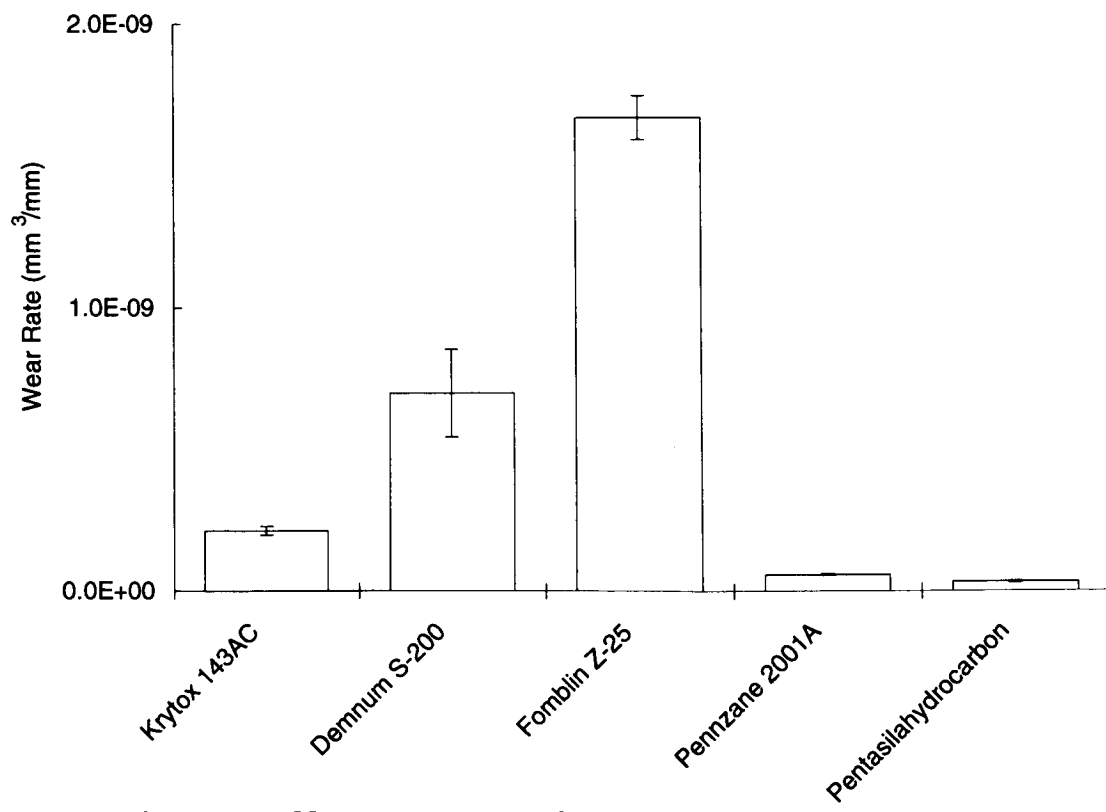
Figure 11. Mean wear rates for a series of space lubricants

308

Future Work

Vapor pressure measurements are being performed on members of this lubricant class. In addition, some low volatility antiwear additives are being developed for incorporation into formulations.

Conclusions

A series of new soluble antiwear additives have been developed for use in perfluoropolyether space lubricants. Use of these materials under boundary lubrication conditions will reduce wear and thus extend bearing lifetimes. A dewetting problem with the synthetic hydrocarbon Pennzane has been verified and a possible mechanism proposed. The effect of several ODC-free cleaning processes on lubricant lifetimes has been determined using a vacuum ball-on-plate apparatus. Two cleaners, Brulin 815GD and super critical fluid CO_2, yielded longer lifetimes compared to a Freon (CFC 113) standard. Two other processes, alumina and UV-ozone, yielded comparable lifetimes compared to Freon. Finally, a new class of synthetic liquid lubricants based on the silahydrocarbons are described and some of their physical and tribological properties are reported.

References

1. Fusaro, Robert L. and Michael M. Khonsari. "Liquid Lubrication in Space." NASA TM-105198, (December 1991).
2. Vernier, C. G. and E. W. Casserly. "Multiply-Alkylated Cyclopentanes (MACs): A new Class of Synthesized Hydrocarbon Fluids." *Lubr. Engr.,* 47, 7 (1991), 586-591.
3. Jones, William R., Jr. "Properties of Perfluoropolyethers for Space Applications." *Trib. Trans.,* 38, 3 (1995), 557-564.
4. Paciorek, K. J. L. and R. H. Kratzer. "Stability of Perfluoroalkylethers." *J. Fluorine Chem.,* 67, (1994), 169-175.
5. Conley, P. L. and J. J. Bohner. "Experience with Synthetic Fluorinated Fluid Lubricants." *Proc. Of the 24th Aerospace Mech. Symp.,* NASA publ. CP-3062, (April 1990), 213-230.
6. Prat, Phillipe. "Contribution a L'Etude de la Lubrification Fluide en Ambiance Spatiale. Approche Experimentale de la Realimentation." Ph. D. Thesis, Laboratoire de Mecanique des Contacts, Lyon, France (1997).
7. Whitaker, A. F., M. Clark-Ingram and S. L. Hessler, Editors. "Second Aerospace Environmental Technology Conference." NASA CP-3349, (March 1997).
8. Carré, D. J. "Perfluoropolyalkylether Oil Degradation: Inference of FeF_3 Formation on Steel Surfaces Under Boundary Conditions." *ASLE Trans.,* 29, 2, (1986), 121-125.

9. Shogrin, Bradley A., William R. Jones, Jr., Pilar Herrera-Fierro, Tzuhn-Yuan Lin and Hajimu Kawa. "Evaluation of Boundary-Enhancement Additives for Perfluoropolyethers." NASA TM 107393, (December 1996).

10. Masuko, M., W. R. Jones, Jr., R. Jansen, B. Ebihara, S. V. Pepper and L. Helmick. "A Vacuum Four-ball Tribometer to Evaluate Liquid Lubricants for Space Applications." *Lubr. Engr.*, 5, 11 (1994), 871-875.

11. Sicre, J., P. Vergne, P. Prat, and M. Pochard. "New Considerations on Fluid Lubricants for Spacecraft Applications." *Proceedings of the 6th European Space Mechanisms and Tribology Symposium*, Zurich, Switzerland, (October 1995), 169-176.

12. Shogrin, Bradley, William R. Jones, Jr. and Pilar Herrera-Fierro. "Spontaneous Dewetting of a Perfluoropolyether." *Trib. Trans.*, 52, 9 (1996), 712-718.

13. Gould, Robert F., editor. *Contact Angle, Wettability, and Adhesion,*. American chemical Society, Washington, D. C. (1964), 24-25.

14. Jones, William R. Jr., Thomas J. Toddy, Roamer Predmore, Bradley Shogrin and Pilar Herrera-Fierro. "The Effect of ODC-Free Cleaning Techniques on Bearing Lifetimes in the Parched Elastohydrodynamic Regime." NASA TM 107322 (September 1996).

15. Pepper, Stephen, Edward Kingsbury and Ben T. Ebihara. "A Rolling Element Tribometer for the Study of Liquid Lubricants in Vacuum." NASA TP 3629, (October 1996).

16. Loewenthal, Stuart, William Jones, Jeffrey Grout, Roamer Predmore and Robert Thom. "Instrument Bearing Life with Non-CFC Cleaners." *Proceedings 4th Int. Rolling Element Bearing Symp.*, Orlando, FL, (April 1997)

17. Didziulis, S.V., J.L. Childs and D.J. Carré. "Effects of Varying Ball Bearing Cleaning Processes on Lubricant Life." Aerospace Corp. Report to be published.

18. Snyder, Carl E., Jr., Lois J. Gschwender, Bruce B. Randolph, Kazimiera J. L. Paciorek, Joseph G. Shih and Grace J. Chen. "Research and Development of Low-Volatility Long Life Silahydrocarbon-Based Liquid Lubricants for Space." *Lubr. Engr.*, 48, 4 (1992), 325-328.

19. Spikes, H.A. "Estimation of the Pressure-Viscosity Coefficients of Two Silahydrocarbon Fluids at Two Temperatures." Imperial College (Tribology Section), London, U.K. Report TS024b/96. (July 1996)

20. Poslowski, Agnieszka K., Bradley A. Shogrin, Pilar Herrera-Fierro and William R. Jones, Jr. "Evaluation of Several Space Lubricants Using a Vacuum Four Ball Tribometer." NASA TM-To be published.

Considerations on Mechanical Reliability

Fabio Panin*

Abstract

Reliability prediction methods for mechanical systems are not as well established as those for electronics. Fundamental differences exist between electronic and mechanical reliability. These differences and some mechanical reliability techniques are reviewed. The hurdles encountered in the reliability calculation of a manipulator joint are described. Topics such as how reliability requirements should be formulated in technical specifications, and some implications of implementing redundancy in the design are discussed.

Introduction

There is voluminous literature on reliability, spanning from theoretical statistical studies to practical engineering investigations. Different approaches to reliability exist because of the different reliability characteristic that is of interest for the case being considered. However, the documentation on reliability prediction methods for mechanical systems is scarce and provides little guidance on the procedures to be followed, whereas for electronic systems these are well-established techniques. In addition, a number of fundamental differences exist between mechanical and electronic reliability, which are often overlooked, such as:
- the wider variety of mechanical component types
- the slimmer databases available
- the lower confidence level associated to the failure data
- the different failure rate distribution function
- the subtle nature of many mechanical failures.

Reliability may be part of an evaluation process, such as a design trade off. If the information or data provided by the reliability engineer has a low confidence level, or it is based on debatable assumptions, the contribution of reliability engineering is scarcely useful. This, in addition to be detrimental to the evaluation process, is negative to the image of the reliability discipline as a whole.

The positive aspect of the lack of well-established techniques is that innovative approaches to mechanical reliability prediction are possible and there is still room for improvement of the current techniques. An effort must be made in fully understanding the process of mechanical failure. The failure mechanism may involve one or more different disciplines such as mechanical failure theories, fracture mechanics, fatigue theory, tribology, material science, physics, chemistry, metallurgy. Failures are often the result of many, other-than-ideal failure mechanisms. This paper discusses the

---

* European Space Technology Center, Noordwijk, The Netherlands

above topics without pretending to fill the mentioned gaps which are currently subject of investigation. Hopefully, the considerations made will be useful to those involved with mechanical reliability.

Differences between mechanical and electronic reliability

The following fundamental differences exist between mechanical and electronic reliability:

1. There is a wide variety of diverse mechanical component types, whereas there are a rather few basic types of electronic components. As a consequence, the mechanical part database is less accurate (because of the lower number of observations for a given part type) and more sparse than the electronic component database.

2. For electronic components, the Constant Failure Rate model is generally adopted, according to which the reliability at time "t" is given by the exponential function:

    $R = \exp(-\lambda t)$

    where "λ" is the failure rate. It follows that the Mean Time Between Failure (MTBF) is given by:

    $MTBF = 1/\lambda$

    This model does not represent adequately failure modes typical of mechanical systems - such as those caused by wear-out, fatigue, or creep. In addition, assuming a constant failure rate implies a smooth loading condition. While electronics often undergo a gradual stress change, many mechanical systems are subject to random or transient loads.

    The Weibull probability distribution function is more suitable to mechanical systems because it represents a non-constant failure rate and because of its versatility to represent a family of various distributions (e.g., Gamma, exponential, Raleigh, Log-normal, normal).

    The normal function models well random variables - such as stress and strength distributions - or many naturally occurring phenomena of symmetric nature.

    The Log-normal function can assume a range of shapes and is a good fit to empirical data.

312

3   For a large number of applications, the main concern about a mechanism failure is more related to wear-out than to a random event, whereas this is typical of an electronic system.

4   Electronic components are generally of very similar quality. Therefore, pooled failure data is very accurate. This is not the case for mechanical items that may vary greatly with the supplier.

5   In electronics/electrical systems, defects are usually "hard to identify but easy to rectify". This is the complete opposite for mechanical systems.

6   For mechanical systems, failures (typically, those of a structural type) may be detected only during post-test investigation, thus making difficult or impossible to estimate the time to failure.

7   For electronic systems, the operating stress band is narrower and more tightly controlled than for mechanical systems. Also, environment-induced stresses can be controlled more easily in the case of electronic systems.

8   Reliability proof tests of mechanical systems are often not possible because the time necessary to have statistically significant data would render testing too costly.

9   Although attempts are made to standardize mechanical components in different systems as an aid to cost reduction, it is rare to find identical components operating under the same conditions in different equipment types. As a consequence, statistical failure data do not allow synthesizing system reliability.

Because of these fundamental differences:
a)   dedicated reliability prediction methods must be used for mechanical system,
b)   such methods need to be more sophisticated than those used for electronics, and
c)   the lack of well-established part reliability data sources and agreed methods render the analyses performed debatable, as the example below shows.

Reliability prediction techniques

The main objectives of reliability prediction are:
-   to perform trade-off studies between various design options
-   to determine the probability of catastrophic failures, major performance degradation or safety hazard
-   to establish component criticality
-   to determine spare usage and repair rates as an input to maintainability analysis.

There are two distinct aspects of reliability:
- part reliability engineering: this analyzes the failures of individual parts to derive failure data about the part population. A part can only fail once, is non-repairable, and is discarded after failure;
- system reliability engineering: this analyzes the failures of an assembly of different parts, which can be repaired and thus may experience successive failures over its lifetime.

The known reliability prediction techniques for mechanical parts are of the following types:
- analysis of test or historical failure data;
- empirical reliability models
- stress/strength interference analysis
- surrogate data sources.

A critical step is how to obtain the necessary information or data. This step is critical because the validity of the assumptions made and the possibility of verifying them depend on it.

Failure data analysis
This is the preferred technique because the data used corresponds to actual or simulated loading conditions, and therefore can be accurate. Failure data can belong to a historical database or result from a dedicated test program, as it is the case of new parts/ systems. The relevant data is the time-to-failure (TTF) distribution which results from life testing. The Weibull distribution has proven effective to characterize mechanical part TTF distributions. Hazard rate time dependency can be analyzed. Design improvements may result by comparing and analyzing the data. Results of failure analyses are also important to investigate failure mechanisms. However, data are often not available and, when available, are unfortunately often grouped. If the design is completely new, a dedicated testing program is required.

Empirical reliability models
These models are based on extensive testing for different combinations of loading, materials, dimensions and other physical parameters, and allow the computation of indicators of part life. A well-known example is the "L_{10}" or "L_{50}" life for bearings. The Weibull distribution can be used. Disadvantages are that models are available only for a few part types, and new materials or processes cannot be accommodated. A model based on failure rates with the application of adjustment factors is also common, mainly because of the simplicity of the calculations. The following generalized expression may be used:

$\lambda = \lambda\_b \ PROD(pi\_i)$

314

where:

λ predicted failure rate

λ_b base failure rate

pi_i   adjustment factors to account for environment, stress, etc.

The model is described in MIL-HDBK-217F, Reliability prediction of electronic equipment, which considers also some electro-mechanical devices. Tables of base failure rates and adjustment factors are provided. Unfortunately, there are very few data sources that can be used as an alternative to MIL-HDBK-217F. A disadvantage of the method is that it does not consider the time-dependent nature of mechanical part failure rates.

An alternative method reduces a time-dependent failure rate into a single average failure rate. This can be assumed to be constant for a specified time period. The average failure rate (or cumulative hazard rate) for a Weibull distribution is:

$$\lambda\_avg = (time^{\alpha-1}) / (\alpha^{\beta})$$

where:

β Weibull shape parameter

time   service life

α a point estimate of life that a certain percentile of population will exceed without failure - such as the Weibull characteristic life, or L10 life.

The main limitation of the method is that the average failure rate is a valid approximation only over a relatively short interval of the service life. For example, to determine the average failure rate of a rolling bearing, the method is applied as follows:

a Identify the bearing characteristics:
   - type
   - dynamic capacity "C" from manufacturer catalogue
   - Weibull slope "β" from manufacturer catalog
   - load life exponent "P" (e.g., 3 for ball bearings, 10/3 for roller bearings)

b Use the standard equation for the bearing "L_{10}" life, to determine the point estimate of bearing life that 90% of the population will complete or exceed without failure:
   $L_{10} = (C/ F)**P$ E6 revolutions
   where "F" is the equivalent radial load

c Convert "L_{10}" in hours, given the speed in rev/hr

d Determine the Weibull characteristic life "α":

   $\alpha = L\_f / ((-\ln(1-f))**(1/\beta))$

e Finally, calculate the average failure rate "λ_avg" with the formula above.

315

Stress/ strength interference (SSI) analysis

SSI analysis is able to design and quantitatively predict the reliability of mechanical components. The applied stress and the material strength are characterized by statistical distributions to account for their variability due to natural scatter. The method can be applied virtually to any mechanical component. The following is necessary:
- engineering knowledge of stress distribution
- engineering knowledge of strength distribution (alloy, design life, loading type, surface finish, heat treatment, operating temperature, stress concentration factors).

Acquiring such a knowledge is a critical step, because the accuracy of the results strongly depends on the assumed stress and strength standard deviations. Tables exist for fatigue strength distribution that include the effect of heat treatment, surface finish, stress concentrators and temperature. The area of intersection of the stress and strength probability distribution functions is called "interference" and represents the probability that a random observation from the stress distribution exceeds a random observation from the strength distribution. The reliability estimation is the interference complement to one. The application of the method takes several forms depending on the assumptions made on the stress and strength distributions.

Case 1
- stress: the standard deviation is negligible compared to the mean stress (that is, the scatter in service stress is small).
- strength: a two-parameter distribution is adopted

Case 2
- stress: normal distribution. The standard deviation is a fixed percentage of the mean stress, such as 5% (this case covers those applications where the stress scatter is appreciable). The actual standard deviation should be determined experimentally for the case in hand, if this is possible.
- strength: distribution parameters are selected from the tables.

Case 3
- stress: cyclic, with variable magnitude.
- strength: distribution parameters are selected from the tables.

SSI analysis may be used to evaluate part dimensions and physical features. Unfortunately this method has not yet found wide-spread use and is applied generally only where the consequences of a potential failure are considered severe (e.g., loss of human life, irreversible environmental damage) perhaps because engineering analyses are traditionally based on a deterministic approach.

An effective tool for the determination of part failure rates is the combination of SSI analysis with a Failure Modes and Effect Analysis (FMEA). As an initial step, the functional analysis of the system is performed to identify the potential failure modes. Then, characteristic parameters are associated to the identified functions. A failure

316

corresponds to one or more parameters exceeding allowable limits. The identification of these limits defines the failure modes. Table 1 (non-exhaustive) applies to a pressure regulator.

Then, the component(s) involved with a given failure modes are identified, and those design characteristics determining the failure are identified. The individual stress/strength analyses of the mechanism components are performed to calculate their failure probability. Finally, the overall failure probability is calculated.

The advantage of this method, which effectively links structural engineering with statistics, is that it allows decision-making under uncertainties. No new structural analyses are necessary: it is sufficient to treat the relevant parameters as probabilistic variables.

Table 1: Pressure regulator failure modes

Function	Characteristic Parameter	Failure Mode
F1: to switch from open to close (and vice versa) to maintain downstream pressure below upper limit	Regulated pressure	$P < P$ min
F2: to switch from close to open to maintain downstream pressure above lower limit	Regulated pressure	$P > P$ max
F3: to prevent leakage when closed	Leak rate	$L < L$ max

Surrogate data sources
An average failure rate can be calculated by grouping the total number of failures occurred in a cumulative time. Data is generally collected from a wide range of applications and operating stress profiles and then grouped based on the similarity in part type and environment. A first shortcoming of the method is that the environment and part type referred may not correspond to the particular application considered. As a result, the accuracy of the prediction is low. In addition, the exponential distribution is usually assumed to represent the failure model, and therefore a constant failure is obtained. If the actual time to failure data was available, the Weibull distribution would be more appropriate.

Another short coming is the lack of detailed description of the parts. This is the least desirable method of predicting mechanical part reliability. No recommendations on design improvements may be drawn as an outcome of the application of this method. However, the method is quick, inexpensive and effective for non-critical or low-failure rate parts.

Example: manipulator joint reliability prediction

An interesting example of the difficulties encountered in performing mechanical reliability prediction is given by the Manipulator Joint Subsystem (MJS) of the European Robotic Arm (ERA). The MJS provides articulation and actuation to the arm. Three MJS types exist: two for the two wrists and one for the elbow. The wrist type includes a roll joint, a pitch joint, and a yaw joint, in addition to an electronics box. Each joint includes a structural unit, a motor and brake unit, thermal equipment, and harness.

The wrist MJS[1] envelope is a 1408-mm long, 348-mm-diameter cylinder, and its mass is 280 kg. The output torque is 50 to 350 Nm, depending on the joint velocity. The joint strength is 1785 N and 1300 Nm (any direction). The nominal power consumption is 30W. Four planetary stages are used, each with a reduction ratio between 3:1 and 5:1, giving a total reduction ratio of 450:1. Lubrication is wet.

The resulting design is quite complex and is a hard-to-achieve compromise among a number of conflicting requirements such as high output torque, low input power, small envelope, low mass, high torsional stiffness, and high motion stability. None of the mechanical components used are redundant, however the complete MJS is replaceable in orbit. The reliability targets specified in the MJS requirements specification are:
- wrist   0.9875
- elbow   0.9972

whereas the ERA system reliability target is 0.75, over a total lifetime of 10 years. The intended aim of the reliability prediction [1] which has been performed is to identify the reliability-critical items, and determine the MTBF. The databases used for part failure rates are MIL-HDBK-217F for electronic equipment, and (in order of preference) the ESA-PSS-302 [2] and Nonelectronic Part Reliability Data (NPRD) [3] for mechanical parts. The Weibull function is used for the failure rate distribution, but the shape parameter is set to 1.0 which means a constant failure rate.

The predicted duty cycle is based on the following five operational modes
- dormant and unpowered   (10 yrs)
- dormant and powered   (1 yr)
- active   (1000 hrs)
- breaking   (4168 hrs)
- static torque   (0.6 hrs)

There is no agreed method on how to handle this. Two different methods are followed for the electronic unit and the mechanical unit. For the electronic unit, a dormancy factor is introduced [4] to account for "space-active to space-passive" scenarios, which ranges from 0.02 to 0.80 depending on the component type. A sensitivity analysis is

---

[1] The following information is updated to March 1996.

318

performed to assess how the predicted reliability is affected by the choice of the dormancy factor. It turns out that the dependency from the value chosen is strong, therefore the choice is critical. Unfortunately, there is no agreed rationale for this choice and the method, when used to verify the compliance with the reliability requirement, is debatable. It could however be used in a comparative trade-off among different design solutions of the electronic unit.

For the mechanical unit, the Contractor assumes a continuous operational mode and uses the part count method to calculate the reliability. For the gearbox, the characteristic lifetime "L_{10}" of the bearings is used in the exponential formula to derive their failure rate, and NPRD is used for the gearwheels and other teeth couplings. To account for the specified duty cycle, the following methodology is then devised.

Due to the electrical power dissipation, there is a temperature difference between internal motor elements and ambient. Accordingly, two temperature extremes are calculated, from which an average temperature is derived. It is then assumed that the unit spends 30% of its life at each extreme temperature, and the remaining at the average temperature. The reliability is calculated as the arithmetic mean of the values corresponding to three temperatures. Unfortunately, the value resulting from this calculation is less then the required target. When the time percentages are adjusted, the calculated reliability finally exceeds the target.

Notwithstanding the several objective difficulties which are part of the problem - such as the intermittent and complex duty cycle - and the uncertainties afflicting a number of key parameters - such as the temperature profile - the described reliability prediction is a quite sterile exercise insofar it is not an acceptable verification of the reliability requirement, and does not provide insight on reliability-critical items. Eventually, due to the low confidence in the failure rate data, critical items are identified on the basis of engineering judgment.

The lesson learned from this example is that when there is not a well-established reliability technique and an agreed part reliability data base, a quantitative reliability prediction should not be required by the customer. Instead, well-formulated and verifiable reliability requirements should be included in the technical specification, as discussed below.

Failure mechanisms

The use of failure rate data or reliability prediction techniques is not "a replacement for sound reliability engineering and design practice", as pinpointed by [3]. "A knowledge of life limiting failure mechanisms and how these mechanisms will behave in the intended use environment is also necessary." [3] Table 2 shows the most common failure mechanisms (adapted from [5]).

Table 2: Failure mechanisms

1	force and/ or temperature-induced elastic deformation
2	yielding
3	ductile rupture
4	brittle fracture
5	buckling
6	fatigue (high and low- cycle, thermal, surface, impact, corrosion, fretting)
7	corrosion (stress, chemical attack, galvanic, pitting, erosion, cavitation, etc.)
8	wear (adhesive, abrasive, corrosive, surface fatigue, deformation, impact)
9	brinnelling, galling, seizure, spalling
10	impact
11	creep
12	thermal relaxation or shock
13	radiation damage

These are actually macro-mechanisms that contains a number of more specific, other-than-ideal failure mechanisms. This is apparent when tribology-related failures - by far the largest share of mechanical system breakdowns - are considered. Tribological failures very often include wear, and "wear is not a single process, but a number of different processes that can take place independently or in combination, resulting in material removal from the contacting surfaces through a complex combination of local shearing, plowing, gouging, welding, tearing, and others" [5].

Failures can be classified in a number of ways, for example depending on the failure-inducing agent that is considered:
- force (steady, transient, cyclic, random)
- time
- temperature (low, room, high, steady, transient, cyclic, random)
- environment

The dependency on time is of particular significance because a gradual reduction in the margin between strength and stress or a gradual deterioration of the part allows a warning period during which the failure may be detected. A generic failure mechanism begins with the occurrence of an initiator failure event which, in turn, determines a sequence of other failure events. These eventually result in the catastrophic, macroscopic failure of the part. If one of the failure events is detected, the failure mechanism can be stopped before the macroscopic failure occurs. This observation is the basis for a number of failure-prevention techniques, such as the periodic inspection of fracture cracks of structural elements.

When an entire satellite is considered, it has been concluded [6] that, on the basis of a number of observations, the first four reasons for failures are, in decreasing order:
1.   poor design at system level
2.   poor knowledge of the environmental conditions and loads
3.   human error
4.   piece parts failure
Unfortunately, still according to [6], "the order in which the space business has expended resources to prevent failures is just the reverse ... we spend most of our reliability resources buying and tracking expensive parts ... and we spend as little as possible on the people who actually design, build, and test rockets and satellites". When the lowest bidder is chosen, it is wise to wonder about the quality of the output product.

Poor system design means, mainly, a poor understanding of the interactions between the sub-systems. This is an "interface effect" resulting from the excessive effort spent on the detail sub-system design relative to that devoted to understanding how the sub-systems work together (under non-nominal and degraded conditions as well as nominal ones). An example is given by the often overlooked study of transient events - both mechanical and electrical - and the resulting lack of protections. The addition of these, when made at a late stage, may have a non-negligible impact on the project.

Misjudgment of the environment has the potential for causing gross, catastrophic failures because of both the low margins of safety adopted for space applications and a chain reaction effect due to the close interrelation of satellite subsystems. The vibration and thermal environment should be a primary concern. Human error can be considered as another type of environment [6].

Considerations

Reliability requirements in technical specifications
Reliability can be achieved in service only if it has been taken fully into account in the design stage. In fact, no matter how closely the manufacturing is controlled by the Quality Assurance function, and how the end product is installed, operated, and maintained, the upper reliability limit is the one inherent in the design [7]. The best approach consists therefore in defining clearly the reliability requirements in the technical specifications, already at the beginning. This is a prerequisite to fruitfully integrate the reliability engineering activities with the design activities, with the aim of impacting the design by identifying its weaknesses.

Reliability requirements must be formulated with precise statements which are predictable, measurable and verifiable. The following are examples of qualitative statements which have been found in specifications applicable to the development of space hardware - spanning from earth-observation instruments to complete satellites:
- "The design shall provide maximum reliability for the specific application"

- "The design shall achieve a degree of safety equivalent to that of two-failure tolerance"
- "The function shall be performed with a sufficient degree of built-in redundancy"
- "Two failure tolerance shall be provided to the maximum extent practical"

Due to their vagueness, these requirements have little meaning and their implementation in the design can only be arbitrary. The definition of reliability stands on the specification of the following four characteristics:
- function: this must be clearly defined and understood because it is essential to the definition of failure
- environment: its definition, to be complete, must include packaging, transportation, handling and the user
- time: this should not only cover the period of expected operation, but also usage parameters such as distance, cycles, stand-by profile, etc.
- probability: the failure prediction is associated to the estimation of the probability of its occurrence

In particular, the specifications should cover the items of Table 3. Items from 6 to 16 are sometimes neglected. For example, the first issue of the system requirements document of a satellite for demonstration of in-orbit autonomy did not cover monitoring and fault detection, isolation and recovery. Fortunately this lack was identified before the release of the final issue.

A preventative approach
The ultimate goal of reliability engineering should be to prevent failures, rather than strive to keep the failure probability low. Broadly speaking, failures can be of two types: systematic and random. While the former can be virtually eliminated by design, the latter can only be minimized.

To eliminate systematic failures, a sufficiently high safety factor (whose value depends on the application criticality) is adopted for component sizing, to allow for all the unknown or unmodelled or uncertain factors of the environment or the parts properties and characteristics. An example is friction, which can vary within a wide range even in laboratory conditions[2]. Additional factors are used to estimate the worst-case resistive torques.

Random failures can be minimized through redundancy. However, clear, well-accepted criteria to determine which mechanism component should be redundant have not yet been formulated. For example, while according to some specialists bearings should be redundant, to others this is not a practical design solution. A

---

[2] "Anybody who thinks they can calculate friction coefficients is a fool", quote from the European Space Tribology Laboratory.

common guidelines is: "All active components should be redundant"[3]. Deviations from this guidelines are often made because its implementation may not be feasible. Obviously, design margins cannot be used as an alternative to redundancy to minimize random failures.

Table 3: Reliability-related topics in technical specifications

1	functional requirements
2	operational requirements
3	environmental requirements
4	test requirements (including stress levels and accept/ reject criteria)
5	design margins (and derating factors for electric/ electronic components)
6	quantitative reliability requirements
7	failure consequence severity (project risk policy)
8	failure tolerance (of hardware and software)
9	fault detection, isolation and recovery
10	monitoring (of mission performance- and safety- critical parameters)
11	failure propagation across interfaces (internal interfaces among subsystems and external interfaces with the carrier system)
12	maintainability requirements (for both ground and in-orbit operations) (e.g., accessibility, preventive/ corrective tasks, special tools/ skills, spares/ replaceable units, limited-life items)
13	reliability and maintainability analyses
14	reliability- and maintainability- critical items
15	validation of non-proven designs by analysis and test
16	part selection (preferred parts)

Why redundancy?

There are different definitions of redundancy. The common engineering meaning is the available number of ways to perform a function. However, the Webster's dictionary defines redundant as "exceeding what is necessary". When this is read as "achieving the desired performance through over design", the definition includes applying safety factors and using a safe-life approach. The primary objective to implement redundancy is to improve the chances for success. In this case, redundancy is an

---

[3] A component is called active if, as a result of its failure, the mechanism is prevented from functioning. It follows that active components are: those carrying electrical power or signals (electric motors, actuators, initiators, sensors, switches), latches, springs.

essential part of the performance requirements and close interaction between the designer and the reliability engineer is necessary. There are cases, however, where redundancy is necessary to meet externally-imposed requirements which cannot be negotiated. This is the case typically of the safety requirements imposed by the carrier/ launcher authority onto the payload/ spacecraft organization. In these cases redundancy is part of the safety requirements.

It is unfortunately common that, when redundancy is not part of the performance requirements nor is externally-imposed, redundancy requirements are overlooked in the technical specifications. This lack should be overcome by a cooperative effort of the reliability engineer and the design engineer aimed at assessing the system behavior under those non-nominal or degraded conditions caused by potential failures. This task is actually part of a FMEA. Once the failure effects are identified, according to the traditional FMEA approach, redundancies are adopted to provide the failure tolerance required. However, when no failure tolerance is specified, the assignment of redundancies can only be somewhat arbitrary. Instead, alternative designs should be devised and investigated to establish if those failures do not occur. In general, the new designs will have/introduce other failure modes. At this point, the severity of the failure consequences and their probability of occurrence must also be considered, to select the preferred design solution. This will have the lower consequence severity and/or probability of occurrence. In particular, by considering the latter in the trade, the negative effect of an increased part count is accounted for.

By following this process, a net reliability improvement can be obtained - usually at the cost of only an additional design effort, whereas merely introducing redundancy in a design in general translates into penalties, such as mass increase, larger envelope, and greater development effort. In some cases, it may also result into a lower efficiency and reliability due to the higher part count. (This latter case cannot be tolerated and may be resolved through some radical design change.) These penalties should be traded against the benefits of a reliability increase and improved safety.

The approach described is handled in a qualitative way. A more rigorous and quantitative approach is called selective redundancy. This is based on the assessment of the relative failure rates of the critical components. "A substantial reliability improvement can be achieved by introducing only a few redundant components, with an affordable price in terms of increased complexity. The reliability improvements obtained through selective redundancy is generally nearly as good as those for the fully redundant approach." [8]

On the false redundant designs
In addition to the differences between mechanical and electrical reliability discussed at the outset, there is yet another one deserving consideration. It may be the case that "space-qualified" mechanical parts or EEE components which meet the applicable requirements are not available commercially, and the estimated development and qualification cost or time are not compatible with the project available budget or

324

planning. In these case, reliability - and quality in general - becomes a hot topic. Should redundancies be implemented in the attempt to compensate for the supposedly lower reliability of those parts/ components with little or no "previous space heritage"? Which "extra precautions to compensate for the use of unqualified components" should be taken? Often, in these cases, the contractor proposes to implement redundancies "for the most delicate items", in addition to their environmental ruggedization. While the second measure is reasonable and allows to improve reliability significantly, the first measure is fictitious. In fact, it cures parts failure and not functional failures. The fundamental difference between these two failure types may be non-obvious and become readily apparent by examining the reliability block diagram of the system in hand. This diagram shows the system functional paths: the entire path corresponding to the failure mode considered should be redundant.

A fully redundant design is obviously more complex than a non- or partially- redundant one, and thus is afflicted by the penalties mentioned above. In addition, a redundant design is not usually the contractor's favorite because of its inherent higher cost. However, especially in an open competition, a redundant design sells well. The result is a compromise where the overall design is boasted as redundant where actually only individual components - as opposed to entire functional paths - are redundant against their failure.   While for electronic systems, such as printed circuits, establishing their "true redundancy" is a non-trivial task, for mechanical (and, more generally, electro-mechanical) systems this is easier once a block diagram is built from the drawings of the general layout.

For example, a very common mechanism type is the power transmission. The design of a redundant power transmission is not a straightforward task. Incorporating redundancy into an electrical or fluid power transmission is relatively trouble free. Switching power to the redundant patch to maintain a continuous power supply, or by-passing a jammed relay or valve is a simple design task. However, isolating a jammed mechanism and switching to a back-up system to allow continuation of its function is more difficult, some times not practically possible. Remotely-controlled jam-removal methods can be devised, but these must also be failure tolerant. The complexity of the design increases dramatically. For example, if a pin puller is used for jam removal, redundant initiators must be used, and devices must be provided to capture the jammed members. Eventually, the resulting overall reliability may be degraded - because of the increased system complexity - to such an extent to render the redundant design not attractive.
A recommended design approach is to use the lowest number of well-proven, simple means to perform the given function. These must have "a sufficiently high inherent reliability", this meaning "a reasonably high, and quantifiable, confidence in their performing the desired function".

However, it may be hard to put this approach into practice in some cases. For example, let's consider a hatch closing mechanism used in a manned module. A loop

325

of latches and a single power drive are sufficient to realize the functions required (opening/ closing, resistance to applied loads, etc.). However, it is likely that a double failure tolerance be required for those failures involving crew safety. This requirement becomes the design driver for the whole mechanism and forces to include a number of overriding and safing devices that add a considerable complexity to the originally simple design.

Conclusions

As a result of the differences between mechanical and electronic reliability, dedicated prediction methods must be used for mechanical systems, which need to be more sophisticated than those used for electronics. The available methods have been briefly reviewed. A promising approach links structural engineering and statistics by combining SSI analysis with FMEA, but has not yet found wide-spread use. In addition, there are not standardized methods, nor agreed reliability data sources. Mainly for these reasons, there are cases where reliability prediction can result in a rather useless exercise and therefore should not be a contractual requirement. Especially in these cases, care should be taken for the inclusion and formulation of reliability requirements in technical specifications. Finally, considerations have been made on the implications of implementing redundancy in mechanical systems.

Acknowledgments

Many people and readings have contributed, directly or indirectly, to the generation of the ideas presented (quotes have been used). Mentioning some would be unfair to the others, therefore the author wishes to thank all the persons with whom he has worked during the last years.

References

1. ERA Reliability assessment report, HS-AP-ERAB-211-ETEL, 5.1.96
2. ESA PSS-01-302 "Failure rates for ESA space systems" (unpublished draft)
3. *Nonelectronic Part Reliability Data*, Reliability Analysis Center, Rome Laboratory, N.Y.
4. *Reliability engineer's toolkit*, Reliability Analysis Center, Rome Laboratory, NY
5. J. A. Collins: Failure of materials in mechanical design
6. R. Fleeter "Mr. Murphy on small spacecraft and rocket reliability" *Launchspace magazine*, March 1997
7. A. Venton "Pursuing reliability in mechanical equipment design" *Mechanical reliability*, edited by T. R. Moss
8. J. C. Hammond "A broad based actuator concept for spaceflight application" NASA CP-2273

Ullage Rocket Jettisoning Mechanism for a Typical Launch Vehicle

N.P. Giri, G. Narayanan, Sanhosh J. Nalluveettil, George Koshy
and M. K. Abdul Majeed[*]

Abstract

In a typical launch vehicle developed by the Indian Space Research Organization, during the first stage separation, ullage rockets are used to give positive acceleration to the ongoing vehicle for the reliable starting of the second-stage liquid engine. The ullage rockets are jettisoned from the vehicle once their function is over. A mounting and jettisoning mechanism has been developed for these ullage rockets. Two rockets are mounted on a frame which transfers the thrust. The frame along with the ullage rockets is jettisoned when a ball lock mechanism is released by actuating a pyro pin pusher mechanism. The jettisoning mechanism is unique as it uses a single frame for two ullage rockets, a hinge and separation mechanism, and a pyro pin pusher for single point release (Fig. 1). The mechanism has undergone a number of qualification tests and has functioned successfully in all the flights of the launch vehicle. This paper covers the design details, theoretical studies, results of testing, lessons learned, and performance analysis of the mounting and jettisoning mechanism developed.

Introduction

During stage separation in launch vehicles, when the liquid fueled upper stage engine is ignited, a positive acceleration to the ongoing stage is usually given to ensure its reliable starting. This can be achieved by firing small solid rockets called ullage rockets mounted to the liquid stage. They have relatively low thrust and short burn time. After burn out, the ullage rockets are jettisoned from the ongoing stage to improve payload. In one of ISRO's launch vehicles, where the first stage is a solid motor and the second stage is liquid fueled, the first stage separation system [1,2] uses Flexible Linear Shaped Charge (FLSC) to cut the stage, and retro rockets to give reverse acceleration for the spent stage. Four ullage rockets mounted to the second stage give a positive acceleration of 0.1g to the ongoing stage, which ensures reliable starting of the second stage liquid engine. Development of a mounting system for the ullage rockets and a jettisoning mechanism to separate them after their function was required. The ullage rockets are mounted in pairs to the stage through a jettisonable frame called an 'A' frame. The ball lock mechanism connects the frame to the inter stage. The spent rockets, along with the frame, is hinged out from the vehicle by releasing the ball lock mechanism with a pyro pin pusher. The spring thrusters mounted to the frame and the acceleration of the ongoing stage give the necessary jettisoning energy required for collision-free separation. The system has to meet a

---

[*] All authors: Indian Space Research Organization, Vikram Sarabhai Space Center, Thiruvananthapuram, India

many functional requirements, and has to undergo a number of qualification tests before the flight.

Functional Requirements

• Smooth transfer of ullage rocket thrust to the vehicle. The nozzle of the rocket is canted at 8 degrees. Maximum thrust along the motor axis is 15.5 kN. The motor burns for 5 to 8 seconds.
• Accommodate motor expansion and inter stage compression during flight.
• Collision-free jettisoning of spent ullage rockets. The liquid engine nozzle protrudes down by 3.7 m from the ullage motor separation plane.
• Withstand flight aero-thermal environment.

System Description

Four ullage rockets are mounted in pairs on Inter Stage (IS) 1/2U at two diametrically opposite locations. A frame acts as an intermediate link between ullage rockets and IS. Two ullage rockets are mounted on a single A frame (Fig. 1). Thrust is transferred from the rocket flange to the thrust transfer bracket provided at the A frame. The motor forward end is held in position by a bracket called the forward support arm, which permits the axial expansion during motor firing. The thrust pins provided at two legs of the A-frame transfers thrust from the frame to the thrust transfer brackets provided on the interstage. The A-frame is resting on a hinge pin bracket mounted on IS at the bottom and it can hinge about the bracket during separation. A ball lock mechanism holds the A-frame at top center which constrains radial movement. Two compressed spring thrusters are provided on either side of the ball lock mechanism to give jettisoning energy. Jettisoning is done by actuating the pyro pin pusher that releases the ball lock mechanism and due to the spring energy, the frame along with the spent ullage rockets start hinging out. The hinge is designed in such a way that jettisoning takes place at 60° from the ongoing vehicle. The separation is collision free and the dynamics involved in the separation are discussed later. The mounting between A-frame and IS is designed in such a way that it can accommodate an IS compression up to 6 mm during flight. The system is preloaded axially at the bottom and laterally at the spring thruster locations.

Design Specifications

- Axial preload of 6000 N at aft end
- Lateral preload of 2500 N
- Jettisoning energy by two spring thrusters
      Spring stiffness: 11.2 N/mm + 5%
      Initial deflection: 67 mm
      Final deflection: 15 mm
- Jettisoning angle: 60° to interstage
- Jettisoning speed: 0.9 m/s

- Axial growth allowed: 6 mm
- Lateral holding by ball lock mechanism
- Pin pusher specifications
        Thrust rating: 2000 N
        Stroke: 16 mm
        Pin diameter: 8 mm

The individual subsystems are designed to meet the above requirements. The present design gives a jettisoning speed of 0.94 m/s during flight and 0.82 m/s during ground test. The details of the subsystems are described below.

Subsystems

Spring thruster

Spring thruster assembly, shown in Figure 2, comprises of the spring, inner housing, outer housing, ball end and cover plate. The outer housing is bolted to the cover plate. The special bolt preloads the ball end and thus prevent lateral movement.
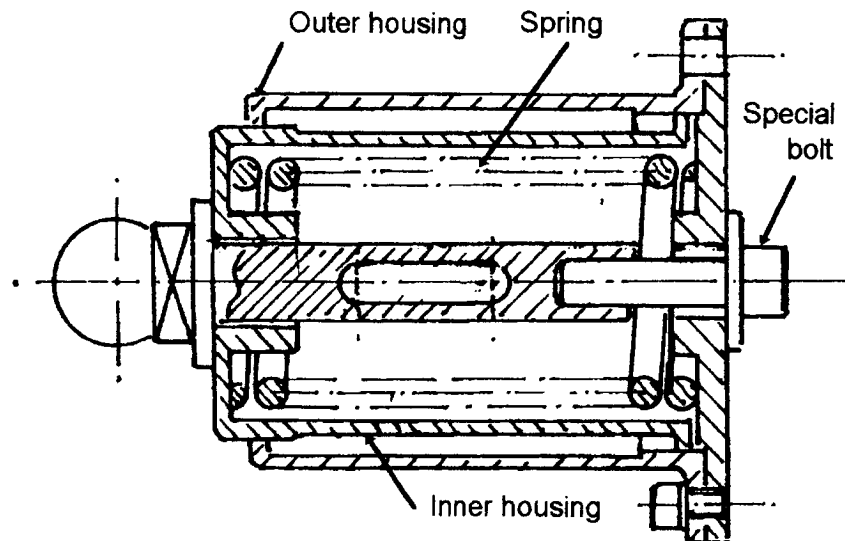
Figure 2. Spring thruster assembly

Ball lock mechanism

The assembly consists of a piston, spring, inner housing, outer housing, collar nut, cap nut, and balls (Fig. 3). The outer housing is bolted to the IS 1/2U through cylindrical spacers to accommodate axial movement due to inter stage compression. The inner housing is bolted to the A-frame. The piston is retained in position by a shear screw. A cap nut prevents the entry of foreign matters and reserves the space for the piston to move. A collar nut preloads the ball lock axially against vibration. The outer housing is provided with grooves and inner housing has holes to accommodate balls. The balls are held in the locked position by the piston (between inner housing and spherical housing), thus preventing the jettisoning of ullage rockets.
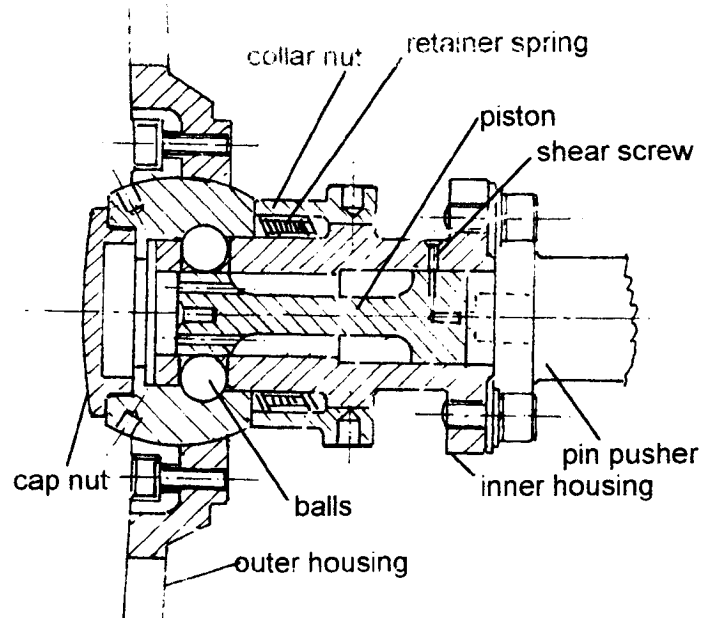
**Figure 3. Ball Lock Mechanism**
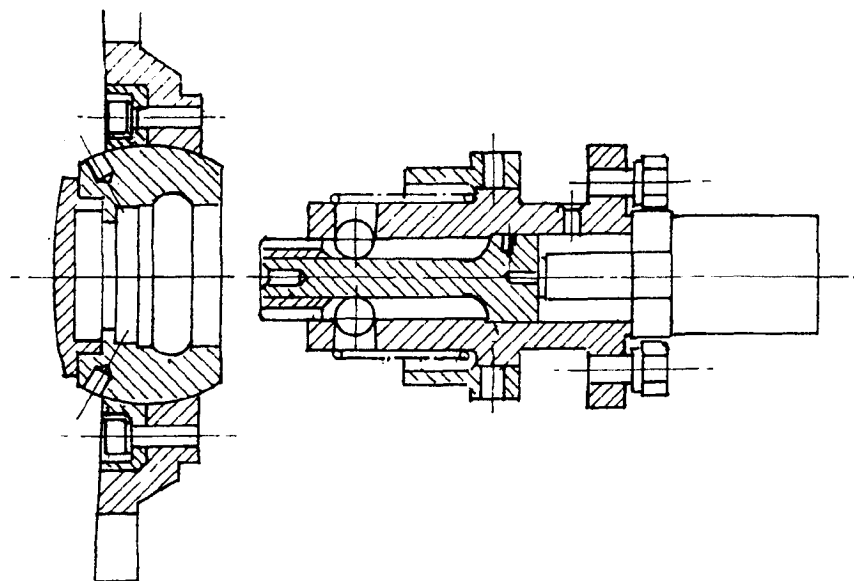
Figure 4. Ball Lock Mechanism after Release

A retaining spring is placed between the collar nut and the inner housing to contain the balls during jettisoning. When the pyro pin pusher is actuated, the screw shears and the piston moves releasing the balls. As a result, the A-frame, along with the

330

spent ullage rockets, is jettisoned out. The outer housing subassembly remains with the ongoing stage. The mechanism after release is shown in Figure 4. Four steel balls are used to lock the system laterally. The ball lock mechanism is designed to carry a lateral load of 4620 N.

Pyro pin pusher
The pyro pin pusher (Fig. 5) is mounted on the A-frame and pushes the piston of the ball lock mechanism to release it. The pin pusher is electrically initiated and has redundancy in initiation. Pyro cartridges are fired to apply pressure on the pin pusher piston to move with the required thrust after shearing the screw.
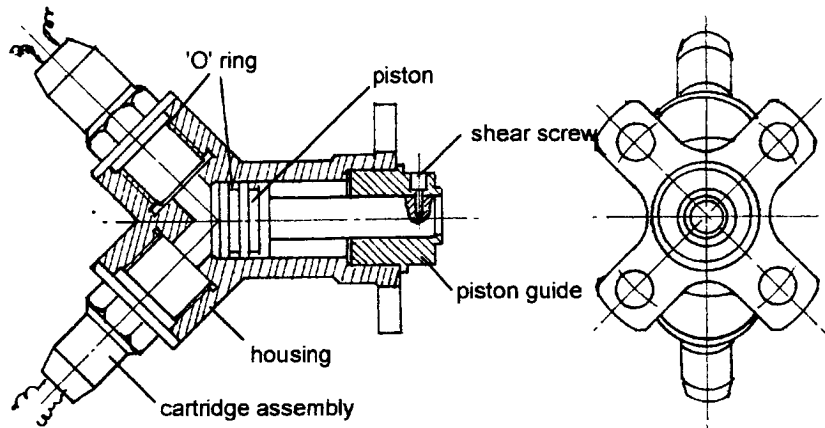
Figure 5. Pin pusher

Jettisoning Dynamics

The dynamics of ullage rocket separation presented here differs significantly from that of other separating bodies. Unlike the general rocket-stage separation, the spent system hinges about the accelerating parent vehicle. The spring thrusters provided on the frame supply the necessary energy for separation. Under the action of the springs and the acceleration of the ongoing stage, the spent ullage system on the frame rotates about the hinge on the inter stage.

After having undergone rotation by a pre-specified angle, the frame gets released form the hinge and their subsequent motion is free from constraints. A detailed study of the separation dynamics of the system was carried out to optimize the parameters like spring stiffness, stroke jettisoning angle, etc. during the design phase [1,3].

External forces and moments are a consequence of inertial pull, aerodynamic effects, thrust and the forces induced by the separation mechanism. Since we are interested in the relative motion of the ullage system with respect to the main stage over short duration (typically around 1s), the gravitational field would have little effect and hence has been neglected. For the same reasons, for an ideally controlled ongoing stage being considered here, its acceleration vector is assumed to be constant and remain

parallel to the longitudinal axis. Finally, since liquid stage ignition occurs at significantly high altitudes, aerodynamic forces are neglected as they would be rather small.

Trajectory of the separated body has been simulated for various design parameters. It is observed that separation angle (the angle at which the spent ullage is hinged out from the vehicle) has a good impact on the separation clearance (clearance between second stage nozzle and separated body). It was observed that the lateral velocity of the jettisoned body increases with separation angle and reaches the maximum value at optimal angle 31.31°. Further increase in angle results in decreasing speed. The optimal angle could not be implemented due to some mechanical constraints. The present system is designed to hinge out at an angle of 60°, which has a separation clearance of 700 mm. The trajectory simulation was carried out for various separation parameters and Figure 6 shows two typical cases.


a. Trial

K= 7 N/mm   a= 1.20g
x₁= 81 mm   ø = 120°

b. Design

K= 11.2 N/mm   a= 1.20g
x₁= 67 mm   ø = 60°
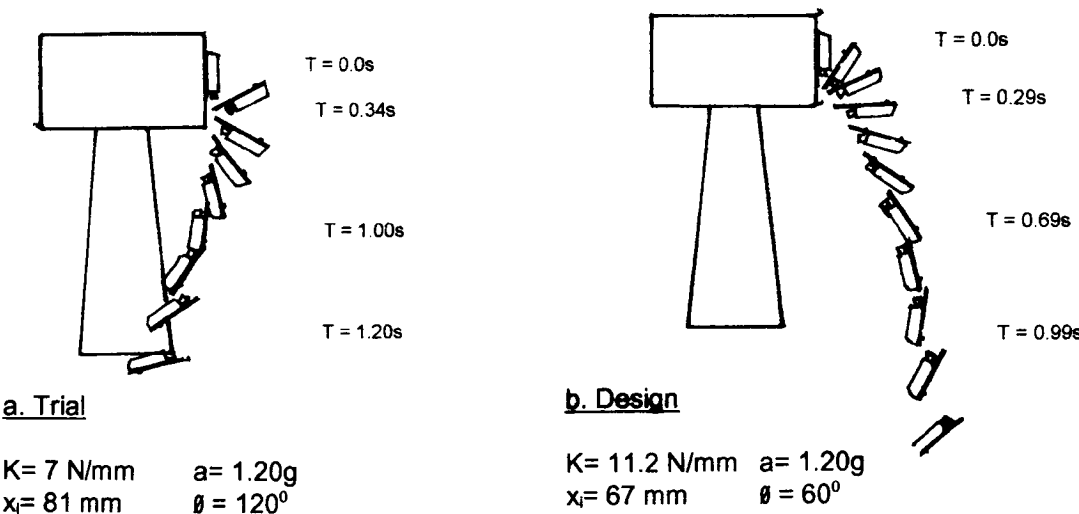
Figure 6.   Simulation

The influence of stored spring energy on the system performance is also analyzed. It is noted that very large energy is required to achieve significant improvement in system performance. It is concluded that increasing the spring energy is not an effective way of improving system performance. Ground test situation is also simulated where the relative longitudinal acceleration drops to $9.81 m/s^2$. It is noted that clearance is more comparable to flight.

Qualification Program

The ullage rocket mounting and jettisoning system had undergone a number if qualification tests [2] like structural test, parallel firing test, vibration test, acoustic test, pyro shock survivability test, and jettisoning test. A brief description of the various tests is given below.

Structural Test

In the structural test, the system was tested using a fixture for 1.2 times thrust load. All system elements were found intact after the test. The test set up is shown in Figure 7. A second structural test was done for 1.2 times flight load using actual interfaces along with interstage qualification tests. In the test, 5 mm interstage compression was noticed and consequently the system was modified to accommodate this, as the system could accommodate only 2 mm as per preliminary design.
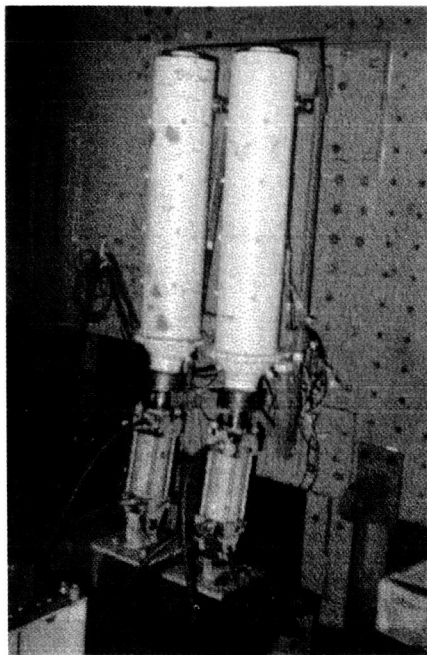

Figure 7. Structural Test
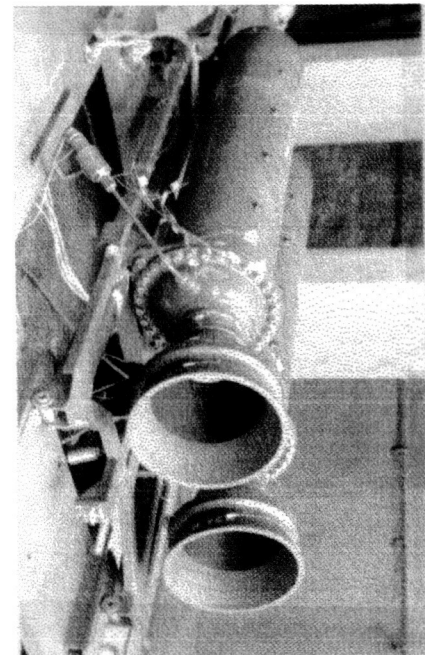
Figure 8. Parallel Firing Test

Parallel Firing Test

Parallel firing of two ullage rockets mounted on the A-frame has been carried out. The system was found to withstand the motor thrust loads and the performance of jettisoning system was confirmed by actuating the pin pusher after the test. The test set up is shown in Figure 8.

Vibration/Acoustic Test

A vibration test of the system was conducted with mass simulation ullage motors mounted to IS 1/2U. The test was carried out in all three axes. The test was conducted for sine levels of 1.8g and random levels of 6.3g. A Pre and post-resonance survey was also conducted. The test set up is shown in Figure 9.

Yielding was noticed at IS 1/2U stringer where the hinge bracket of the system was mounted. Corrective action was taken by strengthening the crown of stringer by introducing a 15CDV6 steel sheet. All other mountings were intact.
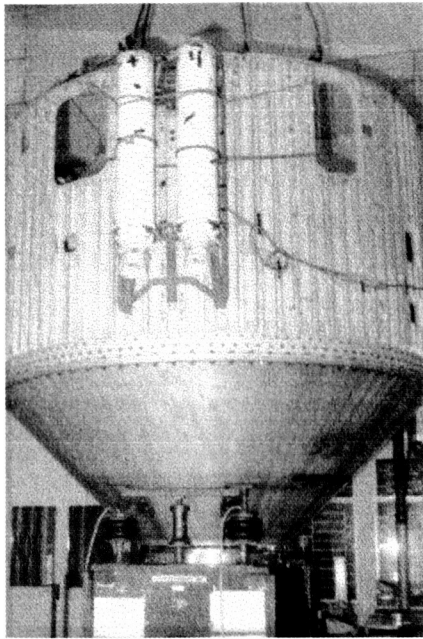
Figure 9. Vibration Test   **Figure 10. Shock Survivability Test**

In the acoustic test, after subjecting to qualification levels 156 dB along with the inter stages, ullage rockets were jettisoned by actuating the pyro pin pusher.

Ullage Rocket Jettisoning Tests
Ten ullage rocket jettisoning tests were conducted in which five used mechanical pin pushers and the remaining five used pyro pin pushers. They indicated proper functioning of the mechanism. In the parallel firing test, after 20 s of burn out of motors, the system was jettisoned in a horizontal position.

Pyro Survivability Test
The ullage rockets are mounted close to the first stage separation plane so it has to survive the large pyroshock by the FLSC during stage separation. In order to qualify the system in a shock environment, the jettisoning system along with live ullage rockets was mounted on the interstage and the FLSC separation test was conducted [Figure 10].

The ullage rocket jettisoning mechanism assembly is shown in Figure 11. Shock on ullage rockets was monitored during first stage separation tests 01, 02 & 03. A typical shock value at pin pusher location is 50g for a duration of 10 ms. The mounting system with empty ullage rockets was jettisoned after each separation test [Figure 12]. The live ullage motors subjected to shock have been removed from the test set up and

non-destructive testing was carried out to assess the grain integrity. After NDT, motors were fired and the characteristics were found acceptable.
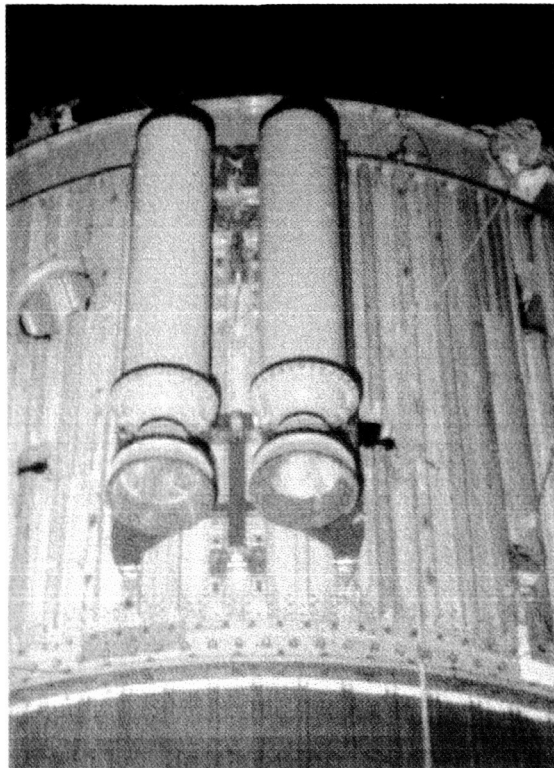

Figure 11. Jettisoning System Assembly
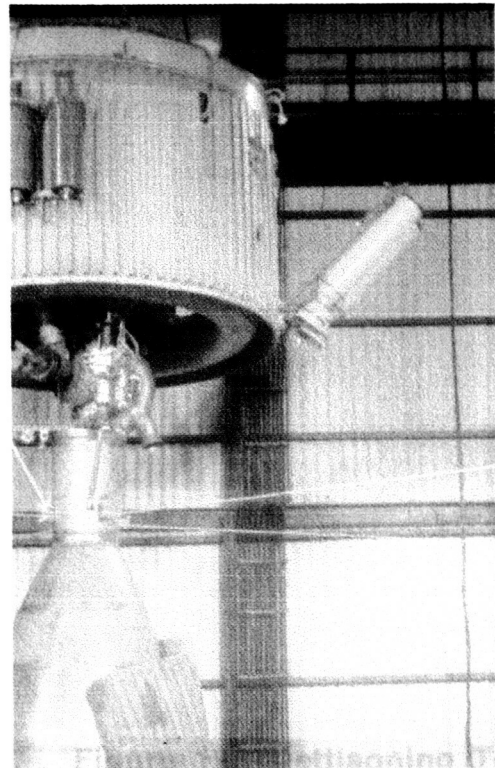
Figure 12. Jettisoning Test

Flight Performance

The system has successfully functioned during flights conducted by the launch vehicle [4,5,6]. Functioning and thrust transfer from ullage rockets are confirmed with data from flight telemetry on motor pressure [Figure 13].

The vehicle acceleration [Figure 14] and fire currents further ascertain the functioning of rockets. Physical separation of ullage rockets from the inter stage is verified by monitoring the connector mating status of the separation connectors mounted between the A-frame and inter stage [Figure 15]. The pin pusher functioning was confirmed from fire currents.

In one of the developmental flights, maximum roll disturbance of 2.6 deg/sec was observed on the vehicle during ullage rocket functioning. Since ullage rockets are mounted on the 'A' frame, the nozzles are given a skew angle in addition to the cant angle. The skew angle ensures that the thrust axis of the ullage rockets passes through the center of the vehicle and thus eliminates the roll moment. Since the skew angle was provided on the motor-nozzle assembly, there were two types of ullage motors: left skewed and right skewed. As the skew angle is only 5.6 degrees, which is too small to visually differentiate, there was a chance for wrong assembly of motors,

which can result in roll moments. To avoid the possibility of human error in assembly, motors were made identical and skew was incorporated in mounting the A frame. Subsequent flights with this modification did not cause unacceptable roll moments [Figure 16].
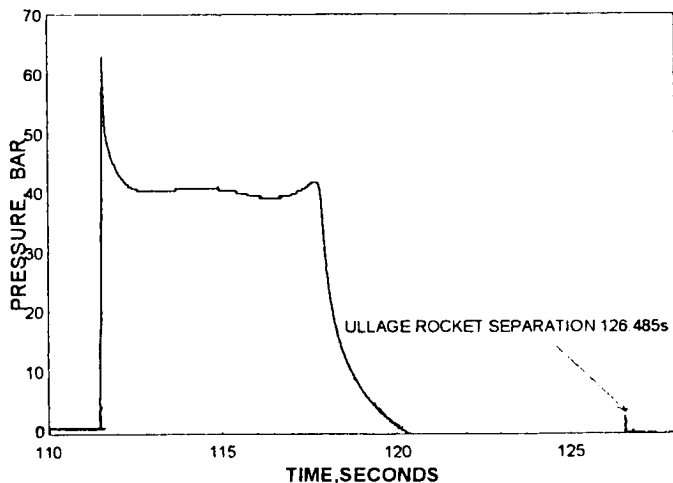


Figure 13.   Ullage Motor Pressure
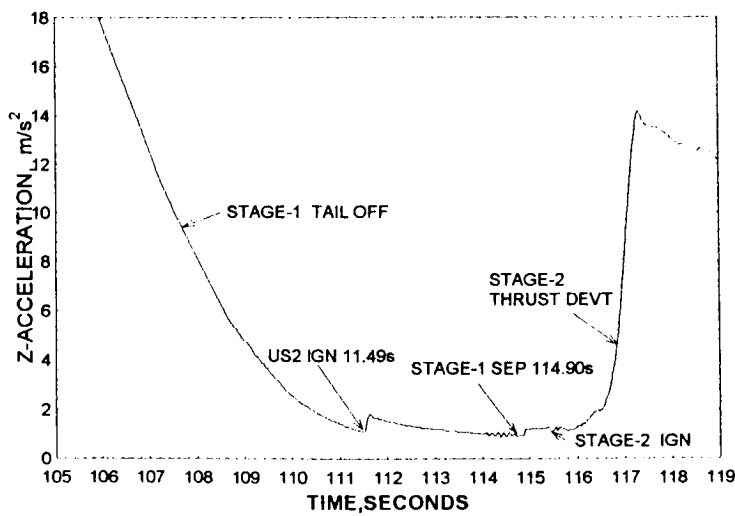

Figure 14.   Vehicle Acceleration

336
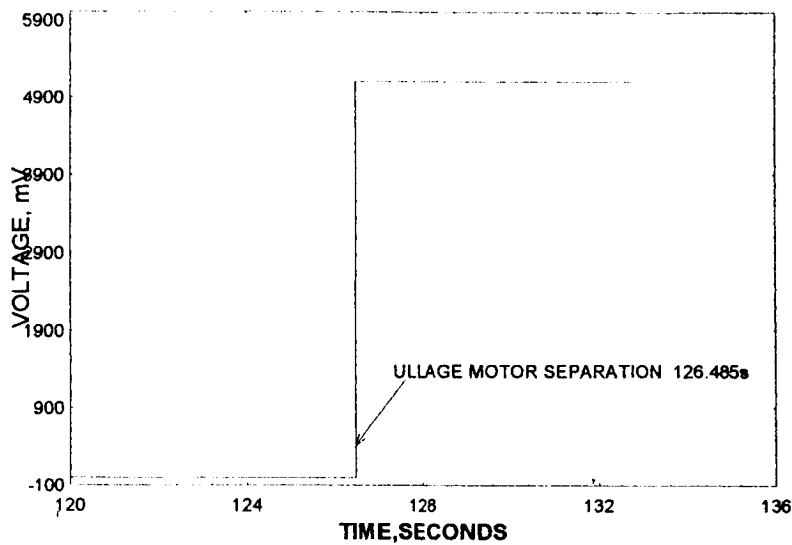
Figure 15.   Connector Mating Status
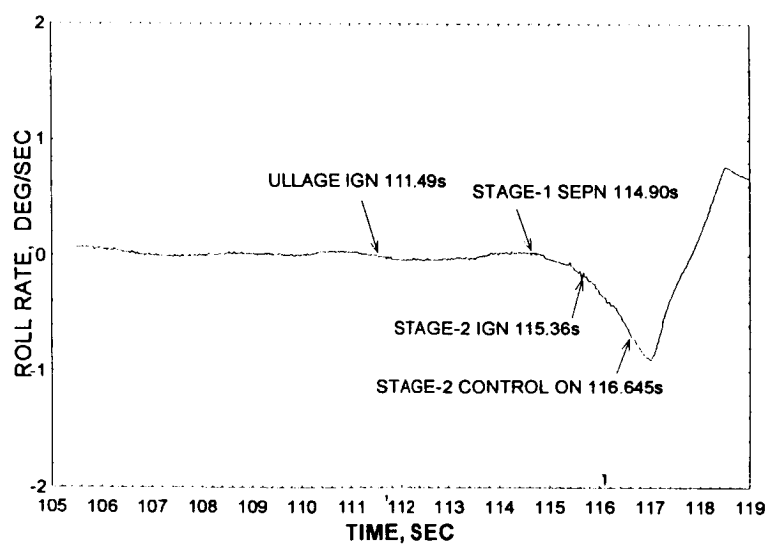
Figure 16.   Roll Rate

Conclusion

The development, qualification, and flight performance of an ullage rocket jettisoning mechanism was discussed. The mechanism is different from conventional separation systems as it uses a single frame to mount two ullage rockets, hinge out and separation mechanism and single point release with pyro pin pusher. The development and qualification program was the learning ground to understand the system better and overcome the limitations by suitable modifications. The system is now confidently used on operational flights of the launch vehicle.

Acknowledgments

References

1. VSSC:ASMD:DR:046:88 (Internal Report)
2. VSSC:ASMG:PR:073:93 (Internal Report)
3. VSSC:ASMG:TR:310:93 (Internal Report)
4. VSSC:SAS:2 Dec 93 (Internal Report)
5. VSSC:ASMG:GR:109:94 (Internal Report)
6. VSSC:ASMG:TR:05:96 (Internal Report)

International Space Station Blanket Restraint System: Successful Mechanism Qualification and Process Development Through Analysis and Simple Characterization Tests

Daniel P. Schmidt[*]

Abstract

The Blanket Restraint System (BRS) is a system of seven spring-actuated retractable mechanisms designed to restrain the International Space Station's solar arrays during launch. Each of the BRS mechanisms retract on orbit prior to solar array deployment. Several units from the initial production run failed acceptance test performance criteria. An analysis to completely characterize the relationship between pin geometry and performance was then initiated. The analysis provided the capability to predict the acceptance test performance at least three months before actual acceptance and could determine which of the manufacturing processes, if any, were degrading performance. The analysis also provided the basis for a modification to the geometry of the assembly that would greatly improve performance. The qualification was completed on the new design at load levels that were twice requirements.

Introduction

The International Space Station features eight of the largest space based solar arrays ever flown (Figure 1). These flexible solar arrays are deployed much like an accordion and provide a large extended surface area versus stowed volume when compared to rigid arrays. However, due to the overall weight of these specific arrays, the solar blankets need additional support during launch beyond typical flexible array stowage that uses preloaded blanket compression to prevent array movement. The Blanket Restraint System (BRS) is a system of seven spring-actuated retractable mechanisms designed to restrain the International Space Station's solar arrays during launch (Figure 2). Each of the BRS mechanisms retract on orbit prior to solar array deployment. The blanket cannot be deployed before retraction of the BRS pins. The core of the BRS mechanism pin consists of two pins, the expandable pin and the taper pin. The expandable pin is stainless steel with twelve slots cut longitudinally along the length of the pin. The titanium taper pin is inserted into the expandable pin thereby producing expansion and a tight fit into the blanket assembly for support during launch (Figure 3). Upon release, the pins are forced apart by a spring providing 223 N separation force so that the taper pin is withdrawn from the expandable pin. This allows the expandable pin to sufficiently reduce in outside diameter, then both pins are withdrawn from the blanket assembly by a second spring, and the array can unfold. The mechanism must meet several requirements including an on orbit retraction under a 223 N sideload due to blanket differential thermal expansion.

---

[*] Lockheed Martin Missiles & Space, Sunnyvale, California

Stowed Configuration

During Deployment
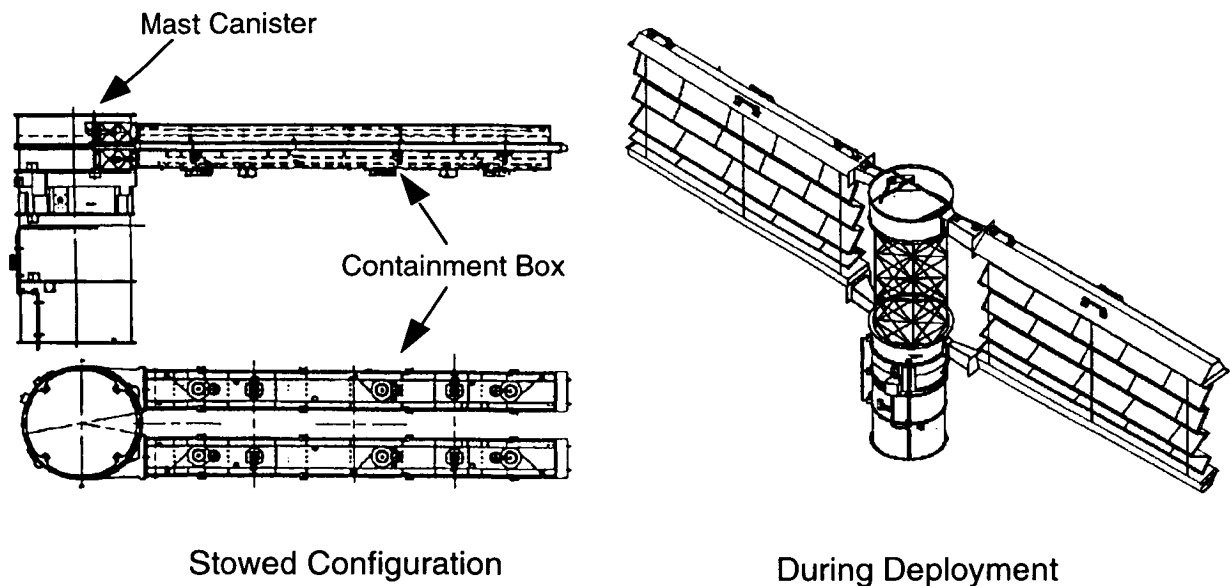
**Figure 1. Space Station Solar Array Wing Assembly**
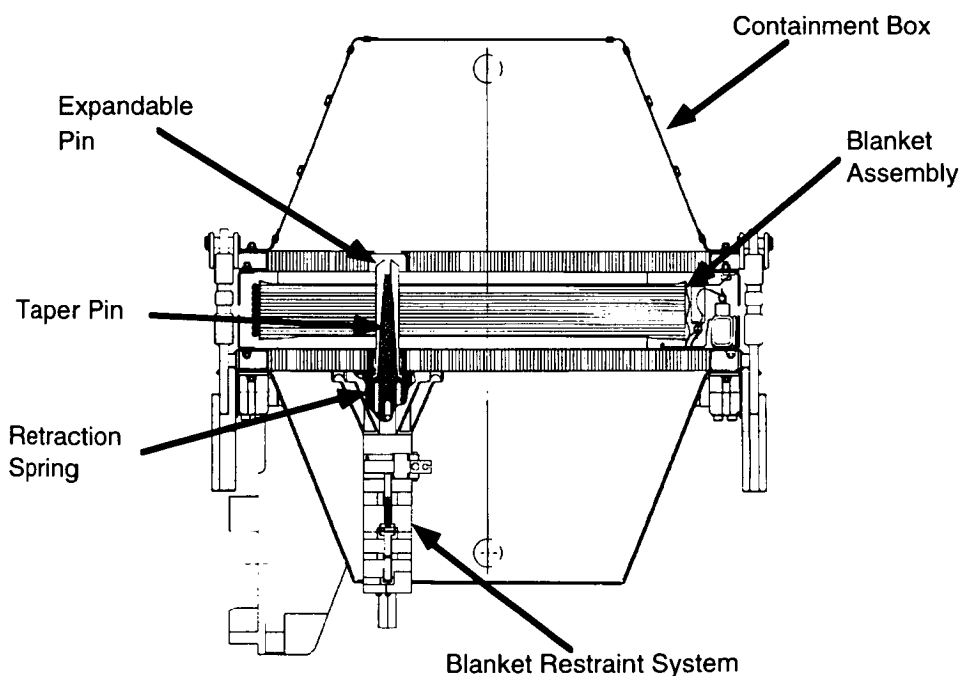
**Figure 2. International Space Station Solar Array Blanket Containment Box Cross Section Showing Restraint Location**

340
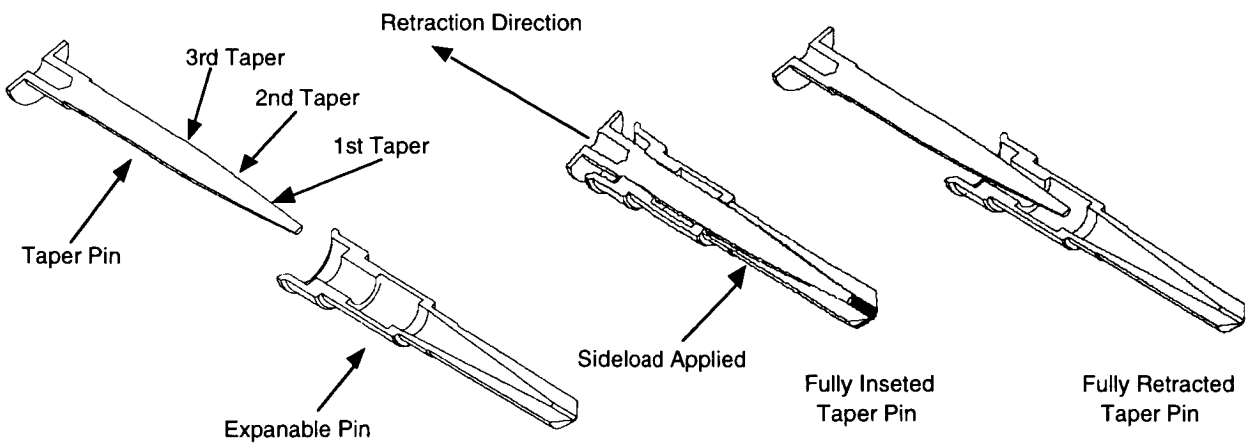
Figure 3. Insertion of Taper Pin into Expandable Pin.

Blanket Restraint System - From Development to Qualification

Development

Three development assemblies were built and successfully tested to requirements. However, one assembly was precariously close to the lower limit of performance. This was attributed to a shift in internal loading due to the application of the sideload. Minor modifications to the design were made including smoother surface finishes and a slight change of taper pin geometry to counteract the sideload. These modifications were seen as performance enhancements and hence development testing was not repeated as all three assemblies performed acceptably. At this point, the development of the mechanism was considered complete (Johnson, et al. 1994).

A full engineering unit of the Solar Array Wing Assembly including a full set of seven BRS mechanism assemblies was constructed to qualify the wing assembly and its components. Each BRS mechanism assembly is acceptance tested before installation into the wing assembly to assure proper performance. The main portion of the BRS mechanism acceptance test consisted of one demonstrated retraction under a 223 to 245 N sideload. The sideload testing is performed in the BRS Test Fixture (Figure 4). A Blanket Simulator which is tensioned by the jack screw shown in the figure is used to mimic the sideload forces. During the acceptance tests of the BRS assemblies to be installed in the engineering wing, the first flight-similar wing to be assembled, several units experienced high resetting forces. The resetting force is the force required to fully insert the taper pin into the expandable pin thereby expanding the assembly, preloading the separation spring, and setting the pins ready to retract. This undesired discrepancy lead to additional testing consisting of several sideload tests on the development units. It was found that the lubrication, impinged dry-film
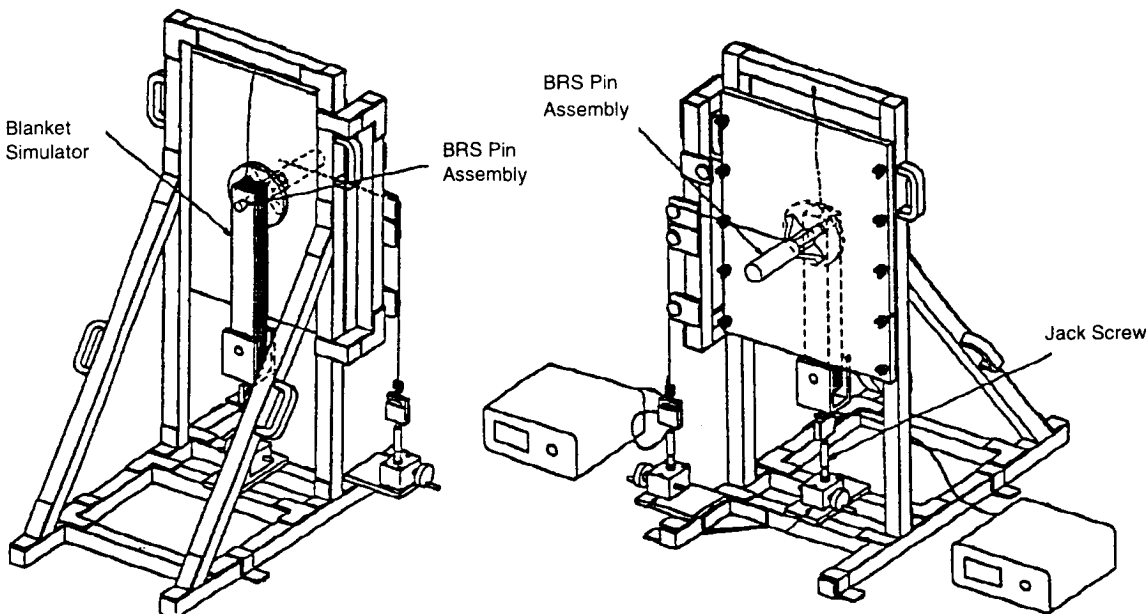
Figure 4. Sideload Acceptance and Qualification Test Fixture

Molybdenum disulfide, was wearing after several cycles, degrading pin performance and culminating in the higher reset forces.

Closer attention to the lubricated surfaces showed that the inherent geometry of the contact areas was contributing to lubricant wear. The area of contact in the assembly is between the tangs of the expandable pin and the conical surface of the tapered pin. The tangs in the expandable pin are formed by slicing twelve pie-shaped wedges in a hollow, tapered cylinder. The tangs have a circular inner surface in their relaxed state, as seen in the first cross section in Figure 5.
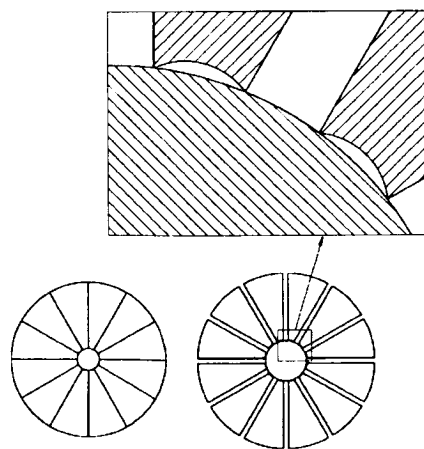

Figure 5. Cross Section of Expandable Pin During Insertion of Taper Pin

When the tapered and expandable pins are assembled, the tapered pin pushes the tangs outward to provide a tight grip on the array, but also changing the tang geometry. The inner surface of the tangs is machined to a smaller diameter in its relaxed state than the diameter of the tapered pin, so there is a surface mismatch during expansion. The contact area for each tang is reduced to two ridges along the outer corners of each wedge, as seen in the second cross section of Figure 5. These small areas of high pressure contact were responsible for increased friction and the accelerated lubricant wear.

Lapping and Honing Operations

A lapping operation was added to the pin processing in order to increase the contact area of the pin interface and reduce lubrication wear. The lapping operation wears the inner surface of the tangs against the tapered pin so the surfaces will mate properly. The tapered pin is inserted into the expandable pin after being coated with a coarse grit lapping compound, and is then rotated and removed. This cycle is repeated 175 times in clockwise and counterclockwise directions, with finer and finer lapping compounds. The result is the inner circumference of the expanded tangs expressly matches the profile of the tapered pin with which it was lapped.

A honing process was also added to improve the surface finish and thereby decrease the coefficient of friction between the taper and expandable pins. The honing operation is done in a pressurized fixture with an abrasive flow media which sands away a thin outside layer while reducing any raised surface features (Figure 6). The honing machine pumps a specified amount of media through the expandable pin. This procedure ensures the expandable pins are as smooth and as frictionless as possible.

As a precaution, an engineering inspection was also added which consisted of coating the taper pin with layout dye and inserting the taper pin into the expandable pin. By giving the taper pin a slight rotation, the tines of the expandable pin would rub on the dye. The amount of removed dye on the taper pin indicated the characteristics of the pin interface. This test was known as the Dye Test. The modifications were again considered improvements and due to schedule constraints, flight and qualification production commenced concurrently.

Restart of Production

Once these modifications were in place, fabrication was started on several batches of flight assemblies. Approximately six months after the modifications, three pin assemblies failed to retract with a 223 N sideload during the acceptance testing, foreshadowing a qualification failure. The qualification testing of a BRS pin consisted of four total sideloaded retractions and 26 nonloaded retractions. Thermal

Normal Media   Backflow
Flow Direction   Situation
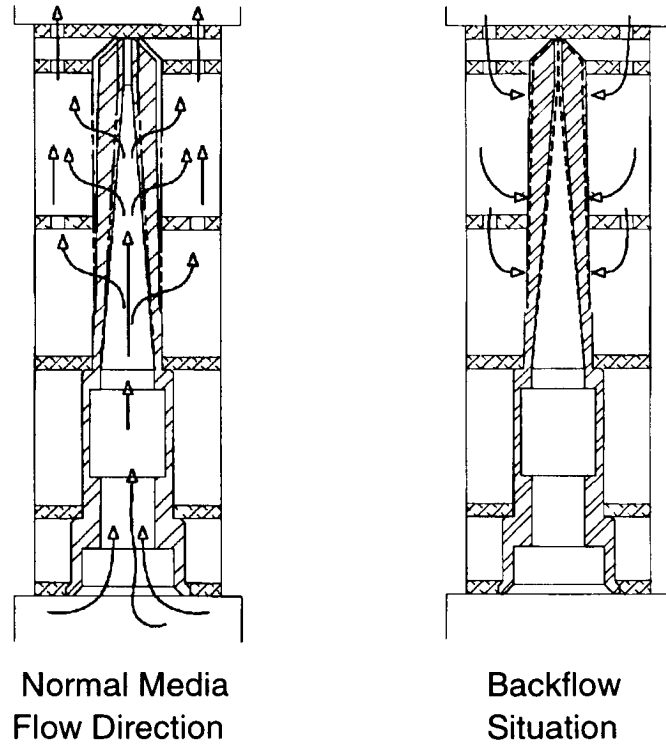
Figure 6.   Flow Honing Operation

performance was to be qualified on the first flight wing during wing assembly thermal vacuum test.

Analysis

Because of the failures, an analysis to completely characterize the relationship between pin geometry and sideload capability was initiated. To begin, the tines of the expandable pin, which are essentially cantilever beams, were modeled as sixty discrete sections along the length of the tine. This was done to account for the varying cross sectional area and inertial changes along the length of the tines. The moment of inertia about the neutral axis was then calculated for each section. A program was subsequently completed to sum the moments along the length of the tine, essentially creating a moment diagram. This method allowed forces to be applied at the center point of each discrete section. Once the moment diagram and the inertia at each section were known, the deflections were calculated utilizing the moment-area method. The model was verified initially by hanging a 13 N weight on the end of six different tines of two different pin assemblies. The deflection was measured at various points and compared to predicted values. Figure 7 represents the moment inertia diagram for this specific loading case. From this figure, the effects of the variable cross-section can be seen. If the beam had a constant cross-section, the applied loads would show linear behavior on the moment/inertia diagram. The predicted deflections versus actual deflections of several pins are shown in Figure 8.

344
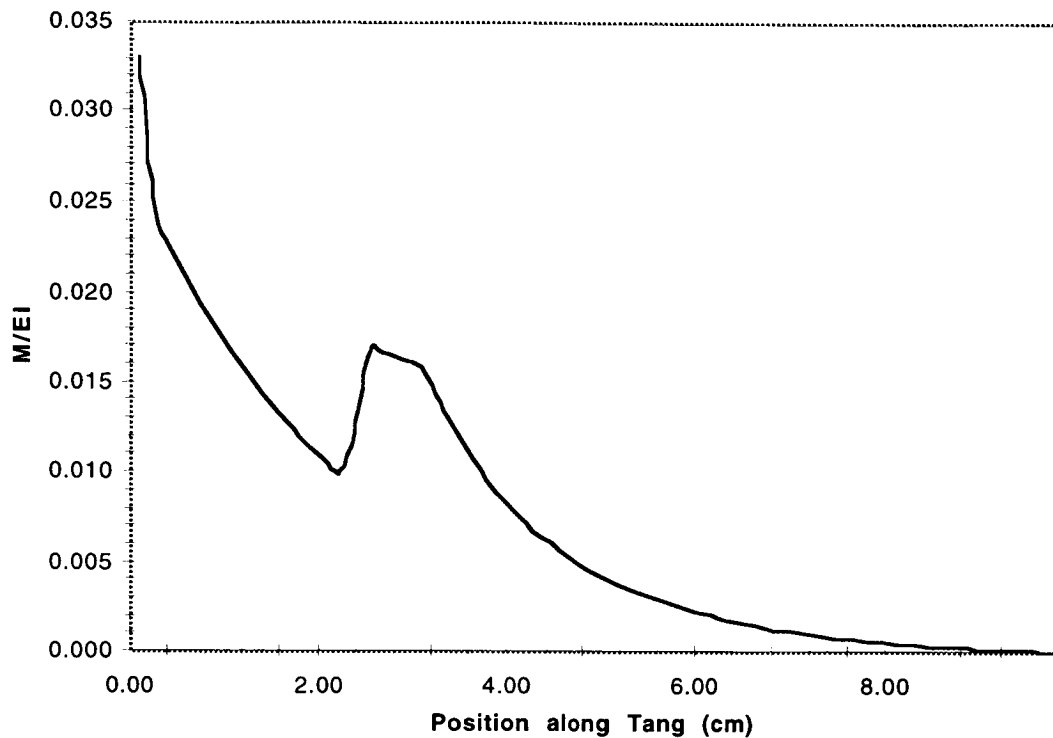
Figure 7. The Moment Divided by the Product of the Modulus of Elasticity and the Moment of Inertia Curve for Test Loading Case
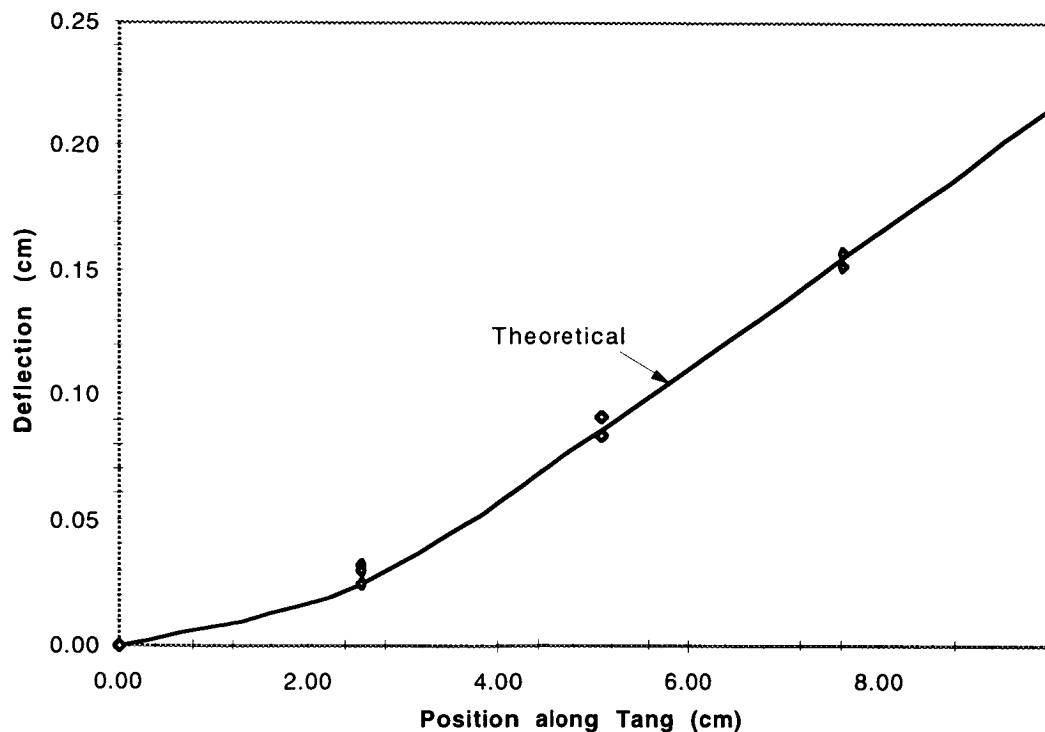

Figure 8. Predicted versus Actual Deflection for Test Loading Case

Next, the model was refined to include predictions for the force required to insert a tapered pin into an expandable pin. This was done by a simple free body diagram. The taper pin has three different tapers along the length of the pin which affect the resultant component of friction and applied forces in the axial direction (Figure 3). As the taper pin is inserted into the expandable pin, first contact between the pins is made at the tip of the taper pin. As the taper pin is pushed further into the expandable pin, the contact point will move back along the taper pin depending on pin geometry. Several assemblies were tested by measuring the force required to insert and retract the expandable pin. Figure 9 shows such a force profile for one representative pin. From several graphs of this nature, an estimation of the coefficient of friction can be made since only the sign of the friction term has changed between insertion and retraction. From this data, the starting coefficient of friction between the pins was estimated to be 0.26.

By comparing the actual dimensions of a taper/expandable pin assembly and by using the model described, the final contacting regions along the length of the pin were found. Accounting for the taper angles and the forces required to expand the expandable pin based on the contacting region, the force required to insert and retract a tapered pin into an expandable pin was now predictable based on pin geometry.

The ultimate goal, however, was to predict the sideload capability of an assembly. The
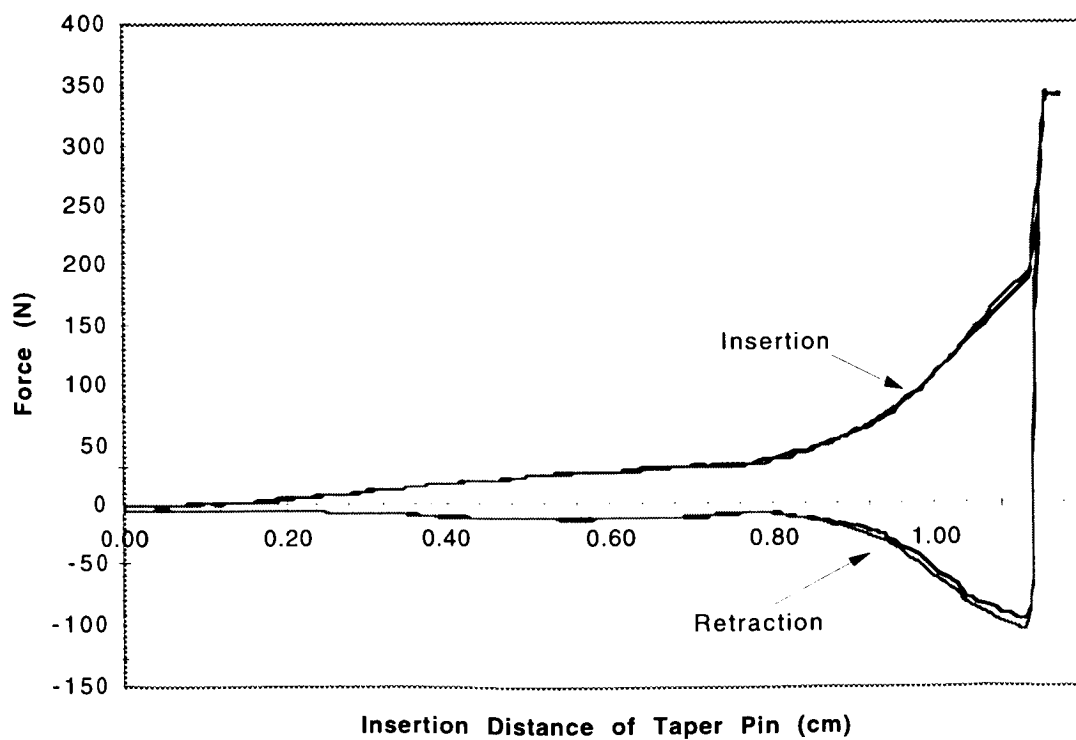

Figure 9. Insertion and Retraction Force Profile for Pin 1014

sideload capability is the maximum external force that can be applied to the pin assembly due to blanket thermal growth and still allow the taper pin to retract from the expandable pin. This calculated prediction was accomplished by placing additional load on the pin, simulating a sideload, until the predicted retraction force equaled the available spring force in the separation spring. When a sideload is applied to a pin assembly that does not have contact along the length of the blanket assembly, the expandable pin will deform to transfer the loads to the taper pin along its length. For this reason, the model was enhanced to determine the stress at each discrete region. The stresses at each section were determined by multiplying the already calculated deflections by the modulus of elasticity.

Two examples of actual predictions follow to show the mechanics of the method. Both pin number 1008 and 1028 conform to the blue print requirements, yet per the Dye Test, pin number 1008 showed the most contact at 4.2 cm from the tip while pin 1028 showed contact 2.2 cm from the tip of the tapered pin. The diameter change of the tips of the expandable pins during expansion were measured using a caliper. Based on these measured values the program predicted a retraction force capability of 436 N for pin 1008 and 663 N for pin 1028. Pin number 1008 actually tested at a maximum sideload capability of 458 N. Pin 1028 was tested up to 579 N but was tested no further due to fears of overstressing the test fixture at that time.

The nearly linear dependence of sideload capability on non-sideload retraction force soon was discovered. The theoretical curve versus actual data is shown in Figure 10.
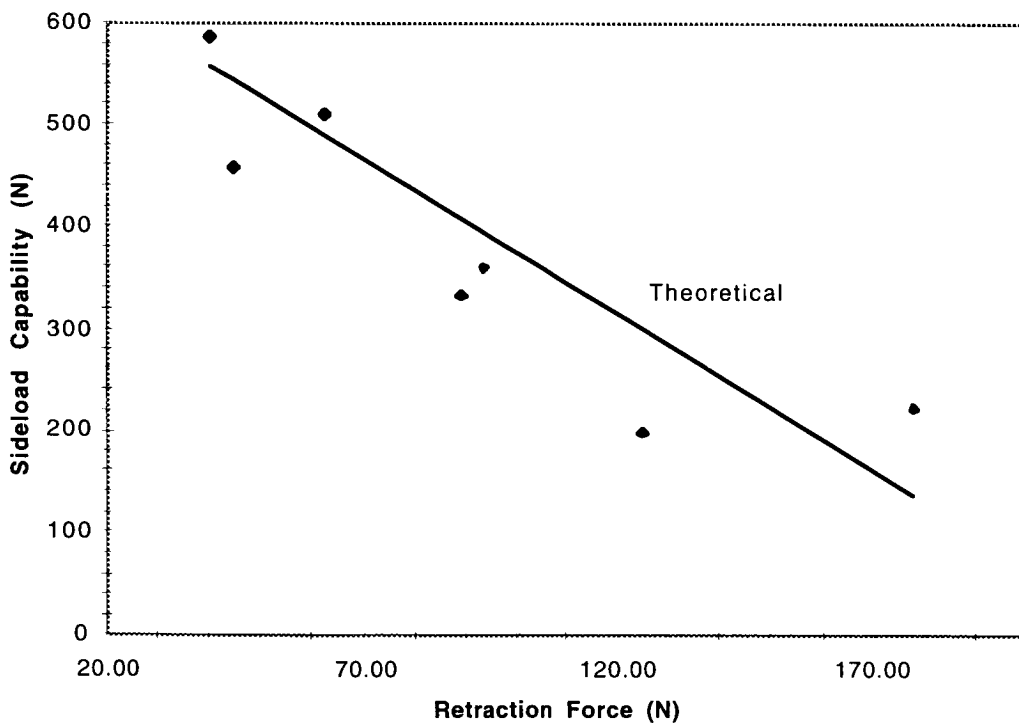

Figure 10. Sideload Capability versus Non-sideloaded Retraction Force

As the contacting region of the pin moves back along the tapered pin, sideload capability falls. The results were intuitive since a taper pin contacting at the tip of the expandable pin's tines would have less contacting forces. This is analogous to a cantilever beam which is easier to deflect by placing a force at the free end of the beam versus placing the force near the fixed end. The contact region can also be related to the insertion force profile. Figure 9 demonstrates this effect. As the taper pin is initially inserted into the expandable pin, the insertion forces start to linearly increase. As the transition is made to the second taper, a new linear curve is followed as the taper pin is inserted. By performing the Dye test on this pin assembly it can be found that contact on this particular pin is near the end of the second taper which is consistent with this insertion force profile.

As seen above, the prediction of sideload capability is highly dependent on the interface and slight dimensional variation between the pins. The tapered pin, being a CNC lathed part is usually within a few micrometers consistently; however, the internals features of the expandable pin have been shown to span the tolerance range without much consistency. Due to this fact, along with the calculated sensitivity of the variation, predictions had to be made across the tolerance range paying particular attention to the expandable pin machining method.

Another subtlety of the design was realized through the analysis. If a pin were to have contact away from the tip of the taper pin, not only would sideload capabilities be low, but the deflection model predicted the ends of an expandable pin's tine to be raised significantly off the surface of the taper pin. This was in fact observed in low performing pins. Thus, the softness of the expandable pin tip while the taper pin was fully inserted became another subtle way of determining contact regions and hence ultimate performance.

A new test was conceived based on these newly discovered performance indicators; a simple, yet accurate test of ultimate performance consisting of a 65 N spring being placed between the two pins (Figure 11). With the taper pin fully inserted into the expandable pin, the pins needed to separate without a sideload friction contribution. If this were so, at least 156 N would be left in the retraction spring to pull against the sideload. After the analysis was completed, the value of this test seemed to be obvious. If there is a need to pull against a sideload, then the retraction spring should not be required to use most of its available energy simply pulling the non-loaded assembly apart.

Lastly, with the analysis confirmed, a newly profiled taper pin was designed based on forcing contact to the tip. The final design was a compromise between removing material from the taper pin on the second and third taper sections versus stress build up during sideload deformation. The new profile also took into account manufacturing process capability for holding tolerances. Acceptable stresses and sideload capability were designed into the new taper pin across the tolerance range. The final design modification was a diameter reduction of 17.8 micrometers on the second taper and

348

| 65 N spring placed around taper pin | Expandable pin ready for insertion | Taper pin fully inserted | Successful completion of 65 N Spring Test |
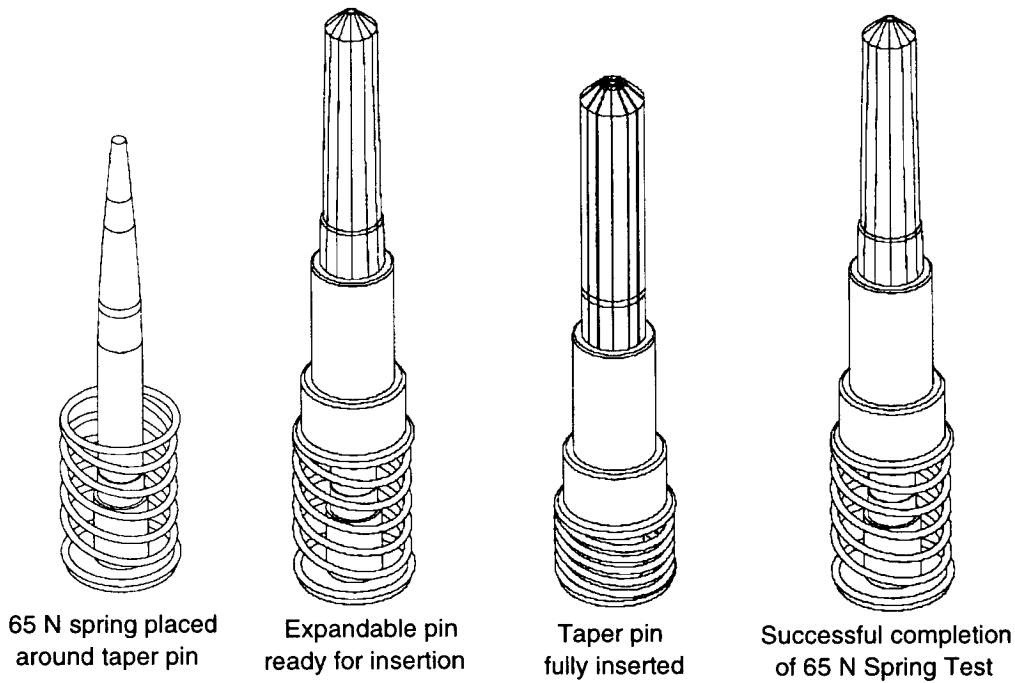
Figure 11.   Demonstration of 65 N Spring Test

38.1 micrometers on the third taper. This final profile was then verified in the sideload test fixture where the assembly performed 25 retractions with a sideload of between 223 and 334 N without lubrication. Flight assemblies which could not be reworked to the new design became non-flight items and were used to gain confidence in the prediction between sideload capability and retraction force.

The 65 N spring test was now also used to monitor the processes early in the assembly of all flight pins. There was now the capability to determine if the assembly would pass at least three months before actual acceptance and which of the processes, if any, were degrading the predicted performance.

Second Restart of Production

Taper pins in the already built assemblies were then machined to the new dimensions and re-lubricated.   Manufacturing of the new design commenced. Two of the first batch of six newly designed assemblies failed the 65 N retraction force test after the abrasive honing operation. The repeat of the Dye Test showed the contacting region of these two pins had been changed since the honing process. An investigation into the process was then conducted. It was found that all of the pins were processed using a bi-directional flow honing machine which pumped media through the part in the forward direction at 4.83e6 N/m^2. The stress prediction for forward flow at nominal processing pressure of 4.83e6 N/m^2 predicted stresses lower then the pins' yield stress. However, the vendors normal processing included both forward and reverse flows; and the machines were designed to automatically reverse once the specified amount of media was pumped through the part. During the processing of the
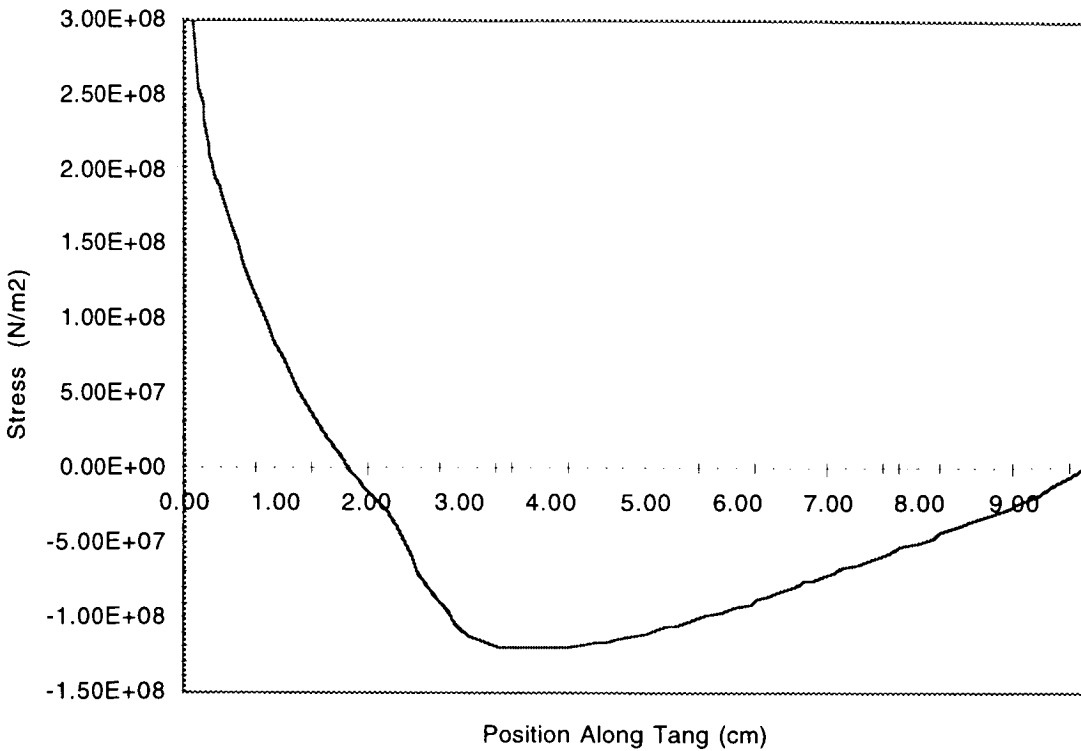
Figure 12. Stress Profile of Expandable Pin Tang during 1.55e6 N/m² Backflow

expandable pins, the machine needed to be manually stopped. If the operator did not stop the machine at the specified amount, the machine automatically reversed and would start pressurizing the exterior of the expandable pin, causing the tines to close off much like a reed valve. Since the media would not be able to reach the inside of the pin, the tines would then deform inwards. Predicted stresses for such a situation are shown in Figure 12. As seen in this figure, yielding is achieved at around 1.55e6 N/m². The result of this deformation was that the contacting region of the assembly moved toward the root of the tine resulting in high retraction forces and lower side load capabilities. This was the reason the two pins failed the 65 N retraction force after the first batch of pins went through the operation after the re-design. As a test of the back flow hypothesis, a scrap pin was processed with two seconds of reverse flow, resulting in the collapse of the pin and subsequent failure of the 65 N retraction force test. The flow honing machine was then modified so the automatic reversal was disabled. This backflow disabling is now a part of the standard operating procedure.

The typical time from beginning of production of a BRS pin assembly to acceptance tests is eight months. Therefore, eight months of manufacturing time plus additional re-engineering time would be lost if a component was to fail and require a complete re-design. However, after the restart of production, the engineers now had two simple non-destructive tests to monitor the predicted performance of the assemblies before and after each process. The 65 N Spring Test and the Dye Test were used as quality

350

assurance to characterize the impacts of each process on the ultimate performance of the pin assemblies. Other processes such as lapping and polishing were also monitored in this fashion. Passage of the 65 N Spring Test three months before the assembly is ready for acceptance tests assures successful acceptance. To this date, none of the nearly 70 pin assemblies built to the new design have failed the 65 N Spring Test. If the flow reversal problem had not been caught until acceptance tests of the first batch, over twenty pins would have to have been scrapped at $7,000 a pin assembly and a six month BRS assembly schedule slip would have impacted end-item hardware delivery.

Qualification Results
The analysis lead to confidence in the design which lead to a more intense qualification program to allow a relaxing of the thermal modeling precision needed to accurately predict the induced sideloads. The qualification was changed to include the baseline plan in addition to many sideloaded retractions at increasing sideloads until the unit failed to retract. The qualification assembly, unit 1034, Figure 13, was selected out of the first batch of 24 assemblies. This qualification unit was selected because it showed the furthest contact point from the tip of all assemblies. Another assembly was selected that showed contact at the tip. This assembly, unit 1028, was run through the complete qualification program to ensure no deformation of the tines would occur if contact was only at the tip of the taper pin. Unit 1034 performed near the predicted sideload capability of 516 N sideload capability, over twice the requirement. The qualification assemblies were disassembled and inspected and showed no signs of damage: the lubrication showed little signs of wear. The wing assembly has since been tested in the thermal vacuum environment with all BRS assemblies performing properly.

Lessons Learned

Several lessons were learned form the successful qualification of the BRS mechanism. First, the performance of a friction based mechanism is very sensitive to dimensional variations along the contacting interfaces of the components. A diameter reduction of 38.1 micrometers on one component in the BRS assembly lead to a more then two fold improvement in performance.

Another result of this high sensitivity is that a large sample size is needed to gain the full cross-section of production performance variation. Three units were constructed during BRS mechanism development, variations in performance were observed but not understood. It was not until the start of production that it became apparent that the development program did not accurately bound the ensuing variations in performance.

Only a complete and accurate model would analytically predict such phenomenon in a friction based mechanism. Once an accurate model is constructed, sensitivity of dimensional variations on performance can be predicted. This leads to a deeper

understanding of the important parameters in the design and the creation of simple tests which can be used to not only predict final performance but also used to monitor manufacturing processes. By understanding important performance variables of the BRS mechanism, requirement compliance was increased from 75% to 100%.

Lastly, processes which are meant to improve performance might actually degrade performance. A simple test which characterizes end performance can be of great value in determining process impacts on a mechanism.

33/2642
Blanket Restraint System
(BRS)
qualification assembly
5843260-506 CCA 21116-1034
02/04/97

Figure 13. Qualification Assembly after Completing Qualification Tests

References

1. Johnson, M., Haugen, B., and G. Anderson. "Space Station Freedom Solar Array Containment Box Mechanisms." *Proceedings of the 28th Aerospace Mechanisms Symposium*, (May 1995), pp.1-16.

Acknowledgments
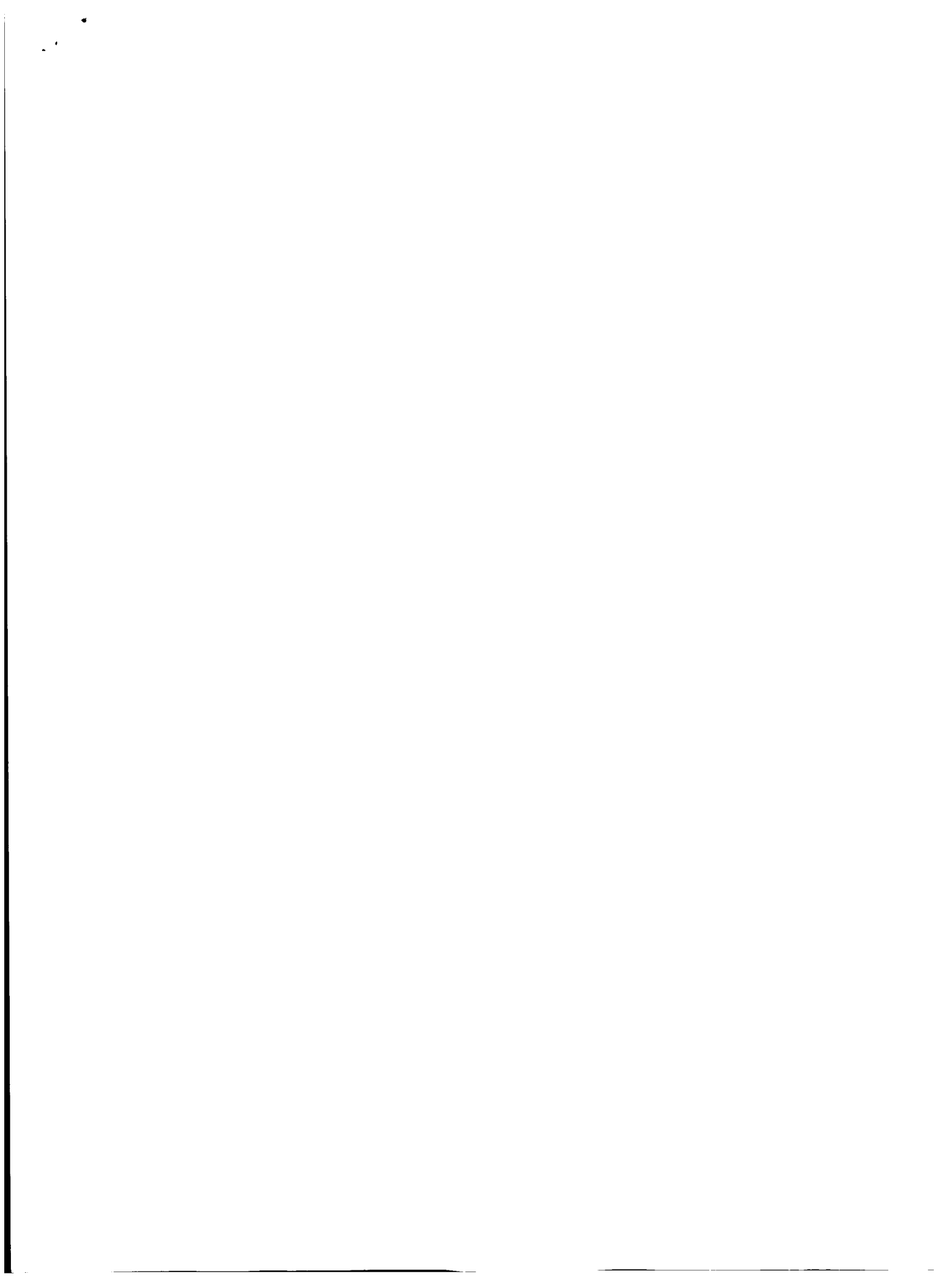
Space Station Remote Manipulator System Qualification Model Joint Test Program

J. Marc Devlin[*]

Abstract

This paper describes the Space Station Remote Manipulator System (SSRMS) Qualification Model Joint Test Program. The SSRMS is provided by the Canadian Space Agency as part of the Space Station Mobile Servicing System. The Qualification Model (QM) Joint is representative of the seven joints that drive the Space Station Remote Manipulator System (Figure 1) providing positioning control and accuracy. The joints are complete electromechanical systems with on-board redundant computers, drive motors, reduction gear systems and a "through-joint" electrical harness which can accommodate joint rotation of ±270 degrees. The QM Joint test program was required to expose the SSRMS joint to a rigorous test program that, when completed, would verify all of the unit design specification requirements and ultimately design certification. Since the QM program was a very large endeavor in scope, this paper tries to cover enough of the interesting and significant events that give a flavor for the whole.

Introduction

The QM Joint test program presented many technical challenges that were magnified by the pressures of schedule and budget. Very specific and unique mechanical and electrical test hardware had to be developed in order to accomplish the various test procedures required. The difficulty of developing specific mechanical test fixtures was compounded by the requirement to use as much of the Engineering Model (EM) hardware as possible to reduce budget, bearing in mind the fact that between engineering model and QM build, the joint interfaces went through a major redesign to accommodate on-orbit maintenance. Incorporated into the test philosophy was the understanding that the QM test program would prove out most of the procedures and associated test script software to be used for Flight Joint acceptance testing. An automated test approach was implemented where possible since 7 flight and 2 spare joints were required for SSRMS. The QM Joint test program was started 13 May 1996 and completed approximately 7 months later on 17 December 1996.

Joint Design Overview

The 7 joints incorporated into the SSRMS have identical designs with the one and the only exception being that the Yaw joint is 13.33 cm. longer than the Roll and Pitch joints.

[*] SPAR Aerospace Limited, Space Systems Division, Brampton, Ontario, Canada
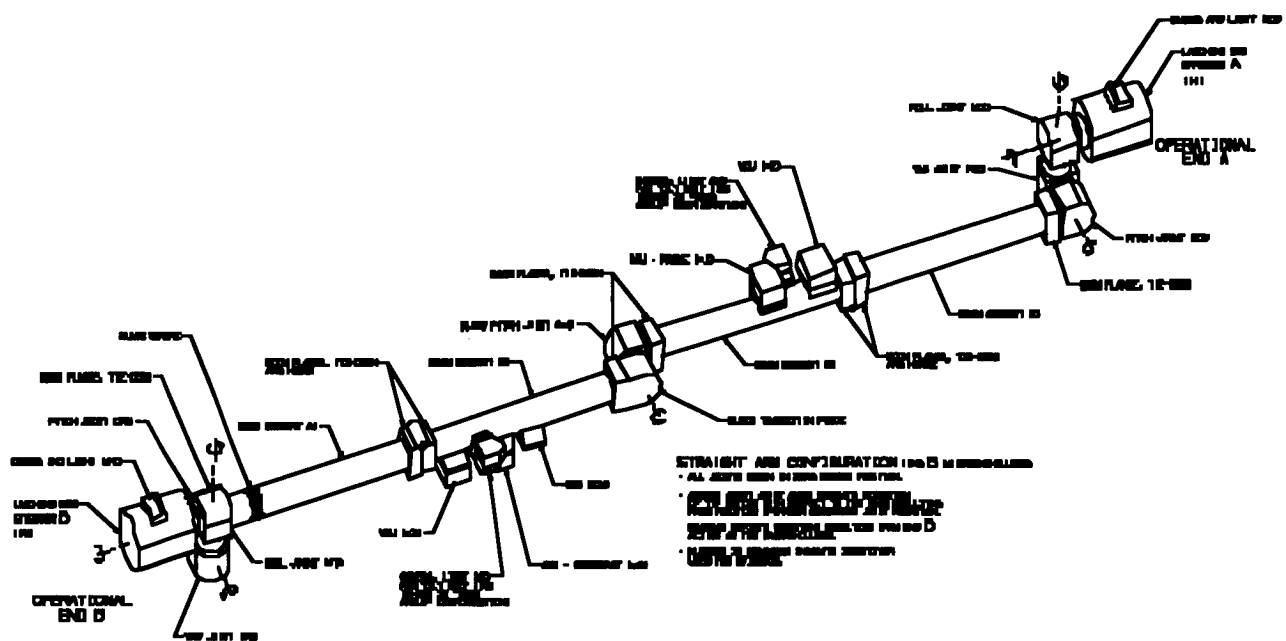
Figure 1. The SSRMS showing the locations of the 7 joints
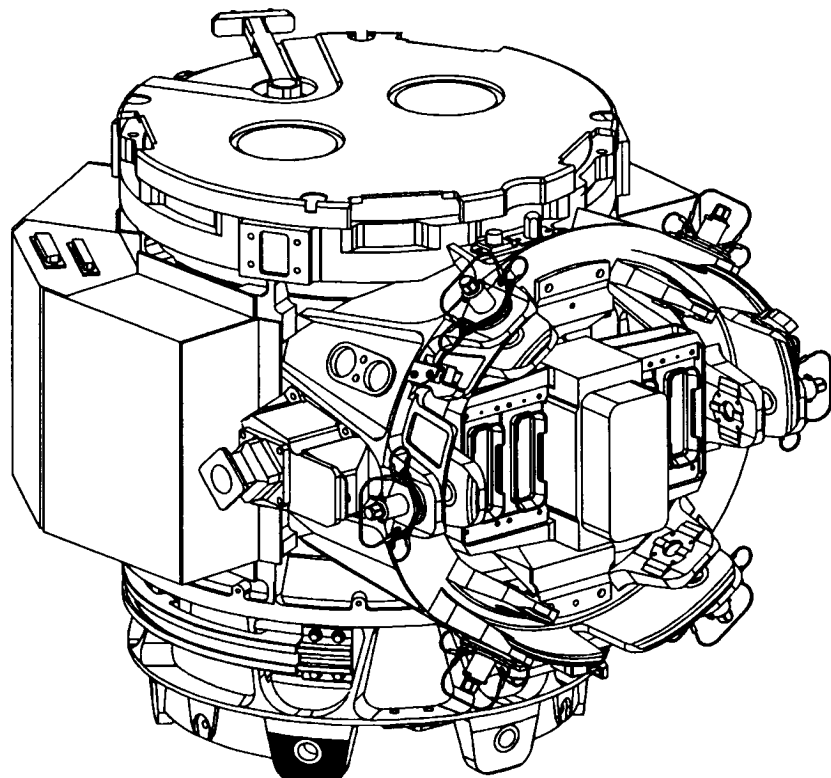
Figure 2. A typical SSRMS roll/pitch joint with thermal protection kit removed.

Each joint has primary and redundant motor modules (JMM) and joint electronic units (JEU). The final joint drive torque of 2545 Nm is achieved with 2 planetary gear systems located in series. Joint torque is transferred through the joint inner housing which rotates within the joint outer housing. A maximum joint rotational capability of ±270 degrees is accomplished with a through joint harness cassette system mounted within the joint inner housing. Joint interfaces are of a 6 bolt lug and clevis design which satisfy the requirement for the joint to be an orbital replaceable unit (ORU). The joint interfaces are at right angles to one another (Figure 2).

Additionally, the joints have a joint angle resolver for joint positioning, retractable mate de-mate system to facilitate ORU changeout, extra vehicular activity (EVA) drive for manual joint rotation, and a joint ambiguity sensor to indicate relative position in the event of a power down.

The Joint Control Software (JCS) resides in the JEU and can be configured to allow the joint to be commanded in Rate Mode, Position Mode, Limp Mode or Vernier Mode. SSRMS payload characteristics are communicated to the JCS by specifying one of several Payload Parameter Sets (PPS).

QM Joint Test Program Overview

The QM joint test program was comprised of the individual test procedures listed and completed in the sequence shown below:
- Initial Joint Checkout Test
- Joint Mechanical Offset Measurement (a JEU downloadable parameter necessary to correlate mechanical "zero" with electrical "zero")
- Joint Ambient Unloaded and Loaded Performance Test
- Joint Baseline Test (a subset of the functional tests used to verify joint performance as required in all of the subsequent test procedures, i.e. between each axis vibration testing)
- Joint QM Vibration Test
- Joint On-Orbit Stiffness and Backlash Test
- Joint EMI/EMC Test
- Joint Thermal Vacuum Test
- Joint Thermal Cycling Test
- Joint Static Launch Load Test

The Initial Checkout Test and the Mechanical Offset Measurement were performed at the Spar manufacturing facility in Ste. Anne de-Bellevue, Quebec prior to shipping the joint to the David Florida Laboratories (DFL) in Ottawa, Ontario to complete the QM joint test program.

The goal of the program was for fully automated testing incorporated into as many of the baseline performance test procedures as possible. In the automated test scenario,

the joint test computer would send the joint a string of commands that were coded into the various test scripts. As the joint performed the commanded task sequence, data from the joint 1553 communication bus, and from the various test rig and environmental test sensors, were collected by the joint test computer in 50 ms frames. The computer then compared the joint performance achieved with the acceptable specification parameters and generated a report indicating either a pass or fail. In the event of a failure, a Discrepancy Notice was raised and a Material Review Board was convened to discuss the problem and plan a course of action.

Baseline performance tests were the tests most desirable to automate since these were repeated many times over the course of the QM joint test program. Baseline performance tests verified that joint performance was acceptable during and after environmental testing and structural loading.

QM Joint Test Rig

The loaded performance tests, on-orbit structural test and static launch load tests were completed with the joint installed on the QM Joint Test Rig (QJTR). The QJTR is a complex high-fidelity test rig designed to test the mechanical characteristics of the joint and has the capability of applying load to the joint and determining the torque generated by the joint. The typical joint set-up on the QMJTR is shown in Figure 3.
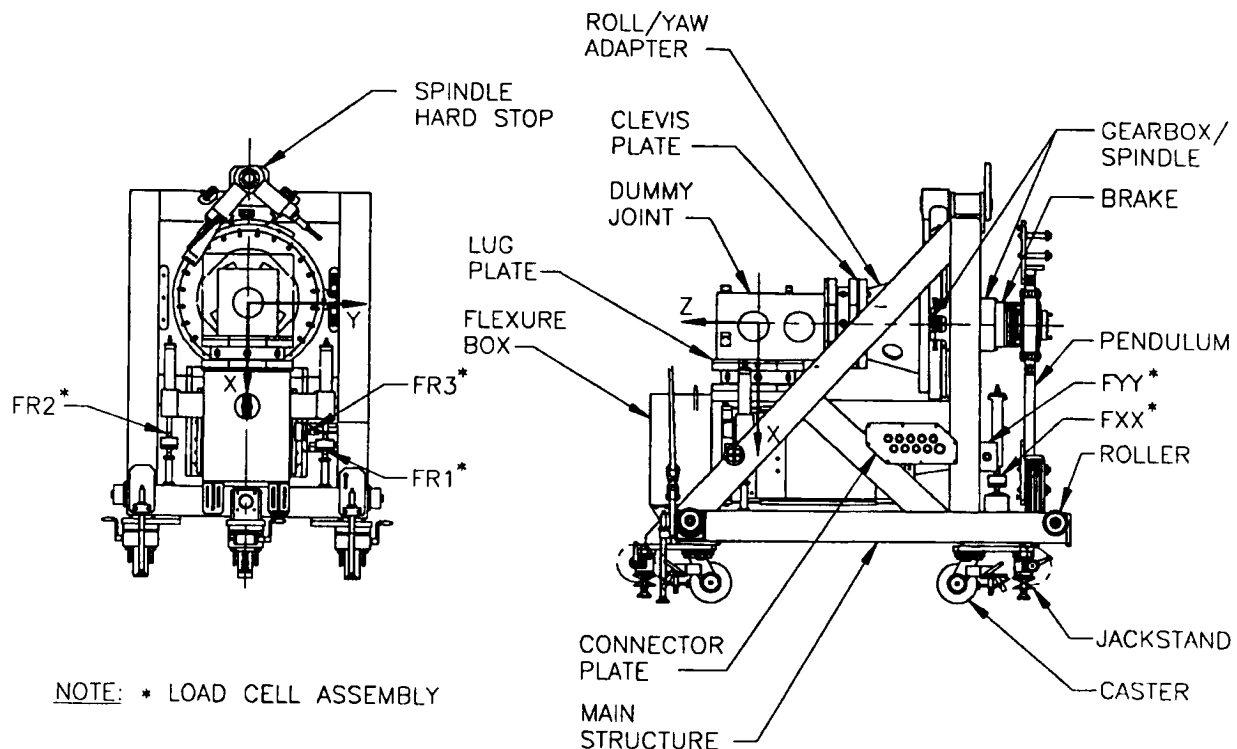

Figure 3.   The typical joint test set-up on the QJTR

The fixed end (clevis) of the joint was attached to the angled support of the QJTR flexure box while the rotating end (lug) was attached to the roll/yaw adapter that was bolted to the face plate of the gearbox/spindle. The rotating end of the joint was thus coupled to the QJTR pendulum through the gearbox. The joint would turn the gearbox (gear ratio of 5.625:1) which raised the pendulum. When the pendulum reached the top of its rotation and began to move down, the joint provided dynamic braking to limit the speed of the pendulum. The QJTR could therefore test four modes of joint operation; torque applied by the joint in the direction of rotation (forward drive), and torque opposite to the direction of joint rotation (backdrive), for both directions of joint rotation.

The QJTR had been originally designed and built to support Engineering Model joint testing. The redesign of the rig to accommodate the QM joint was extensive primarily because of the change to the joint ORU interface geometry. The EM joint ORU interfaces consisted of curvic couplings preloaded by 4 bolts per interface. The change in the joint design to lug and clevis interfaces necessitated major structural changes to the rig to maintain the joint drive axis in line with the rig spindle even though the ORU interface center-line had been moved out by several inches.

Cross-axis bending moments were applied about both of the axes perpendicular to the joint drive axis. These bending moments were applied to the joint to verify structural strength and to verify its ability to rotate under cross-axis moments. Cross-axis moments were applied by manually adjusting screw jacks at the narrow end of the flexure box cone.

Shear forces on the joint were kept below 890 N to simulate on orbit conditions. This was accomplished in the QJTR by incorporating flexures in the flexure box and load cell assembly designs, which permitted limited movement under low load. The flexure box has two pairs of flexures, permitting flexure in the X and Y directions. The flexure box was supported on the main structure by five load cell assemblies, each consisting of a load cell mounted between two flexure bars. These load cell flexure bars permit flexure in the Z direction and accommodate manufacturing tolerances. Cross -axis bending moments and torque output were measured by the load cells which were connected to signal conditioning amplifiers. Resolution of loads was in the range of 100 N (approximately 3.9 % of maximum torque capability).

A fail-safe 24 Vdc spring set brake located on the high speed shaft of the rig spindle /gearbox drive axis was able to stop joint and pendulum rotation at any time. The spindle face plate had a lug locking feature that allowed it to be rigidly locked out for joint stiffness and backlash measurements.

All of the components in the QJTR were thermal vacuum compatible. The main rig structure is of an open nature to maximize the thermal radiation path to the joint from the thermal vacuum chamber shroud and minimize any masking effect excessive structure may have had.

The Pendulum was attached to the high speed shaft and provided an adjustable external bi-directional torque load to the joint. Load adjustments were made by adding or removing stainless steel weights at the end of the pendulum and/or changing from the standard pendulum arm to the mini pendulum arm. The load could be varied up to a maximum of 5670 Nm using combinations of weights and pendulums.

The SSRMS was designed to handle an extremely broad range of inertial loads up to and including the ability to berth the Space Shuttle to the Space Station. It was impractical to expose joints to that extreme level of inertial loading so thorough testing of joint performance with PPS values corresponding to the lower range of inertias were downloaded. Simulations and analysis of the data obtained here was used to verify joint performance for the highest inertial cases.

Significant Enhancements to Specific Test Methodology

Over the course of the test program, sometimes events occurred that would render the existing test procedure unworkable. In these cases, "work arounds" had to be devised that would capture the technical intent of the original procedure yet would result in a minimum cost and schedule impact. Some of the situations in which this sequence of events proved successful are described in this section.

The intent of the QM joint static launch load test was to prove that the joint could withstand loads in each axis of up to 1.4 times the design ultimate loads without a catastrophic failure. Ultimate loads are the maximum loads that the unit has been designed to be exposed to. The original idea for achieving the static load limit in the Z-axis (joint drive axis) was to apply the load to the pendulum of the QJTR by rotating the pendulum screw jack. The resultant load path would be through the joint housing and drive train with the JMM brakes preventing rotation at the opposite or drive end. Unfortunately, the JMM brakes are designed for vacuum and do not provide enough braking torque in an ambient atmospheric environment to react the applied static loads.

The solution was to remove one of the JMM's and replace it with a locking mechanism (Figure 4). This mechanism was inserted into the first stage planetary gearbox polygon interface and could be locked thus pinning this end of the joint drive train. The mechanism could also be released and allowed to run free for a post-static load test functional check of performance in which the joint was powered by the remaining JMM.

The QJTR was designed to operate inside the 2.44m x 2.44m thermal vacuum chamber at DFL. The nature of thermal vacuum testing dictates that a typical test set-up is designed in such a way that all of the testing can be completed without having to

re-open the chamber between tests. If multiple set-ups are required the test becomes prohibitively long and expensive.
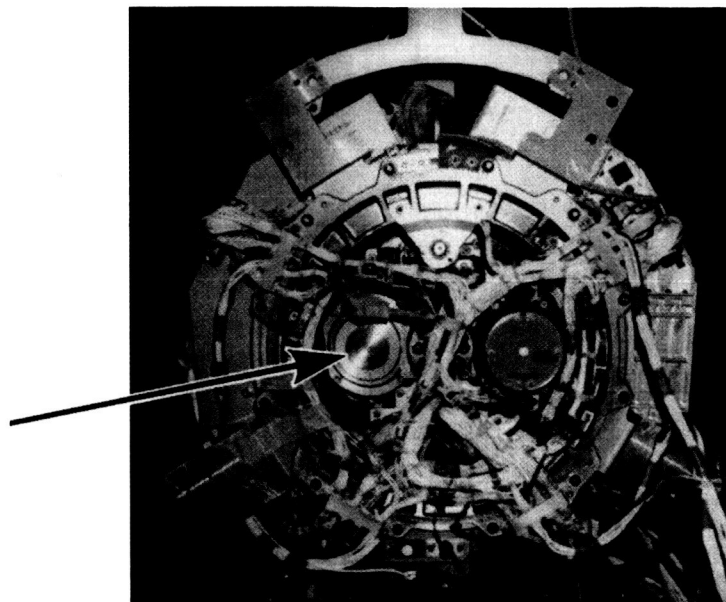

Figure 4. View of the exposed joint fixed end with the rotational locking mechanism installed. The locking mechanism (indicated by arrow) is shown located left of center and the JMM is shown located right of center.

The QM joint baseline set of tests were developed such that all of the joint test parameters could be determined with only one mass loaded onto the QJTR pendulum. This was done to eliminate any need to change set-ups for specific joint test parameters while the joint was in the thermal vacuum chamber (Figure 5). Stopping and starting thermal vacuum testing to change test set-ups would have had a severe impact on the test schedule and would have been a relaxation of the requirement for the test to be continuous in nature.

The test that was made most difficult without the ability to vary pendulum mass was the joint brake upper and lower limit test. The pendulum mass was calculated such that when the pendulum was positioned with its mass parallel to the horizontal, and the QJTR brake released, the joint could rotate downward with gravity defeating the friction brake. If no rotation occurred, then the minimum joint braking lower limit of 1600 Nm had been achieved.

Having calculated the pendulum mass to facilitate a relatively easy determination of the lower brake limit made the upper brake limit inherently more difficult to determine. The downward force provided by the pendulum mass had to be enhanced to allow verification of the minimum upper brake limit of 2600 Nm. Downward force of the mass

was augmented by commanding the JMM to drive the pendulum downward. The amount of current required to drive the JMM with the required amount of force was carefully calculated and then programmed into the JEU as a current limit (1.6 amps). The variables under consideration for this calculation were JMM motor constant at cold and hot QM temperatures, predicted brake friction, and QJTR gearbox inertia.
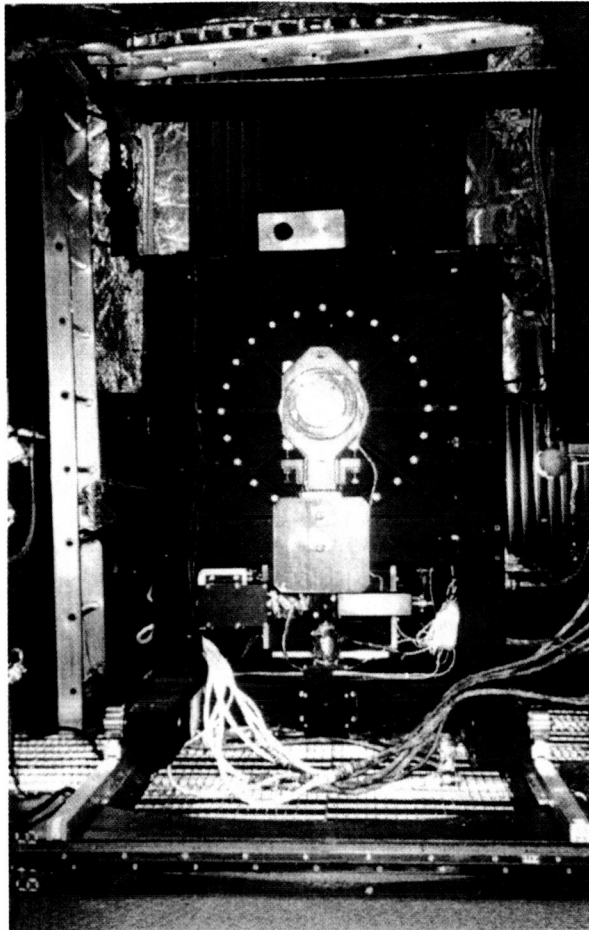

Figure 5.   QJTR installed in the thermal vacuum chamber showing pendulum with mass in vertically down position.

Care had to be taken to predict the right motor current to achieve as close to 2600 Nm as possible. Excessive downward force could have caused a runaway condition damaging the joint. This test was repeated many times under ambient conditions to achieve the right combination of variables to ensure success under thermal vacuum conditions.

An important component of the Baseline tests for the joint was the Limp Mode test. When the joint is in Limp Mode, it must be backdrivable by a force not exceeding 265 Nm. This joint requirement derives from an SSRMS requirement to be able to

362

capture a "free-flyer". This capture operation requires the SSRMS to grapple an approaching free flying satellite (or similar vehicle). During the grapple operation, all of the joints must be capable of being freely backdriven to prevent damage to the arm.

Under ambient conditions, the joint was able to meet the 265 Nm requirement with substantial margin. In the Thermal Vacuum environment, we anticipated the joint to pass, but the relative margin was expected to be much smaller because the backdrivability of the joint is very dependent on temperature, with cold being the worst case. In anticipation of a possible need for extra "thermal control" requirements, the following provisions were made.

Prior to going into the thermal vacuum chamber, the QJTR was fitted with several heating pads fastened to various parts of the rig structure. Thermocouples were located adjacent to each of the heaters so that heater power could be closely monitored and controlled.

In between the Joint and the lug and clevis adapter plates were 0.95 cm sheets of NEMA 12 insulating material. An Infra Red (IR) light bank was suspended over the joint on the rig and targeted at the joint (Figure 6). Additional heaters were located on the joint side of the joint to rig interfaces. The joint was intended to transition temperatures much more rapidly than the large thermal mass of the QJTR. The surrounding shrouds of the thermal vacuum chamber remained at between -60 degrees C and -70 degrades C for the full duration of the thermal vacuum test.
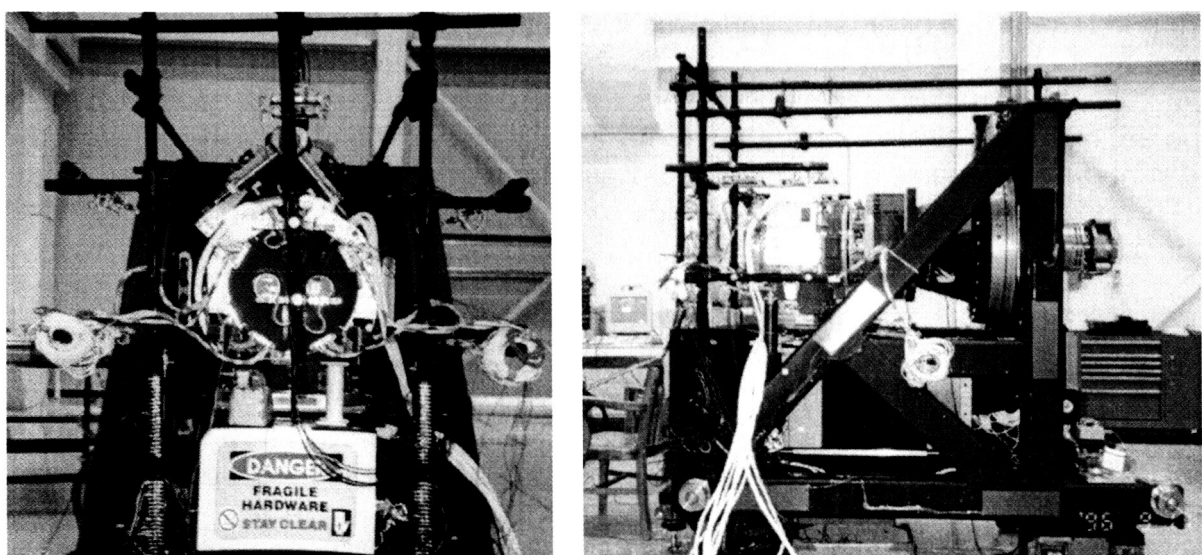

Figure 6. The joint installed on the QJTR prior to being installed in the thermal vacuum chamber. The infra red light bank and additional rig heaters can be seen.

363

When the first Limp Mode test was attempted in thermal vacuum at the cold soak temperature of -36 degrees C, the joint failed yielding a Limp Mode torque of 320 Nm. Upon examining the thermocouple data, it was realized that the temperature delta between the joint and rig at the rig rotating interface was approximately -40 degrees C. This was most probably causing large misalignment loads in the QJTR spindle and gearbox making the Limp Mode results appear much higher than they really were. It was decided that the rig had to be brought up to a temperature approximating that of the joint and the temperature balanced over the entire structure of the rig. The Limp Mode test was repeated with these modifications to the procedure and the joint passed at 250 Nm for all of the subsequent cold and hot cycles.

Qualification of ORU Expandable Diameter Fasteners

The ORU expandable diameter fasteners (EDF) were qualified as part of the QM joint test program. The EDF's are used as the fastener that connects one joint to another at the lug and clevis interface. Each ORU interface consists of 6 EDF's joining the lugs and clevises of the 2 mating joints (Figure 7). The holes in the lug and clevis features of the joint housings that take the EDF's are precisely machined Inconel bushings. The EDF's have the unique capability of being easily removed on- orbit yet provide crucial load and stiffness transfer at the ORU interface points required for SSRMS stiffness and hence tip accuracy.

The EDF's are expanded in the bushing hole by torquing the EVA nut to 40 Nm. A locking pellet within the EDF core pin prevents the EVA nut from backing off after the required torque has been set. Lanyards fasten the EDF to the joint thereby providing a tether feature for on-orbit removal during on-orbit changeout scenarios.

One set of 6 EDF's was designated as the qualification set and they were installed on the joint during assembly. The lug and clevis adapter plates required for use on the QJTR and the vibration fixture functioned as the mating halves of another joint thereby simulating the joint to joint interface.

Each time a series of tests that were part of the QM joint test program were performed and completed, the torque on the EDF's was checked by backing off the EVA nut with a calibrated dial type torque wrench. The torque was then reset for the next set of tests. In this manner the EDF's were exposed to the full QM joint test program.

Analysis of the EDF torque data indicated that the breakout torque was lower than preload torque. Although this was expected the magnitude of the reduction was larger than expected. The EDF's experienced break out torque reduction of approximately 33% to 50% of preload torque. The results were consistent throughout the test program regardless of the environmental nature of the test. No degradation in stiffness, static load or vibration test performance was observed. The post QM

364

vibration low-level sine sweep completed after each axis of joint vibration showed no evidence of reduced EDF stiffness or preload.

Retracted Position

Engaged Position
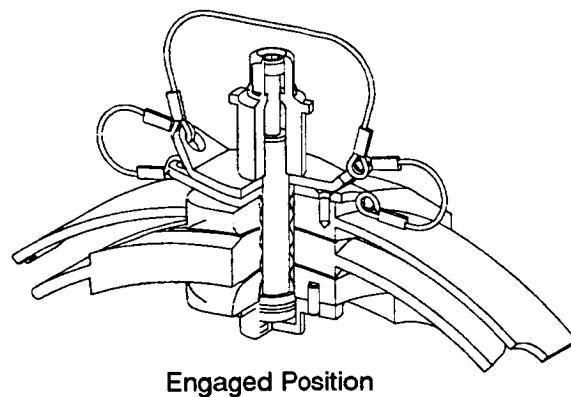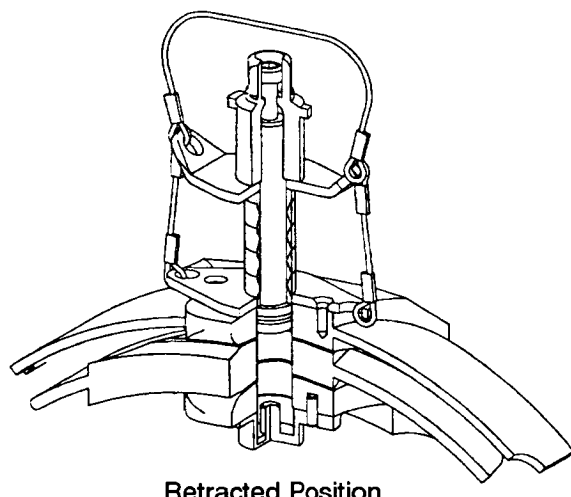
Figure 7. QM joint Expandable Diameter Fastener as installed on joint lug and clevis interface.

The reduced breakout torque of the EDF was considered to be normal behavior and an inherent result of the EDF design. Even non-fight EDF's used for ground support equipment exhibited this behavior when checked.

Conclusions

The QM joint test program proved that the joint met or exceeded all of its performance requirements.

The Static Launch Load test was the final sequence of tests in the QM Joint Test program. Pass/Fail criteria for this test was to demonstrate that no catastrophic failure had occurred as a result of the static loading. The robust nature of the joint design was demonstrated when it was commanded to rotate after the static loads had been applied. The joint moved to the commanded position without displaying any signs of performance degradation.

The automated nature of the test program proved to be a success. Once the test scripts had been debugged, the application of the baseline tests at each of the required intervals shortened overall test duration considerably. The Passing or Failing of a test was determined immediately and time required for interpretation of results was in most cases significantly reduced.

The lessons learned from the QM program were applied directly to the Flight Acceptance test program. Many of the test scripts were transferred directly. Improved Test methodologies that were worked out for the QM program were transferred directly to the FM program.

The breakout torque for the Expandable Diameter Fasteners was 33% to 50% lower than predicted. Although lower than predicted this proved to be normal and an acceptable aspect of the EDF design. In all cases the reduced breakout torque did not reduce stiffness, static load or vibration test performance.

The QM joint test rig functioned as designed enabling the testing of all of the joint design and performance specifications.

References

1. Greenwood, Donald T. "Principles of Dynamics." Prentice-Hall International Series in Dynamics, 1965.
2. Dally, James W. and Riley, William F. "Experimental Stress Analysis." McGraw-Hill Book Company. 1978.
3. Thomson, William T. "Theory of Vibration With Applications." Prentice-Hall Inc.,1981.
4. Oberg, Erik, Jones, Franklin D., Horton, Holbrook L. and Ryffel, Henry H. "Machinery's Handbook." Industrial Press Inc., 1992.

S27-54

168120

Human Habitat Positioning System
for NASA's Space Flight Environmental Simulator

336887

W.F. Caldwell*, J. Tucker**, P. Keas[+]

16 p.

Abstract

Artificial gravity by centrifugation offers an effective countermeasure to the physiologic deconditioning of chronic exposure to microgravity; however, the system requirements of rotational velocity, radius of rotation and resultant centrifugal acceleration require thorough investigation to ascertain the ideal human-use centrifuge configuration. NASA's Space Flight Environmental Simulator (SFES), a 16-meter (52-foot) diameter, animal-use centrifuge, was recently modified to accommodate human occupancy. This paper describes the SFES Human Habitat Positioning System, the mechanism that facilitates radius of rotation variability and alignment of the centrifuge occupants with the artificial gravity vector.

Introduction

"Explore and settle the Solar System, achieve routine Space travel, and enrich life on Earth through people living and working in Space." In its Strategic Plan, NASA resolutely claims that we have a home in outer space; however, the quest to understand how the human body adapts to microgravity environments continues to offer many of the greatest challenges to space exploration.

NASA's Human Exploration and Development of Space (HEDS) Enterprise acknowledges that the key to understanding how humans shall survive in Space, lies in our understanding of *gravity*: "Objective 1: Understand the fundamental role of gravity and the space environment in biological systems."[1] To date, NASA has accumulated over 125,000 hours of manned-space flight.[2,3] Our experience in microgravity has proven that the exposure of the human body to weightlessness will produce significant physiological changes in various systems of the body, including muscle atrophy, bone loss, and vestibular and cardiovascular reactions.

These physiologic alterations have been the focus of numerous research studies. Most methods used to monitor or prevent their occurrence have involved fluid and electrolyte supplements, drugs, physical exercise, and lower body negative pressure.[4-6] These methods, however, have apparently been effective in treating only the symptoms of the physiologic deconditioning. The partial effectiveness of our experiments suggests that the best solution to offset the undesirable effects of a weightless environment is to artificially produce the forces in which the body systems have developed (i.e., produce an artificial gravity).

---
* NASA Ames Research Center, Moffett Field, CA
** Gates/Arrow Distributing, Hayward, CA
[+] Sverdrup Technology, Inc., Moffett Field, CA

The centrifugal acceleration, a_n, developed in the rotating environment of the centrifuge (See Figure 1) generates a centripetal reaction force that, although different in nature, is equivalent to the gravitational force of attraction identified in Newton's Law of Universal Gravitation ($F=Gm_1m_2/r^2$).
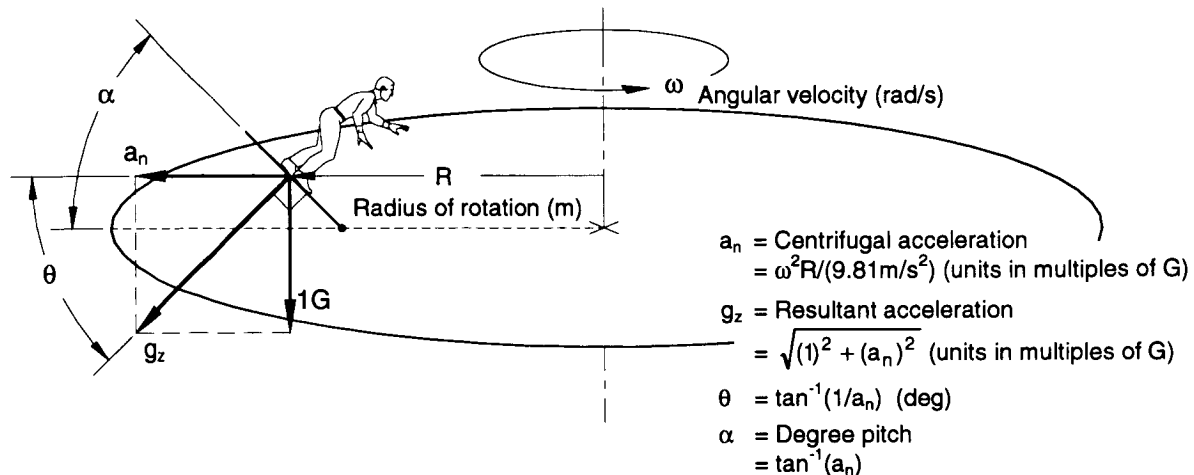

Figure 1. Centrifuge Dynamics of Constant Velocity

For the demands of space exploration, centrifugation offers a viable solution to the problems of physiologic deconditioning that humans experience in microgravity; however, the design of human-rated centrifuges requires careful consideration. Owing to the relatively high costs of developing large structures, a centrifuge of the smallest radius, capable of generating the required accelerations, would most likely be the design of choice. Unfortunately, as the radius of rotation is shortened, the rotational velocity is increased and, consequently, a number of shortcomings are realized, including:

- Increased variance in head-to-toe gravity gradient imposed on centrifuge occupants
- Increased perception of rotating environment on behalf of centrifuge occupants, many times resulting in motion sickness
- Increased influence of coriolis accelerations (change in tangential velocity as a result of change in radius of rotation)

In addition to size considerations, the required magnitude of the resultant acceleration, g_z, of a human-use centrifuge requires thorough investigation. Use of a centrifuge that is capable of an acceleration equal in magnitude to that of Earth-normal gravity (1G) could potentially require extended exposure durations as an effective countermeasure to the effects of a microgravity environment. It has been proposed that the necessary acceleration requirement may have a time-intensity summation effect, and exposures greater than 1G may be useful in shortening the required amount of periodic exposure.[5,7]

368

In order to identify the design parameters of a centrifuge that will provide the most efficient and effective countermeasures to offset, or protect against, the deconditioning of the human body exposed to microgravity, an experimental program needs to be established for the study of human adaptation to artificial gravity. Although there are a number of human-use centrifuges in existence, most are of a gondola-type design, in which a single-person cab is located on a rotating arm of fixed radius. The gondola centrifuges are capable of variable speed, and hence variable acceleration; however, the ideal configuration of a research facility used for artificial gravity experimentation would also incorporate the capability of variable radius of rotation.

The NASA Ames Research Center, of Moffett Field, California, has recently pursued a project to provide such a facility. By upgrading one of its animal-use centrifuges, the 52ft Centrifuge Space Flight Environmental Simulator (SFES), NASA shall provide a human-rated facility to address the questions associated with human adaptation to artificial gravity.

In addition to two newly-constructed Human Habitats, each capable of accommodating a crew of four persons, the upgraded design of the SFES incorporates Human Habitat Positioning Systems to satisfy the requirements of both variable radius of rotation and correct g_z orientation for habitat occupants. The purpose of this paper is to describe the Human Habitat Positioning System, and the design methodology used to satisfy the facility requirements.

SFES Facility Overview

The 52-foot Centrifuge Space Flight Environment Simulator is NASA's largest animal-research centrifuge. The facility has provided over 35,000 hours of operational use since its initial construction in 1966. The simulator's construction basically consists of a hollow rotating cylinder, 16 m (52 ft) in diameter, and 3 m (10 ft) in ceiling height. Figure 2 depicts the original construction of the SFES. The entire rotating system is structurally tied to its central spindle, which is supported by two 61-centimeter (24-inch) diameter tapered-roller bearings. Rotation of the SFES is accomplished via a 56-kilowatt (75-horsepower) DC motor, engaged to the outer perimeter of the Main Platform, providing simulator rotational velocities of up to 2.1 rad/s (20 rpm).

The original SFES configuration incorporated ten radially-aligned tracks, each supporting one or two cages (See Figure 3). Initially designed to support hypergravity related research for such specimens as rodents, rabbits, chickens and dogs,[8] the SFES has recently undergone several modifications to accommodate human occupancy. Integral to the simulator's capability of supporting human subjects, a project was initiated to design, construct and install two Human Habitats (See Figure 4). Each Human Habitat incorporates the use of a Human Habitat Positioning System, the mechanism that facilitates radius of rotation variability and alignment of habitat occupants with the artificial gravity vector, the system of which is the focus of this article.
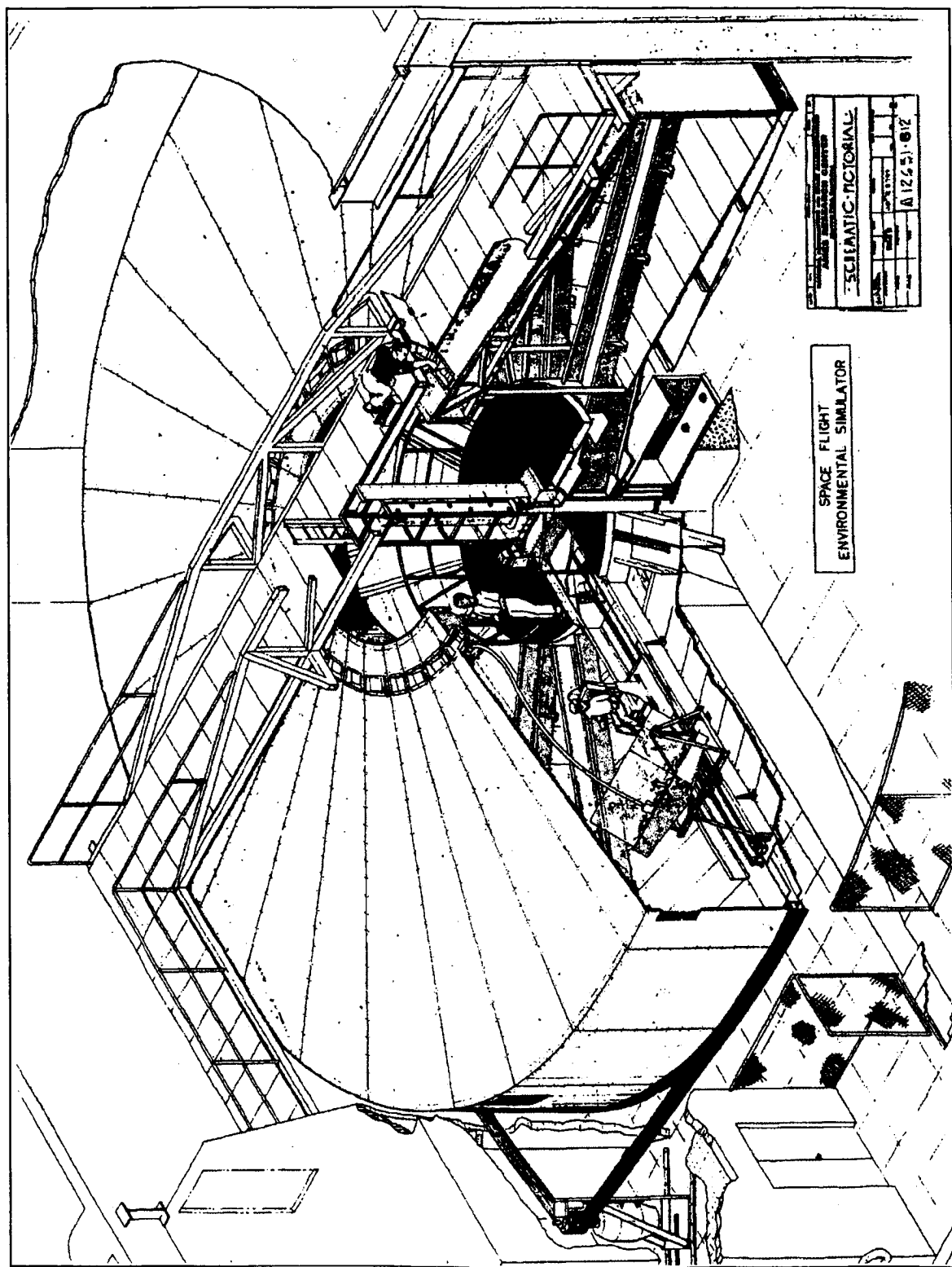
Figure 2. SFES Original Configuration

SPACE FLIGHT
ENVIRONMENTAL SIMULATOR
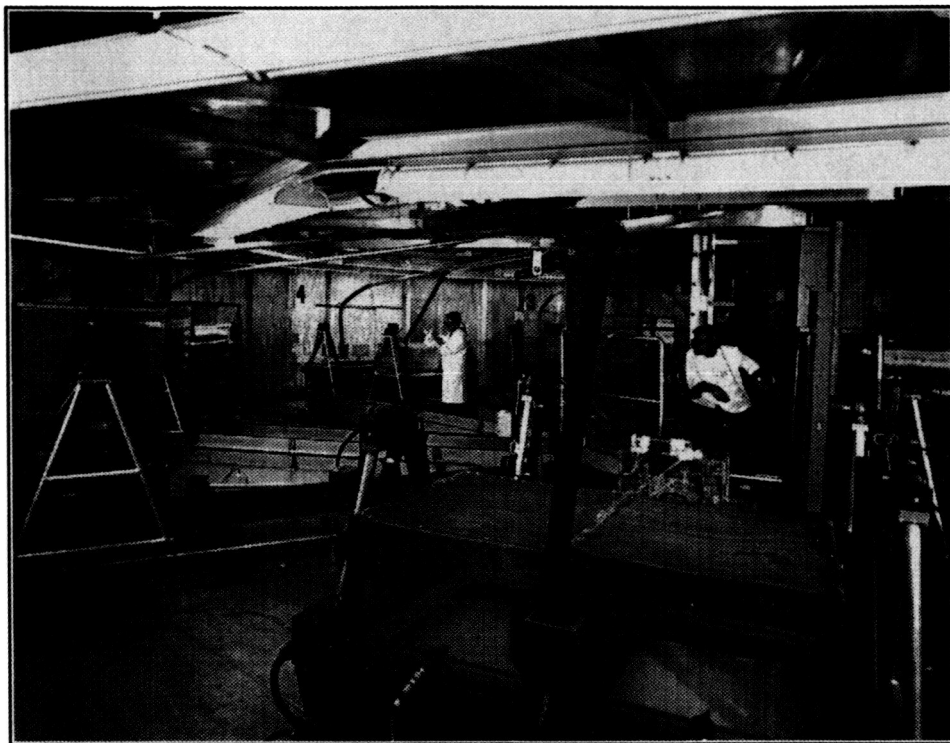
Figure 3. SFES Original On-Board Configuration

2.8 m (9 ft)

7.6 m (25 ft)

3.4 m (11 ft)
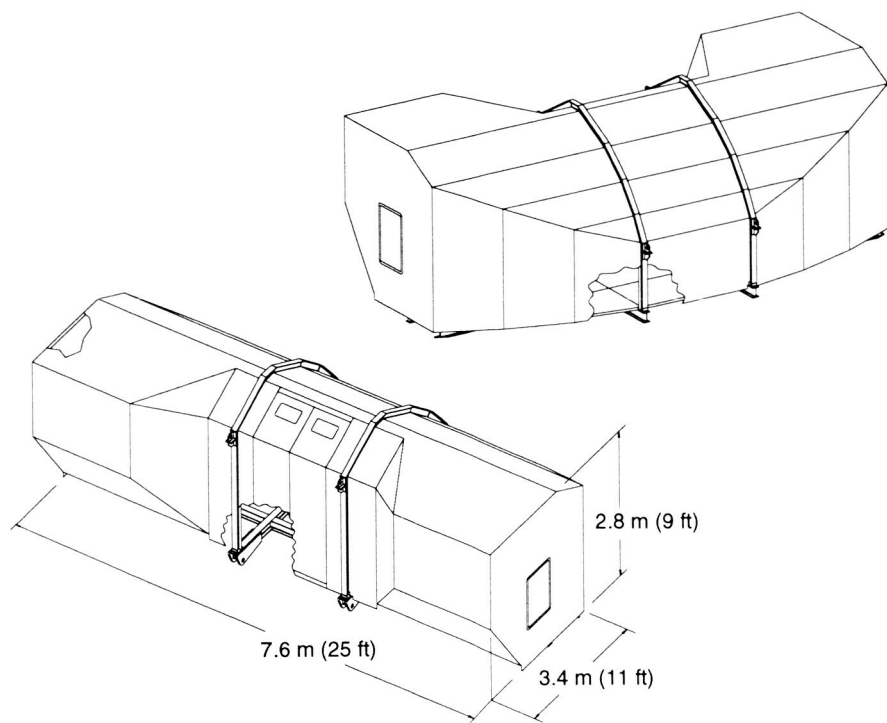
Figure 4. SFES Human Habitat

Human Habitat Positioning System Requirements

In addition to the fundamental need to vary the radius of rotation of the Human Habitat, several functional and design requirements governed the development of the Human Habitat Positioning System. The primary requirements are listed below:

- Support the Human Habitat, with crew of four plus payload hardware
- Package mechanism assembly to maximize range of radial positioning with minimal compromise to Human Habitat design
- Given centrifuge rotational velocity range, provide sustained "g" field environment of 1G to 2G, for periods of up to twelve months
- Incorporate closed-loop attitude control, providing automatic pitch angle adjustment within the range of 0° (1G) to 60° (2G), in response to change in centrifuge rotational velocity
- Integrate with existing simulator, minimizing modifications to centrifuge structure and surrounding facility
- Employ fail-safe mechanisms to reduce risk of hazard

System Description

Relative positioning of each Human Habitat on-board the SFES main platform is accomplished by the Human Habitat Positioning System. Each Human Habitat Positioning System is comprised of a Radial Positioning System and an Attitude Control System. For purposes of describing functional performance, a coordinate system is established for the SFES, as shown in Figure 5.
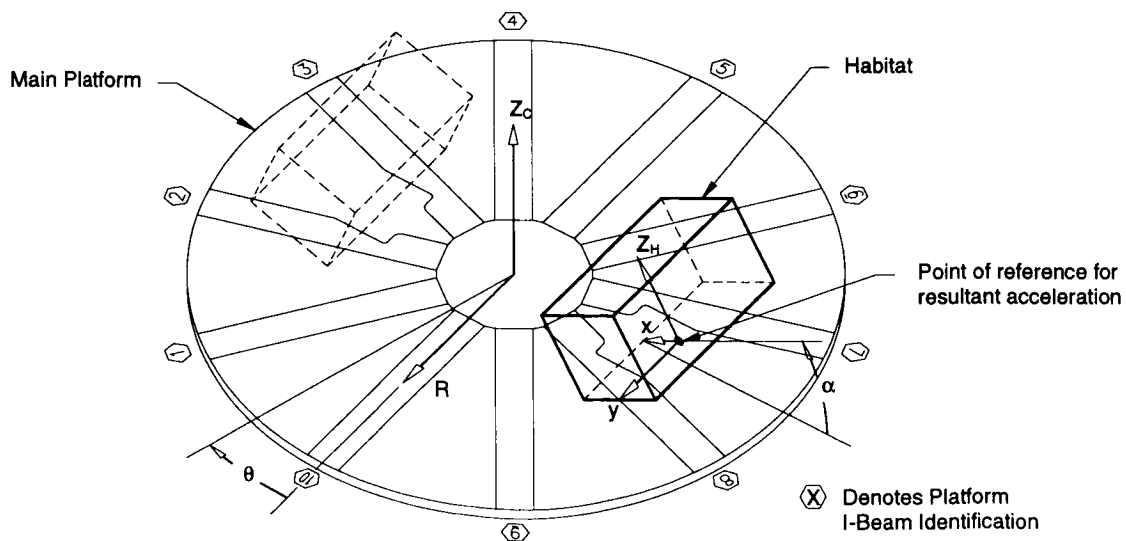

Figure 5. SFES Coordinate System

372

Radial Positioning System

The Radial Positioning System (RPS) facilitates translational positioning of the Human Habitat along the SFES main platform, in the radial direction, R (See Figure 6). Each of the two Human Habitats can be independently positioned within the range 4.6 to 6.4 m (15 to 21 ft), as measured from the centrifuge's axis of rotation to the habitat's interior floor midpoint. The Human Habitat is mounted to a Habitat Carriage Assembly that incorporates linear bearings and tracks, aligned in the R direction. A single 63.5 mm (2 ½ in) diameter acme screw, 5.5 m (18 ft) in length, mounted parallel to the linear bearings, drives the habitat and carriage assembly outward or inward, respectively increasing or decreasing the habitat's radius of rotation. Rotation of the RPS acme screw (i.e., change in habitat radial position) is accomplished via a crank handle fastened to the inboard end. Although the present configuration of the RPS requires manual adjustment of habitat radial position, the design permits future upgrade of motorized control. The low efficiency of the acme screw (i.e., relatively high thread pitch) prohibits back-driving of the system when subjected to centrifugal loads, ensuring a fixed location for each habitat.
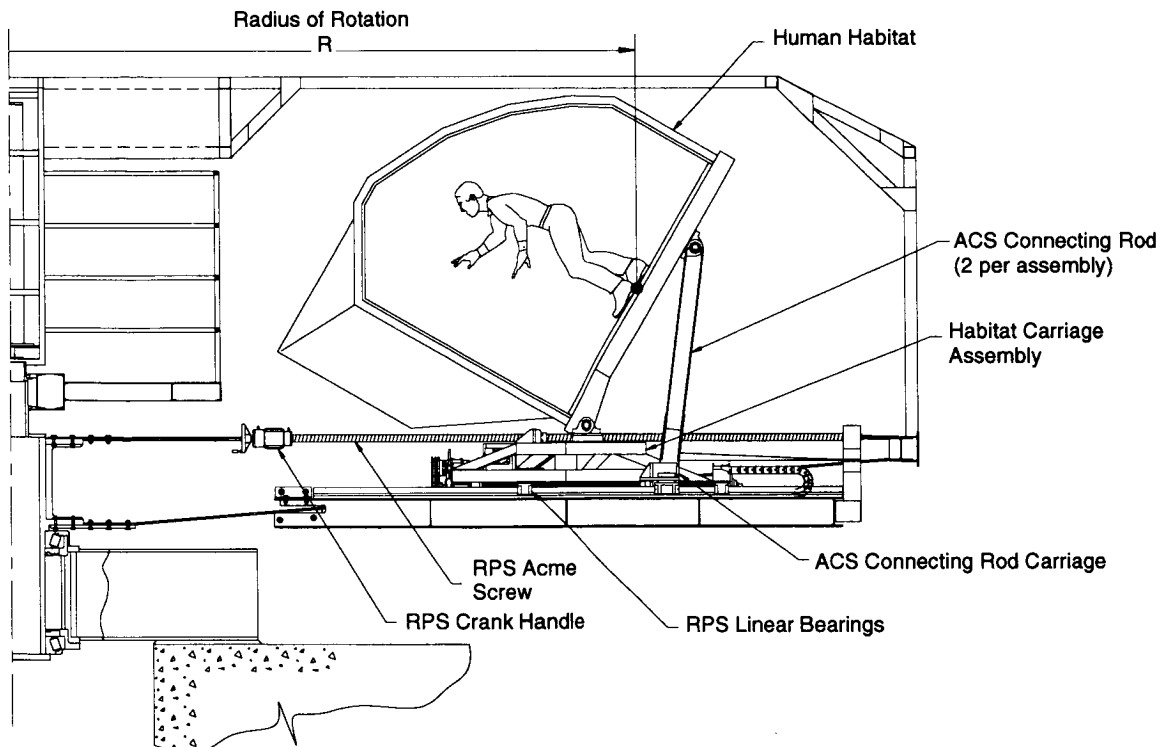
**Figure 6. Human Habitat Positioning System**

Attitude Control System

The purpose of the Human Habitat Attitude Control System (ACS) is to provide the means of pitch adjustment for the Human Habitat, within the range of $0° < \alpha < 60°$. The ACS consists of an assembly of mechanical drive components that emulate a slider-crank mechanism (See Figures 6 and 7). Change in the habitat's pitch angle, α, is

accomplished via rotational motion of the input shaft of the ACS right-angle gear box. Rotational input to the gear box provides rotational motion of two parallel acme screws that drive the Connecting Rod Carriage (i.e., "slider"), radially inward or outward, along the bearing tracks utilized by the RPS. The linear motion of the Connecting Rod Carriage provides either a raising or lowering action of the outboard side of the habitat, with the load transmitted through two Connecting Rods. Change in the Human Habitat pitch is consequently an emanation of the Connecting Rod Carriage motion, where rotation of the habitat occurs about the hinged connection of its lower, inboard edge to the Habitat Carriage Assembly.

Closed-loop control of the ACS (discussed in detail, below) accommodates automated pitch adjustment of each Human Habitat, as a function of centrifuge speed.
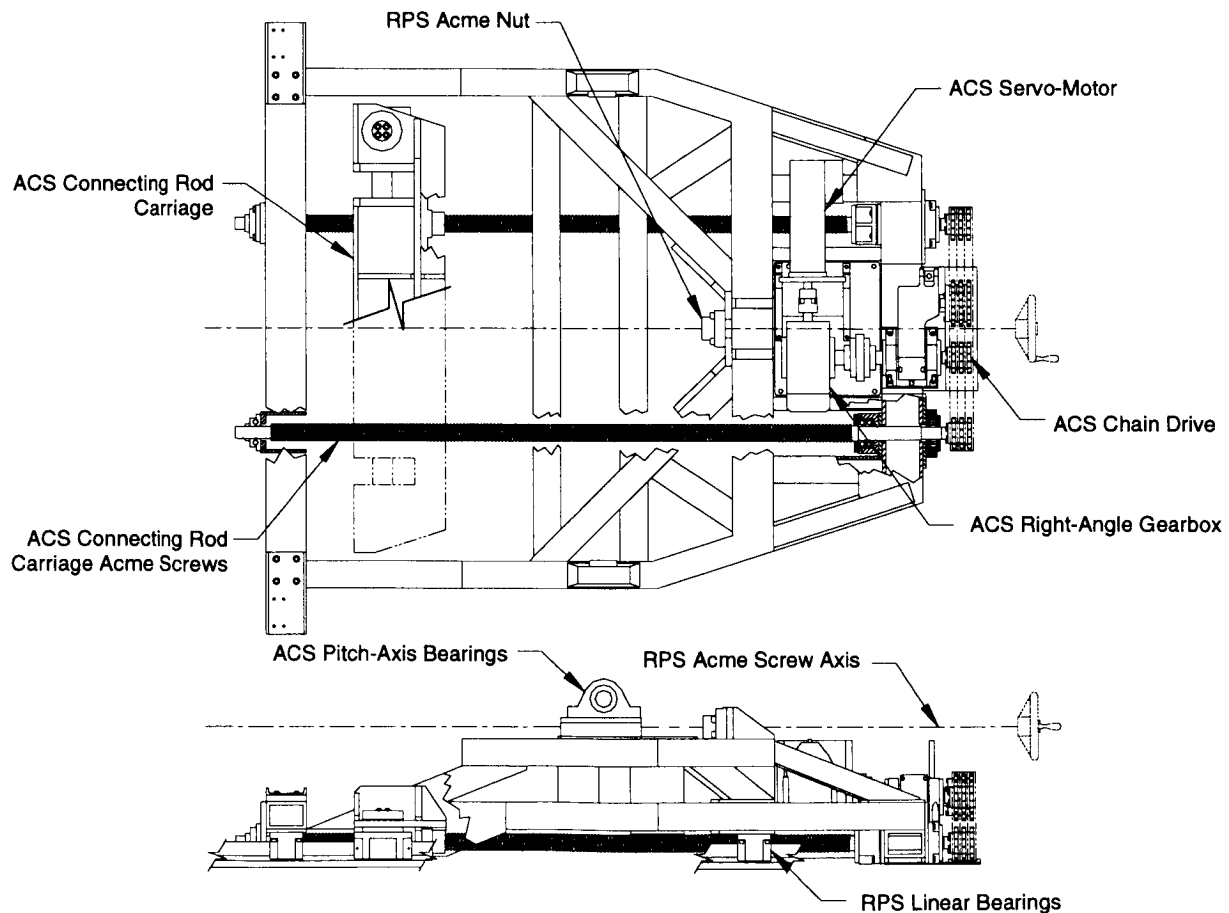

Figure 7. Human Habitat Carriage Assembly

Operation

Typical operation of the Human Habitat Positioning Systems is conducted in the following manner:

1) Obtain desired radial position by manual adjustment of RPS.
2) As the rotational velocity of the SFES changes (e.g., during startup, shutdown, or mid-experiment), the ACS provides automatic adjustment of habitat pitch, to maintain proper orientation of the Human Habitat with respect to the resultant acceleration vector.

Design Considerations

The design of the SFES Human Habitat Positioning System was a process that was mutually dependent upon the design of the other SFES systems. In order to establish compliance with the system requirements, while minimizing structural modifications to the SFES, its design was conducted concurrently with that of the Human Habitat, Main Platform, and the centrifuge roof and wall structures. The top-level design parameters of system mass and selection of mechanism were derived from the system dependencies and design requirements.

System Mass

The maximum permissible mass for the Human Habitat Positioning System was derived from the habitat payload requirement and the minimum factor of safety associated with loading of the SFES Main Platform. In addition to a crew of four persons, each habitat is required to support experiment racks, furniture, appliances and miscellaneous provisions to support human life and hypergravity experiments for periods of extended duration. Using a payload requirement of 15,570 N (3500 lb) and an estimated maximum weight of the Human Habitat, of 11,120 N (2500 lb), a stress analysis of the main platform was performed to back-calculate the maximum permissible weight of the Human Habitat Positioning System. Using combined accelerations of centrifugal loading, potential seismic activity (per the Uniform Building Code[9]), and Earth's 1G, a weight budget for each Human Habitat Positioning System was established as 15,570 N (3500 lb), with 4450 N (1000 lb) allocated to the RPS and 11,120 N (2500 lb) allocated to the ACS. Compliance to the weight budget satisfies factor of safety design requirements of 3.0 on Yield Stress and 4.0 on Ultimate Tensile Stress, while maintaining a slight margin for potential needs of increased mass.

Mechanism Selection

As is the condition of most gondola-type centrifuges, the SFES was designed to provide an artificial gravity of vector orientation similar to that of Earth-normal gravity (i.e., acting in a head-to-toe direction for an upright individual). The rotating environment of a centrifuge produces an artificial gravity of magnitude, g_z, and direction, θ, determined by the vector sum of Earth's 1G and the centrifugal acceleration, as shown in Figure 1. The required pitch, α, of a habitat is established by the need to maintain a perpendicular orientation of g_z with the floor of the habitat. To provide a 2G resultant acceleration for

occupants of the SFES Human Habitat, using the habitat's internal floor midpoint as the point of reference, a pitch angle of $\alpha = 60°$ is required.

Typical design of animal and human centrifuges incorporate passive means of accomplishing the required attitude, where the cab or habitat subjected to the combined accelerations is allowed to rotate freely about the y-axis. The resulting pitch angle is developed as a function of centrifugal acceleration and the relative location of the payload center of gravity, with respect to the axis of pitch rotation. The occupants of the SFES Human Habitat will be allowed to freely move about their living space. In addition, on-board equipment and provisions could be moved about. Consequently, a shift in the relative location of the Human Habitat's center of gravity will most likely occur. Therefore, an active (i.e., mechanically controlled) system was identified as the required means of pitch control. An active Attitude Control System permits user-selected pitch orientation of the habitat, independent of center of gravity location, and provides a stable platform for occupants to conduct normal activities, eliminating undesirable affects, such as motion sickness, associated with the rocking motion of a gimbaled habitat.

A slider-crank mechanism was selected as the means of accomplishing the required attitude adjustment of the SFES Human Habitat. In addition to satisfying the required $0° < \alpha < 60°$ pitch adjustment capability, the slider-crank mechanism offers an operating envelope that does not impair range of radial motion of the Human Habitats. As shown in Figure 8, the full ranges of both pitch adjustment and radial positioning are accommodated with minimal modification to the SFES roof and wall structure. The incorporation of acme screws in the mechanism design provides positive locking of habitat attitude, and prevents back-driving of the system.

Automation of the ACS is accomplished by a DC brushless servo-motor and drive, Compumotor series Z930. The system utilizes closed-loop control to zero-regulate the lateral acceleration imparted on the Human Habitat by a change in SFES angular velocity. A linear accelerometer is mounted to the underside of the habitat floor, directly beneath the floor midpoint, aligned with the habitat's x-axis. As a change in SFES angular velocity occurs, the resulting +/- voltage signal of the accelerometer invokes a command to the servo-motor. The servo-motor subsequently generates either a clockwise or counter-clockwise rotational motion to the input shaft of the ACS gearbox, with direction dependent upon polarity of the accelerometer signal, ultimately increasing or decreasing the Human Habitat's pitch angle, until the accelerometer signal (i.e., lateral acceleration) is nullified. The vector of the resultant acceleration, as experienced by the occupants of the habitat, is thereby held normal to the habitat floor.

The ACS permits a controlled offset of the resultant acceleration. The human occupant standing directly above the G-level point of reference experiences a head-to-toe gravity gradient of magnitude ratios as high as 1:1.3. For example, a 1.8-meter (6-foot) individual standing upright within a Human Habitat positioned at a radius of rotation, R = 4.6 m (15 ft), may experience a 2G resultant acting at his or her feet, while

376

R = 4.6 m (15 ft)

R = 4.6 m (15 ft)

R = 6.4 m (21 ft)

R = 6.4 m (21 ft)

1G Configuration ($\alpha = 0°$)

2G Configuration ($\alpha = 60°$)
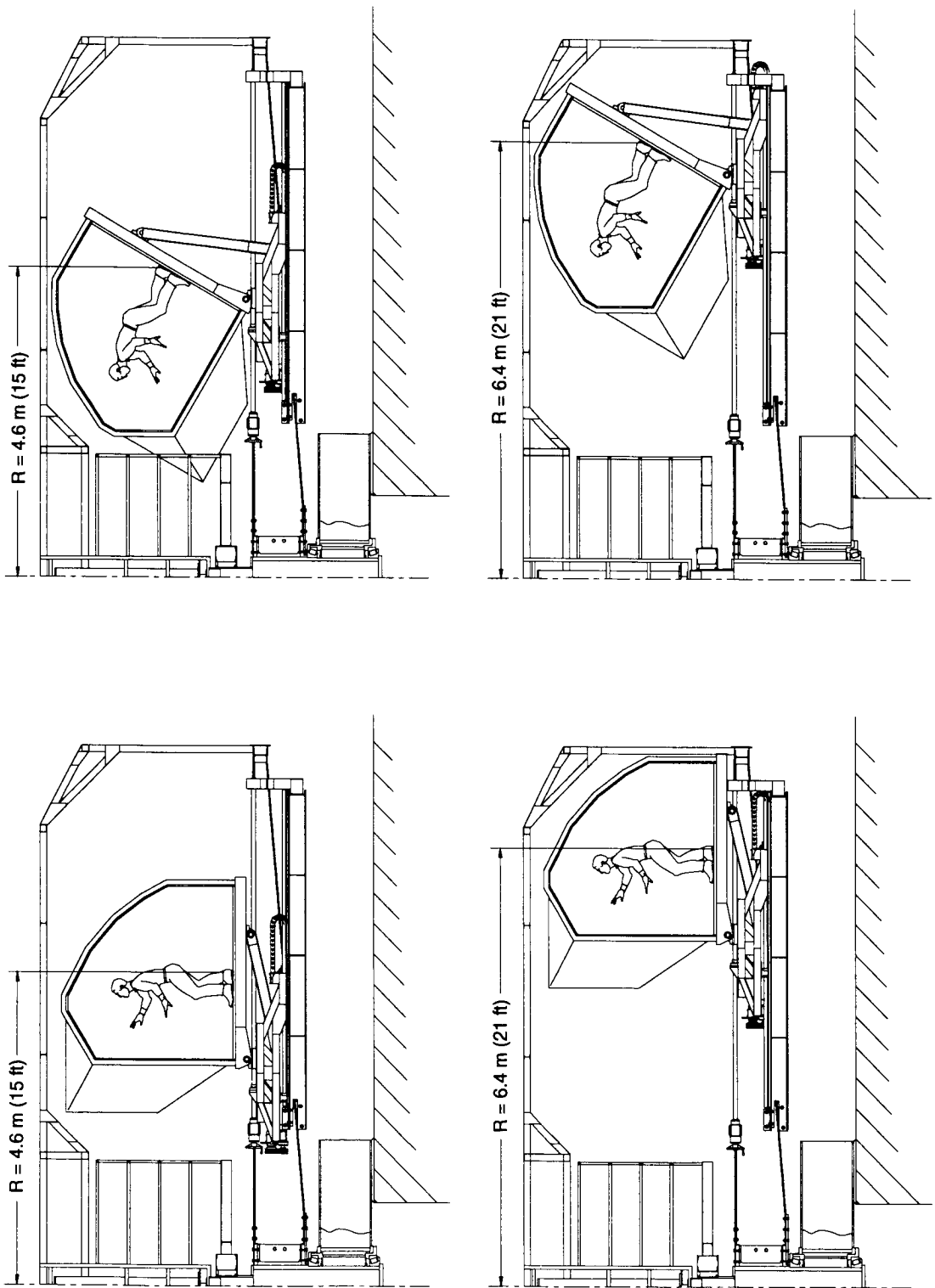
Figure 8. Human Habitat Positioning System Operational Envelope

377

simultaneously experiencing a 1.5G resultant (of different vector orientation) acting at his or her head. The offset function of the ACS provides a G-regulated pitch adjustment of the Human Habitat, for controlled placement of the point of reference of the resultant acceleration.

The design of the Attitude Control System permits manual jog tilt control, indication of habitat inclination angle, habitat normal and lateral acceleration indication, tilt range limits, lateral acceleration limits and a redundant control scheme.

Mechanism Analysis and Modeling

Upon selection of a slider-crank mechanism as the means of attitude control, and as the system design achieved a maturity in which a general layout could be established, a detailed kinematic analysis was performed. The analysis was used to evaluate dynamic loads and power requirements, and proved to be a valuable tool in the iterative design process of the ACS.

The modeled representation of the Attitude Control System is shown in Figure 9. The primary components are modeled in a manner that accounted for inertial, gravitational, and centrifugal loads. The corresponding mechanism loop equation for the model is:

$$B - Di - He^{i\phi} + Ce^{i\theta} = 0 \qquad\qquad (1)$$

where real and imaginary components define geometrical relationships for the local cartesian system of coordinates. The equation is differentiated with respect to time to generate velocity and acceleration relationships.

A FORTRAN code was developed to evaluate reaction loads between the mechanism components, at incremental time steps. Variable input parameters for the code included length and weight of primary components, centrifuge angular acceleration, and component radial position (determined as a function of habitat R and α). Using a desired minimum duration of 120 seconds for the SFES to obtain the required rotational velocity for a 2G resultant acceleration, output data was generated to predict servo-motor requirements. As observed in the sample output charts of Figure 10 (sample data from 1G to 2G startup at R = 6.4m), the modeled analysis predicts the following minimum performance requirements for the attitude positioning servo-motor:

> Minimum Torque Capacity: 275 N•m (203 ft•lb)
> Minimum Speed Capacity: 21 rad/s (200 rpm)
> Minimum Power Capacity: 2.0 kW (2.7 hp)

The ACS design enables pitch adjustment with a high-torque, low-speed demand for start-up configuration, and, conversely, a low-torque, high-speed demand for final positioning. Consequently, pitch adjustment is accomplished with relatively smooth and

378

Human Habitat

Connecting Rod

CG_H

Z_H

x

α

θ

CG_{CC}

Z_C

ϕ

R

D

CG_{HHC}

CG_{CRC}

Habitat Carriage Assembly

B

Connecting Rod Carriage

MECHANISM ASSEMBLY

R_H

a_{2X}

F_{2A}

P_{2A}

a_{2Y}

a_n

1G

P_{3A}

F_{3A}

R_{CR}

a_{3X}

a_{3Y}

a_n

1G

C

C_X

θ

F_{3B}

F_{2C}

ϕ

H_X

H_Y

P_{2C}

H

P_{3B}

HABITAT

CONNECTING ROD

F_{1C}

R_{HC}

P_{1C}

P_{ACME1}

Y_{ACME}

a_n

Y_C

Y_{CG}

1G

N_{BRG1}

X_{CG}

N_{BRG2}

X_C

X_{BRG}

R_{CRC}

θ

P_{3B}

F_{3B}

a_n, P_{ACME2}

1G, $-N_{BRG3}$

CONNECTING ROD
CARRIAGE

HABITAT CARRIAGE
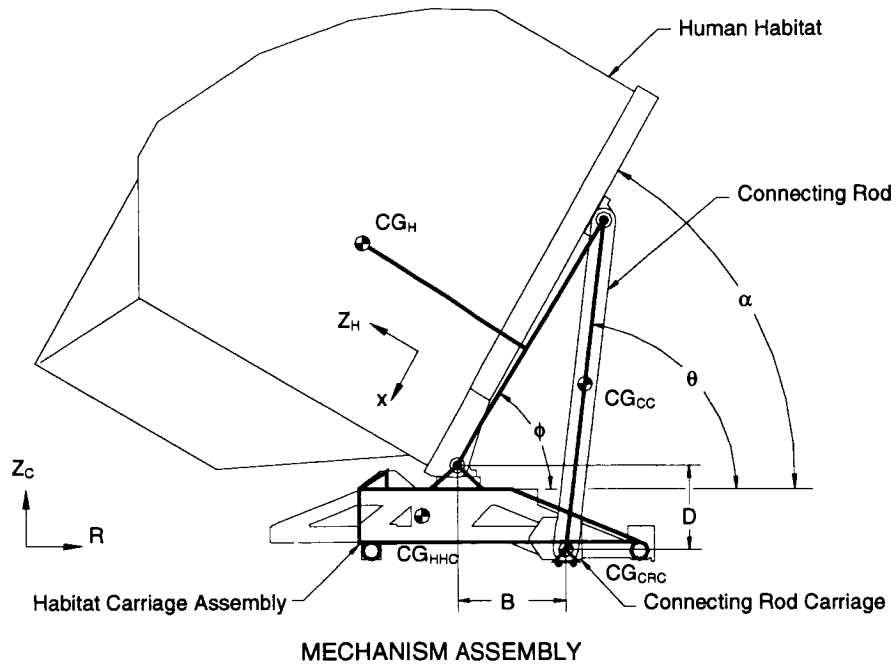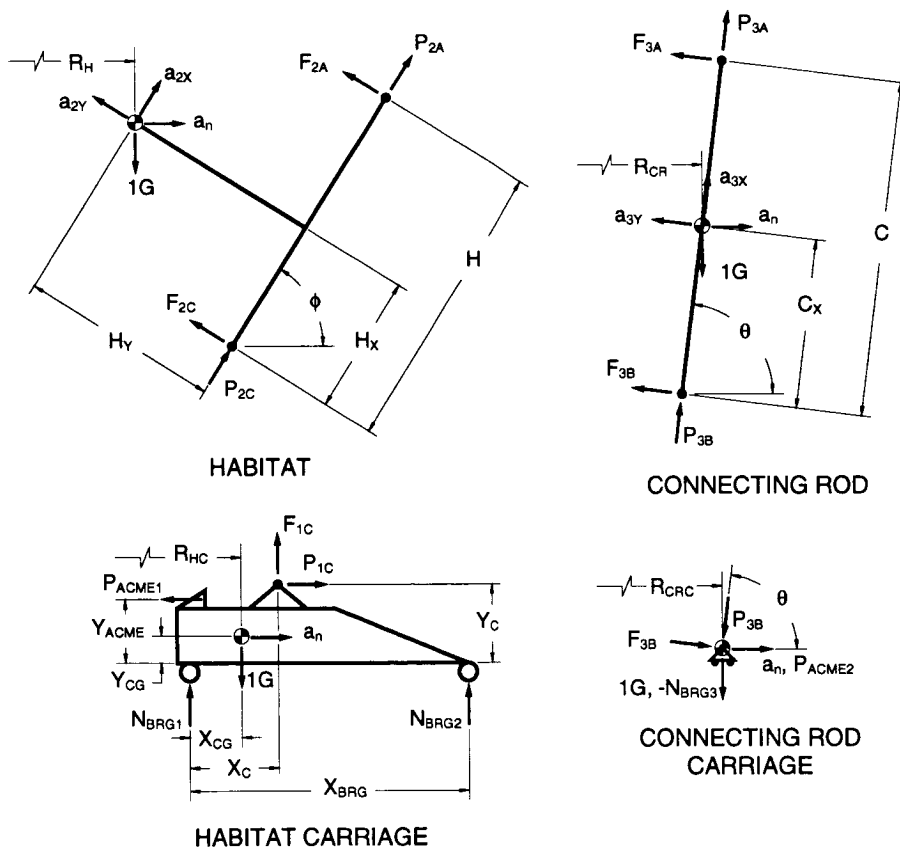
Figure 9. ACS Mechanism Model
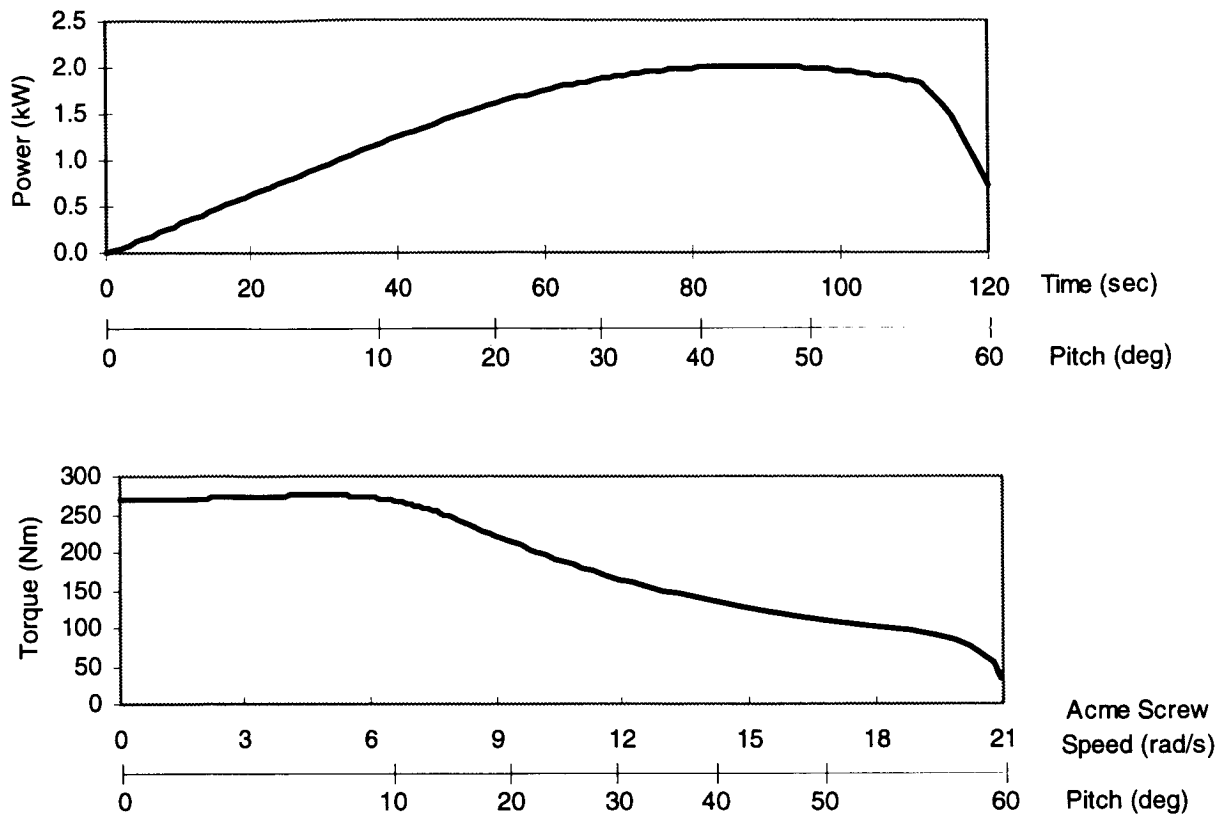
**Figure 10. Kinematic Analysis of ACS
Start-up at R = 6.4 m for 2G Resultant**

uniform power demands. Combined with the non-linear function of applied load (i.e., centrifugal acceleration), the maximum power required by the ACS is computed to occur approximately mid-span of the 0° to 60° adjustment; more precisely, at $\alpha = 42°$. In addition to predicting performance requirements for the attitude positioning motor, the output data was reviewed for worst case profiles (i.e., maximum loading) for subsequent stress analysis of the positioning system components.

Project Status

As principal investigator requirements help determine interior design and layout of Human Habitats, the SFES facility is presently undergoing its first phase of operational testing. Facing an initial need to support animal hypergravity experiments, tests are conducted with the Human Habitats arranged in an empty, stowed configuration. The primary objectives of the initial phase of testing is to verify the structural integrity of the redesigned SFES and assess tuning requirements and performance verification of the SFES Main Drive System. Upon completion of the upcoming animal hypergravity experiments, the human-rating certification process of the SFES shall commence.

380

Conclusion

The modified SFES is soon to embark on its initial phases of qualification and acceptance testing for human occupancy. Experiment proposals are currently being solicited, as researchers eagerly await the ribbon-cutting of this "new" facility.

The incorporation of the Human Habitats, and the innovative design of the Human Habitat Positioning Systems, help fortify the Space Fight Environmental Simulator's position among the world's unique research facilities. By complimenting the facility's capability of variable rotational velocity (hence, variable resultant g_z acceleration), with the functionality of variable radius of rotation and controlled g_z alignment, the Human Habitat Positioning System shall provide the scientific community the ideal tool for artificial gravity research. With design and construction totaling a fraction of the cost of developing a completely new facility, the modified SFES can help provide only a positive return on investment into future space exploration programs.

References

1. NASA Human Exploration and Development of Space (HEDS) Enterprise Mission Statement, NASA Strategic Plan, 1996.

2. NASA Historical Data Book, NASA SP-4012, 1988.

3. NASA Public Affairs Office, Space Shuttle Mission Chronology, 1997.

4. Miquel, J., and Souza, K.A., "An Overview of Gravitational Physiology," NASA TM-102849, 1991.

5. Burton, R.R., "A Human-Use Centrifuge for Space Stations: Proposed Ground-Based Studies," Aviation, Space, and Environmental Medicine, 1988, 579-582.

6. Cardus, D., Diamandis, P., McTaggart, W.G., and Campbell, S., "Development of an Artificial Gravity Sleeper (AGS)," Physiologist, Supplement, ISSN 0031-9376, 1990, vol 33, S-112, S-113.

7. Burton, R.R., and Meeker, L.J., "Physiologic validation of a Short-Arm Centrifuge for Space Application," Aviation, Space, and Environmental Medicine, 1992, 476-481.

8. Oyama, J., "Response and Adaptation of Beagle Dogs to Hypergravity," Life Sciences and Space Research XIII; Proceedings of the Seventeenth Plenary Meeting, 1975

9. Uniform Building Code, International Conference of Building Officials, 1994.
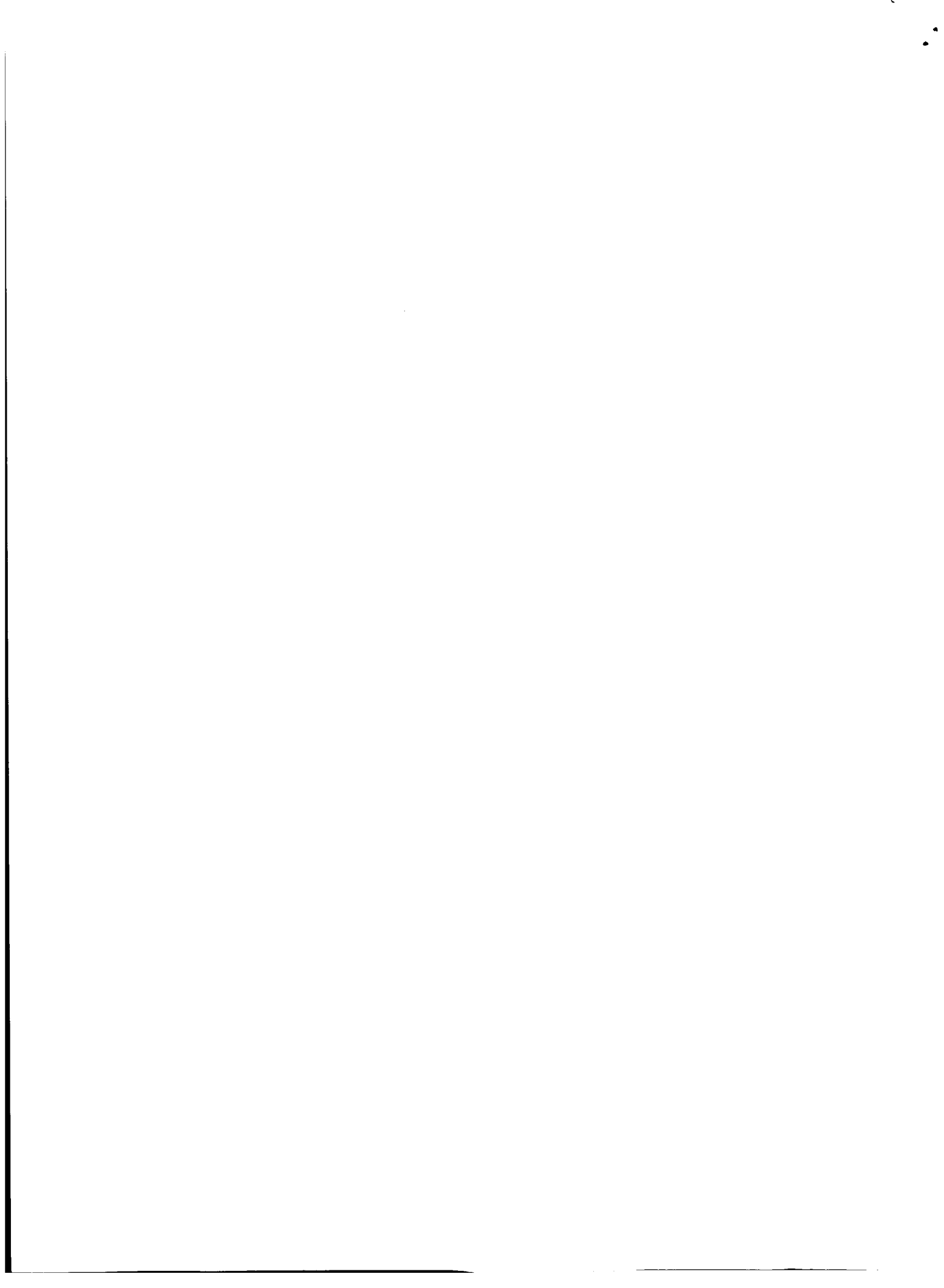
Testing of the Automated Fluid Interface System

A. S. (Nick) Johnston*, Tony R. Tyler*

Abstract

The Automated Fluid Interface System (AFIS) is an advanced development prototype satellite servicer. The device was designed to transfer consumables from one spacecraft to another. An engineering model was built and underwent development testing at Marshall Space Flight Center. While the current AFIS is not suitable for spaceflight, testing and evaluation of the AFIS provided significant experience which would be beneficial in building a flight unit.

Introduction

The Automated Fluid Interface System (AFIS) project was an advanced development program aimed at developing a prototype satellite servicer for future space operations. This mechanism would be capable of transferring propellants, cryogens, fluids, gasses, electrical power, and communications from a tanker unit to the orbiting satellite. The development of this unit was a cooperative effort between Marshall Space Flight Center in Huntsville, Alabama, and Moog, Inc. in East Aurora, New York.

Currently the US does not have an automated capability for consumable transfer on-orbit. This technology would benefit both Space Station and long duration satellites. AFIS is unique in that it provides that capability. An engineering model was built and underwent substantial development testing at Marshall Space Flight Center.

Testing and evaluation of the AFIS provided significant experience which would be beneficial in building a flight unit. This paper presents the results of that testing and subsequent lessons learned. An evaluation of the unit and recommended design improvements are included.

AFIS Description

The AFIS is consists of an active and passive side. The active side is on the tanker and the passive side is on the spacecraft. The face cover of each side is octagon shaped and measures 66.04 cm (26 inches) across the flats. The active side weighs approximately 16.33 kg (36 pounds) and the passive side weighs 7.7 kg (17 pounds) without couplings. Figure 1 shows both sides of the AFIS positioned and ready for engagement. The initial alignment of the two halves is done by the docking mechanism.

Figure 2 depicts an exploded view of the active side of the AFIS. This side contains all components requiring electrical power and/or control and is composed of a chassis

---

* NASA/Marshall Space Flight Center, Huntsville, Alabama

and a carriage assembly. The chassis is hard mounted to the spacecraft structure, provides a structure for the carriage assembly to ride on, and contains a rotating cover which protects the couplings.
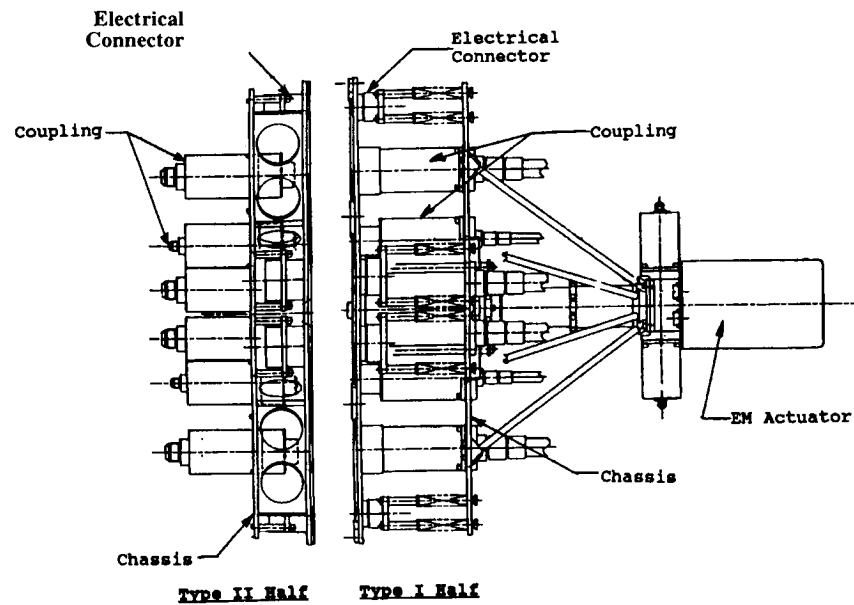

Figure 1: Both AFIS sides (or halves)
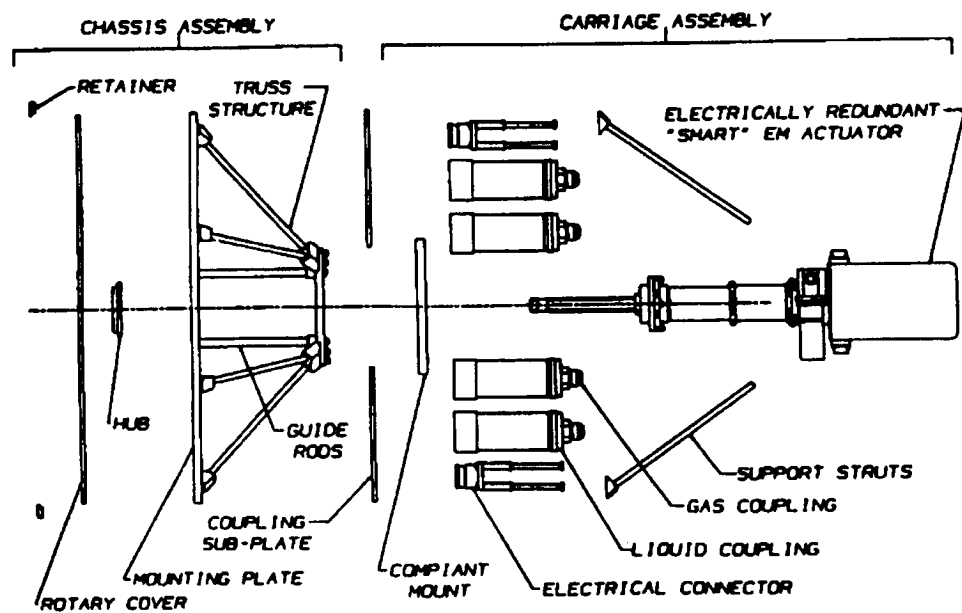
Figure 2: Exploded View of AFIS Type I Half

The carriage assembly also contains the couplings and connectors. This assembly is stiffened by a truss assembly and is compliantly mounted to the chassis assembly. The compliant mounting allows the AFIS to adjust for misalignments resulting from the docking mechanism.

The main component of the carriage assembly is an electromechanical actuator that powers and controls all AFIS functions. This actuator performs the following tasks:

- Rotates covers on both the spacecraft and tanker side.
- Locks/unlocks the two sides together.
- Engages/disengages couplings and connectors.
- Aligns the tanker and spacecraft sides of AFIS.
- Carries the loads from fluid transfer.
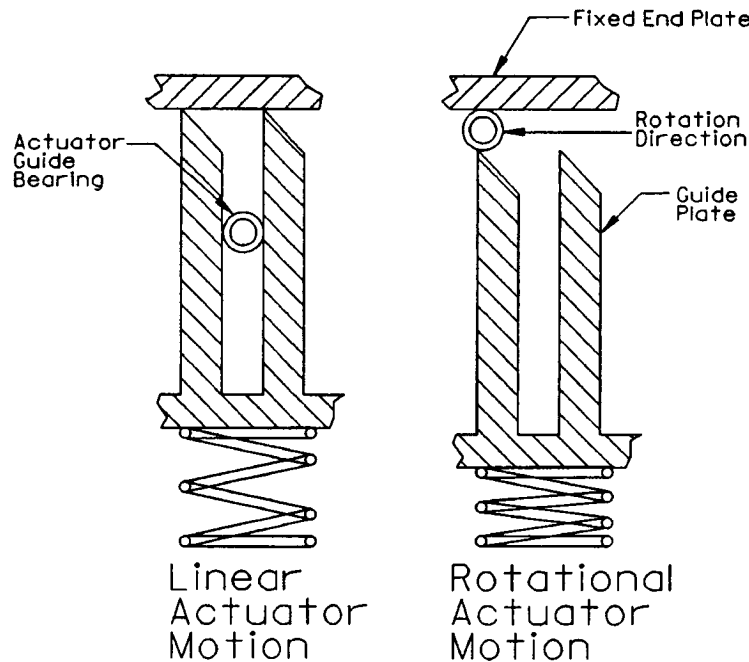
Figure 3: Actuator Rotation Mechanism

The actuator is unique because it provides linear motion and an additional rotary motion at the end of stroke. The actuator drive mechanism is a typical ball screw actuator driven by motors through worm gears. The ball screw is attached to a square rod. The mounting is such that initially the ball screw nut rotates and the ball screw translates linearly with a guide bearing captured in a guide plate slot. Rotation at the end of stroke is illustrated in Figure 3. At the end of travel, the bearing contacts the end plate. Because the bearing can no longer translate linearly, it rotates in a clockwise direction. The bearing forces the retaining guide plate down by means of a sloped surface. The guide bearing can then move to the next slot and the retaining plate returns to its normal position because of the spring. A limit switch stops the

motors and reverses their direction once rotation has occurred. Because the opposing retaining plate surface is not sloped, the bearing must stay in the retaining plate slot for linear translation during actuator retraction. The guide bearing, with square rod, now translates linearly down the guide plate.

The passive side of the AFIS requires no power or control and was designed to be simple and lightweight. Moving parts are limited to a rotating cover which is rotated by the active side.

The operation of the AFIS is controlled by three signals: "Enable", "Engage", and "Disengage". The AFIS has redundant electronics and motors which are selected by choosing different channels. When the AFIS is disengaged, as shown in Figure 4a, the carriage assembly is preloaded against the back of the rotating covers. This allows the floating carriage to withstand the launch vibration loads. When the "engage" command is received by the actuator, a square shaft is extended across the interface as shown in Figure 4b. Once this actuator is fully extended, it protrudes into the square of center hub on the passive side. The actuator then rotates 45 degrees which rotates both covers and locks the two sides together. The two halves are locked together because the 45 degree rotation now allows the corners of the actuator rod tip to contact against the center hub. The actuator then begins retracting. Because the end of the actuator is now fixed at the center hub, the carriage assembly of the active side (with couplings) begins to move across the interface towards the passive side. The engagement is complete when all couplings are engaged as is shown in Figure 4c. Disengagement is simply the reverse of engagement.
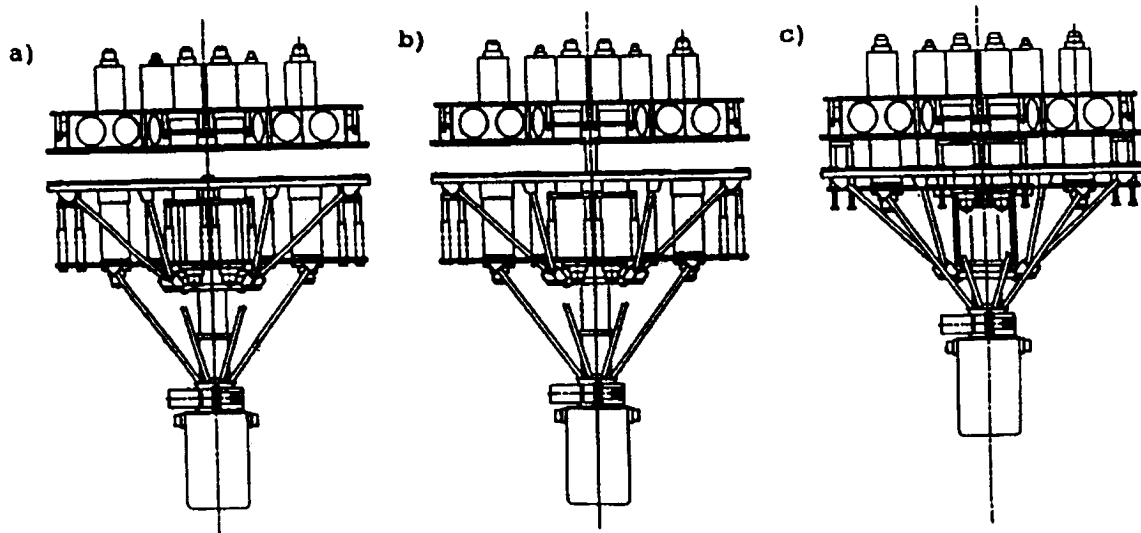

Figure 4: AFIS Engagement.

Misalignment Test

The initial alignment of AFIS is dictated by the docking mechanism. Most docking mechanisms typically have some tolerance in the position of any reference point after docking. Additional misalignments are caused by thermal and structural deflections. The AFIS must be able to engage under the worst case misalignment from these effects.

The AFIS was designed to operate with the Three Point Docking Mechanism (TPDM) and the Remote Grapple Docking Mechanism (RGDM). The misalignment envelope given for these docking devices was:

Axial -   6.35 mm (0.25 in)
Lateral Offset -   2.54 mm (0.10 in)

This envelope provided an indication of the ability of the device to operate with external misalignments. Of course this envelope is device specific and using another docking system, such as the Orbiter Docking System (ODS), would change these numbers. The misalignment envelope is also strongly influenced by the location of the AFIS relative to the docking system. This is a design specific requirement that cannot be completely addressed by a generic set of misalignment criteria.

AFIS engagements were completed with each of the required misalignments independently and combined. All engagements were successful. The "floating" carriage of the active half of the AFIS adequately adjusted for the misalignments. However, the AFIS does not completely isolate the fluid and electrical couplings from this misalignment. The connectors and couplings are still required to provide some (but smaller) misalignment capability.

Docking Test

In order to evaluate the compatibility of AFIS with a docking system and the ability of the AFIS to transfer fluids, a demonstration docking and engagement was accomplished in the flight robotics facility of the MSFC. The active side was integrated into a tanker spacecraft mock-up. This mock-up was stationary and contained a TPDM. This mounting arrangement is shown in Figure 5. A truss structure and tubular frame were used to attach the AFIS.

The passive side of the AFIS was mounted on a mobile cart which contained a trunnion arrangement compatible with the TPDM. The mobile cart floated on air bearings and was propelled by air thrusters. The mobile cart was then docked to the mock-up using an Automatic Rendezvous and Docking system developed at the MSFC. Once docked, the AFIS was engaged and power and air were successfully transferred across the interface. This demonstration placed the AFIS in the horizontal orientation. Because the AFIS was designed for microgravity, several changes were required for this test. Even with these changes, the actuator sag prevented any misalignment studies during this demonstration.
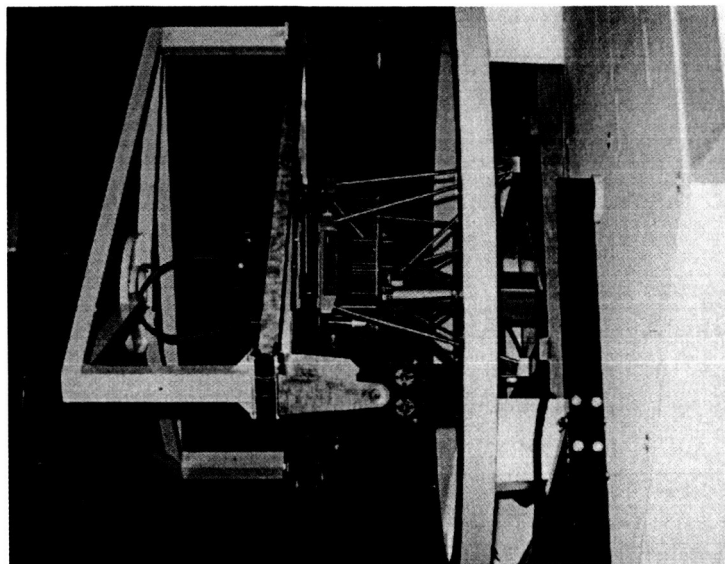
Figure 5:   Demonstration Docking and AFIS Engagement

This test successfully demonstrated that the AFIS can be integrated with the TPDM. It also demonstrated gas and power can be transferred across the interface. The AFIS performed well even in the horizontal orientation docking maneuver.

Load Testing

The AFIS was integrated into a force measuring frame for the purposes of determining the loads that would be imposed onto the docking mechanism and to characterize the force profile of an AFIS engagement. The load frame utilized strain gauges mounted on simple supporting beams to determine the forces in three axes. Of interest was the ability of AFIS to isolate the docking mechanism from connector loads that can be extreme.

Figure 6 shows a force profile of an AFIS engagement with no couplings on the Type II half or flexhoses. Point A shows where the spring in the Type II half is being compressed as the actuator rod extends across interface. Cover rotation and the reversal of the actuator direction is designated by point B. As the rod retracts, the spring load is released until the rod bottoms on the Hub interface. The load then reverses direction due to the weight of the carriage (Point C). Because the test was performed in a 1-g environment, the forces measured reflect the weight of the carriage assembly on the tanker side. This load would not be present in a microgravity environment.

Figure 7 shows the same engagement sequence but with couplings and flexhoses. Point A shows the initial contact of the actuator with the Type II half. These initial forces indicate a slight misalignment between the two halves due to flexhose loads.

388

After rotation, forces in the z direction are unchanged from Figure 6 which demonstrates that the AFIS carries all z direction loads from the couplings. The significance of this is that the spacecraft and docking systems are isolated from the coupling and transfer loads which can be very large. Engagement continues until point B where the couplings begin engagement. The increase in x and y forces are due to coupling misalignments and flexhose loads.
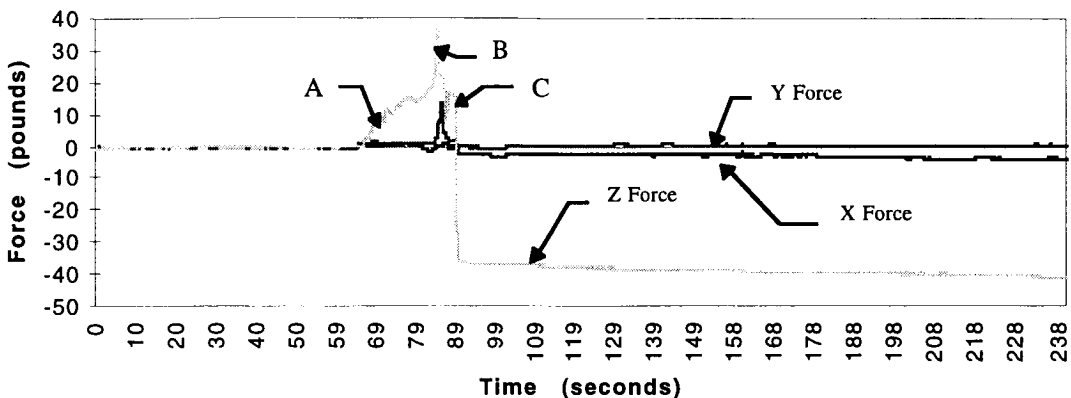
Figure 6: Force profiles of an AFIS engagement without Coupling Loads
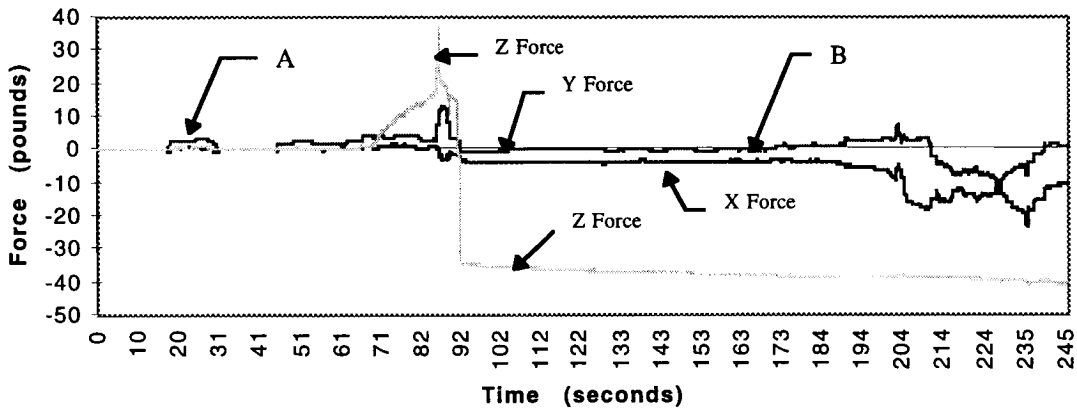
Figure 7: Force profiles of an AFIS engagement with Couplings and Flexhoses

Thermal Testing

Test Parameters

The AFIS underwent thermal vacuum testing at the MSFC Environmental Test Facility (ETF). An estimate of temperature range was developed by Thermal Engineering and Design Branch personnel at MSFC. The temperatures for AFIS covers were 89°C and -60°C. The numbers were developed with four main assumptions:

389

1. The face of the AFIS (cover) could be exposed to either full sun (with albedo and earth infrared) or to deep space (no albedo or earth infrared).
2. Reasonable inner satellite temperatures were assumed to be -20°C to +50°C. This assumption was based on past experience.
3. Most satellites specify a maximum interface conductance. 0.635 cm (1/4 inch) thick fiberglass isolators were added underneath the mounting plate for simulate this conductance.
4. The Materials and Processes Laboratory at MSFC measured the optical properties of the cover. For the temperature calculation, a solar absorbtivity of 0.527 and an emissivity of 0.85 were used.

These temperature ranges were developed assuming only the AFIS front plates and covers would be exposed to the outside space environment. The surfaces below the AFIS mounting plates would be exposed to the spacecraft inner environment. The inner surfaces would still be affected by cover conduction and radiation. Since the AFIS would be mounted on two separate spacecraft, three separate cases were required.

- Two "hot/cold" cases, in which one AFIS part had been exposed to sun and the other in shade, and vice versa.

- A "cold/cold" test was necessary for the case where each part was shaded.

A "hot/hot" was not tested because the geometry of the test vehicles would block at least one AFIS half from full sun. These scenarios are considered worst case. In reality, the spacecraft would probably be docked for a period of time before transfer is attempted. This time would allow the AFIS halves to equalize in temperature with little exposure to deep space or full sun.

Test Set-up
A test fixture was developed that allowed the AFIS halves to be separated for thermal conditioning. (Figure 8) The concept worked well, the only change being a sheet of mylar to screen off the AFIS surfaces while separated. The test fixture was a welded aluminum cage. The cage was sized for Thermal Vacuum Chamber 7 (V7) of the MSFC ETF. A translation table with thermal vacuum rated motor was used to move the bottom AFIS (active half) from the thermal conditioning position to the engagement position. Heat lamps were mounted on the cage to allow differential heating. A box surrounded each AFIS half with only the cover exposed to mimic a spacecraft installation. Additional heat lamps were mounted alongside the boxes to allow for simulated spacecraft heating of AFIS internal parts. Compressed air, liquid nitrogen, and electrical power were the consumables chosen for transfer during testing. After engagement these supplies would be transferred across the interface to demonstrate refueling.

The following is a general description of ETF testing. The AFIS was mounted into the test fixture and inserted into the chamber. Motor power, thermocouples, and AFIS telemetry were connected through the chamber walls. AFIS was translated, engaged and a motor profile (of AFIS engagement) recorded. AFIS halves were translated apart and the chamber was evacuated. Chamber cooling then started. At -60° C, the

AFIS would be translated together, and engaged. After a successful engagement, the AFIS would be disengaged, translated apart, and one side heated to 89°C. The AFIS would be again translated together and engaged. Then the other side would be heated while the other cooled and a final test begun. The AFIS mechanism would provide engagement feedback, and the motor current would be monitored for AFIS mechanical binding. A plot of the motor voltage is shown as Figure 9. The first peak (A) is cover rotation. The spring resistance of the connectors can also be seen before engagement (B). (C) shows cover rotation on disengagement.
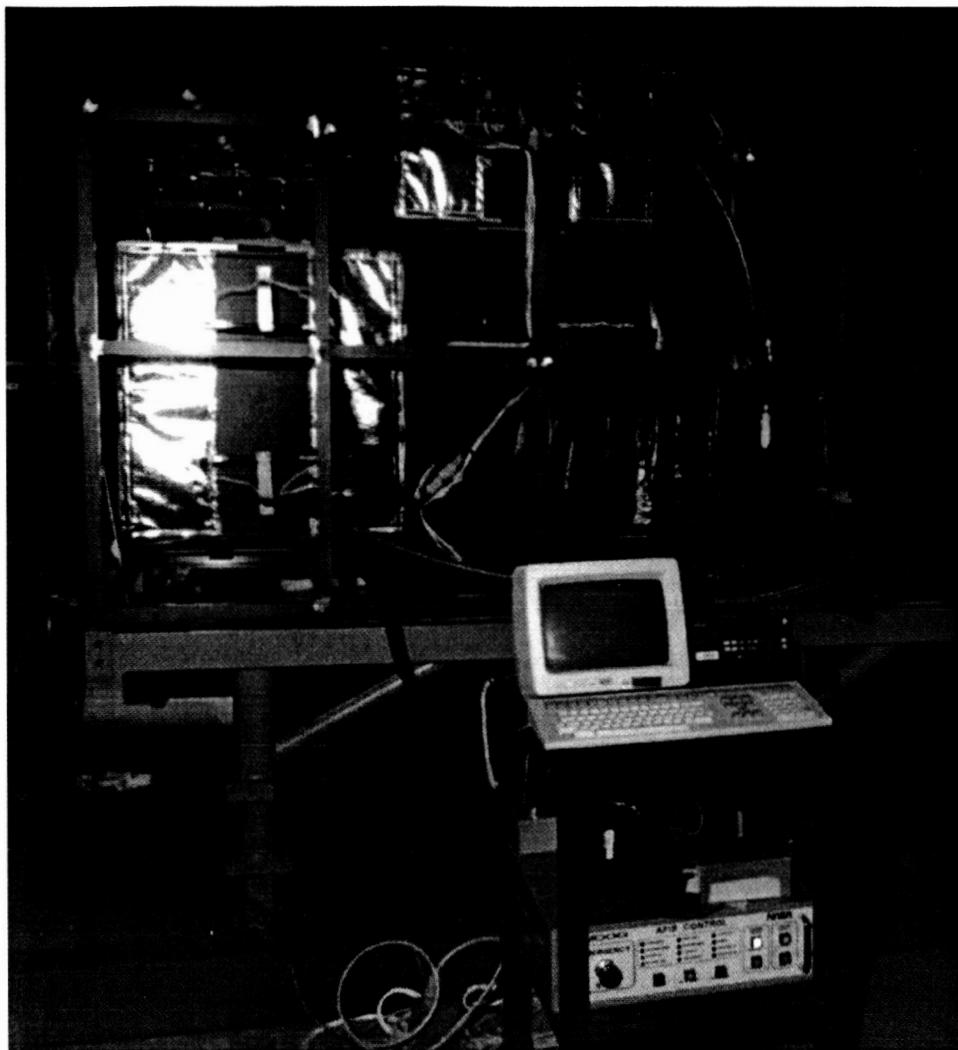

Figure 8: Thermal Vacuum Test Setup

Test 1
AFIS successfully engaged in ambient vacuum conditions. Croygens, gas, and power were also successfully transferred. Table translation failure occurred at cold/cold. After pressurization and trouble shooting, the test was repeated with periodic translations to check table. When the table began to stall the AFIS was translated

together and left for remainder of the test. The goal cover temperatures could not be reached without the ability to separate halves.
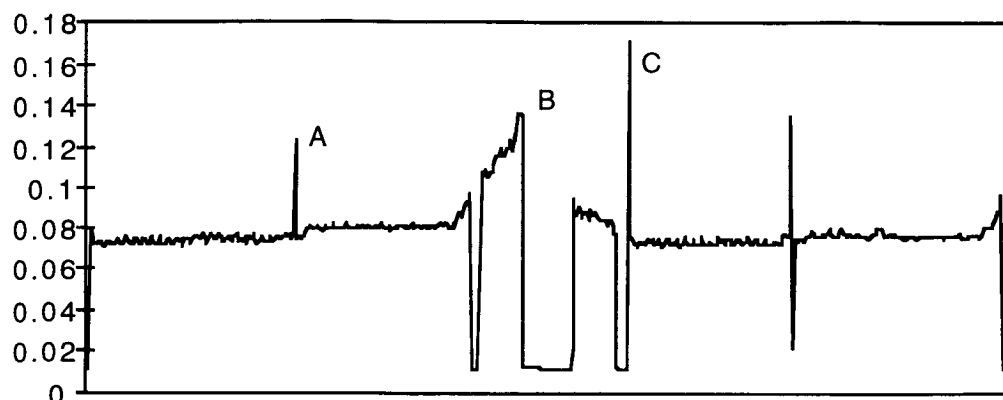

Figure 9: Motor Voltage Plot

An AFIS engagement was attempted at an intermediate cold/cold temperature but before successful engagement the actuator motor stalled and test was ended. Upon inspection the AFIS cover had been damaged.

During the post test investigation the following problems were discovered.
1. The support bearing on end of the ball screw was corroded. Evaluation of the hardware determined the translation table guide rails provided adequate support and the failed bearing was not required for this application. It was removed from the setup.
2. A benchtest showed bowing of translation table due to different coefficients of expansion. This bowing was corrected by floating the ends of the table and relocating attachment hardware to the engagement position.
3. The ball screw balls were corroded. New stainless steel balls were inserted and lubricated with molybdenum disulfide.
4. Thermal analysis showed excessive shrinkage of support frame would cause AFIS alignment requirements to be exceeded. Insulation, heaters, and thermocouples were installed on the frame to control frame expansion.
5. Cover damage was caused by coupling impact with the rotating cover. The coupling interference was caused by cover misalignment after rotation. A new cover was manufactured and installed. The failure due to cover misalignment could not be isolated to a single cause; however, frame expansion was possibly one source. If the test fixture was colder than the AFIS boxes, the resulting contraction would have driven the AFIS shaft in the passive side too far, increasing rotation resistance.

Repeatability of cover rotation at this time in ambient began to degrade slightly. A misalignment was bad enough to cause connector-to-cover impact roughly one of ten times. Information about cover alignment was needed to protect against further damage. AFIS was moved to a thermal chamber (Sunspot/V8) with a viewing plate

392

and a lever switch was added to the mechanism to indicate when cover rotation was acceptable during the test.

Test 2
Test 1 was repeated except no fluid transfer was attempted because the new chamber not plumbed for it. Table translation was successful. Frame thermal control was also successful. At the first cold/cold test, AFIS cover rotated slowly and misaligned. During a second attempt, AFIS stopped functioning completely. Upon investigation a broken motor brush braid was discovered upon each motor. The brushes were replaced and refurbished.

Due to the problems with cover rotation at cold conditions and the uncertainty of the cause, AFIS was moved to a thermal humidity chamber for more accessibility during testing. This chamber was limited to ambient pressure.

Thermal test
The thermal chamber allowed access to measure torque and troubleshoot the device. A major concern of the test was possible condensation on the electronics when opening the door at cold temperatures for torque measurement. This problem was alleviated by purging with dry missile air and by covering the door with a sheet of plastic with hand access ports. The AFIS electronics were also enclosed and insulated in order to maintain them at the required warmer temperatures. The AFIS demonstration stand was suitable for the thermal test. With minor modifications it fit into the thermal humidity chamber (also located at the MSFC ETF). The thermal chamber did not allow for testing of AFIS halves at different temperatures but it did allow for cold/cold testing at -60°C and a hot/hot test at 80°C. The chamber was capable of higher temperatures but the test temperature was limited due the electronics.

Thermal Test 1
The AFIS active side was placed in the chamber and cooled to -60°C. An AFIS engagement cycle was attempted and torque were measured. Excessive torque were measured at cover rotation. The cover was removed and the test repeated with same results. It was then apparent the problem was within the actuator. With further investigation it was discovered the guide bearings used for actuator rotation were binding.

These bearings were stainless steel sleeve bearings with a vespel insert. A stainless steel shoulder screw was used as the bearing shaft. Bench testing showed that the bearings seized on the shafts at cold temperatures. The vespel coefficient of expansion was greater than stainless steel and the bearing would seize on the shaft due to insufficient clearances.

These bearings were replaced with an alternate ball bearing. The ball bearings provided lower rolling resistance and were stainless steel. Bench testing proved low temperature operability.

Thermal Test 2
Retest of test 1 was completed with new bearings and the AFIS functioned nominally under cold conditions. The AFIS temperature was increased to 80°C to test the hot/hot case. This time the cover rotated repeatedly at the end of actuator stroke. The test was stopped and AFIS was brought to ambient temperature. Failure investigation revealed the limit switches were not activating due to expansion problems. The limit switches were adjusted. New cold/cold and hot/hot tests were successful.

Final Thermal Vacuum Test
In preparation for the final thermal vacuum test, the AFIS was functionally tested in the chamber under ambient conditions. AFIS cover alignment was erratic. At times, the motor would stall. The stall problem was determined to be an interference between the cover and the retainer brackets caused during installation of the cover. The top and bottom retainer brackets were machined to increase clearance and dry film lubricant installed to decrease friction. The stall problem was fixed and cover rotation improved enough to continue thermal vacuum testing.
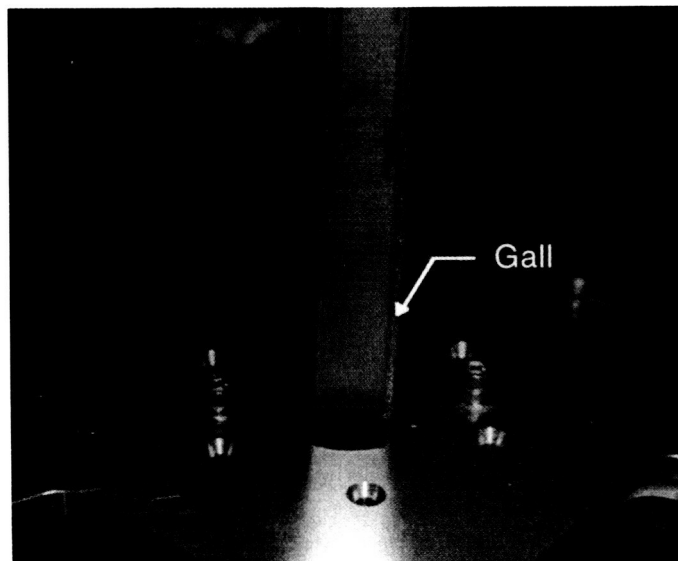

Figure 10: Actuator Rod Galling

Cold/cold, hot/cold, and cold/hot engagements were successfully completed during testing. The objectives of the test were achieved but the following anomalies were still noted:
- The rotation of the covers was still erratic with some engagements requiring multiple attempts. Some of this problem can be attributed to wear from a high number of cycles.

394

- During the hot/cold test, the actuator shaft hung on the center hub of the active half. Upon release, the carriage would drop causing a large shock impulse. Visual inspection after testing revealed mechanical wear and galling on the actuator shaft. A visible grove was worn in the center hub collar and the protective coating was removed on the shaft (Figure 10).

Life cycle

Life cycle testing was not formally done and the number of cycles is not known. It was estimated that the AFIS performed several thousand cycles due to demonstrations, load test, thermal vacuum test, and trouble shooting. For comparison consider on space station a fluid transfer device needed to operate 120 cycles (8 flights a year times 15 year lifetime). The realistically expected life of the AFIS was far surpassed. Many of the problems experienced at the end of testing can be attributed to wear. After the final thermal test, the AFIS was completely disassembled. Noticeable wear was seen on the worm gear, shaft gear, and bevel gears. Wear was also seen on the 45 degree surface of the guide that allows actuator rotation.

Conclusions

AFIS Design Evaluation

The AFIS testing completed at MSFC provided insight into the strengths and weaknesses of the design. The AFIS design proved to be a simple and lightweight device which met its initial design goals. It proved capable of transferring power, data, gases, fluids and cryogens across the interface. The simplicity of having a single actuator accomplish all tasks was a major strength. The design can be easily scaled to fit an application. A full scale AFIS active half could even mate with a smaller AFIS satellite half. The AFIS is very flexible in coupling arrangement.

One of the primary weaknesses was the active half cover design. Cover alignment was unreliable. This problem intensified later in the life of the mechanism. There are several reasons for this unreliability:

1. The design provided inadequate bearing surface between the actuator shaft and the center hub of the active AFIS half. This interface allowed for shaft movement (to correct misalignment between the AFIS halves), rotated the cover and provided a means of preloading the connectors on the back of the cover for stowage. The complexity of this interface compromised its reliability.
2. Any play between the hub and shaft is magnified at the outer radius of the cover.
3. The resistance to cover rotation is dependent on sliding friction which can vary significantly with temperature, contamination, surface finish, materials, and the normal force.
4. Inertial loads are greater at the center of the hub due to the increased moment arm.

Another weakness was a lack of feedback. Cover alignment, shaft position, AFIS halves alignment, and stall indicator would have been useful information. For testing the AFIS was moved to a larger thermal vacuum chamber with camera and viewing port for shaft and cover location. A contact switch was also added to help determine cover alignment. A resistor mounted in the actuator power lines gave motor current and stall indication. AFIS halves alignment was verified before test, but real time information was needed.

A weakness of the actuator was the loss of mechanical advantage at actuator rotation. The ball screw provides good mechanical advantage during linear translation but this advantage is lost at rotation. This loss of mechanical advantage also results in a faster, more uncontrolled rotation. The faster rotation increases inertial loads and increases the tendency of the cover to overshoot.

Testing Lessons Learned
During preparation for the thermal vacuum test, inadequate attention was given to the support equipment. The primary focus was on preparing the AFIS. The consequences were loss of schedule and money. With proper review, the following problems could have been avoided.

- The AFIS test frame needed to be thermally controlled because the AFIS halves required separation to within a certain tolerance. After the first thermal test, controllable heaters were mounted on the frame, along with thermocouples. The frame then had dacron netting and mylar wrapped around it for insulation. Additional thermocouples on the frame provided redundancy.

- The original frame was sized to fit snugly inside the first thermal chamber. No additional room was available for engineering personnel to get inside the chamber to service AFIS, or for connector hookup. Such an amount of space would have been desirable.

- Thermal lamps needed to be isolated from each other. The AFIS covers had two separate banks of lights to heat the covers independently. However, radiation from one set of lights slowed cooling on the other set. This problem was fixed by hanging a sheet of mylar between the lights.

Another valuable lesson learned was the value of feedback during testing. Without cover feedback, the ability to visually confirm cover alignment was essential. Even if the covers were only slightly misaligned the edges would catch the electrical connectors. The first AFIS tanker half cover was broken because the connector/cover interference was not seen and the motor was strong enough to damage the cover. After the first thermal vacuum test, the AFIS was moved to a thermal chamber with a viewport. A camera was later mounted inside the chamber for a close-up view of the cover. While a thermal vacuum camera is expensive, AFIS used an ambient CCD

camera mounted inside a metal bellows that reached inside the chamber. The bellows had a glass plate at the end for the camera viewing and dry facility air was run inside the bellows for moisture control. A heater also kept the camera at the proper operating temperature. The bellows with camera inside was hard mounted to a stand inside the chamber to give a view of the cover.

Monitoring of the actuator was required in order to determine stall and motor performance. Resistors were added to the actuator power lines to allow for motor monitoring. Real time monitoring of the voltage was the only way to tell when motor stall occurred. This feedback also indicated motor load. This feedback was invaluable.

A valuable tool in trouble shooting the AFIS was the thermal chamber. It provided access to the hardware during testing and subsystem isolation which proved essential in determining the actuator bearing problem. Initially, the electronics condensation was a concern but was alleviated with proper precautions.

Recommendations for a Flight Design
The following is a brief list of recommended changes to incorporate in a flight design.

Cover rotation was a constant problem during thermal testing and after extensive testing. Smaller covers should improve the alignment problem due to the smaller moment arm and less inertia. An increased bearing surface at the actuator rod interface would reduce error. Cover frictional effects could be minimized by incorporating rolling surfaces. A separate motor, actuator or solenoid could be used to rotate the cover and eliminate the mechanical advantage loss by the current design. However, some simplicity and reliability may be lost. Incorporating a cover hard stop could be simple way to ensure alignment. Unfortunately, the current design of a cover that continually rotates in the same direction makes this improvement difficult.

With the current design, a very important improvement would be feedback on rotation. Some indication of proper cover alignment is needed, particularly if fuel and oxidizer will be passing through connectors. A stepper motor may provide a way to correct slight alignment problems. Visual inspection is not adequate considering the closeness of the mating covers, on orbit lighting changes, and the need for total automation.

Other useful indications would be for shaft position, stall, and type I to type II alignment. The shaft could incorporate magnetic or resistive type sensors to provide a gross position indication. Alignment sensors between the AFIS halves would ensure the docking mechanism has correctly aligned the AFIS before an engagement is attempted.

For Shuttle or space station applications some method of quick detach would be required. An AFIS failure could prevent the spacecraft from undocking. The current

design has redundant electronics and extravehicular activity (EVA) operation but has a single mechanical drive system. Also, binding of the actuator rod in the Type II half has not been addressed. This problem of quick separation could easily be addressed by placing an EVA removable hub in the Type II interface, or by pyrotechnic mounting bolts on the Type II half itself.

Another recommendation is that the electronics could be detached from the mechanism and moved into another environment, such as the aft flight deck on the Shuttle. This would relax thermal constraints on the electronics.

Since Thinkpad computers are already available on the Shuttle, they could be used to control the AFIS and for graphical feedback of cover position, shaft position, and stall.

References

1. "Automated Fluid Interface System for Satellite Servicing" by T.D. Bechtel and T.R. Tyler. Published at the Joint Army Navy NASA Air Force Symposium in October, 1990.
2. "Development and Testing of the Automated Fluid Interface System" by Martha A. Milton and Tony R. Tyler. Published at the 27th Aerospace Mechanisms Symposium in May, 1993.

REPORT DOCUMENTATION PAGE

Public reporting burden for this collection of information is estimated to average 1 hour per response, including the time for reviewing instructions, searching existing data sources, gathering and maintaining the data needed, and completing and reviewing the collection of information. Send comments regarding this burden estimate or any other aspect of this collection of information, including suggestions for reducing this burden. to Washington Headquarters Services, Directorate for Information Operations and Reports, 1215 Jefferson Davis Highway, Suite 1204, Arlington, VA 22202-4302, and to the Office of Management and Budget, Paperwork Reduction Project (0704-0188), Washington, DC 20503.

1. AGENCY USE ONLY (Leave blank)	2. REPORT DATE May 1998	3. REPORT TYPE AND DATES COVERED Conference Publication

4. TITLE AND SUBTITLE

32nd Aerospace Mechanisms Symposium

5. FUNDING NUMBERS

6. AUTHOR(S)

Edward A. Boesiger, Compiler

7. PERFORMING ORGANIZATION NAME(S) AND ADDRESS(ES)

NASA John F. Kennedy Space Center
Kennedy Space Center, Florida 32899

8. PERFORMING ORGANIZATION REPORT NUMBER

9. SPONSORING/MONITORING AGENCY NAME(S) AND ADDRESS(ES)

National Aeronautics and Space Administration
Washington, D.C. 20546

10. SPONSORING/MONITORING AGENCY REPORT NUMBER

NASA CP-1998-207191

11. SUPPLEMENTARY NOTES

Cosponsors: Lockheed Martin Missiles and Space, Sunnyvale, CA 94088, and the Aerospace Mechanism Symposium Committee. Conference Coordinator: Sterling Walker, Director, Engineering Development Directorate, Kennedy Space Center

12a. DISTRIBUTION/AVAILABILITY STATEMENT

Unclassified - Unlimited
Subject Category 15

12b. DISTRIBUTION CODE

13. ABSTRACT (Maximum 200 words)

The proceedings of the 32nd Aerospace Mechanism Symposium are reported. NASA John F. Kennedy Space Center (KSC) hosted the symposium that was held at the Hilton Oceanfront Hotel in Cocoa Beach, Florida on May 13-15, 1998. The symposium was cosponsored by Lockheed Martin Missiles and Space and the Aerospace Mechanisms Symposium Committee.

14. SUBJECT TERMS

15. NUMBER OF PAGES
408

16. PRICE CODE

17. SECURITY CLASSIFICATION OF REPORT Unclassified	18. SECURITY CLASSIFICATION OF THIS PAGE Unclassified	19. SECURITY CLASSIFICATION OF ABSTRACT Unclassified	20. LIMITATION OF ABSTRACT

NSN 7540-01-280-5500

Standard Form 298 (Rev. 2-89)
Prescribed by ANSI Std. Z39-18
298-102